NASA/CP-1998-207654

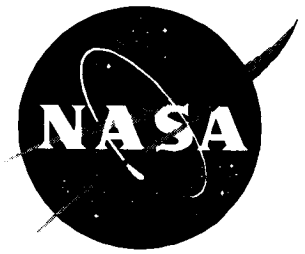

Fourth International Symposium on Magnetic Suspension Technology

Edited by
Nelson J. Groom
Langley Research Center, Hampton, Virginia

Colin P. Britcher
Old Dominion University, Norfolk, Virginia

May 1998

The NASA STI Program Office . . . in Profile

Since its founding, NASA has been dedicated to the advancement of aeronautics and space science. The NASA Scientific and Technical Information (STI) Program Office plays a key part in helping NASA maintain this important role.

The NASA STI Program Office is operated by Langley Research Center, the lead center for NASA's scientific and technical information. The NASA STI Program Office provides access to the NASA STI Database, the largest collection of aeronautical and space science STI in the world. The Program Office is also NASA's institutional mechanism for disseminating the results of its research and development activities. These results are published by NASA in the NASA STI Report Series, which includes the following report types:

- TECHNICAL PUBLICATION. Reports of completed research or a major significant phase of research that present the results of NASA programs and include extensive data or theoretical analysis. Includes compilations of significant scientific and technical data and information deemed to be of continuing reference value. NASA counter-part or peer-reviewed formal professional papers, but having less stringent limitations on manuscript length and extent of graphic presentations.

- TECHNICAL MEMORANDUM. Scientific and technical findings that are preliminary or of specialized interest, e.g., quick release reports, working papers, and bibliographies that contain minimal annotation. Does not contain extensive analysis.

- CONTRACTOR REPORT. Scientific and technical findings by NASA-sponsored contractors and grantees.

- CONFERENCE PUBLICATION. Collected papers from scientific and technical conferences, symposia, seminars, or other meetings sponsored or co-sponsored by NASA.

- SPECIAL PUBLICATION. Scientific, technical, or historical information from NASA programs, projects, and missions, often concerned with subjects having substantial public interest.

- TECHNICAL TRANSLATION. English-language translations of foreign scientific and technical material pertinent to NASA's mission.

Specialized services that help round out the STI Program Office's diverse offerings include creating custom thesauri, building customized databases, organizing and publishing research results . . . even providing videos.

For more information about the NASA STI Program Office, see the following:

- Access the NASA STI Program Home Page at ***http://www.sti.nasa.gov***

- Email your question via the Internet to help@sti.nasa.gov

- Fax your question to the NASA Access Help Desk at (301) 621-0134

- Phone the NASA Access Help Desk at (301) 621-0390

- Write to:
  NASA Access Help Desk
  NASA Center for AeroSpace Information
  7121 Standard Drive
  Hanover, MD 21076-1320

NASA/CP-1998-207654

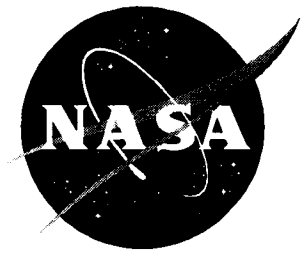

Fourth International Symposium on Magnetic Suspension Technology

Edited by
Nelson J. Groom
Langley Research Center, Hampton, Virginia

Colin P. Britcher
Old Dominion University, Norfolk, Virginia

Proceedings of a symposium sponsored by the National Aeronautics and Space Administration, Washington, D.C., the National Aerospace Laboratory, Tokyo, Japan, and the National High Magnetic Field Laboratory, Tallahassee, Florida, and held in Gifu City, Japan
October 30–November 1, 1997

National Aeronautics and
Space Administration

Langley Research Center
Hampton, Virginia 23681-2199

May 1998

The use of trademarks or names of manufacturers in this report is for accurate reporting and does not constitute an official endorsement, either expressed or implied, of such products or manufacturers by the National Aeronautics and Space Administration.

Available from the following:

NASA Center for AeroSpace Information (CASI)
7121 Standard Drive
Hanover, MD 21076-1320
(301) 621-0390

National Technical Information Service (NTIS)
5285 Port Royal Road
Springfield, VA 22161-2171
(703) 487-4650

INTRODUCTION

The 4th International Symposium on Magnetic Suspension Technology was held at The Nagaragawa Convention Center in Gifu City, Japan, on October 30 - November 1, 1997. The symposium was sponsored by the Guidance and Control Branch of the Langley Research Center, in coordination with NASA Headquarters, the National Aerospace Laboratory (NAL), Japan, and the National High Magnetic Field Laboratory (NHMFL) operated by Florida State University. The symposium was hosted by the National Aerospace Laboratory.

The organizing committee consisted of the following people:

Nelson J. Groom, Symposium Co-Chairman
NASA
Langley Research Center
Hampton, VA 23681-0001

Hideo Sawada, Symposium Co-Chairman
National Aerospace Laboratory
Chofu, Tokyo, 182
JAPAN

Jack E. Crow, Symposium Co-Chairman
National High Magnetic Field Laboratory
Tallahassee, FL 32306-4005

Colin P. Britcher, Technical Program Co-Chairman
Dept. of Aerospace Engineering
Old Dominion University
Norfolk, VA 23529-0247

Atsushi Nakajima, Technical Program Co-Chairman
National Aerospace Laboratory
Chofu, Tokyo, 182
JAPAN

Sandy Johnson, Administrative Co-Chairman
NASA
Langley Research Center
Hampton, VA 23681-001

Kendall Sherman, Administrative Co-Chairman
NASA Langley Research Center
Hampton, VA 23681-0001

Takashi Kohno, Administrative Co-Chairman
National Aerospace Laboratory
Chofu, Tokyo, 182
JAPAN

An international steering committee assisted in selecting and reviewing submitted abstracts and in structuring the symposium sessions. The steering committee consisted of the following people:

Isaiah Blankson
NASA Lewis Research Center
MS: 5-9
21000 Brookpark Road
Cleveland, OH 44135

Karl Boden
KFA-IGV
Siemensstr .20
Julich 52428
GERMANY

James Downer
SatCon Technology Corporation
161 First St.
Cambridge, MA 02142-1221

Robert A. Kilgore
CES-Hampton
359 Marlfield Circle
Hampton, VA 23669-1733

Alexander V. Kuzin
Moscow Aviation Technological Institute
Petrouka, 27
Moskow, K-31, 103737
RUSSIA

Chin E. Lin
National Cheng Kung University
No. 1 University Road
Tainan, Taiwan
REPUBLIC OF CHINA

Roland Siegwart
Swiss Federal Inst. of Technology
EPFL
DMT-IMT
1015 Lausanne
SWITZERLAND

David Trumper
Massachusetts Institute of Technology
Room 3-455
77 Massachusetts Ave.
Cambridge, MA 02139

Sigeharu Enkyo
National Aerospace Laboratory
7-44-1 Jindaijihigashi-machi
Chofu, Tokyo, 182
JAPAN

Hans Schneider-Muntau
National High Magnetic Field Laboratory
1800 E. Paul Dirac Dr.
Tallahassee, FL 32306-4005

The goal of the symposium was to examine the state of technology of all areas of magnetic suspension and to review recent developments in sensors, controls, superconducting magnet technology, and design/implementation practices. The symposium included 13 sessions in which a total of 35 papers were presented. The technical sessions covered the areas of maglev, controls, high critical temperature (T_c) superconductivity, bearings, magnetic suspension and balance systems (MSBS), levitation, modeling, and applications. A list of attendees begins on page xiii.

The first symposium in this series was organized by NASA Langley Research Center and held at Langley Research Center, Hampton, Virginia, on August 19-23, 1991. The proceedings of the first symposium are available as NASA Conference Publication 3152, Parts 1 and 2. The second symposium in the series, also organized by NASA Langley Research Center, was held at the Westin Hotel in Seattle, Washington, on August 11-13, 1993. The proceedings of the second symposium are available as NASA Conference Publication 3247, Parts 1 and 2. The third symposium, organized by NASA Langley Research Center and hosted by the National High Magnetic Field Laboratory was held at the Holiday Inn Capital Plaza in Tallahassee, Florida, on December 13-15, 1995. The proceedings of the third symposium are available as NASA Conference Publication 3336, Parts 1 and 2.

CONTENTS

SESSION 4--Bearings-1
Chairman: Toru Namerikawa, Kanazawa University

SESSION 5--MSBS-1
Chairman: Hideo Sawada, NAL

SESSION 6--Levitation
Chairman: Takeshi Mizuno, Saitama University

SESSION 7--Maglev-2
Chairman: Hans Schneider Muntau, NHMFL

SESSION 8--Modeling-1
Chairman: Colin P. Britcher, Old Dominion University
Atsushi Nakajima, NAL

SESSION 9--Maglev-3
Chairman: Nelson J. Groom, NASA Langley

SESSION 10--Controls-2
Chairman: Colin P. Britcher, Old Dominion University

SESSION 11--High Tc-2
Chairman: Hans Schneider-Muntau, NHMFL

SESSION 12--Bearings-2
Chairman: Yohji Okada, Ibaraki University

SESSION 13--Applications
Chairman: Nelson J. Groom, NASA Langley

LIST OF ATTENDEES

Masaaki Akatsuka
Mitsubishi Precision Co., Ltd.
3-3-16, Mita
Minato-ku
Tokyo
JAPAN
81-3-3453-6426

Vijayan Baburaj
University of Tsukuba
Institute of Eng. Mechanics
Tsukuba 306
JAPAN
0296-63-5266
babu@kz.taukuba.ac.jp

Sergei A. Belov
Osaka Sangyo University
Dept.of Information Systems Eng.
3-1-1, Nakagaito
Daito-shi, Osaka 574
JAPAN
0201005374
belov@h-ps011.ise.osaka-sandai.ac.jp

Dale V. Bloodgood
Old Dominion University
Dept. of Aerospace Engineering
Norfolk, VA 23529-0247
757-683-3720

Colin P. Britcher
Old Dominion University
Dept. of Aerospace Engineering
Norfolk, VA 23529-0247
757-683-4916
c.p.britcher@larc.nasa.gov

Jean H. Chabas
Railway Technical Research Institute
2-8-38 Hikari-cho
Kokubunji-shi
Tokyo 185
JAPAN
0425-73-7299
chabas@rtri.or.jp

H. Ming Chen
Mohawk Innovative Technology Inc.
437 New Karner Rd.
Albany, NY 12205-3833
518-862-4289

Akira Chiba
Science University of Tokyo
Department of Elec. Engineering
2641 Yamazaki
Noda Chiba 278
JAPAN
81-471-24-1501
chiba@ee.noda.sut.ac.jp

M. D. Driga
University of Texas at Austin
Dept. of Elec. Eng. & Comp. Eng.
ENS434
Austin, TX 78712
512-471-6943
driga@ece.utexas.edu

Shigeharu Enkyo
National Aerospace Laboratory
7-44-1 Jindaijihigashi-machi
Chofu-shi
Tokyo 182
JAPAN
81-422-47-5911

Nobuo Fujii
Kyushu University
Hakozaki 6-10-1
Fukuoka 812-81
JAPAN
81-92-642-3914
fujii@ees.kyushu-u.ac.jp

Hiroyuki Fujimoto
Railway Technical Research Institute
2-8-38 Hikari-cho
Kokubunji-shi
Tokyo 185 JAPAN
81-425-73-7297
fujiimoto@rtri.or.jp

Yoshiteru Fukao
Kobe Steel Ltd.
2-3-1 Shinhama
Arai-chi Takasago-shi
Takasago
JAPAN
0794-45-7815
yoshi-fukao@topics.kobeko.co.jp

Satoru Fukata
Kyushu University of Design
Dept. of Engineering Design
4-9-1 Shiobaru
Minami-ku Fukuoka 815
JAPAN
81-92-641-1101

Thomas Gempp
ETH Zurich
Laboratory of Elec.Eng. Design (EEK)
Technoparkstrasse 1
Zurich CH-8005
SWITZERLAND
41-1-445-1383
gempp@eek.ee.ethz.ch

Pindoria K. Govind
SRL
10-13 Shinonome 1-chome
koh-kr, Tokyo 135
JAPAN
81-335-305713
govind@injapan.net

Nelson J. Groom
NASA Langley Research Center
Mail Stop 161
Hampton, VA 23681-0001
757-864-6613
n.j.groom@larc.nasa.gov

Tobias Habisreuther
Institut fur Physikalische
Hochtechnologie
P.O.Box 400239
Jena D-07702
GERMANY
49-364-302-729

Maciej Hippner
University of Natal
Department of Elec. Engineering
Durban 4041
SOUTH AFRICA
27-31-260-1244
mhippn@eng.und.ac.za

Hiroshi Horiuchi
Keio University
3-14-1 Hiyoshi, Kohoju-ku
Yokhama, Kangawa
Tokyo 120
JAPAN
045-563-1151
hori@sum.elec.keio.ac.jp

Eichi Ito
Science University of Tokyo
Dept. of EE Faculty of Sci and Tech
2641 Yamazaki
Noda Chiba 278
JAPAN
81-471-1501

Yukikazu Iwasa
Keio University
3-14-1 Hiyoshi
Kohuku-ku
Yokohama 223
JAPAN
045-563-1141 x2279

Mituru Iwaya
HSST Development Corporation
Kokuryu Shibakoen Bldg. 3F
Shibakoen 2-6-15
Minato-ku, Tokyo 105
JAPAN
81-3-5403-1430

Sandra G. Johnson
NASA Langley Research Center
Mail Stop 161
Hampton, VA 23681-0001
757-864-6222
s.g.johnson@larc.nasa.gov

Hironori Kameno
Koyo Seiko Co., Ltd.
No. 24-1 Kokubu-Higanjo-cho
Kashiwara, Osaka 582
JAPAN
81-729-78-5018

Kemchi Katoh
Electro-Magnetic Control Division
4-2-1, Honfujisawa
Fujisawa-shi
Kanagawa
JAPAN
81-466-83-7645

Shin Katsumata
Sundstrand Aerospace
4747 Harrison Avenue
MS 773-6
Rockford, IL 61125-7002
815-394-2734

Yoshiyuki Kawamura
Fukuoka Institute of Technology
Higashi-ku
Fukuoka 811-02
JAPAN
092-606-1313 (x3131)

Chan-Joong Kim
Superconductivity Research Lab
Korea Atomic Energy Research Inst.
Yusung Taejon 305-600
SOUTH KOREA
82-42-868-8908

Ernst G. Knolle
Knolle Magnetrans
2691 Sean Court
S. San Francisco, CA 94080
415-871-9816
knolle@crl.com

Takashi Kohno
National Aerospace Laboratory
7-44-1 Jindaijihigashi-machi
Chofu-shi
Tokyo 182
JAPAN
0422-47-5911
kohno@nal.go.jp

Tetsuya Kunimasu
National Aerospace Laboratory
7-44-1 Jindaijihigashi-machi
Chofu-shi
Tokyo 182
JAPAN
0422-47-5911
kunimasu@nal.go.jp

Haigun Lee
Massachusetts Institute of Technology
Bldg. NW14-2508
170 Albany St.
Cambridge, MA 02139
617-253-4185
hlee@pfc.mit.edu

Junho H. Lee
Kanazawa University
2-40-20 Kodatsuno
Kanazaw a 920
JAPAN
81-762-34-4850
junho@fmsun1.ec.t.kanazawa-u.ac.jp

Takeshi Mizuno
Saitama University
Faculty of Engineering
255 Shimo-Okubo
Urawa 338
JAPAN
81-48-858-3455
mizar@mech.saitama-u.ac.jp

Mikihiko Mori
National Aerospace Laboratory
7-44-1 Jindaij-higashi machi
Chofu-chi Tokyo 182
JAPAN
81-422-47-5911

S. C. Mukhopadhyay
Kanazawa University
Lab. of Magnetic Field Control & Applic.
Kodatsuno 2-40-20
Kanazawa 920
JAPAN
81-762-34-4943
chandra@magstar.ec.t.kanazawa-u.ac.jp

Masato Murakami
ISTEC
Superconductivity Research Lab
1-10-13 Shinonome, Koto-ku
Tokyo 135
JAPAN
81-3-3454-9284

Shin Murakami
Shimane University
Matsue 690
JAPAN
0852-32-8913
smurakam@riko.shimane-u.ac.jp

Ken Nagashima
ISTEC
Superconductivity Research Lab
1-16-25 Shibaura
Minato-ku, Tokyo 105
JAPAN
81-3-3454-9284
QZG14305@niftyserve.or.jp

Hideo Nakai
Toyota Central R&D Labs
Nagakute, Achi 480-11
JAPAN
0561-62-4137
h-nakai@mosk.tytlabs.co.jp

Atsushi Nakajima
National Aerospace Laboratory
7-44-1 Jindaiji-Higashi-machi
Chofu, Tokyo 182
JAPAN
81-442-47-5911 (x2548)
nakajima@nal.go.jp

Toru Namerikawa
Kanazawa University
Dept. of Electrical & Computer Eng.
2-40-20, Kodatsuno
Kanazawa 920
JAPAN
81-76-234-4849
toru@t.kanazawa-u.ac.jp

Kentaro Nishi
Keio University
Sawa Laboratory
Yokokama kouhoku-hu
Hiyoshi 3-14-1
JAPAN
81-45-563-1151

Takahisa Ohji
Kanazawa University
Facility of Engineering
Kanazawa Ishikawa 920
JAPAN
096-234-4943
ohji@magstar.ec.t.kanazawa.u.ac.jp

Hiroyuki Ohsaki
The University of Tokyo
Dept. of Electrical Engineering
7-3-1 Hongo Bunkyo-ku
Tokyo 113
JAPAN
03-3812-2111
ohsaki@ohsaki.t.u-tokyo.ac.jp

Yohji Okada
Ibaraki University
Faculty of Engineering
4-12-1 Nakanarusawa Machi
Hitachi 316
JAPAN
81-294-38-5025
okada@mech.ibaraki.ac.jp

Christian Redemann
ETH Zurich
Lab for Elec. Eng. Design (EEK)
Technoparkstrasse 1
Zurich CH8005
SWITZERLAND
41-1-445-1352
redemann@eek.ee.ethz.ch

Reiko Saitoh
National Aerospace Laboratory
7-44-1, Jindaijihigashi-machi
Chofu-shi
Tokyo 182
JAPAN
81-422-47-5911

Tetsuzo Sakamoto
Kyushu Institute of Technology
Department of Control Engineering
Tobata
Kitakyushu 804
JAPAN
81-93-884-3182
sakamoto@cntl.kyutech.ac.jp

Yukio Sakaue
Gifu University
Gifu-City
Yanagido 1-1 501-11
JAPAN
058-293-2706

Misako Satoh
National Aerospace Laboratory
7-44-1, Jindaijihigashi-machi
Chofu-shi
Tokyo 182
JAPAN
81-422-47-5911

Koichiro Sawa
Keio University
3-14-1 Hiyoshi
Kohoku-ku
Yokohama 223
JAPAN
81-45-563-1141

Hideo Sawada
National Aerospace Laboratory
7-44-1 Jindaijihigashi-machi
Chofu-shi
Tokyo 182
JAPAN
81-0422-47-5911
sawada@nal.go.jp

Jean-Francois Schneider
French Embassy in Japan
4-11-44 Minami-Azabu
Minato-ku, Tokyo 106
JAPAN
03-5420-8886

Hans Schneider-Muntau
National High Magnetic Fields
Laboratory (NHMFL)
1800 E. Paul Dirac Drive
Tallahassee, FL 32306-4005
904-644-0863

Kendall W. Sherman
NASA Langley ResearchCenter
Mail Stop 162
Hampton, VA 23681-0001
757-864-4447
k.w.sherman@larc.nasa.gov

Joachim F. Sobotzik
Technical University of Darmstadt
Pekrsenshape 30
Darmstadt D-64287
GERMANY
49-65-63973

Hitoshi Takahashi
National Aerospace Laboratory
7-44-1 Jindaijihigashi-machi
Chofu-shi
Tokyo 182
JAPAN
0422-47-5911

Yoshio Takai
Toshiba Corporation
1, Toshiba-cho, Komukai
Saiwai-ku
Kawasaki-shi
Kanagawa
JAPAN
81-44-548-5123

Hideo Takatsuka
HSST Development Corporation
2-6-15, Shibakohen
Minato-ku
Tokyo
JAPAN
81-3-5403-1427

Ms. Takeda
Knolle Magnetrans
2691 Sean Court
S. San Francisco, CA 94080
650-871-9816

Masatsugu Takemoto
Science University of Tokyo
Chiba Lab, Dept. of Elec. Eng.
2461 Yamazaki
Noda Chiba 278
JAPAN
81-471-24-1501
j7397632@ed.noda.sut.ac.jp

Ryuichi Tanaka
Mitsubishi Precision Co., Ltd.
345 Kamimachiya
Kamakura-City
Kantawa 247
JAPAN
0467-43-8907
rtanaka@mpcnet.co.jp

Takumi Tanida
HSST Development Corporation
2-6-15, Shibakohen
Minato-ku
Tokyo
JAPAN
81-3-5403-127

Hidekazu Teshima
Nippon Steel Corporation
Advanced Technology Research Labs
3-35-1 ida, Nakahara-ku
Kawasaki 211
JAPAN
81-44-777-4111

Richard D. Thornton
Massachusetts Institute of Technology
Room 10-005
77 Massachusetts Avenue
Cambridge, MA 02139
617-253-4639
thornton@MIT.EDU

Masahiro Tosa
National Res. Inst. for Metals (NRIM)
1 Sengen
Tsukuba 305
JAPAN
81-298-59-5073
tosa@nrim.go.jp

Hirochika Ueyama
Koyo Seiko, Co., Ltd.
24-1 Kokubu, Higanj-cho
Kashiwara
Osaka 582
JAPAN
81-729-78-5018
ueyama@tec.koyo-seiko.co.jp

Rafael Vives Fos
Grupo de Investigacion en Electr
Avanzada
Universidad Politecnica de Valencia
Camino de Vera 14
Valencia 46022
SPAIN
34-6-387-7068
rvives@upvnet.upv.es

Chieko Watanuki
National Aerospace Laboratory
7-44-1, Jindaijihigashi-machi
Chofu-shi
Tokyo 182
JAPAN
81-422-47-5911

Mr. Yamashita
Knolle Magnetrans
2691 Sean Court
S. San Francisco, CA 94080
650-871-9816

Hiroki Yoshida
Gifu University
Gifu-City Yanagido
1-1 501-11
JAPAN
058-293-2906

Satoru Yoshida
Knolle Magnetrans
2691 Sean Court
S. San Francisco, CA 94080
650-871-9816

Takai Yoshio
JAPAN
044-548-5123
eth@uchu.komukai.toshiba.co.jp

Junko Yoshioka
3-35-2 Lioka-shinden
Morioka-City Iwate 020
JAPAN

Session 1 -- Maglev 1

Chairman: Nelson J. Groom
NASA Langley Research Center

POSSIBILITY OF A SUPERCONDUCTING BULK MAGNET FOR THE MAGLEV TRAIN

Hiroyuki Fujimoto
Railway Technical Research Institute,
2-8-38 Hikari-cho, Kokubunji-shi, Tokyo 185, Japan
Also, Superconductivity Research Laboratory, ISTEC,
1-16-25 Shibaura, Minato-ku, Tokyo 105, Japan

ABSTRACT

Superconducting magnets which use high critical temperature, T_c, oxide superconductors are promising for industrial applications including the magnetically levitated (Maglev) train. Since the discovery of high T_c superconductors in 1986, much effort has been devoted to developing materials with a high critical current density, J_c. Recent development shows that rare-earth $REBa_2Cu_30_{7-x}$ and light rare-earth $LREBa_2Cu_3O_{7-x}$ superconductors prepared by melt processes have a high J_c at 77 K in high magnetic fields. A wide variety of applications of (RE)-Ba-Cu-O superconductors have been proposed. Further, (LRE)-Ba-Cu-O bulk superconductors melt-processed in a reduced oxygen atmosphere, named oxygen-controlled-melt-growth (OCMG) process are very promising for high field application as a superconducting permanent magnet with liquid nitrogen refrigeration. Compared to a good quality melt-grown REBCO bulk, LREBCO bulks exhibit larger J_c in high magnetic fields and much improved irreversibility field, H_{irr}, at 77 K, implying that more effective flux pinning can be realized in a commercially feasible way. In this paper, we discuss the possibility of a superconducting bulk magnet for the Maglev train in the aspect of a preliminary design of the bulk magnet and also melt processing for REBCO and LREBCO bulk superconductors and their characteristic superconducting properties.

INTRODUCTION

Magnetization of $REBa_2Cu_3O_{7-x}$ (RE: Rare Earth, REBCO) superconductors [1] with a high critical current density (J_c) results in a strong bulk magnet. Therefore, the superconducting bulk magnet or the superconducting quasi-permanent magnet for the magnetically levitated (Maglev) train [2-3] with liquid nitrogen refrigeration could be realized, instead of Nb-Ti coils which require liquid helium as a coolant. Further a large $LREBa_2Cu_3O_{7-x}$ (LRE: Light Rare Earth, e.g. Nd, Sm, Eu, Gd, LREBCO) bulk superconducting magnet is believed to trap very high magnetic fields - over 5 T at 77 K. If that happens, it will have a great impact on future transport systems.

It has been expected to apply the REBCO bulk to a superconducting magnetic bearing, a flywheel, a motor, high field magnetic shielding, and a superconducting bulk magnet. [4] The trapped magnetic field of the superconducting bulk magnet with a large single domain has been reported to be superior to that of a conventional permanent magnet. It is known that the superconducting bulk magnet can generate a higher magnetic field with increasing critical current density and volume of the bulk superconductor. Activation processes by using a pulsed magnetic field in zero field cooling, or a static magnetic field in a zero field or field cooling are prospective methods [4-5].

Many of the high critical temperature (T_c) superconductors show superconductivity at temperatures higher than liquid nitrogen, 77 K. In sintered YBaCuO, J_c is low because of the existence of weak links such as grain boundaries, and defect structures. However, recent development shows that melt-processed REBCO [6-9] and LREBCO [10-12] superconductors have a high J_c at 77 K in high magnetic fields. Solidification processes for producing REBCO and LREBCO superconductors are effective for obtaining a high J_c. Although some superconducting compounds from the Bi-Sr-Ca-Cu-O and Tl-Ba-Ca-Cu-O systems exhibit higher T_c in comparison with the RE-Ba-Cu-O system (e.g. Y-system), they are considered inadequate for bulk-type applications at 77 K because their irreversibility lines are drastically depressed over a wide temperature range [13-14].

In the present paper, important points in melt processing of the RE-system and the LRE-system are described. Properties of oxygen-controlled-melt-growth (OCMG)-processed LREBCO superconductors [10-12] and their characteristic flux pinning are also presented. Further, the possibility of a superconducting bulk magnet for the magnetically levitated (Maglev) train, or magnetic levitation system is discussed [15].

BULK SUPERCONDUCTORS AND MELT PROCESSES

In this section, melt processing for the LRE-systems and characteristic superconducting properties of melt-grown LREBCO bulk superconductors, mainly for NdBCO, are briefly described. Melt processing has been a key processing route for the fabrication of bulk high-temperature superconductors required for practical applications. A solidification technique for the Y-Ba-Cu-O system (Y-system) has been developed [4], known as the melt-textured growth (MTG) process [6] with a large J_c value $\geq 10^4$ A/cm^2 at 77 K and 0 T, the quench and melt growth (QMG) [7-8], the melt-powder-melt-growth (MPMG) [9] process with a large J_c value $\geq 3 \times 10^4$ A/cm^2 at 77 K and 1 T. The melt process opened the possibility of various monolithic bulk applications operative with liquid nitrogen refrigeration.

While reported J_c values of melt-processed YBCO superconductors have already surpassed the lower limit for practical applications, J_c enhancement over the order of 10^5 A/cm^2 and its less severe degradation in high fields at 77 K are still required for both better performance and a safety margin. As a promising process, an oxygen-controlled-melt-growth (OCMG) process for the $LREBa_2Cu_3O_{7-x}$ systems (LRE-systems, LRE: Nd, Sm, Eu) was developed [10-12]. In comparison with optimally melt-processed YBCO superconductors, OCMG-processed LREBCO superconductors exhibit larger J_c in high magnetic fields and much improved irreversibility field (H_{irr}) at 77 K for the applied field (H) parallel to the c-axis of the crystal (H//c), implying that stronger flux pinning can be realized in a commercially feasible way.

The OCMG process was developed to solve the fundamental problem of a depressed T_c with a broad superconducting transition of LREBCO superconductors when they were melt-processed in air. The OCMG process was also found to be effective in achieving high T_c phase in other LRE-systems. Significant effects of the oxygen partial pressure, $p(O_2)$, controlled during melt processing, on T_c and the superconducting transition behaviors are displayed for the Nd-Ba-Cu-O system. Reduced oxygen atmospheres are obviously effective in fabricating NdBCO superconductors with high T_c and the sharp transition. After melt processing in a flowing mixed gas of 1% O_2 in Ar ($p(O_2)= 10^{-2}$ atm) and subsequent oxygen annealing, a high T_c phase with sharp transition could be reproduced. The highest onset T_c of 96K with sharp transition was achieved [10-12]. The same effect was also observed for other LREBCO superconductors, particularly for Sm and Eu. Since $p(O_2)$ must be controlled during the process in the OCMG process, melt processing in air has been favored. For this point, we have just recently succeeded in fabricating fairly good quality NdBCO bulks with the melt process in air [16].

For practical applications, the improvement in the mechanical properties is also essential. The strength and the fracture toughness of YBCO are considered to be improved by Ag addition in the melt growth of the crystal from the partial molten state [17]. The size and the distribution of Ag particles in the crystal can be determined by controlling the growth rate or undercooling.

PROPERTIES OF BULK SUPERCONDUCTORS

Trapped Magnetic Field of REBCO

A significant magnetic field can be trapped by a superconductor when it exhibits large flux pinning forces. Figure 1 shows the field distribution of an MPMG-processed YBCO sample at 77 K, after being field-cooled in an external magnetic field of 3 T which was subsequently removed. The trapped field

distribution was measured using a Hall probe. At the center of the sample, a magnetic field of 1.4 T is trapped, showing that the material becomes a quasi-permanent magnet [4].

At the present stage, YBCO bulk superconductors have a relatively low H_{irr} at 77 K which limits the maximum achievable trapped field. However, LREBCO bulk superconductors show much higher H_{irr}, which should make these superconductors applicable for this purpose [10-12].

Critical Current Density, J_c of REBCO and LREBCO

High J_c has been a major issue for high-temperature superconductors for practical applications. The critical current is an extrinsic superconducting property which can be controlled by defect type, amount and distribution. Figure 2 shows a typical J_c–B curve for OCMG-processed NdBCO superconductors at 77 K. We followed the usual MPMG processing procedure except for the $p(O_2)$ control. For a comparison, the J_c–B curve of a good quality MPMG-processed YBCO sample is also displayed [18-19]. The J_c–B curve was obtained from the dc magnetization hysteresis (M-H) loops measured by a SQUID magnetometer. It is shown that while J_c of the NdBCO is lower in low fields compared to the MPMG-processed YBCO, it becomes higher in high fields.

This behavior is also common to other OCMG-processed LREBCO (LRE: Sm, Eu) samples and is closely related to the existence of the anomalous secondary peak effect in the M-H loops for H//c. In other words, much stronger pinning in high field regions is realized.

We believe that there exists a slight chemical variation and thus Nd-substituted Ba regions of low T_c are distributed in the high T_c matrix of OCMG-processed NdBCO superconductors, and that these regions will be driven normal in high fields and turn into effective flux pinning sites. The field necessary for these regions to be driven normal depends on chemical composition. This is the origin for the anomalous second peaks, the field-induced pinning.

For further enhancement of J_c, we have approached with two different methods; one is by microstructure control and the other by thermal processing control. The control method for the $Nd_4Ba_2Cu_2O_{10}$ (Nd422) second phase particles in the Nd123 matrix is important, since it is known that the Y211 refinement is effective in J_c improvement. The control of thermal processing conditions in a given $p(O_2)$ is important primarily for the achievement of sample homogeneity in large grains and also closely related to the secondary peak position.

Trapped Magnetic Field of YBCO and SmBCO

A significant amount of magnetic field can be trapped by a LREBCO bulk superconductor when it exhibits large flux pinning forces as mentioned above. Figure 3 shows the field distributions trapped by an MPMG-processed YBCO and an OCMG-processed SmBCO sample for a comparison [20]. A single mountain-like distribution of trapped fields evidences that both samples are single textured domain without weak links. Samples were first field-cooled in the liquid nitrogen with an external field of 3.5 T. Subsequently, the applied field was decreased to 3 T and held for measuring the trapped field, and finally removed to 0 T again for the measurement. The trapped field distribution was measured using a Hall probe.

From Fig. 3, we can see a very interesting difference in the trapped fields between two samples at 3 T, although there is no apparent difference at 0 T. That is, in the external field of 3 T, while YBCO can trap only a negligible field, SmBCO can trap a significant amount of magnetic flux (about one third of the maximum trapped field at 0 T). The reason is ascribed to higher J_c in high fields for SmBCO in comparison with YBCO. This result obviously represents that OCMG-processed LREBCO bulks can trap much higher field than YBCO at 77 K in the case that the sample dimension is similar. It is estimated that fields greater than 5 T can be trapped at 77 K, if optimally-processed large bulks are produced from these materials, because LREBCO bulk superconductors show much higher H_{irr}.

Pulsed Magnetization of YBCO

Pulsed Magnetization is one of the prospective methods for having a sample with large trapped fields. An electromagnet made of copper wire can generate a high magnetic field by pulsed current without liquid helium and superconductors. Figure 4 shows one example of the two-dimensional distribution of the trapped magnetic field over the YBaCuO sample surface, in a pulsed magnetic field of 1.2 T [5]. A pulsed magnetic field was applied perpendicular to the YBaCuO superconductor prepared by the Melt-Powder-Melt-Growth (MPMG) process at 77 K. A period of the pulsed current of zero to peak and peak to zero was 340 μsec. The sample size is 10 mm × 10 mm × 1 mm. After the sample was magnetized, the two-dimensional distribution of the trapped magnetic field over the YBaCuO sample surface was measured by a scanning microsize Hall sensor with an active area of 50 μm × 50 μm at an interval of 0.5 mm. The distance between the Hall sensor and the sample surface was 2.5 mm.

At 1.2 T, it is seen that the whole sample is magnetized, and the distribution has a 4-fold symmetry which indicates the homogeneous superconducting properties of the sample. A maximum remnant magnetic

field of 0.15 T was obtained at the center of the sample surface. The maximum trapped magnetic field by a static magnetic field also reached approximately the same value. Therefore, the pulsed magnetization was shown to be effective. The maximum trapped magnetic field increased with an increasing applied magnetic field, and showed a peak. Then the trapped field decreased with a further increase of pulsed magnetic field [5].

SUPERCONDUCTING BULK MAGNET

Maglev is a super high-speed non-contact transport system with a combination of superconducting magnets (SCM) and linear motor technology. The Maglev system is levitated, guided, and propelled by magnetic forces acting between the superconducting magnets and the ground coils such as the levitation/guidance coils and the propulsion coils. The SCM is one of the most basic elements of the Maglev, and the enhancement of reliability and durability of the SCM is a major research and development issue. Two SCMs with on-board refrigerators are mounted on each bogie of the train, and each SCM consists of four superconducting coils with a pole pitch of 1.35 m. The pole size is 1×0.5 m, and each pole is composed of a race-track coil made of NbTi superconducting wires in a persistent current mode at 4.2 K. The magnetomotive force is 700 kA [2-3].

One of the prospective designs is a racetrack coil made of high T_c superconducting wires similar to the NbTi coil. Another one is a superconducting bulk magnet, or a superconducting quasi-permanent magnet. Magnetization of REBCO superconductors with a high J_c would result in a strong bulk magnet, e.g. a superconducting bulk magnet for the Maglev train. In the case of the superconducting bulk magnet, each pole will be composed of small bulk superconductors, because the size of the bulk at present is reported to be up to 100 mm in diameter.

Figure 5 shows a model of a superconducting bulk magnet, when the diameter (d) of a bulk is 100 mm, and the thickness (t) is 20 mm. Each pole consists of 8×4 bulks. The distribution and the magnitude of magnetic fields are then calculated for the bulk magnet composed of bulk superconductors. Magnetic fields for the conventional SCM composed of race-track coils are also calculated for a comparison. The effects of the size and the current density of the bulk superconductor on generated magnetic fields are studied. A perpendicular component of the magnetic field generated by the bulk magnet through the ground coils on the guideway is calculated by the Biot-Savart law. A constant current density without magnetic field dependence is assumed by the Bean model. The gap between the surface of the bulk and the center of the ground coil takes 150 mm for the levitation/guidance coil, and 222 mm for the propulsion coil.

Figure 6 shows the distribution of calculated magnetic fields, B_y at the center of the levitation/guidance coil for the case of 8 × 4 bulks, when the current density of the bulk is 1 A/mm^2. The distribution of the magnetic field of the bulk magnet was almost the same as that of the conventional race-track magnet. Figure 7 shows the distribution of calculated magnetic fields, B_y at the center of the levitation/guidance coil when each pole consists of 4 × 2 bulks, 200 mm in diameter, and the current density of the bulk is 1 A/mm^2. When the diameter of the bulk becomes large and the number of the bulks per pole is reduced, the magnitude of magnetic fields, B_y increases. However, the fluctuations in the magnetic fields also increase within each pole as shown in Fig. 7 [15].

As a result, the current density necessary for the SCM of the Maglev train is estimated to be larger than 10^5 A/cm^2 for d = 100 – 200 mm and t = 20 mm. The generating magnetic field depends on the diameter and the thickness of a bulk, and the required current density decreases with increasing thickness and size of a bulk. Currents flowing through the outer region of the bulk contribute much more to generating magnetic fields than those through the inner region. It should be noted that mechanical properties limit the trapped magnetic field, that is J_c, due to the electromagnetic force.

Therefore, for designing the SCM of the Maglev train, increasing the critical current density and the size and thickness of bulk superconductors is a key issue. The strength of a bulk superconductor is also important together with increasing J_c.

In addition to the material properties, the magnetization method of a bulk is a basic issue for the bulk magnet. One of the methods is a pulsed magnetization. Trapped field properties by the pulsed magnetic field are briefly described above in YBCO superconductors prepared by the MPMG process. Another method is the magnetization of superconductors in a static magnetic field by a SCM. Furthermore, a cooling temperature for operation and an arrangement of bulks are also important for planning an outline of a SCM. An arrangement of hollow cylindrical bulks are one of the outline plans of a SCM, because the current flowing through the outer region of a bulk contributes more to generating magnetic field.

CONCLUSIONS

Up to date, major applications of high-temperature superconductors have been confined to products in the form of wires and thin films. However, recent development of melt-processed REBCO and LREBCO bulk superconductors with a high J_c at 77 K and high magnetic fields has initiated the possibility of various applications in the bulk monolithic form, such as magnetic bearings, flywheels and superconducting bulk

permanent magnets. In this paper, we discussed the possibility of the superconducting bulk magnet in the Maglev train.

(LRE)-Ba-Cu-O bulk superconductors melt-processed in a reduced oxygen atmosphere (OCMG process) are very promising for high field applications. LREBCO bulks exhibit higher J_c in high magnetic fields and much improved irreversibility field, H_{irr} , at 77 K. The control of microstructure by altering the amount, size, and shape of the second phase (Nd422 for Nd, LRE211 for Sm, Eu) would lead to reduction of cracks, improvement of mechanical properties, further enhancement in J_c , and so forth. The addition of Ag to REBCO and LREBCO superconductors is considered to be effective for improving the strength of the bulk. Through the optimization of processing, further improvements in T_c , J_c and H_{irr} as well as mechanical properties such as the flexural strength and the fracture toughness would be realized. The homogeneity and size of the bulk superconductor is also a key issue to be overcome.

Summarizing the results of calculation for the bulk magnet, a magnetic field is generated by the bulk magnet composed of small oxide-superconducting bulks, and the distribution of the magnetic field is almost the same as that of the conventional race-track magnet. The magnitude of the magnetic field generated by the bulk magnet depends on the size and the critical current density of the bulk superconductor. Therefore, it is significant to improve the critical current density and to increase the size of bulk superconductors. The strength of a bulk superconductor is also important together with increasing J_c. Furthermore, magnetization methods, cooling temperatures for operation, and arrangements of bulks are major issues for designing a SCM.

Since a large LREBCO bulk superconducting magnet is believed to trap very high magnetic fields - over 5 T at 77 K, LREBCO and REBCO superconductors will surely promote the application of bulk high-temperature superconductors in high magnetic fields. The superconducting bulk magnet for the Maglev train is expected to be one of the most important prospective applications.

ACKNOWLEDGEMENTS

The author would like to thank all of the collaborators, Dr. M.Murakami of SRL, ISTEC for leading the work, and Dr. N.Sakai , Mr. K.Nagashima, Mr. S.Takebayashi, Mr. N.Hayashi, Dr. H.Kojo, and Mr. K.Waki in SRL-ISTEC, and also Dr. S.I.Yoo, Mr. K.Nemoto, Mr. T.Ban, Dr. Y.Nakamura, Mr. H.Kamijo, Mr. T.Higuchi, and Mr. K.Kawano in RTRI for intensive experimental and analytical work, and discussions. This work was partially supported by NEDO for the R&D of Industrial Science and Technology Frontier Program.

REFERENCES

1. S. Gotoh, M. Murakami , H. Fujimoto, and N. Koshizuka : J.Appl.Phys., **72** (1992) 2404.
2. for example, H.Nakashima : Advances in Superconductivity **V** (Springer-Verlag, Tokyo, 1993) p.1211.
3. H. Nakashima, and A. Seki : Proc. 14th Intl. Conf. on Magnetically Levitated Systems, MAGLEV '95, 11. 1995, p. 31.
4. M.Murakami ed. : Melt Processed High-Temperature Superconductors (World Scientific, 1992).
5. H. Fujimoto, K. Kawano, T. Higuchi, K. Nagashima, and M. Murakami : to be published in Proc. M^2S-HTSC-V, 2.28-3.4.'97 at Beijing, China.
6. S. Jin, T.H. Tiefel, R.C. Sherwood, M.E. Davis, R.B. van Dover, G.W. Kammlott, R.A. Fastnacht, and H.D. Keith : Appl. Phys. Lett., **52** (1988) 2074.
7. M.Murakami, M.Morita, K.Doi, K.Miyamoto and H.Hamada : Jpn.J.Appl.Phys., **28** (1989) L399.
8. M.Morita, M.Tanaka, S.Takebayashi, K.Kimura, K.Miyamoto, and K.Sawano : Jpn.J.Appl.Phys., **30** (1991) L 813.
9. H.Fujimoto, M.Murakami, S.Gotoh, N.Koshizuka, T.Oyama, Y.Shiohara and S.Tanaka : Advances in Superconductivity **II**, T. Ishiguro and K. Kajimura eds. (Springer-Verlag, Tokyo, 1990) p. 285.
10. S. I. Yoo, N. Sakai, H. Takaichi, T. Higuchi, and M. Murakami: Appl. Phys. Lett., **65** (1994) 633.
11. S. I. Yoo, M. Murakami, N.Sakai, T. Higuchi, and S. Tanaka : Jpn. J. Appl. Phys., **33** (1994) L1000.
12. M. Murakami, S. I. Yoo, T. Higuchi, N.Sakai, M. Watahiki, N. Koshizuka, and S. Tanaka : Physica C, **235-240** (1994) 2781.
13. for example, H.Maeda, and K.Togano eds. : Bismuth-Based High-Temperature Superconductors, (Marcel Dekker Inc., NewYork, 1996).
14. for example, A.M. Hermann, and J.V. Yakhmi eds. : Thallium-Based High-Temperature Superconductors (Marcel Dekker Inc., NewYork, 1996).
15. H. Kamijo, K. Nemoto, and H. Fujimoto : Advances in Superconductivity **IX** (Springer-Verlag, Tokyo, 1997) p. 1473.
16. H. Kojo, S. I. Yoo, and M. Murakami : submitted to Appl. Phys. Lett. (1997).
17. Y. Nakamura, T. Ban, S.I. Yoo, and H. Fujimoto : Advances in Superconductivity **IX** (Springer-Verlag, Tokyo, 1997) p. 701.
18. S.I. Yoo, H. Fujimoto, N. Sakai, and M. Murakami : J. Alloys and Compounds, **250** (1997) 439.
19. S.I. Yoo, T. Higuchi, H. Fujimoto, and M. Murakami : Quarterly Report (QR) of RTRI, **38**, 3 (1997) 141.
20. K. Nagashima, N. Hayashi, S.I. Yoo, H. Fujimoto, and M. Murakami : presented at Intl. Workshop on the Processing and Applications of Superconducting (RE)BCO Large Grain Materials, July 1997, Cambridge, U.K.

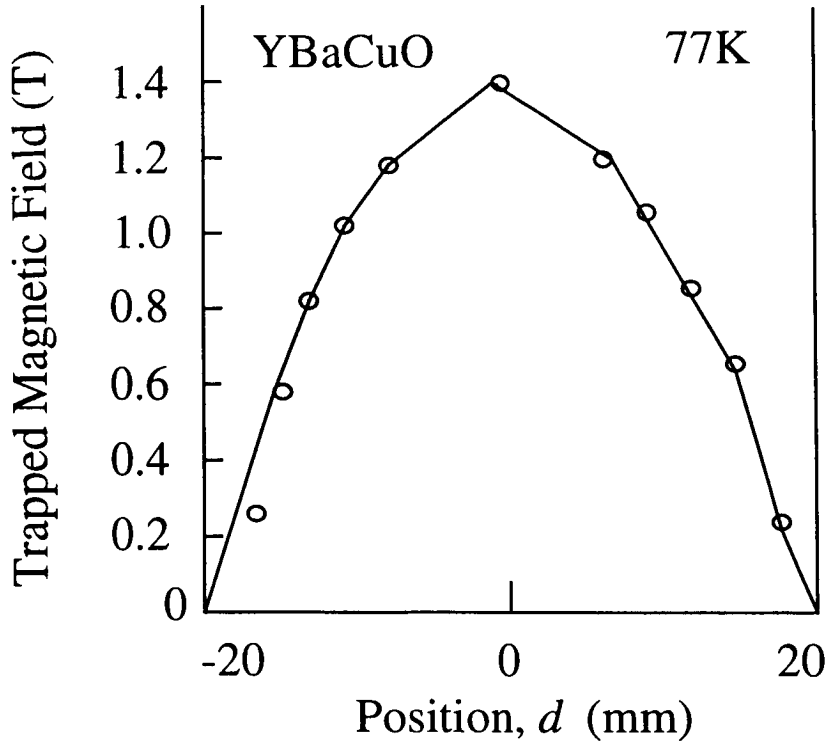

Figure 1. Trapped field distribution of an MPMG-processed YBCO superconductor at 77 K.

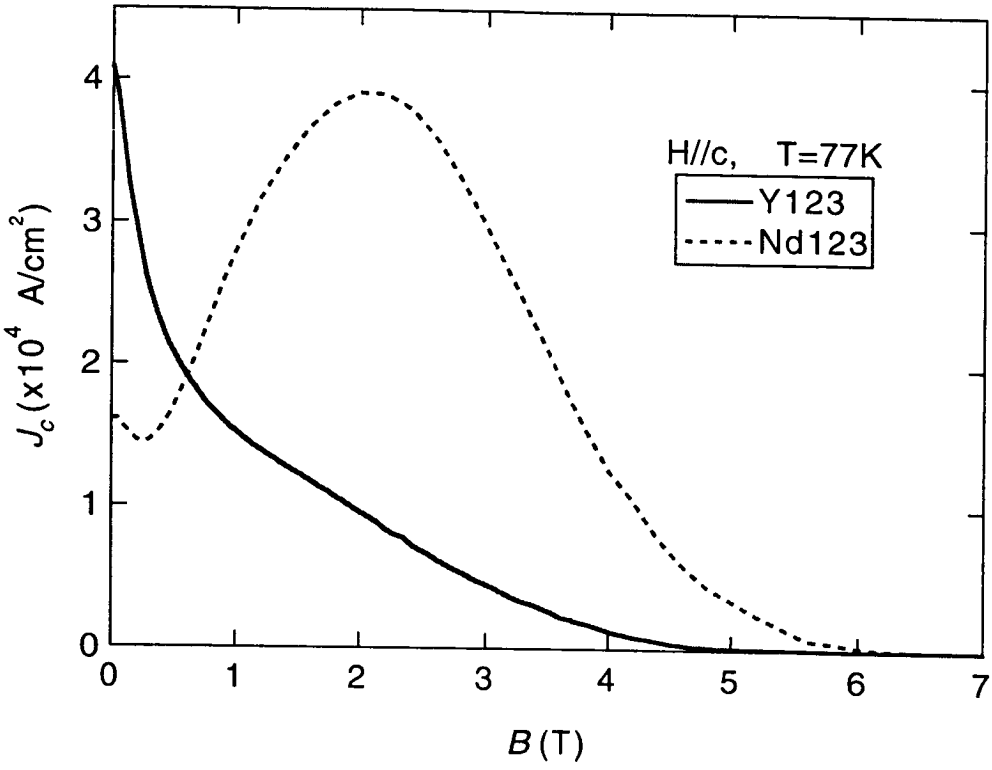

Figure 2. Typical J_c-B curve for OCMG-processed NdBCO superconductors at 77 K. For a comparison, the J_c-B curve of a good quality MPMG-processed YBCO sample is also displayed.

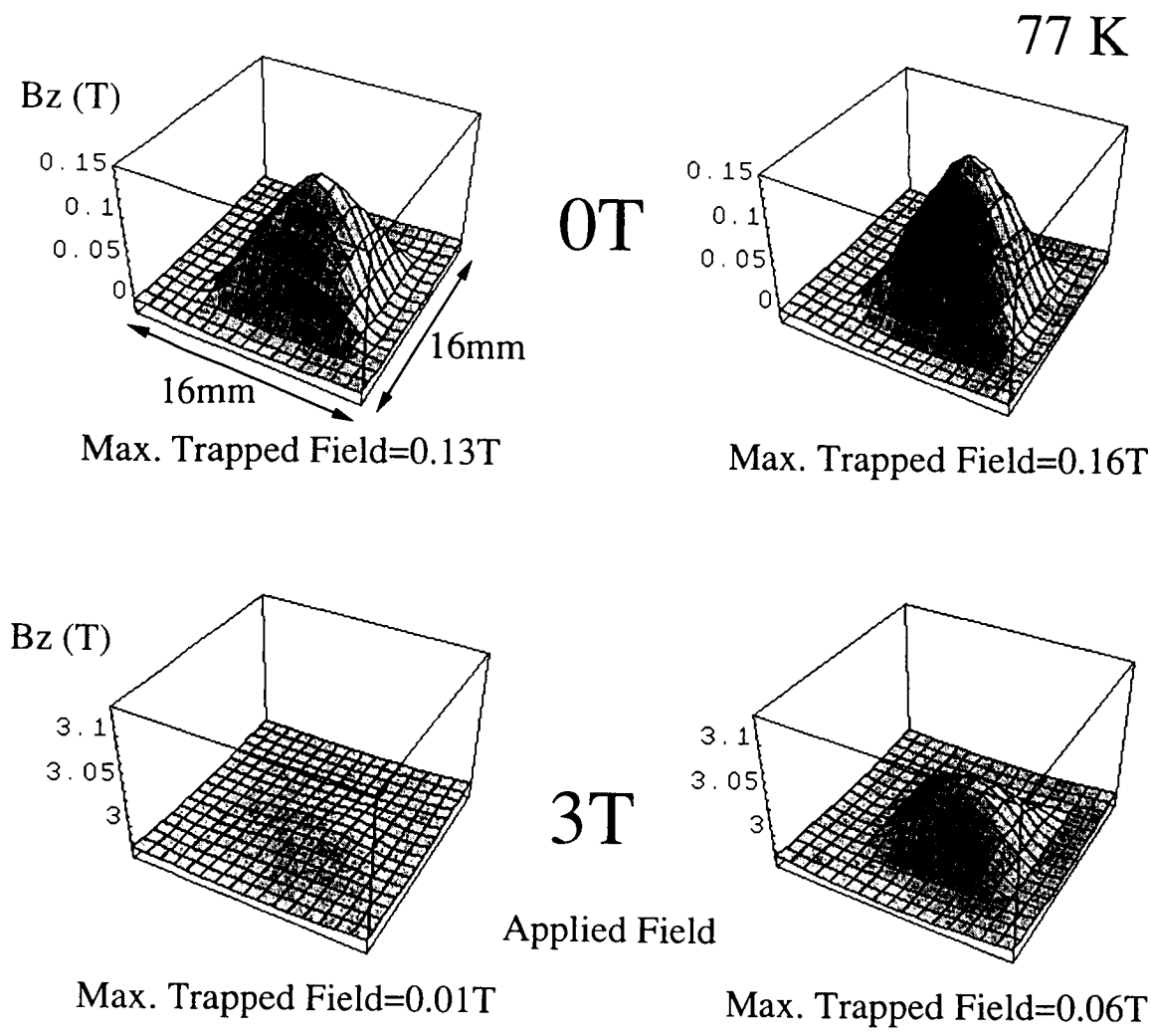

Figure 3. Field distributions trapped by an MPMG-processed YBCO and an OCMG-processed SmBCO sample for a comparison at 77 K.

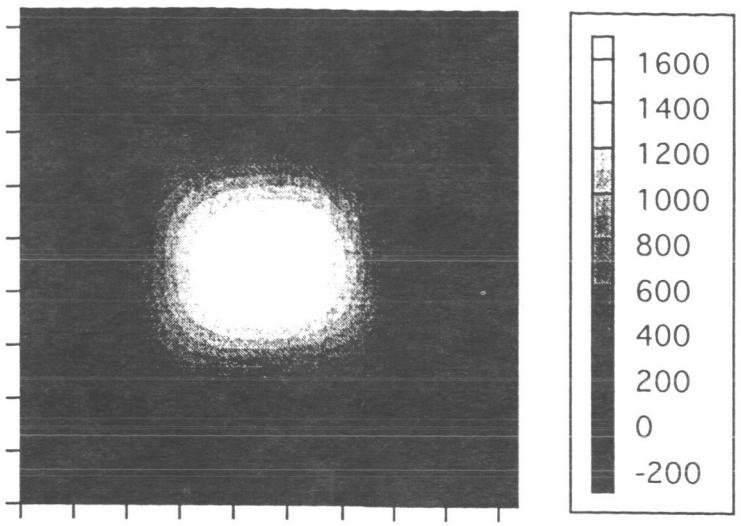

Figure 4 Two-dimensional distribution of the trapped magnetic field over the YBaCuO sample surface at a pulsed magnetic field of 1.2 T.

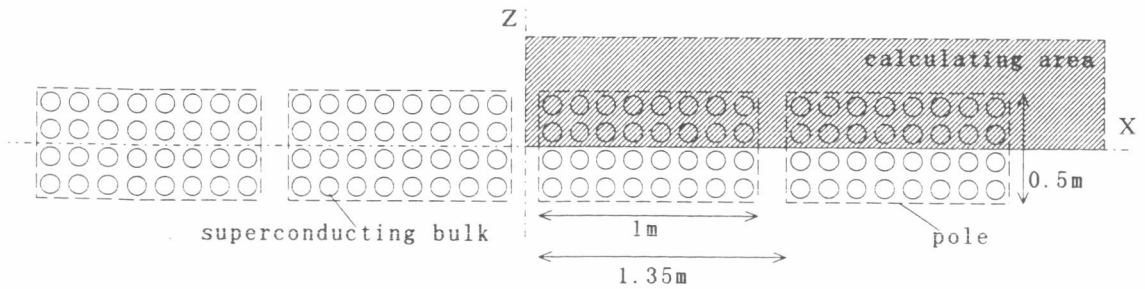

Figure 5. Model of bulk magnets, when the diameter of a bulks is 100 mm, each pole is composed of 8 × 4 bulks, and the bulk magnet is composed of 4 poles with a pitch of 1.35 m.

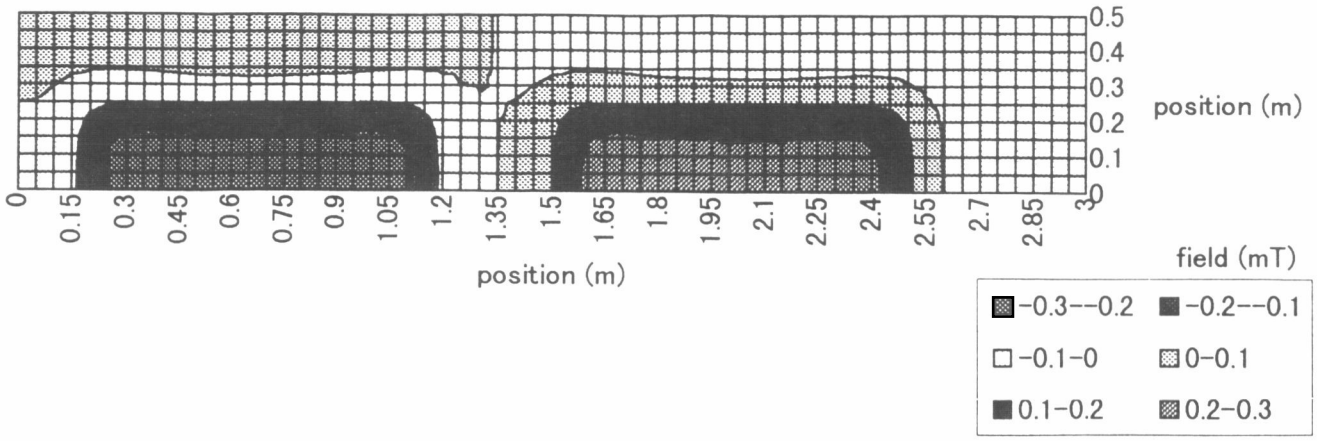

Figure 6. Distribution of calculated magnetic fields, $\mathbf{B_y}$ at the levitation/guidance coils. Each pole is composed of 8 × 4 bulks, 100mm in diameter and 20mm in thickness, and a current density of 1 A/mm^2 in the bulk is used.

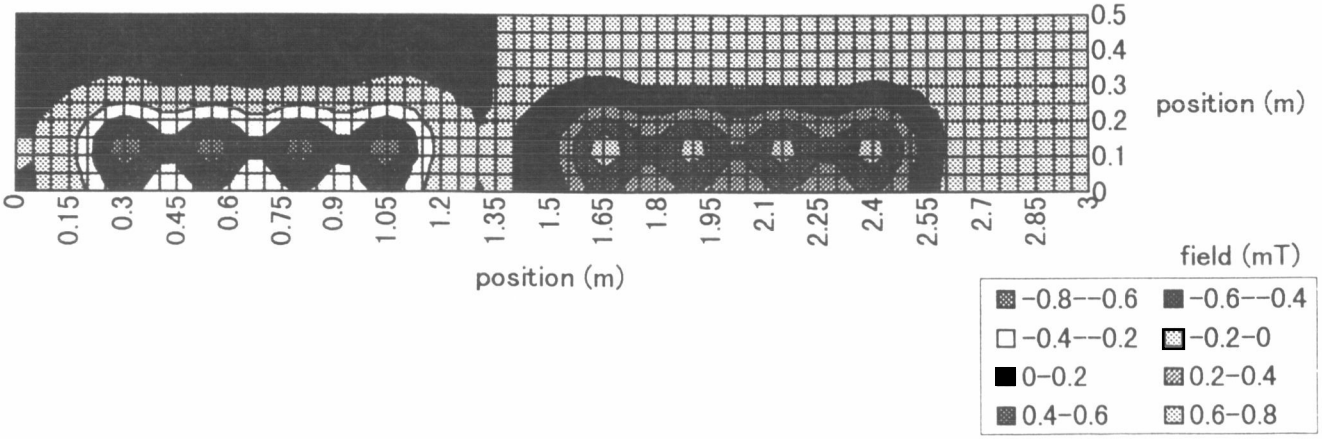

Figure 7. Distribution of magnetic fields, $\mathbf{B_y}$ calculated at the levitation/guidance coils. When each pole is composed of 4 × 2 bulks which are 200 mm in diameter and 20 mm in thickness, and the current density of the bulk is 1 A/mm^2.

THE HSST MAGLEV TRAIN - DEVELOPMENT, TECHNOLOGY AND PROSPECT

Mituru Iwaya
HSST Development Corporation
Tokyo, Japan

Masao Tanaka
Chubu HSST Development Corporation
Nagoya, Japan

SUMMARY

The High Speed Surface Transport (HSST) is a magnetically levitated and linear motor propelled vehicle for mass transit. It has superior environmental adaptability over traditional wheeled vehicles. It was first developed by Japan Air Lines in 1975 as the HSST-01 and the following development efforts have resulted in the latest version of HSST-100L. The Ministry of Transport in Japan made an announcement in 1993 that the HSST poses no technical problems concerning its commercial use. It is now awaiting practical operation.

INTRODUCTION

To prepare for the 21st century, an innovative system designed from a totally unique perspective is necessary. The High Speed Surface Transport (HSST) had adopted magnetic suspension technology and realized a contactless and frictionless transportation system. Floating in the air, suspended and propelled by magnetic force, it is expected to bring us unique merits in our society. Its magnetic suspension system is a combination of normal conducting electromagnets and mild steel anchor rails. Its control is similar to that in other normal conducting magnetic suspension systems.

HISTORY OF DEVELOPMENT

Starting with Small Test Vehicles

The HSST's development was started by Japan Air Lines (JAL) in 1972. At that time, the opening of New Tokyo International Airport (Narita) was planned, and research and development of a high speed railroad was started for the access transit system to connect the 60km distance between the airport and downtown Tokyo.

At first, we conducted some experiments with small model units. In 1975, the first test vehicle called HSST-01 (a two-seater car, Photo 1) was constructed in JAL's aircraft maintenance factory. As shown in Fig. 1, it was made of aluminum alloy with a 1 ton gross weight. It has, on the lower part of the body, two lines (left and right) of electromagnets for levitation and one Linear Induction Motor (LIM) at the body center. A run test was performed on the test track constructed at Higashi-Ogishima in Kawasaki City. After various verification tests, it succeeded in running at a speed of over 300km/h (unmanned condition) in 1978.

During this period, a new vehicle, the HSST-02 (Photo 2), was built for the purpose of a riding experience open to the public. As shown in Fig. 2, it had 8 passenger seats and the gross weight was 2 tons. It was used for both technical tests and public relation purposes. The HSST-02 vehicle had a secondary suspension system to improve passenger's ride quality. This vehicle provided maglev experiences to many guests which were mainly leading persons in various areas, including the King and Queen of Sweden.

Major test items were completed in 1980 giving many useful results. We decided to terminate the tests in Higashi-Ogishima and the test site was closed in March 1981.

Aiming at Mass Transportation

The next stage was a larger vehicle which had the capability of mass transportation. The design and manufacturing of the HSST-03 (Photo 3) vehicle used a Module concept which was considered for use in future commercial vehicles. As shown in Fig. 3, the main feature of the Module concept was to build up units called "Modules" combining the functions of both levitation and propulsion. The HSST-03 was equipped with six modules. With more modules, the vehicle can enlarge its capacity, and with less modules, it can diminish the capacity. The HSST-03 was built as a test vehicle. However, its design was also targeted to provide the potential for commercial operations.

The HSST-03 was completed in 1984, and various run tests were conducted using the track constructed at the site of International Exposition in Tsukuba City. Then, it became part of the '85 Tsukuba Science Expo (March to September of 1985) and it was operated for demonstrations in which it provided the maglev ride experiences to 600,000 passengers including the Japanese Emperor and Prime Minister. In the next year, the HSST-03 was also operated for demonstrations at the '86 Transport Expo in Vancouver, Canada, and it was further demonstrated in Aoi Fair (local exposition) in Okazaki, Japan, in 1987. Through the demonstrative operations open to the public during three consecutive expositions, the HSST-03 carried 1.5 million passengers with total running distance of 24,000 km.

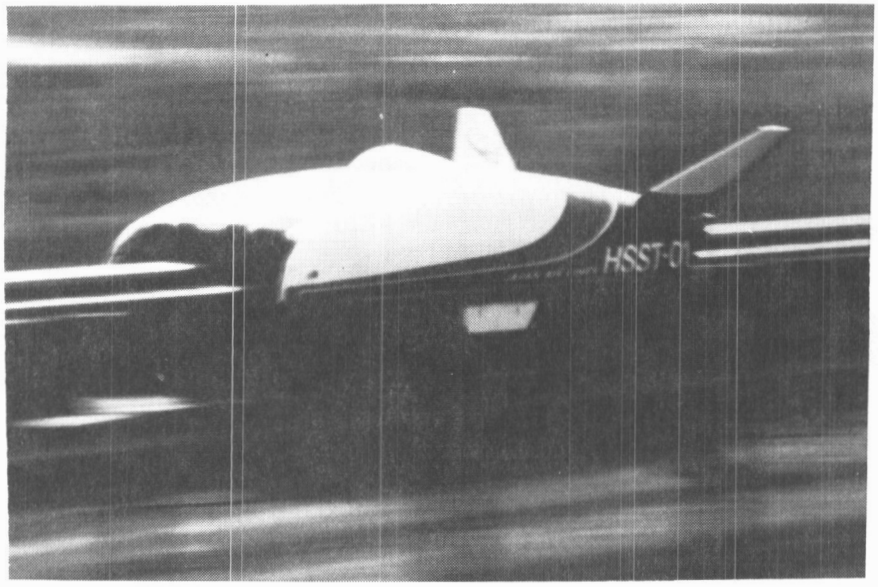

Photo.1 HSST-01 in Ogishima Test Center

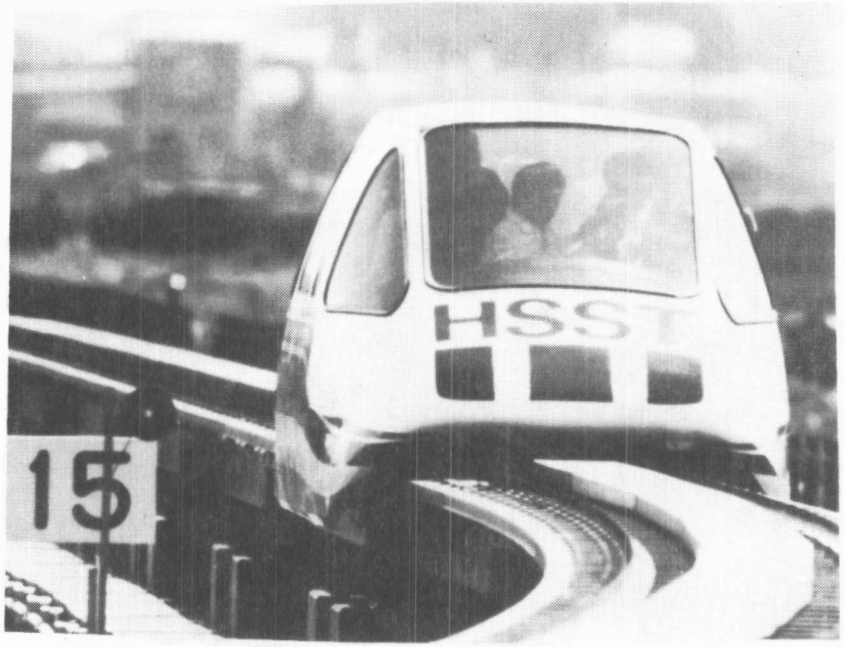

Photo.2 HSST-02 in Ogishima Test Center

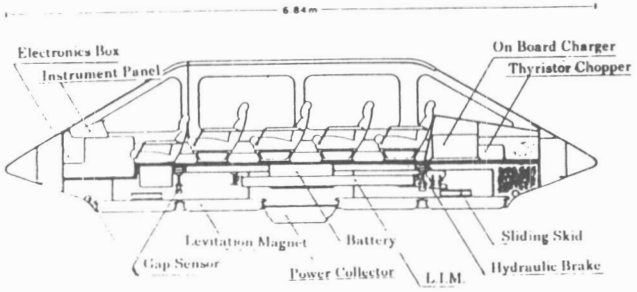

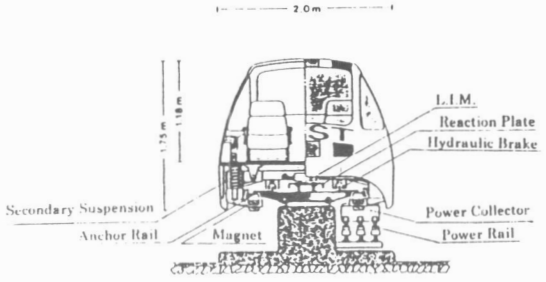

Fig.2 HSST-02 System

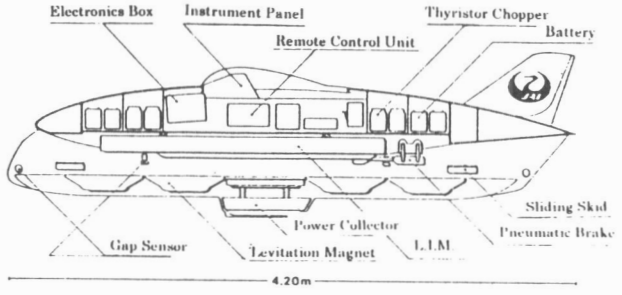

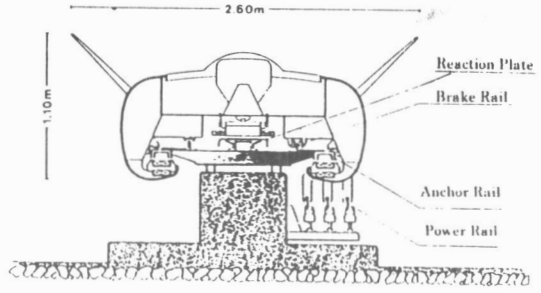

Fig.1 HSST-01 System

Photo.3 HSST-03 in Vancouver Expo '86

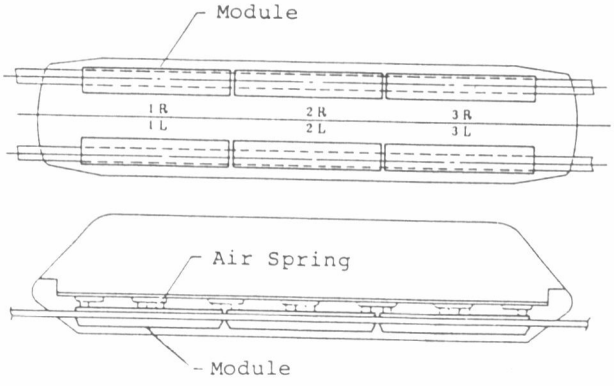

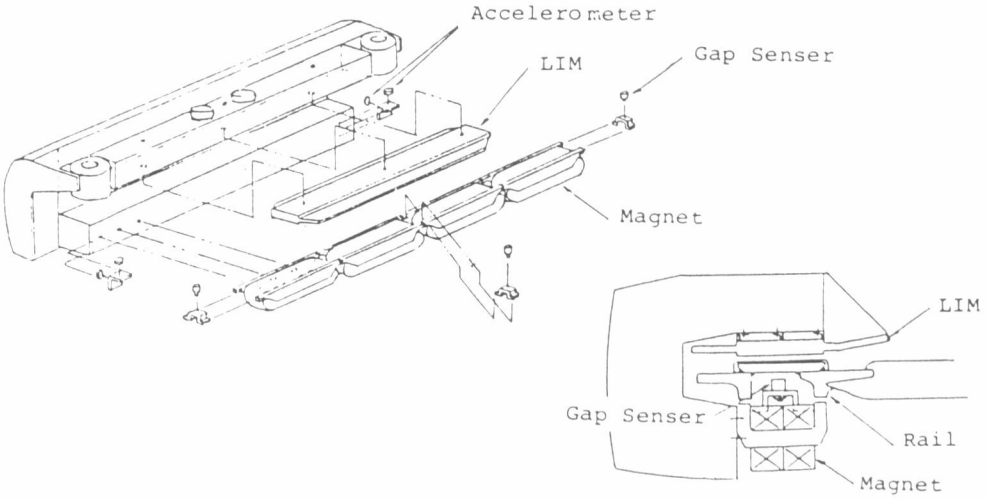

Fig.3 Module System in HSST-03

Establishing a New Corporation for HSST

In 1985, just after the closing of the '85 Tsukuba Science Expo, a small company named HSST Corporation was founded to promote HSST's development and sales, and it inherited all of the HSST businesses from JAL. In this new company, the design of the HSST-04 (Photo 4) vehicle was started. It was a 70-seat single car similar to the monorail system in exterior shape, and had the potential to be operated for commercial operations. Therefore, the design improvements added on HSST-04 over HSST-03 were those such as the adoption of the on-board type propulsion power source (ground side type for HSST-03), the elevated guideway structure (spread footing track for HSST-03), etc. The HSST-04 joined a local exposition held in Kumagaya City, Saitama Prefecture in 1988, and it carried 240,000 passengers during its two-month term.

In 1989, the HSST-05 (Photo 5) was designed and built with a concept similar to the HSST-04. It was fundamentally based on the same technology as HSST-04 except that HSST-05 was a two-car train and was much closer to a commercial train for daily operations. In the same year HSST-05 joined the '89 Yokohama Expo. It is worth noting that HSST operations during the '89 Yokohama Expo were performed as scheduled public transportation with a railroad business license issued by the Ministry of Transport of Japan. The HSST-05, a two-car train with 158 seats, carried 1.26 million passengers during a 191-day term. Both the HSST-04 and HSST-05 were prototype vehicles which belonged to the HSST-200 type with potential to cruise long distances at 200km/hour speed.

Through the operations in the above mentioned expos, HSST's high quality in safety and reliability, and its superb compatibility to the environment have been witnesses and confirmed by many people.

Preparation for HSST's Application to Commercial Operations

In 1990, Aichi Prefecture expressed its intention to investigate the adoption of the HSST system to its newly planned line. Accordingly, Aichi Prefecture, Nagoya Railways, and HSST Corporation founded CHSST (Chubu HSST Development Corporation) to conduct verification tests of the HSST system. The first vehicle type to be tested was the HSST-100S (Photo 6) which is an urban type transit system with a gross weight of 15 tons (per car), with a nominal capacity (per car) of 75 passengers (standard) including 24 seated (refer to the drawing). Concurrently, to investigate the HSST's maturity/compatibility for commercial applications, Aichi Prefecture organized a special investigation committee whose members were specialists of the government (Ministry of Transport, Ministry of Construction) and Aichi Prefecture itself, university professors, and engineers of companies concerned including HSST.

CHSST constructed a 1500m long test guideway in Nagoya City for the various running tests. The tests were conducted there from 1991 to 1993, and more than 100 items were investigated covering a wide range of operation modes including the vehicle and guideway. Test results were

Photo.4 HSST-04 in Saitama Expo '88

Photo.5 HSST-05 in Yokohama Expo '89

Photo.6　HSST-100S in CHSST Test Center

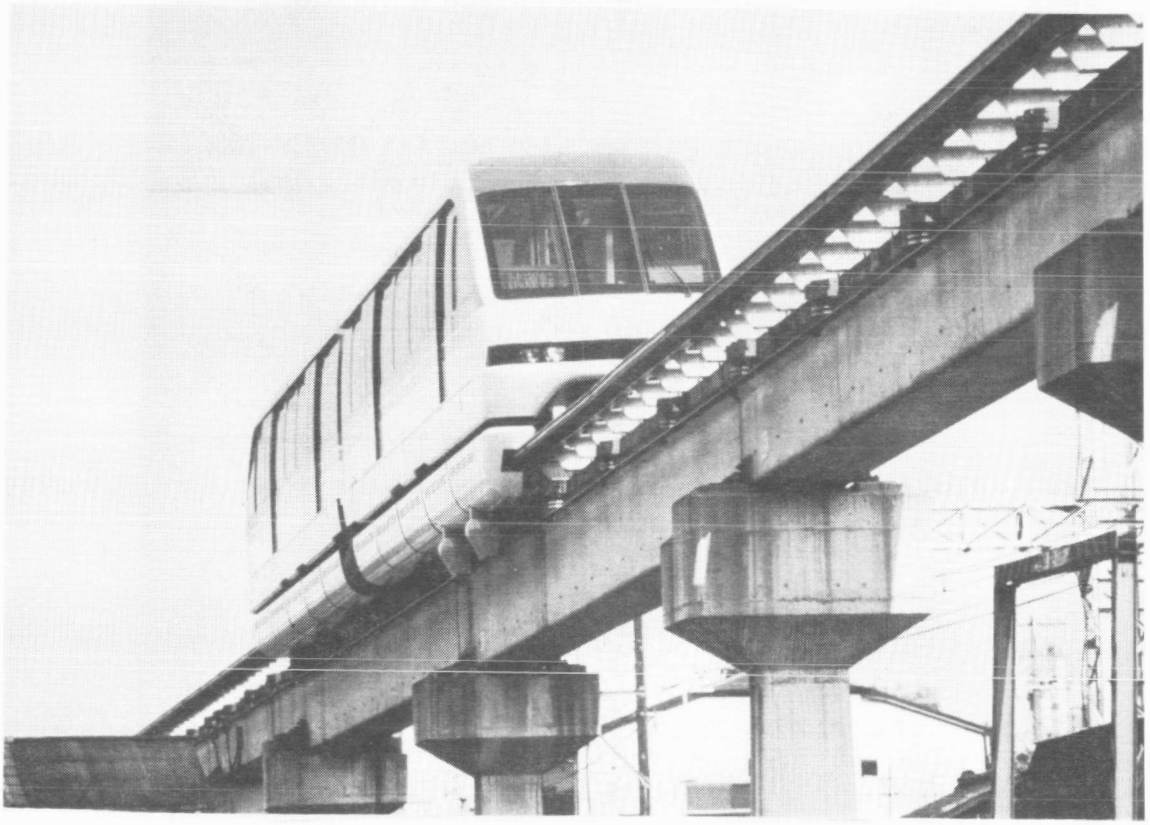

Photo.7　HSST-100L in CHSST Test Center

investigated by the committee, and it issued two reports in 1992 and 1993, respectively. The committee judged that the HSST-100 system was technically mature enough for commercial application though small improvements were required for a few items.

In parallel to the above committee, the Ministry of Transport organized another committee, which announced in 1993 that the HSST system was applicable for commercial application without any technical problems. Then the required legal actions were taken through the amendment of the law/regulations concerned for maglev application to commercial operations.

To further speed-up the HSST's development for commercial application, a new company with 12.1 billion yen capital, called "HSST Development Corporation" was founded in January 1993 by the investment of 52 companies including JAL and Nagoya Railways as the top share-holders. After inheriting all HSST businesses from HSST Corporation, it has been promoting the technologies and sales of the HSST system. For the better sales, HSST Development has added a new type vehicle, the HSST-100L (Photo 7) which can meet wider market demands, with a longer car body with more passenger capacity. The HSST-100L prototype vehicle (two-car train) has been operated on the Nagoya test track for the running tests and endurance tests since 1995, and it has provided, through demonstration runs, many visitors with a comfortable maglev ride [1],[2].

The total running distance of the HSST-100S is 61,724km and that of the HSST-100L is 29,306km as of September 10, 1997.

MAGNETIC SUSPENSION IN HSST

Levitation Magnet

The HSST is equipped with "Modules" which have the similar functions of a bogie of conventional rolling stock. Each module is equipped with four electromagnets. One module has 2.5 tons of levitation capability for HSST-100 vehicle. A 15 ton-car can be supported by six modules.

The main component of the module is an assembly of electromagnets. Table 1 shows the specification of each one of four electromagnets of the HSST-100. The HSST uses an electromagnet which is a so-called "U-shaped Magnet" with its core cross section shaped like a "U". Compared with the "Salient Pole Magnet" with a quadrant shaped magnet core cross section, the "U-shaped Magnet" has the following characteristics. Regarding Lift/Weight Ratio, the "U-shaped" is inferior to the "Salient". On the other hand, the "U-shaped" is similar in structure, for the "U-shaped" has the functions of both vertical levitations and lateral guidance. Furthermore, magnetic drag during a high speed run is less with the "U-shaped" than with the "Salient".

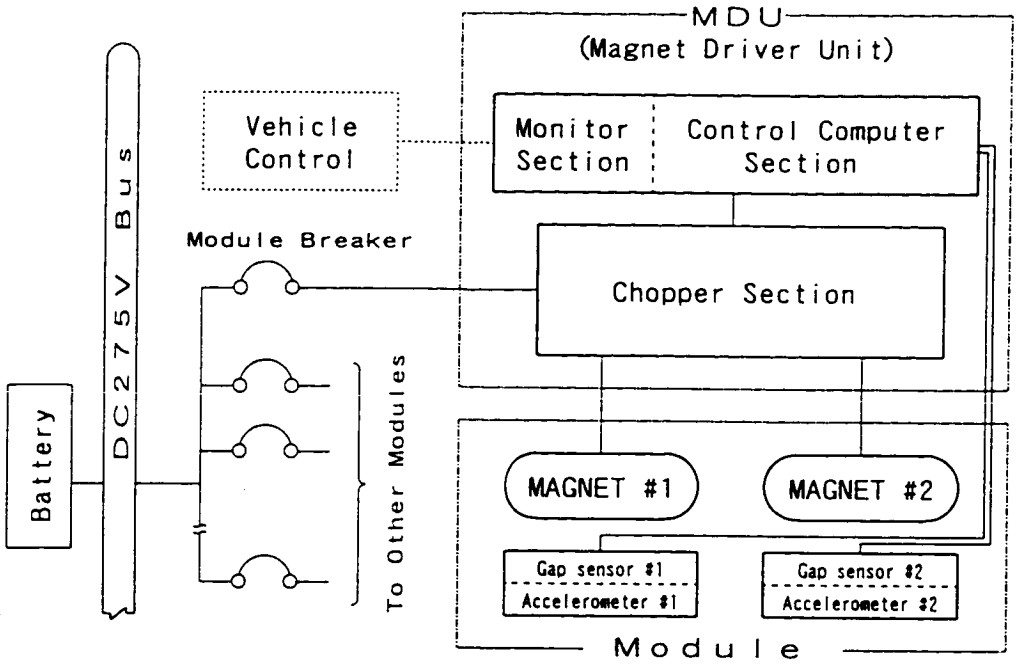

Fig.4 Levitation and Guidance System

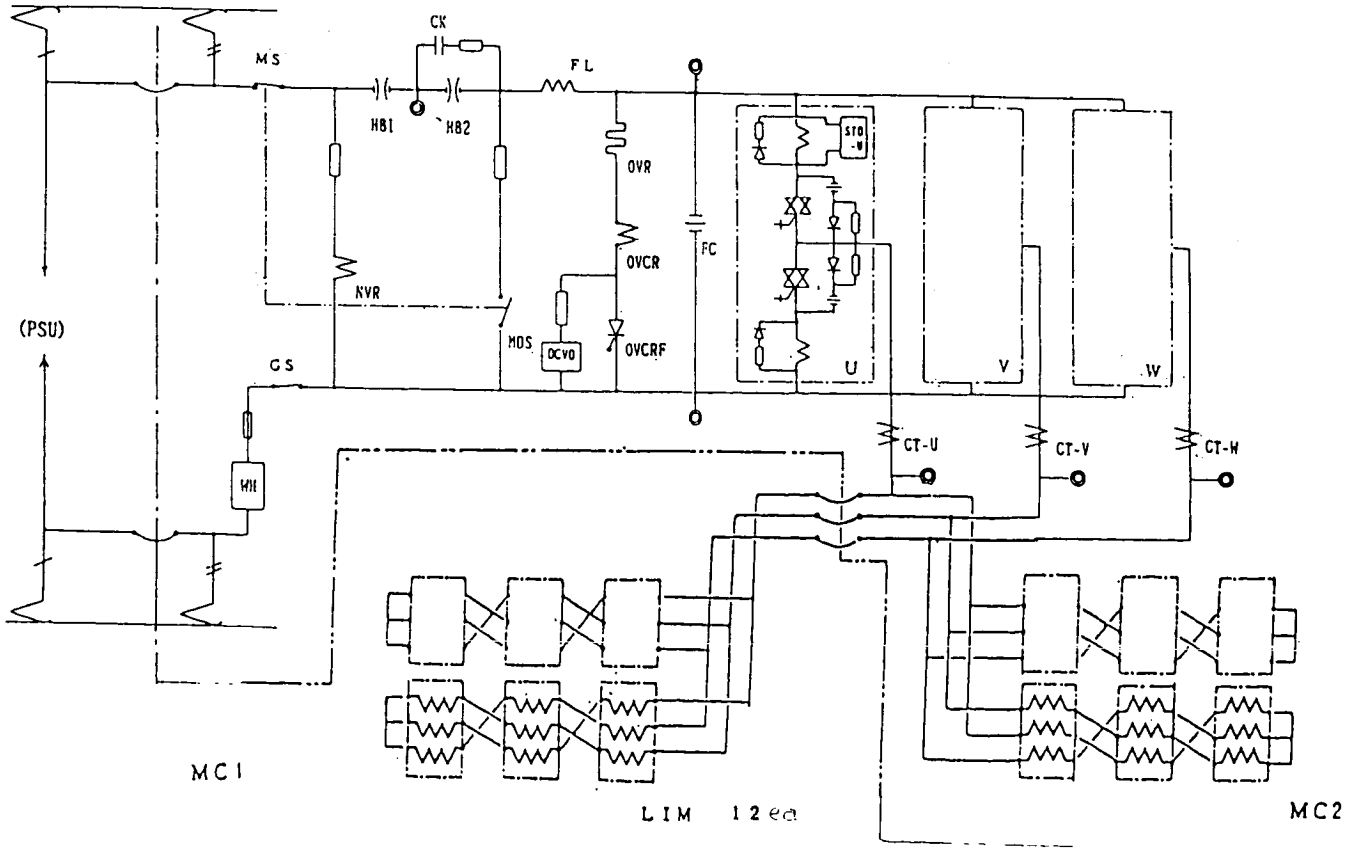

Fig.7 Propulsion System of the HSST-100S

Levitation Control System

Attractive levitation has no natural stability. It requires a feedback control system with sensors. The HSST uses, for this purpose, gap sensors and accelerometers mounted on the surface of the magnet. Fig. 4 shows the block diagram of the levitation system. Sensors detect the movement of magnet and send its signal to the MDU (Magnet Driver Unit). The data is processed in the Control Computer Section and the resulting voltage is sent to the Chopper Section. The Chopper regulates the 275VDC supply voltage in accordance with Pulse Width Modulation (PWM). This regulated power is fed to the magnet coil. The 275VDC supply power is backed up with batteries.

The control system is proportional-integral-derivative (PID). The main signal is the gap between magnet and steel rail. Its proportional element determines magnet position from the rail. The integral element ensures the magnet position accuracy against disturbance such as load change caused by passenger increase/decrease. The differential element has a damping effect to prevent vibration. Accelerometers further ensure damping characteristics of the magnet.

CHSST TEST CENTER AND OPERATION TESTS

Test Center

The Chubu HSST Development Corporation constructed the HSST Test Center in Nagoya in 1991. Fig. 5 shows its profile. The track is approximately 1.5km length, which is sufficient to attain a speed of over 100km/h. It incorporates lateral and vertical curves, 100mR and 700mR respectively, which represent the major allowable mainline curvature for the HSST-100S vehicle. A switching device near the car shed leads a vehicle to a branch line of 25mR horizontal curve which represents the minimum allowable radius in the maintenance yard. Rail gauge is 1.7m.

Test Vehicle HSST-100S

Fig. 6 shows the configuration of the HSST-100S, which was the first vehicle system to be tested in Nagoya. This vehicle has two cars, MC1 and MC2 (Motor Control 1 & 2), with a maximum capacity of 67 passengers per car. The car length of 8.5m was determined chiefly by the minimum curve radius of 25mR. The design speed is 110km/h. The car body is made of aluminum alloy. The gross weight is 15 tons per car.

The levitation system is shown above. Here Fig. 7 shows the propulsion system of the HSST-100S. A car has six modules and each module has one LIM. A total of 12 LIMs are connected in three series and four parallel. Trolley power voltage is 1500VDC which is inverted to VVVF through GTO inverters. Maximum frequency is 90Hz, maximum current 800A. It is incorporated with regenerative braking control and weight adaptive compensation control. This system is backed up by a hydraulic mechanical braking system. Thus the acceleration and deceleration rate is maintained constant as long as the trolley power supply is sufficient [3].

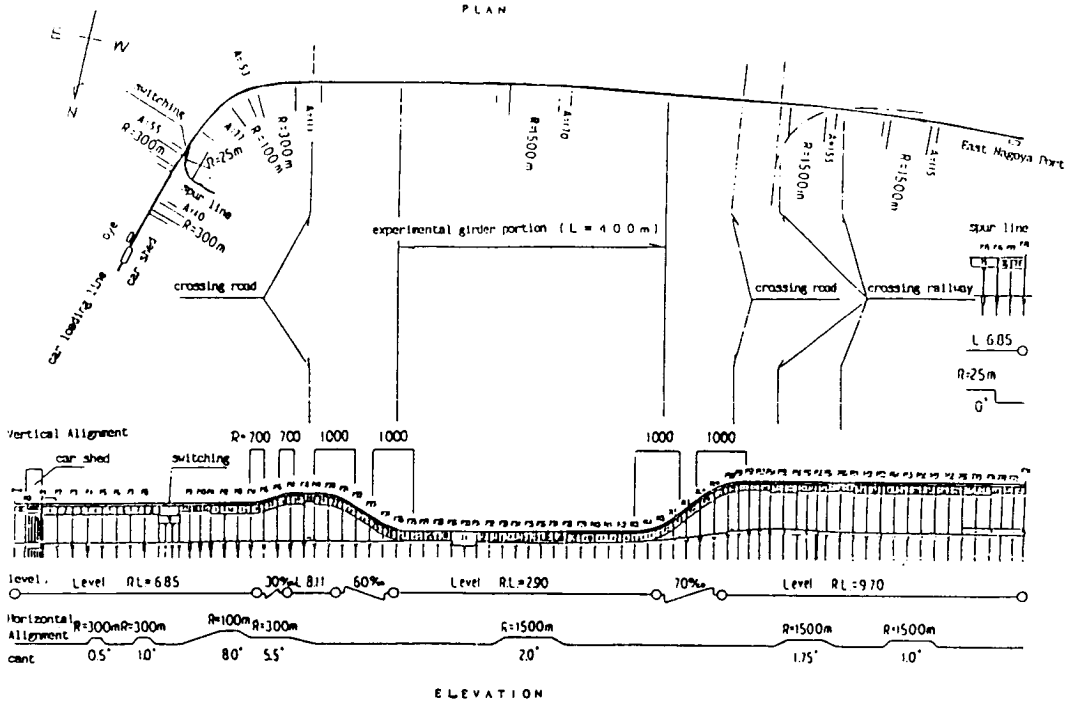

Fig.5 Horizontal Plan and Vertical Elevation of Test Track in Nagoya

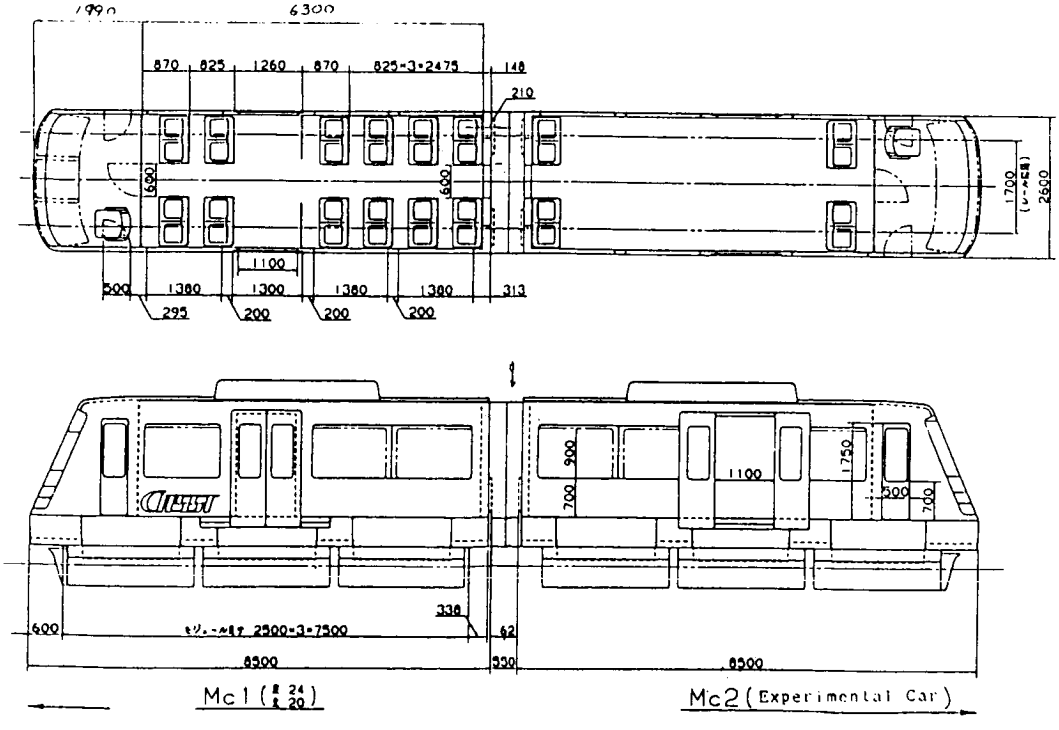

Fig.6 HSST-100S Vehicle

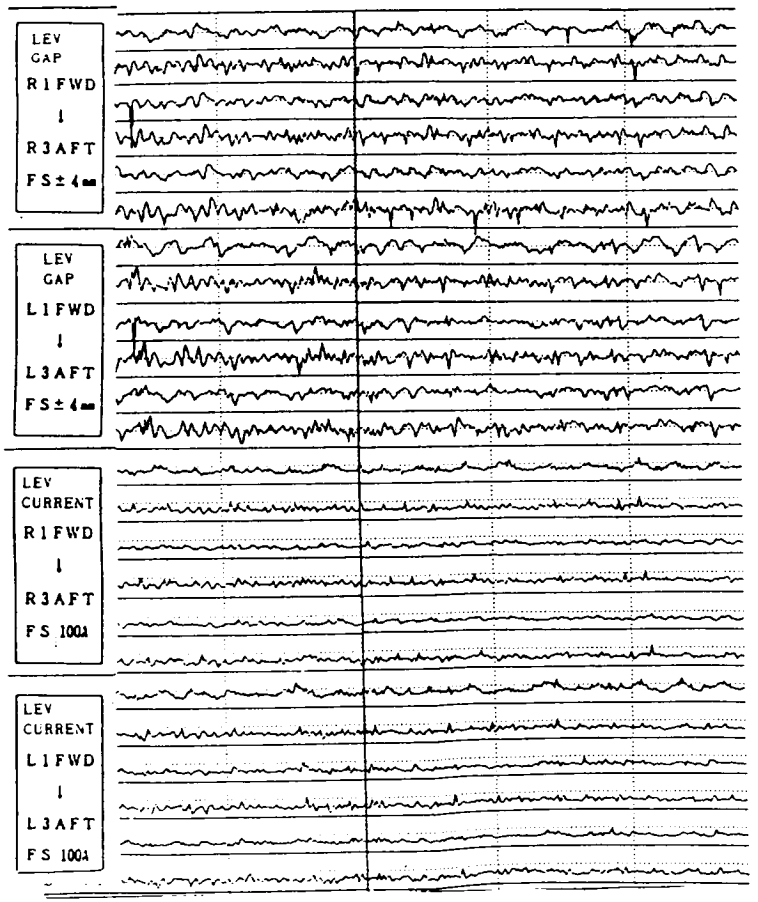

Fig.9 Propulsion and Braking Behavior - 100km/h, Empty Load

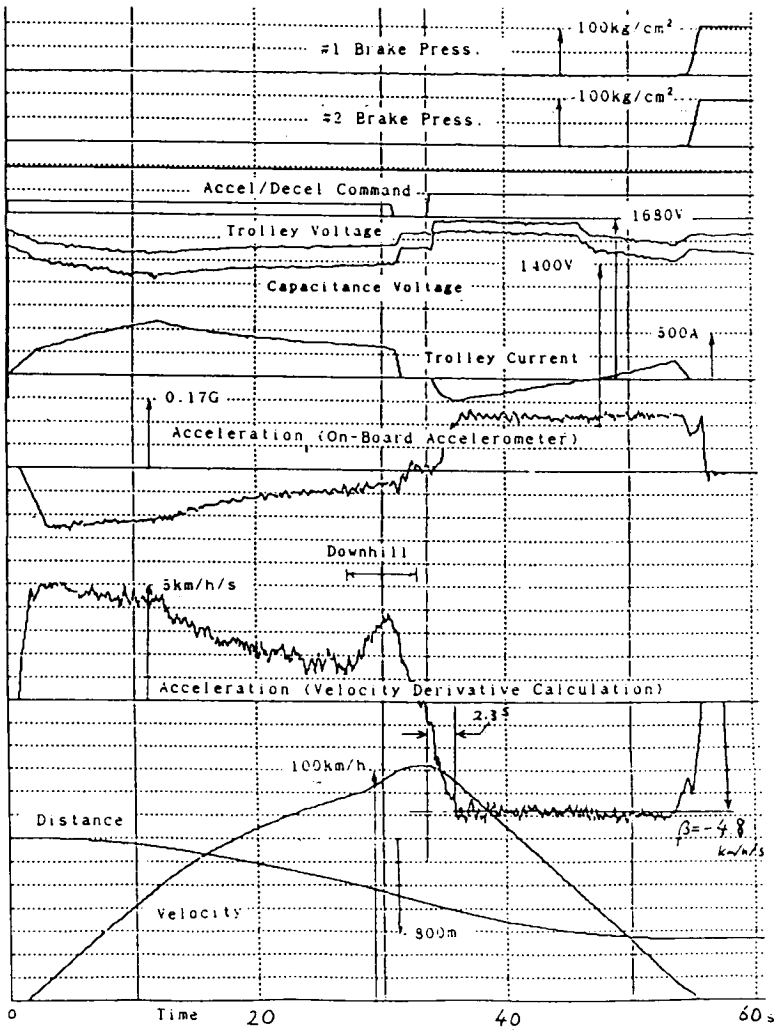

Fig.8 Magnet Gap and Current Fluctuation - 100km/h, Full Load

Operation Test Results - Levitation and Propulsion (Tested in 1992 on HSST-100S)

Fig. 8 shows the test result of a levitation gap fluctuation at 100km/h. Upper half oscillations are the output signal of gap sensors equipped on each module. The center line means a standard gap of 8mm and full scale values are +/- 4mm. The lower half are output signals of the current detector of the chopper. The scale is 0-100A. We can see that magnet gap fluctuation at 100km/h is less than 4mm and the vehicle can run without contact to the rail. The RMS average of the magnet gap proved to be less than 1mm.

Fig. 9 shows propulsion and braking behavior of the vehicle. We can see the general running pattern of the vehicle from this figure. In this case the vehicle started from the west end of the track. Acceleration becomes 5km/h/s at 2 seconds after starting. It begins to decrease at 10 seconds after starting with 50km/h of velocity where trolley current begins to decrease on account of VVVF voltage saturation. The vehicle speed reaches 100km/h at the 500m (35 seconds) point. This location is the bottom of the east downhill because, just prior to the top speed, the on-board accelerometer maintains constant acceleration while the velocity derivative acceleration shows a sharp increase. Braking is engaged just after top speed. Deceleration is maintained at 4.8km/h/s until the car stops at 900m (55 seconds) point. During the braking mode, trolley current flows in a negative direction which means regenerative braking, however it soon comes to a positive direction (power feeding braking) and, at last, zero when the vehicle stops. Hydraulic brake pressure rises at this moment which means the braking function changes from deceleration to parking.

FUTURE PROSPECT OF HSST

The HSST's basic feature is contactless running. As a result, it has many advantages over conventional railway systems. Fig. 10 summarizes these features of HSST. Low noise emission, low inner and outer vibration - in short, outstanding adaptability to the environment seems to be the most remarkable feature of the HSST when we consider the latest social conditions.

A magnetic suspension train is being developed also in Germany and Korea. In Japan, the JR group is developing another type of vehicle system with superconducting magnetic suspension. We believe that such a tendency is in accordance with the social needs for better quality in transport [4].

Currently, HSST has some projects of practical operation. Domestic projects are in Oofuna, Nagoya and Hiroshima, etc. Overseas projects are in the U.S.A., Mexico and Brazil, etc. They are under investigation at this time. We hope we will be able to inform you of the first practical application of HSST very soon.

Type	Normal Conducting and Attractive
Core Material	Mild Steel
Pole Width	28 mm
Pole Length	616 mm
Coil Material	Electric Aluminum
Coil Turn	304T
Rated Air Gap	8 mm
Attractive Force	625 kg (per one magnet)
Weight	65 kg (per one magnet)

Table 1 Levitation Magnet of HSST-100

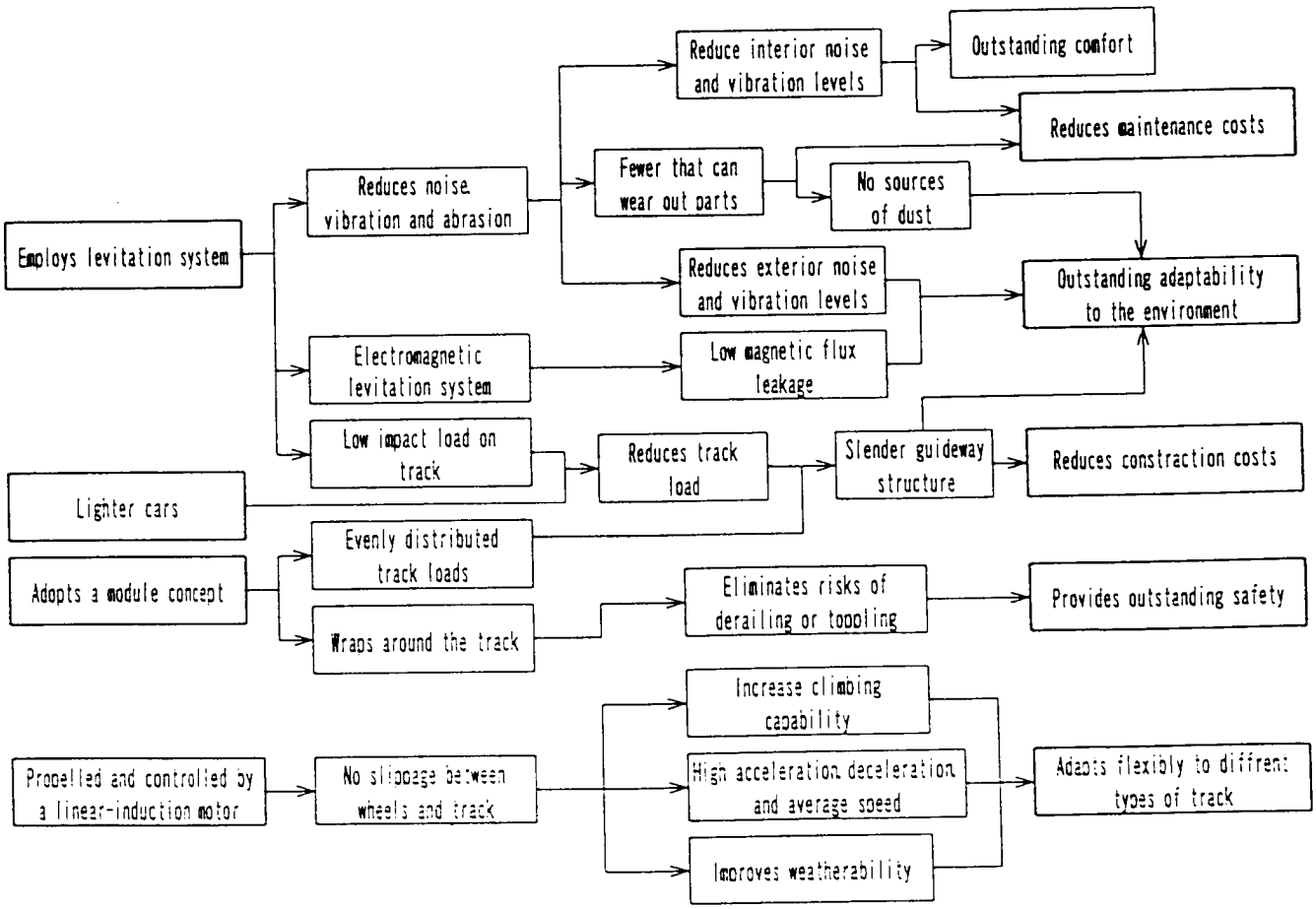

Fig.10 Special Features of the HSST system

REFERENCES

[1] E. Masada, "Development of Maglev and Linear Drive Technology for Transportation in Japan," Maglev '95, Bremen

[2] T. Seki, "The Development of HSST-100L", Maglev "95, Bremen

[3] J. E. Paddison, "Comparison of the Suspension Design Philosophies of Low Speed Maglev Systems," STECH '96, Birmingham

[4] HSST Development Corporation, Internet Homepage http://www.jalgroup/gr/HSST/index.htm

Session 2 -- Controls 1

Chairman: Atsushi Nakajima
National Aerospace Laboratory (NAL)

TWO DIMENSIONAL DRIVE MOTOR WITH CIRCULAR CORE

N. Fujii and T. Kihara
Dept. of Electrical and Electronic Systems Eng., Kyushu University
Fukuoka, 812-81, Japan

SUMMARY

A surface induction motor is described that has smooth force for any directional drive including rotation, compared with other surface motors. This motor has a toroidal core with an armature winding as a primary member, and a secondary reaction plate composed of a conducting plate and a back iron plate. The thrust and normal force characteristics are studied by using a test facility and two-dimensional electromagnetic analysis. This surface motor has a relatively high utilization factor for the thrust in spite of the circular shape. Compared with a single-sided linear induction motor, the performance of the magnetic circuit is the same or better, and the thrust is larger than that of two linear motors in a relatively small number of slots of the primary core. The large attractive normal force is suitable for magnetic suspension making use of the circular shape.

INTRODUCTION

Some motors called surface motors or planar motors for two-dimensional drive are being developed [1]-[3]. The authors have proposed the surface induction motor with a toroidal core as a primary core [4]. The secondary member is composed of a flat conducting plate with no directional qualities and a back iron plate as a secondary yoke. The primary member is composed of a toroidal core and armature winding which can be supplied current in every coil. Two types can be used for the method of armature winding; one of which is a ring winding supplied current at each slot and another of which is a double-layer winding supplied current to each coil.

In this paper, the basic structure of surface motors and the simple type surface motor are shown respectively including the circuit for power supply. The thrust and normal force characteristics for linear motion are shown at standstill by using two-dimensional electromagnetic analysis [5], which are confirmed by experimental results. Characteristics for typical examples for current supply to the winding are studied for both double-layer winding type and ring winding type. To estimate the performance of the surface motor, it is compared with a single-sided linear induction motor. The effects of the thickness of conducting plate and the length of air gap are studied respectively. The distribution of normal force density is studied for the use of the magnetic levitation.

STRUCTURE AND WORKING PRINCIPLE OF THE SURFACE MOTOR

Figure 1 shows a schematic diagram of the surface induction motor. This motor has a toroidal core with armature winding as a primary member, and a secondary reaction plate composed of a conducting plate and back iron plate. In the figure the primary core is placed under the secondary plate to use the attractive normal force for magnetic levitation. The armature winding is supplied current in every coil in each slot for any directional motion. Two types of winding methods as shown in Figure 2 are conceivable. Figure 2(a) shows the (Gramme) ring winding. Figure 2(b) shows a double-layer winding as well as an ordinary axial-air-gap-type rotating motor.

The ring winding is a suitable method based on the operational principle of this surface motor although this winding is difficult to make. For rotating motion, all coils are used for ordinary rotating magnetic field in the same way as a rotating motor as seen in Figure 3(a). For linear motion, the winding is separated into two groups over each half of toroidal core for the axis of linear motion, then a partial traveling magnetic field is generated in every winding group as shown in Figure 3(b). In practical use, all windings will be supplied current for larger force even for a linear drive.

A conventional double layer winding also can be used, but each coil is supplied power independently. Figure 4 shows a sample of supply method of current for a linear motion. There is an overlap region of both windings around the axis of linear motion.

Figure 5 shows a basic power supply circuit for the surface motor with ring winding. Figure 6 shows a basic inverter circuit for the surface motor with double layer winding. The supplied power is controlled for each coil.

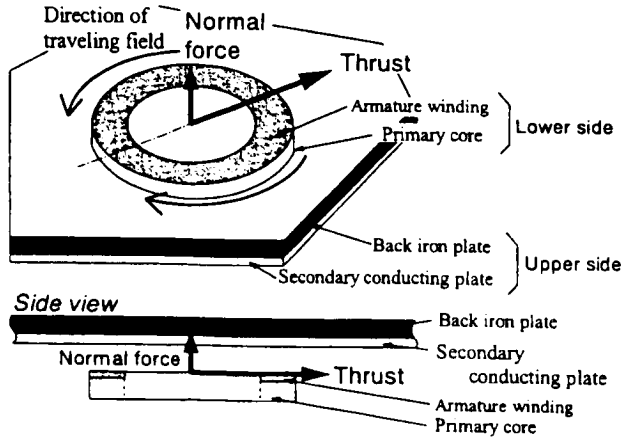

Fig. 1 Proposed surface induction motor.

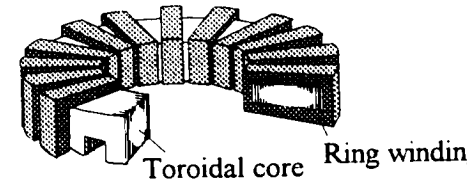

(a) Ring winding type

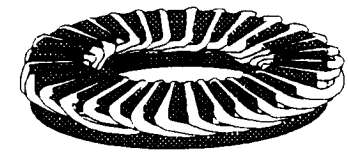

(b) Double-layer winding type

Fig. 2 Primary member of the surface motor.

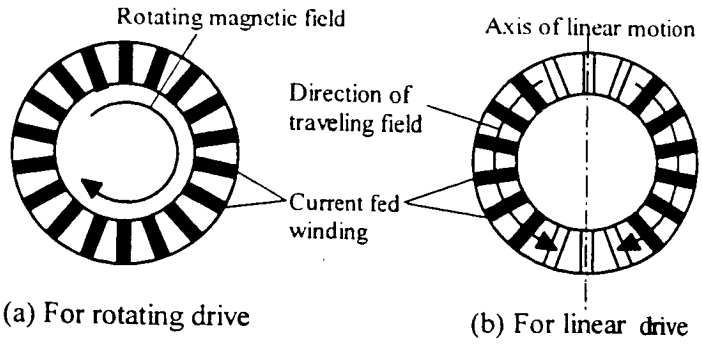

Fig. 3 Current supply method to armature windings.

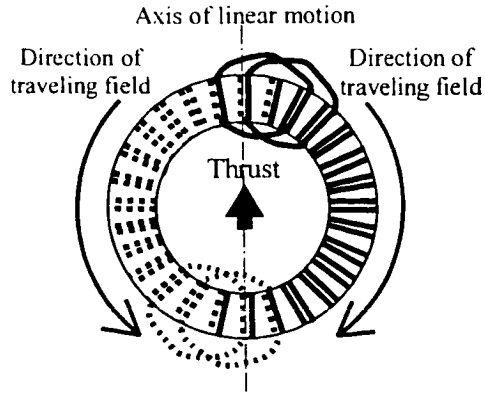

Fig. 4 Current supply method for double-layer winding type.

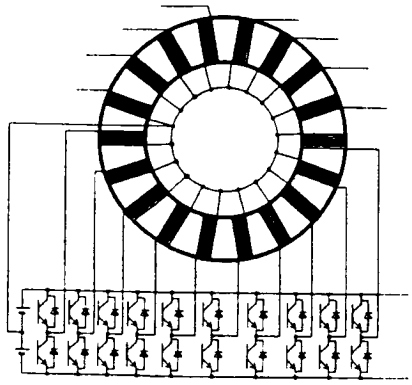

Fig. 5 Basic inverter circuit for the ring winding type.

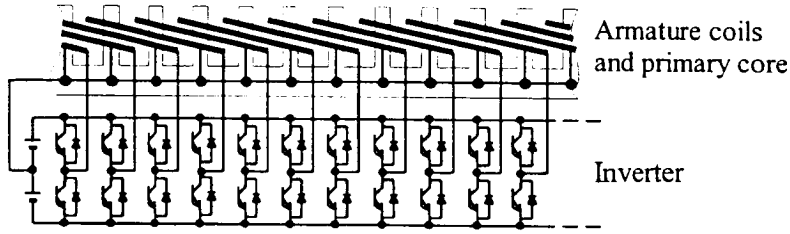

Fig. 6 Basic inverter circuit for the double-layer winding type.

Simple Type Surface Induction Motor

By limiting the two functions of the linear drive as fixed direction translation and rotation, the simple forms are obtained as shown in Fig.7. The simple type has two groups of ordinary three-phase windings. In Figure 7(a), the current is supplied to two groups of windings from two inverters respectively, and each traveling field can be controlled individually. Figure 7(b) shows the method of supply by one inverter using a three-phase sequence changeover switch. For linear motion, each winding is excited to generate the different direction of traveling magnetic field, and for rotation the two groups of windings are excited to generate the rotating field over all.

Figure 8 shows the simple type surface motor with four groups of three-phase armature windings. Two groups of windings, related by diagonal position to each other, are connected. This type is also supplied three-phase current by two inverters to the two electrical groups of windings. For forward motion, the traveling field in each winding is generated in the direction

shown in Figure 8(a). The necessary traveling field for the transverse motion is obtained by the change of only the three-phase sequence of Inverter A, as shown in Figure 8(b). For the diagonal motion, the current is supplied from only one inverter, as shown in Figure 8(c).

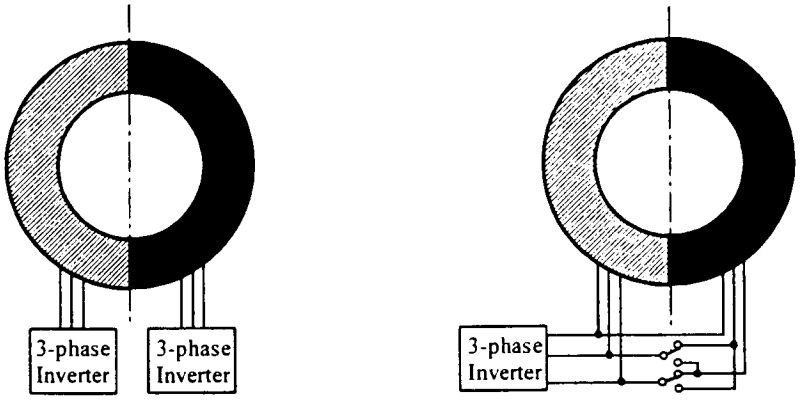

(a) Two inverters configuration (b) One inverter configuration

Fig. 7 Simple type for one direction linear motion and rotating motion.

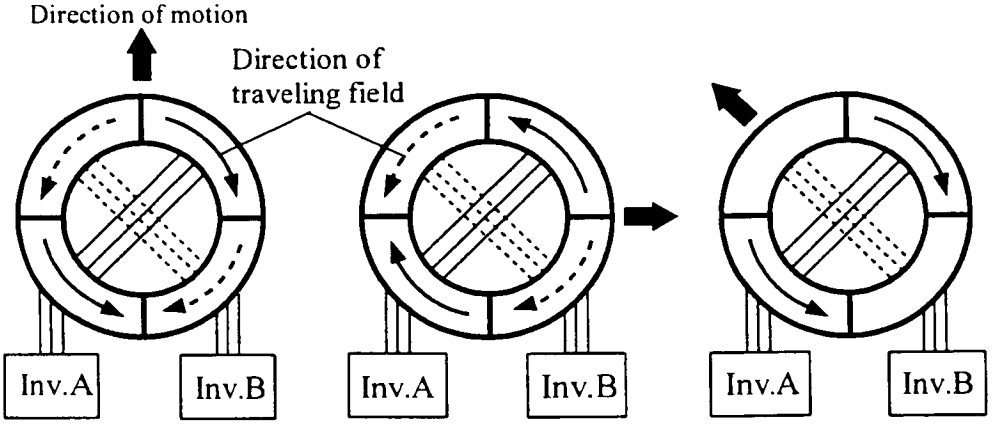

(a) For forward motion (b) For transverse motion (c) For diagonal motion

Fig. 8 Simple type for three directions of linear motion.

NUMERICAL EXAMPLE AND ARRANGEMENT OF WINDING

This paper deals with the surface induction motor of the test facility. The number of slots is 24, and other detailed parameters are shown in Table 1. A three-phase supply is assumed for the armature winding. There are many different supplies for current. Figure 9 shows four examples of current supply to each coil for linear motion in the case of double-layer winding. Here the arrangement is expanded to a linear model. The name S4 means that the axis of linear motion is at the center of a slot and the coil arrangement is four poles per one-side winding. T3 means that the axis of linear motion is at the center of a tooth and the current-fed coil arrangement is three poles per one-side winding. In S4 and T4, right-side winding is marked by the gray color in order to clear the boundary.

Table 1 Numerical example for the surface motor.

Name	Numerals
Primary core	
Av. Diameter of core	D_a = 120mm
Width of core	h = 25mm
Height of core	d_c = 53mm
Width of tooth	w_t = 9.5mm
Width of slot	w_s = 6.5mm
Number of slots	N_s = 24
Armature windings	
Turns / coil	N_t = 69turns
Turns / slot	138 turns
Secondary	
Material of conducting plate	Copper
Thickness of the conductor	d_2 = 2mm
Thickness of back iron	d_1 = 5mm

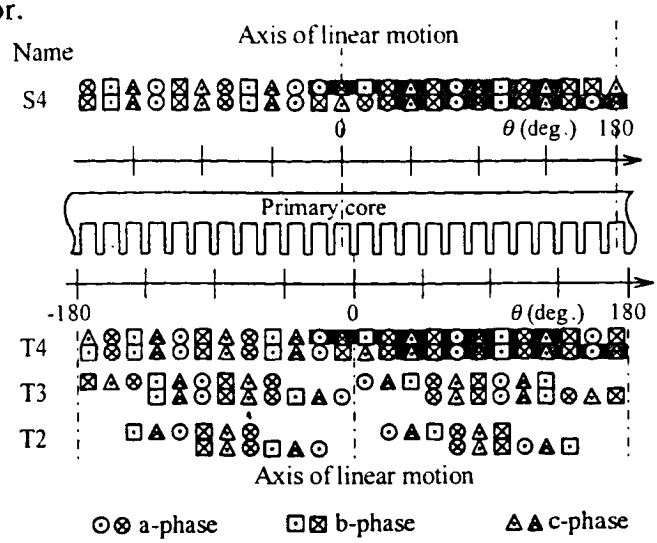

Fig. 9 Examples of three-phase current supply to each coil for linear motion.

CHARACTERISTICS OF THE SURFACE MOTOR

The following calculated values were obtained by using two-dimensional electromagnetic analysis using Fourier Series of surface current for the winding [5].

Flux Density Distribution

Figure 10 shows the distribution of magnetic flux density on the surface of the primary core in the direction of circumference for the case of type S4 without secondary plate. The measured values were obtained by using a Hall element. It is confirmed that the number of poles is four per one side. Large ripples appear in the distribution because of slot harmonics. The calculated values agree with the measured values.

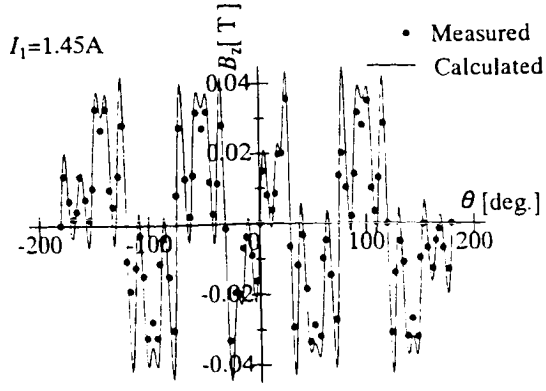

Fig. 10 Flux density distribution.

Figure 11(a) and Figure 11(b) show the thrust and the normal force characteristics respectively at standstill for linear drive operation for type S4. The condition is that the coil current is fixed at 2.5A and the air gap between the primary core and the secondary conducting plate is 1mm. The calculated values agree with the measured values. The thrust of more than 98% of the maximum thrust is obtained in the frequency range from 24Hz to 38Hz. The normal force is an attractive force between the primary core and secondary plate. The normal force decreases largely as frequency increases. The value of normal force varies from 25.9N to 17.0N in the frequency range of 24Hz to 38Hz. The ratios of the normal force to the thrust are 4.16 at 24Hz and 2.72 at 38Hz respectively. The ratio of the surface motor is generally larger than that of linear induction motor.

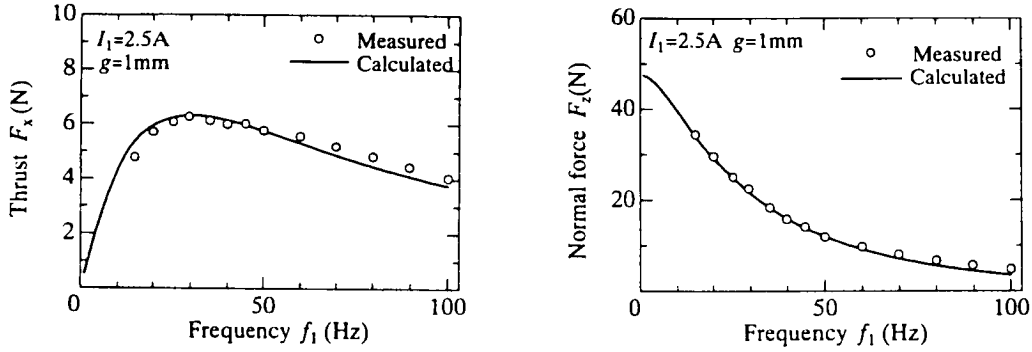

(a) Thrust (b) Normal force

Fig. 11 Thrust and normal force versus frequency for type S4 at standstill for linear drive.

Figure 12 shows the force characteristics as functions of frequency for type T4, T3 and T2. In the thrust characteristics shown in Figure 12(a), the maximum thrust of T2 with two poles is about 1/2 of that of T4 with four poles in spite of different utilization factors for thrust. The maximum thrusts per one pole for T4, T3 and T2 are 1.67N, 1.81N and 1.69N respectively. That is, T4 is a worst case from the standpoint of utilization for thrust because of the circular core. In T2, it is a worst case for the arrangement of winding because of the large single-layer region. In the normal force in Figure 12(b), the attractive forces at 30Hz for T3 and T2 are 0.71 and 0.41 times respectively as large as that of T4.

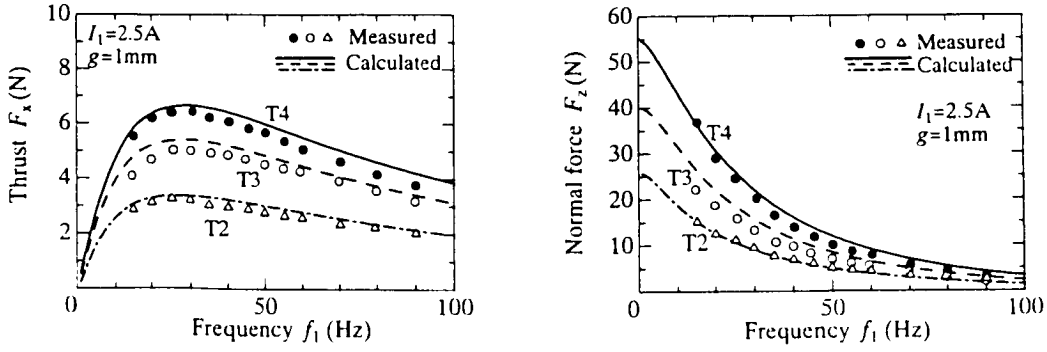

(a) Thrust (b) Normal force

Fig. 12 Force – frequency characteristics for type T4, T3 and T2 respectively.

Figure 13 shows force characteristics as functions of current for type T4, T3 and T2. In Figure 13(a), the thrust increases in proportion to the square of current in this range. In the normal force shown in Figure 13(b), there is a quantitative difference between the calculated values and measured values because magnetic saturation is not considered in the analysis.

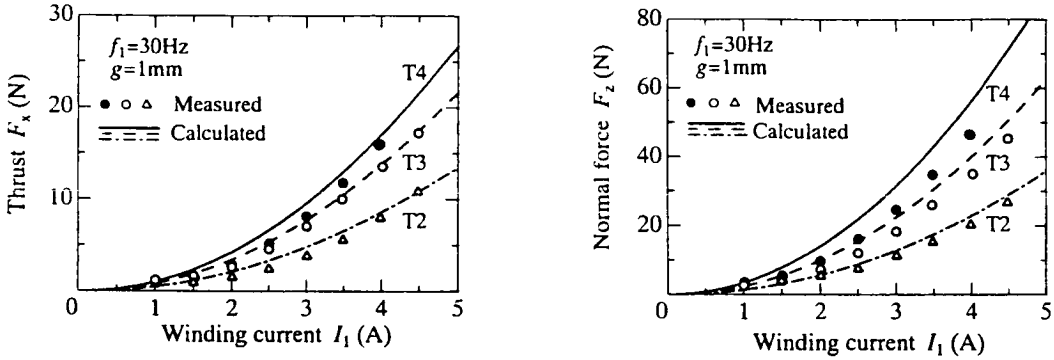

(a) Thrust (b) Normal force

Fig. 13 Force – current characteristics for type T4, T3 and T2 respectively.

This surface motor has two kinds of axes of linear motion, that is, one expressed by type S is at the center of slot and the other expressed by type T is at the center of tooth. Figure 14 shows the comparison the forces of type S4 and T4. In both thrust and normal force, the forces of S4 and T4 are almost equal. This is desirable because the force does not vary with the direction of motion.

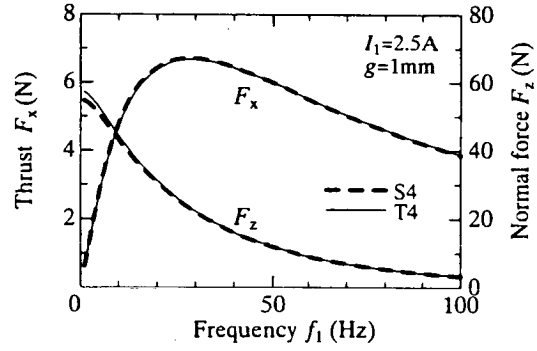

Fig. 14 Comparison between the forces of type S4 and T4.

Evaluation of the Thrust

Figure 15 shows the calculated utilization factor defined as a ratio of the thrust F_x to the tangential force F_t. The utilization factors for T4, T3 and T2 at 30Hz that gives maximum thrust are 74%, 83% and 90% respectively.

Figure 16 shows the ratio of thrust of the surface motor and that of single-sided linear induction motor as functions of total number of slots. The conditions are that the magnetomotive force of each coil, the slot pitch and the pole pitch are fixed at the values shown in Table 1 respectively for the double-layer winding. For two-dimensional motion using a conventional linear motor, four linear

motors would be generally used, with two parallel motors used for every x- or y- directional motion. The solid line shows the ratio of thrust of the surface motor T4 to the total thrust of two linear motors with core length of half circumference of the toroidal core. The broken line shows for one linear motor with the length of circumference of the toroidal core. The thrust of the surface motor is larger than that for two linear motors in the number of slots 24 or less in spite of circular core because all slots are used effectively.

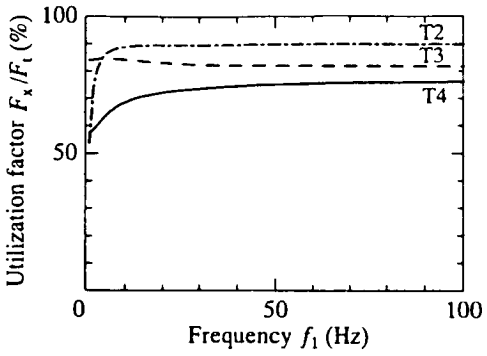

Fig. 15 Utilization factors of thrust for T4, T3 and T2 respectively.

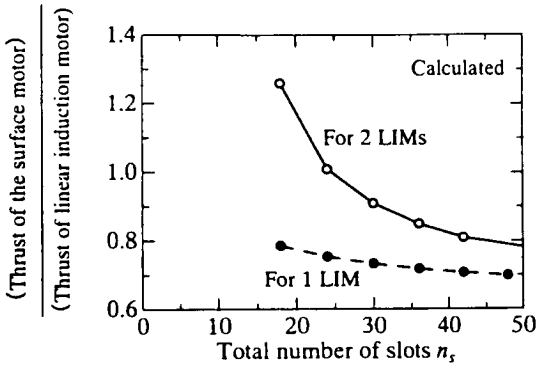

Fig. 16 Comparison between thrust for the surface motor and linear induction motor.

Forces for the Surface Motor with Ring Winding

Figure 17(a) and 17(b) show the thrust and the normal force of the surface motor with ring winding respectively. The parameters are those of Table 1, the number of turns per coil is 138, equal to the number of turns per a slot in this case. RT4, RT3 and RT2 mean 4-pole, 3-pole and 2-pole supply of current respectively in the ring winding type. That is, all 24 coils are used for RT4 and 12 coils are used for RT2. The maximum thrusts of RT3 and RT2 are 0.84 times and 0.61 times of that of RT4, these ratios are larger than those for double-layer winding in Figure 12(a). The normal forces at 30Hz for approximately maximum thrust of RT3 and RT2 are 0.70 times and 0.46 times of that of RT4, these ratios are almost equal to those for double-layer winding in Figure 12(b).

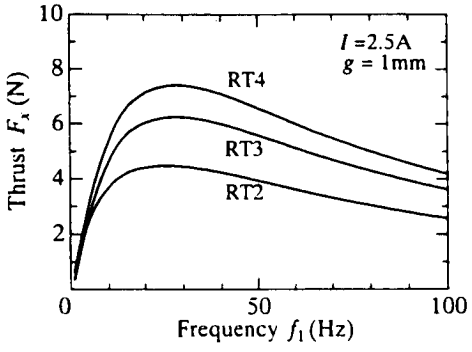

(a) Thrust

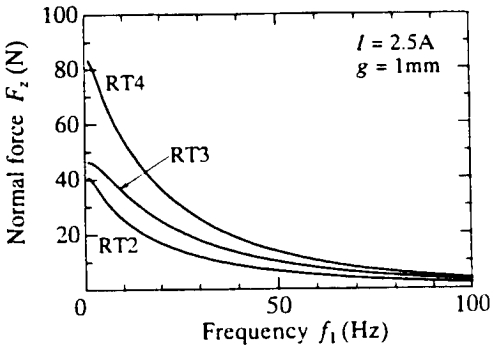

(b) Normal force

Fig. 17 Force characteristics of the ring winding type surface motor with 4-pole, 3-pole and 2-pole respectively.

Figure 18 shows the comparison between the forces of the double-layer winding type T4 and the ring winding type RT4.The ring winding type has about ten percent larger force for the maximum thrust and for the normal force at 30Hz respectively compared with the double-layer winding type.

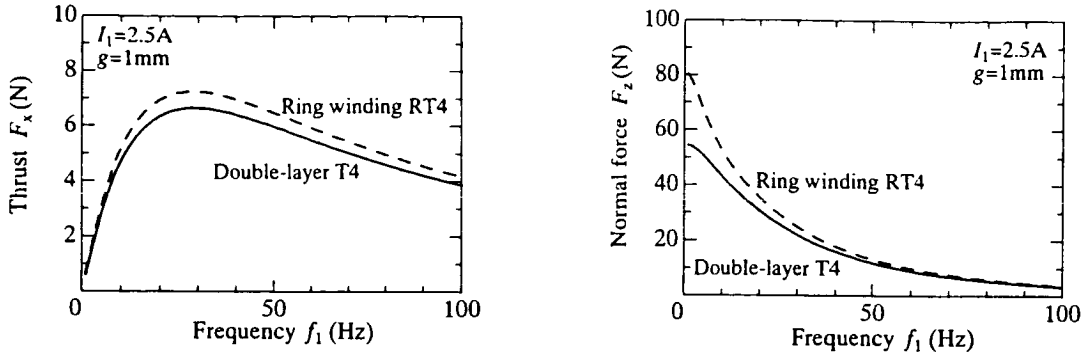

(a) Thrust (b) Normal force

Fig. 18 Comparison between forces of the double-layer winging type and the ring winding type.

Effect of Thickness of Conducting Plate

Figure 19 shows the effect on the thrust and the normal force of the thickness of copper plate as a secondary conducting plate. The conditions are that the supply current is fixed at 2.5A in the type T4, the conductivities of copper and back iron are 5.273×10^7 S/m and 9.524×10^6 S/m respectively. The frequency at the maximum thrust for each thickness d_2 increases as the thickness decreases because the secondary resistance increases. The extreme value for maximum thrust is obtained at the conductor thickness of 0.5mm, as shown in Figure 19(a). The normal force increases as the conductor thickness decreases, as shown in Figure 19(b). The ratio of thrust to normal force for each conductor is approximately proportional to the frequency, as shown in Figure 19(c). The ratios for d_2 = 2mm and d_2 = 0.5mm at maximum thrust are 0.30 and 0.16 respectively.

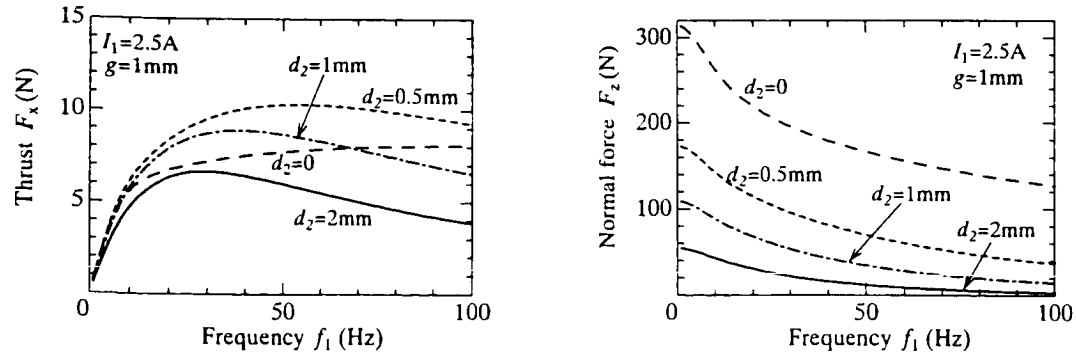

(a) Thrust (b) Normal force

Fig. 19 Forces for various thickness of conducting plate.

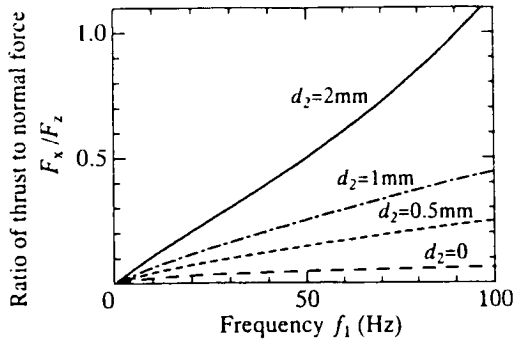

(c) Ratio of thrust to normal force

Fig. 19 Forces for various thickness of conducting plate.

Effect of Length of Air Gap

Figure 20 shows the effect on the thrust and the normal force of type T4 of the length of air gap. The current is fixed at 2.5A. The frequency at maximum thrust for each air gap increases about 5Hz each as the air gap decreases by 0.5mm, because the magnetizing reactance decreases. The maximum thrust at each air gap is 1.21 times for g=0.5mm, 0.86 times for 1.5mm and 0.61 times for 3mm compared to that for g=1mm, as shown in Figure 20(a). The effect of length of air gap on the normal force is larger than that on thrust, as shown in Figure 20(b). The normal force at each maximum thrust is 1.48times for g=0.5mm, 0.72times for 1.5mm and 0.33times for 3.0mm compared to that for g=1mm. The ratio of thrust to normal force is almost independent on the air gap in the frequency 40Hz and less, and is proportional to frequency as shown in Figure 20(c).

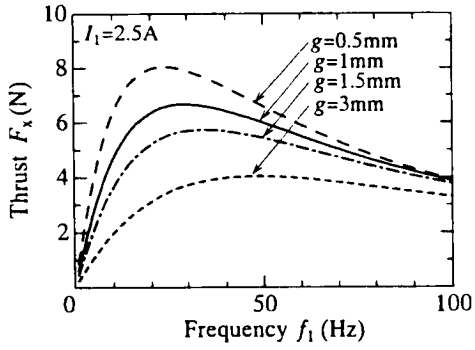

(a) Thrust

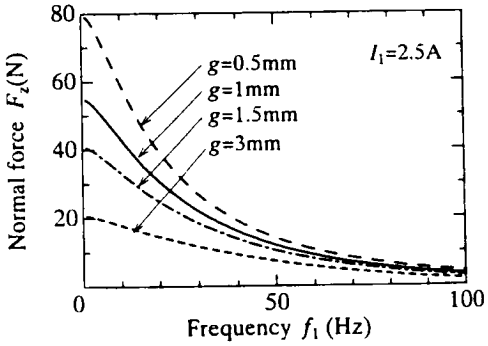

(b) Normal force

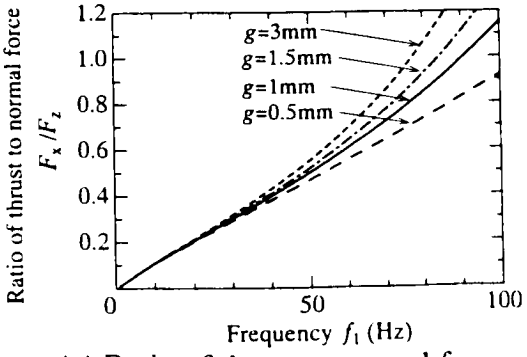

(c) Ratio of thrust to normal force

Fig. 20 Forces for various air gap

Distribution of Normal Force Density

To use the large attractive type normal force for magnetic levitation , since this shape is suitable for stable suspension, the distribution of force density is studied. Figure 21(a), 21(b), 21(c) and 21(d) show the space distributions in the circumferential direction of the normal force of type S4,T4 T2 and RT4 respectively for the linear motion. The axis at $\theta = 0$ is the front end of motion on the axis of linear motion, and $\theta = \pm 180°$ is the rear end of traveling field on the axis of linear motion. All coils are supplied the same current of 2.5A. There is a difference between the distributions around the axis of linear motion for S4 shown in Figure 21(a) and T4 shown in Figure 21(b) because of the interference between two winding groups. In the case of a two-pole supply, there is no interference as shown in Figure 21(c). In the ring winding, the ripple appears in the distribution because of the influence of alternating magnetic field. In all types, the normal forces for right-side and left-side of the axis of motion are in equilibrium.

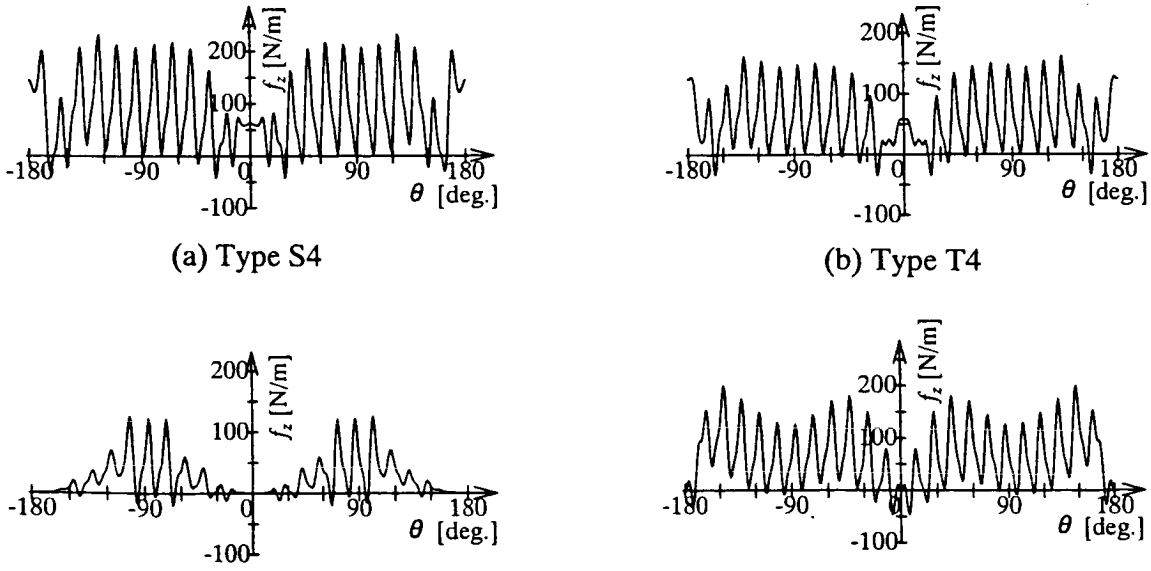

(a) Type S4

(b) Type T4

(c) Type T2

(d) Type RT4

Fig. 21 Distribution of normal force density in circumference direction in the case of linear motion.

Figure 22(a) and 22(b) show the distribution of the tangential force and the normal force respectively for every region of 30 degrees. In the tangential force, from which the thrust is produced, the force distribution around the middle of each group of winding is uniform for the double-layer winding S4 and T4. The tangential force distribution of ring winding is not uniform because of alternating field. On the other hand, the attractive normal force around the front end $\theta = 0$ is smaller than that around the rear end $\theta = \pm 180°$ in all types, as shown in Figure 22(b). Some technique will be required for the magnetic levitation.

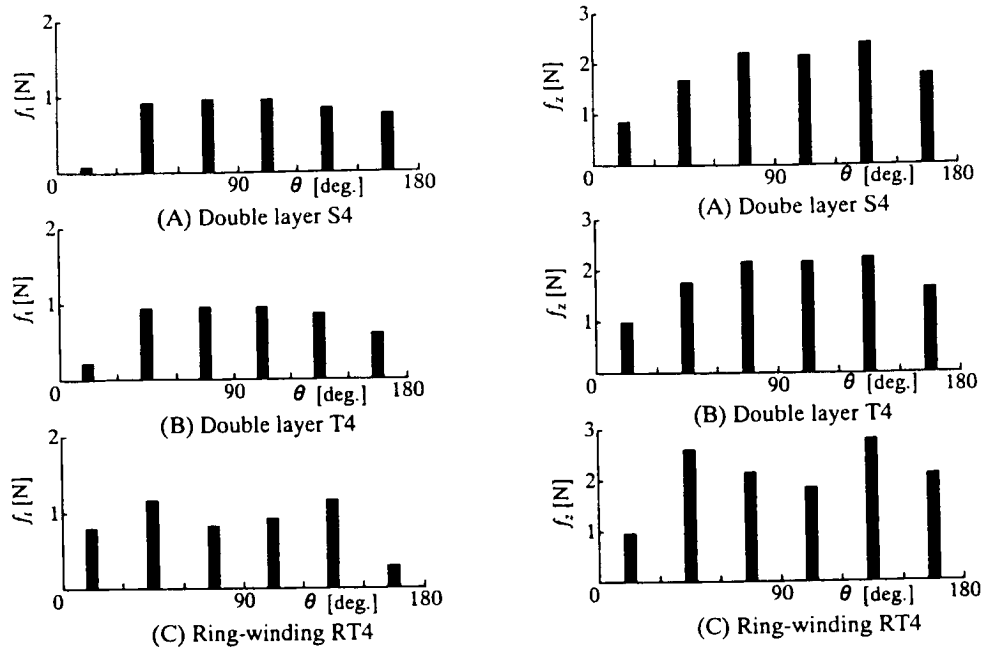

(a) Tangential force (b) Normal force

Fig. 22 Distribution of force for every region of 30 degrees.

CONCLUSIONS

This surface induction motor has the following good characteristics, although the driving circuit is complicated.

1. The quality of the magnetic circuit is the same or better compared with that of a linear induction motor.
2. This surface induction motor has a relatively high utilization factor of 74% or more for thrust in spite of a circular core.
3. The thrust is larger than that for two linear motors with length of semicircle of the toroidal core in relatively small number of slots 24 or less.
4. There is little difference in thrust and normal force for any directional motion.
5. As the ratio of normal force to thrust is large, the attractive normal force should be used for magnetic suspension making use of the circular shape.

ACKNOWLEDGMENT

This study has been supported partially by the Grant-in-Aid for Scientific Research (B) from the Ministry of Education, Science, Sports and Culture of Japan.

REFERENCES

[1] Y. Ohira, Y. Yamamoto, K. Takeuchi, H. Yamada: "Magnetic Circuit Analysis of X-Y Linear Induction Motor", Trans. IEE of Japan, Vol.109-D, pp.675-681 (1989)

[2] D. Ebihara, T. Watanobe, M. Watada: "Approximated Three-dimensional Analysis of Stepping Surface Motor", Trans. IEE of Japan, Vol.114-D, pp.1235-1241 (1994)

[3] D. Trumper, W. Kim, M. E. Williams: "Design and Analysis Framework for Linear Permanent-Magnet Machines", IEEE Trans. on IA, Vol.32 pp.371-379 (1996)

[4] N. Fujii, K. Nishimura, Y. Imazu: "Surface Induction Motor for Two-dimensional Plane Drive Including Rotating Operation", National Convention Record IEE Japan - Industry Application Society, No.211, pp.899-903 (1994)

[5] N. Fujii, T. Kihara, M. Fujitake: "Electromagnetic Analysis of Surface Induction Motor", IEE of Japan Technical Meeting on Linear Drives, LD-97-51, pp.33-38 (1997)

A DESIGN AND CHARACTERISTICS OF SWITCHED RELUCTANCE TYPE BEARINGLESS MOTORS

Masatsuga Takemoto, Ken Shimada, Akira Chiba
Chiba Laboratory, Department of Electrical Engineering
Faculty of Science and Technology,
Science University of Tokyo

Tadashi Fukao
Tokyo Institute of Technology

SUMMARY

Switched reluctance type bearingless motors have been proposed. The principle of radial force generation is explained on a stator with differential winding configurations. The radial force is a function of the radial force winding current and the motor current, as well as the rotor rotational position. If salient poles are unaligned, the radial force is the minimum. In this condition, fringing fluxes play an important role. In this paper, the theoretical equations of radial forces are derived with a close examination of the flux distribution. Based on results of FEM analysis, a simple mathematical equation is proposed to express fringing fluxes neglecting magnetic saturation. The radial force and current relationships are derived with the fringing effects. The derived equations are found to be effective especially at unaligned positions.

I. INTRODUCTION

Recently, various bearingless motors have been proposed, for example, reluctance [1], induction [2-4], permanent magnet [5-6], etc. These motors each have nice characteristics of their own. Recently, there has been interest in switched reluctance motors. For very special environments, switched reluctance motors have superior possibilities, because switched reluctance motors have several advantages such as fail safe, rotor robustness, low cost and possible operation in high temperatures or at high rotational speeds [7-8].

Moreover, switched reluctance motors have nice possibilities as bearingless motors. In principle, torque is generated by magnetic attraction of rotor and stator poles. In this process, significant amounts of radial force are generated. Thus, in practice, switched reluctance motors are famous for noises and vibration because fairly high radial force is exerted in the air-gaps. It is very possible to take advantage of these high radial forces for bearingless motors.

Switched reluctance motors have a stator with concentric windings around salient poles. Thus, if currents in the concentric windings of each pole are controlled independently, both radial force and torque can be controlled. To the author's best knowledge, this idea was originally proposed by Prof. Higuchi [9] in 1989. The same idea can also be seen in [10]. The ideas are good for only low rotational speed motors such as torque drives and positioning drives. In the case of power conversion, rotational speeds are high so that motor back E.M.F. is high. Thus, it is unavoidable to increase the voltage ratings of drive inverters to have fast control of radial forces. In practice, voltage and current ratings of drive inverters should be minimized to be cost competitive. Then, instantaneous current control is difficult at high rotational speeds. The current control can be fast enough for torque control; however, it cannot be fast enough for radial force control required in magnetic suspension.

Professor Higuchi also proposed a stepping motor with magnetic suspension windings [11]. His idea took advantage of the multi-pole per stator tooth configuration in variable reluctance motors. Radial force is not influenced by motor current due to having several poles for a stator tooth. This motor is good for positioning drives as he proposed, however, not for power conversion because of many poles, high inductance as well as high leakage fluxes. For power conversions, switched reluctance motors have stator and rotor combinations of 12/8, 8/6, or 6/4, with only one pole for a tooth.

It is important to apply recent ideas of differential windings of bearingless motors to switched reluctance motors to be practical and reduce voltage and current required for magnetic suspension. A stator winding configuration with differential windings for switched reluctance motors with one pole for a stator tooth has been proposed by the authors [12]. Principles of radial force production were explained. The relationships between radial force and current were found to be dependent to rotor rotational positions unlike Prof. Higuchi's [11]. If rotor and stator poles are aligned, radial force is effectively produced. However, radial force is low at unaligned positions. For successful magnetic suspension, radial force must be controlled at any rotational position. Successful control can then be realized by integrated digital controllers. Thus, analysis of unaligned positions is very important.

In this paper, effects of fringing fluxes are examined using FEM analysis. Then, a simple mathematical equation is proposed for further analysis. Relationships between radial force and current around unaligned positions are derived. These relationships are confirmed in experiments.

II. PRINCIPLES OF PROPOSED MACHINES

A. Configuration of a stator core and windings

Fig. 1 shows a cross section of stator and rotor cores on a prototype machine. The iron cores of a stator and a rotor are made up of laminated silicon steel which is simply stamped out to salient pole form. The laminated silicon steel has a thickness of 0.35mm. The stack length is 50mm. It is noted that the stator has 12 poles and the rotor has 8 poles.

Fig. 2 shows the A-phase winding configuration. The motor winding current i_{ma} flows into four coils connected in series. One coil is three paralleled wires having a diameter of 0.8mm and 14 turns in series. On the other hand, radial force winding currents i_{sa1} and i_{sa2} flow into two coils, respectively. These coils are separately wound around each stator tooth. These coils are two paralleled wires having a diameter of 0.8mm and 11 turns in series. The B-phase winding configuration is situated on one third rotational position of the A-phase. The C-phase winding configuration is situated on two thirds rotational position of the A-phase. The axes a_1 and a_2 of a perpendicular coordinate can be defined based on the A-phase winding configuration. In this case, the axes α and β are aligned with a_1 and a_2, respectively. In addition, the axes of coordinates b_1, b_2, c_1 and c_2 can be defined based on the B- and C-phase windings, respectively.

B. Principles of radial force generation

Fig. 3 shows the principles of radial force production of the proposed bearingless motors. Stator teeth and rotor teeth of this figure are situated in the aligned position. The symmetrical 4-pole fluxes are produced from the 4-pole motor winding current i_{ma}. These thick solid lines show the instantaneous flux direction of the 4-pole magnetic field at a certain moment. The symmetrical 2-pole fluxes are also generated from 2-pole radial force winding current i_{sa1}. These broken lines show the instantaneous flux direction of the 2-pole magnetic field for radial position control.

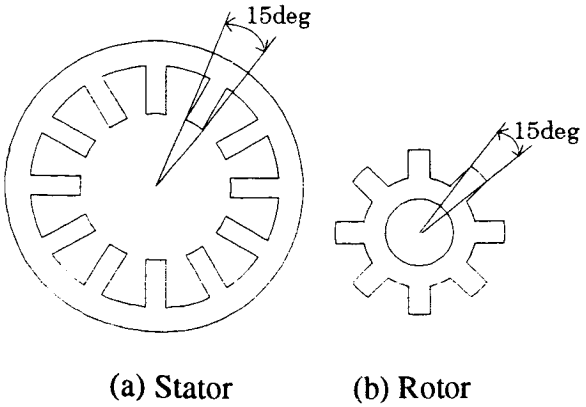

(a) Stator (b) Rotor

Fig. 1 Cross section of a prototype machine.

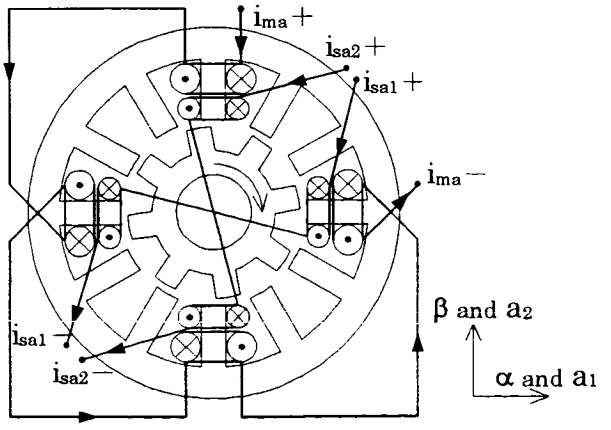

Fig. 2 A-phase winding configuration.

The rotor radial position control with a negative feedback loop can be explained as follows. If the rotor moves toward the negative direction in the α-axis from the stator center, the flux distribution in the air-gap is unbalanced. A radial force toward the negative direction in the α-axis is generated. In order to balance with this force, a positive current i_{sa1} is fed in the 2-pole radial force winding, which produces the 2-pole fluxes as shown in Fig. 3. Therefore, the flux density in the air-gap 1 is increased, because the direction of the 2-pole fluxes is the same as that of the 4-pole fluxes. On the contrary, the flux density in the air-gap 2 is decreased, as the direction of the 2-pole fluxes is opposite to that of the 4-pole fluxes. This superimposed magnetic field results in the radial electromagnetic force F acting to the rotor in the α-direction.

On the other hand, a radial force opposite to the α-direction can be produced with a negative current i_{sa1} in the 2-pole radial force winding. Moreover, a radial force in β-direction can be produced by 2-pole radial force winding current i_{sa2}. Thus, radial force can be produced in any desired direction.

The above is the case of A-phase, in the same way, this principle can be applied to the B- and C-phase. The direction of a radial force on the B- and C-phase differs from that on the A-phase. Therefore, transformation of coordinates is required. In switched reluctance motors, all three phases are not excited at one moment. Rather, only one out of three phases is excited at a low speed. If at least one of three phases is excited, the radial force can be produced in any desired direction with the proposed winding configuration. It is noted that the air-gap flux density depends on the rotor rotational position. The stator and rotor poles are aligned in Fig. 3. High radial force can be produced in this condition, however, radial force is reduced at unaligned positions. At unaligned positions, fringing fluxes play an important role.

III. DERIVATION OF INDUCTANCES

A. Magnetic equivalent circuit

Fig. 4 shows a cross section of a prototype machine superimposed by a magnetic equivalent circuit and each phase winding configuration. Voltage sources show magnetomotive forces (MMFs) of the 4-pole motor windings and the 2-pole radial force windings, in addition, permeances of air-gaps are expressed as resistances.

Fig. 5 shows a magnetic equivalent circuit only for the A-phase, which is extracted from Fig. 4. The definitions of Fig. 5 are as follows:

N_m number of turns of the motor winding.
N_b number of turns of the radial force winding.
i_{ma} an instantaneous current of the motor winding.
i_{sa1} an instantaneous current of the radial force winding on the a_1-axis.
i_{sa2} an instantaneous current of the radial force winding on the a_2-axis.
P_{a1}~P_{a4} permeances of air-gaps at A-phase winding poles.
ϕ_{a1}~ ϕ_{a4} magnetic fluxes of each tooth.

Only A-phase magnetic equivalent circuit is used to have a simple calculation in this paper. This is possible because switched reluctance motors have little mutual inductance among the A-, B-, and C-phases.

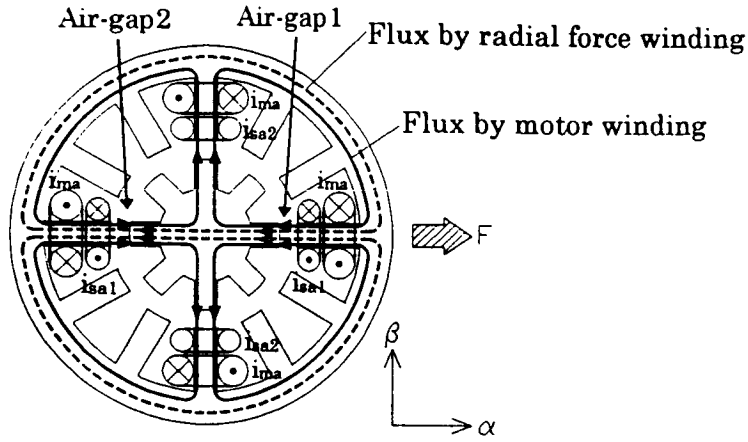

Fig.3 Principle of radial force generation.

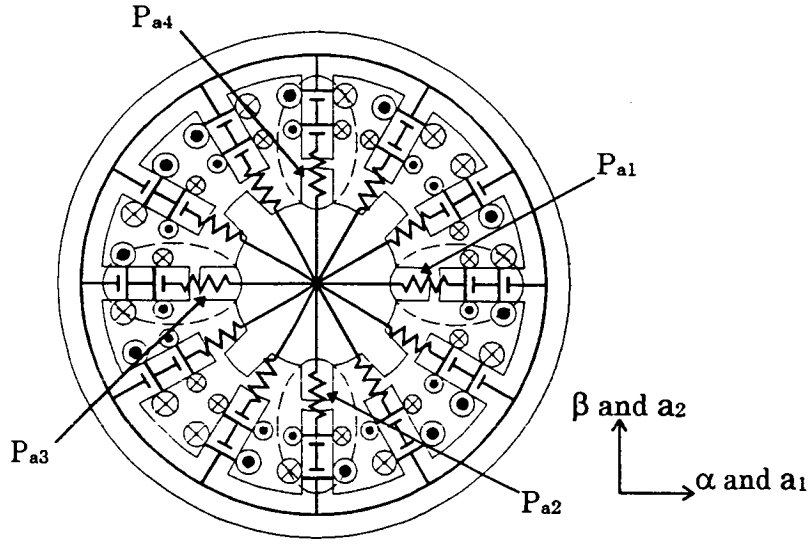

Thick solid lines : Magnetic equivalent circuit.
Broken lines : M.M.F. and permeance of A-phase.

Fig.4 Winding configuration and a magnetic equivalent circuit.

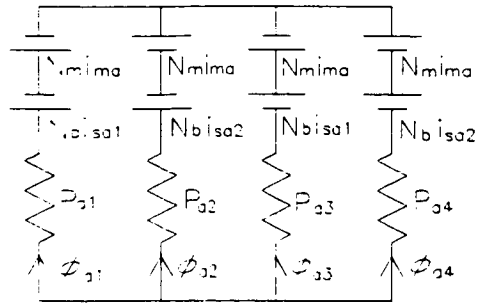

Fig.5 A magnetic equivalent circuit of A-phase.

The following equations (1)~(3) are given from Fig. 5, because a sum of the magnetomotive forces in each branch is equal to another one.

$$\frac{\phi_{a2}}{P_{a2}} - N_m i_{ma} + N_b i_{sa2} = \frac{\phi_{a1}}{P_{a1}} + N_m i_{ma} + N_b i_{sa1} \tag{1}$$

$$\frac{\phi_{a3}}{P_{a3}} + N_m i_{ma} - N_b i_{sa1} = \frac{\phi_{a1}}{P_{a1}} + N_m i_{ma} + N_b i_{sa1} \tag{2}$$

$$\frac{\phi_{a4}}{P_{a4}} - N_m i_{ma} - N_b i_{sa2} = \frac{\phi_{a1}}{P_{a1}} + N_m i_{ma} + N_b i_{sa1}. \tag{3}$$

Because a sum of the magnetic fluxes is equal to zero, it can be written as,

$$\phi_{a1} + \phi_{a2} + \phi_{a3} + \phi_{a4} = 0. \tag{4}$$

ϕ_{a1}~ϕ_{a4} can be derived from the equations (1)~(4) as,

$$\phi_{a1} = \frac{-P_{a1}}{P}\left[2N_m(P_{a2}+P_{a4})i_{ma} + N_b(P_{a2}+2P_{a3}+P_{a4})i_{sa1} - N_b(P_{a2}-P_{a4})i_{sa2}\right] \tag{5}$$

$$\phi_{a2} = \frac{P_{a2}}{P}\left[2N_m(P_{a1}+P_{a3})i_{ma} + N_b(P_{a1}-P_{a3})i_{sa1} - N_b(P_{a1}+P_{a3}+2P_{a4})i_{sa2}\right] \tag{6}$$

$$\phi_{a3} = \frac{-P_{a3}}{P}\left[2N_m(P_{a2}+P_{a4})i_{ma} - N_b(2P_{a1}+P_{a2}+P_{a4})i_{sa1} - N_b(P_{a2}-P_{a4})i_{sa2}\right] \tag{7}$$

$$\phi_{a4} = \frac{P_{a4}}{P}\left[2N_m(P_{a1}+P_{a3})i_{ma} + N_b(P_{a1}-P_{a3})i_{sa1} + N_b(P_{a1}+2P_{a2}+P_{a3})i_{sa2}\right] \tag{8}$$

where P is a sum of the permeances P_{a1}~P_{a4}.

Next, in order to calculate inductances, it is required to derive flux-linkages of each winding from the above equations. Consequently, the flux-linkage ψ_{ma} corresponding to motor winding current i_{ma} can be written from Fig. 5 as,

$$\psi_{ma} = (-\phi_{a1} + \phi_{a2} - \phi_{a3} + \phi_{a4})N_m. \tag{9}$$

Substituting the equations (5)~(8) into the equation (9) yields,

$$\begin{aligned}\psi_{ma} = {} & \frac{4N_m^2(P_{a1}+P_{a3})(P_{a2}+P_{a4})}{P} i_{ma} + \frac{2N_m N_b(P_{a1}-P_{a3})(P_{a2}+P_{a4})}{P} i_{sa1} \\ & - \frac{2N_m N_b(P_{a1}+P_{a3})(P_{a2}-P_{a4})}{P} i_{sa2}.\end{aligned} \tag{10}$$

Similarly, the flux-linkages ψ_{sa1} and ψ_{sa2} of the radial force windings can be written from Fig. 5 as,

$$\psi_{sa1} = (-\phi_{a1} + \phi_{a3})N_b \tag{11}$$

$$\psi_{sa2} = (-\phi_{a2} + \phi_{a4})N_b. \tag{12}$$

Substituting the equations (5)~(8) into the equations (11) and (12) yields,

$$\begin{aligned}\psi_{sa1} = {} & \frac{N_b^2\{P_{a1}(P_{a2}+2P_{a3}+P_{a4}) + P_{a3}(2P_{a1}+P_{a2}+P_{a4})\}}{P} i_{sa1} \\ & + \frac{2N_m N_b(P_{a1}-P_{a3})(P_{a2}+P_{a4})}{p} i_{ma} - \frac{N_b^2(P_{a1}-P_{a3})(P_{a2}-P_{a4})}{P} i_{sa2}\end{aligned} \tag{13}$$

$$\psi_{sa2} = \frac{N_b^2\{P_{a2}(P_{a1}+P_{a3}+2P_{a4})+P_{a4}(P_{a1}+2P_{a2}+P_{a3})\}}{P} i_{sa2} - \frac{2N_mN_b(P_{a1}+P_{a3})(P_{a2}-P_{a4})}{p} i_{ma} - \frac{N_b^2(P_{a1}-P_{a3})(P_{a2}-P_{a4})}{P} i_{sa1}. \quad (14)$$

Self-inductances and mutual inductances are given from coefficients of i_{ma}, i_{sa1} and i_{sa2} in the equations (10), (13), and (14).

$$L_{ma} = \frac{4N_m^2(P_{a1}+P_{a3})(P_{a2}+P_{a4})}{P} \quad (15)$$

$$L_{sa1} = \frac{N_b^2\{P_{a1}(P_{a2}+2P_{a3}+P_{a4})+P_{a3}(2P_{a1}+P_{a2}+P_{a4})\}}{P} \quad (16)$$

$$L_{sa2} = \frac{N_b^2\{P_{a2}(P_{a1}+P_{a3}+2P_{a4})+P_{a4}(P_{a1}+2P_{a2}+P_{a3})\}}{P} \quad (17)$$

$$M_{(ma,sa1)} = \frac{2N_mN_b(P_{a1}-P_{a3})(P_{a2}+P_{a4})}{p} \quad (18)$$

$$M_{(ma,sa2)} = -\frac{2N_mN_b(P_{a1}+P_{a3})(P_{a2}-P_{a4})}{p} \quad (19)$$

$$M_{(sa1,sa2)} = -\frac{N_b^2(P_{a1}-P_{a3})(P_{a2}-P_{a4})}{P} \quad (20)$$

where,

L_{ma}	the self-inductance of motor winding "ma".
L_{sa1}, L_{sa2}	the self-inductance of radial force windings 'sa1' and 'sa2'.
$M_{(ma,sa1)}$	the mutual inductance between motor winding 'ma' and radial force winding 'sa1'.
$M_{(ma,sa2)}$	the mutual inductance between motor winding 'ma' and radial force winding 'sa2'.
$M_{(sa1,sa2)}$	the mutual inductance between radial force winding 'sa1' and radial force winding 'sa2'.

B. Assumption and calculation of the permeance

Each permeance shown as P_{a1}~P_{a4} can be divided into three parts of permeances P_1~P_3 as shown in Fig. 6. P_2 and P_3 represent fringing path permeances. P_1 represents the permeance between poles. The following assumptions are considered in calculation.

(1) Magnetic saturation can be neglected.
(2) The rotor displacement is small enough compared with the air-gap length.
(3) Flux paths which do not link a rotor can be neglected.
(4) Flux paths between stator poles and rotor interpolar area can be neglected.

(5) Fringing fluxes only at the aligned position can be neglected, because an air-gap length is very short.

The assumed magnetic paths in the previous paper are made up of straight and circular lines. On the contrary, the assumed magnetic paths in this paper are composed of elliptical lines using a variable 'k'. In the previous paper, k is equal to 1. However, the variable k is dependent to the rotor rotational position and the air-gap length. The definitions of variables in Fig. 6 can be summarized as follows;

θ_a	rotor rotational position.
l_g	air-gap length.
r	radius of the rotor poles.
t	a position on a rotor circular surface.
dt	a derivative of t.
dP_2, dP_3	permeances of the infinitesimal width of the assumed magnetic path.

In Fig. 6, the fringing flux path has a width of dt and kdt at rotor and stator surfaces, respectively. k is a constant to determine the shape of ellipse. Thus, it is important to find the value of k. Fig. 7 shows flux paths obtained from FEM analysis. Fig. 8 shows an enlarged magnetic path at the pole edge. k can be calculated from each flux path in Fig. 8. FEM analysis is carried out with the air-gap lengths of 100μm, 220μm and 300μm to see the dependence of fringing fluxes to the air-gap length.

Fig. 9 shows the relationship between k and t derived from results of FEM analysis. Fig. 10 shows the relationship between k and t/l_g.

Regardless of l_g, k is found to be dependent to only t/l_g. Next, an average length of the flux path can be written with a simple approximation that an average of lengths of the semimajor and semiminor axes of the ellipse represent radius as,

$$l = \frac{\pi}{4}\left(t + l_g + kt\right) \tag{21}$$

where l is an average length of the magnetic path. This equation can be also written as,

$$\frac{l}{l_g} = \frac{\pi}{4}\left(1 + \frac{t}{l_g}\left(1 + k\right)\right). \tag{22}$$

Fig. 11 shows the relationship between l/l_g and t/l_g. It is seen that all the points are located in a line. The relationship between l/l_g and t/l_g can be approximated such that l/l_g and t/l_g have linear relationships. A simplified equation can be written as,

$$\frac{l}{l_g} = c\frac{t}{l_g} + \frac{\pi}{4} \tag{23}$$

where 'c' is a constant of 1.49. Substituting the equation (23) into the equation (22) yields,

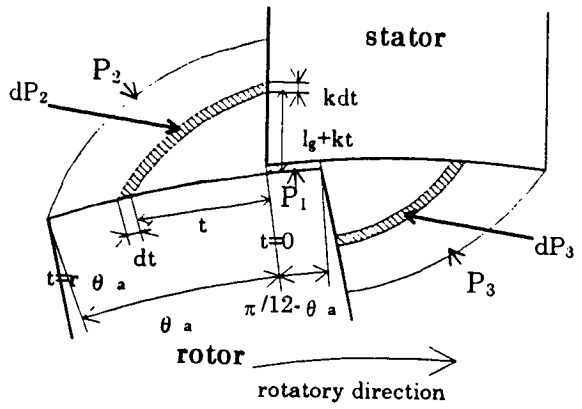

Fig.6 The assumed magnetic paths and permeances P_1~P_3.

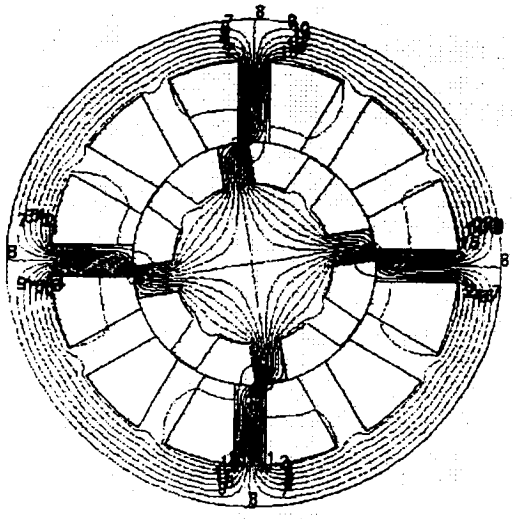

Fig.7 Flux distribution.

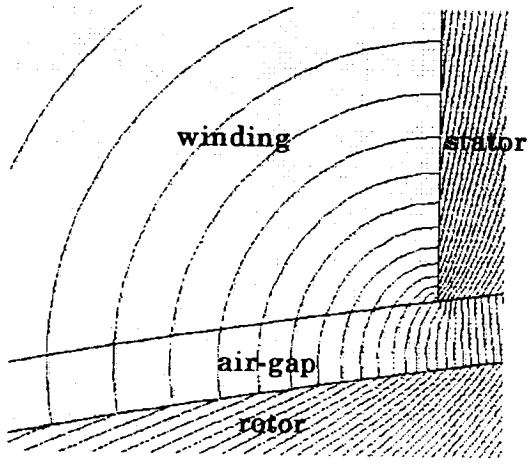

Fig.8 Enlarged flux paths.

$$k = \frac{4}{\pi}c - 1. \tag{24}$$

A cross section area of dP_2 can be approximated in the following equation (25).

$$s = \frac{h(dt + kdt)}{2} \tag{25}$$

where 's' is the cross section area of dP_2, 'h' is a stack length. Therefore, the relationship between $dP_2 \times l_g$ and t/l_g can be written as

$$dP_2 \times l_g = \frac{\mu_0 \times s}{l} \times l_g \tag{26}$$

where μ_0 is the permeability in the air. Substituting equations (22)~(25) into equation (26) yields,

$$dP_2 \times l_g = \frac{\delta \mu_0 hc}{\pi} \times \frac{1}{4c\dfrac{t}{l_g} + \pi} dt. \tag{27}$$

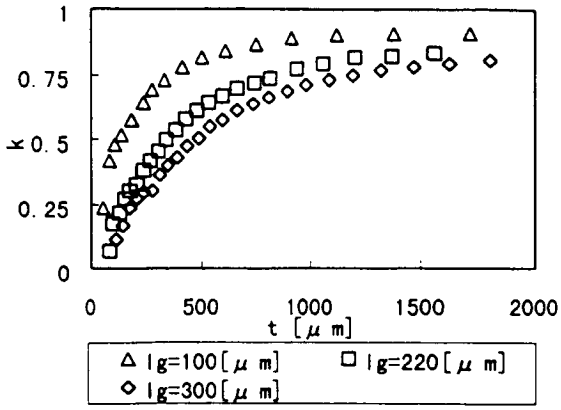

Fig.9 Relationship between k and t.

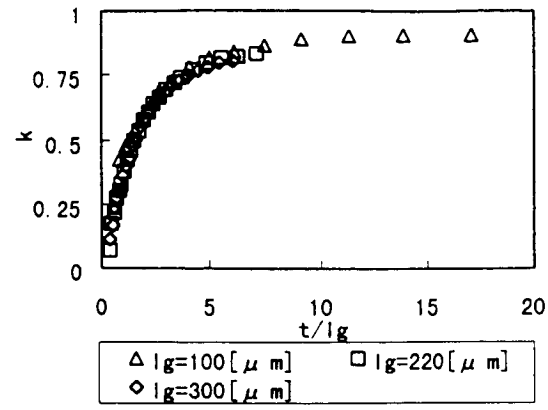

Fig.10 Relationship between k and t / l_g.

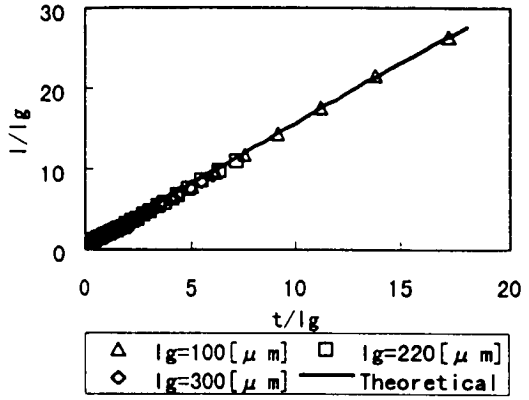

Fig.11 Relationship between l / l_g and t / l_g.

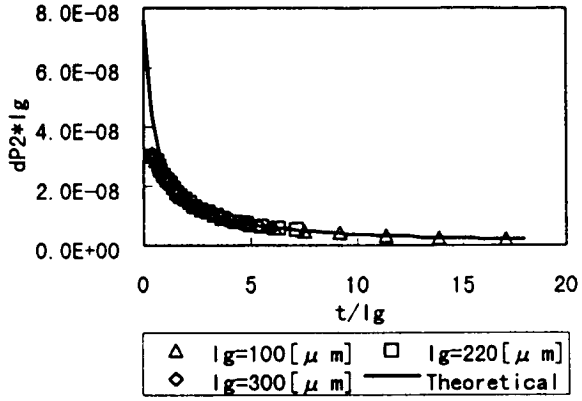

Fig.12 Relationship between $dP_2 \times l_g$ and t / l_g.

Fig. 12 shows the relationship between $dP_2 \times l_g$ and t/l_g. From Fig. 12, it is seen that the theoretical curve corresponds to the results of FEM analysis. Therefore, it is noted that the assumption of the equation (24) is effective. The equation (27) can be written as,

$$dP_2 = \frac{8\mu_0 hc}{\pi} \times \frac{1}{4ct + \pi l_g} dt . \tag{28}$$

The permeance P_1 of the air-gap between a rotor and stator poles can be derived as,

$$P_1 = \frac{\mu_0 hr\left(\frac{\pi}{12} - \theta_a\right)}{l_g} \tag{29}$$

where r is a radius of rotor poles. The permeance P_2 can be calculated from the equation (28) as

$$P_2 = \int_0^{r\theta_a} dP_2 . \tag{30}$$

Substituting the equation (28) into the equation (30) yields,

$$P_2 = \frac{2\mu_0 h}{\pi} ln\left(\frac{4cr\theta_a + \pi l_g}{\pi l_g}\right). \tag{31}$$

Similarly, the permeance P_3 can be derived considering symmetrical fringing flux paths as

$$P_3 = \frac{2\mu_0 h}{\pi} ln\left(\frac{4cr\theta_a + \pi l_g}{\pi l_g}\right). \tag{32}$$

The total permeances P_A is the sum of $P_1 \sim P_3$, thus,

$$P_A = P_1 + P_2 + P_3. \tag{33}$$

Therefore, from the equations (29) ~ (33),

$$P_A = \frac{\mu_0 hr\left(\frac{\pi}{12} - \theta_a\right)}{l_g} + \frac{4\mu_0 h}{\pi} ln\left(\frac{4cr\theta_a + \pi l_g}{\pi l_g}\right). \tag{34}$$

It is noted that P_{a1}, P_{a2}, P_{a3}, and P_{a4} are the equal to P_A if a rotor is positioned at the stator center.

C. Derivation of inductances

Substituting $l_0 \pm \alpha$ and $l_0 \pm \beta$ into the air-gap length l_g in the equation (34), the permeances $P_{a1} \sim P_{a4}$ are given, considering rotor radial displacements as,

$$P_{a1} = \frac{\mu_0 hr(\pi - 12\theta_a)(l_0 + \alpha)}{12{l_0}^2} + \frac{4\mu_0 h}{\pi} ln\left(\frac{4cr\theta_a(l_0 + \alpha) + \pi {l_0}^2}{\pi {l_0}^2}\right) \tag{35}$$

$$P_{a2} = \frac{\mu_0 hr(\pi - 12\theta_a)(l_0 - \beta)}{12{l_0}^2} + \frac{4\mu_0 h}{\pi} ln\left(\frac{4cr\theta_a(l_0 - \beta) + \pi {l_0}^2}{\pi {l_0}^2}\right) \tag{36}$$

$$P_{a3} = \frac{\mu_0 hr(\pi - 12\theta_a)(l_0 - \alpha)}{12{l_0}^2} + \frac{4\mu_0 h}{\pi} ln\left(\frac{4cr\theta_a(l_0 - \alpha) + \pi {l_0}^2}{\pi {l_0}^2}\right) \tag{37}$$

$$P_{a4} = \frac{\mu_0 hr(\pi - 12\theta_a)(l_0 + \beta)}{12{l_0}^2} + \frac{4\mu_0 h}{\pi} ln\left(\frac{4cr\theta_a(l_0 + \beta) + \pi {l_0}^2}{\pi {l_0}^2}\right) \tag{38}$$

where l_0 is the average air-gap length, α and β are the rotor displacements in the α- and β-axes, provided that l_0 is large enough to α and β. Substituting the equations (35)~(38) into the equations (15)~(20) yields,

$$L_{ma} = 2{N_m}^2\left(\frac{\mu_0 hr(\pi - 12\theta_a)}{6l_0} + \frac{8\mu_0 h}{\pi} ln\left(1 + \frac{4cr\theta_a}{\pi l_0}\right)\right) \tag{39}$$

$$L_{sa1} = {N_b}^2\left(\frac{\mu_0 hr(\pi - 12\theta_a)}{6l_0} + \frac{8\mu_0 h}{\pi} ln\left(1 + \frac{4cr\theta_a}{\pi l_0}\right)\right) \tag{40}$$

$$L_{sa2} = {N_b}^2\left(\frac{\mu_0 hr(\pi - 12\theta_a)}{6l_0} + \frac{8\mu_0 h}{\pi} ln\left(1 + \frac{4cr\theta_a}{\pi l_0}\right)\right) \tag{41}$$

$$M_{(ma,sa1)} = N_m N_b \left(\frac{\mu_0 hr(\pi - 12\theta_a)}{6{l_0}^2} \alpha + \frac{8\mu_0 h}{\pi} ln\left(\frac{4cr\theta_a(l_0 + \alpha) + \pi {l_0}^2}{4cr\theta_a l_0 + \pi {l_0}^2} \right) \right) \quad (42)$$

$$M_{(ma,sa2)} = N_m N_b \left(\frac{\mu_0 hr(\pi - 12\theta_a)}{6{l_0}^2} \beta + \frac{8\mu_0 h}{\pi} ln\left(\frac{4cr\theta_a(l_0 + \beta) + \pi {l_0}^2}{4cr\theta_a l_0 + \pi {l_0}^2} \right) \right) \quad (43)$$

$$M_{(sa1,sa2)} \approx 0 . \quad (44)$$

IV. DERIVATION OF RADIAL FORCES

A. Derivation of the theoretical equations of radial force

It is possible to construct a 3 x 3 inductance matrix from the derived self-inductances and mutual inductances in the equations (39)~(44). The 3 x 3 inductance matrix can be written as,

$$[L] = \begin{bmatrix} L_{ma} & M_{(ma,sa1)} & M_{(ma,sa2)} \\ M_{(ma,sa1)} & L_{sa1} & M_{(sa1,sa2)} \\ M_{(ma,sa2)} & M_{(sa1,sa2)} & L_{sa2} \end{bmatrix} \quad (45)$$

where, [L] is the 3 x 3 inductance matrix. The radial forces F_α and F_β can be derived from the derivatives of the stored magnetic energy with respect to displacements α and β, respectively. The stored magnetic energy can be written using the equation (45) as,

$$W_a = \frac{1}{2} \begin{bmatrix} i_{ma} & i_{sa1} & i_{sa2} \end{bmatrix} [L] \begin{bmatrix} i_{ma} \\ i_{sa1} \\ i_{sa2} \end{bmatrix} \quad (46)$$

where W_a is the stored magnetic energy. Thus, the radial forces F_α and F_β are given, substituting the equations (39)~(44) into the equation (46), yields,

$$F_\alpha = \frac{\partial W_a}{\partial \alpha} = N_m N_b \left(\frac{\mu_0 hr(\pi - 12\theta_a)}{6{l_0}^2} + \frac{32\mu_0 hrc\theta_a}{\pi\left(4rc\theta_a(l_0 + \alpha) + \pi {l_0}^2\right)} \right) i_{ma} i_{sa1} \quad (47)$$

$$F_\beta = \frac{\partial W_a}{\partial \beta} = N_m N_b \left(\frac{\mu_0 hr(\pi - 12\theta_a)}{6{l_0}^2} + \frac{32\mu_0 hrc\theta_a}{\pi\left(4rc\theta_a(l_0 + \beta) + \pi {l_0}^2\right)} \right) i_{ma} i_{sa2} . \quad (48)$$

The following points are clear from the equations (47) and (48).

(1) The radial forces F_α and F_β are directly proportional to the products of motor winding current i_{ma} and radial force winding currents i_{sa1} or i_{sa2}. Therefore, the radial forces can be controlled by radial force winding current. Let us define a radial force constant K_f as $F_\alpha / (i_{ma} i_{sa1})$ and $F_\beta / (i_{ma} i_{sa2})$.

(2) The radial force constant K_f is dependent on rotor rotational position θ_a. The first term in the parentheses originates from the permeance between rotor and stator poles. Thus, the first term is dominant, and decreases linearly as θ_a increases. At $\theta_a = \pi/12$, the first term becomes zero. Note that the equations (47) and (48) are valid only $0 \le \theta_a \le \pi/12$ (15deg). If $\theta_a > \pi/12$, then the first term is zero. In this condition, rotor poles are not facing stator poles. The second term corresponding to fringing paths now plays an important role.

(3) In low speed operations, motor current is usually injected during $0 \le \theta_a \le$ 15deg to produce torque efficiently. Thus, it is important to examine K_f in this condition, especially θ_a is around 15deg.

B. The measurement and the examination of the radial forces

A test machine was built and the magnetic suspension realized with DC current in A-phase windings. In this situation, weights are hung to apply radial force as shown in Fig. 13. An average current in the radial force windings is measured. In every rotational position, weights are increased and then decreased while the average current is measured. The hysteresis influence is small enough to obtain relationships between radial force and radial force winding current. Then, K_f is obtained from the Least-Square Error method. A ratio of lengths from the fulcrum to the mechanical force application point and the central point of the active area is 2.316:1. This ratio is considered.

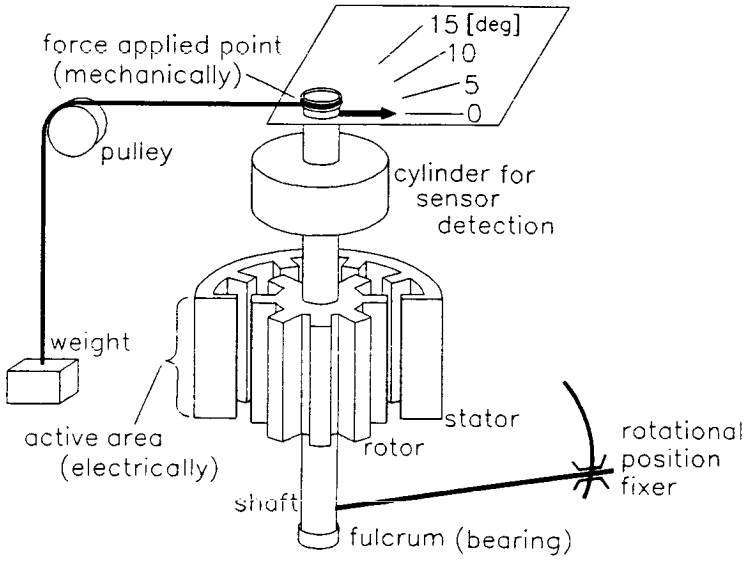

Fig. 13 A model of the experiment.

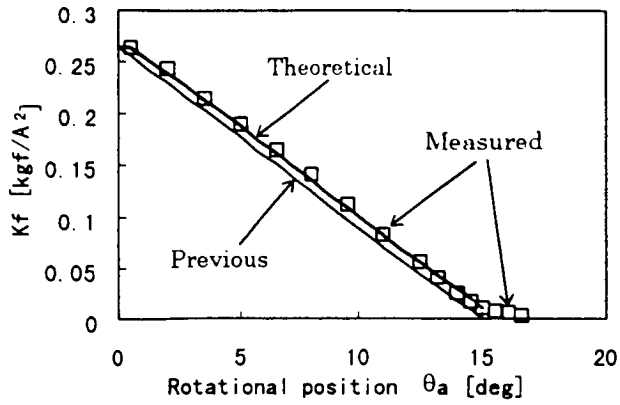

Fig.14 Relationship between K_f and θ_a.

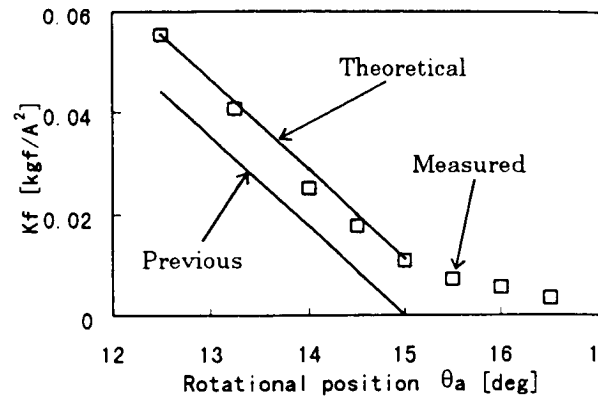

Fig.15 Magnification of unaligned position.

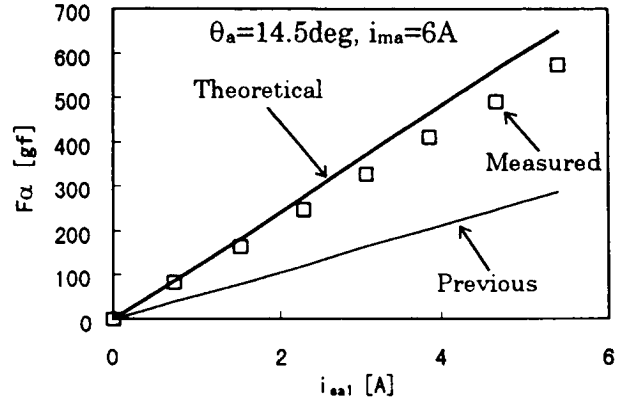

Fig.16 Relationship between F_α and i_{sa1}.

Fig. 14 shows the relationship between the radial force constant K_f and the rotor rotational position θ_a. Fig. 15 shows the magnification in a range of θ_a = 12.5~15deg. Fig. 16 shows the relationship between the radial forces F_α and the radial force winding current i_{sa1} at θ_a = 14.5deg. The theoretical value in the previous paper [12] is also drawn. This value is originated from only the first term in the parentheses of the equations (47) and (48). It is seen that the proposed calculation is especially effective in a range of θ_a = 13~15deg. As the accurate inverse function of K_f is required in controller to keep constant loop gain, while a test machine is rotating, accurate theoretical estimation is important. The second term in the parentheses is found to be effective to derive the radial force constant, especially at unaligned positions.

V. CONCLUSIONS

In this paper, the theoretical equations of radial forces are derived with a close examination of flux distribution. Based on results of FEM analysis, simple mathematical equations are proposed to express fringing fluxes. Relationships between radial force and current around unaligned positions are derived with the fringing effects. It is stated that the derived equations are especially effective at unaligned positions. These relationships are confirmed in experiments.

REFERENCES

[1] Ichikawa O., Michioka C., Fukao T., and Chiba A., "A Decoupling Control Method of Radial Rotor Position in Synchronous Reluctance Type Bearingless Motors", IPEC-Yokohama'95, pp.347-351, 1995.

[2] A. Chiba, R. Furuichi, Y. Aikawa, K. Shimada, Y. Takamoto, and T. Fukao, "A Stable Operation of Induction Type Bearingless Motors under Loaded Conditions", IEEE Trans. of Industry Applications, Vol.33, No.44, pp.919-924, 1997.

[3] A. Chiba, R. Miyatake, S. Hara, and T. Fukao, "Transfer Characteristics of Radial Force of Induction Type Bearingless Motors with Four-Pole Rotor Circuits", Fifth International Symposium on Magnetic Bearings,Kanazawa, pp.319-325, 1996.

[4] R. Schöb, "Applications of the Lateral-Force-Motor (LFM)", IPEC-Yokohama'95, pp.358-363, 1995.

[5] M. Ooshima, A. Chiba, T. Fukao, and M. Azizur Rahman, "Design and Analysis of Permanent Magnet-Type Bearingless Motors", IEEE Transactions., Indus. Electr., Vol.IE-43, No.2, pp.292-299, 1996.

[6] T. Ohishi, Y. Okada, and S. Miyamoto, "Levitation Control of IPM Type Rotating Motor", Fifth International Symposium on Magnetic Bearings, Kanazawa, pp.327-332, 1996.

[7] Eike Richter and Caio Frreira, "Performance Evaluation of a 250kW Switched Reluctance Starter Generator", IEEE IAS'95, pp.434-440, 1995.

[8] Kaushik R., "Propulsion System Issues in Electric and Hybrid Vehicle Applications", IPEC-Yokohama'95, pp.93-98, 1995.

[9] T. Higuchi, H. Kawakatsu, and T. Iwasawa, "A study on magnetic suspension of switched reluctance motor", IEE of Japan, Annual Meeting Record 684, pp.(6-122)-(6-123), 1989 (in Japanese).

[10] Mark A., James P. F., Eike Richter, and Kiyoung Chung, "Integrated magnetic bearing / switched reluctance machine", U.S. Patent 5,424,595, 1994.

[11] T. Higuchi and T. Komori, "z-θ positioning contactless actuator", Proc. of 6th Robot Institute of Japan, pp.281-282, 1988 (in Japanese).

[12] K. Shimada, M. Takemoto, A. Chiba, and T. Fukao, "Radial Forces in Switched Reluctance Type Bearingless Motors", The 9th Symposium on Electromagnetics and Dynamics, pp.547-552, 1997 (in Japanese).

Session 3 -- High Tc 1

Chairman: Masato Murakami
ISTEC

ELECTROMAGNETIC INTERACTION BETWEEN PERMANENT MAGNETS AND BULK Y-Ba-Cu-O SUPERCONDUCTORS

Ken Nagashima*, Tomohiko Murayama#, Tsuyoshi Otani*
and Masato Murakami*
* Superconductivity Research Laboratory, ISTEC
1-16-25, Shibaura, Minato-ku, Tokyo 105, Japan
now at Shikoku Electric Power Company
2-5 Marunouchi, Takamatsu-shi, Kagawa 760, Japan

ABSTRACT

We have measured the electromagnetic force (EMF)[1] between Nd-Fe-B magnets and bulk Y-Ba-Cu-O superconductors, by varying magnet configurations such as the number of poles, the thickness of magnets and back iron yokes, the number of subsectioned magnets and the shape of bulk superconductors and studied the effects of these variables on the EMF. The EMF is strongly dependent on the magnet configuration, and therefore for the design of magnetic bearings in a superconducting flywheel system, it is very important to optimize the arrangement of permanent magnets for achieving a large EMF.

INTRODUCTION

Stable levitation or suspension of a heavy object in midair can be realized using a combination of a strong permanent magnet and a bulk superconductor with high critical current density (J_c) [1]. Recent progress in the fabrication of good quality large Y-Ba-Cu-O bulk superconductors with high Jc made it possible to levitate a person at 5 cm gap[2], and the force density has already reached 1kg/cm^2 [3]. Several applications with levitation have been proposed and those are magnetic bearings, flywheels, and transport systems. The feasibility studies of these systems have already been performed worldwide [4]. In particular, a super conducting flywheel system for energy storage is attractive when superconducting magnetic bearings are installed,since the rotational loss of the bearing can be greatly reduced. For this reason, a number of superconducting flywheel systems have been constructed and subjected to field testing [5],[6]. Through these studies, it has been confirmed that rotational loss of the superconducting flywheel system can really be reduced to a very small value [7]. However, for practical applications it is also very important to increase the stored energy, which requires a large EMF.

It is known that the EMF between a superconductors and a magnet is given by

$$F = \int m \nabla H dv \qquad (1)$$

[1]Editors Note: The standard abbreviation for electromotive force is emf (all lower case letters). Hence, the nonstandard abbreviation for electromagnetic force, EMF, uses all upper case letters to distinguish it from electromotive force.

In one dimension, this equation is simplified as

$$F = m\frac{dH}{dx} \tag{2}$$

where m is the magnetic moment of a superconductor, and dH/dx is a field gradient produced by a magnet. A number of studies have been conducted for the electromagnetic interaction between a single magnet and a single superconductor [8],[9]. Numerical simulation has also been conducted and found to be in good agreement with the experimental results [10]. In most experiments, however, the relative position of a permanent magnet and a superconductor is symmetric with their central axes fixed on the same line.

In contrast to such a simple case, the configuration of magnets/superconductors for practical flywheel is more complicated and the position of bulk superconductors and permanent magnets is off-axis.

In the present study, we then prepared various flywheels, in which Nd-Fe-B magnets with different configurations are assembled in an aluminum plate, and measured the EMF between these flywheels and bulk Y-Ba-Cu-O superconductors as a function of the gap in order to deduce a generic trend in the EMF.

EXPERIMENTAL

Bulk Y-Ba-Cu-O superconductors with the cation ratio of Y: Ba: Cu = 1.8: 2.4: 3.4 were prepared with the top-seeded melt-growth (TSMG) method, the details of which are described elsewhere [11],[12]. In the TSMG process, prior to the melt-growth process, a $SmBa_2Cu_3O_y$ seed crystal is positioned at the center of the pellet so that the c-axis of the seed is aligned perpendicularly to the top surface. With this technique, a large single-grain Y-Ba-Cu-O bulk with the c-axis oriented parallel to the pellet surface can be fabricated.

In order to study the effect of the size and shape of superconductor on the EMF, we prepared two kinds of YBCO bulks: 4.5 cm in diameter and 2.0 cm in height; and 4 cm square and 2 cm in thickness. For EMF measurements, these superconductors are placed in a thermally insulating container, as schematically shown in Fig. 1. In this arrangement, the c-axis of Y-Ba-Cu-O bulks is directed parallel to the magnetic field of permanent magnet, whereby induced currents mainly flow within the a-b plane, that is a preferred orientation for the supercurrent flow.

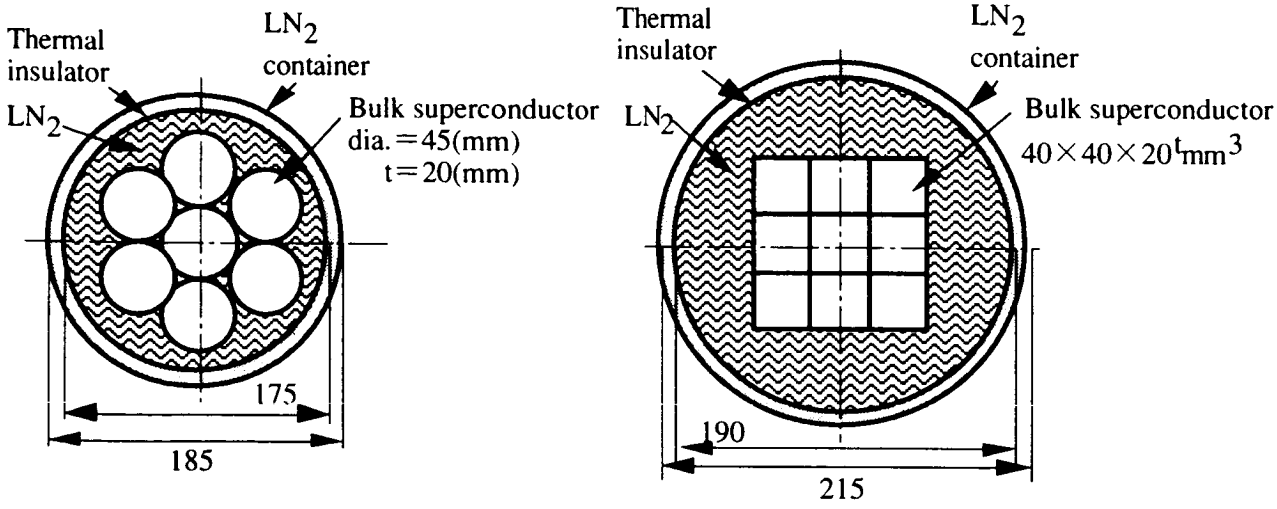

(a) Disk bulks (b) Rectangular bulks

Fig 1. Arrangements of superconductors.

Table 1. Specification of permanent magnets used in this study.

Magnet No.	Number of Poles	Thickness of Yoke	Thickness of Magnets	Weight of Magnets	Notes
No.1	1	0mm	10mm	1.15kg	
No.2	1	0mm	15mm	1.57kg	
No.3	1	0mm	34mm	3.27kg	
No.4	1	10mm	15mm	2.22kg	
No.6	1	8mm	15mm	1.71kg	2 subsectioned
No.7	1	8mm	15mm	1.78kg	3 subsectioned
No.8	2	8mm	10mm	1.58kg	
No.9	2	8mm	15mm	2.00kg	
No.11	2	8mm	34mm	3.57kg	
No.12	2	8mm	15mm	1.94kg	spacer 3 mmt
No.13	2	8mm	15mm	1.87kg	spacer 6 mmt
No.14	3	8mm	15mm	1.99kg	
No.15	4	8mm	15mm	1.98kg	

Flywheel (Permanent Magnets)

In order to study the effect of magnetic field distribution, we have prepared flywheel disks with various magnet configurations, as specified in Table 1 and also schematically presented in Fig 2. Permanent magnets used in the present experiment were Nd-Fe-B with B_r = 1.3 T.

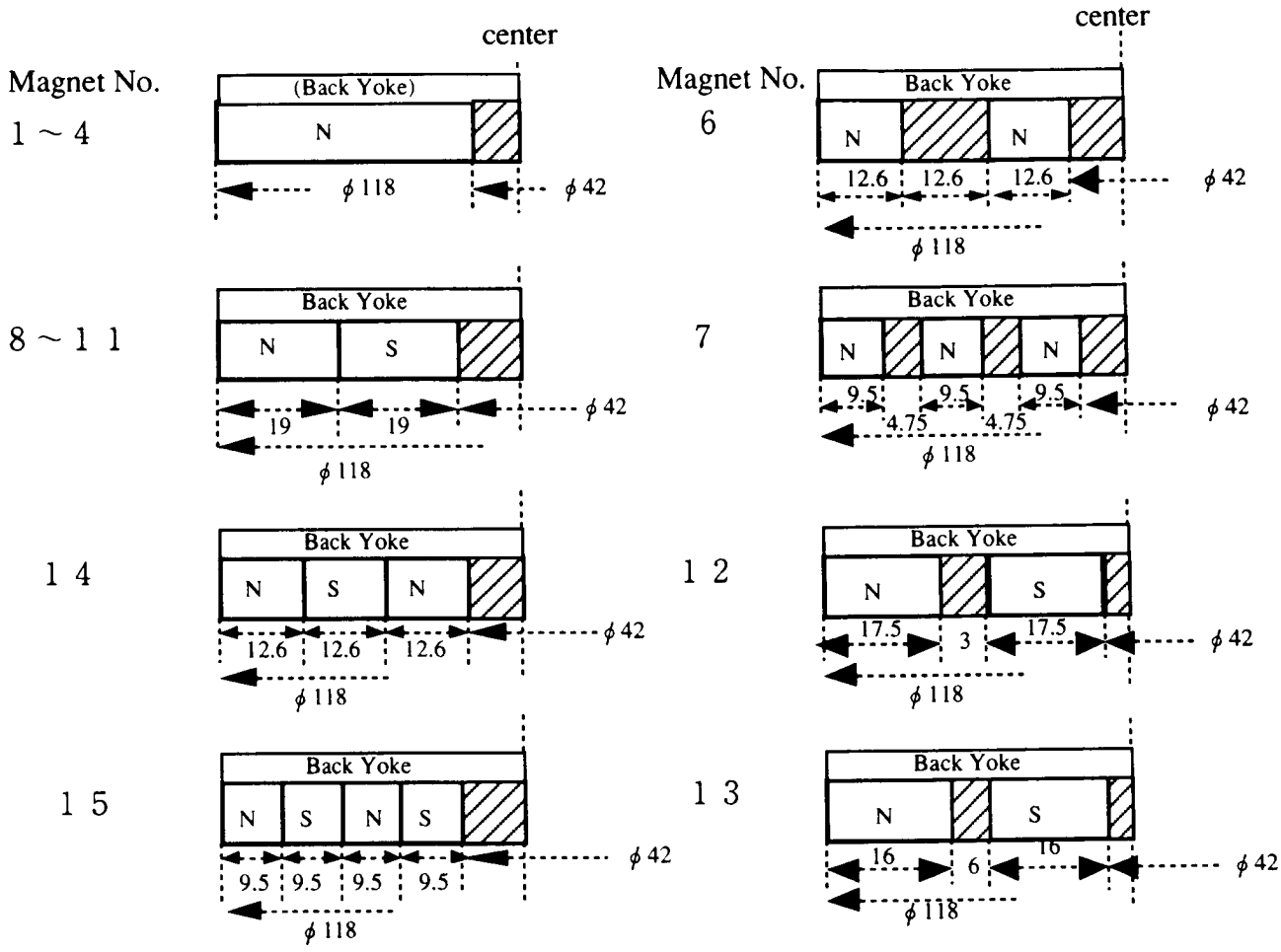

Fig 2. Configurations of permanent magnets.

Measurement of Repulsive Force

Figure 3 shows a schematic of the apparatus (Shimadzu Autograph AGS-100D) for the EMF measurements between the flywheel and bulk superconductors. Here, the flywheels are attached to a load cell and brought toward bulk superconductors which are arranged and glued to the thermal insulating container and cooled by liquid nitrogen, as already illustrated in Fig. 1.

EMF measurement procedure was as follows. Bulk superconductors are cooled in liquid nitrogen

in zero field while keeping the distance far enough to avoid the effect of the field generated from the magnet. Next the flywheel is moved to the position 50mm above the superconductors and then moved toward the superconductors for EMF measurements. The gap is automatically controlled by a computer and the EMF is continuously recorded as a function of the gap with a data acquisition system during both descending and ascending processes.

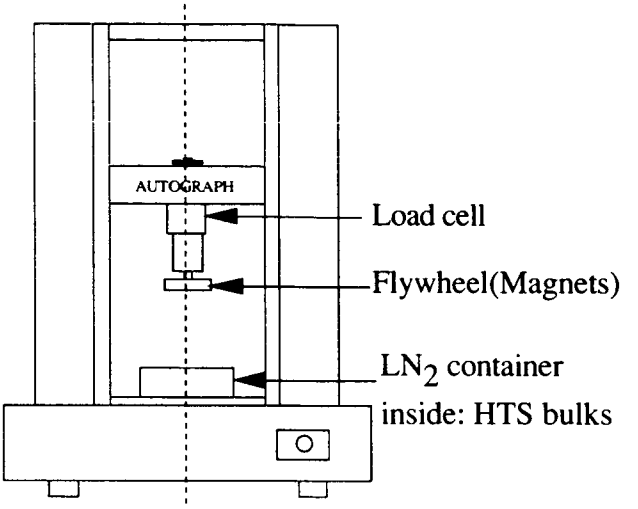

Fig 3. The schematic of the experimental setup.

RESULTS AND DISCUSSION

The Effects of Arrangement and Shape of Superconductors

Figure 4 shows the relationship between the force density and the magnet/superconductor gap for disk and rectangle bulks. Here we used three kinds of magnets with different thickness (No. 1, No.2 and No. 3). And the force density is the amount of repulsive force divided by the area of arranged bulk superconductors. It is clear from the figure that the force density curves for two different superconductors almost overlap, indicating that the shape of the superconductor has a very small effect on the EMF. We could not see any appreciable difference due to the shape of superconductors for almost all the magnets studied in the present study, which shows that the effect of the shape is negligible for the EMF.

The source of EMF is the interaction between the induced currents and magnetic field. Induced currents can flow within the pinned superconductor only at the surface layer. The penetration depth of induced (or shielding) currents is a function of J_c of the superconductor. In one dimension, the penetration depth (dx) is given by the following equation:

$$\frac{dB}{dx} = \mu_0 J_c \qquad (3)$$

where μ_0 is the permeability of vacuum, and dB is the external magnetic induction. The EMF is also given by the equation (2), in which m is the magnetization of a superconductor. Here it should be born in mind that the magnetization of the superconductor is obtained because the interior region is shielded by the induced currents. Figure 5 is a schematic illustration of the magnetization of the superconductor, in which dx is the penetration depth in the equation (3) and the internal field gradient (dB/dx) gives J_c. Y-Ba-Cu-O superconductors used in this experiment exhibit J_c of 30000 - 50000 A/cm^2 at 77 K and 0.1 - 0.5 T, which is the field strength used in this experiment. The penetration depth is thus in the order of 0.1 mm, which is much smaller than the dimension of the superconductors, showing that the most volume can be shielded by induced currents. Therefore, even if we change the shape of the superconductor, there will be no drastic change in the magnetization per unit volume, which is the reason that the shape of a superconductor has a small effect on the EMF.

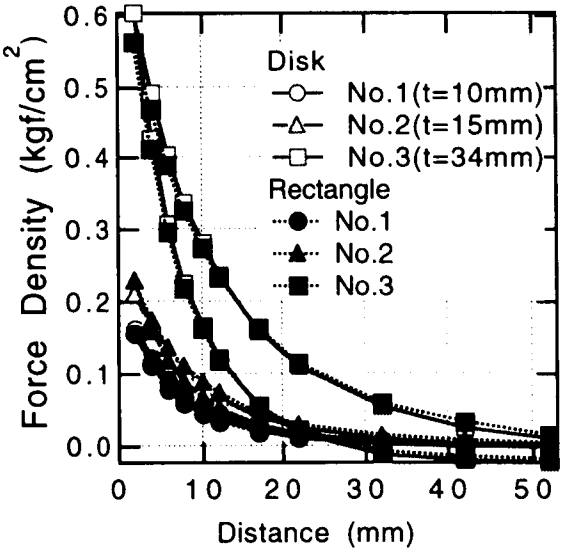

Fig 4. Relationship between the force density and the magnet/superconductor gap for disk and rectangle bulks.

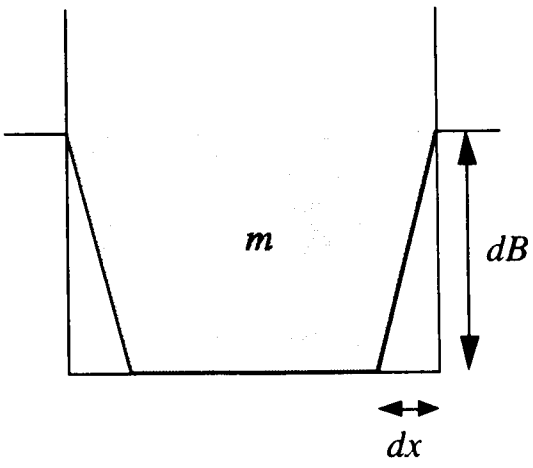

Fig 5. Schematic illustration of the magnetization of the superconductor.

Effect of Thickness of Single-pole Permanent Magnets

It is well known that as the thickness of permanent magnet is increased, the demagnetizing effect (or the geometrical effect) is reduced. Therefore the magnetic field at the surface of magnet pole

increases with increasing the thickness, as shown in Fig 6. Accordingly the repulsive force has the tendency to increase as the thickness of permanent magnet is increased (see Fig. 4). This shows that the EMF can simply be increased by increasing the thickness of the magnet. As an economical way to increase the effective thickness of the magnet, it is common to attach an iron yoke to the back of a magnet. Figure 7 shows the effect of the effective thickness on the EMF (magnets No.2 and No.4). It is clear that the EMF could also be increased simply by increasing the yoke thickness. However, it should also be born in mind that the weight of the levitated magnet increases with increasing magnet thickness. This suggests that we should take account of the EMF per unit volume rather than the EMF per unit area when the weight of the levitated magnet is important.

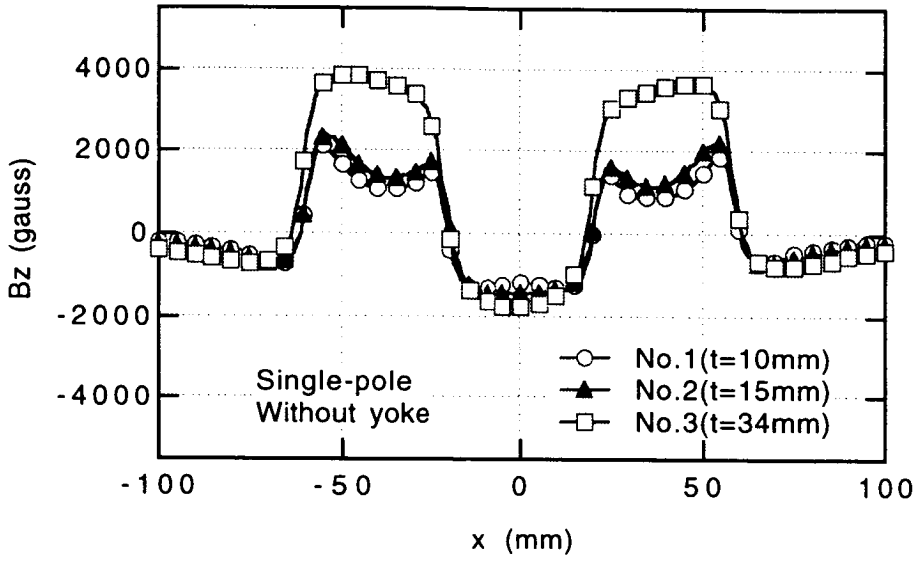

Fig 6. Magnetic field distribution at the surface of flywheel (Gap=2.8mm).

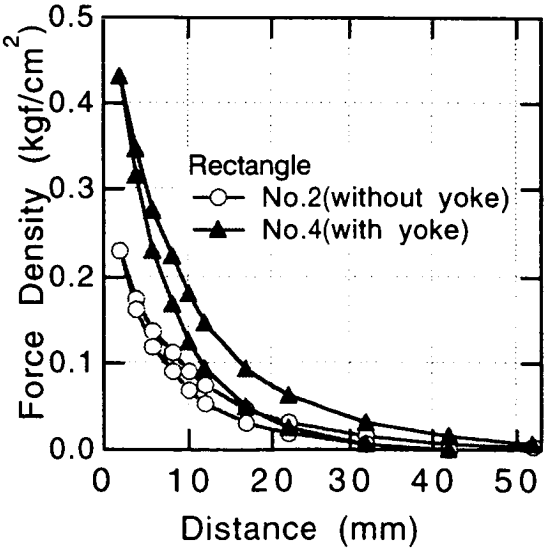

Fig 7. Force density vs. the magnet/superconductor gap.

Effect of Thickness of Double-pole Permanent Magnets

Figure 8 shows magnetic field distribution of double-pole magnets. For these magnets, an iron yoke with 8mm thickness was attached to increase the effective thickness. Like the case of a single-pole magnet, the peak magnetic field strength increases with increasing magnet thickness. Accordingly, the EMF increases with increasing magnet thickness as shown in Fig. 9, although the effect of magnet thickness was not so drastic compared with a single pole magnet. It is also notable that while the EMF is large for a single-pole magnet even at a relatively large gap, for a double-pole magnet the EMF is smaller in a large gap region but steeply increases with decreasing gap and surpasses the value of a single-magnet when the gap is below 5 mm. Such behavior can easily be understood in terms of the difference in the field distribution for single and double-pole magnets as shown in Fig. 10. For a double-pole magnet, the field and the field gradient are very strong only near the surface due to the fact that magnetic flux generated from one pole cannot diverge and must direct the pole with the opposite sign, and therefore the EMF is very strong in a small gap region and decays quickly with the gap. In contrast, for a single-pole magnet, since the magnetic flux spans a longer distance, the EMF does not decay with the gap like a double-pole magnet, instead the EMF near the surface is smaller. These results clearly show that for the design of a flywheel, the necessary gap for magnet/superconductor is important for optimization of the magnet arrangement in order to achieve a large EMF under operational conditions.

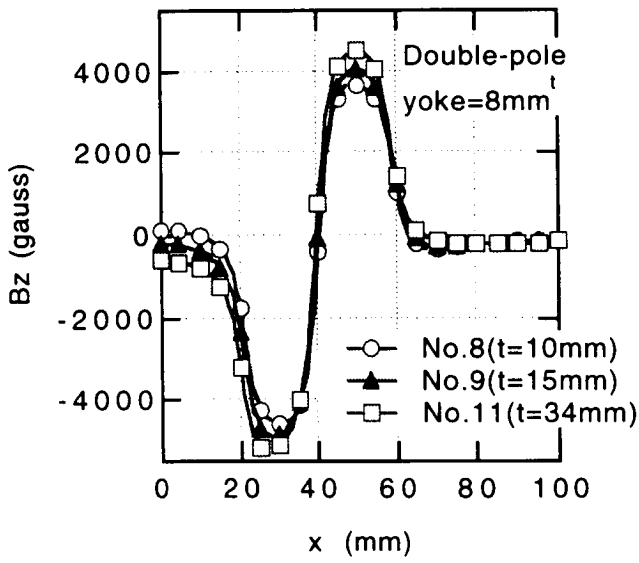

Fig 8. Magnetic field distribution(Gap=2.8mm).

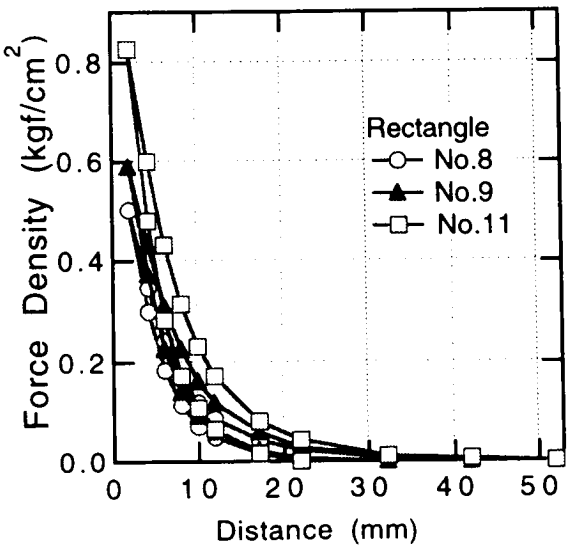

Fig 9. Force density vs. the magnet/bulks gap.

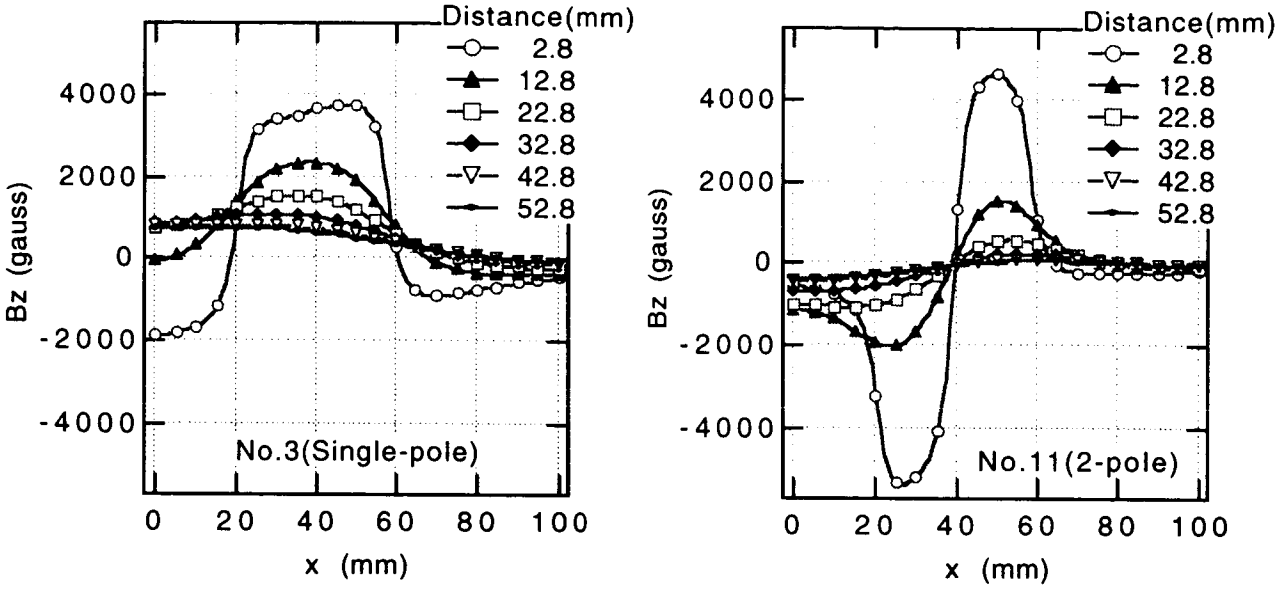

Fig 10. Gap dependence of magnetic field distribution.

The Effects of Number of Poles

Figure 11 shows the magnetic field distribution of the magnets with different pole numbers: magnets No.4, No9, No.14 and No.15. At the gap of 2.8 mm, the peak field strength is not a simple function of the number of poles. As discussed above, the field is localized for multi-pole magnets near the magnet surface, and the field distribution is strongly affected by the width of each pole and also the thickness of the magnet. Here, except for single-pole magnet, the effective thickness of multi-pole magnets is constant. When the number of poles is increased, the effective distance between two neighbor poles is reduced and the field will tend to be more localized near the surface. The fact that the peak field strength of a four-pole magnet (No. 15) is smaller than two- or three-pole magnets (No. 9 and No.14) at 2.8 mm gap may indicate that the most field cannot span this gap for a four-pole magnet.

Figure 12 is a relationship between the force density and the gap for these magnets. In a large gap region, a single-pole magnet gives the highest force density, which can be understood by the fact that magnetic field can span a longer distance. In a small gap region, there are several interesting features. First, the force density of a four-pole magnet is the smallest. Second the largest force density is recorded for a double-pole magnet below 5 mm gap. These results show that a simple increase in the pole number is not effective in increasing the EMF. It is also interesting to note that the EMF strength near the magnet surface is the largest for a double-pole magnet and the smallest for a four-pole magnet, which contrasts with the idea of simple field localization, and indicates that magnetic flux density in free space may be small for multi-pole magnets, which should be taken into

account for the design of flywheels.

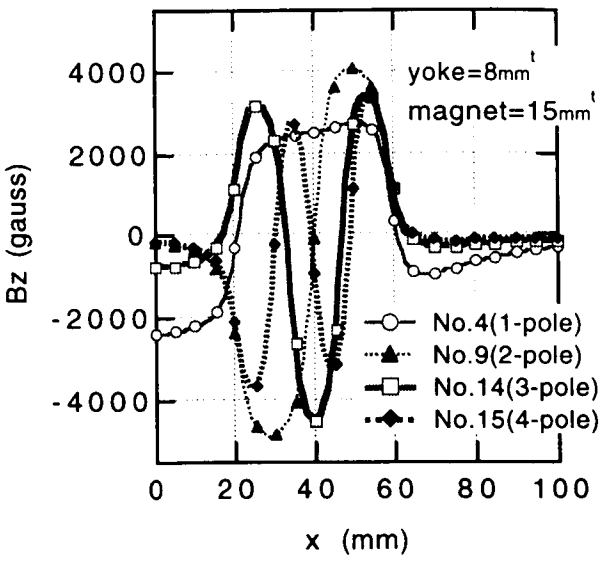

Fig11. Magnetic field distribution at the surface of flywheel (Gap=2.8mm).

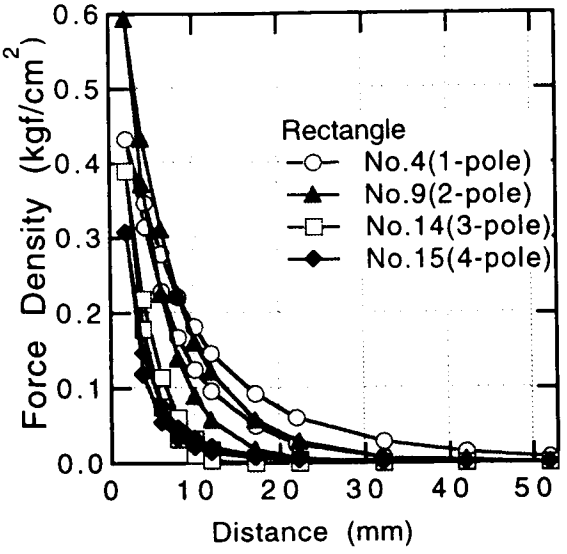

Fig12. Force density vs. the magnet/bulks gap.

The Stiffness of Flywheel

For the application of flywheel, the EMF along the radial direction or the stiffness is also important. In the present experiment, it was difficult to directly measure the stiffness, however, a general trend we found is that the levitation of the flywheel with multi-pole magnets is more stable than single-pole magnets, indicating that the stiffness is large for multiple-pole magnets.

According to equation (2), the EMF along radial direction (F_x) can be given by

$$F_x = \frac{m}{\mu_0}\frac{dB_z}{dx} \qquad (4)$$

and therefore, the distribution of dB_z/dx is one of the important parameters to evaluate the stiffness. Figure 13 shows the variation of dB_z/dx along a radial direction for single-pole (No.3) and a four-pole (No.15) magnet. As clearly be seen in the figure, the peak height is much higher for a four-pole magnet, indicating that the stiffness is higher. Thus an increase in the pole number is effective in enhancing the radial stability, although it was not so effective in increasing the EMF for levitation.

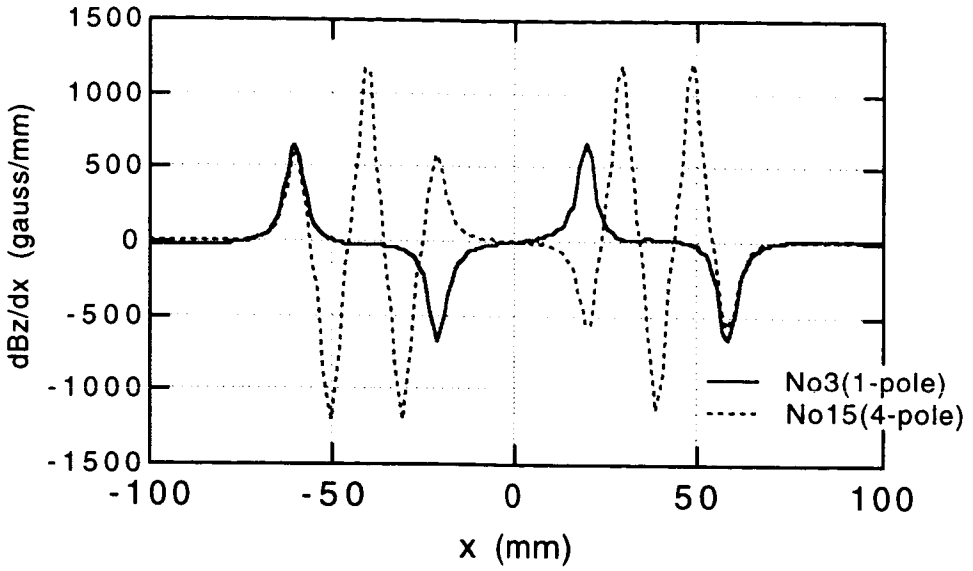

Fig 13 The dB_z/dx distribution of permanent magnets (Gap=2.8mm).

Effect of Subsectioned Magnets

The demagnetizing effect can also be reduced by increasing the effective magnet height, that is, to subsection the single-pole magnet part of magnet No.2 like the magnets No.6 and No.7, the configuration of which is already presented in Fig.2. The magnetic field strength at the surface will be increased by such treatment. Figure 14 shows the magnetic field distribution of these magnets at 2.8mm gap. Compared to a single-pole magnet, subsectioned magnets exhibit higher peak field, however, the peak field of the magnet subsectioned in three sectors is lower than that of two-subsectioned magnet. This can be understood by considering the fact that the total magnet volume, and therefore the total flux density is reduced by subsectioning the magnet, and this loss in the total flux density is responsible for a low magnetic field strength of three-subsectioned magnet.

Figure 15 shows the relationship between the force density and the gap for these magnets. Despite the increased field strength, an increase in the force density due to the subsection treatment is very small. The effect may become clear when the force density is normalized with the effective surface area of the subsectioned magnet. In conclusion, the subsectioning is not so effective in increasing the EMF. However, in manufacturing a flywheel for practical use, it is customary to insert a spacer between the magnets to support the mechanical strength of Nd-Fe-B magnets, since their strength is of order 8 kg/mm^2 and much smaller than that of engineering materials. In this context, the fact that the EMF was not reduced by inserting the spacer is favorable for the design of practical flywheel.

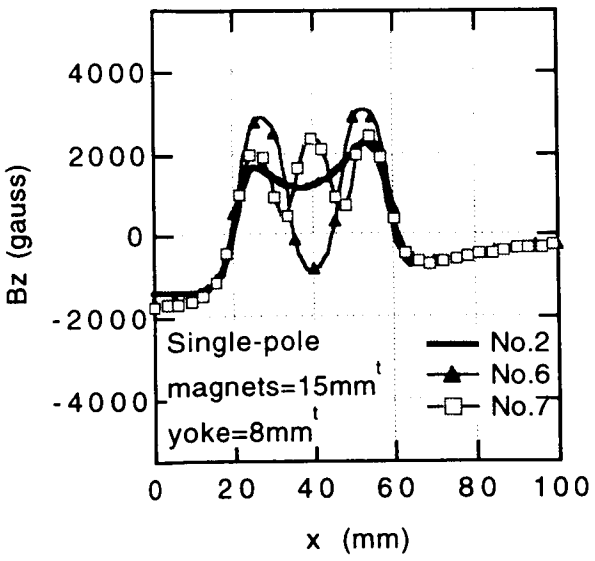

Fig14. Magnetic field distribution at the surface of flywheel (Gap=2.8mm).

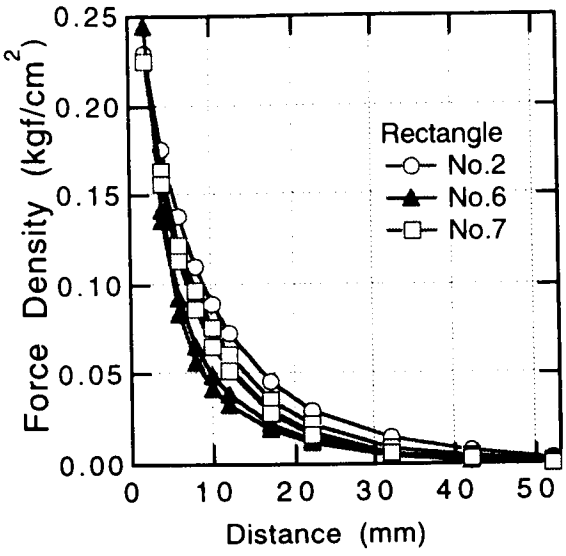

Fig15. Force density vs. the magnet/bulks gap.

Effects of a Spacer for Double-pole Magnet

We have also studied the effect of a spacer on the EMF of a double-pole magnet, and the configuration of the magnets (No. 12 and No. 13) is already presented in Fig. 2. Figure 16 shows the field distribution for magnets No. 9, No. 12, No. 13. It is clear that the field distribution is almost identical, showing that the effect of a spacer is very small. As a result, the effect of a spacer on the force density is also quite small for a double-pole magnet, as shown in Fig. 17. Such small effect of a spacer may be in part due to a relative small width ratio of the magnet to the spacer for the present experiment, and clear effect may be seen if the width of spacer is increased. The magnetic flux lines cannot be curved by a small angle, that is, the critical angle exists for the bending of magnetic flux, and therefore when the south and north poles are aligned with their axes parallel to each other like the case of the present study, magnetic flux near the S/N boundary cannot come out of the magnet, so that the contribution of the magnet near the boundary to the external field is negligibly small. In other words, the magnetic field will not be reduced even when we insert the spacer for the construction of practical flywheel.

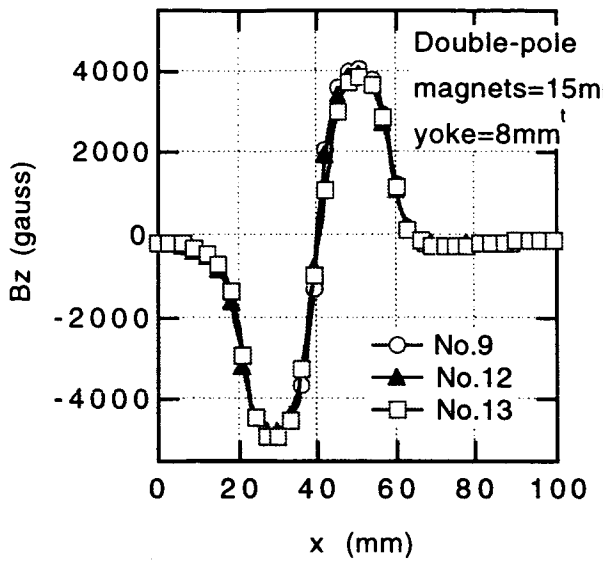

Fig16. Magnetic field distribution at the surface of flywheel (Gap=2.8mm).

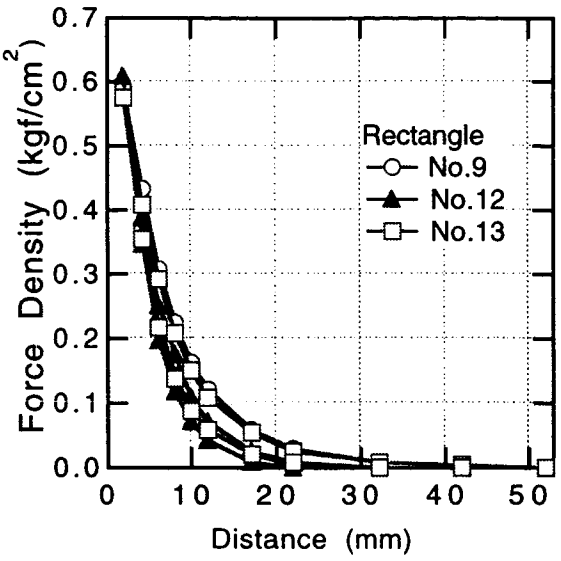

Fig17.Force density vs. the magnet/bulks gap.

SUMMARY

From the present experiments, several interesting features could be deduced as to the electromagnetic interaction between multiple magnets and multiple superconductors. First, the EMF was almost independent of the shape of the superconductors with high J_c. Second the EMF was strongly dependent on the magnet configuration, in that the field distribution was the most important factor to govern the EMF. For the design of the flywheel as well as other levitation systems, it is important to optimize the thickness, the width, the number of poles of magnet for achieving a large EMF. It should also be born in mind that the optimal magnet configuration is the function of the gap, at which the system is operated.

ACKNOWLEDGMENTS

The authors are grateful to Sumitomo Special Metals for the design of the flywheel magnets used in the present study. This work was supported by NEDO for R&D of Industrial Science and Technology Frontier Program.

REFERENCES

1. Murakami, Masato ed.: *Melt Processed High-Temperature Superconductors.* World

Scientific Publ. Co., Pte. Ltd., 1992.

2. Yoo, S.I.; Fujimoto, H.; Sakai, N.; Murakami, M.: Melt-processed LRE-Ba-Cu-O superconductors and prospects for their applications. *J. Alloys and Compounds,* vol. 250, 1997 pp. 439-448.
3. Kondoh, A.; Kagiya, S.; Takaichi, H.; Sakai, N.; Murakami, M.: YBaCuO with Large Magnetic Repulsive Force. *Advances in superconductivity 5*, Springer-Verlag Tokyo, 1993 pp. 1301-1304.
4. Nagaya, S.; Hirano, N.; Takenaka, M.; Minami, M.; Kawashima, H.: Fundemental Study on High Tc Superconducting Magnetic Bearings for Flywheel System. *IEEE Trans. Appl. Supercond.* vol. 5, No. 2, June 1995, pp. 643-649.
5. Bornemann, H. J.; Urban, C.; Boegler, P.; Ritter, T.; Zaitsev, O.; Weber, H.; Rietschel, H.: High speed superconducting flywheel system for energy storage. *Physica C* , vol. 235-240, 1994, pp. 3455-3456.
6. Bornemann, H. J.; Tonoli, A.; Ritter, T.; Urban, C.; Zaitsev, O.; Weber, K.; and Rietschel, H.: Engineering Prototype of a Superconducting Flywheel for Long Term Energy Storage. *IEEE Trans. Appl. Supercond.* vol. 5, No. 2, June 1995, pp. 618-621.
7. Hull, J. R.; Mulcahy, T. M.; Uherka, K. L.; Abboud R. G.: Low Rotational Drag In High-Temperature Superconducting Bearings. *IEEE Trans. Appl. Supercond.* vol. 5, No. 2, June 1995, pp. 626-629.
8. Hiebel, P.; Tixador, P.; Brunet, Y.; Chaud, X.; Beaugnon, E.; de Rango, P.; Ducloux, F.; Tournier, R.: Characterization of magnetically textured YBaCuO pellets and permanent magnet configurations for applications to magnetic bearings. *Physica C* , vol. 235-240, 1994, pp. 3449-3450.
9. Matsuura, K.; Homma, N.; Sawada, N.; Tsuchimoto, M.; Yamada, K.; Honma, T.: Observations of Suspension and Levitation Effects of Bulk HTSCs in microgravity Experiments. *Advances in superconductivity 7*, Springer-Verlag Tokyo, 1995 pp. 821-824.
10. Tsuchimoto, M.; Homma, N.; Matsuura, K.; and Matsuda, M.: Numerical Evaluation of Levitation Force of a Thin Film High Tc Superconductor. *Advances in superconductivity 9*, Springer-Verlag Tokyo, 1997 pp. 1389-1392.
11. Morita, M.; Sawamura, M.; Takebayashi, S.; Kimura, K.; Teshima, H.; Tanaka, M.; Miyamoto, K.; and Hashimoto, M.: *Physica C* , vol. 235-240, 1994, p. 209.
12. Morita, M.; Tanaka, M.; Takebayashi, S.; Kimura, K.; Miyamoto, K.; and Sawano, K.: *Jpn. J. Appl. Phys.*, vol. 30[5A], 1991, p. 813.

MODELING OF HTSC-BASED IRON CORE FLUX-CANCELING ELECTRODYNAMIC SUSPENSION FOR MAGLEV

Marc T. Thompson, Ph.D.[1]
Consultant
19 Commonwealth Road Watertown, MA 02172
(617) 923-1392
marctt@mit.edu

Richard D. Thornton, Sc.D.

Massachusetts Institute of Technology
77 Massachusetts Avenue, Room 10-050
Cambridge, MA 02139
thornton@mit.edu

Magnemotion, Inc.
142V North Road
Sudbury, MA 01776
mmi-rdt@magnemotion.com

SUMMARY

The design and analysis of a new iron core "flux-canceling" magnetic suspension suitable for high-temperature superconductors (HTSC) is described. A 1/5-scale model of this suspension has been designed and tested with a high-speed rotating wheel test facility. A new low-cost multiple-loop guideway has been tested and lift, drag, and guidance forces have been measured at operating speeds approaching that of a full-scale train. These results are compared to predictions based on simple circuit models, with good results.

A vertical control system has been designed and tested to improve ride quality through differential control of the magnet currents. The test fixture has also been used to validate the concept of lift generation at zero train velocity by AC excitation of the main magnet coils. Scaling laws have been applied to the results and predictions made for a full-scale HTSC suspension operating at 40K. Further work in this area may help overcome one of the fundamental limitations of electrodynamic (EDS) Maglev --- the fact that there is zero levitation force at zero train velocity and a low speed suspension is needed.

INTRODUCTION

Magnetic levitation for high speed ground transportation (Maglev) has been an active area of research and development for over 30 years. This new transportation mode has been proposed as an alternative to air, automobile, and high-speed train travel. Various experimental and a large number of theoretical studies have been done. Work has been continuous in Japan and Germany, while U.S. research support has been sporadic. The development in the past 10 years of high-temperature superconductors may alter the economics of high-speed ground transportation for the better. The goal of this work has been to design and test a novel prototype electrodynamic magnetic suspension using high-temperature superconductors and an iron core.

[1] Formerly from the Laboratory for Electromagnetic and Electronic Systems, Massachusetts Institute of Technology, Cambridge, MA 02139

ElectroDynamic magnetic suspension, called EDS Maglev and referred to as repulsive Maglev because it relies on repulsive magnetic forces, has the capability of allowing high speed transportation with a relatively large gap between the vehicle and guideway. In 1966 Danby and Powell proposed an EDS system using superconducting magnets with a "null flux" suspension that offered reduced magnetic drag. Subsequent researchers in the U.S., Japan, Germany, UK and Canada have developed further innovations, but there are still a number of technical problems that need resolution.

To date the only commercial Maglev implementations have used the electromagnetic suspension (EMS) in which electromagnets support a vehicle with attractive forces to steel guideways. While EMS may be a preferred option for lower speed designs, it has the fundamental disadvantage of requiring a small gap between the vehicle and guideway, typically less than a centimeter, and requires active control to maintain the gap. The promise of EDS is that this gap can be increased by a factor of 5 or more, and therefore guideway tolerances are relaxed and cost might be reduced. Another purported advantage of EDS is that it can be inherently stable and not dependent on feedback control to maintain a constant gap. Unfortunately, this advantage is not as real as it appears because all EDS designs are highly underdamped and, in certain cases, even unstable. Other disadvantages of EDS are higher power requirements for suspension, higher external magnetic fields, and the need for a separate low speed suspension.

The foremost problem for all high speed ground transportation systems is the high cost of guideway construction, but this key issue is not unique to Maglev. Many researchers are now convinced that if Maglev technology were fully developed it would be less expensive than a high speed train if all installation and operating costs are compared. This is particularly true if the Maglev system can provide shorter travel times which in turn attracts more users so that the capital cost per user is reduced. The reason for the EMS preference has been its apparently lower cost because it uses a relatively simpler technology with fewer unknowns. German Maglev developers have shown that EMS can operate successfully at speeds over 400 km/hour, so the problem is to improve EDS to the point that, for high speed travel, it has substantial advantages other than that of a larger gap.

We believe that a successful EDS design must face squarely the following problems:

- The cost of manufacturing and installing suspension and propulsion components on the guideway must be reduced to an absolute minimum;
- The suspension system must have a power loss that is comparable to that for EMS;
- All EDS suspension designs are highly underdamped and it is imperative to find practical means to damp oscillations and provide high ride quality;
- External magnetic fields associated with onboard superconducting magnets must be reduced particularly in the passenger compartments;
- It is highly desirable to eliminate the need for a separate low speed suspension system because this adds to the cost, weight and complexity of both the vehicle and guideway;
- Any superconducting vehicle magnets must be able to operate reliably in a hostile transportation environment.

This and two other companion papers in these *Proceedings* report the latest results of MIT research to develop an improved EDS design that addresses all of these issues.

SYSTEM OVERVIEW

This section describes the design and modeling of the multiple-loop guideway and development of circuit models to predict behavior of a full-scale flux-canceling Maglev system based on high-temperature superconducting coils. The guideway is composed of multiple conductive copper coils arranged vertically, and the train magnets are arranged in a dual-row N-S-N-S arrangement (*Fig. 1a*). The magnets in the test facility have a pole pitch $p = 0.126$ meter. When the train is in the vertical null position at $z = z_o$ and traveling in the $+y$ direction, there is no net flux through the levitating coils, and no net current induced around the loop. However, if the train's vertical position deviates from equilibrium, the net changing flux through the loop induces currents in the loop. The Lorentz force is a restoring force in this structure, with the magnetic suspension acting as a linear spring with spring constant k_z. The suspension behaves like a mass and a linear spring, with a resulting resonant frequency $\sqrt{k_z / M}$ where k_z is the magnetic spring constant and M is the total suspended mass.

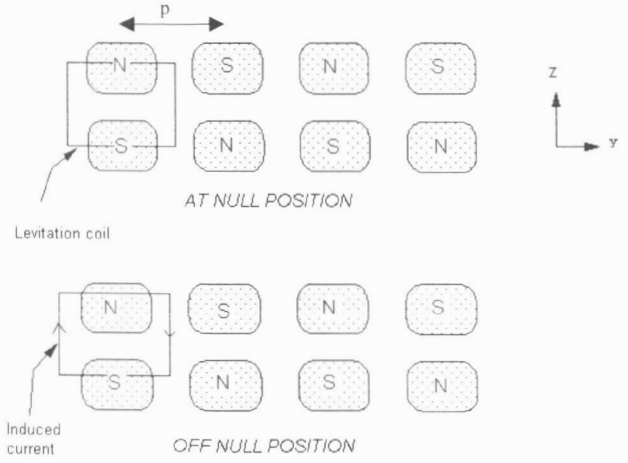

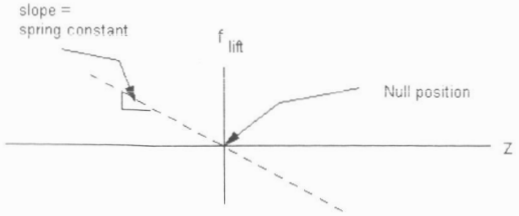

(a) Top: train at null position, no induced currents. Middle: train above null position. Currents are induced, creating a restoring force. Bottom: magnetic spring constant

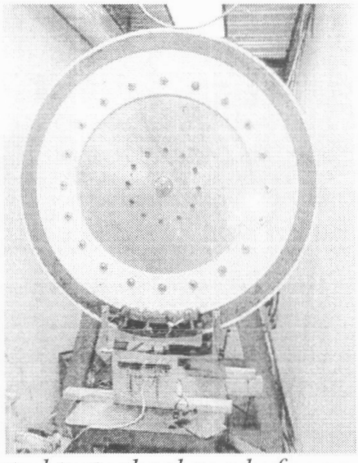

(b) Completed test wheel ready for operation

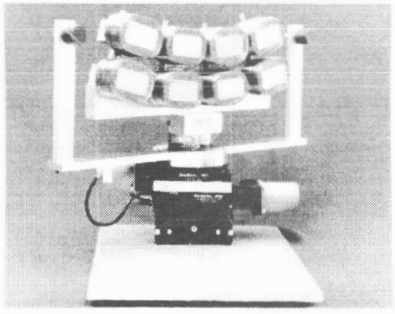

(c) Iron-core magnet, mounted to multi-axis force sensor, showing capacitive position sensors

Fig. 1. Flux-canceling Maglev topology

Guideway Coil Implementation

The guideway coils are constructed out of sheets of 0.093" thick copper, with the conductor pattern cut with a water jet and the resultant layers brazed (*Fig. 2a*). The two layers were insulated by a thin layer of non-conductive paint. The induced current path is around the thin loops on the top

layer, through the brazed rim, and around the thin loop in the bottom layer. Therefore, the electrical integrity of the rim has a large effect on the efficient operation of the guideway.

Circuit Models and Scaling Laws

Simple models may be used to demonstrate the effects of mutual coupling between guideway loops on the Maglev forces and drag peak velocity. Using a 3-coil model (*Fig. 2c*), the transfer ratio between loop current and voltage in the sinusoidal steady state is:

$$sL\begin{bmatrix} 1 & k_{12} & k_{13} \\ k_{12} & 1 & k_{12} \\ k_{13} & k_{12} & 1 \end{bmatrix} + R\begin{bmatrix} 1 & r_{12} & r_{13} \\ r_{12} & 1 & r_{12} \\ r_{13} & r_{12} & 1 \end{bmatrix} = \begin{Bmatrix} v_1 \\ v_2 \\ v_3 \end{Bmatrix} \qquad [1.]$$

The self inductance of each loop is L and the loop-loop mutual inductance $M_{ij} = k_{ij}L$ where k_{ij} is the loop coupling coefficient which is less than 1. The effects of mutual resistance are modeled by the off-diagonal term r_{ij}. The natural frequencies and mode shapes of this structure are found by solving the resultant Eigenvalue problem.

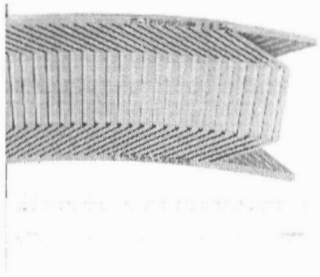

(a) Prototype guideway section showing two copper layers bolted and brazed along the edge

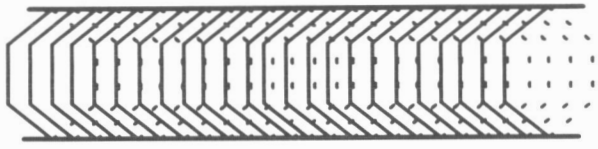

(b) Linearized geometry of guideway coils

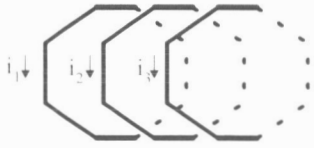

.85 cm

(c) Broken up into individual coils (exploded view)

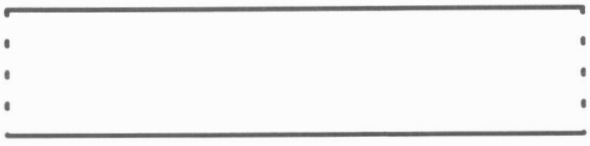

(d) Rim

Fig. 2. Guideway geometry and modeling

For the purposes of calculating guideway coil self and mutual inductances to fill the inductance matrix, approximate models were developed for this guideway structure. Although the inductances can be calculated by finite element analysis, this method gives little insight into scaling laws. Therefore, simple approximations were developed which may be used as a practical design tool.

Known solutions exist for inductor geometries such as disk coils and filamentary loops. A realizable geometry for which tabulated results exist is the round loop with rectangular cross section,

with mean radius a, axial thickness b, and trace width c (*Fig. 3a*). The self-inductance of this loop may be calculated using techniques outlined in [Grover, pp. 94], where the inductance is found to be:

$$L = 0.1aPF \qquad [2.]$$

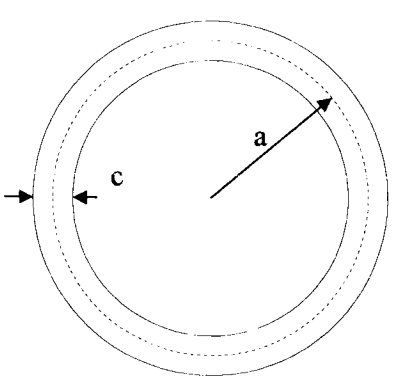

Depth b into paper

(a) Top view of disk coil

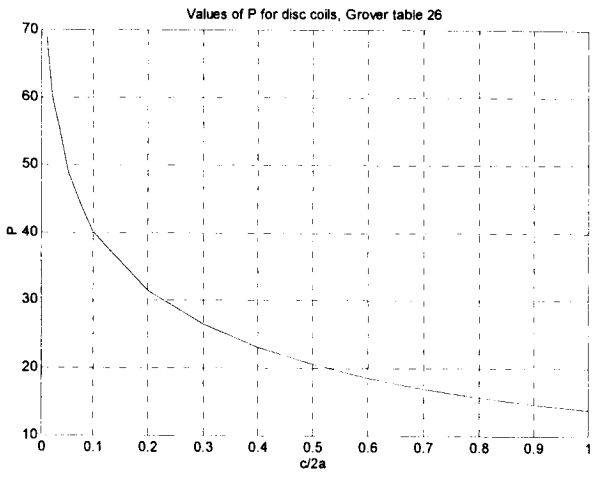

(b) Function P, for disk coils

Fig. 3. Modeling of circular coil with rectangular cross section

For this calculation, a is in meters and L is in μH. P is a function of the coil normalized radial thickness $c/2a$ (*Fig. 3b*) and applies to a coil of zero axial thickness ($b = 0$), and F accounts for the finite axial length of the coil. For $b << c$ and $c << a$ (coils resembling thin disks) the factor $F \approx 1$, an important limiting case. Therefore, for a coil with double the mean radius, there will be a corresponding doubling of the inductance.

The goal of this exercise is to approximate the complicated guideway loop geometry by a geometry where analytic expressions are available. The calculation for the circular disk coil with rectangular cross section was applied to a single loop of the guideway. Shown in *Fig. 4a* is the actual geometry of one guideway loop coil which spans one pole pitch $p = 12.6$ cm. The procedure for finding an approximate equivalent disk coil (*Fig. 4b*) is as follows:

• Calculate the circumference of the actual coil, using the mean distance to each coil element from the center	$l_{total} = 36.1$ cm
• Find the mean radius of a circular coil which has the same perimeter	$a = 5.75$ cm
• Calculate the mean radial thickness of the coil	$c = 0.39$ cm
• Find P as a function of $c/2a = 0.0337$, interpolating from Grover Table 26, pp. 113	$P = 53.87$
• Find F as a function of $c/2a$ and $b/c = 0.6082$, using Grover Table 24, pp. 108	$F = 0.9182$

This methodology is designed to match the self-inductance of the actual guideway coil with a circular coil. Results (*Table 1*) show good agreement between measurements made using an actual coil, finite element analysis on the coil, and the approximate calculation.

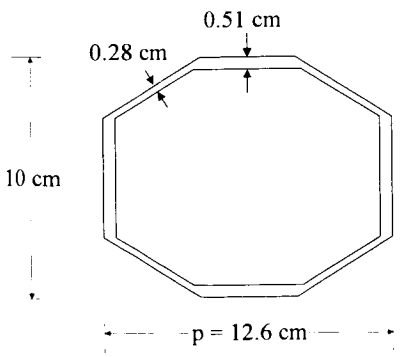

(a) Actual linearized geometry of one pole-pitch wide primitive guideway loop

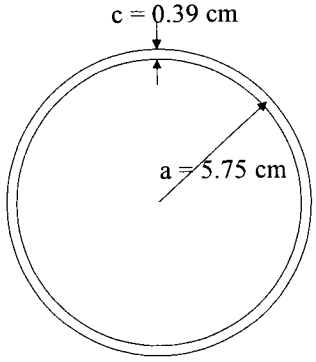

(b) Approximate model, using disk coil enclosing same perimeter

Fig. 4. Coil model, showing primative coil section and disk coil used for modeling

Table 1. Comparison of calculations on coil geometries

Measured inductance @ 10 kHz	***Grover Calculation (using circular disk coil)***	***Finite Element Analysis (using actual guideway coil geometry)***
259 nH	276 nH (see above)	280 nH

In order to calculate the mutual inductance between coils, further approximations were made by modeling the circular disk coil by a thin filament near the center of the cross-section of the disk. An approximate formula for the calculation of the self-inductance of a filamentary loop was first given by J.C. Maxwell [Maxwell, pp. 342], where:

$$L = \mu_o a\left\{\ln\left(\frac{8a}{r}\right) - 2\right\} \qquad [3.]$$

where a is the radius of the loop in meters and r is the radius of the wire. A paper by T. R. Lyle in 1913 shows that the filament approximation will give the self-inductance of any circular coil with rectangular cross section to any degree of accuracy when the mean coil radius is substituted for a and the geometric mean distance (G.M.D.) is substituted for r. The values of mean radius and G.M.D. are adjusted depending on the mean radius and the cross-section profile of the coil. The same reasoning can be applied to find the mutual inductance between filamentary loops, as in the early papers by S. Butterworth and A. Campbell. Using these approximation methods, the resultant self and mutual inductances were found (*Fig. 5*) and used to fill a 15×15 inductance matrix. The self and mutual resistances for the 15 loops was calculated and the resistance matrix was filled. These matrices were used to calculated forces, dominant time constants, and the drag peak velocity with results described later in this paper.

Once the inductance and resistance matrices are found and solved, the vectors corresponding to loop currents are used to calculate lift and drag forces. Lift force is found by:

$$< f_z(\omega) > = \frac{l}{2} \sum_{j=1}^{15} \mathrm{Re}\left\{ i_j(j\omega) B_j^*(j\omega) \right\} \qquad [4.]$$

where l is a length scale associated with the horizontal length of the coil, i_j is the induced current in the jth coil, and B_j is the average field acting on the induced current. The drag force is found by evaluating the power dissipated in the guideway coils, or:

$$< f_x(v) > = \sum_{j=1}^{15} \frac{|i_j|^2}{2Rv} \qquad [5.]$$

where v is linear velocity and R is the loop resistance.

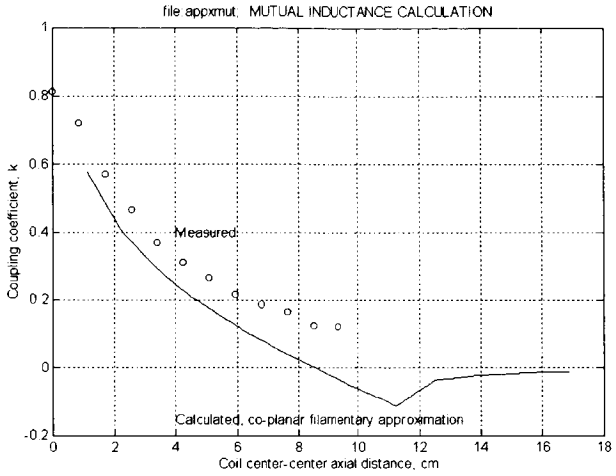

Fig. 5. Comparison of calculated (solid line) to measured guideway coil-coil mutual inductance Mutual inductance calculation based on approximations in [Butterworth]

MAGLEV TEST PROGRAM AND TEST RESULTS

Details of the test fixture including speed control of the test wheel and operation of the data acquisition system are discussed in [Kondoleon, et. al., 1995] and a companion paper in these *Proceedings*. The goals of the test program were to:

- Measure forces and moments for the magnets in different equilibrium positions and for different linear velocities using a force sensor.
- Test the viability of using AC excitation of the magnet coils to achieve significant lift force at zero train velocity.
- Test the viability of actively controlled high temperature superconducting magnets in a magnetic secondary suspension by testing the magnet with copper coils and a low-friction air bearing.

Basic Maglev Tests using Force Sensor

The result of several test wheel runs is shown in *Fig. 6*. In *Fig. 6a*, the magnet was set below the null position, and a positive lift force is measured. In *Fig. 6b*, the magnet was set +1.25 cm above the null position and a negative lift force is measured. The drag force shows a peak at approximately 20-25 meters/second. Also of note is the guidance force, which is a significant fraction of the lift

force. In *Fig. 6c*, the magnet was set near the null position, and the lift and drag forces are minimized accordingly.

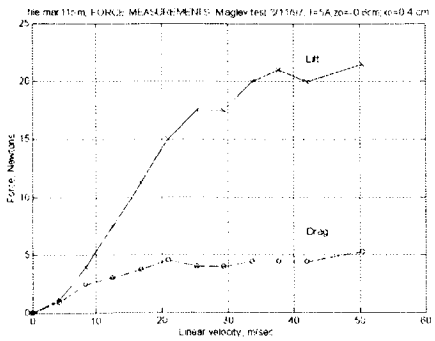

(a) Magnet below null position at z = -0.4 cm

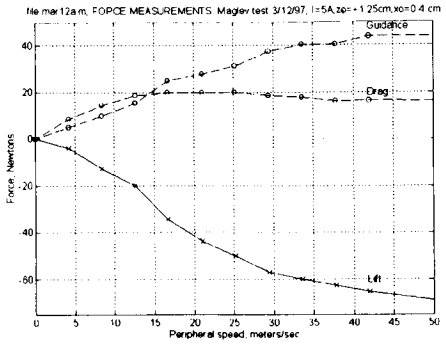

(b) Magnet above null position at z = 1.45 cm

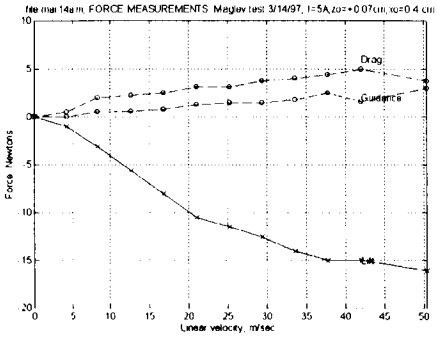

(c) Magnet slightly above null position at z = 0.27 cm

Fig. 6. Lift, drag, and guidance force measurements. I = 5A per coil, NI = 2,750 A-turns per coil, all 8 coils energized

The important results from this test are that the drag peak velocity is approximately 20-25 meters per second, which is significantly lower than the maximum test wheel speed. Therefore, data has been taken at speed significantly higher than the drag peak velocity. This critical velocity will decrease significantly for a full-scale Maglev magnet. The dependence of drag peak velocity with magnet size can be predicted with scaling laws developed later in this paper. Also, the guidance force for this configuration is a significant fraction of the lift force. This may enable a design without additional guidance coils.

The result of a calculation based on the electrodynamic model described previously is shown in *Fig. 7*, and compared to measured data taken with the test wheel in the range 0 - 600 RPM (0 - 50 meters/second). There is good agreement for the 15-coil model for the lift force f_z and the drag force f_y. The simple circuit model predicts a drag peak velocity of approximately 15 meters/second, while the measured drag peak is approximately 20-25 meters/second. The accuracy of the drag force can be further improved by accounting for parasitic eddy currents in the guideway rim, effects that are not considered by the circuit model.

Referring to *Fig. 7*, the excitation vector (top left) is approximately a half-sinusoid, corresponding to the applied magnetic field integrated over the area of the guideway loops. The

shape of this vector insures that only first and second modes will be excited, due to the orthogonality of natural modes. Measurements on drag force (bottom right) bear this out, as the measured drag peak velocity was approximately 25 meters/second and the electrodynamic model predicts ~40 meters/second. Higher-order modes are at significantly higher natural frequencies.

The lift force model shows good agreement with experiment in the 0-50 meter/second range, although there is divergence at higher velocities. This may be due to the effects of higher-order modes at higher frequencies, but further study is warranted.

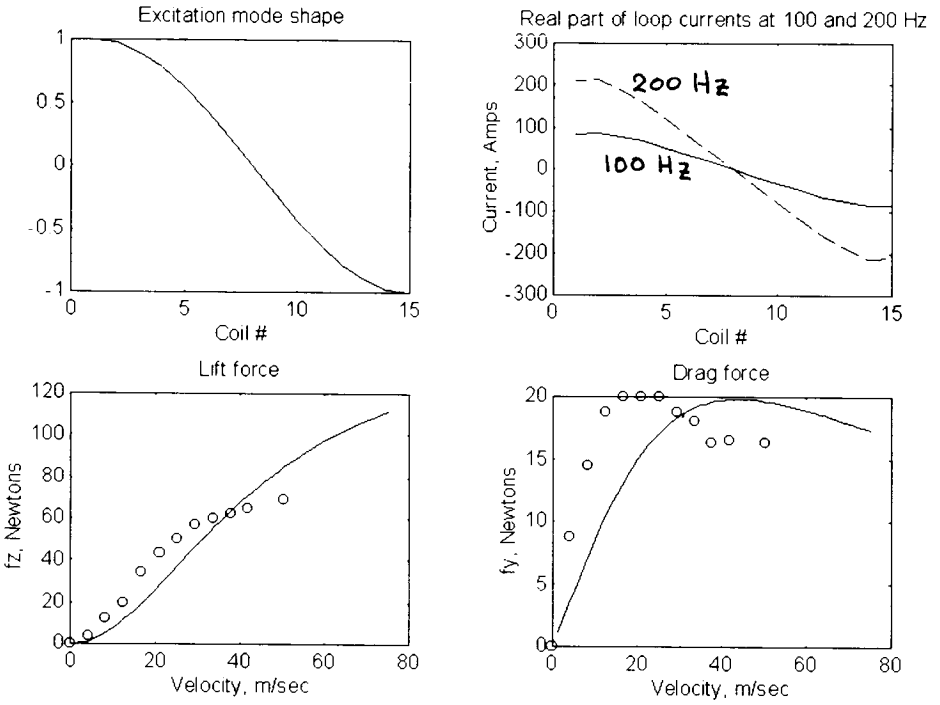

Fig. 7. Predictions of electrodynamic model with magnet +1.25 cm above null position Upper left, coil excitation vector {v}; Upper right, induced loop currents {I} at 100 Hz and 200 Hz Lower left, comparison of measured to calculated lift force vs. velocity; Lower right, comparison of measured and calculated drag force vs. velocity

Use of Scaling Laws for Full-Scale System

The goal of this section is to predict performance of a full-scale Maglev system based on scaling laws, simple guideway coil geometries, and test results from the 1/5 scale-model magnet. Results may be extrapolated from calculations on simple resistance-inductance circuits, as the previously mentioned measurements have proven this approximate technique to be valid. It is assumed that in scaling up the system, every linear dimension in the guideway and magnet is scaled by the factor ℓ.

As shown previously, the inductance of a disk inductor has the form:

$$L \propto aPF \qquad [6.]$$

where a is the mean coil radius. If all dimensions of the inductor are scaled by the factor ℓ, the inductance also scales by the same factor as P and F remain constant. The self-resistance of the loop is given by:

$$R \approx \frac{2\pi a}{\sigma bc} \qquad [7.]$$

and this resistance scales as $1/\ell$. The resultant time constant of the loop (given by L/R) scales as ℓ^2, and shows that large scale inductors will be more efficient than small ones. Given this scaling, the EDS drag peak velocity is expected to scale as $1/\ell$, although the effects of parasitic eddy currents will modify this somewhat.

The number of coil turns (N) scales with the winding area, or as ℓ^2. The average guideway field scales as ℓ, due to the ℓ^2 factor increase in turns, and the ℓ increase in pole pitch. The induced voltage V_i around a guideway loop may be expressed as:

$$V_i = j\omega B_0 A \propto l^3 \qquad [8.]$$

where B_0 is the average magnetic field, and A is the area of the guideway loop. In the high-speed limit, the induced current is limited by the inductance of the coil, as:

$$I_i \approx \frac{V_i}{j\omega L} \propto l^2 \qquad [9.]$$

The lift force is due to the product of the induced current, the applied magnetic field, and the length scale, or:

$$f_z \propto I_i B_0 l \propto l^4 \qquad [10.]$$

The maximum lift force scales as ℓ^4, which also could be inferred from evaluating the magnetic pressure acting on the iron polefaces. The drag force scales as $I_i^2 R$, or as ℓ^3 and hence the lift/drag ratio at cruising speed scales as ℓ. Other parameters such as scaling of lift/drag and lift-to-weight ratio may also be inferred from the test results. A summary of the scaling laws is shown in *Table 2*.

Using these scaling laws, performance of a full-scale magnet based on copper coils and on HTSC coils operating at 40K has been predicted (*Table 3*). The extrapolation from our 1/5-scale test results to 1.0 scale copper and for copper operating at 77K is straightforward if limitations imposed by air cooling of the copper magnets are not considered. It is unlikely that the number of Ampere-turns shown for the full-scale copper magnet would be achieved in practice due to the heat transfer limitations of air or water cooling.

It is assumed that the copper coils operating at 77K have the same power dissipation as 1.0-scale copper coils operating at room temperature. Therefore, a higher coil current is possible at 77K since the conductivity of copper at liquid nitrogen temperature is only 13% of the room temperature value. This assumes that there is sufficient copper area exposed to the boiling liquid nitrogen. An

upper limitation[2] for allowable power dissipation in the copper coil is the peak nucleate boiling heat transfer flux, which for liquid nitrogen is $q_{pk} \sim 15$ Watts/cm^2 [Iwasa, pp. 113].

The performance of a silver-sheathed HTSC magnet operating at 40K is extrapolated from the copper coil results and from available data taken from tests on HTSC coils and samples of HTSC tape. The achievable current density in HTSC at 40K is much higher than that in HTSC at 77K (approximately by a factor of 2-6 from published data). For the same number of Ampere-turns, less material will be needed for the HTSC design, resulting in a lighter coil. Current HTSC tapes are available with critical current $I_c = 40$ Amperes at 77K corresponding to a critical current density significantly higher than that supported by copper at 77K. A value of $I = 100$ Amperes or higher seems reasonable for an HTSC coil design at 40K given current technology [Iwasa, 1997]. Further improvement may be made by adjusting the dimensions of the core, as the full winding area will not be needed.

The performance of the predicted 1.0-scale HTSC magnet at 40K is comparable to that of the Japanese MLU002 test vehicle, which operates with an MMF of 700 kA-turns while generating a levitating force of 196 kiloNewtons [He, et. al, pp. 7]. The advantage to the iron-core HTSC design is that less Ampere-turns and less superconducting material is needed, and there is the possibility of actively controlling the magnet currents to achieve acceptable ride quality.

Table 2. Scaling law summary for EDS Maglev scaled by factor ℓ
Primed coordinates are for the scaled-up system

Parameter	***Constitutive Relation***	***Scaling law***
Guideway loop self-inductance, L	$L \propto \ell PF$	$L' = \ell L$
Guideway loop self-resistance, R	$R \propto 1/\sigma\ell$	$R' = R/\ell$
Guideway dominant time constant, τ	$= L/R \propto 1/\ell^2$	$\tau' = \tau/\ell^2$
Effective frequency at guideway, ω		$\omega' = \omega/\ell$
Drag peak velocity		$v_{pk}' = v_{pk}/\ell$
N, turns	$\propto \ell^2$	$N' = \ell^2 N$
Average field normal to guideway, B_o	$\propto NI/\ell \propto \ell$	$B_o' = \ell B_o$
Induced guideway loop voltage, V_i	$\propto j\omega B_o \ell^2 \propto \ell^2$	$V_i' = \ell^2 V_i$
Max. induced loop current, I_i	$\propto V_i/j\omega L \propto \ell^2$	$I_i' = \ell^2 I_i$
Lift force at cruising speed, f_z	$\propto B_o I_i \ell \propto \ell^4$	$\propto B_o I_i \cdot \propto \ell^4$
Drag force at cruising speed, f_y	$\propto I_i^2 R \propto \ell^3$	$\propto I_i^2 R \propto \ell^3$
Lift/drag ratio at cruising speed	$= f_z/f_y$	$\propto \ell$

[2] Assuming that the winding has sufficient ventilation space for the liquid nitrogen to vent

Table 3. Scaling law summary applied to test data
Comparison between 1/5 scale suspension test results, 1.0-scale copper magnet operating at room temperature, 1.0 scale copper at 77K, and HTSC at 40K (Cooling weight not included)

Parameter	***1/5-scale model***	***1.0 scale copper***	***1.0 scale copper, 77K***	***HTSC @ 40K***
Guideway loop self-inductance, L	280 nH	1.4 μH	1.4 μH	1.4 μH
Guideway loop self-resistance, R	0.0007 Ω	0.00014 Ω	0.00014 Ω	0.00014 Ω
Loop time constant, τ	0.4 msec	10 msec	10 msec	10 msec
Levitation coil turns, N	550 turns	13750	13750	1500
Levitating coil operating current, I	5 Amps	5	14.4	136[1]
Levitation power dissipation	680 Watts	85 kW	85 kW	0
NI, each coil	2750 A-turn	68750	198,450	198,450
Current density in winding, λJ	275 A/cm^2	275	800	7500
Average field normal to guideway, B_o	0.067 Tesla	0.335	0.96	0.96
Lift force at v = 100 m/s, f_z	70 Newtons	43.8 kN	365 kN	365 kN
Drag force at drag peak, f_y	20 Newtons	2.5 kN	20.8 kN	20.8 kN
Drag peak velocity v_{pk}	25 m/sec	5 m/sec.	5 m/sec.	5 m/sec.
Drag force at v = 100 m/sec	9.4 N	249 N	2.1 kN	2.1 kN
Lift/drag ratio at v = 100 m/s	7.4	175.4	175.4	175.4
Magnet core weight	29 kg	3625	3625	3625
Coil weight	8 kg	1000	1000	106
Total magnet weight[2]	37 kg	4625	4625	3731
Magnetic drag power @ 100 m/sec	0.94 kW	24.9 kW	208 kW	208 kW
Guideway power, kW/ton of lift	120 kW/ton	5.07	5.07	5.07
Lift/weight ratio	0.19	0.97	8.0	10.0

1. Assuming HTSC tape is of same cross sectional area as 18 gauge wire; for comparison only
2. Cryostat weight not included

Results of Dynamic Tests Using Air Bearing and Control System

In another set of experiments, the magnet was mounted to an air bearing which allowed low-friction vertical motion of the magnet. The control current source was connected as in *Fig. 8a*. The advantage of driving the control current at these points is that that mutual coupling reduces the power required to change the coil currents and control the lift force.

Each of the coils was energized with 6 Amps DC by the main power supply V_m. With the air bearing energized and the control system deactivated, the vertical magnet position was perturbed approximately +1 centimeter from the equilibrium position and the resultant transient decay of magnet position was observed (*Fig. 8a*). The oscillatory behavior is at 1.15 Hz with a damping ratio of approximately 1%, corresponding to the expected underdamped EDS response.

A similar experiment was run, but with the control system operating (*Fig. 8c*). Vertical position of the magnet was measured with a frictionless LVDT and a P.I.D. controller which controlled the current source I_c. The resultant magnet vertical position response is much more

damped ($\varsigma \sim 40\%$) showing that the control system is operating correctly. Further improvement can be made in the transient response by adjusting the loop parameters.

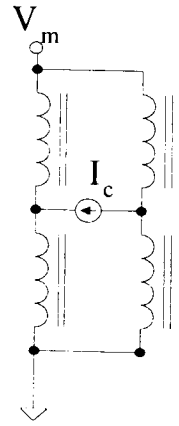

(a) Wiring

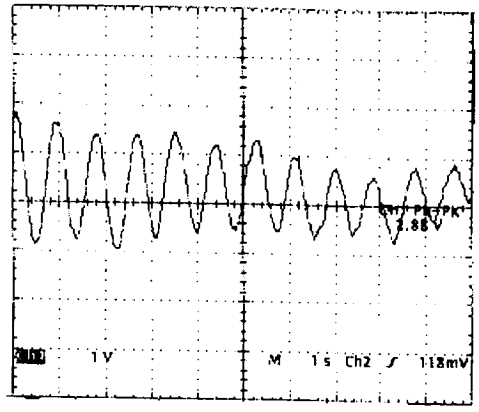

(b) Control system not activated, initial deflection 1 cm; oscillation frequency 1.15 Hz

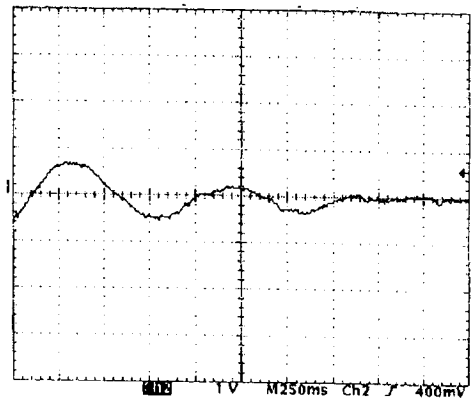

(c) Control system operational

Fig. 8. Test of vertical control system

AC Lift Measurements

Further tests were run to determine if significant lift is possible at zero train velocity by exciting the levitation coils with AC currents. Generating lift at zero velocity is desirable, as this can remove the need for a low speed suspension. The fact that high temperature superconductors are robust with regard to AC losses is a further motivation, as such control is difficult using low temperature superconductors due to quenching.

For this series of tests, the coils were wired as in *Fig. 9a*. The coils were wired so that for the first half cycle of the sinewave current excitation, the top two coils are in a North-North arrangement, and the bottom two coils are energized South-South. For this configuration, if the guideway is offset from the null position, there is a net changing flux through the guideway loops and hence a restoring force.

Results of AC lift measurements are shown in *Fig. 9b* for various equilibrium displacements from the null position, and for excitation frequencies of 10, 20, 50 and 100 Hz. A maximum frequency of 100 Hz was chosen[3] as this is the approximate equivalent frequency of the Maglev drag peak, and higher frequencies will not result in significantly higher lift. The data shows that lift comparable to that achieved by electromagnetic induction by motion can be achieved, however at the cost of high power delivery from the magnet current source. Scaling laws can be used to show that a full-scale magnet with eight coils each with $NI = 165{,}000$ (corresponding to $N = 2062$ turns and $I =$ 80 A p-p) will generate approximately 1 ton of lift with a lift-to-weight ratio of 0.28 at 100 Hz (*Table 4*). With $NI = 495{,}000$ A-turns p-p, a magnet lift-to-weight ratio of ~2.5 will be achieved for a full-scale magnet based on an HTSC coil. The primary losses will be switching losses in the driving electronics, and AC losses in the levitation and guideway coils. The actual lift-to-weight ratio will

[3] If the operating frequency is known and does not change, a series capacitor can be added to resonate with the inductive load to reduce the large reactive voltage required to drive the magnet coil.

be less due to the weight of the cooling system, and further study is required to determine the extent of power losses in the HTSC coil due to switching.

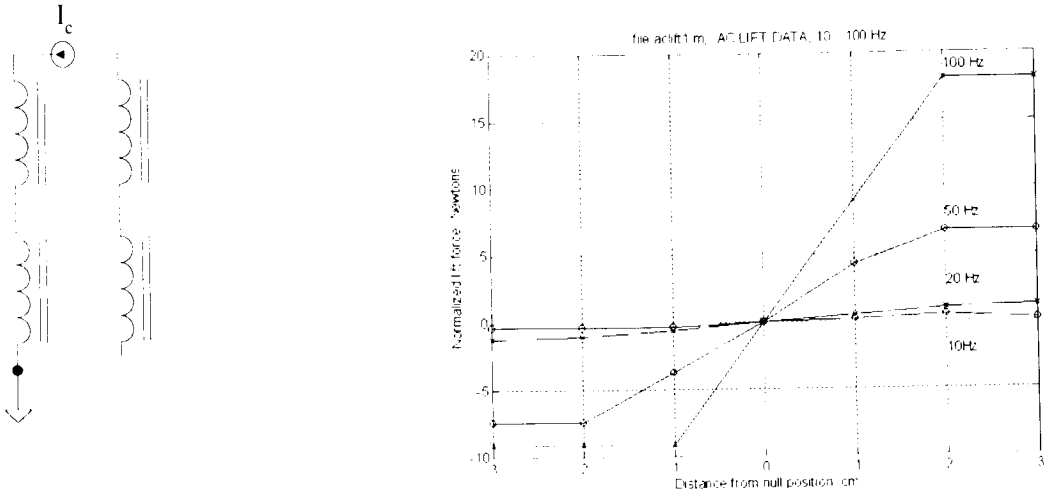

(a) Magnet wiring for AC lift measurements *(b) Test results for AC lift*

Fig. 9. AC lift measurements at 10, 20, 50 and 100 Hz

Table 4. Scaling laws applied to AC lift measurements (Cryostat weight not included)

	1/5-scale copper, I = 12A, 100 Hz	***1.0 scale HTSC @ 40K, I=80A p-p, 100 Hz***	***1.0 scale HTSC @ 40K, I=240A p-p, 100 Hz***
Ampere turns, p-p	6,600	165,000	495,000
Lift force	17 N	10625 N	95,625 N
Lift/weight ratio	0.05	0.28	2.5

CONCLUSIONS

Results from these series of Maglev tests show that there is good agreement between predictions based on simple circuit models with measurements taken on the test fixture for lift force, drag force, and magnetic drag peak. The models could be improved by doing additional finite-element analyses and extending the 15-coil model so that the infinitely long guideway is better approximated.

The use of an iron core offers significant advantages such as rapid attenuation of the far magnetic field. Furthermore, the iron core reduces the mass of superconducting material needed for a given guideway field. The iron can be used to reduce the magnetic field impinging on the coils so that the critical current is maximized.

Vertical force can be controlled by differential control of the magnet currents. Vertical position can be actively damped by utilizing an active magnetic secondary suspension. Use of HTSC may overcome the limitations imposed by mechanical secondary suspensions. The guidance force

measured was a significant fraction of the lift force. Similar reasoning could be used to design a guidance system, for horizontal train control, based on flux-canceling concepts.

It is possible to generate lift with AC currents using this configuration. The robustness of HTSC with regard to AC losses may make AC lift a viable alternative to low-speed mechanical suspensions. However, cooling requirements will probably limit the duration for which AC lift may be operated. Scaling laws were derived which show that the performance of an HTSC-based design at 40K may be comparable to that of low-temperature superconducting designs, with the advantage of less weight and the possibility of using AC lift for low-speed suspension.

ACKNOWLEDGMENTS

Thanks are due to the U.S. Department of Transportation, Federal Railroad Administration, through the Volpe National Transportation Systems Center, Cambridge, MA, which funded this work.

REFERENCES

[1] S. Butterworth, "On the Coefficients of Self and Mutual Induction of Coaxial Coils," *Philosophical Magazine*, vol.29, 1915, pp. 578-592

[2] S. Butterworth, "On the Coefficients of Mutual Induction of Eccentric Coils," *Philosophical Magazine*, series 6, vol.31, 1916, pp. 443-454

[3] A. Campbell, "On the Use of Variable Mutual Inductances," *Philosophical Magazine*, vol. 15, 6th series, 1908, pp. 155-171

[4] F. W. Grover, *Inductance Calculations: Working Formulas and Tables*, Dover Publications, Inc., New York, 1946

[5] J. L. He, D. M. Rote, and H. T. Coffey, "Study of Japanese Electrodynamic-Suspension Maglev Systems," *Argonne National Laboratory report ANL/ESD-20*, April 1994

[6] Y. Iwasa, *Case Studies in Superconducting Magnets*, pub. by Plenum Press, New York, 1994

[7] Y. Iwasa, personal communication, 1997

[8] A. Kondoleon, D. Seltzer, R. D. Thornton, and M. T. Thompson, "Development of a Large Scale High Speed Wheel Test Facility," *Proceedings of the Third International Symposium on Magnetic Suspension Technology*, NASA Conference Publication 3336, part 2, pp. 523-534, Dec. 13-15, 1995

[9] T. R. Lyle, "On the Self-Inductance of Circular Coils of Rectangular Section," *Philosophical Transactions*, vol. 213A, (1913) pp. 421-435

[10] J. C. Maxwell, *A Treatise on Electricity and Magnetism*, vols. 1 and 2, Dover Publications

[11] M. T. Thompson, "High Temperature Superconducting Magnetic Suspension for Maglev," Ph.D. Thesis, Department of Electrical Engineering and Computer Science, Massachusetts Institute of Technology, May 1997

[12] M. T. Thompson and A. Kondoleon, "Test Results from a Large Scale, High Speed EDS MAGLEV Wheel Test Facility," these *Proceedings*

[13] R. D. Thornton, D. Perreault, T. Clark, "Linear Synchronous Motors for Maglev," *U.S. Dept. of Transportation, Federal Railroad Administration Report DOT/FRA/NMI-92/13*, January 1993

[14] R. D. Thornton and M. T. Thompson, "Magnetically Based Ride Quality Control for an Electrodynamic Maglev Suspension," these *Proceedings*

(**Editors Note**: This paper was presented by Hans Schneider-Muntau of the NHMFL. Unfortunately, only the abstract is available since the text of the paper was not received by the time of publication of the proceedings.)

Progress in High Temperature Superconductivity for Magnet Applications

Justin Schwartz, Florida State University, National High Magnetic Field Laboratory, 1800 E. Paul Dirac Drive, Tallahassee, FL 32310

Abstract

High temperature superconductors (HTS) have progressed greatly in the 10 years since their discoveries. Bi-Sr-Ca-Cu-O conductors are fabricated on long length-scales with transport critical current density (J_c) sufficient for technical applications. Recent breakthroughs with Y-Ba-Cu-O have led to incredibly large transport J_c in short lengths, which, if scaleable, would lead to a plethora of new applications. Hg-Ba-Ca-Cu-O materials have significantly larger critical temperature (T_c) than other HTS materials (up to 135K), and have the potential to be a significant second-generation conductor.

In this paper, the status of HTS conductor development is reviewed with a focus on applicability to practical magnet systems. Issues such as scale-up, mechanical properties, thermal properties (*i.e.*, stability and quench behavior), and intrinsic superconducting properties, are discussed. Progress on system applications of Bi-Sr-Ca-Cu-O conductors (*e.g.*, motors and high field solenoids) and on the latest developments with Y-Ba-Cu-O coated conductors are reviewed. Recent breakthroughs in the processing of Hg-Ba-Ca-Cu-O materials with metallic substrates or sheaths are also presented and the practicality of using a high-toxicity material in commercial systems is analyzed.

Session 4 -- Bearings 1

Chairman: Toru Namerikawa
Kanazawa University

DESIGN OF A STATOR-CONTROLLED MAGNET BEARING

H. Ming Chen
Mohawk Innovative Technology, Inc.
Albany, NY

ABSTRACT

The subject bearing has a laterally movable stator which consists of a permanent magnetic ring axially polarized and two disks made of magnetic material. The radial magnetic flux at air gaps between the stator and rotor form an unstable bearing. To make it stable, the stator is mounted on mechanical springs and motion-controlled by feeding back the rotor displacement. The motion control actuators are likely the stationary electromagnetic types. A design methodology for the new bearing concept is presented herein with emphasis on sizing the system parameters for stability. The bearing is best suited for supporting vertical rotors, such as those of energy or momentum storage flywheels. It has a simple rotor structure, minimal eddy-current loss, and electronically maneuverable stiffness and damping.

INTRODUCTION

A conventional active magnetic bearing (AMB) has stationary electromagnetic poles around its rotor. In rotation, the rotor surface material comes in and out of the magnetic flux of the protruding poles. The changing flux in the surface material generates heat due to magnetic hysteresis and eddy current. The latter not only causes heat loss but also delays the control response of the electromagnets. To reduce the eddy current effect, the conventional AMB cores are usually made of silicon steel laminations. The eddy current heat loss on high speed rotors can be a serious problem, because it is difficult to dissipate in vacuum. It may generate high rotor temperature causing stress and other thermal related problems. Using a homopolar AMB with extended pole edges in the circumferential direction may reduce the eddy current heat, but can not totally eliminate it. Note that the heat is proportional to the square of rotor speed times number of poles. This has led to the use of continuous ring pole permanent magnet (PM) bearings. Since the magnetic flux of the ring-shaped poles is not interrupted during rotation, the eddy current and hysteresis core losses can be kept to a minimum. As an example, two radial PM ring bearings have been designed for a flywheel energy storage power quality application [1]. These bearings have stationary and rotating disks packed with many axially polarized PM rings. They are expensive to fabricate and have centrifugal stress concern at high speeds. Also, they are soft and have no damping; their large axial negative stiffnesses require oversized active thrust magnetic bearings.

Herein a new PM bearing concept called stator-controlled magnetic bearing (SCMB) is presented. As shown in Figure 1a, the stator consists of two disks made of magnetic material such as silicon steel, and each disk has a center hole served as a magnetic pole. A PM ring with axial polarization is sandwiched between the two disks . The rotor is simply a circular cylinder made of magnetic material

with an outer diameter slightly smaller than the stator disk holes. The magnetic flux circulating through the annular air gaps form an unstable magnetic bearing with a negative stiffness. To make a stable bearing as demonstrated by Oka and Higuchi [2], the stator should be mounted on mechanical springs and its motion be controlled with feedback of the rotor motions. The latter are measured by using two displacement sensors. The actuators for controlling the stator motions are likely a stationary type of AMB as shown by the concept variation in Figure 1b. The actuators are not the main interest of this paper. The focus here will be on how to design a stabilizing controller and how to size the bearing proper and the actuator capacity. Note that the rotor leans on a backup bearing when the stator is not under control.

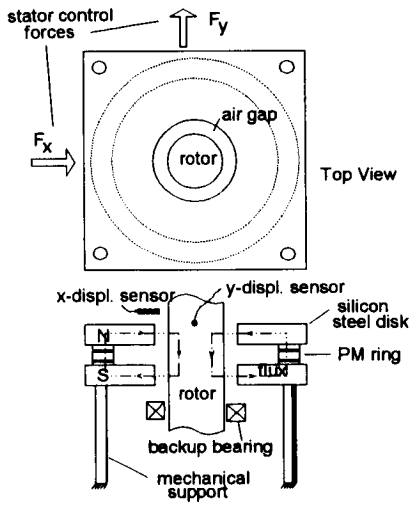

Figure 1a. Stator-controlled magnetic bearing concept

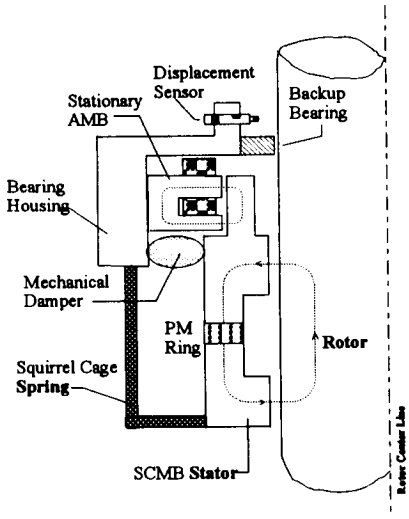

Figure 1b. SCMB practical implementation

FORMULATION OF STATOR-CONTROLLED MAGNETIC BEARING

There are two stator motion-control axes which are assumed to be independent of each other. The dynamics of each control axis can be represented by Figure 2. The equations of motions are the following:

$$M_s X_s'' = K_m(X_s - X_b) - F_s \tag{1}$$

$$M_b X_b'' = -K_m(X_s - X_b) - KX_b - CX_b' + F \tag{2}$$

where

M_s = rotor mass at bearing
M_b = stator mass
X_s = rotor displacement

X_b = stator displacement
' = differentiate once with respect to time
" = differentiate twice with respect to time
K_m = stiffness coefficient of magnetic field in air gaps
K = stiffness coefficient of stator mechanical support
C = damping coefficient of stator mechanical support
F_s = static load on rotor
F = stator control force.

For the stator feedback control, the rotor displacements relative to ground are measured in two orthogonal directions as shown in Figure 1a. A PID (proportional, integral, derivative) control scheme is appropriate for the application and the stator control force is represented by (3).

$$F = C_p X_s + C_d X_s' + C_i \int X_s dt \qquad (3)$$

where

C_p = proportional constant
C_i = integral constant
C_d = derivative constant
t = time.

The first priority of the bearing design is to make a stable control system by choosing a proper set of PID constants. For evaluating stability, the static force F_s in equation (1) may be ignored. Taking Laplace transform of (1), (2) and (3), and combining the three transformed equations, the following normalized system characteristic equation is obtained:

$$S^5 + CS^4 + (K-\mu-1)S^3 + (C_d-C)S^2 + (C_p-K)S + C_i = 0 \qquad (4)$$

where $\mu = M_b/M_s$. All the parameters in (4) are normalized or dimensionless quantities as defined below. The sign "==>" means "imply".

$S \Longrightarrow S/B_s$ (S=Laplace variable, $B_s=\sqrt{K_m/M_s}$)
$C \Longrightarrow C/\sqrt{K_m M_s}$
$C_d \Longrightarrow C_d/\sqrt{K_m M_s}$
$K \Longrightarrow K/K_m$
$C_p \Longrightarrow C_p/K_m$
$C_i \Longrightarrow C_i/K_m B_s$.

The above normalization is done with respect to the magnetic field stiffness (or negative spring rate) K_m and the rotor mass M_s which are the basic given quantities of the bearing system. The artificial

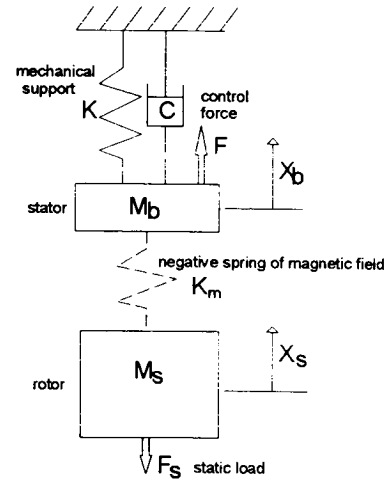

Figure 2. Control axis representation

parameter B_s provides a calibration of the frequency location of the lowest system mode. The bearing design work is to choose a set of values for six parameters, i.e., μ, K, C, C_p , C_d and C_i , so that equation (4) has stable roots which all lie in the left half of the S-plane.

SYSTEM SIZING METHOD

Out of the six parameters, only the mass ratio μ may be independently chosen. The stator mass relative to the rotor mass which includes two disks, one PM ring and a part of the mechanical support, can be estimated. The remaining five normalized parameters can be determined by using the pole-placement method. A desirable set of five roots of the normalized equation (4) may include a pair of reasonably damped complex conjugate roots and three negative real roots. To demonstrate the method, let's consider the following "desirable" five roots:

$$S = -0.3 \pm 0.5j \; ; \quad -0.6 \; ; -0.6 \; ; \quad -1.0$$

Then the system characteristic equation can be re-created below:

$$(S+0.3+0.5j)(S+0.3-0.5j)(S+0.6)^2(S+1.0) = 0$$

or

$$S^5 + 2.8S^4 + 3.22S^3 + 2.144S^2 + 0.8464S + 0.1224 = 0 \qquad (5)$$

Comparing (5) to (4), we obtain:

$$C/\mu = 2.8 \; ; \; (K-\mu-1)/\mu = 3.22 \; ; \; (C_d-C)/\mu = 2.144 \; ;$$

$$(C_p-K)/\mu = 0.8464 \; ; \; C_i/\mu = 0.1224$$

Let's choose the stator mass to be 1/8 of the rotor mass M_s , i.e., $\mu = 0.125$. Then the five normalized system parameters are:

$$C = 0.35 \; ; \; K = 1.5275 \; ; \; C_d = 0.618 \; ; \; C_p = 1.6333 \; ; \; C_i = 0.0153$$

NUMERICAL EXAMPLE AND TRANSIENT SIMULATION

To test the performance of the system with the above parameters, a transient simulation of the rotor lifting off a backup bearing in a SCPM bearing has been performed. The transient results as presented in Figure 3 to Figure 5 show the rotor and stator displacements and the associated forces in one of the two orthogonal axes. The force exerted on rotor by stator is defined as $F_m = K_m(X_s-X_b)$. The system has parameters as chosen above and it has a rotor mass M_s = 10 Kg (22 lb) and a negative stiffness $-K_m$ = $-7\text{x}10^5$ N/m (-4000 lb/in) in the PM-created magnetic field. A static force, i.e. F_s=4.45 N (1 lb) is applied to the rotor to show the integral control effect. Before lift-off, the rotor leaned on a backup

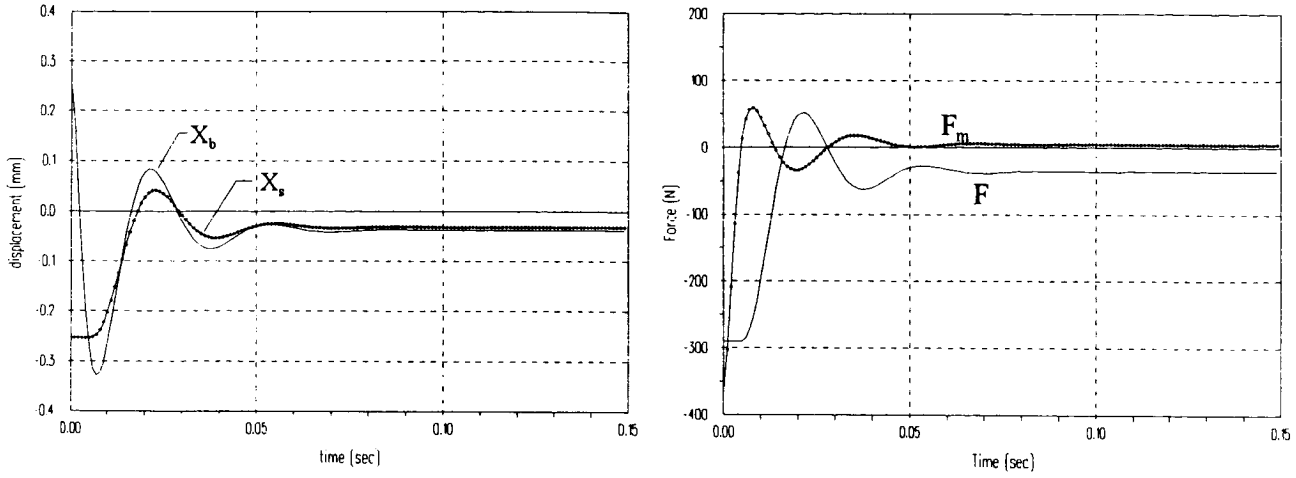

Figure 3. Lift-off transient without integral control

bearing 0.25 mm (0.010 inch) away from the center, while the stator leaned on an opposite side stop, also 0.25 mm away. The stator moved over toward the shaft side to create lifting force when the control began. The over-shooting rotor displacements in Figure 3 are the result of the chosen complex conjugate root pair being not well damped. The figure also shows the importance of the integral control. Without it, a large static force can make the rotor so eccentric that the rotor may not be able to lift off the backup bearing. The static displacement offset also causes a static control force (F). The rotor eccentricity inside the stator is opposite to the static load direction. This phenomenon is also a common feature in sensor-less magnetic bearings [3].

Figure 4 shows that with integral control, the steady-state shaft displacement and control force are eliminated.

In the case of Figure 5, the shaft backup bearing clearance was reduced by a factor of two, i.e., from ±0.25 mm to ± 0.125 mm. Comparing Figure 3 with Figure 5, it is interesting to learn that the maximum control force was also reduced by a factor of two.

Every bearing has its stiffness and damping properties, and so does a SCMB. Obviously, when the stator is not under control, a SCMB bearing has a negative stiffness coefficient ($-K_m$) and no damping.

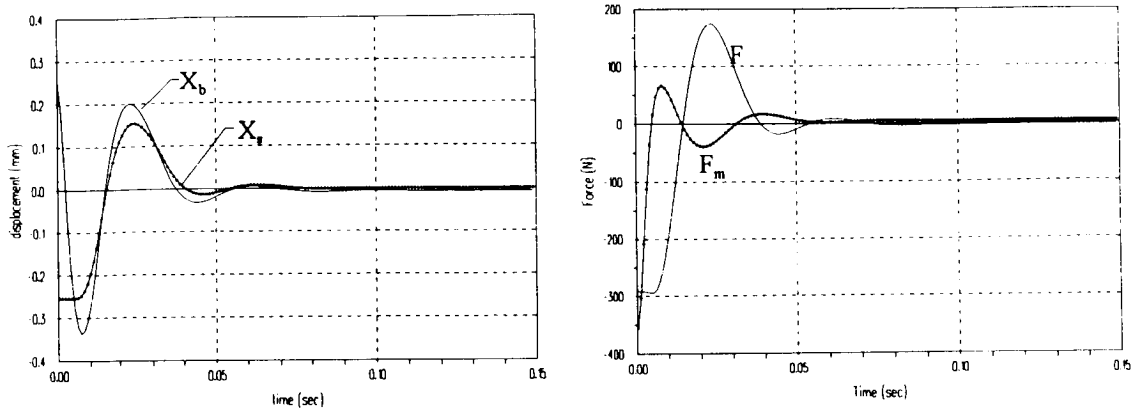

Figure 4. Lift-off transient with integral control

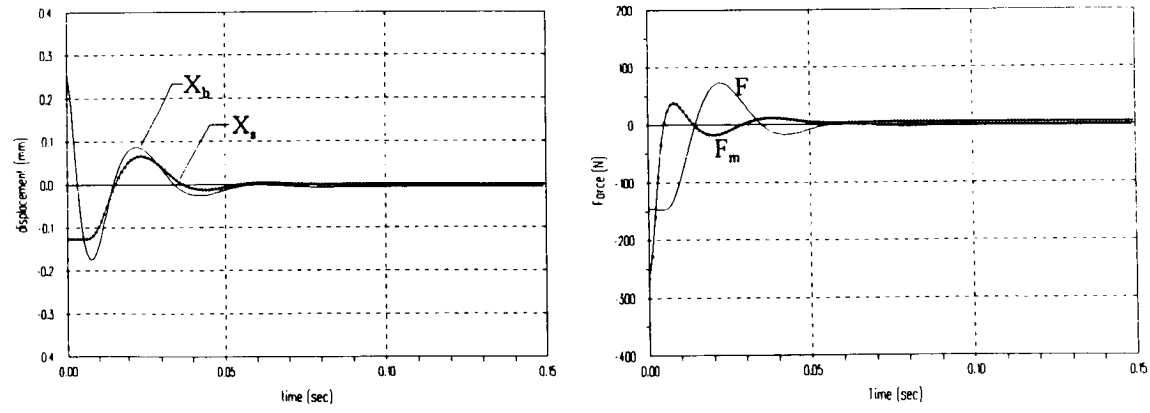

Figure 5. Lift-off transient with less shaft excursion

When the stator is under control, it can be readily shown that the effective SCMB dynamic stiffness is:

$$K_{dyn} = K_m (X_b - X_s)/X_s$$

$$= K_m[(C_p-K)+(C_d-C)S+C_i /S -M_bS^2]/[M_bS^2+CS+(K-K_m)] \quad (6)$$

Apparently, the dynamic stiffness is a function of the stator mass M_b among other parameters. For the above example, the normalized dynamic stiffness (K_{dyn}/K_m) is plotted in Figure 6. The phase plot in this figure shows that positive damping only occurs at the system natural frequency, i.e., in a normalized frequency range between 0.3 to 1.2. One can extend this range by choosing other sets of system roots to cover other system natural modes, if needed.

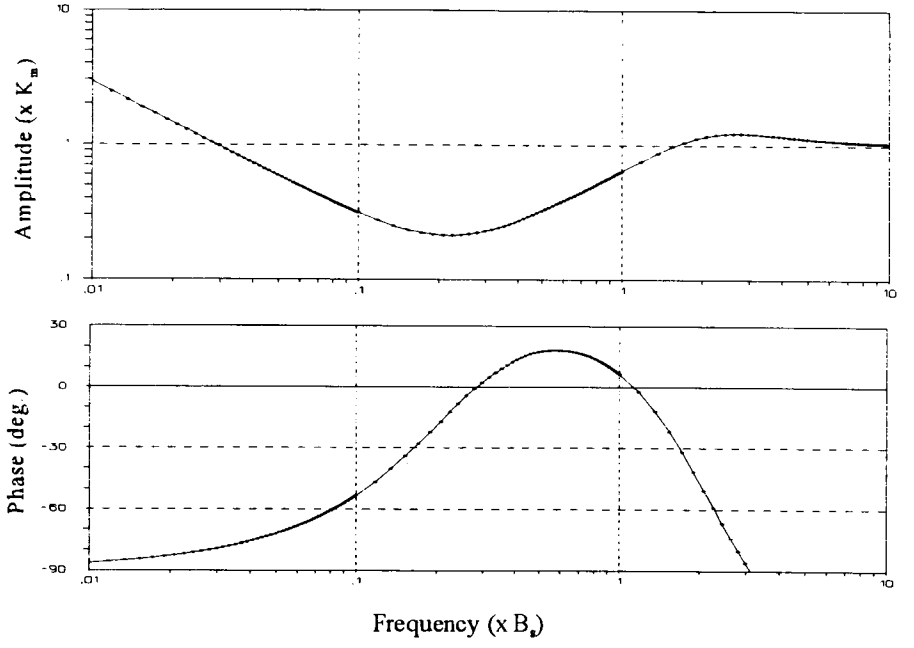

Figure 6. SCMB dynamic property

BEARING COMPONENT DESIGN

The key parameter of a SCMB is the magnetic stiffness K_m which dictates the size of the bearing. The bearing design work starts with a given value of K_m which relates to a given rotor mass. The magnetic stiffness is a function of the magnetic flux density (B in Tesla), the nominal concentric air gap (g in meter), and the circular pole area (A in meter squared). It has a closed-form solution as presented in [4] which may be simplified as:

$$K_m = (AB^2/2\mu_o)/g \qquad \text{N/m} \tag{7}$$

where

$A = \pi DL$ = circular pole area of one disk, m^2
D = rotor diameter, m
L = axial thickness of one stator disk, m
μ_o = permeability of free space = $4\pi x10^{-7}$ Tesla/A-T

Iterative calculations are involved in using (7) and choosing the proper values of rotor diameter, disk thickness, air gap and achievable flux density. Once the flux density B is determined, the sizes of a PM ring, i.e., its thickness and axial area, may be estimated using a conventional method where flux leakage factors are considered.

The clearance (g_b) between the rotor and a backup bearing is smaller than the magnetic air gap g. For a given stator support stiffness (K), the required actuator force capacity is directly proportional to the clearance or approximately equal to "Kg_b". Therefore, the backup bearing clearance should be kept to a minimum as practically possible.

A SCMB can be made with axial bearing stiffness if small tooth pairs are machined on both the rotor and the stator disk inner diameters. This reluctance centering type of passive bearing has been studied and documented in [5]. Therefore, using radial SCMBs, an active thrust magnetic bearing may be spared.

CONCLUSIONS

The stator-controlled magnetic bearing concept has a laterally moveable stator without protruding poles to face the rotor. The annularly distributed radial magnetic flux provided by a permanent magnet ring in the air gaps are uniform circumferentially. There is no concern of eddy current or magnetic hysteresis losses. Since it is an actively controlled magnetic bearing, its stiffness and damping properties can be electronically manipulated. Therefore it is ideal for supporting high speed rotors, such as those of momentum and energy storage flywheels.

In this paper, a method has been presented on how to design the new bearing concept. The presentation included a concise formulation of the rotor and stator control dynamics and a procedure for determining the system parameters to achieve stability. Through numerical simulations, it has been shown that the inherently unstable bearing would work under proper stator motion control. Also presented were how to size the bearing proper and the required actuator force capacity.

REFERENCES

1. Chen, H.M. & Walton, J.: Novel Magnetic Bearings for a Flywheel Energy Storage System. presented at *ISROMAC-6*, Honolulu, Feb. 25-29,1996.

2. Oka, K. and Higuchi, T.: Magnetic Suspension System with Permanent Magnet Motion Control. *Proceedings of the 4th International Symposium on Magnetic Bearings*, pp317-320, 1994.

3. Chen, H. M.: Design and Analysis of a Sensorless Magnetic Damper. presented at *ASME Turbo Expo*, June 5-8, 1995, Houston, Texas, 95GT180.

4. Knospe, C.R. and Stephens, L.S.: Side-Pull and Stiffness of Magnetic Bearing Radial Flux Return Paths. *ASME, Journal of Tribology*, 1994.

5. Walowit, J.A. and Pinkus, O.: Analytical and experimental Investigation of Magnetic Support System. Part 1: Analysis. *ASME Journal of Lubrication Technology*, Vol. 104, pp.418-428, 1982.

RADIAL ACTIVE MAGNETIC BEARING FOR OPERATION WITH A 3-PHASE POWER CONVERTER

Reto Schöb
Sulzer Electronics AG
Winterthur, Switzerland

Christian Redemann
Laboratory for Electrical Engineering Design (EEK)
Swiss Federal Institute of Technology
Zürich Switzerland

Thomas Gempp
Laboratory for Electrical Engineering Design (EEK)
Swiss Federal Institute of Technology
Zürich Switzerland

SUMMARY

In order to reduce costs, radial active magnetic bearings have been proposed which are formed by only three electromagnets. Unfortunately it is not possible to operate the three coils with a 3-phase power converter, since the sum of the coil currents does not equal zero. Three independent amplifier channels are needed for the control of this arrangement. In this paper, a radial magnetic bearing is proposed which can be operated by commercial 3-phase power amplifiers. By the use of an arrangement of bias coils, it is possible to make the sum of the three currents become zero. Some problems related to this bearing arrangement as well as their solutions are discussed and shown using the example of two prototype bearings.

MOTIVATION

In a radial active magnetic bearing, usually four independent electromagnets are arranged around the rotor. They are operated either by four unipolar power amplifiers or by two bipolar amplifiers. A simplification can be achieved by the arrangement of only 3 electromagnets. Such arrangements have been shown for example in [1] and [2]. In this case still three independent unipolar power amplifiers are needed for the control of one radial bearing. Unfortunately, it is not possible to operate the three coils with a 3-phase power converter. However, it would be very attractive to operate magnetic bearings with 3-phase power converters, mainly because of two reasons:

- 3-phase converters are used in huge quantities for electrical drives and are therefore available at very low prices. Today they are even cheaper than dc power amplifiers.

- Modern 3-phase servo amplifiers incorporate high performance digital processors like signal processors. These processors would offer enough calculation power for the control of active magnetic bearings. This means that a 3-phase servo amplifier could be easily transformed into a magnetic bearing controller merely by exchanging software.

THE NEW APPROACH

In this paper, a radial magnetic bearing is suggested which can be operated by 3-phase power amplifiers. Its basic principle is shown in figure 1. Figure 2 shows how the coils are connected to a 3-phase power converter.

There is one major point which has to be considered with the implementation of the bearing by using a 3-phase power converter. In a 3-phase system, the sum of the phase currents must equal zero. This is the case whether the winding coils are connected either in a star configuration with a floating start point or in a triangular configuration. It means that only two out of the three phase currents (i_u, i_v, i_w in figure 1) can be independently controlled. The third phase current equals the negative sum of the two others. At first glance this seems to be no problem for the radial bearing, since only two degrees of freedom should be controlled.

The equation system which shows the relationship between the magnet forces (F_u, F_v, F_w) and the resulting forces in the two directions x and y (F_x, F_y) is undetermined:

$$F_x = F_u - \frac{1}{2} F_v - \frac{1}{2} F_w \qquad (1)$$

$$F_y = \frac{\sqrt{3}}{2} F_v - \frac{\sqrt{3}}{2} F_w \qquad (2)$$

A further condition is possible, for example that the sum of all magnetic forces equals zero. If the magnetic forces were proportional to the winding currents, the bearing could easily be operated as a 3-phase system. However, this would mean that the electromagnets can generate attractive forces as well as repulsive forces, depending on the sign of the current. But since the magnetic forces are proportional to the power of two to the winding current, only attractive forces can be generated. A better idea is to let the sum of all magnetic forces and therefore the sum of the winding currents equal a constant, positive value. However, in this case the currents no longer form a 3-phase system and the windings cannot be driven by a 3-phase power converter.

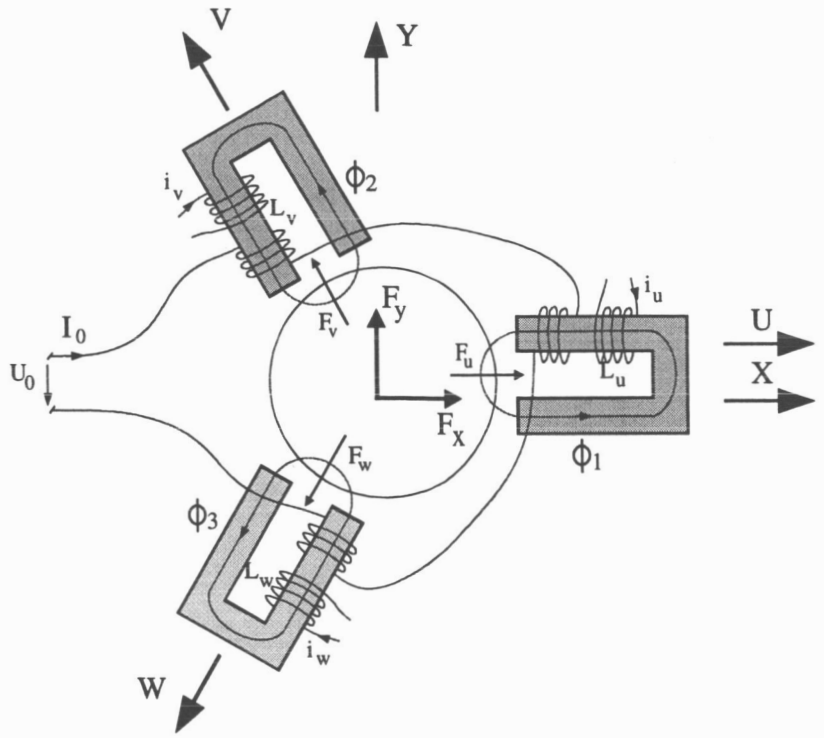

Figure 1. Functional principle of the radial magnetic bearing for 3-phase operation

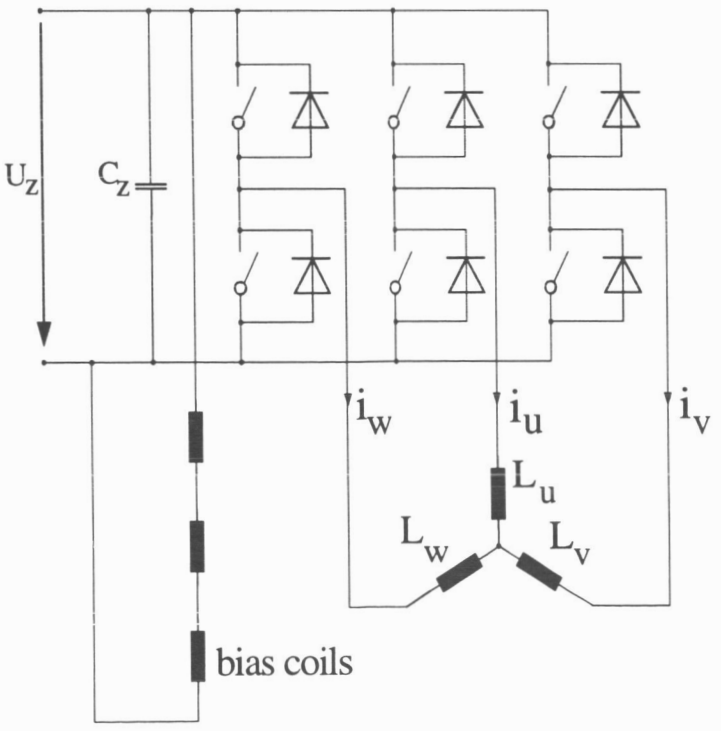

Figure 2. Connection of the bearing coils to the 3-phase power converter

The idea is now to generate a constant magnetomotive force in all of the three electromagnets by separate premagnetization coils which are connected in series directly to the dc link (see figures 1 and 2). The linearized equations for the magnet forces are then:

$$F_u = k\,(i_u + i_0) \tag{3}$$

$$F_v = k\,(i_v + i_0) \tag{4}$$

$$F_w = k\,(i_w + i_0) \tag{5}$$

If these equations are inserted in equations 1 and 2, it can be seen that the premagnetization current i_o disappears in the resulting force formulas.

$$\begin{aligned} F_x &= k\left((i_u + i_0) - \frac{1}{2}(i_v + i_0) - \frac{1}{2}(i_w + i_0)\right) \\ &= k\left(i_u - \frac{1}{2}\,i_v - \frac{1}{2}\,i_w\right) \end{aligned} \tag{6}$$

$$\begin{aligned} F_y &= k\frac{\sqrt{3}}{2}(i_v + i_0) - k\frac{\sqrt{3}}{2}(i_w + i_0) \\ &= k\frac{\sqrt{3}}{2}\,i_v - k\frac{\sqrt{3}}{2}\,i_w \end{aligned} \tag{7}$$

Now, the condition for a 3-phase system is applicable.

$$i_u + i_v + i_w = 0 \tag{8}$$

With equations 6, 7 and 8, the equations for the three phase currents with the forces F_x and F_y as parameters can be evaluated:

$$i_u = \frac{2}{3k}F_x \tag{9}$$

$$i_v = \frac{1}{3k}(-F_x + \sqrt{3}\,F_y) \tag{10}$$

$$i_w = \frac{1}{3k}(-F_x - \sqrt{3}\,F_y) \tag{11}$$

$$\begin{bmatrix} i_u \\ i_v \\ i_w \end{bmatrix} = \frac{2}{3k} \begin{bmatrix} 1 & 0 \\ -\frac{1}{2} & \frac{\sqrt{3}}{2} \\ -\frac{1}{2} & -\frac{\sqrt{3}}{2} \end{bmatrix} \cdot \begin{bmatrix} F_x \\ F_y \end{bmatrix} \qquad (12)$$

If the equation system is written in a matrix form (equation 12), it is obvious that the currents form a 3-phase system. They can be evaluated by a simple 2- to 3-phase transformation from the set-values (X_s and Y_s) of a position controller. The basic control scheme of the 3-phase bearing is shown in figure 3.

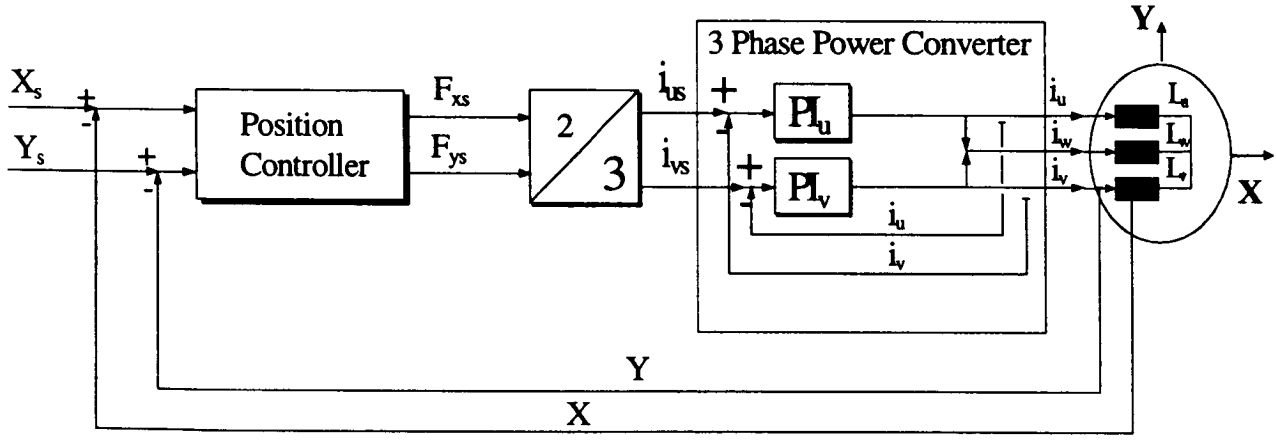

Figure 3. Control scheme of the 3-phase radial bearing

NONLINEARITY AND CROSS-COUPLING

The linear equations 6 and 7 are based on the assumption that the force changes are directly proportional to the changes in currents. However, this assumption is valid only for small changes of the current and as long as the rotor is placed in the center of the three electromagnets. In reality, the magnetic forces are proportional to the magnetomotive forces (which are dependent on the phase currents as well as on the premagnetization current) by the power of two. Also, they are inversely proportional to the power of two of the air gaps. These dependencies lead to a nonlinear behavior of

the bearing forces for high currents as well as for large displacements of the rotor. Figure 4 shows the calculated displacement-force graph of a test bearing in X-direction. The figures 5 and 6 show current-force graphs of the same bearing for two different premagnetization currents and for several rotor positions. Effects of magnetic material saturation are not considered in these calculations. The graphs show that the linearity of the bearing becomes better with a higher premagnetization current, and worse with a rise of the displacement and the control current.

There are similar nonlinearities in all active magnetic bearings. A robust controller can handle them without problems. Several methods to compensate these nonlinearities have been proposed for example in [3] and [4]. However there are two differences between the behavior of 4-phase bearings and the discussed prototype bearing. One difference is the strong asymmetry related to the displacement as well as to the control current which are shown in the X-direction (Figures 4-6). However a robust controller can deal even with these asymmetries as long as there is no change of sign of the forces as shown in figure 5. Figures 7 and 8 show the displacement-force graphs and the current-force graphs of the prototype bearing in the Y-direction. What might be at first surprising is the fact that these graphs are perfectly symmetrical. They are fully comparable to a 4-phase bearing. The behavior of the bearing is completely different in the X-direction and in the Y-direction and it is much easier to find a stable controller for the Y-direction than for the X-direction. However, the asymmetry of the system could be easily compensated by nonlinear compensation with a look-up table.

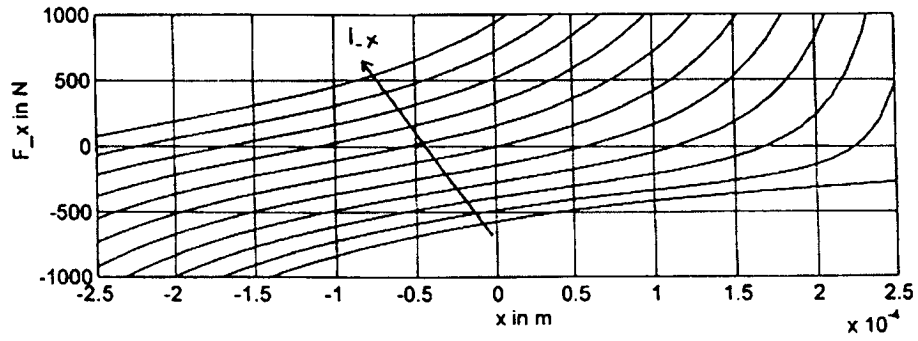

Figure 4. Calculated displacement-force graph of test bearing in X-direction

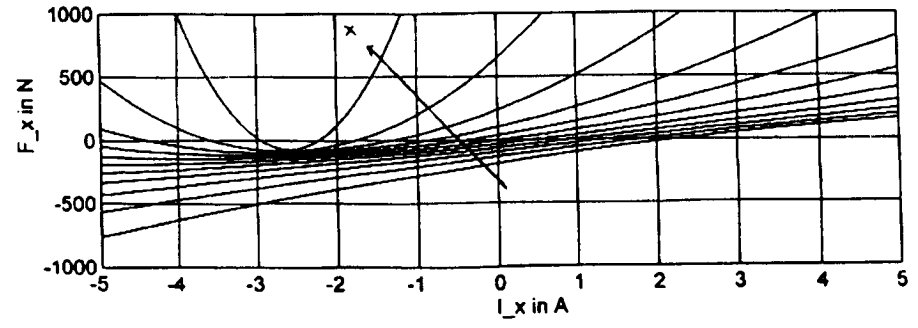

Figure 5. Current-force graph of test bearing in X-direction for premagnetization current of 3 A

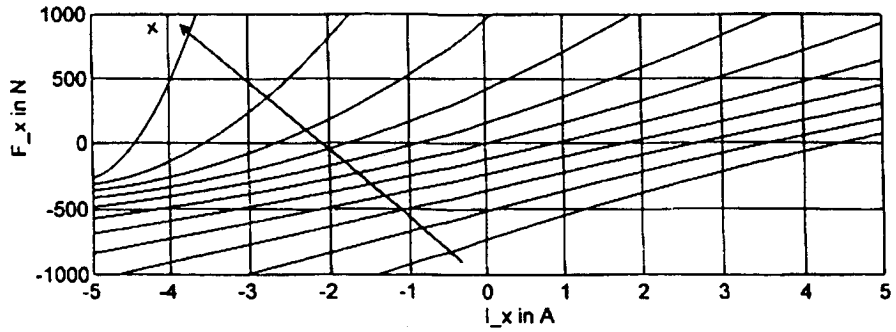

Figure 6. Current-force graph of test bearing in X-direction for premagnetization current of 6 A

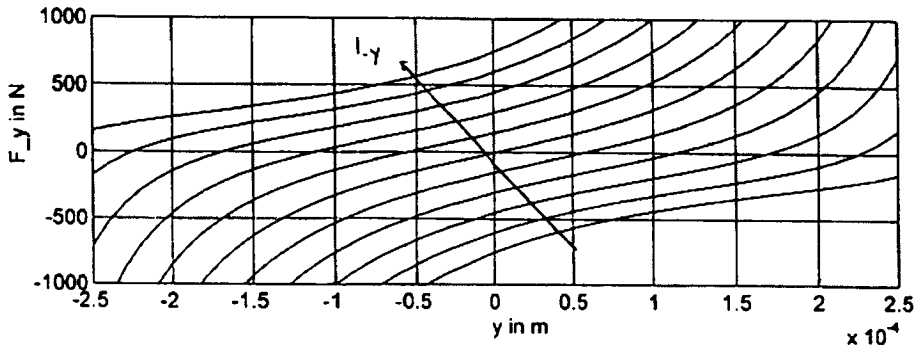

Figure 7. Displacement-force graph of test bearing in Y-direction

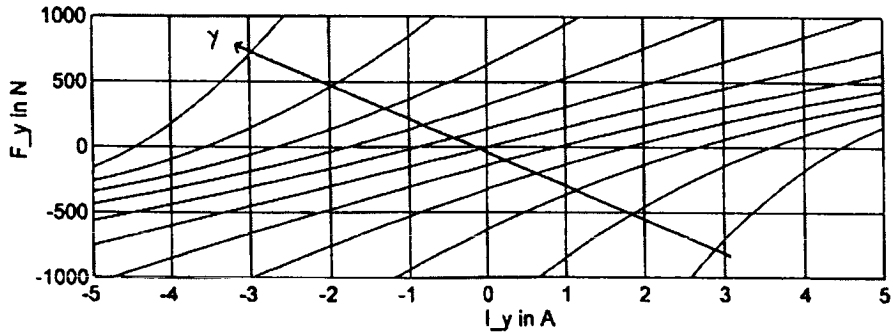

Figure 8. Current-force graph of test bearing in Y-direction

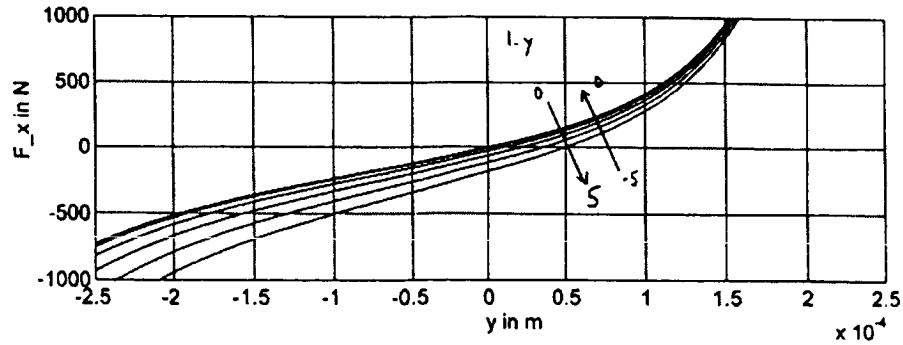

Figure 9. Cross-coupling from Y-current and Y-displacement to force in X-direction

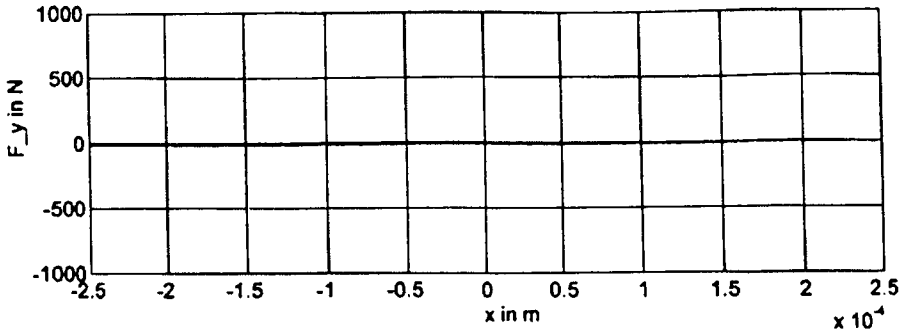

Figure 10. Cross-coupling from X-current and X-displacement to force in Y-direction

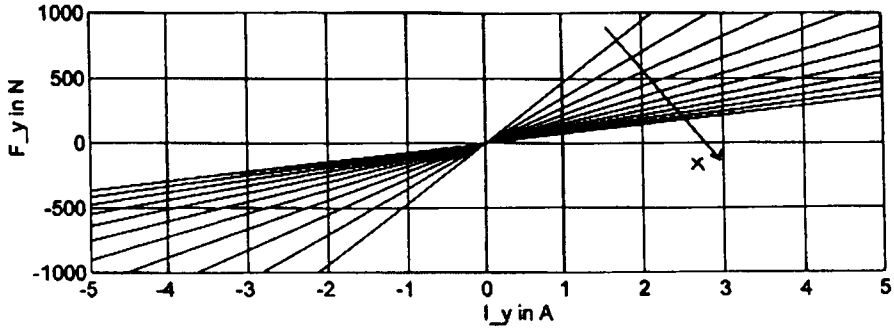

Figure 11. Dependence of current-force graphs in Y direction on X-current and X-displacement

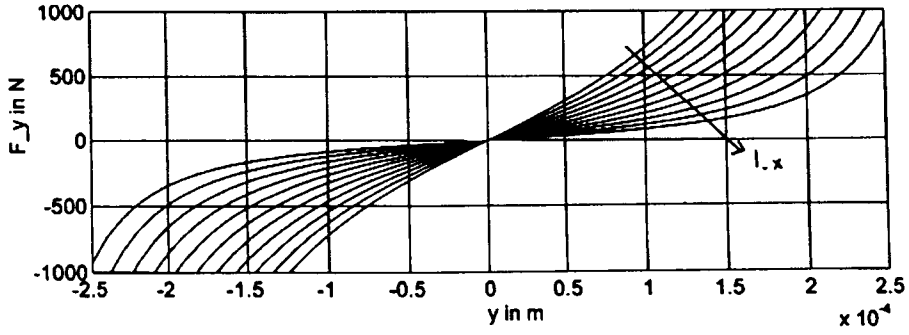

Figure 12. Dependence of displacement-force graphs in Y-direction on X-current and X-displacement

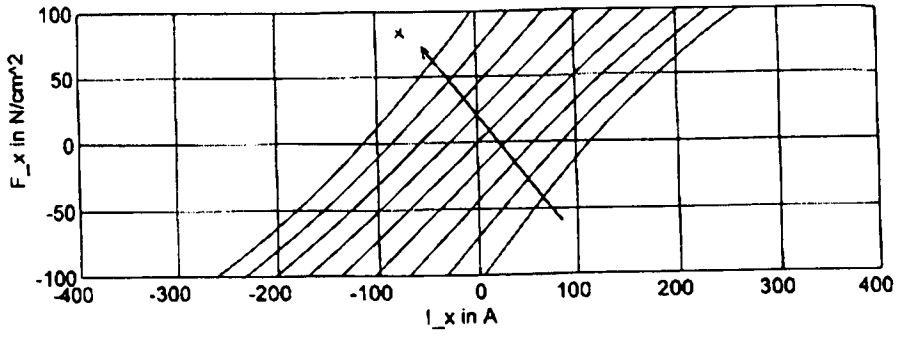

Figure 13. Calculated current-force graph for 3-phase/12-pole radial bearing

The main problem with the discussed arrangement is the fact that its asymmetry also leads to cross-coupling between the two bearing axes. Figure 9 shows the forces of the bearing in X-direction as a function of the displacement and the control current in Y-direction. In a symmetrical arrangement (4-phase bearing) without cross-coupling the force in X-direction would be fully independent of changes of control current and position in Y-direction. This means it would remain zero. Figure 9 shows however a high dependence mainly on the rotor position. There is no cross-coupling from X-axis to Y-axis as long as there is no Y-current or displacement (figure 10). However, there is an influence on the current-force slope k_{iy} as well as on the displacement-force slope k_{sy} which can be seen in figures 11 and 12.

The reason for the strong cross-coupling is the wrong assumption of a linear dependence between the magnetic forces in the electromagnets and the related control currents on which our model and the 3-2-phase transformation were based. For control of 4-phase bearings the same assumption is commonly made. But because of the geometrical symmetry of the magnet arrangement a nonlinearity does not lead to cross-coupling.

A simple solution for the problem would be an underlaid flux(force)-control of magnets. However, such a control scheme would require independent control of all three winding currents. It would not be compatible with a 3-phase system. A mathematical decoupling in a digital controller should be possible without the requirement of much calculation power by gain scheduling based on a look-up table. Here the drawback would be the necessity of a good knowledge of the system and a high sensitivity to parameter changes.

A 3-PHASE BEARING WITHOUT CROSS-COUPLING

A better solution to the problem of cross-coupling is the design of a symmetrical arrangement of the 3-phase system. One solution is the arrangement of six magnets around the rotor. In this case two opposite magnets are connected to the same phase of the 3-phase converter. The principle of this bearing is shown in figure 14. Figure 15 demonstrates a practical implementation of this bearing type in the form of a large outer rotor bearing. The load capacity of this bearing is 3000 N, the stator diameter is 350 mm and the air gap is 1.5 mm. Figure 13 displays the calculated current-force graph for this bearing. It is very linear and perfectly symmetrical to displacements. The 12-pole arrangement shows virtually no cross-coupling effects. For the large bearing the 12 poles are no disadvantage. However, for smaller bearings it would be an advantage to have fewer poles. Figure 16 shows a 6-pole bearing with a 3-phase winding and low cross-coupling. This type of bearing was designed and tested for the support of a linear slider (figure 17).

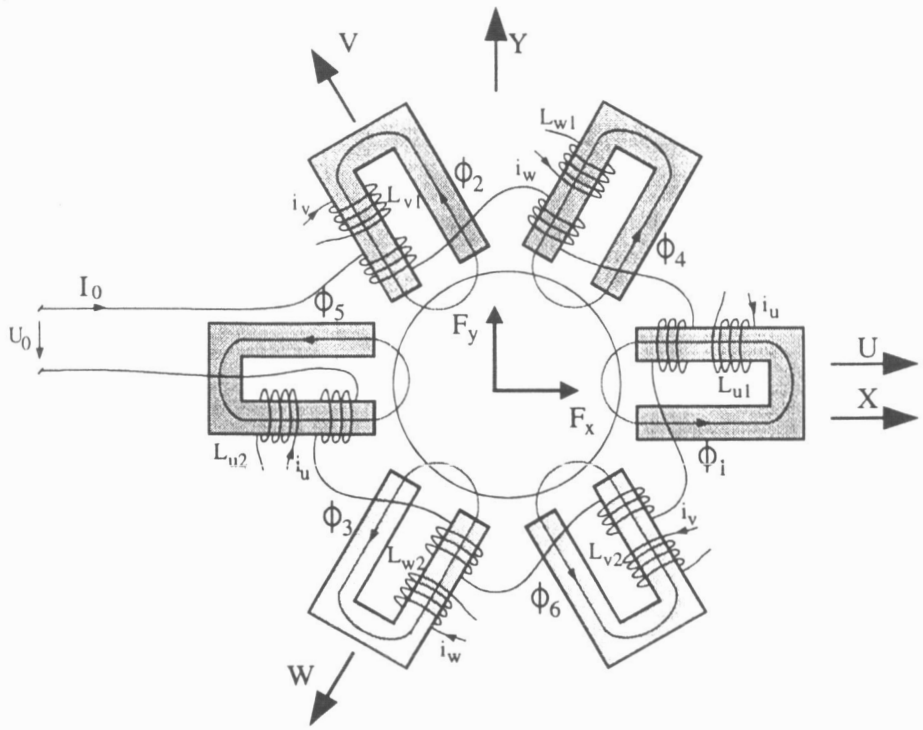

Figure 14. 3-phase radial bearing with reduced cross-coupling (12-pole arrangement)

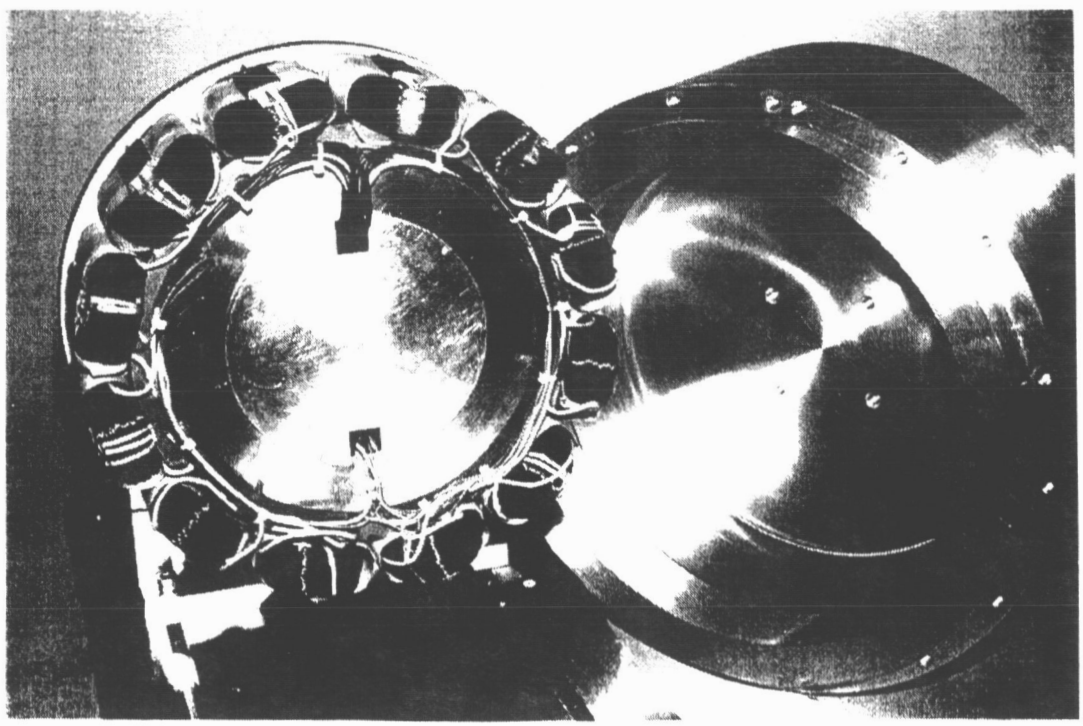

Figure 15. 3-phase/12-pole outer rotor type radial bearing with reduced cross-coupling

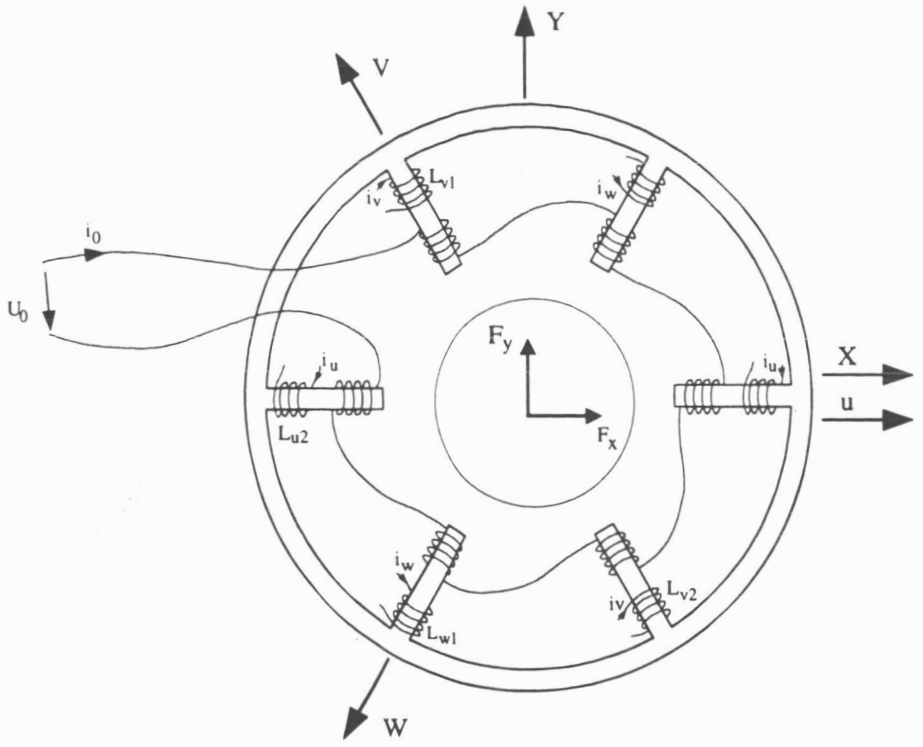

Figure 16. 3-phase radial bearing with reduced cross-coupling (6-pole arrangement)

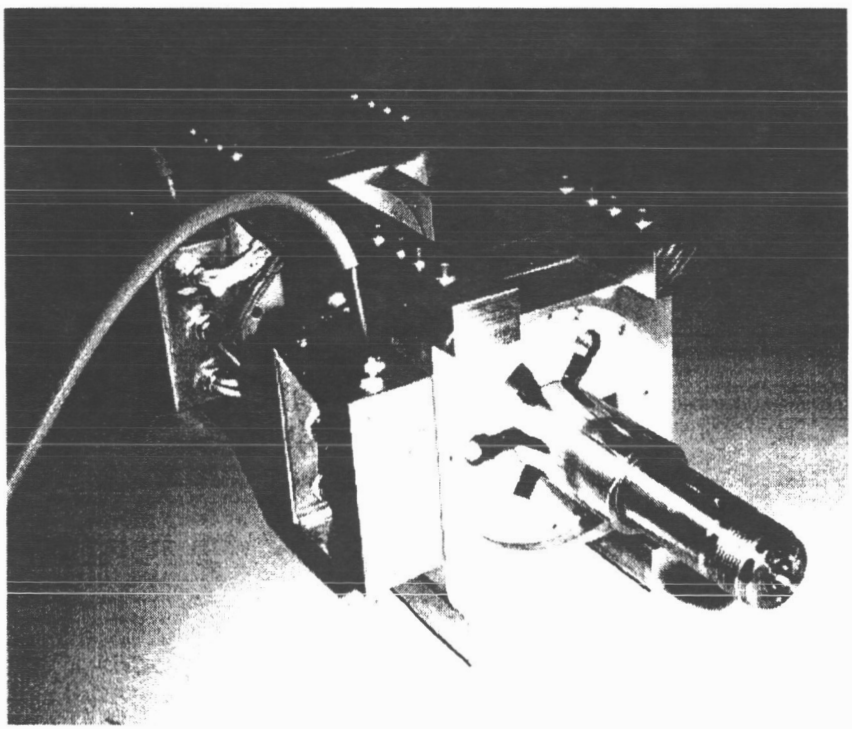

Figure 17. Linear slider supported by two 3-phase/6pole radial bearings

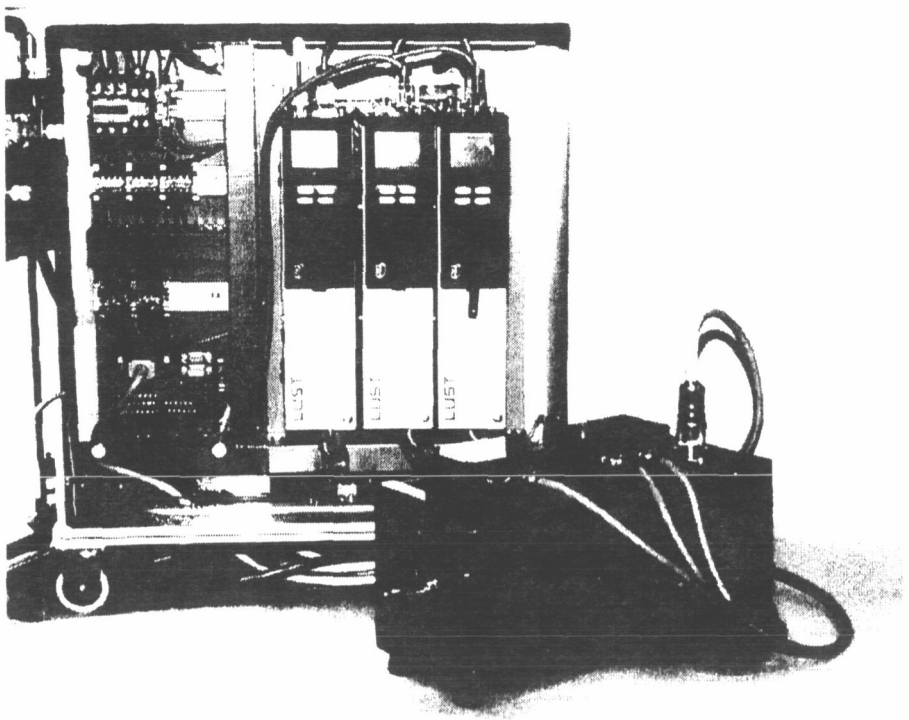

Figure 18. Magnetic bearing controller based on 3-phase servo amplifiers

CONTROL ELECTRONICS

Figure 18 shows a magnetic bearing controller for five spatial degrees of freedom. It is entirely based on commercial 3-phase servo amplifiers by LUST Drive Technology (MC7000 series). The only hardware modification of the 3kVA converters is an additional 2-channel sensor card (for the position sensing of the rotor) which is plugged into an extension slot. Everything else is accomplished by software. All control parameters are stored on a chip card and can be easily set. The controllers can exchange data by a high speed serial link. Several field bus interfaces are available for this system. The power range of the servo amplifiers starts at 1.4kVA and ends at 44 kVA.

ACKNOWLEDGEMENT

The project was supported by the Laboratory for Electrical Engineering Design (EEK) of the Swiss Federal Institute of Technology (ETH) in Zurich and the companies Sulzer Electronics AG., Winterthur (Switzerland) and Lust Antriebstechnik GmbH, Lahnau Germany.

REFERENCES

1. Ueyama, H.: EP O 612 928
2. Bühler, P. et al.: Digital Control for Low Cost Industrial AMB Applications, 5th Int. Symposium On Magnetic Bearings, Kanazawa, August 1996
3. Boeringer A.: DE 31 14 426 A1
4. Habermann, H.; and Brunet, M.: US 4,308,490

A MEASUREMENT OF VA REQUIREMENTS IN AN INDUCTION TYPE BEARINGLESS MOTOR

Eichi Ito[1] Akira Chiba[1] Tadashi Fukao[2]

[1]Department of Electrical Engineering
Faculty of Science and Technology
Science University of Tokyo
2641 Yamazaki Noda Chiba Japan 278
Tel. +81(471)24-1501 Ext. 3700
Fax. +81(471)25-8651

[2]Department of Electrical and
Electronic Engineering
Tokyo Institute of Technology
Ookayama Meguro Tokyo Japan 152
Tel. +81(3)5734-2188
Fax. +81(3)5734-2903

SUMMARY

Bearingless motors are electrical motors combined with magnetic bearing functions. In order to produce radial force, radial force windings are wound in a stator of a 4-pole induction motor. In this paper, voltage and current are measured at the radial force winding terminals of a test machine. It is found that the volt-ampere requirement is only 0.0059 times of that of the motor terminals.

INTRODUCTION

Bearingless motors are electrical motors combined with magnetic bearing functions [1,2]. In order to produce radial force, 2-pole windings are wound in a stator of conventional 4-pole induction motors. With a current in the 2-pole windings, the 4-pole revolving magnetic field is unbalanced. Flux distributions are actively made unbalanced and the resulting radial force is effectively used for magnetic suspension of the rotor shaft. The amplitude and direction of the radial force are adjusted with negative feedback circuits employing rotor radial position detectors. In this system, one of the main concerns is how much current and voltage are required at the additional 2-pole winding terminals.

Voltage and current requirements were previously reported to be experimentally 5% of motor excitation VA by the authors [3]. However, the measured rms values were far from the theoretical values of 0.1% because of unfortunately high shaft unbalance and radial position sensors. In this paper, a test machine is built to verify the theoretical values. A shaft of the test machine is carefully balanced. It is also equipped with radial position sensors with less noise. As a result, voltage and current requirements to support its shaft are found to be only 0.0059 (0.59%) times the motor excitation VA in a test machine. Test results indicate the effectiveness of a simple theoretical calculation to estimate VA requirements of bearingless motors.

SYSTEM CONFIGURATION AND VA REQUIREMENTS

Fig. 1 shows a system block diagram of a simple bearingless motor drive. In part of the motor controller, the motor windings are driven by a current controlled voltage source inverter which supplies sinusoidal currents with variable frequency. The amplitude of exciting current is kept constant in no-load operations. The three-phase current commands i_{um}*, i_{vm}*, and i_{wm}*

are generated employing the 2-phase to 3-phase transformation. Suppose the rms value of sinusoidal currents in 4-pole windings is I_m, then the rms line-to-line voltage of motor winding terminals V_m is written, assuming sinusoidal voltage as,

$$V_m = 2\sqrt{3}\omega L_{mm} I_m \qquad (1)$$

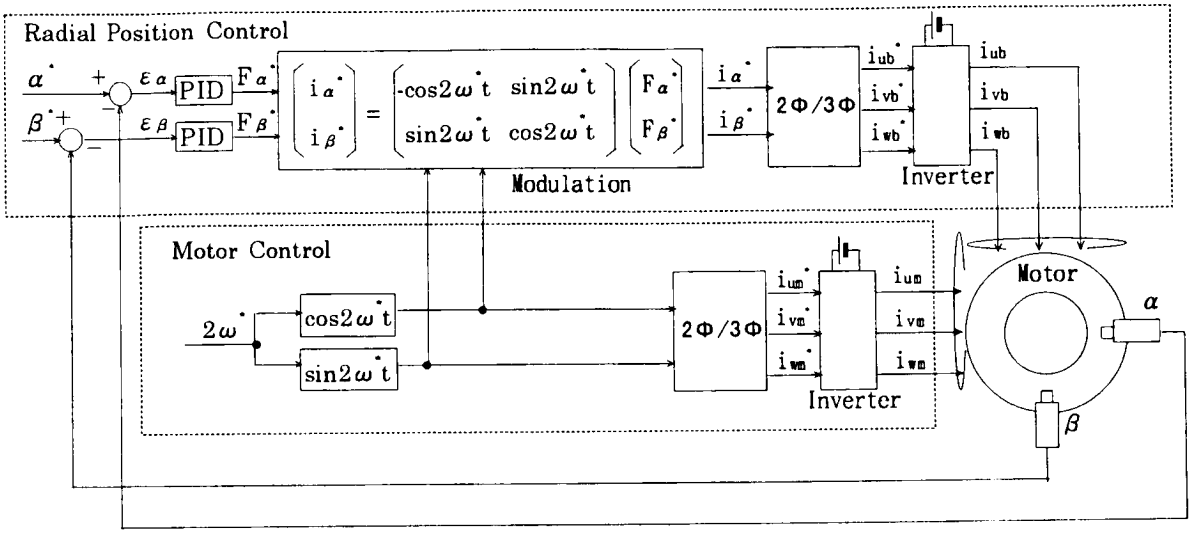

Fig. 1 System of radial position control.

where, L_{mm} is a magnetizing inductance of 4-pole motor windings and ω is the mechanical angular speed of the shaft [rad/s]; and V_m is proportionally increased as ω is increased. Voltage and current requirement, VA_m of the 4-pole motor windings is a product of the line current and terminal voltage. Then, Va_m can be defined as,

$$VA_m = \sqrt{3} V_m I_m . \qquad (2)$$

Substituting (1) into (2) yields,

$$VA_m = 6\omega L_{mm} I_m^2 . \qquad (3)$$

Note that the unit of VA_m is volt-ampere [VA]. The VA_m is also proportional to ω.

In the radial position controller, rotor radial displacements α and β are detected by radial position sensors. The detected radial positions are compared with radial position commands α^* and β^*, which are usually set to zero. The errors ε_α and ε_β are amplified in Proportional-Integral-Differential controllers. The radial force commands F_α^* and F_β^* are generated. From these radial force commands, the instantaneous current commands I_α^* and I_β^* of the 2-pole radial force windings are generated with a modulation block. The inverter is controlled by the 3-phase current commands i_{ub}^*, i_{vb}^* and I_{wb}^* and supplies the currents i_{ub}, i_{vb} and i_{wb} of the radial force windings. Then radial forces corresponding to the references are generated in bearingless motors.

The rms current I_b of 2-pole windings depends on the generated radial force. Let us suppose that only static radial force is generated. Thus, the current waveform is sinusoidal with angular frequency of 2 ω. The relationship between radial force F[N] and I_b[A] can be written as,

$$I_b = \frac{F}{3MI_m} \tag{4}$$

where, M is a derivative of mutual inductance with respect to radial position. It is seen that if radial force F is constant as in the case of the gravity force of a shaft, I_b is constant. The rms value V_b of fundamental line-to-line voltage at the radial force winding terminals is a product of an impedance and I_b. Neglecting winding resistance, V_b is written as,

$$V_b = 2\sqrt{3}\omega L_{mb} I_b \tag{5}$$

where, L_{mb} is magnetizing inductance. It is seen that V_b is proportional to ω. The voltage and current requirements of 2-pole radial force windings Va_b are written as,

$$VA_b = \sqrt{3} V_b I_b. \tag{6}$$

Substituting (5) into (6) yields,

$$VA_b = 6\omega L_{mb} I_b^2. \tag{7}$$

Substituting (4) into (7) yields,

$$VA_b = 6\omega L_{mb}\left(\frac{F}{3MI_m}\right)^2 \tag{8}$$

If F is constant, Va_b is proportional to ω. If ω is constant and F is changed, Va_b is proportional to F squared. VA_m is also proportional to ω as seen in (3). Then, a VA Ratio VA_b/VA_m is independent of rotational speed. VA_b/VA_m can be obtained from the equations (3) and (6).

$$\frac{VA_b}{VA_m} = \frac{6\omega L_{mb} I_b^2}{6\omega L_{mm} I_m^2}. \tag{9}$$

Reducing (9) yields,

$$\frac{VA_b}{VA_m} = \frac{L_{mb} I_b^2}{L_{mm} I_m^2}. \tag{10}$$

If F is constant, VA Ratio is constant because I_b is constant from (4). If F is increased, VA Ratio is proportional to F squared because VA_b is proportional to F squared although VA_m remains constant.

CONSTRUCTION OF THE TEST MACHINE

Fig. 2 shows the cross section of a constructed test machine. Two bearingless motor units are constructed on a vertically arranged shaft. Radial positions of upper shaft end are controlled by a bearingless motor. On the other hand, thrust and radial positions in a lower

shaft end are supported by a pivot bearing. Only an upper unit of bearingless motor units is tested. Radial position sensors are constructed above the upper bearingless motor unit. A touch down bearing is installed on the upper part in order to support the rotor shaft in an emergency. The air gap between rotor and touch down bearing is 100 μ m. In the bearingless motor unit, both 4-pole and 2-pole three-phase windings are wound in stator slots. The rotor has 4-pole short circuit paths to act as a 4-pole induction motor. The shaft weight including two rotors is 5.2kg.

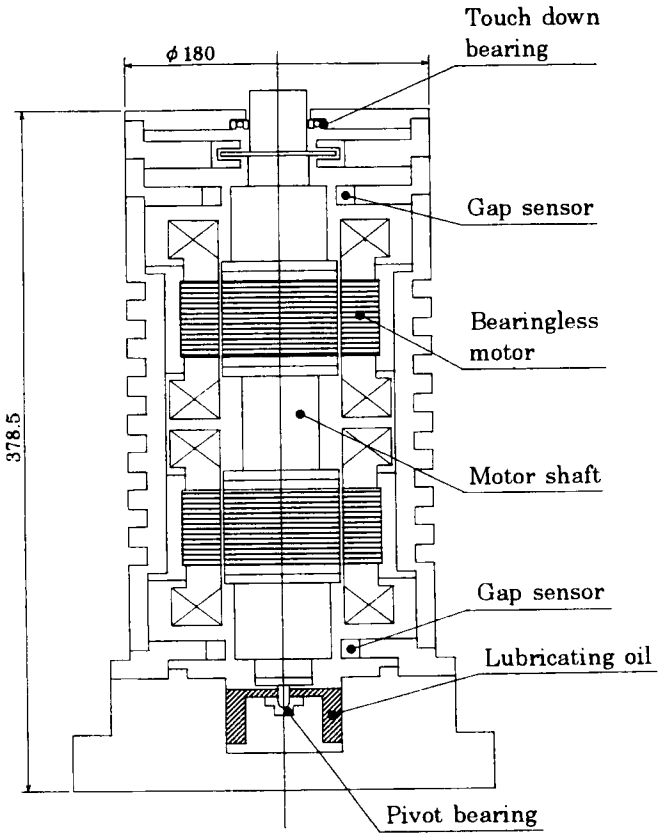

Fig. 2 Cross section of a test machine.

A MEASUREMENT OF VA REQUIREMENTS AT 4-POLE MOTOR WINDINGS

Fig. 3 shows a system block diagram of a test system. Both 4-pole motor windings and 2-pole radial force windings are connected to voltage source inverters through digital power meters. Voltage and current rms values as well as input powers are measured. Each frequency component of current and voltage is also measured by a FFT analyzer. DC terminal voltage can be adjusted to reduce harmonics. In the 2-pole system, inductances are connected between an inverter and a digital power meter because a voltage requirement at 2-pole radial force windings is much smaller than the adjustable voltage range of the inverter. The terminal voltage was initially designed to be low enough to force line current to follow its command. As a result, the voltage is found to be fairly low. Thus, the currents follow these commands. However, DC terminal voltage can be reduced up to 20V. Thus, the voltage measurements are disturbed by harmonics. In order to avoid the undesirable harmonics, DC terminal voltage may be decreased. Thus, the inductances are connected in series.

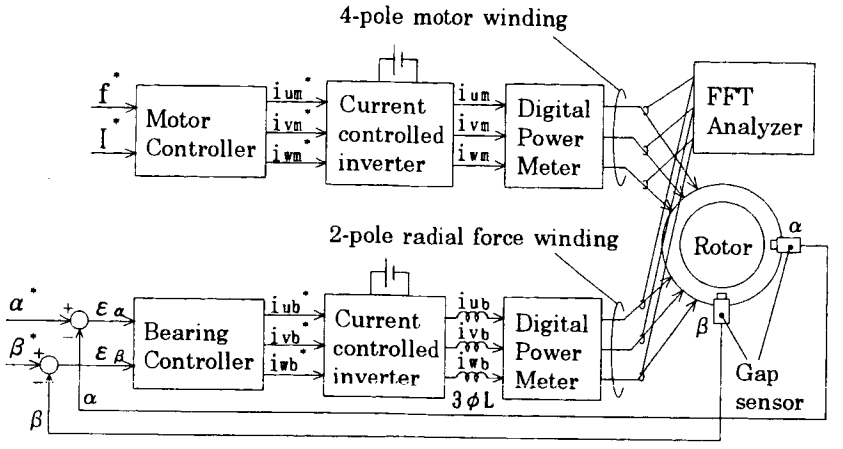

Fig. 3 The structure of the test system.

Fig. 4 shows the line currents at the 4-pole motor winding terminal. It is seen the rms values are approximately 14.0A in all speed ranges. It is also seen that fundamental components are 13.6A in all speed ranges. Note that the frequency of the fundamental components is nearly as high as twice the rotor rotational speed (2ω).

Fig. 5 shows the terminal voltage of the 4-pole motor windings. Because the rms values of terminal voltage are measured by a digital power meter, DC voltage is adjusted as small as possible to reduce harmonics while motor currents follow these commands. Although the best efforts have been made, there still remain a few harmonics. Then, measured rms voltage is slightly higher than the measured fundamental voltage. It is seen that voltages increase proportionally as rotational speed increases. Theoretical values are calculated from the equation (1). The value of magnetizing inductance of 4-pole motor windings L_{mm} is shown in the Table I. These are measured from a no load test. It is seen that the rms values of terminal voltage are higher than theoretical values by about 5V because the current controlled voltage source inverter includes harmonic components.

Fig. 6 shows the voltage and current requirements at the 4-pole motor windings. The required VA can be calculated by substituting measured current values in Fig. 4 and voltage values in Fig. 5 into the equation (6). It is seen that the voltage and current requirements also increase proportionally as rotational speed increases.

Fig. 7 shows voltage and current waveforms at 10,200 r/min. It is noted that the rms value of current is about 14A and that of terminal voltage is about 26V. The voltage drop at motor winding terminals is caused by that of Insulated Gate Bipolar Transistors (IGBTs).

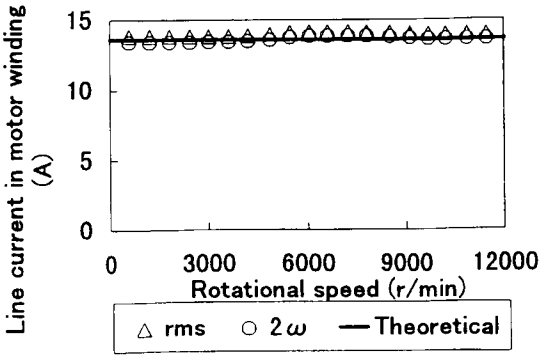

Fig.4 Current at motor windings.

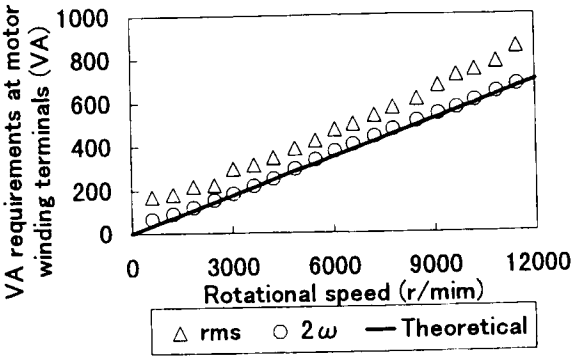

Fig.6 Voltage and current requirements at motor windings.

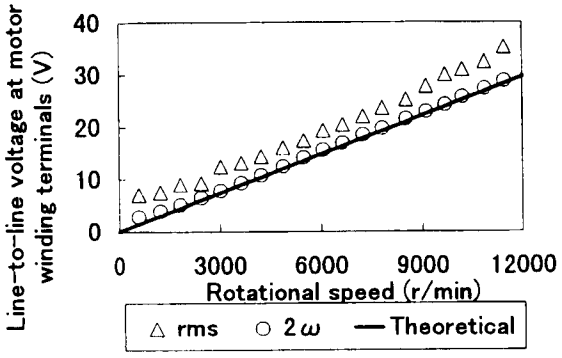

Fig.5 Terminal voltage at motor windings.

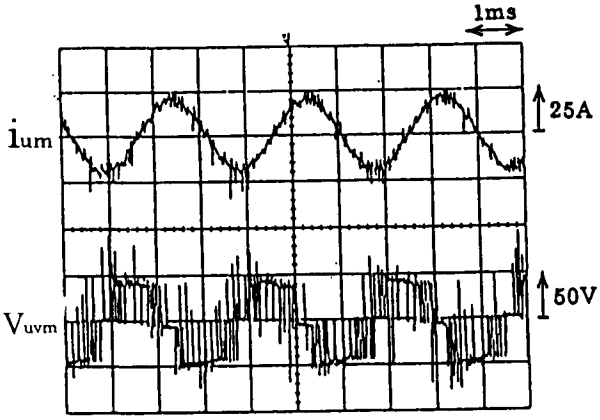

Fig.7 Waveforms at 10,200r/min.

Table I Motor parameters.

Parameter	Values
L_{mm}	0.50(mH)
L_{mb}	0.38(mH)
M'	0.60(H/m)

MEASUREMENTS OF VOLT-AMPERE REQUIREMENTS AT RADIAL FORCE WINDING TERMINALS

In the section, voltages, currents and Volt-Ampere (VA) requirements at radial force winding terminals are measured. In the voltage and current waveforms, it is suggested that values are influenced by mechanical unbalance in a certain speed range. Thus, voltage and current values are measured by a variety of equipment. Fundamental and second harmonic components of rotational frequency are measured by a FFT analyzer. Rms values are also measured by digital power meters with a wide frequency range.

As a result, it is shown that the measured second harmonic values have a good correspondence to theoretical values. The measured rms values are larger than the theoretical values. The discrepancy is mainly caused by mechanical unbalance and PWM harmonics.

Radial force winding current with rotational and static forces

If the rotor shaft is free from radial force, any current should not flow in the 2-pole radial force windings. In practice, this is not true because there are currents caused by a negative feedback circuit. Fig. 8 shows the waveforms of radial positions α and β, and radial force commands F_α^* and F_β^* when a static force of 2.6kgf is applied in the β-direction. When a static force is applied in the β-direction, a radial force having an amplitude which is equal to the static force is generated opposite to the β-direction. In Fig. 8, it is noted that radial positions and these commands have variations. The fundamental component of the variation is synchronized to the rotor mechanical speed. It means that radial force commands are automatically generated to suppress disturbance forces caused by the mechanical unbalance. It is also noted that F_β^* contains negative DC values. This DC value is generated to produce static force. It is important to derive theoretical current representation when both static and rotational radial forces are applied to a shaft.

Let us suppose a static force F_s is applied to a shaft. This force can be the weight of the rotor shaft. Let us also suppose that an amplitude of rotational radial force is F_ω which is generated by negative feedback controllers having rotational shaft displacements. The angular frequency of F_ω is exactly the same as the mechanical angular speed of the shaft. When static and rotational radial forces are applied, the radial force commands are written as,

$$F_\alpha^* = F_\omega \sin \omega t \qquad (11)$$

$$F_\beta^* = -F_s + F_\omega \cos \omega t. \qquad (12)$$

The instantaneous current command i_ω^* can be obtained by a modulation equation shown in a block diagram in Fig. 1, as,

$$i_\alpha^* = -F_\alpha^* \cos 2\omega t + F_\beta^* \sin 2\omega t. \qquad (13)$$

Note that the rotor speed is assumed to be exactly the same as the speed of revolving magnetic field. This assumption is valid at the no load condition. Substituting (11) and (12) into (13) yields,

$$i_\alpha^* = -F_\omega \sin \omega t \cos 2\omega t - F_s \sin 2\omega t + F_\omega \cos \omega t \sin 2\omega t. \qquad (14)$$

Let us consider the theorem of trigonometric function

$$\sin\omega t\cos 2\omega t = \frac{1}{2}(\sin 3\omega t - \sin\omega t) \qquad (15)$$

and

$$cos\,\omega t\,sin\,2\omega t = \frac{1}{2}(sin\,3\omega t + sin\,\omega t). \qquad (16)$$

Substituting (15) and (16) into (14) yields,

$$i_a^* = -F_\omega\,sin\,\omega t + F_s\,sin\,2\omega t. \qquad (17)$$

It is noted from equation (17) that the fundamental component of radial force winding current originates from the rotational radial force caused by mechanical unbalance. On the other hand, the second harmonic component of the current is originated from static radial force. It is also noted that the third harmonic component is canceled. These results suggest that measurements of fundamental and second components are important to see a cause of current requirements. Thus, in the following section, current is measured by a FFT analyzer to obtain amplitude of the fundamental and second harmonic components. The rms value of the current is also measured by a digital power meter.

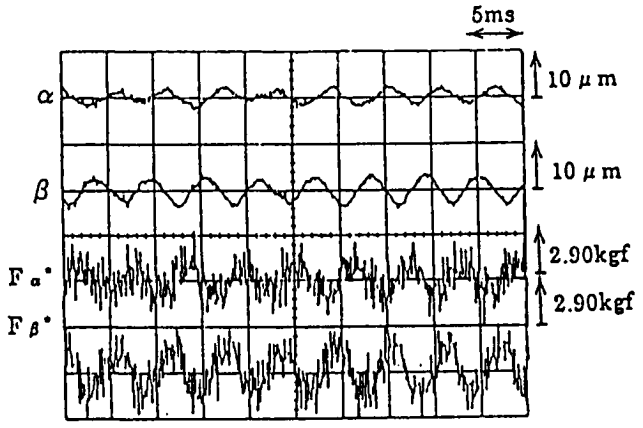

Fig. 8 Waveforms at 10,200 r/min when static force of 2.6kgf is applied.

Voltage, current and VA requirements

Fig. 9 shows the basic experimental setup to apply radial force to the rotating shaft. A mechanical bearing is attached at the top of the shaft. Static radial force is applied through a thread connected to the mechanical bearing. The other end of the thread is connected to a weight through a pulley. Only the upper unit of the two units of a bearingless motor is used in experiments. Thus, the bottom shaft end is supported by a pivot bearing. The height of the upper unit is 219.5mm. The height of the top of the shaft is 353.0mm. Thus, radial force generated in the bearingless motor is about 1.6 times as large as the gravitational force. For example, if a weight of 1.53kg is hung, a static force of 2.6kgf is applied to the upper unit of the bearingless motor. The weight of 2.6kgf is used in this paper, because the whole shaft weighs 5.2kgf including a shaft and two bearingless rotor units.

Fig. 10 shows variations in radial force winding currents with respect to rotational speeds while a constant radial force of 2.6kgf is applied. A solid line is the theoretical value, obtained from the equation (4). The Δ plots indicate the rms values measured by a digital power meter. The □ plots indicate fundamental components (ω) measured by a FFT analyzer, which are originated by mechanical unbalance. The O plots indicate second fundamental components (2ω) measured by a FFT analyzer, which are originated from static force. The second harmonic components are nearly constant in all speed ranges as indicated by theoretical values. The second harmonic components are more dominant compared with fundamental components. The rms values are 30% ~ 40% higher than the second harmonic components because there are not only a fundamental component but also higher harmonic components. It is also seen that the fundamental component reaches the peak value at 6,000 rpm. This result indicates that a critical speed is 6,000 rpm in this machine.

Fig. 11 shows voltage variations in radial force winding terminals with respect to rotational speeds while a constant radial force of 2.6kgf is applied. A solid line is the theoretical values. The theoretical values are obtained from the equation (5). The Δ plots indicate the rms values measured by DPM. The O plots indicate second harmonic component (2 ω) measured by a FFT analyzer. The second harmonic component is increased proportionally as rotational speed increases. Good correspondence is seen between the second harmonic component and theoretical values.

However, it is seen that the rms values of terminal voltage are higher than theoretical values by about 0.5V because of the harmonics of a voltage source inverter. During the experiments, much effort has been expended to adjust DC voltage as small as possible to realize the minimum voltage requirements while the rotor does not touch down. If the DC voltage is too high, the rms value is increased because harmonics are generated by the PWM inverter. If the DC voltage is too low, the line current does not follow its command, then magnetic suspension is out of control. Thus, careful adjustments have been made in the DC voltage of the PWM inverter at every measured point. The voltage increase of 0.5V is understandable in hysteresis type current controlled PWM inverters.

Fig. 12 shows variations in radial force winding voltage and current requirements with respect to rotational speeds while a constant radial force of 2.6kgf is applied. A solid line is the theoretical values obtained from the equation (6). The Δ plots indicate the product of measured rms voltage and current. The O plots indicate the product of voltage and current of second harmonic components. The calculations of volt-ampere are based on equation (6). Thus, theoretical values are proportional to the rotational speeds. The second harmonic component corresponds to the theoretical values. The rms values are about twice as high as theoretical values at the top speed.

Fig. 13 shows variations in VA ratio with respect to rotational speeds while a constant radial force of 2.6kgf is applied. A solid line is the theoretical values obtained from the equation (9). The Δ plots are calculated from the measured rms values. The VA ratio is calculated as VA_b/VA_m. The VA_m was previously shown in Fig. 6. The VA_b is shown in Fig. 12. The O plots are calculated from the second harmonic components. VA ratio is nearly constant in all speed ranges. This fact verifies that the VA ratio is independent of rotational speed. At a speed of 10,200 rpm, VA ratio is theoretically 0.0039. In experiments, VA ratio is 0.0059 in rms values and 0.0043 in the second harmonic component values. The

second harmonic value of 0.43% is close to the theoretical value. The rms value of 0.59% is 1.6 times the theoretical value. The discrepancy is caused by harmonics in voltage waveforms, mechanical unbalance, sensor noises and imperfection of controllers.

Fig. 14 shows the waveforms of radial positions α and β and current at radial force winding terminals. It is seen that i_{ub} contains the fundamental and second harmonic components.

Table II summarizes frequency component analysis of current and voltage at the radial force winding terminals. It is shown that the second harmonic components of current are most significant compared with other components. On the other hand, the voltage waveform contains not only the second harmonic component but also higher harmonic components because of the harmonics of a voltage source inverter.

Fig. 15 shows voltage and current waveforms at 10,200 rpm. It is seen that the voltage waveform contains significant harmonics. It is noted that the rms values of current are about 1.4A and that of terminal voltage is about 2.0V.

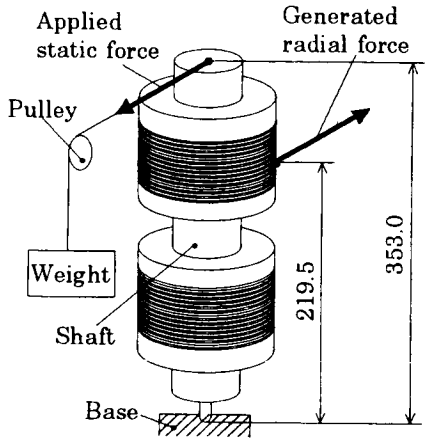

Fig.9 Mechanical radial force application.

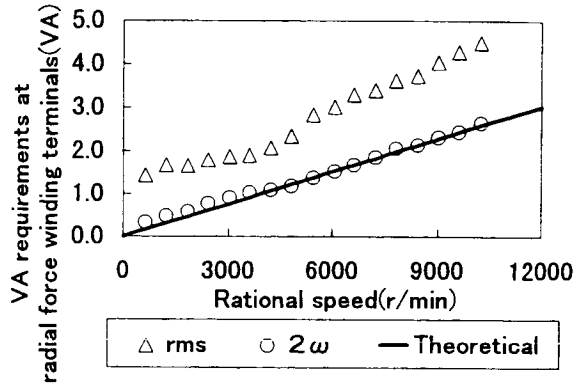

Fig.12 VA requirements at radial force winding terminals with radial force of 2.6kgf.

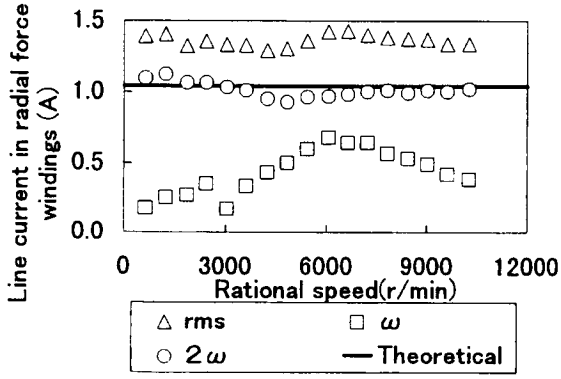

Fig.10 Line currents in radial force windings with radial force of 2.6kgf.

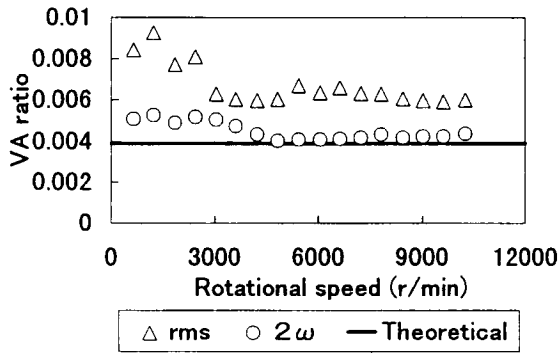

Fig.13 VA Ratio at 2.6kgf .

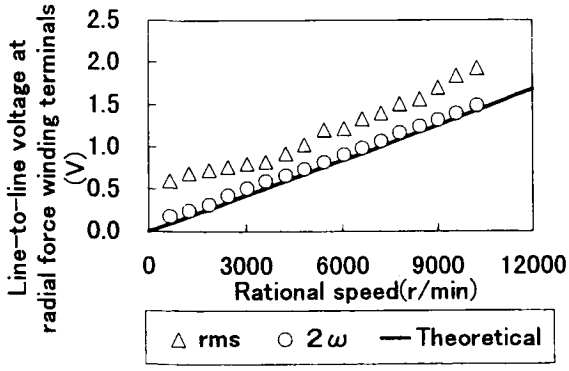

Fig.11 Line-to-line voltage at radial force winding terminals with radial force of 2.6kgf.

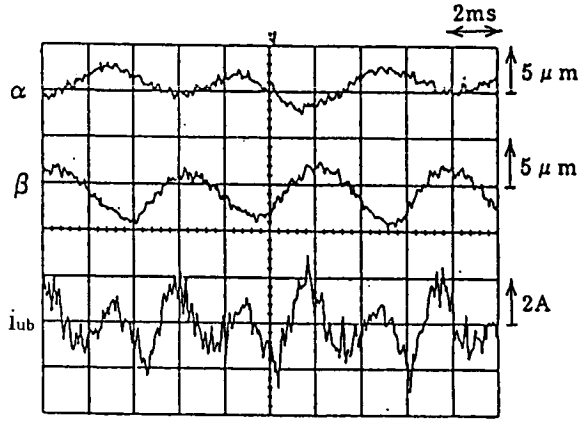

Fig.14 Waveforms at 10,200r/min when static force of 2.6kgf is applied.

Table II Frequency components at radial force winding terminals.

Frequency component	I_{ub}(A)	V_{uvb}(V)
Fundmental component	0.38	0.18
2	1.02	1.49
3	0.10	0.10
4	0.05	0.06
25	-	0.82
27	-	0.75

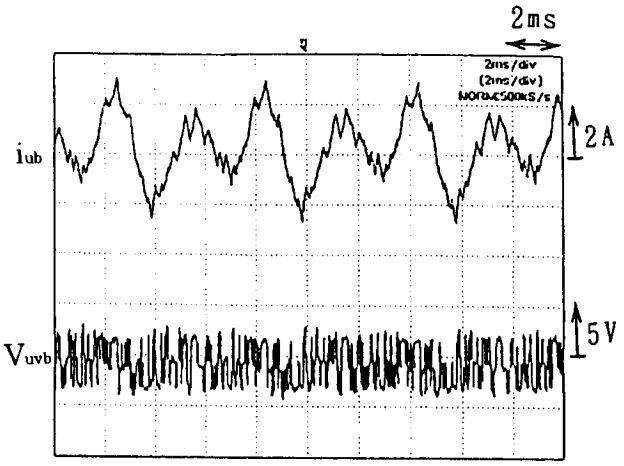

Fig.15 Waveforms at 10,200r/min when static force of 2.6kgf is applied.

Table III summarizes voltage, current, VA and VA ratio of a unit at a speed of 10,200 rpm with a radial force of 2.6kgf. Good correspondence is seen between measured second harmonic values and theoretical values. In the comparison of measured rms values and theoretical values, a good correspondence is seen only in motor winding current. A 30% increase is seen in the rms current values in radial force windings. This increase is caused by cyclic variations in shaft displacements due to mechanical shaft unbalance. The 30% increase is seen in line-to-line voltage of motor windings because of harmonics caused by PWM inverters. A 60% increase is seen in line-to-line voltage in the radial force winding terminals. One of the reasons for the increase is harmonics in a PWM inverter. The other reason is an increase of the rms current in the radial force windings. As a result, the 60% increase is seen in the VA ratio.

The index of VA ratio of 0.59%, i.e., 0.0059 can be explained employing an example. Suppose an induction motor has an output of 1.5kW. Also, suppose the exciting current of the motor is 800VA. Then, 800 x 0.0059 = 4.7VA is required to the radial force winding terminals for all three phases. If 200V line-to-line voltage is employed in an inverter, with optimization of number of turns and diameters of radial force windings, the required rms current can be derived as

$$I = 4.7 / (200\sqrt{3})$$
$$= 0.014.$$

Only 0.014A is required.

Table III
Voltage, current and VA at 10,200 r/min with 2.6kgf.

		Motor windings	Radial force windings
Measured 2ω component	V_f	25.7V	1.49V
	I_f	13.6A	1.0A
	$\sqrt{3}V_fI_f$	605VA	2.6VA
	VA ratio	0.43%	
Measured rms values	V_{rms}	31.0V	1.94V
	I_{rms}	14.0A	1.3A
	$\sqrt{3}V_{rms}I_{rms}$	752VA	4.4VA
	VA ratio	0.59%	
Theoretical	V_t	28.3V	1.44V
	I_t	13.6A	1.0A
	$\sqrt{3}V_tI_t$	666VA	2.6VA
	VA ratio	0.39%	

CONCLUSION

Voltage and current requirements were significantly higher than theoretical values in a previous paper because of unfortunately high shaft unbalance and radial position sensor noise.

In this paper, a test machine with precise mechanical balance and low noise sensors is described. The test machine was driven up to 10,200 rpm. The fundamental and second harmonic components of voltage and current were measured and the rms values of voltage and current were also measured by digital power meters. The volt-ampere (VA) requirements were also measured. The ratio of VA requirements, i.e., the VA at radial force winding terminals divided by VA at motor terminal is found to be only 0.0059.

ACKNOWLEDGMENT

The authors wish to thank Mr. Ryoji Miyatake, who was a student in Master Course in electrical engineering in the Science University of Tokyo, for his contributions.

REFERENCES

[1] R. Schob, and J. Bichsel: "Vector Control of the Bearingless Motor," Fourth International Symposium on Magnetic Bearings, Zurich 1994.

[2] Y. Okada, K. Dejima, and T. Oshima: "Analysis and Comparison of PM Synchronous Motor and Induction Motor Type Magnetic Bearings," IEEE Trans. IA-31, No. 5, pp. 1047-1053, 1995.

[3] Y. Takamoto, A. Chiba, and T. Fukao: "Test Results on a Prototype Bearingless Induction Motor with Five-Axis Magnetic Suspension," Proceedings of 1995 International Power Electric Conference (IPEC-Yokohama '95) Vol. 1, pp.334-339, April 7, 1995 Pacifico Yokohama.

Session 5 -- MSBS 1

Chairman: Hideo Sawada
National Aerospace Laboratory (NAL)

ROLL MOTION RESTRAINT SYSTEM FOR NAL 0.6m MSBS

Takashi Kohno, Hideo Sawada, Tetsuya Kunimasu
National Aerospace Laboratory
7-44-1, Jindaijihigashi-machi, Chofu-shi, Tokyo 182 JAPAN

SUMMARY

Suspension of a wind tunnel model and control of its motion in 5 degrees of freedom is realized in the NAL 0.6m MSBS but roll motion of the model is not controlled. Controlling the roll motion by adding additional magnets for roll control is realized in some small facilities including the NAL 0.1m MSBS, but it is not suitable for large wind tunnels. A mechanical roll motion control system for the 0.6m MSBS is described and simulation and experimental results are presented.

INTRODUCTION

Magnetic Suspension and Balance System (MSBS) for wind tunnel testing can avoid the support interference problem and has many other advantages in future wind tunnel tests. At National Aerospace Laboratory (NAL), a MSBS for the 0.1m x 0.1m test section has been developed and has succeeded in suspending and controlling the motion of a model in 6 degrees of freedom. 0.6m MSBS is designed for testing in a larger test section. Figure 1 shows the arrangement of the electromagnets of the NAL 0.6m MSBS. A model containing a cylindrical magnet is at the center of the test section and the magnetic field from the electromagnets surrounding the test section provides the lifting force that suspends the model. The position and the motion around the y-axis and z-axis of the model is controlled by modifying the current supplied to each electromagnet by digital automatic control using a personal computer. However, the magnetization of the model is equal around the x axis so the motion around x axis (roll motion) of the model causes no change of the magnetic force acting on the model. So the roll motion cannot be controlled. In wind tunnel testing, roll motion caused by some fluctuation must be considered, so some means to constrain the roll motion is necessary.

Containing another magnet besides the main magnet that obtains lifting force or using a main magnet that is not cylindrical gives the gradient of magnetization in the direction perpendicular to x-axis and enables control of the roll motion by modifying the surrounding magnetic field. Such a way to control the roll motion is realized in some facilities successfully. (Ref. 1,2) At NAL 0.1m MSBS, Sawada et.al. succeeded in controlling the motion in 6 degrees of freedom by using a model containing 4 small magnets besides the main magnet. (Ref. 3) Figure 2 shows the model used in the 0.1m MSBS and the test of the roll motion control.

In controlling the roll motion in this way, when the MSBS and the model are enlarged, a required current to the electromagnet increases proportionally to the increasing size of the test section. When the magnetic field from the main magnet becomes stronger, it deducts the effect of radial magnetization for the roll control and make the required electric supply much greater. This system has another problem that causes coupling between the roll

motion and other modes. On the other hand, when the MSBS becomes larger, using large models makes it easier to contain some mechanical system in the model. So a mechanical system that controls the roll motion is designed for introduction of large scale MSBS.

DESIGN & SIMULATION

Figure 3 shows the general idea of the mechanical roll motion restraint system. In this system, the roll rate of the model is measured by the gyro and the measured roll rate is fed to the control circuit. The signal from the controller drives the DC motor with a flywheel to cancel the roll motion of the model. The controller is currently a digital controller on a personal computer and is connected by electric wire. But to keep the advantage of the MSBS, no mechanical connection is allowed, so in the future, it will be necessary to implement a controller as an analog circuit contained in the model or to communicate with the PC through a telemetry system as shown in Figure 4. In order to keep the roll-rate to zero, feedback control is necessary. Figure 5 shows the control loop for roll motion as block lines.

In order to prove the feasibility of such a system, a computer simulation was carried out. The results are shown in Figure 8 with the results of the experiment. It shows that this system has the capacity to suppress the roll motion of the model. But some results of the simulation showed that when a static moment around x axis is acting on the model, the rotation of the flywheel increases as time and reaches the maximum rotation. This will make it impossible to control the roll motion. In real cases, the distribution of the magnetization in the magnet is not equal and causes some roll moment acting on the model as a function of ϕ. It is necessary to avoid the influence of the constant moment by waiting to start controlling until the model is stable under no control or by reducing proportional control gain in exchange for tolerable degeneration of the control authority.

IMPLEMENTATION

Using the results of the simulation, a prototype of the mechanical roll motion restraint system was designed for the NAL 0.6m MSBS. To make it easy to introduce such a system, commercial products were used. In order to avoid the influence of the surrounding magnetic field, a fiber optic gyro (FOG) and coreless DC motor were used. The FOG used in this system is TA7319N1 produced by Tamagawa Seiki Co., Ltd.

Figure 6 shows the general arrangement of the system. A 55mm diameter cylindrical model is used in the NAL 0.6m MSBS and we tried to put the whole system in the 55m diameter cylinder, but we could not get the FOG that can be contained in the ϕ 55m model. So we contained the system in another 75mm diameter, 150mm long cylinder and aligned it to the model with the longitudinal axis in common. The 20mm difference in diameter is of course intolerable, but it is because of the size of FOG only so downsizing of the FOG will permit the application of such a system to the model less than 75mm in diameter. A ϕ 90mm diameter superconducting solenoid model has been introduced to 0.6m MSBS so this test also makes sense as the preparation of applying this system to the superconducting solenoid model. The cylinder is made of aluminum.

Figure 7 shows the prototype of the roll motion restraint system. In order to avoid any connection from what is not contained in the model, the power source also must be contained in the model. A commercial 9V dry cell is used and a DC-DC converter is used to produce required constant voltage. The results of the numerical simulation showed it possible to control the system by simple PI compensator. So it is not very difficult to implement the compensator circuit as an analog electric circuit. But for simplification of the system, a digital control system implemented on the personal computer is selected at first. An electric cable connection is used to monitor the roll rate and to send control signals. But it will be replaced by a telemetry system when this system is applied to wind tunnel testing.

The lifting ability of the NAL 0.6m MSBS with its ϕ 55mm diameter model is limited to 700g but the weight of the roll control system exceeded the limit. So some parts made of stainless steel were replaced by parts made of aluminum and lightening holes added. Finally the weight of the model is 650g.

EXPERIMENTS

Before suspending the model containing the roll motion restraint system in the MSBS, a test of a vertically hung model is carried out to prove the possibility to restrain the roll motion under the influence of the magnetic field caused by the main magnet of the model. Figure 8 shows the method of testing. The model with the mechanical roll motion restraint system is hung by the string and can rotate around the x-axis. The test was carried out for some control parameters of the feedback control loop.

Figure 9 shows the roll-rate ($d\phi$) in degree per second, roll (ϕ) in degree and control command in voltage. The initial value of the roll rate 20 [deg/sec] is given and the control is turned on when the amplitude of the roll rate is maximum. Because of the elasticity of the string suspending the model, the roll motion is reduced without any control. But the results of the test show that this system reduces the roll motion much faster. The magnetic field of the main magnet contained in the model did not cause any influence on the performance of this system. The strength of the magnetic field from the main magnet is superior to that from the electromagnets surrounding the test section. So the results were sufficient for constant magnetic field, but the effect of the fluctuation of magnetic field strength is not evaluated in this test.

However the results of the test showed a large difference from the results of the simulation. Especially, the required time to restrain the roll motion is longer than that in the simulation and it did not shorten as the proportional gain of the control loop increased. It is thought to be caused by the error in estimating the inductance of the DC motor, delay from the electric circuit to drive the motor, and non-linearity of the motor around the point where the rotation is equal to zero. The oscillation with small amplitude is still present even when the control is effective. It is supposed to be caused by non-uniformity of the model and the coupling between the roll motion and the pendulum motion of the model. Some results of the test show that the saturation of the rotation of the motor makes the running time of this system short especially when Kp is set at a higher number to obtain a good response. But increasing the weight of the flywheel makes it possible to obtain more torque from the same gradient of the rotation.

Figure 10 shows the results of the calibration test in the 0.1m MSBS. According to this, the roll moment acting on the model is 0.05 ~ 0.1 [mN•m/A]. The result of the experiment for the mechanical roll motion restraint system shows that the maximum torque acting on the model is about 2mN•m. When the 0.1m MSBS model is enlarged for the 0.6m MSBS, and taking the difference of the performances of the 0.1m MSBS and 0.6m MSBS into account, it corresponds to 5 ~ 20[W]. On the other hand the maximum power of the motor is 2.4 [W] and the gyro requires 2.0 [W], so the mechanical roll motion restraint system requires 4.4 [W]. When the model becomes larger, the method using a magnet for roll control needs to have the magnet similarly enlarged. But in the mechanical roll motion restraint system, only the flywheel needs to be enlarged similarly. The weight of the flywheel itself is 10% of that of the whole system, and it is easy to increase the weight of the flywheel. The mechanical roll motion restraint system is expected to cause less coupling, because it does not change the current to the electromagnets that is also used for controlling other modes of motion.

CONCLUDING REMARKS

A mechanical roll motion restraint system has been designed for use in the large scale MSBS that requires strong magnetization of the model. The results of a numerical simulation proved the possibility of such a system. A prototype of the system was made and tested under the situation that the model is hung vertically. The results showed that this system controls the roll motion in the constant magnetic field. This prototype is larger than the standard model in diameter and has some connection by electric cables. But these problems can be solved for large MSBS.

As the next step, a test with the model suspended in the MSBS is required. It may cause problems from the fluctuating magnetic field strength, coupling with other modes of motion, and electric noise from power supply. Further, this system will be applied to the superconducting solenoid model that has been introduced to the 0.6m MSBS.

REFERENCE

1) M. J. Goodyer: The Generation of Rolling Moments with the Superconducting Solenoid Model. NASA CR-172520, 1985.

2) M. J. Goodyer: Roll Control Techniques on Magnetic Suspension Systems. Aeronautical Quarterly, Vol. 18, Feb. 1967, Pt. 1, pp. 22-42.

3) H. Sawada: Rolling Moment Control in the NAL 10cm x 10cm Magnetic Suspension and Balance System. NAL TR-1164, 1992.

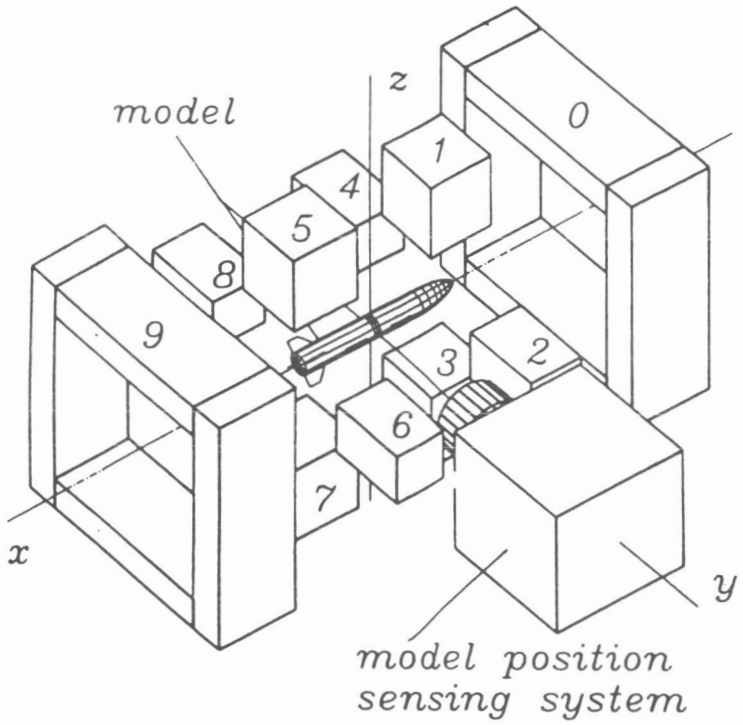

Fig.-1 Arrangement of the Electromagnets of the NAL 0.6m MSBS

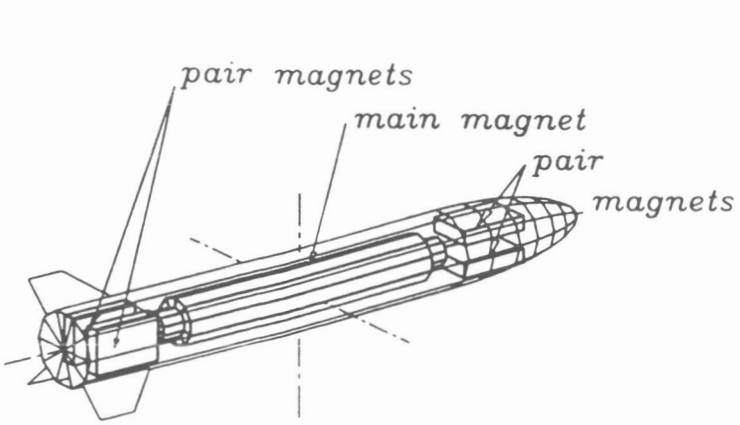

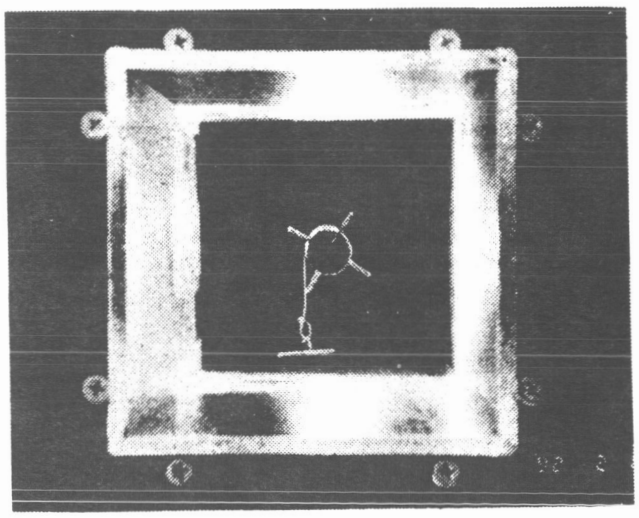

Fig.-2 Roll motion control at the NAL 0.1m MSBS (ref. 3)

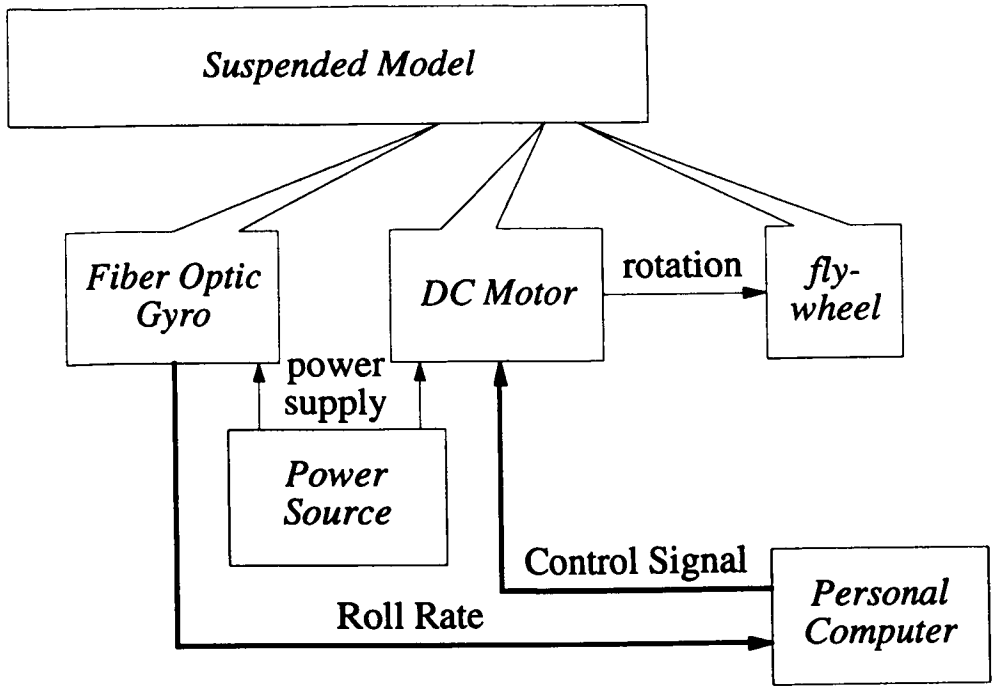

Fig.-3 General idea of the mechanical roll motion restraint system

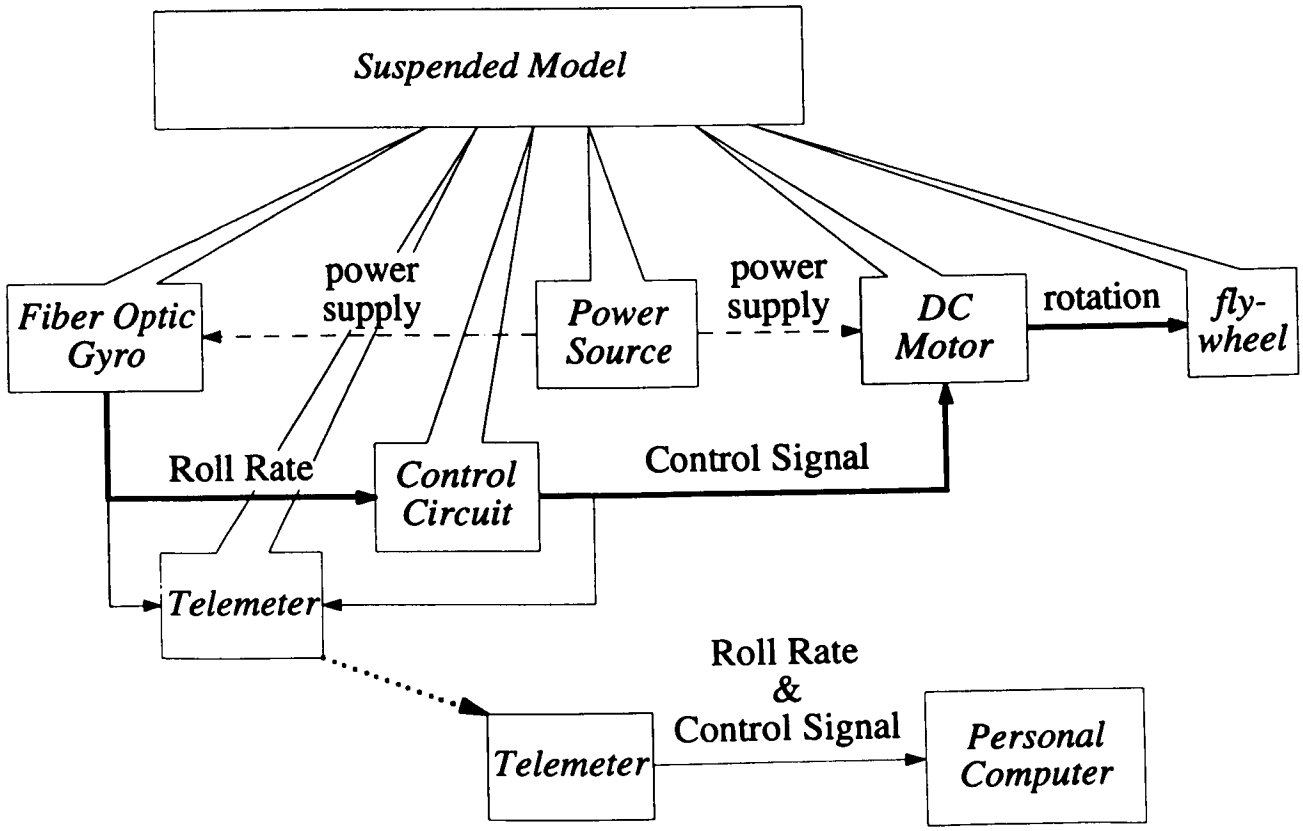

Fig.-4 Future plan of the mechanical roll motion restraint system

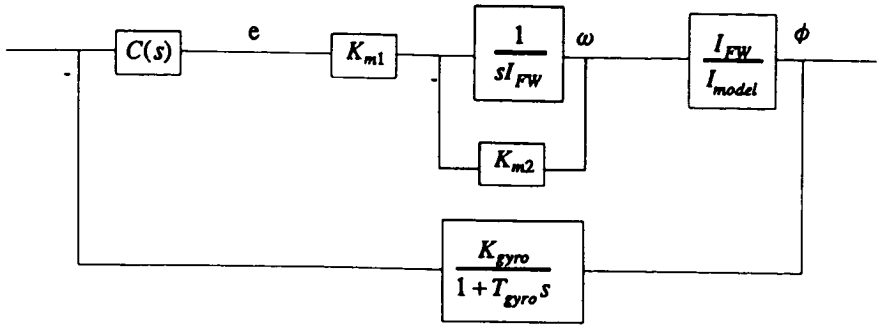

K_{m1} : torque-roll rate coefficient
K_{m2} : voltage-torque coefficient
I_{FW} : Inertia Momemt of the Flywheel
I_{model} : Inertia Momemt of the Model
K_{gyro} : Gain of the Gyro
T_{gyro} : Time Constant of Gyro

Fig.-5 Block lines of the roll control loop

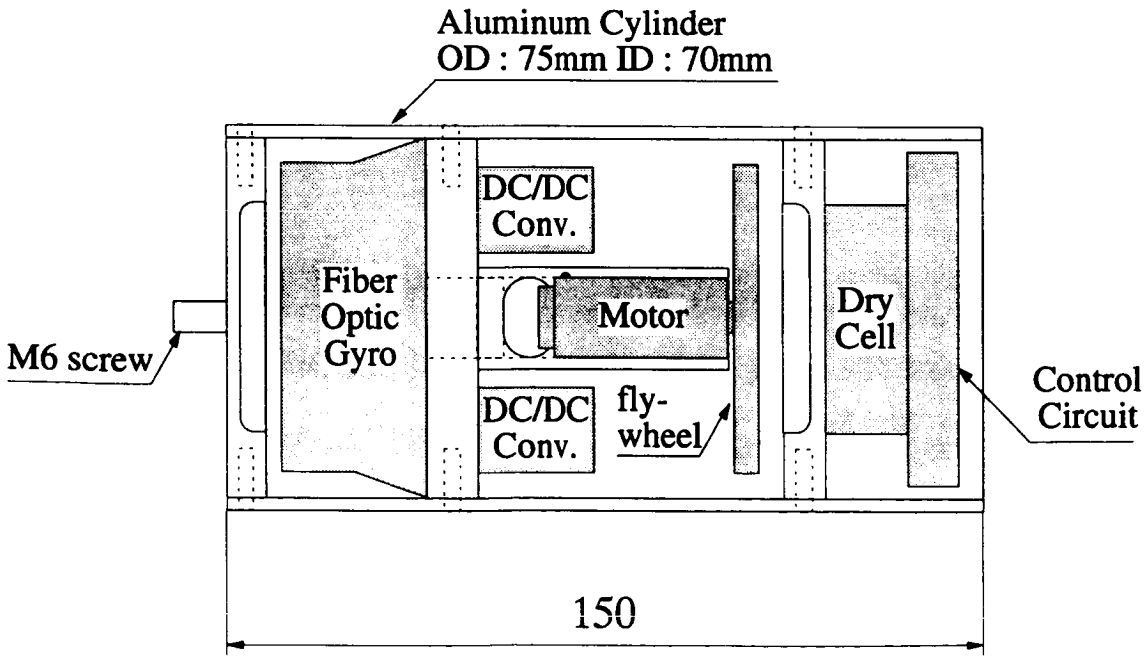

Fig.-6 General arrangement of the mechanical roll motion restraint system

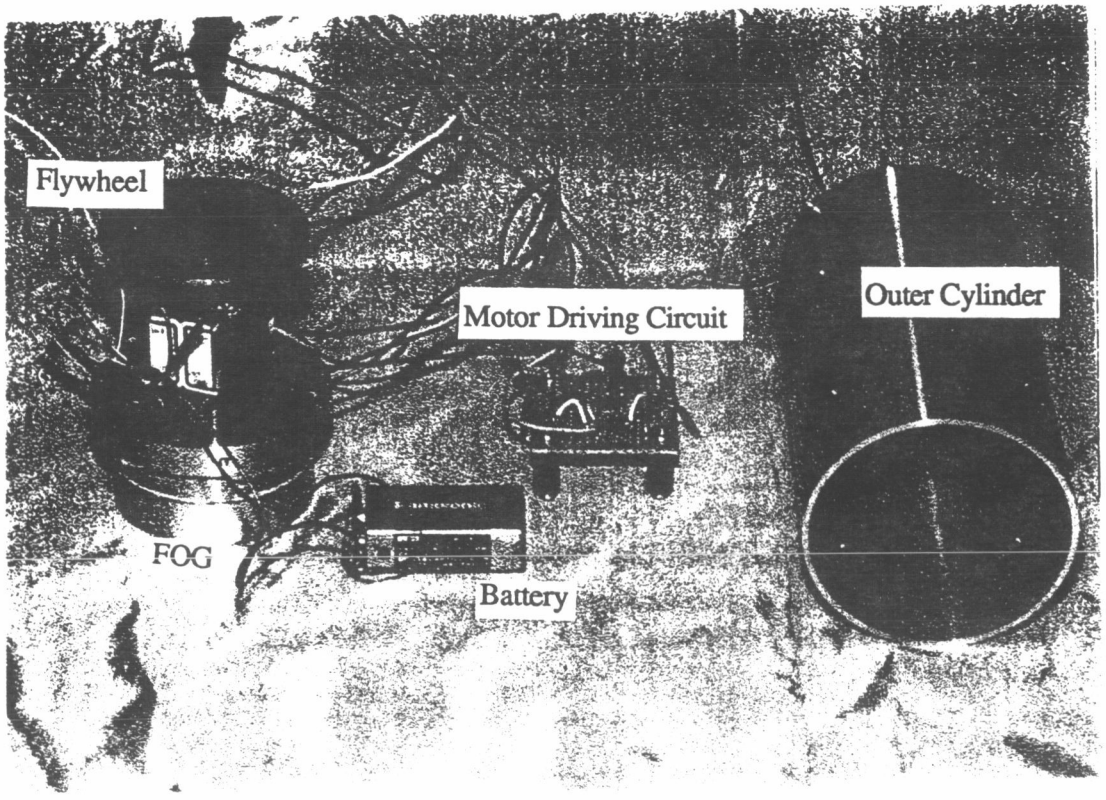

Fig.-7 Picture of the prototype

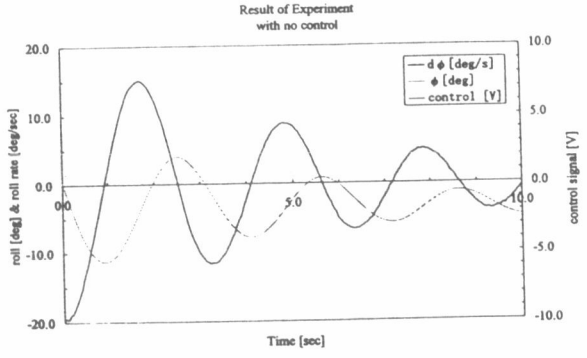

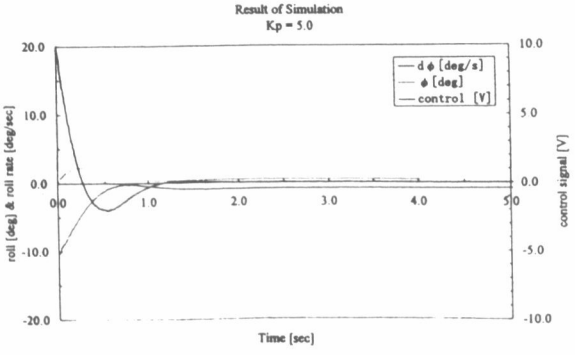

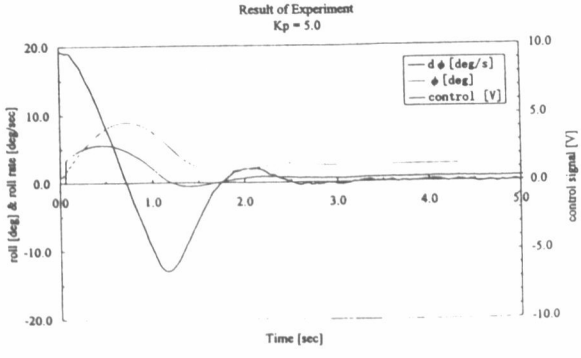

Fig.-8 Results of the simulation and experiment

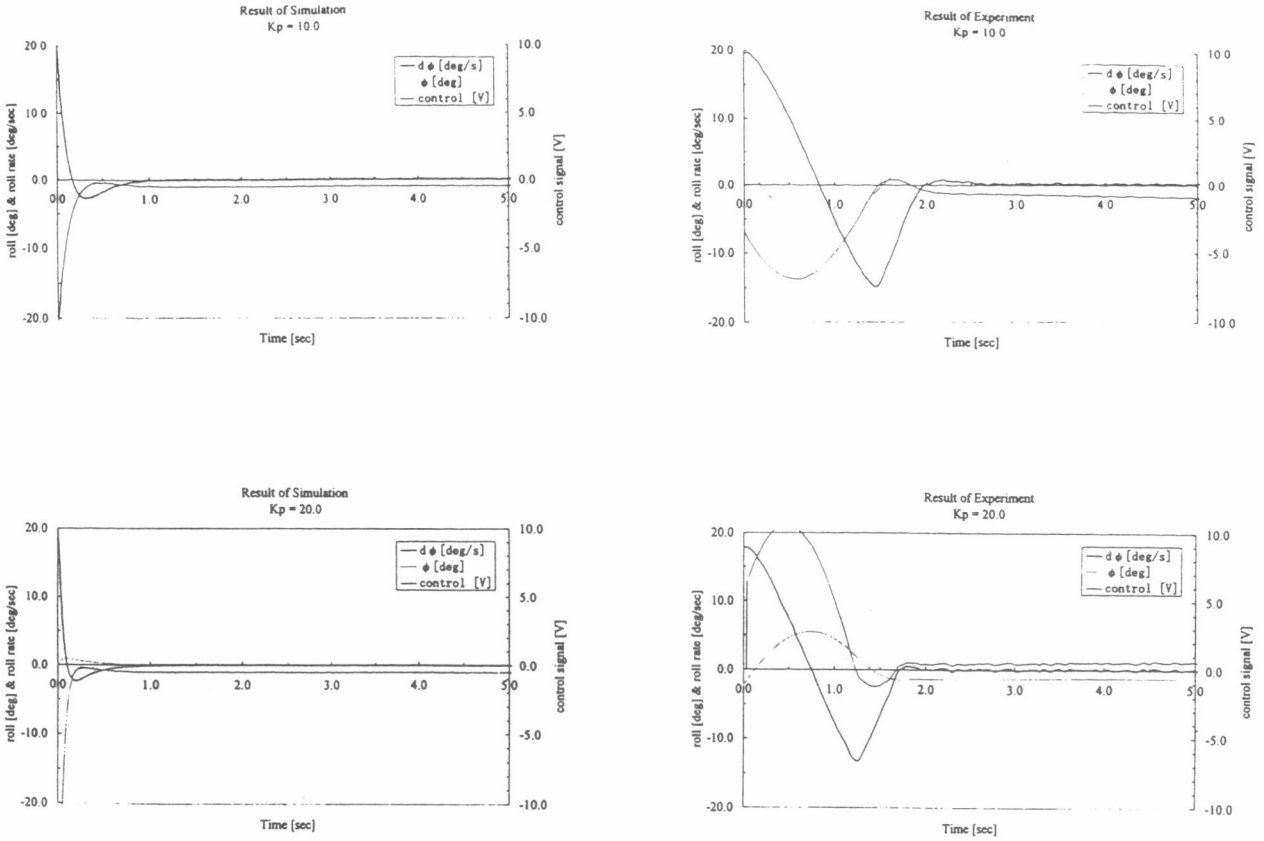

Fig.-8 Results of the simulation and experiment

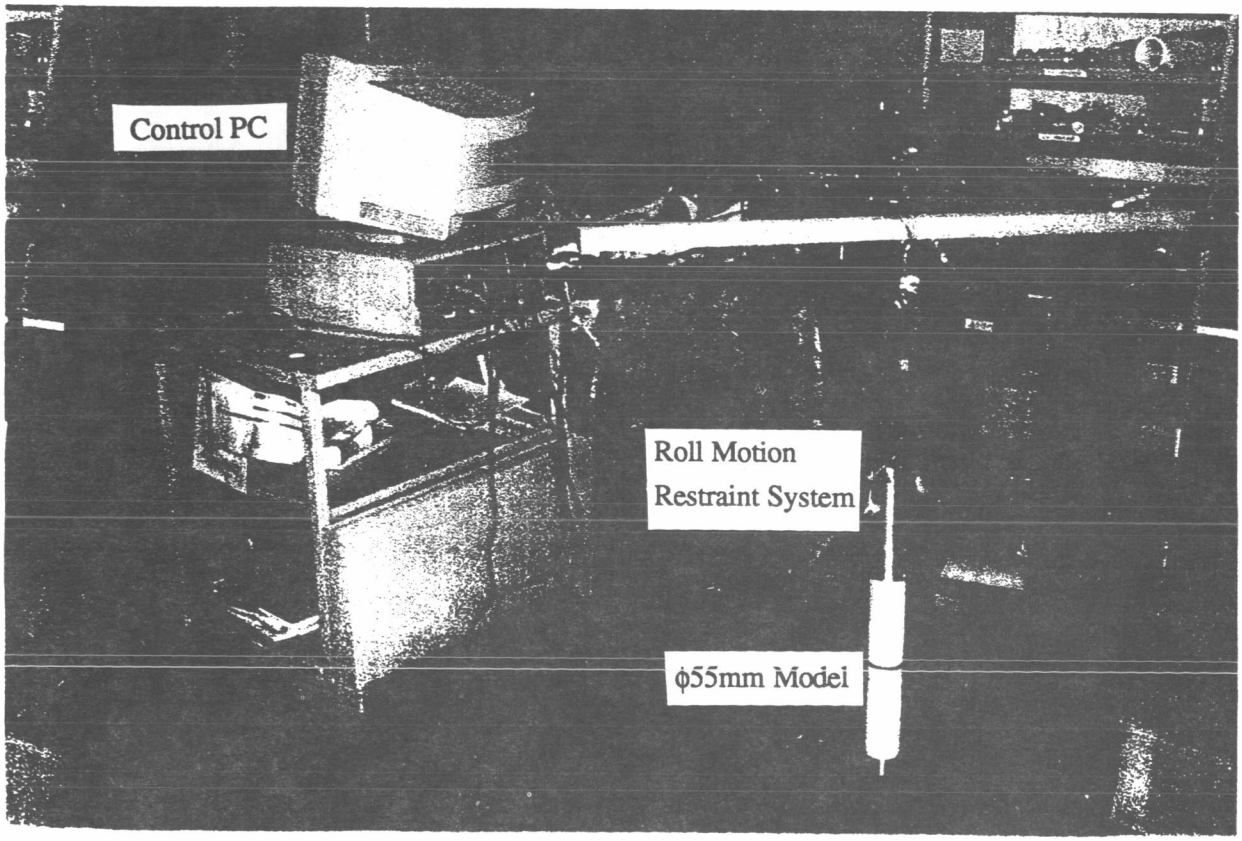

Fig.-9 Testing by hung model

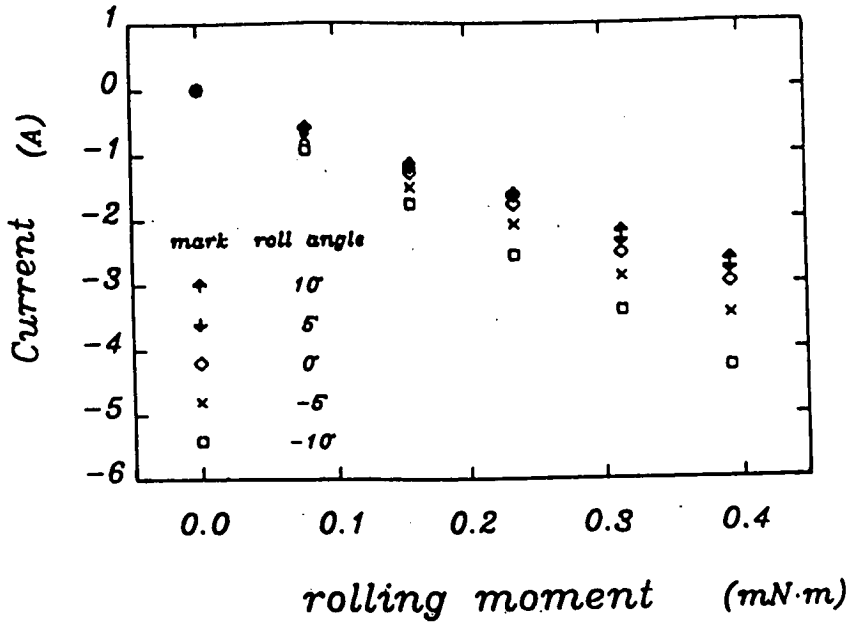

Fig.-10 Calibration test of roll moment in the 0.1m MSBS (ref. 3)

Wind Tunnel Magnetic Suspension and Balance Systems with Transversely Magnetized Model Cores

Colin P. Britcher
Department of Aerospace Engineering
Old Dominion University

Abstract

This paper discusses the possibility of using vertically magnetized model cores for wind tunnel Magnetic Suspension and Balance Systems (MSBS) in an effort to resolve the traditional "roll control" problem. A theoretical framework is laid out, based on previous work related to generic technology development efforts at NASA Langley Research Center. The impact of the new roll control scheme on traditional wind tunnel MSBS configurations is addressed, and the possibility of demonstrating the new scheme with an existing electromagnet assembly is explored. The specific system considered is the ex-MIT, ex-NASA, 6-inch MSBS currently in process of recommissioning at Old Dominion University. This system has a sufficiently versatile electromagnet configuration such that straightforward "conversion" to vertically magnetized cores appears possible.

Background

For many years, the "roll control" problem has hindered the development of wind tunnel Magnetic Suspension and Balance Systems (MSBS). This problem arises due to the natural tendency to place magnetic cores in the fuselage of aircraft models, magnetized along their long axis, i.e. the axis of the fuselage. This leads to a problem in generation of roll torque (torque about the axis of the fuselage), since the relevant moment equation provides no direct torque component for axisymmetric model cores :

$$\vec{T} \approx Vol\,((M_x,0,0) \times \vec{B}) \quad (axial\ \vec{M}) \tag{1}$$

A wide variety of techniques for generation of roll torque have been tried over the years, usually based on the introduction of transverse magnetization of some kind, or on the reduction of the degree of axial symmetry of the model core. Previous techniques are briefly summarized in a Addendum to this paper.

During the last few years, a series of laboratory-scale demonstration magnetic levitation systems have been designed and constructed at NASA Langley Research Center, in support of a program aimed at developing improved technology required for magnetic suspension of objects at large gaps and over large ranges of orientation. The first of these systems was called the Large Angle Magnetic Suspension Test Fixture (LAMSTF [1,2]), and relied on control in five degrees-of-freedom, the equivalent of the "roll" axis being

free (uncontrolled). Later systems have demonstrated that full six-component control can be achieved with a cylindrical permanent magnet core magnetized transversely. i.e. perpendicular to the axis of symmetry.

It is important to note that the choice of transverse magnetization has only been made practical by the introduction of new magnetic materials over the past two decades or so. For practical systems, high magnetizations (remanences) are required, eliminating ferrite materials from consideration. High remanence, but relatively low coercive force materials, such as the Alnico types, would be wholly unsuitable, due to the high demagnetizing factors developed by the proposed geometry. By contrast, rare-earth cobalt (ReCo) and neodymium-iron-boron (NdFeBo) materials exhibit high remanences and extremely high coercive forces and are therefore virtually immune to demagnetization.

Theoretical Framework

The force and torque on dipole-like permanent magnet cores is given by :

$$\vec{F} \approx Vol(\vec{M}.\nabla\vec{B}) \tag{2}$$

$$\vec{T} \approx Vol(\vec{M} \times \vec{B}) \tag{3}$$

Where the magnetic cores exhibit reduced levels of symmetry, such as a slender, transversely magnetized cylinder, additional contributions to torque arise, due to interactions between the core magnetization and second-order field gradients. A specific case of interest is that of a slender cylindrical core with its principal axis oriented along the suspension system's x-axis (the wind tunnel axis), but with transverse magnetization, aligned in the z-direction (vertical in the wind tunnel), as shown in Figure 1. The additional torque term (acting about the axis of magnetization) can be shown to be [3,4]:

$$T_z \approx \int_{length} M_z\,(B_{yz}\,x - B_{xz}\,y)\,d(Vol)\ \ (vertical\ \vec{M}) \tag{4}$$

or, where B_{yz} varies uniformly along the length (l) of a core of radius a :

$$T_z \approx Vol\left(M_z\left(\frac{l^2}{12} - \frac{a^2}{4}\right)B_{xyz}\right) \tag{5}$$

Inspection of equation 5 shows that the torque arises due mostly to a longitudinal gradient of lateral forces. As suggested above, a six-degree of freedom levitation system using this torque generation scheme for control of the magnetic core about its axis of magnetization has been built and demonstrated. The working designation of this system, which is illustrated in Figure 2, is the "6DOF 8C/2L" - referring to a 6 degree-of-freedom configuration with 8 control coils and two fixed-current levitation coils.

Application to Wind Tunnel Magnetic Suspension and Balance Systems

This paper explores the possibility of applying the torque generation scheme described above to wind tunnel MSBSs. Specifically, the magnetic core is assumed to be mounted in the aerodynamic model's fuselage as usual, but magnetized vertically, instead of axially as has been the virtually universal practice. Large rolling moments can be now be generated by application of transverse fields. The governing equation for moment production from dipole-like interactions is similar to that shown previously :

$$\vec{T} \approx Vol\,((0,0,M_z) \times \vec{B})\ (vertical\,\vec{M}) \qquad (6)$$

Inspection reveals that the "missing" torque component is now that about a vertical axis; the equivalent of "yaw" in the aerodynamic sense. Force and torque components are clarified in Figure 3.

The Old Dominion University 6-inch MSBS

This system was designed by Stephens et.al. in the 1960's and operated for many years at the MIT Aerophysics Laboratory [5,6]. In the 1980's the system was relocated to NASA Langley Research Center and was recommissioned in support of a wind tunnel MSBS research and development program. Limited aerodynamic testing was undertaken [7], prior to a termination of NASA's effort, and subsequent transfer of the entire facility to ODU. The MSBS with its low-speed wind tunnel are both illustrated in Figure 4.

Despite its age, the electromagnet assembly is still one of the most sophisticated ever constructed, with considerable efforts made in the original design to provide a significant degree of separation of field and field gradient components by choice of electromagnet configuration. Further, the Electromagnetic Position Sensor (EPS) is still the only successful example of its kind. Recommissioning efforts are currently proceeding, albeit rather slowly.

The electromagnet assembly comprises several subsystems. Two pairs of "saddle" coils[1] are configured to develop transverse fields within the test section. Two assemblies comprising four coils mounted on complex iron yokes are positioned at each end of the test section (upstream and downstream) with the intention of developing lateral gradients in axial fields[2] for generation of lift and lateral forces. A pair of axial (Helmholtz) coils are configured to generate an axial magnetizing field, and a final set of coils (two pairs upstream and downstream) provide an axial gradient in the axial field. These subassemblies and their design functions are illustrated in Figure 5

[1]Electromagnet windings are traditionally referred to as coils
[2]Equivalent to axial gradients in transverse fields

By removing existing electrical interconnections between coils, additional flexibility to generate independent field and field gradient components can be introduced. By way of example, Figure 6 illustrates that the lift coil assemblies, previously used only for production of the "lift" and "sideforce" field gradients, B_{xy} and B_{xz} are actually capable of developing two fields, three field gradients and one second-order gradient, B_x, B_z, B_{xy}, B_{xz}, B_{yz} and B_{xyz}, depending on the relative signs of current in each coil. In effect, each lift coil assembly can act as a dipole-like field source, or a quadrupole-like field source. Action as a monopole-like field source is ruled out on grounds of low efficiency, due to the configuration of the iron yokes.

Field and Field Gradient Generation

Preliminary computational (finite-element) models of the electromagnet sub-assemblies have been developed using the well-proven TOSCA package [8]. Some experimental validations have also been completed [9]. At the present time, each coil set has been modeled separately for convenience. Therefore, although the effect of the iron yokes within the lift coil sets is properly represented, the secondary influences of the yokes on the other coils sets is not. Further development and refinement of the model is clearly necessary.

In a preliminary analysis of system performance, it is acceptable to retain the notion that each coil set is assigned certain limited functions, i.e. develops one or more specific field or field gradient components, with secondary contributions neglected. Following this approach, Table 1 summarizes the principal coil sets involved in the development of each important field and field gradient term. It is seen that the generation of the necessary field and field gradient components for suspension and control of a vertically magnetized model core is possible with this system.

Table 1 - Coil Sets Generating Individual Field and Field Gradient Components

Field	Traditional Function	Proposed Function	Traditional Coil Set Designation
B_x	Magnetizing field	Pitching moment	Magnetizing coils
B_{xx}[3]	Drag force	None	Drag coils
B_y	Yaw moment	Rolling moment	Saddle coils, lift assemblies
B_{xy}	Sideforce	None	Lift assemblies
B_z	Pitch moment	None	Saddle coils, lift assemblies
B_{xz}	Lift force	Axial force	Lift assemblies
B_{yz}	None	Sideforce	Lift assemblies
B_{xyz}	None	Yaw moment	Lift assemblies
B_{yy}	None	None	Saddle coils, drag coils
B_{zz}	None	Lift force	Saddle coils, drag coils

[3]Of course $B_{xx} + B_{yy} + B_{zz} = 0$

The magnitude of the relevant field and field gradient components that can be generated with the existing electromagnet assembly are indicated in Table 2. Data is derived from a combination of original design information [5] with recent analysis and computation [9]. A maximum current of 100 Amps in each coil is used for reference, although this is well within the original design specifications of this system [5]. Note that transverse gradients in transverse fields (such as B_{zz}) can be generated by the saddle coil assembly, or as secondary components by the drag coil pair.

Table 2 - Baseline Capability for Specific Fields and Field Gradients ($I = 100A$)

Force or Moment	Field or Gradient	Magnitude	Data Source
Axial force	B_{xz}	$0.55\,T/m$	Ref. 5
Lateral force	B_{xy}	$0.55\,T/m$	Ref. 5
Lift force	B_{zz} (saddle coils)	$0.7\,T/m$	Estimated using Ref. 9
	B_{zz} (drag coils)	$0.33\,T/m$	Ref. 5
Rolling moment	B_y	$0.054\,T$	Ref. 5
Pitching moment	B_x	$0.14\,T$	Ref. 9
Yawing moment	B_{xyz}	$31.8\,T/m/m$	Computer model in Ref. 9

A typical model core used in this MSBS might be around 5 inches long and 0.75 inches in diameter. Typical core material (NdFeBo) has a working magnetization level around 800 kA/m ($\equiv$ 1 Tesla). The magnitude of the forces and torques that can be generated with axial and vertical magnetization configurations can now be estimated using Equations 2,3, and 5 and the information from Table 2 above. The estimated forces and moments are compared in Table 3.

Table 3 - Baseline Force and Moment Capability

Force or Moment	Magnitude
Axial force	$15.8\,N$
Lateral force	$15.8\,N$
Lift force	$29.7\,N$ (includes saddle and drag coils)
Rolling moment	$1.5\,Nm$
Pitching moment	$4.0\,Nm$
Yawing moment	$1.1\,Nm$
Deadweight	$3.2\,N$

Discussion

The largest force present in typical wind tunnel applications tends to be the aerodynamic lift force, which can be generalized to the aerodynamic normal force in cases where large angle-of-attack ranges are of interest. With transverse magnetization, it is seen that this

force is developed by field gradients of the form B_{ii}, i.e. a vertical gradient in a vertical field, B_{zz}. It is suspected, but not yet proven by example, that this type of field gradient can be generated more efficiently than field gradients of the form B_{ij}, as required in the traditional case of axial magnetization. If this proves to be the case, then roll torque generation can be "added" to wind tunnel MSBSs with zero cost penalty. More detailed analysis of alternative configurations will be required to resolve this point.

Conclusions

The results presented above indicate that the transverse magnetization concept can be demonstrated using the existing 6-inch MSBS electromagnet configuration. By inference, the transverse magnetization concept is worthy of further study.

Acknowledgements

This work was partially supported by NASA Langley Research Center under Cooperative Agreement NCC-1-248. The technical monitor is Nelson J. Groom. The author also wishes to acknowledge the assistance of one of his graduate research assistants, Yan Yang, in the measurements related to the 6-inch system.

References

1. Britcher, C.P.; Ghofrani, M.: A magnetic suspension system with a large angular range. Review of Scientific Instruments, July 1993
2. Britcher, C.P.; Ghofrani, M.; Britton, T.C.; Groom, N.J.: The large angle magnetic suspension test fixture. International Symposium on Magnetic Suspension Technology, August 1991. Published as NASA CP-3152, May 1992
3. Groom, N.J.: Expanded equations for torque and force on a cylindrical permanent magnet core in a large-gap magnetic suspension system. NASA TP-3638, February 1997
4. Groom, N.J.: Simplified analytical model of a six degree-of-freedom large-gap magnetic suspension system. NASA TM-112868, June 1997.
5. Stephens, T.: Design, construction and evaluation of a magnetic suspension and balance system for wind tunnels, MIT-TR-138, Nov. 1969; NASA CR-66903.
6. Covert, E.E.; Finston, M.: Magnetic balance and suspension systems for use with windtunnel models. Progress in Aerospace Sciences, 14, 1973.
7. Schott, T.; Jordan, T.; Daniels, T.: Present status of the MIT/NASA Langley 6-inch MSBS. International Symposium on Magnetic Suspension Technology, August 1991. Published as NASA CP-3152, May 1992
8. Vector Fields Incorporated. TOSCA Reference Manual.
9. Yang, Y.: Research related to multi degree-of-freedom magnetic suspensions. MS Thesis, Old Dominion University, August 1997. Submitted as a NASA CR.

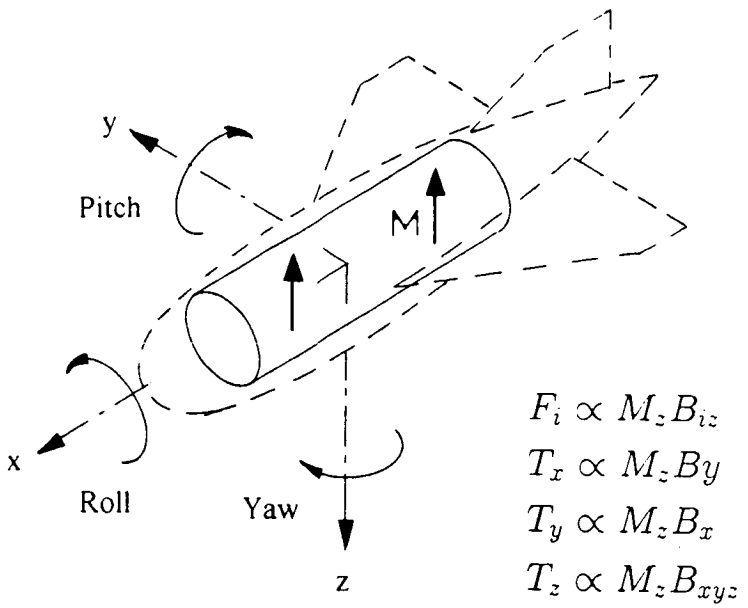

Figure 1 - Transverse Magnetization

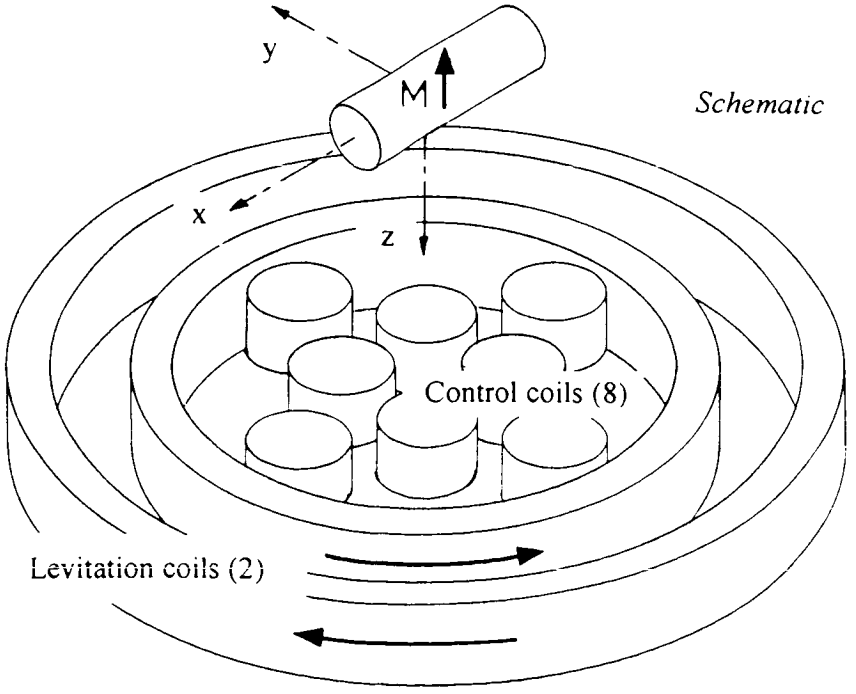

Figure 2 - Schematic Layout of the 6DOF-8C/2L System

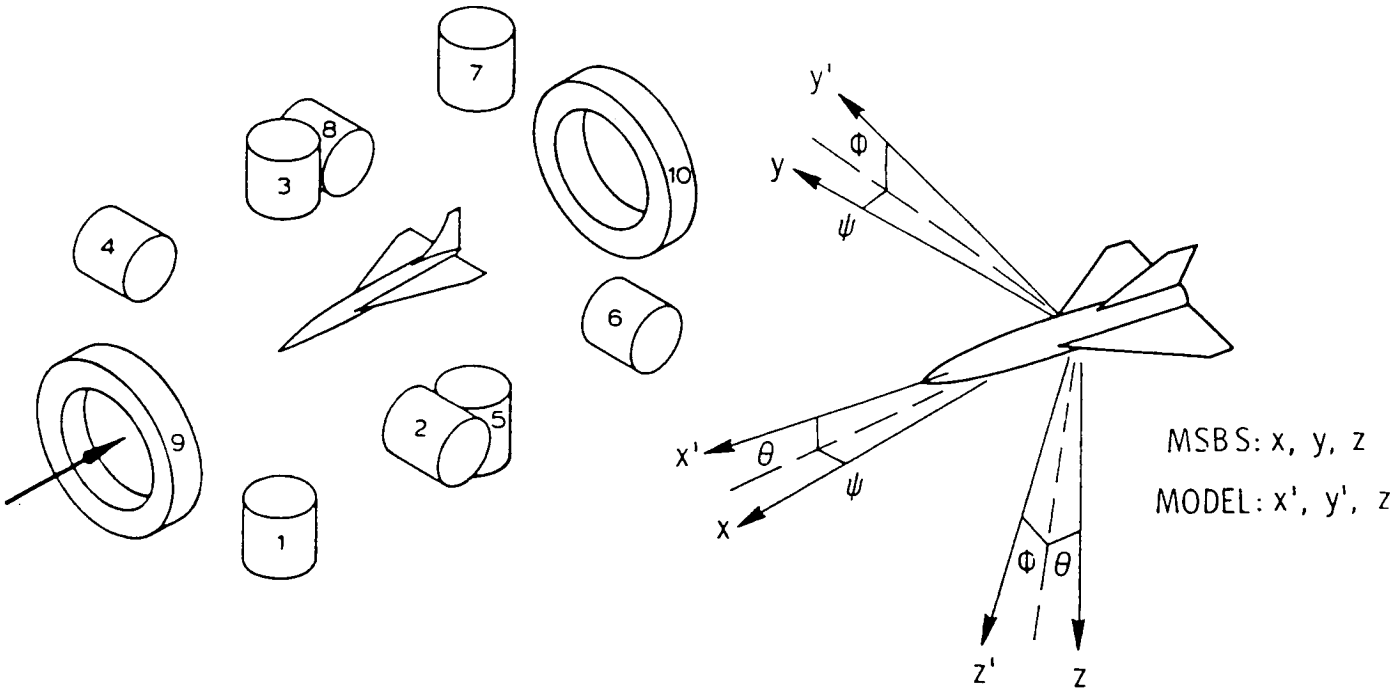

Figure 3 - Force and Torque Components

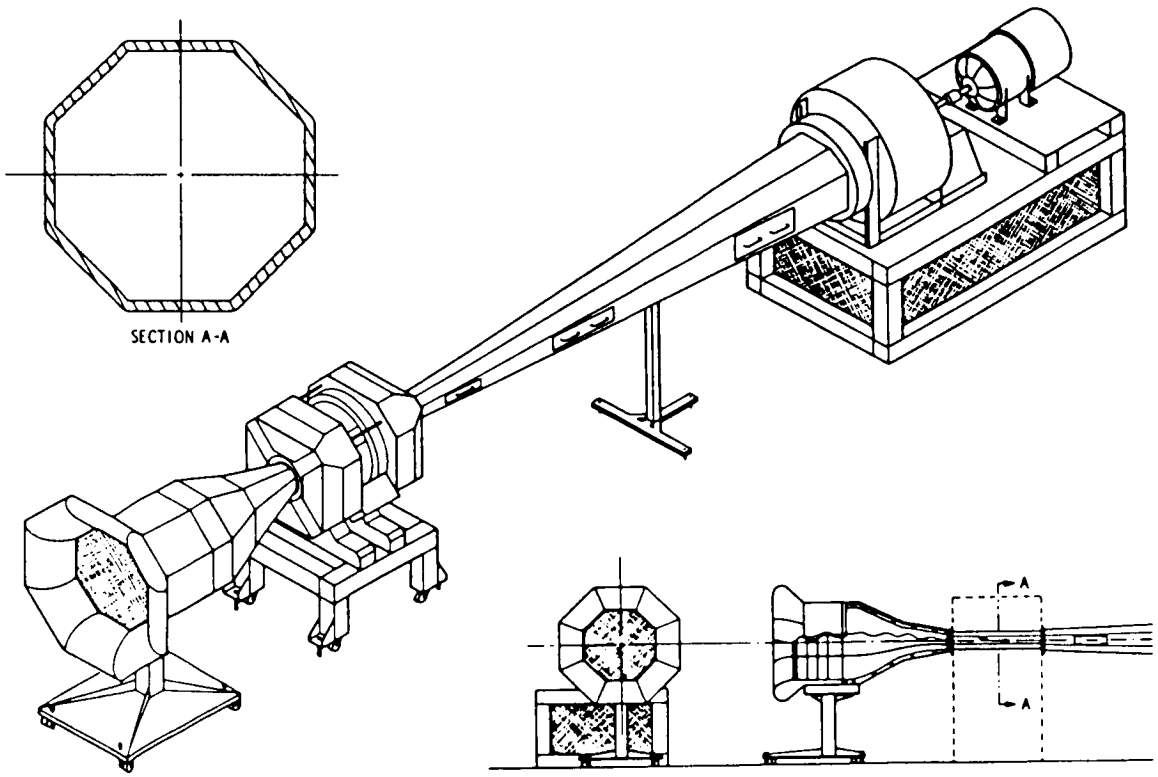

Figure 4 - The ODU 6-inch MSBS

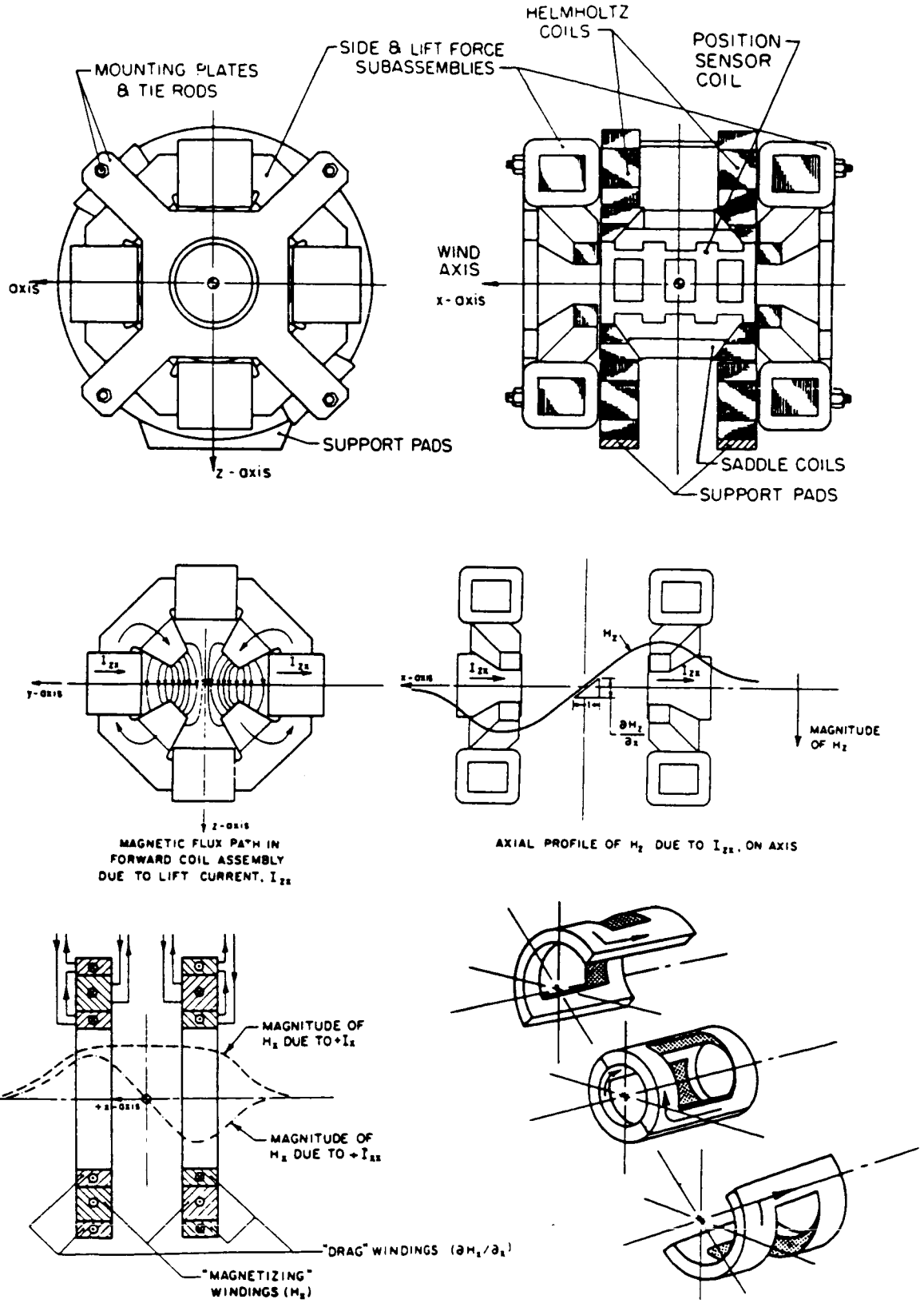

Figure 5 - Electromagnet Cofiguration of the 6-inch MSBS

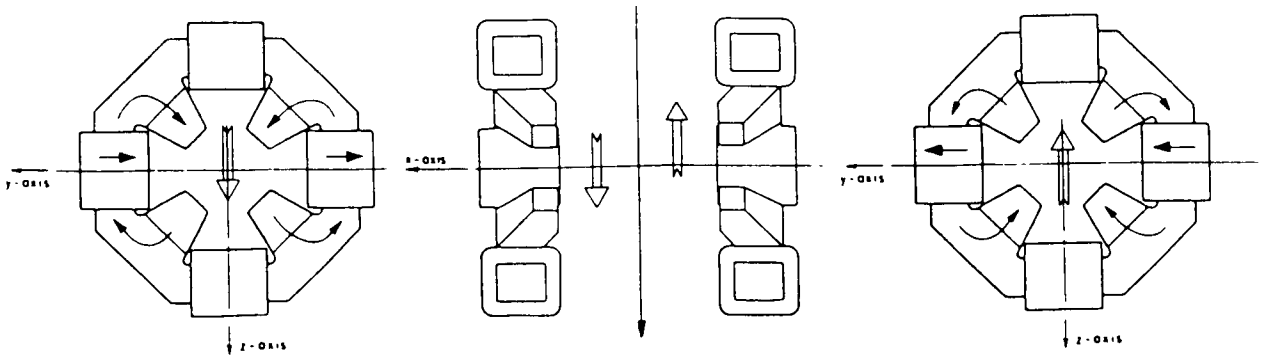

B_{xz} $(B_{yz}\ similar)$

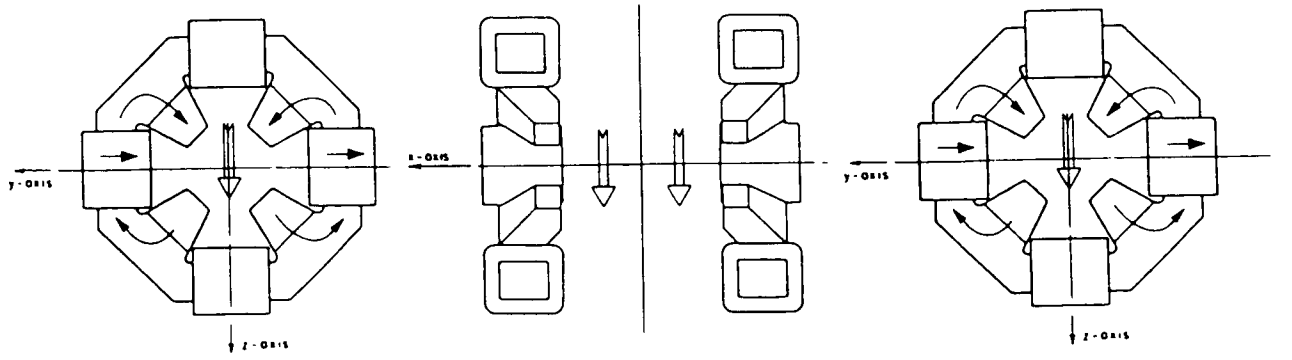

B_z $(B_y\ similar)$

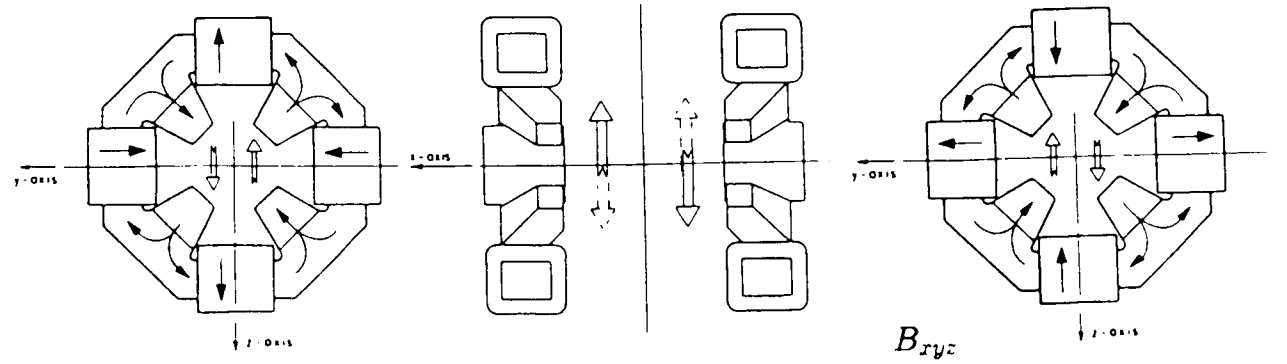

B_{xyz}

Figure 6 - Field and Field Gradient Component Production

ADDENDUM

Roll control techniques suggested or demonstrated in past years include at least the following :

Transverse magnetization methods (interactions with transverse fields)

1.1 "Bent" fuselage cores [A.1, 6]

1.2 Through-wing magnetized wing cores [A.2]

1.3 Spanwise magnets [A.3]

Methods based on reduction in axial symmetry

2.1 Shaped fuselage cores [A.2]

Model-mounted coils

3.1 Passive (battery-powered) wing or fin coils [A.2]

3.2 Active (controlled-current) wing or fin coils [A.2]

3.3 A.C. excited, phase-controlled model-mounted coils [A.1, 6]

3.4 Secondary windings in superconducting solenoids [A.4]

Aerodynamic Systems

4.1 Active aileron control [A.2]

4.2 C_{l_β} control [A.2]

References

A.1 Stephens, T.: Methods of controlling the roll degree of freedom in a wind tunnel magnetic balance. MIT TR-78, July, 1965.

A.2 Goodyer, M.J.: Roll control techniques on magnetic suspension systems. Aeronautical Quarterly, Vol.18, February 1967.

A.3 Britcher, C.P.: Some aspects of wind tunnel magnetic suspension and balance systems with special applications at large physical scale. NASA CR-172154, September 1983.

A.4 Goodyer, M.J.: The six component magnetic suspension system for wind tunnel testing. In High Reynolds Number Flows Using Liquid and Gaseous Helium. Springer-Verlag, 1991.

Session 6 -- Levitation

Chairman: Takeshi Mizuno
Saitama University

MAGNET WHEEL USING PERMANENT MAGNETS FOR REPULSIVE MAGNETIC LEVITATION AND INDUCTION TYPE THRUST

Nobuo Fujii
Dept. of Electrical and Electronic Systems Eng., Kyushu University
Fukuoka, 812-81, Japan

SUMMARY

A revolving permanent magnet type magnetic wheel called the "magnet wheel" is shown, which has both functions of inductive repulsive-type magnetic levitation and thrust. The characteristics of two types of the "tilt type magnet wheel" and the "partial overlap magnet wheel" are studied respectively by using a test facility and three-dimensional numerical analysis. The lift force, the thrust and the lateral force characteristics at standstill are shown versus revolving speed, the mechanical clearance, the conductivity of conducting plate, the arrangement of magnets, the volume of magnets, the tilt angle for the tilt type and the overlap factor for the partial overlap type.

INTRODUCTION

There are many magnetic levitation or propulsion techniques. The author has proposed the "magnet wheel" which is a kind of electromagnetic device with magnetic levitation and propulsion. The magnet wheel produces a rotating magnetic field by mechanically rotating permanent magnets with high coercivity. The induction repulsive-type magnetic lift force is produced by the rotating flux linking to a conducting plate. Simultaneously with the lift force is produced the thrust from the usually detrimental drag torque accompanying copper loss. The author has proposed two variations called "tilt type magnet wheel" and "partial overlap type magnet wheel" respectively [1][2].

Different from these types, a rotating motor type magnetic wheel has been also considered [3]. That is, a synchronous motor is constructed by the outer field-pole of permanent magnets which rotates against the centrally fixed armature winding. With no magnetic shielding, part of the magnetic flux on the outer pole is made to link with a normally placed conducting plate.

The proposed magnet wheel has a large weak point of mechanical rotation, but has the following strong points in induction repulsive type magnetic levitation, which has a self-stability without a complicated controller.

a. This method can produce larger lift force than the weight of mover installed levitation and propulsion device.
b. The useful thrust can be produced from the power required to produce the lift force.
c. The mechanical revolving method enables the operation free of poor power factor typical of ac electromagnets.

A small vehicle model with four magnet wheels of the "partial overlap type" has succeeded in propulsion, levitation and guidance without any control [4].

In this paper, the characteristics of the magnet wheel at standstill are shown, which were obtained by experimental study using a test facility [1] and theoretical study using three-dimensional numerical analysis [5].

WORKING PRINCIPLE OF THE MAGNET WHEEL

The magnet wheel is composed of a rotor with permanent magnets and a conducting plate. Figure 1 and Figure 2 are simplified diagrams of the magnet wheel. The pole faces of the permanent magnets are placed opposite to the conducting plate and are separated by an air gap. When the magnets rotate, the magnetic field which links the conducting plate changes with time producing eddy currents due to induced electromotive force (emf) in the conducting plate. The magnetomotive force (mmf) due to the eddy current faces the magnetic poles of the permanent magnets. The mmf cancels the magnetic flux which traverses from the magnets to the conducting plate, allowing a repulsive levitation force between the magnet wheel and the conducting plate to be produced. In general, a drag torque along the rotation direction will be produced, too. Due to this torque, corresponding amounts of power loss cannot be avoided. To make effective use of the torque, two types of magnet wheels are proposed.

Figure 1 shows the "tilt type magnet wheel", where the permanent magnet rotator (henceforth referred to as "magnet wheel" unless otherwise stated) is inclined to the conducting plate such that there is a varying air gap. Figure 2 shows the "partial overlap type magnet wheel", where the magnet wheel is made to rotate near the edge of conducting plate, so that the rotation region of the magnet wheel partially superimposes the conducting plate. Both types attempt to produce an uneven air gap magnetic flux density distribution in the rotating direction. This uneven distribution will produce a linear force, that is the thrust.

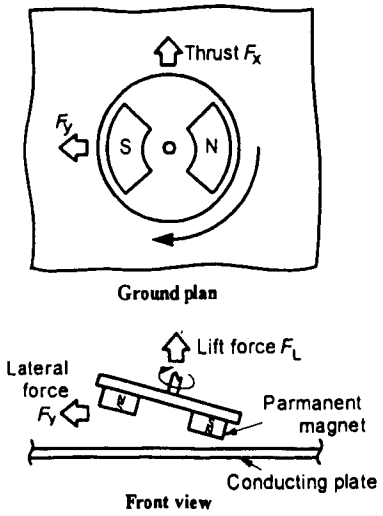

Fig. 1 The "tilt type magnet wheel".

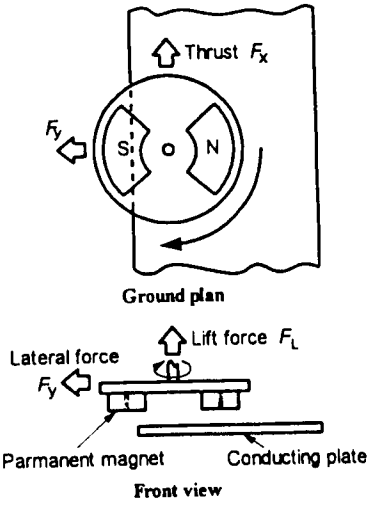

Fig.2 The "partial overlap type magnet wheel".

DATA FOR TESTED WHEEL

Figure 3 shows the form and the dimensions of the tested magnet wheel. 40mm thick neodymium permanent magnets with coercivity of 926kA/m (11,640Oe) and maximum energy product of 345kAT/m (43.3MGOe) are arranged in two poles on a circle of 60mm radius on the disk shaped ferro-magnetic yoke. The magnetization of the permanent magnets is in the direction of the thickness. The surface of the magnet poles is covered by thin non-magnetic stainless steel. This magnet wheel is denoted by the name of MW-A. The following experimental results were obtained by using the test facility installed with this magnet wheel [1].

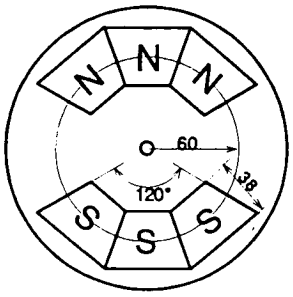

Specification of permanent magnet	
Type	Neodymium type
Maximum energy product	$(BH)_{max}$ =345kAT/m
Coercivity	iH_c = 926kA/m
Thickness	h_M = 40mm

Fig. 3 Dimension and arrangement of permanent magnets of the tested magnet wheel (MW-A).

CHARACTERISTICS

Characteristics of Magnetic Levitation Device of Induction Type

Characteristics at the state of parallel rotation are fundamental, in which the magnet wheel is placed in a parallel condition opposite the conducting plate in the tilt type magnet wheel shown in Figure 1. Numerical three-dimensional electromagnetic analysis [1][5] is used to check the characteristics.

Rotating Speed Characteristics

Figure 4(a) shows the lift force versus rotating speed characteristics for 10mm-thick copper plate (Cu) at mechanical clearance of g_2=15mm and 10mm-thick aluminum (alloy) plate (Al) at g_2=10mm respectively. The conductivity of copper and aluminum (alloy) are 5.27×10^7 S/m and 1.79×10^7 S/m respectively. The copper plate with small resistance gives larger lift force that is saturated at a lower rotational speed compared with aluminum. The lift force for the aluminum plate is in proportion to the rotational speed in this range. The rotational speed of 1,800 rpm is equivalent to 11.3 m/s in the tested wheel. Figure 4(b) shows the drag torque versus rotational speed characteristic for the case of Figure 4(a). The maximum torque appears for the copper plate.

Figure 5 shows the comparison between the computed characteristics for copper plate and aluminum plate respectively over a wide speed range. The classical skin effect is not considered in the calculation because the thickness of conductor is divided into only two layers. The saturated value of lift force is fixed independently of the resistance of conductor, and the rotational speed for saturation is proportional to the resistance of conductor, as shown in Figure 5(a). The maximum drag torque is fixed independently of the resistance, and the rotational speed for the maximum torque is in proportion to the resistance. This is the same phenomenon as the proportional shifting of torque for rotor resistance in a rotating type induction motor.

Figure 6 shows the measured lift force per driving power of the magnet wheel with respect to the rotational speed. The value of lift force per driving power is almost constant independent of the rotational speed, and dependent of the resistance of the conducting plate.

Characteristics for Conductivity of Conducting Plate

Figure 7 shows the relation between the measured lift force per driving power and the surface conductivity, that is the value of conductivity multiplied by the thickness. Cu 10mm means the 10mm-thick conducting plate of copper. The surface conductivity of the 5mm-thick copper plate is almost equal to that of 15mm-thick aluminum (alloy) plate, whose conductivity is 0.34 times as large as that of copper. The lift force per driving power is almost proportional to the surface conductivity.

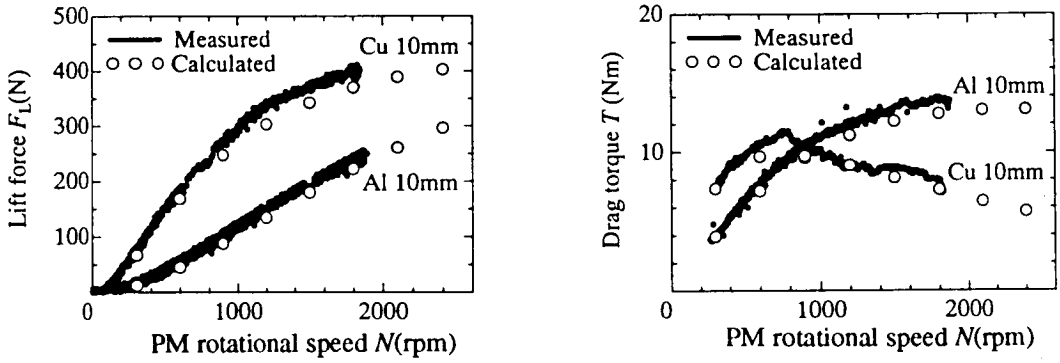

(a) Lift force (b) Drag torque

Fig. 4 Measured lift force and drag torque characteristics compared with calculated values.

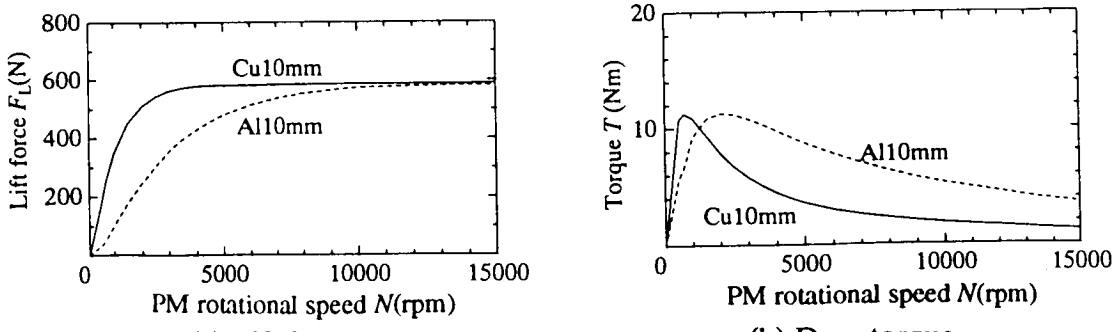

(a) Lift force (b) Drag torque

Fig. 5 Computed lift force and drag torque – rotational speed curves for different secondary conductors.

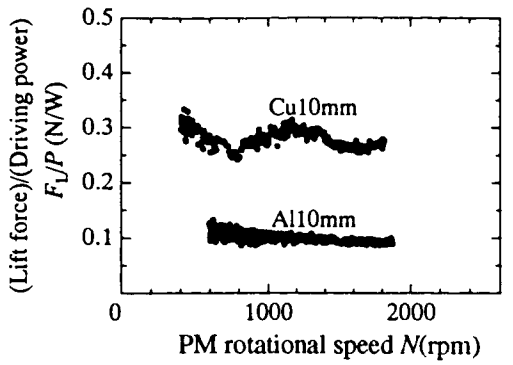

Fig. 6 Lift force per driving power for rotational speed.

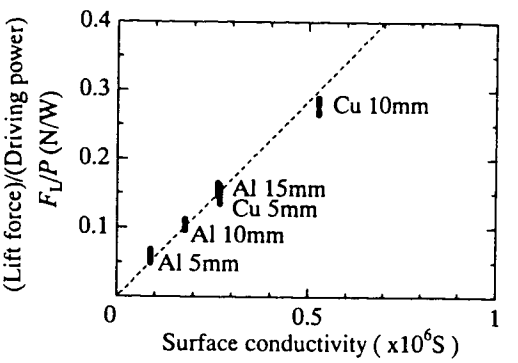

Fig. 7 Lift force per driving power characteristics for surface conductivity.

Influence of Arrangement of Permanent Magnets

Various arrangements of permanent magnets are studied as a parameter for performance of the magnet wheel. Figure 8 shows the five kinds of arrangements of experimental wheels. The MW-B has an arrangement lacking a center magnet of pole of MW-A. The number of poles and the pole pitch are equal to those of MW-A respectively. The total volume of permanent magnets of MW-B is 2/3 as much as the MW-A. The distribution in the direction of the circumference of the magnetomotive force of magnets for MW-B includes a large spatial harmonic component. MW-C is a four-pole arrangement using the magnets of MW-B. The volume of MW-C is equal to that of MW-B. The pole pitch is half of that of MW-A or MW-B. In MW-D and MW-E the thickness of magnets is 20mm, half of that of MW-A. MW-B and MW-C. The number of poles and the pole pitch of MW-D are equal to MW-C. The diameter of MW-E with two-poles is half of the others. The pole pitch of MW-E is equal to that of MW-C or MW-D.

Figure 9 shows the relation between the magnitude of lift force and the total volume of permanent magnets (PMs) for the magnet wheels, using measured values. The rotational speed is fixed at 11.3m/s. The lift force varies as about the 4/3th power of the magnets volume. It seems that the spatial harmonics of flux density of magnets are hardly effective to increase the lift force.

In order to study the influence of the space harmonics of flux distribution, the magnetomotive force of permanent magnets in the direction of circumference is analyzed. The solid line of Figure 10 shows the distribution of magnetomotive force for MW-A. F_m is the amplitude of the magnetomotive force of the magnets. The dotted line represents the fundamental component of the waveform of the solid line. Here the fundamental factor is defined as the ratio between F_m and the root mean square (rms) value expressed by F_1 of the fundamental waveform. That is

$$\text{Fundamental factor}: \quad F_1 / F_m = \frac{\frac{F_{1m}}{\sqrt{2}}}{F_m}$$

Figure 11 shows the relation between the fundamental factor and the lift force per total volume of magnets of one magnet wheel, using measured values. The lift force is approximately proportional to the fundamental factor independently of the resistance of conductor.

Figure 12 shows the relation between the thickness of magnets in the direction of magnetization and the lift force. Here the notations of 2p, 4p and 6p mean 2-pole, 4-pole and 6-pole respectively under the condition that the radius at magnet placement is fixed at 60mm. As the magnet wheel has large magnetic resistance in the magnetic path, the lift force is not saturated even for thick magnets, but the lift force per volume of magnet has an extreme value at some thickness. The value of thickness for the maximum lift force increases as the pole pitch expressed by τ increases.

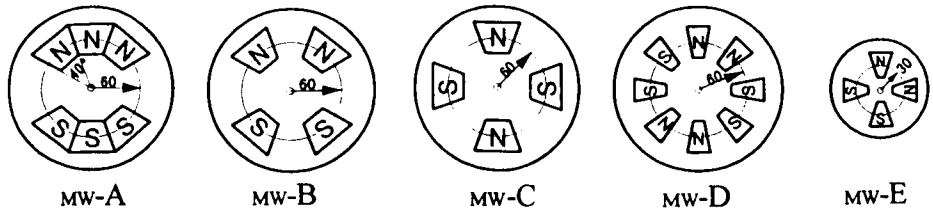

Fig. 8 Name of magnet wheel with different arrangement and size of magnet.

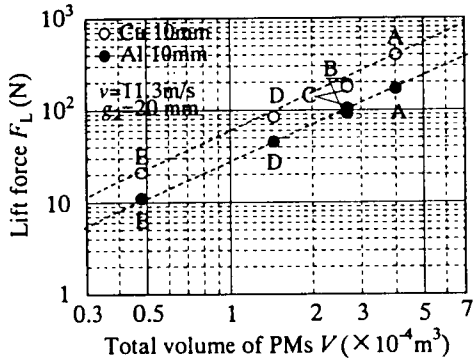

Fig. 9 Relation between magnitude of lift force and total volume of magnets for five magnet wheels.

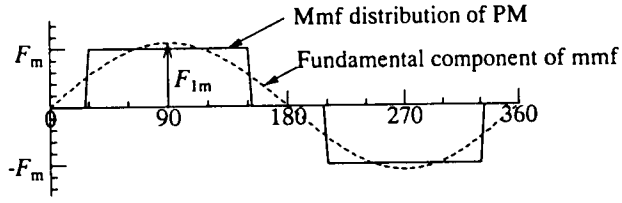

Fig. 10 Magnetomotive force distribution of magnets in the direction of circumference for MW-A.

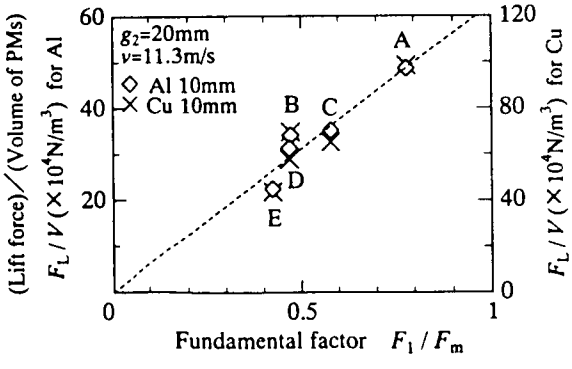

Fig. 11 Lift force per total volume total magnets versus fundamental factor of mmf.

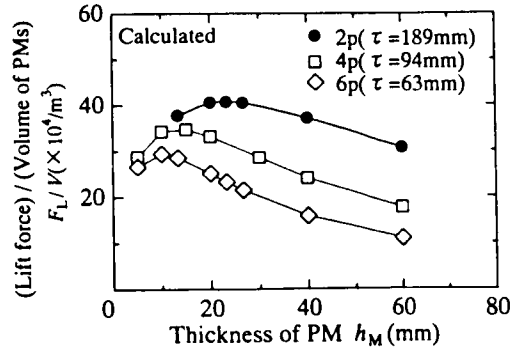

Fig. 12 Lift force per total volume of magnets versus thickness of magnet.

Figure 13 shows the definition of symbols and parameters for the tilt type magnet wheel. The tilt angle is expressed by ϕ. The minimum mechanical clearance between the surface of the magnet wheel and the surface of the conducting plate is expressed by $g_{2,\min}$.

Three Dimensional Force versus Rotational Speed

Figure 14 shows the lift force, the thrust and the lateral force with respect to the rotational speed for the tilt type magnet wheel of MW-A at the condition that the tilt angle is 10 degree, the minimum mechanical clearance is 10mm for 10mm-thick aluminum plate. It can be confirmed that thrust is produced. The lateral force does not appear.

Instantaneous Forces for Revolving Angle Position

Figure 15 shows the instantaneous forces of tilt type magnet wheel which are calculated values. The rotational angle means the mechanical angle that is equal to the electric angle in the case of MW-A with 2-pole. The pulsation appears in the lift force of magnet wheel.

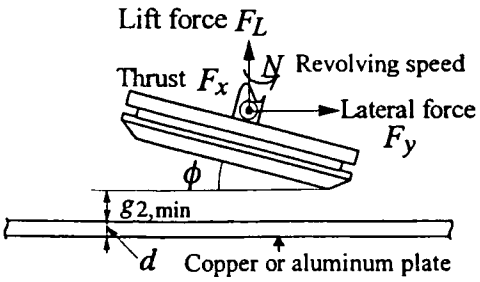

Fig. 13 Definition for the tilt type magnet wheel.

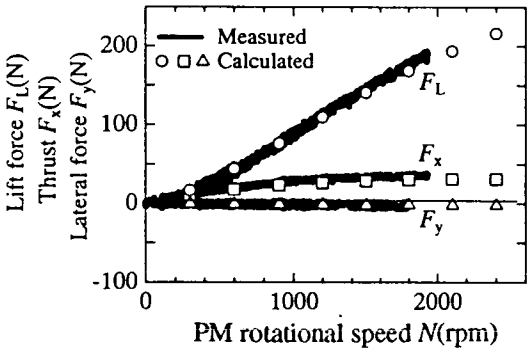

Fig. 14 Force-rotational speed curves for the tilt type magnet wheel at $\phi = 10$ degree.

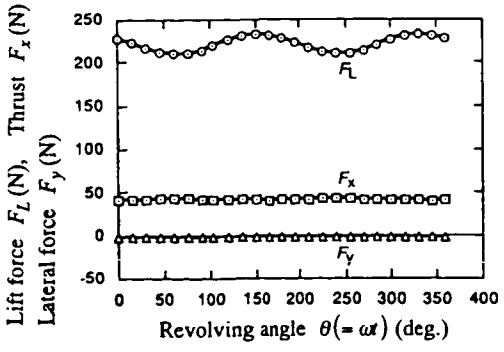

Fig. 15 Fluctuation of forces with rotational angle at the tilt angle of 10 degree and 1,800 rpm.

Characteristics for Tilt Angle and Mechanical Clearance

Figure 16(a) and Figure 16(b) show the measured lift force and thrust with respect to the tilt angle respectively for copper and aluminum plates. The minimum mechanical clearance and the rotational speed are fixed at 10mm and 1,800 rpm respectively. The lift force decreases rapidly as the tilt angle increases. The maximum thrust appears at a smaller tilt angle when resistance of conductor is smaller.

Figure 17(a) and Figure 17(b) show the measured lift force and thrust with respect to the mechanical clearance. The tilt angle is fixed at 15 degrees. The large lift force is produced with a small resistance of conductor and small mechanical clearance compared to the size of magnetic wheel. The thrust characteristics do not differ very much with the resistance of conductor.

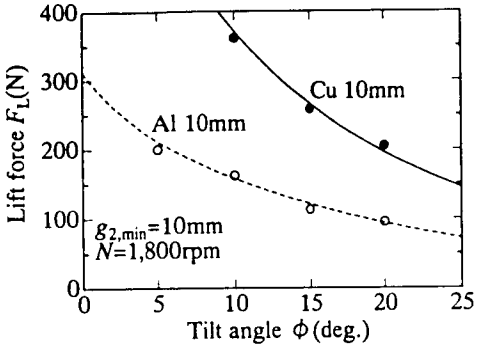

(a) Lift force

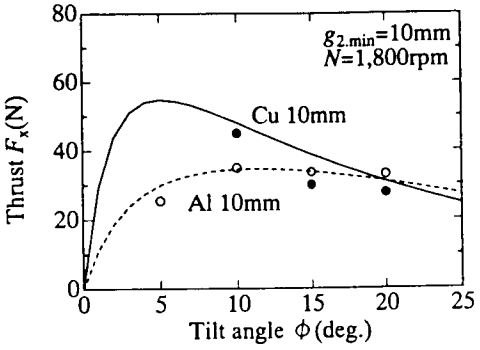

(b) Thrust

Fig. 16 Tilt angle characteristics.

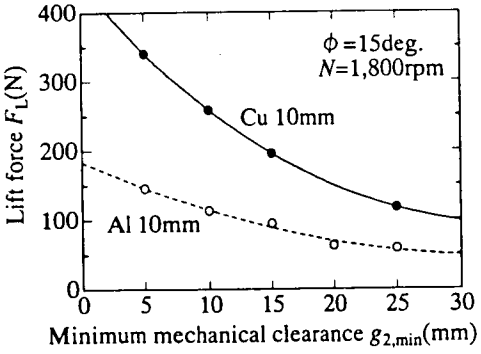

(a) Lift force

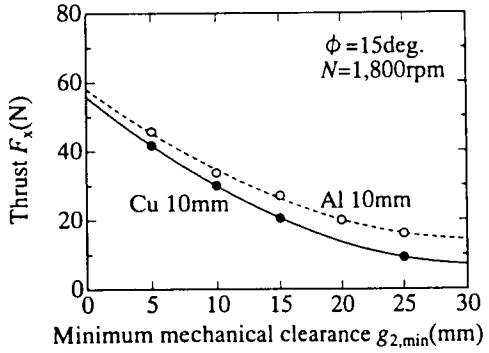

(b) Thrust

Fig. 17 Mechanical clearance characteristics.

Characteristics for Five Arrangements of Magnets

Figure 18 shows the relation between the measured lift force per driving power and the tilt angle for five magnet wheels shown in Figure 8. The lift force per driving power is independent of the tilt angle and the arrangement of magnets.

Figure 19 shows the relation between the tilt angle and the measured transformation for thrust. The transformation is defined as the ratio of the tangential force-induced drag torque to the thrust. The thrust transformation rate increases as the tilt angle increases. The four-pole wheel of MW-C has larger transformation rate compared with two-pole wheel of MW-A.

Figure 20 shows the lift force and the thrust with respect to the total volume of magnets for five tilt type magnet wheels respectively. The tilt angle and the rotational speed are fixed at 10 degree and 11.3m/s respectively. Both lift force and thrust vary as about 4/3th power of the magnets volume as well as the lift force characteristics for the state of parallel rotation shown in Figure 9.

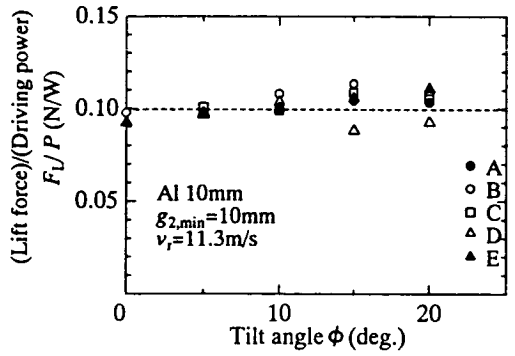

Fig. 18 Lift force per driving power versus tilt angle.

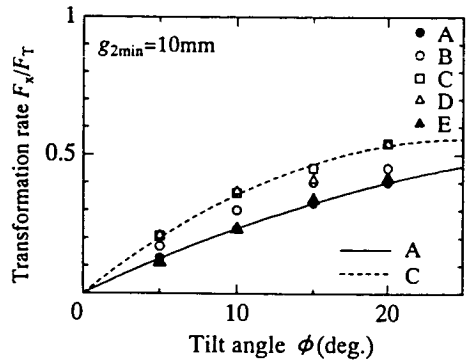

Fig. 19 Transformation rate for thrust versus tilt angle.

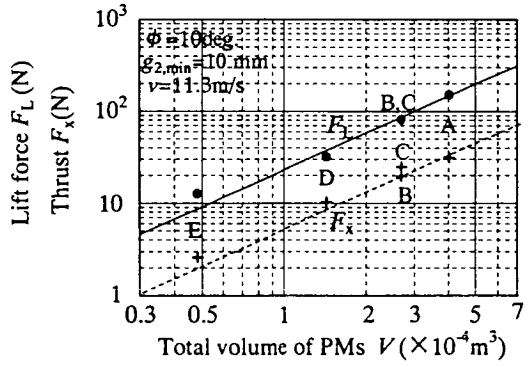

Fig. 20 Measured lift force and thrust for five tilt type magnet wheels.

Characteristics at the "Partial Overlap Type Magnet Wheel"

The directions of forces for the partial overlap type magnet wheel are defined respectively as shown in Figure 21. The overlap area between the magnet wheel and the conducting plate is an important parameter of the partial overlap type magnet wheel. In Figure 21, we let the rotational area of magnetic poles shown by the shadowed portion be S_1, and let the overlap area between S_1 and the conductor region be S_2 shown by the gray portion. Here the overlap factor is defined as $k_y = S_2 / S_1$. At the case that the magnet wheel overlaps the conducting plate completely, $k_y = 1.0$.

Three Dimensional Forces versus Revolving Speed

Figure 22 shows the measured lift force, thrust and lateral force with respect to the rotational speed for the overlap type magnet wheel of MW-A for the condition that the overlap factor is 0.66, mechanical clearance is 15mm for 10mm-thick aluminum plate. It can be confirmed that thrust and the lateral force are produced together with lift force. The lateral force acts in the direction away from conducting plate.

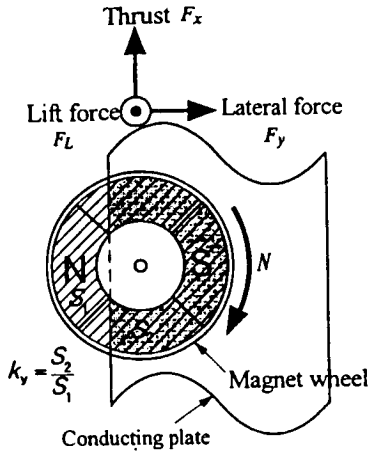

Fig. 21 Definition of direction of forces and the overlap factor k_y.

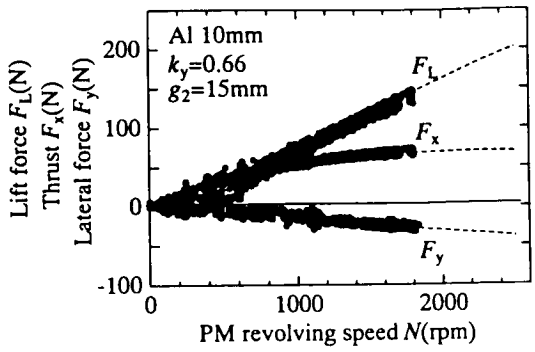

Fig. 22 Measured force-revolving speed curves for the partial overlap type magnet wheel.

Instantaneous Forces for Revolving Angle Position

Figure 23 shows the instantaneous forces of the overlap type magnet wheel with respect to the position of revolving angle at the conditions that the overlap factor is 0.66, mechanical clearance 15mm, rotational speed 1,800rpm for 10mm-thick aluminum plate. The pulsation appears in the lift force and the lateral force. Although the pulsation is relatively large, there will be no problem in the high-speed rotation over 3,000 rpm corresponding to 100 Hz for two-pole wheel.

Characteristics for Overlap Factor and Mechanical Clearance

Figure 24 shows the lift force, the thrust and the lateral force with respect to the overlap factor at the condition that mechanical clearance is 15mm, rotational speed 1,800 rpm for a 10mm-thick aluminum plate. The lift force decreases as the overlap factor decreases. The thrust and the lateral force have extreme values depending on the arrangement of magnets and overlap factor respectively.

Figure 25(a) and Figure 25(b) show the measured lift force and thrust with respect to the mechanical clearance. The overlap factor is fixed at 0.66 which gives almost maximum thrust with relative large lift force. Although the lift force depends largely on the resistance of conductor at the same mechanical clearance, the thrust is less dependent.

Characteristics for Five Arrangements of Magnets

Figure 26 shows the relation between the measured lift force per driving power and the overlap factor for five magnet wheels shown in Figure 8. Although there is some scatter in the measured values with small overlap factor of 0.7 or less, the lift force per driving power is almost independent on the overlap factor and the arrangement of magnets.

Figure 27 shows the relation between the transformation rate for thrust and the overlap factor. The transformation rate at the overlap factor of 0.66 is about 0.5, this means that the wasteful drag torque is about 50% utilized for the thrust. There is a little difference for the arrangement of magnets.

Figure 28 shows the lift force and the thrust with respect to the total volume of magnets for five partial overlap type magnet wheels respectively. The overlap factor, the mechanical clearance and the revolving speed are fixed at 0.66, 15mm and 11.3m/s respectively. Both lift force and the thrust vary as about 4/3 power of the magnets volume as well as the lift force characteristics for the state of parallel rotation shown in Figure 9.

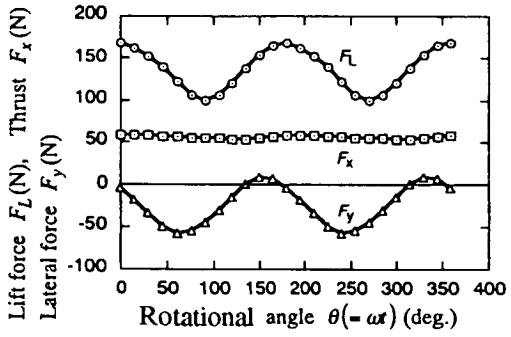

Fig. 23 Fluctuation of forces for rotational angle at the overlap factor of 0.66.

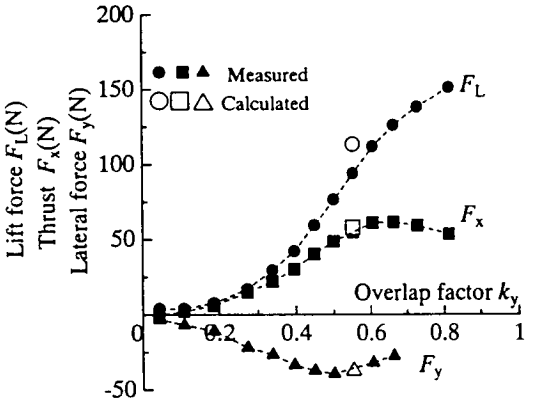

Fig. 24 Lift force, thrust and lateral force - overlap factor characteristics.

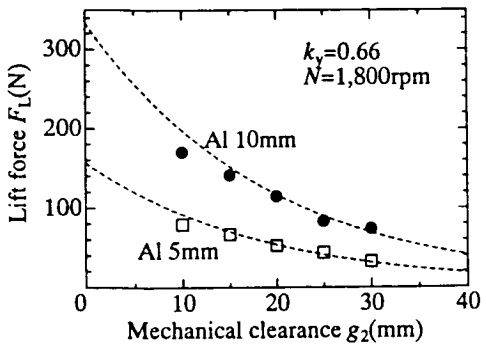

(a) Lift force

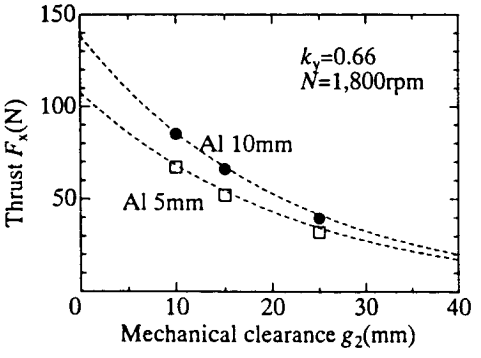

(b) Thrust

Fig. 25 Mechanical clearance characteristics.

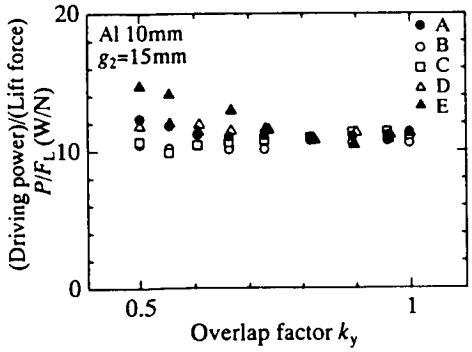

Fig. 26 Lift force per driving power versus overlap factor.

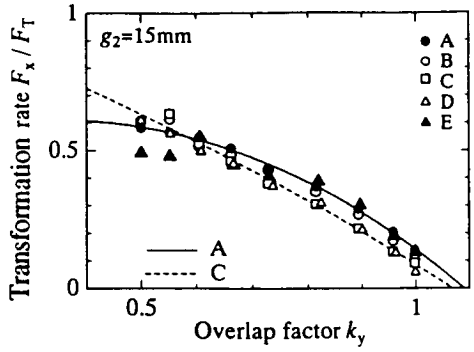

Fig. 27 Transformation rate for thrust versus overlap factor.

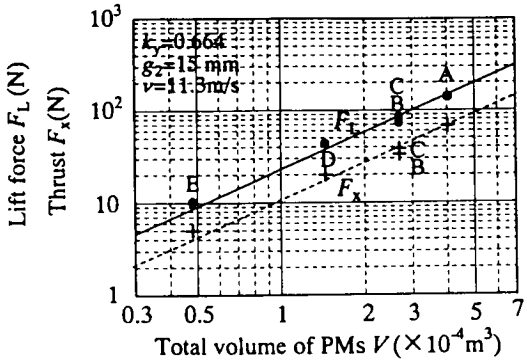

Fig. 28 Measured lift force and thrust for five partial overlap type magnet wheels.

CONCLUSIONS

The following characteristics of the magnet wheel were established;

1. The lift force per driving power doesn't change regardless of the extraction of thrust.
2. The lift force per driving power is approximately proportional to surface conductivity of conducting plate, which is defined as the value of the conductivity multiplied by the thickness.
3. The lift force per magnets volume is approximately proportional to the fundamental factor of mmf distribution of magnet poles. That is, the space harmonics are hardly effective to increase the lift force without increase of power loss.
4. The lift force and thrust are proportional respectively to about 4/3th power of magnets volume.

ACKNOWLEDGMENTS

The author wishes to express thanks to Dr. K. Ogawa for the numerical analysis, who is a associate professor of Oita University. This study has been supported partially by the Grant-in-Aid for Scientific Research (B) from the Ministry of Education, Science, Sports and Culture of Japan.

REFERENCES

[1] N. Fujii, K. Ogawa, T. Matsumoto: "Revolving Magnet Wheels with Permanent Magnets", Electrical Engineering in Japan, Vol. 116, No. 1 pp.106-118 (1996)

[2] N. Fujii, K. Ogawa, K. Naotsuka: "Analysis for Static Characteristics of Magnet Wheels", Trans. IEE of Japan, Vol. 115-D, pp.327-335 (1995)

[3] M. Kawai, H. Ariga: "Equos-lim-car", The invention, Vol. 89, pp.70-77 (1992)

[4] K. Nagashima, H. Kamijo, S. Iikura, H. Hasegawa, H. Shigeeda, H. Nakashima: " Maglev Model Propelled, Levitated and Guided by Magnetic Wheels", 1995 National Conv. IEE, Japan, No.1060

[5] K. Ogawa. Y. Horiuchi, N. Fujii: "Calculation of Electromagnetic Forces for Magnet Wheels", IEEE Transactions on Magnetics, Vol. 33 No. 2, pp.2069-2072 (1997)

XHV INTEGRATED PROCESS WITH MAGNETIC LEVITATION TRANSPORTS

Masahiro Tosa, Akira Kasahara and Kazuhiro Yoshihara
National Research Institute for Metals
1 Sengen, Tsukuba 305, JAPAN.

SUMMARY

Extreme high vacuum (XHV), below 10^{-10} Pa, can result in no surface contamination by adsorption of gases and offer an ideal ultraclean environment which lasts long enough to artificially synthesize advanced materials with atomic manipulation. An XHV integrated process with magnetic levitation transports has been developed in order to transfer substrates long distances from one instrumented vacuum chamber to another without any contamination on the ultraclean substrate surface. The process consists of vacuum chambers, pumps, gauges, gate valves, transports for the main line and sidetrack line and so on. The integrated process has five main line chambers and six sidetrack line chambers with connections to six chambers with instruments. A main line has a connection-chamber to join a main line chamber and a sidetrack line chamber which can attach chambers with such instruments as surface analyzers, film preparation and so on. Magnetic levitation transports are installed into the line chambers because they have no sliding parts to generate dust particles and outgassing which may extensively damage ultraclean substrate surfaces and environments. One transport for the main line electromagnetically levitates a carrier and transfers it by linear motor drive. The other transport for the sidetrack line levitates a carrier by $YBa_2Cu_3O_{7-x}$ superconducting magnet discs and mechanically transfers it by means of pinning effect. The levitation transports can transfer a substrate from one connected chamber to another with a pressure change of less than 10^{-10} Pa.

INTRODUCTION

Extreme high vacuum (XHV) below 10^{-10} Pa which contains few gas molecules and atoms can cause almost no surface contamination by absorption. An excellent laboratory to study and develop advanced materials on an atomic scale can be established in an XHV environment because it can offer and maintain an ideal ultra clean environment for a long enough time to artificially synthesize advanced materials with manipulation of atoms. The study and development of materials on an atomic scale requires many operations such as sample cleaning, deposition, etching, surface analysis, performance testing and so on as well as an XHV environment, but it is impossible to carry out all operations in the same vacuum chamber because the chamber becomes so large due to the installation of all material operation components and instruments into one chamber. It takes a long time to acquire the XHV environment once the chamber is exposed to atmosphere for change of instruments or replacement of the components.

The XHV integrated process, therefore, consists of lots of continuous operations in XHV joined by a transfer system because it is more practical and efficient to carry out each operation in individual connected chambers.

We have successfully developed the extreme high vacuum integrated process with two types of magnetic levitation transports using no sliding mechanism and could transfer a sample in the pressure change of less than 10^{-10} Pa (ref.1). The problem of the first developed XHV integrated process is the limitation that the process can not share more than three connected chambers and requires large space for the installation due to a 2 stage transfer system with sliding magnetic transports to deliver the sample from sidetrack to connected chambers.

The purpose of this work as a second step is to downsize the XHV process to increase the number of the connected chambers by means of simplifying the electromagnetic levitation transport for the main track line and introducing direct sample delivery between the carrier of the side track line and the sample stage of connected chambers.

EXTREME HIGH VACUUM INTEGRATED PROCESS

Figure 1 shows the schematic diagram of the developed XHV integrated process with magnetic levitation transports and Figure 2 shows the whole photograph of the process. The process consists of four main track vacuum chambers connected in series, five sidetrack chambers standing in a row, five coupling chambers, six connected instrument chambers, vacuum pumps, pressure gauges, and valves. The connected instruments with the process are three film preparation chamber (MBE & two RfmsVD) and three surface analysis chambers (SAM, ESCA & AFM). Production of the XHV environment requires a very low outgassing chamber, high sensitivity gauge system, high performance vacuum pumps and so on. Type 316L stainless steel employed as chamber material has no ferritic structure which causes magnetization and little intergranular corrosion at welds because of low carbon content. The surface of the inside wall of the chambers was electrolytically polished in phosphoric-sulfuric acid solution and the chambers were annealed at 823 K in a high vacuum for sufficient outgassing. Metal gate valves are installed between the main track and coupling chambers in order to keep the XHV environment of the track chambers from the ultra high vacuum environment of the connected chambers. Each track chamber is evacuated by a titanium getter pump (pump speed:1.6 $m^3 \cdot s^{-1}$) and an ion pump (pump speed:0.2 $m^3 \cdot s^{-1}$). Figure 3 shows the schematic vacuum pumping system of a unit of a main track vacuum chamber, a sidetrack chamber and a coupling chamber. The properties of extreme high vacuum is evaluated with an extractor gauge and a quadrupole mass spectrometer with the separation of an ion source and a quardrupole analyzer. The chambers were evacuated with ion pumps after the whole system was baked out with a mantle heater system at the temperature of 423 K keeping the turbo pump system in operation.

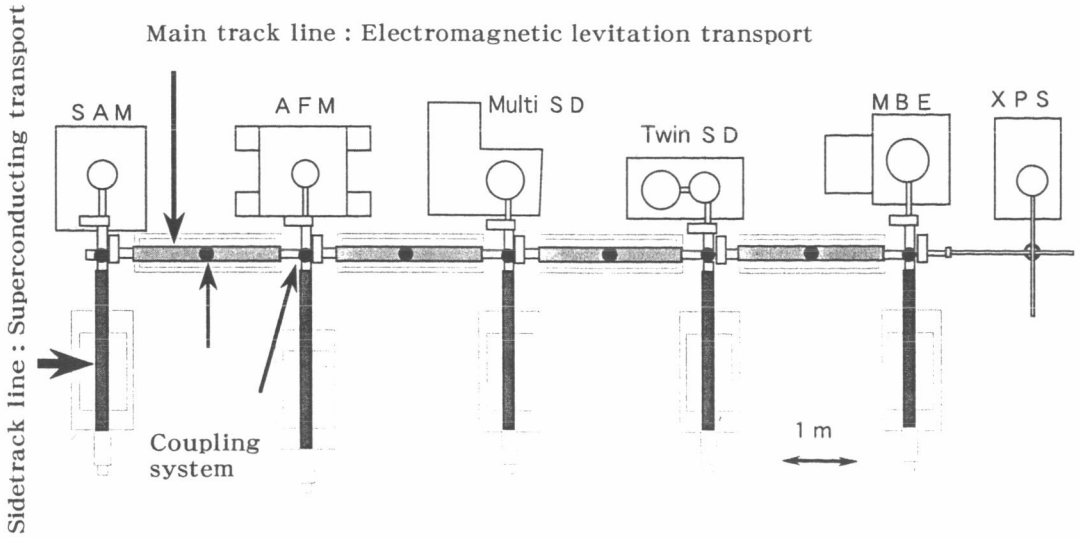

Figure 1 Schematic diagram of the developed XHV integrated process

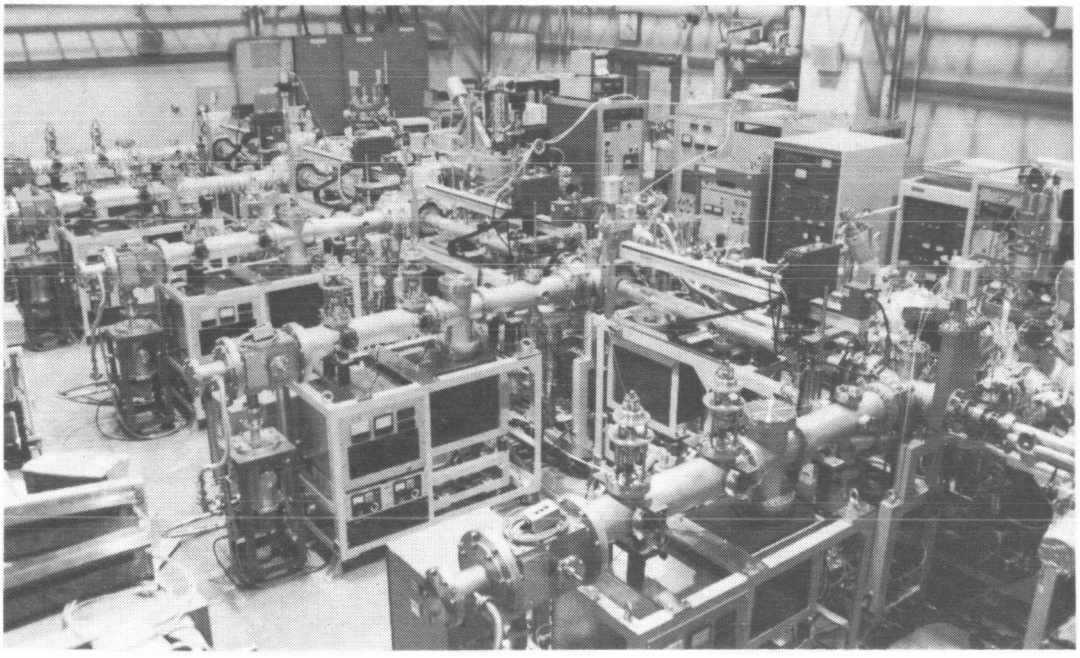

Figure 2 Whole photograph of the XHV integrated process

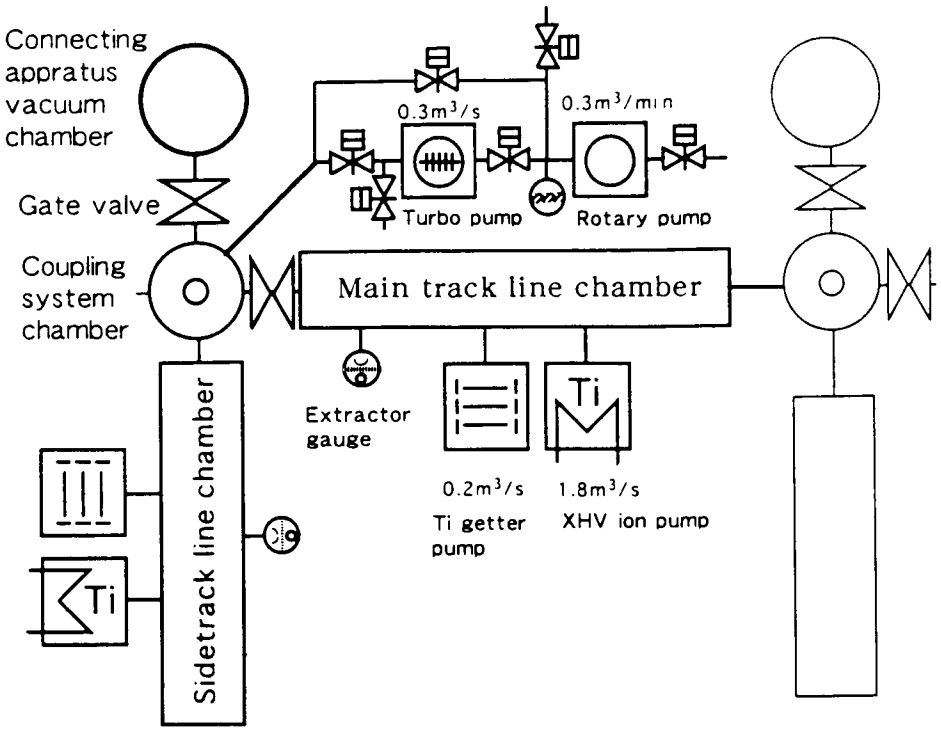

Figure 3 Schematic vacuum pumping system of a unit of a main track vacuum chambers, a sidetrack chamber and a coupling chamber.

LEVITATION TRANSPORT SYSTEM

A transport system to be used in XHV should generate no particles because particles are sources of outgassing as well as contamination. It is necessary to use no sliding components to keep the process XHV. A magnetic levitation transport system can meet the demand as it employs no sliding motion so that XHV may be kept during transport. We adopted two types of magnetic levitation transports, one is an electromagnetic levitation transport and the other is a superconducting levitation transport.

The electromagnetic levitation transport is introduced to each main track vacuum chamber for long-distance transfer and quick start operation. The superconducting magnetic levitation transport is introduced to each sidetrack vacuum chamber for short-distance transfer and stability against mechanical shock. An up and down hoist system by an air cylinder mechanism is introduced to each coupling chamber for the sample delivery among carriers of main track and sidetrack.

Figure 4 shows the schematic of a superconducting levitation transport used for the sidetrack because of the space saving and robust stability against mechanical shock. The transport consists of a sidetrack chamber, a cooler filled with helium gas coolant cooled by a freezer at the back of the chamber and a carrier rod with a sample holder at the head. Three discs of high-Tc $YBa_2Cu_3O_{7-x}$ (YBCO) superconductor driven by a rotating long bolt shaft in the cooler is cooled down below Tc and cause the effect of pinning and the diamagnetism on the three discs of

samarium cobalt attached to the bottom of the carrier. The effect is strong enough to levitate the carrier with a certain gap through the cooler wall and to drag the carrier accurately without any stabilizer. The carrier can transport a sample at the speed of 3 $cm \cdot s^{-1}$.

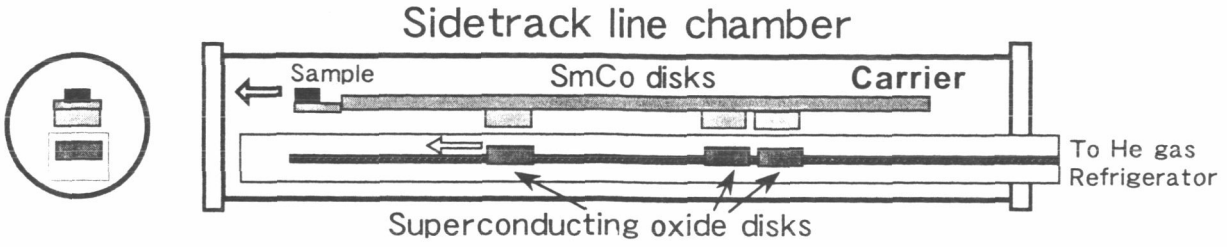

Figure 4 Schematic of a superconducting levitation transport used for the sidetrack

Figure 5 shows the schematic of an electromagnetic transport used for the main track because of easy extension and quick startup. A stator on the track chamber has electromagnets to levitate a carrier in the chamber, a linear synchronous motor above the stator to drive and position sensors as well as gap sensors with electromagnets to stabilize levitating carrier. The electromagnets in the stator control the levitation gap of the carrier about 1 mm between the carrier and chamber wall. The running carrier can stop within the error of 0.5 mm after transporting a sample holder at the top speed of 5 $cm \cdot s^{-1}$.

A sample transfer direction is changed by the hoist system in the order as shown in Figure 6 and the sample is also delivered from the carrier of the sidetrack to the carrier of the main track in the same way by the hoist system.

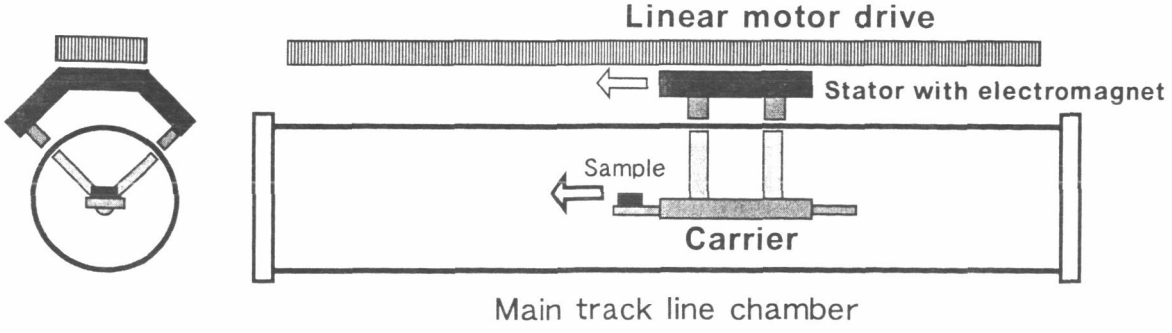

Figure 5 Schematic of an electromagnetic transport used for the main track

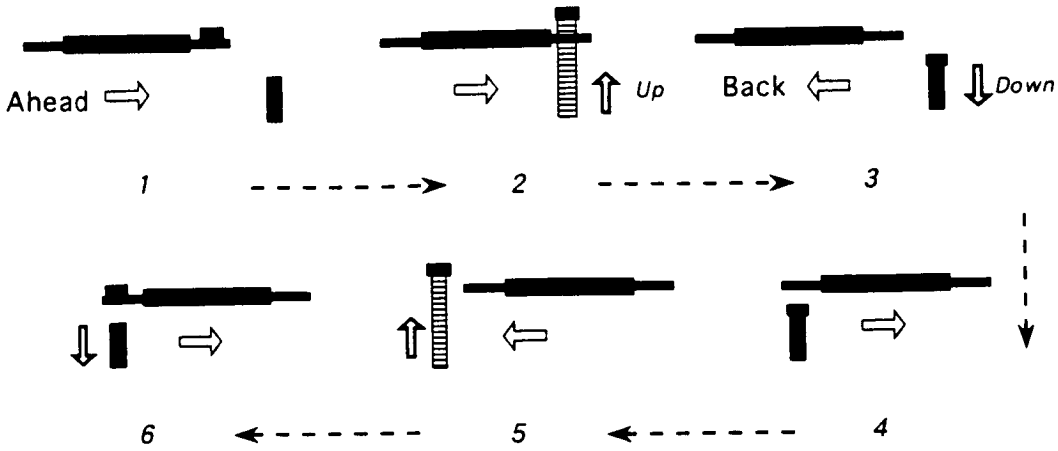

Figure 6 Schematic of change in a sample transfer direction by the hoist system

SAMPLE TRANSPORT CHECK

Operation of sample transport from the sidetrack for SAM to the sidetrack for AFM by way of a main track was carried out and the pressure change during the transport is shown in Figure 7. A change of pressure less than 2.0×10^{-10} Pa was obtained during the levitation transports of sidetrack and main track but the hoist up and down motion caused a large pressure increase of 2×10^{-9} Pa. More perfect outgassing operation of the bellows wall is required because mechanical vibration still releases gas from the wall surface. This indicates that the current system is successful in the transport in an ultra high vacuum though additional improvement of the system is required for the stable transport in XHV.

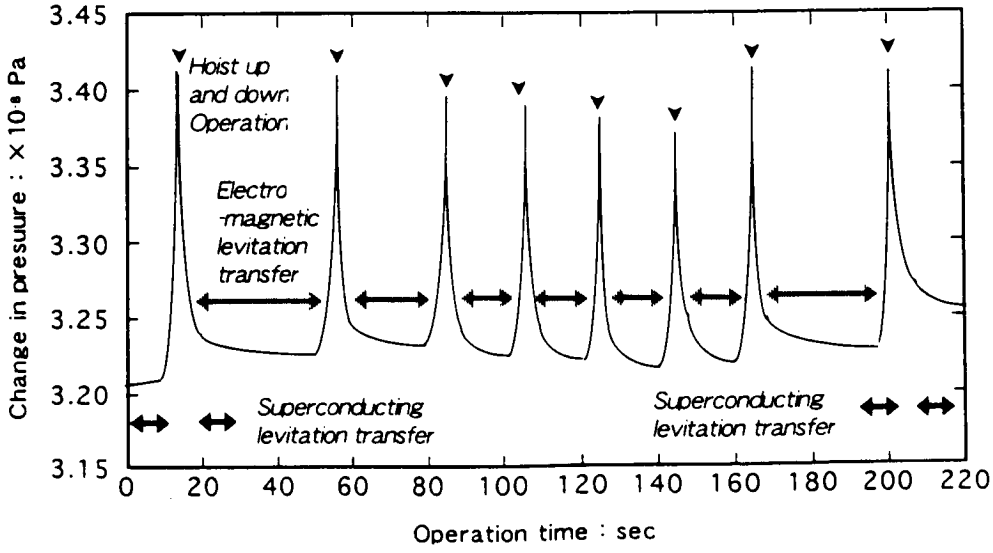

Figure 7 The pressure change during the transport from a sidetrack to another sidetrack by way of a main rack

CONCLUSIONS

We have successfully downsized the XHV integrated process with two types of magnetic levitation transports by direct sample delivery to a connected chamber from a sidetrack, can connect six vacuum instruments, and the pressure change less than 2.0×10^{-10} Pa was obtained when a sample was transported from one sidetrack to another sidetrack by way of a main track.

ACKNOWLEDGMENT

We deeply appreciate the cooperation of ULVAC Ltd's staff, H.Minami, M.Takahashi, M.Nishituji, J.Yuyama and H.Yamakawa, for the development of the XHV integrated process.

REFERENCE

1. M.Tosa, A.Itakura, M.Harada, A.Kasahara and K.Yoshihara, J. Vacuum 47(1996)493.

RESISTIVE AND SUPERCONDUCTING MAGNET CONFIGURATIONS FOR LEVITATION OF WEAKLY DIAMAGNETIC MATERIALS

Y. M. Eyssa and H. J. Schneider-Muntau
National High Magnetic Field Laboratory (NHMFL)
Florida State University,
Tallahassee, FL

SUMMARY

The magnetic fields that can be generated today by superconducting and resistive magnets are so strong that even weakly diamagnetic materials can be levitated. Materials with magnetic susceptibilities in the order of 10^{-5} require a product of field times field gradient of about 1000 T^2/m. Such values are easily obtained in standard 12-20 T, small bore (30-50 mm) resistive and superconducting solenoid magnets, available in many locations. To levitate larger objects, magnets with wider bores and different field configurations than solenoids are necessary, as for instance a split coil magnet with opposite field direction in the two halves. In this study, we characterize the levitation capability of some of the resistive magnets available at the NHMFL. We also examine different configurations, optimized for maximum levitation, such as strong gradient magnets and magnets in racetrack form, with the goal to determine the relationship between the limitation imposed by today's available conductor materials and the size of the body that can be levitated.

INTRODUCTION

High field superconducting and resistive magnets have been known to levitate weakly diamagnetic organic and non-organic materials with susceptibilities as low as 10^{-5}. Previous work at the NHMFL and the university of Nijmengen shows that matter with a specific gravity of about unity, and, therefore also living organisms such as frogs, peanuts and other substances can easily be levitated in fields of 10-16 T [1,2]. The levitation results from a balance between the magnetic force, F_m, acting on every molecule in the levitated specimen, and the gravitational force. Diamagnetism is a general attribute of matter, in a few materials it is covered by additional para- or ferromagnetism. The molecular diamagnetism is caused by electrons adjusting their orbits to reduce their energy in the presence of an external magnetic field. These magnetic levitation forces are many orders of magnitude weaker than forces on ferromagnetic materials.

An object will levitate when its magnetic force balances the gravitational force. The magnetic force per unit volume is related to the field and field gradient as,

$$\vec{F} = x\,(B.\nabla)\vec{B},$$

(1)

where x is the magnetic susceptibility, and $\vec{B}$ is the magnetic field vector. In a solenoidal cylindrical coordinate system the total axial and radial forces, F_r and F_z, integrated over the levitation volume V are,

$$F_r = x\iiint [B_z \frac{dB_z}{dr} + B_r \frac{dB_r}{dr}]dv$$
$$F_z = x\iiint [B_z \frac{dB_z}{dz} + B_r \frac{dB_z}{dr}]dv$$

(2)

The radial force averages to zero and is self-stabilizing due to the homogeneous diamagnetic properties of the levitated material and the assumed symmetry of the suspended body. Though the net radial force is zero, there is a radial magnetic pressure acting on the levitated object. The radial pressure gets higher as the sample volume becomes comparable to the solenoid bore. The axial balancing force is dominated by the $B_z\,(dB_z/dz)$ term and is more uniform for a specimen with a radius small compared to the levitation solenoid bore.

Equating the axial force with the gravitational force, $F_g = \rho g V$, results in a relation between the magnetic susceptibility, the magnet field, bore, configuration, the specific gravity ρ,and the levitated object volume V. In the case of a superconducting magnet, it is convenient to correlate that relation to the maximum winding field, B_{max}, since it is the quantity that determines the superconducting current density. B_{max} in a single solenoid system occurs at the inner radius on the mid-plane. In the case of a resistive magnet, it is natural to correlate the levitation relation to the power consumption of the magnet. In this study we neglect (for both cases, superconducting or resistive magnets) the stress or power density constraints that may impose limits on the maximum field, and leave it for an engineering design to optimize the magnet configuration in view of the stress and power density. Later we show two examples, a small and a large bore resistive magnet system, that have been optimized for maximum central field and can be used to levitate small and medium size objects.

By equating the gravitational and levitation axial forces the lower bound on the magnetic susceptibility x that can be levitated as function of the maximum field or dissipated power W is,

$$x \geq \frac{\rho g}{\lambda_{B_{max}}} \frac{a_1}{B_{max}^2}, \quad or$$
$$x \geq \frac{\rho g}{\lambda_W} \frac{\rho_e a_1^2}{p_f W},$$

(3)

where ρ_e is the conductor electrical resistivity at the operating temperature (typically 2~2.5 x 10^{-8} ohm.m) and p_f is a filling factor accounting for insulation and cooling channels (typically 0.8-0.9).

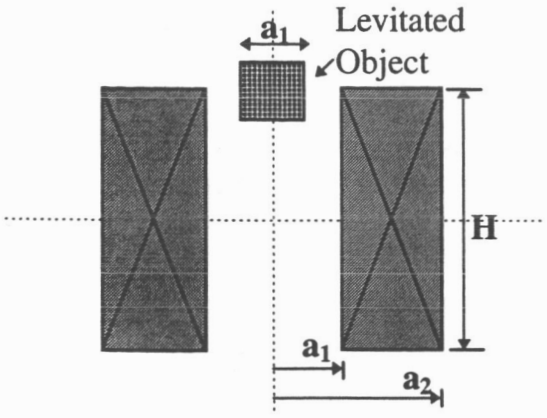

Fig. 1a Levitation in a single solenoid.

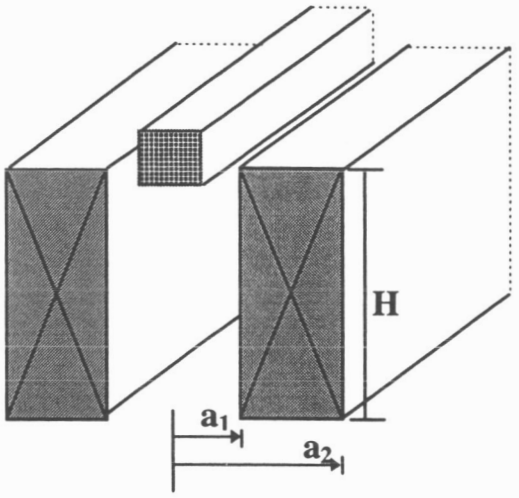

Fig.1b Levitation in a single racetrack magnet

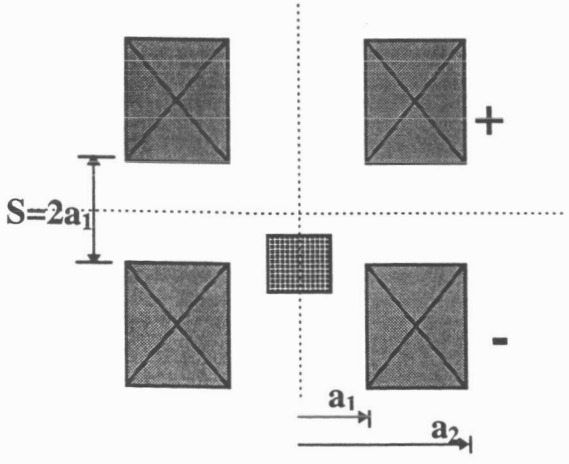

. Fig. 2a Levitation in a split Helmholtz solenoid.

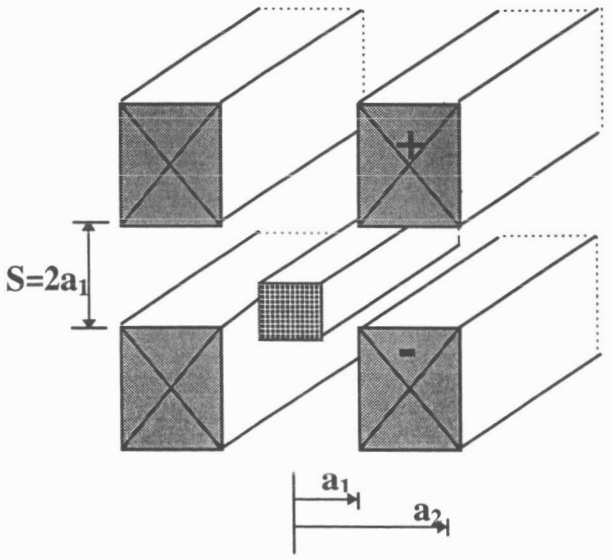

Fig. 2b Levitation in a split Helmholtz race-track magnet

The levitation factor λ is a dimensionless constant that relates to bore diameter, magnet geometry, to field or power. It is a geometry factor, like the Fabry factor, that defines the optimum magnet geometry and allows for a comparison between different magnet designs. We have computed the levitation factor for several solenoidal and racetrack geometries. Solenoids can have uniform current density, or 1/r current distribution (Bitter solenoids $J = J_O\ a_1/r$. J_O is the current density at the inner radius a_1). Fig. 1a shows a sketch of the winding cross-section, and the levitated volume that is centered at the winding opening where we encounter the highest product of B x grad B. The volume occupies a cross-sectional area with length and thickness a_1, i.e., half the bore diameter. The bottom of the levitated volume is at $z = H/2 - a_1/2$ and the top is at $z = H/2 + a_1/2$. This volume has the highest product of field and field gradient. The levitation winding has two aspect ratios; $\alpha = a_2/a_1$ and $\beta = H/2a_1$ where a_2 is the outer radius and H is the height. We also investigated racetrack coils, since they allow to suspend longer objects. We assumed an aspect ratio where each turn circumference is 20 times its radial distance a_1.

In addition to the simple geometry, shown in Fig. 1a and 1b, we have considered a split Helmholtz pair geometry made of two halves with opposite current direction that can be either solenoids with uniform current density, 1/r Bitter type current density, or race-track winding as shown in Fig. 2a and 2b. The split gap between the two halves is kept equal to the inner diameter, or the inner radial spacing in case of a racetrack. The change in the levitation force relative to the convenient choice of a split gap that is slightly different from the bore size, is small and is, therefore, neglected in this article. The levitated volume is centered in the highest product of field times field gradient region that is axially bound by $Z_{min} = -1.4a_1$ and $Z_{max} = -0.4a_1$. The radial width is again a_1.

The levitation factor has been computed for the four geometries shown in figures 1 and 2 for maximum field, i.e., superconducting magnets, or power, i.e., resistive magnets. The results are shown in figure 3a-d and table 1.

Discussion of the Results

The levitation factor for superconducting solenoids with two different current density distributions, and also for two magnet geometries are displayed in Fig. 3a and 3b. It follows that there is no significant difference for the first five cases, and the levitation factor λ is about 2×10^5. The split coil racetrack shows a geometric suspension efficiency of only half of the others. As first approximation it follows from equation (3) that $a_1/B^2 = 2.10^{-4}$ for a susceptibility of 10^{-5}. With today's technology, superconducting magnets can be built that generate 20 T in bores up to 150 mm diameter [3]. This coincides with the above relationship, i.e., we can suspend objects up to 80 - 100 mm diameter. A racetrack coil would have the advantage that longer objects can be levitated. Assuming a length of 5 times the bore diameter, objects of 100 mm x 800 mm would float in a magnetic field. The construction of the superconducting magnet would be a challenging but feasible task, involving over 10 t of conductor and reinforcement structure.

The levitation factors of the resistive magnets (Fig. 3c and 3d) give very similar results for solenoids, i.e., the current density distribution has no impact on the levitation factor. All other geometries, like split and racetrack, have lower efficiencies. Resistive magnets have the advantage that they are not limited in magnetic

field, however, at the expense of excessive power requirements. For example, to levitate a human body using a racetrack resistive magnet with a 500 mm bore and 2.5 m length, the magnet would have to generate a maximum field of 38 T, and the power demand would be of the order of 1000 MW. Stress and power density constraints may increase the power and winding field requirements even more.

As a demonstration of the levitation capabilities at the NHMFL, we show in Fig. 4a and 4b the lower bound on the values of magnetic susceptibilities of materials that can be levitated in our 50 mm and 200 mm bore magnets. In our 50 mm magnet we can levitate diamagnetic materials with $x = 0.5 \times 10^{-5}$ and higher, while in our 200 mm bore x has to be higher than 1.0×10^{-5}. The profile of the levitation force is also shown in Fig. 4. The total volume that can be levitated is limited by the region where $F_z > 1$ and by the bore diameter. For both magnets the useful F_z region is about 30 mm thick, i.e., objects of up to 750 cm^3 can be suspended.

Conclusion

Magnets with small bore diameters have strong gradients. The condition of levitation of diamagnetic matter is, therefore, easy to achieve for small objects. Large bore magnets have lower gradients. To achieve the same B x grad B product the field must be increased. Today's conductor materials set limits on the achievable fields that restrict the object size to about 100 mm diameter for superconducting magnets and to 180 mm diameter for a 20 MW resistive magnet. Large objects would require higher power consumption or unavailable higher field materials in case of superconducting magnets. For example to levitate a human body only resistive magnet in a racetrack configuration could satisfy the field and the volume requirements. A field of almost 40 T is needed, and the continuous power demand would be about 1 GW.

Acknowledgment.

The work was supported by the State of Florida and the National Science Foundation under grant No. DMR 9016241

References

1. M. V. Berry, A. K. Geim, submitted to Eur. J. Phys.

2. J. Brooks, J. Perenboom, private communications.

3. W. D. Markiewicz et al, in "High Magnetic Fields: Applications, Generation, Materials", ed. H. J. Schneider-Muntau, World Scientific, 1997, p. 287-297

Table 1.a Levitation factor in a single solenoid, Bitter solenoid or race track magnet system.

Solenoid	λ_W	λ_W	λ_W	λ_W	λ_W	λ_{Bmax}	λ_{Bmax}	λ_{Bmax}	λ_{Bmax}	λ_{Bmax}
	β=0.6	β=0.8	β=1.0	β=2.0	β=3.0	β=0.6	β=0.8	β=1.0	β=2.0	β=3.0
1.01	2.04E-10	2.04E-10	1.88E-10	1.12E-10	7.71E-11	1.78E+05	2.11E+05	2.23E+05	2.14E+05	1.96E+05
1.1	1.79E-09	1.82E-09	1.69E-09	1.03E-09	7.09E-10	1.75E+05	2.07E+05	2.18E+05	2.08E+05	1.95E+05
1.3	4.08E-09	4.29E-09	4.08E-09	2.58E-09	1.79E-09	1.71E+05	2.00E+05	2.10E+05	1.97E+05	1.84E+05
1.5	5.28E-09	5.71E-09	5.55E-09	3.64E-09	2.54E-09	1.70E+05	1.96E+05	2.05E+05	1.89E+05	1.74E+05
2.0	6.05E-09	6.91E-09	7.00E-09	5.03E-09	3.59E-09	1.68E+05	1.89E+05	1.95E+05	1.74E+05	1.57E+05
3.0	5.04E-09	6.11E-09	6.55E-09	5.50E-09	4.12E-09	1.60E+05	1.79E+05	1.83E+05	1.59E+05	1.38E+05
5.0	3.00E-09	3.82E-09	4.31E-09	4.40E-09	3.63E-09	1.44E+05	1.59E+05	1.64E+05	1.44E+05	1.22E+05
Bitter	β=0.6	β=0.8	β=1.0	β=2.0	β=3.0	β=0.6	β=0.8	β=1.0	β=2.0	β=3.0
1.01	2.04E-10	2.04E-10	1.88E-10	1.12E-10	7.71E-11	1.78E+05	2.11E+05	2.23E+05	2.14E+05	1.96E+05
1.1	1.79E-09	1.82E-09	1.70E-09	1.03E-09	7.10E-10	1.75E+05	2.07E+05	2.18E+05	2.08E+05	1.95E+05
1.3	4.16E-09	4.36E-09	4.14E-09	2.61E-09	1.81E-09	1.71E+05	2.01E+05	2.11E+05	1.98E+05	1.85E+05
1.5	5.52E-09	5.94E-09	5.75E-09	3.74E-09	2.61E-09	1.70E+05	1.97E+05	2.06E+05	1.90E+05	1.76E+05
2.0	6.94E-09	7.80E-09	7.81E-09	5.48E-09	3.89E-09	1.69E+05	1.92E+05	1.98E+05	1.78E+05	1.61E+05
3.0	7.21E-09	8.45E-09	8.79E-09	6.89E-09	5.06E-09	1.65E+05	1.85E+05	1.90E+05	1.67E+05	1.47E+05
5.0	6.50E-09	7.84E-09	8.40E-09	7.37E-09	5.72E-09	1.58E+05	1.76E+05	1.81E+05	1.58E+05	1.36E+05
RT	β=0.6	β=0.8	β=1.0	β=2.0	β=3.0	β=0.6	β=0.8	β=1.0	β=2.0	β=3.0
1.01	4.97E-11	5.43E-11	5.37E-11	3.87E-11	2.84E-11	1.02E+05	1.37E+05	1.59E+05	1.75E+05	1.57E+05
1.1	4.49E-10	4.98E-10	4.98E-10	3.67E-10	2.70E-10	1.03E+05	1.36E+05	1.57E+05	1.70E+05	1.58E+05
1.3	1.09E-09	1.25E-09	1.28E-09	9.82E-10	7.33E-10	1.06E+05	1.36E+05	1.54E+05	1.62E+05	1.50E+05
1.5	1.50E-09	1.76E-09	1.83E-09	1.47E-09	1.12E-09	1.06E+05	1.34E+05	1.50E+05	1.56E+05	1.43E+05
2.0	1.99E-09	2.43E-09	2.64E-09	2.34E-09	1.83E-09	1.07E+05	1.31E+05	1.43E+05	1.45E+05	1.31E+05
3.0	2.12E-09	2.73E-09	3.10E-09	3.18E-09	2.64E-09	1.05E+05	1.25E+05	1.35E+05	1.33E+05	1.17E+05
5.0	1.83E-09	2.45E-09	2.90E-09	3.51E-09	3.21E-09	9.62E+04	1.13E+05	1.21E+05	1.19E+05	1.05E+05

Table 1.b Levitation factor in a split Helmholtz solenoid, Bitter solenoid or race track magnet system.

Solenoid	λ_W	λ_W	λ_W	λ_W	λ_W	λ_{Bmax}	λ_{Bmax}	λ_{Bmax}	λ_{Bmax}	λ_{Bmax}
	β=0.6	β=0.8	β=1.0	β=2.0	β=3.0	β=0.6	β=0.8	β=1.0	β=2.0	β=3.0
1.01	9.76E-11	9.40E-11	8.51E-11	5.00E-11	3.42E-11	1.01E+05	1.23E+05	1.35E+05	1.52E+05	1.56E+05
1.1	8.61E-10	8.42E-10	7.70E-10	4.59E-10	3.14E-10	1.75E+05	2.00E+05	2.06E+05	1.90E+05	1.77E+05
1.3	1.99E-09	2.00E-09	1.87E-09	1.15E-09	7.92E-10	1.75E+05	1.96E+05	2.01E+05	1.81E+05	1.67E+05
1.5	2.59E-09	2.68E-09	2.55E-09	1.62E-09	1.13E-09	1.78E+05	1.95E+05	1.98E+05	1.74E+05	1.59E+05
2.0	3.02E-09	3.27E-09	3.23E-09	2.24E-09	1.58E-09	1.86E+05	1.97E+05	1.96E+05	1.63E+05	1.44E+05
3.0	2.51E-09	2.87E-09	2.99E-09	2.39E-09	1.77E-09	1.97E+05	2.02E+05	1.97E+05	1.52E+05	1.26E+05
5.0	1.39E-09	1.67E-09	1.82E-09	1.76E-09	1.42E-09	2.05E+05	2.05E+05	1.97E+05	1.43E+05	1.11E+05
Bitter	β=0.6	β=0.8	β=1.0	β=2.0	β=3.0	β=0.6	β=0.8	β=1.0	β=2.0	β=3.0
1.01	9.76E-11	9.40E-11	8.51E-11	5.00E-11	3.42E-11	1.01E+05	1.23E+05	1.35E+05	1.52E+05	1.56E+05
1.1	8.63E-10	8.43E-10	7.71E-10	4.59E-10	3.15E-10	1.75E+05	2.00E+05	2.06E+05	1.90E+05	1.77E+05
1.3	2.02E-09	2.03E-09	1.89E-09	1.16E-09	8.01E-10	1.75E+05	1.96E+05	2.02E+05	1.82E+05	1.68E+05
1.5	2.71E-09	2.78E-09	2.63E-09	1.67E-09	1.16E-09	1.78E+05	1.96E+05	1.99E+05	1.76E+05	1.60E+05
2.0	3.44E-09	3.68E-09	3.59E-09	2.44E-09	1.71E-09	1.84E+05	1.97E+05	1.97E+05	1.66E+05	1.47E+05
3.0	3.55E-09	3.95E-09	4.00E-09	3.00E-09	2.18E-09	1.91E+05	2.00E+05	1.98E+05	1.57E+05	1.34E+05
5.0	3.05E-09	3.49E-09	3.64E-09	3.04E-09	2.32E-09	1.96E+05	2.02E+05	1.98E+05	1.51E+05	1.23E+05
RT	β=0.6	β=0.8	β=1.0	β=2.0	β=3.0	β=0.6	β=0.8	β=1.0	β=2.0	β=3.0
1.01	2.29E-11	2.40E-11	2.32E-11	1.60E-11	1.15E-11	3.71E+04	4.80E+04	5.52E+04	7.00E+04	7.47E+04
1.1	2.07E-10	2.20E-10	2.15E-10	1.51E-10	1.10E-10	7.84E+04	9.86E+04	1.12E+05	1.34E+05	1.39E+05
1.3	5.05E-10	5.51E-10	5.50E-10	4.04E-10	2.96E-10	1.07E+05	1.33E+05	1.49E+05	1.49E+05	1.33E+05
1.5	6.97E-10	7.78E-10	7.89E-10	6.03E-10	4.46E-10	1.14E+05	1.38E+05	1.50E+05	1.45E+05	1.28E+05
2.0	9.21E-10	1.07E-09	1.13E-09	9.39E-10	7.16E-10	1.23E+05	1.42E+05	1.50E+05	1.37E+05	1.17E+05
3.0	9.53E-10	1.16E-09	1.27E-09	1.22E-09	9.82E-10	1.34E+05	1.48E+05	1.52E+05	1.29E+05	1.06E+05
5.0	7.42E-10	9.36E-10	1.07E-09	1.20E-09	1.06E-09	1.43E+05	1.53E+05	1.54E+05	1.23E+05	9.51E+04

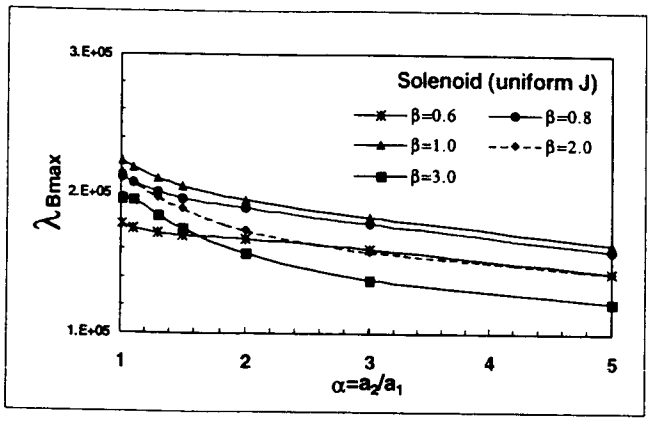

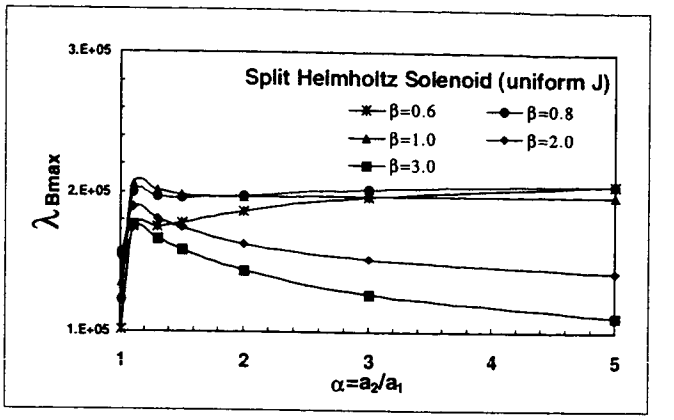

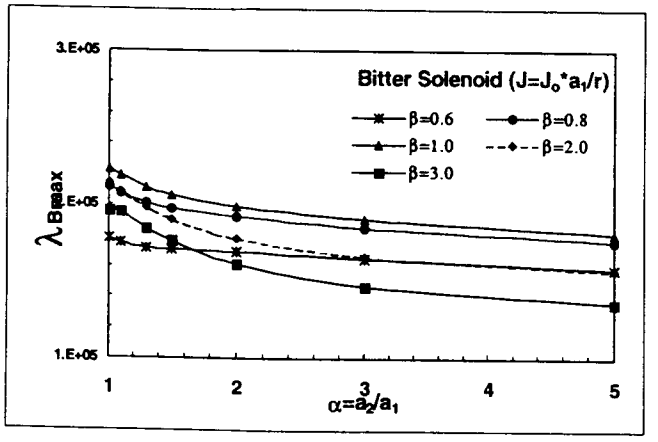

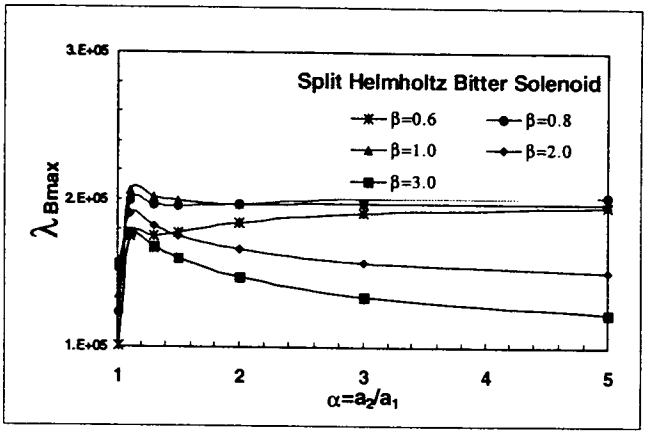

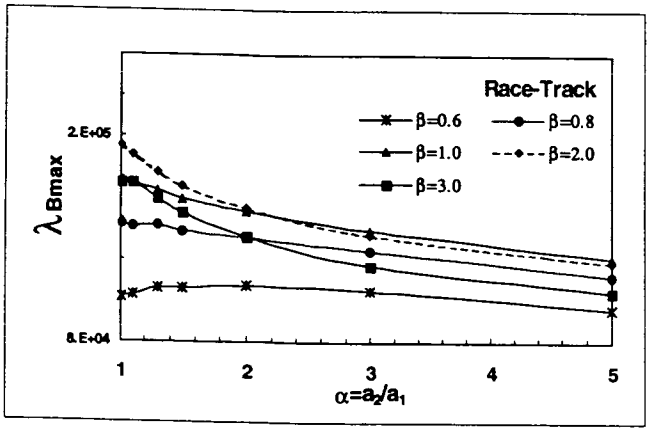

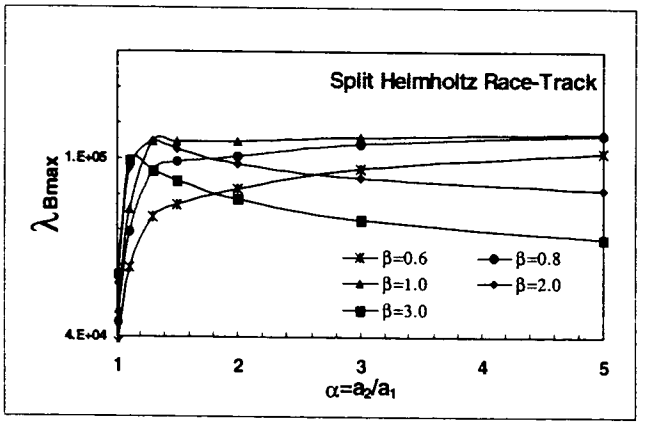

Fig. 3a Levitation factor for Helmholtz split pair relative to maximum winding field, B_{max}.

Fig. 3b Levitation factor for single coils relative to maximum winding field, B_{max}.

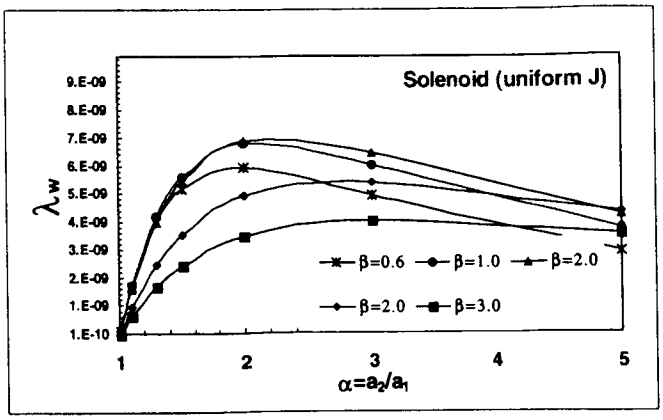

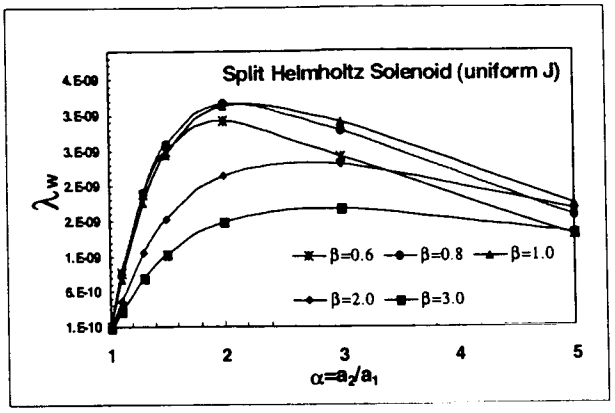

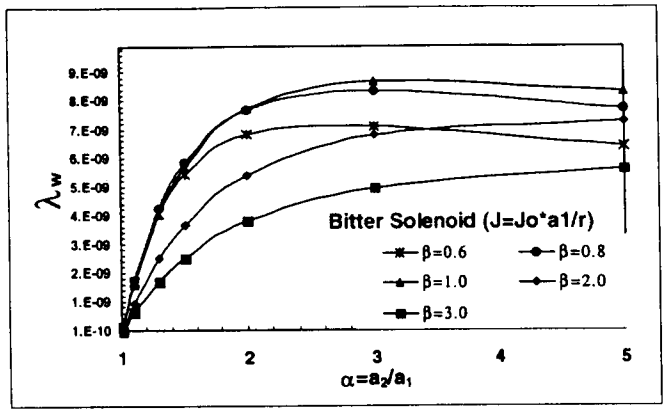

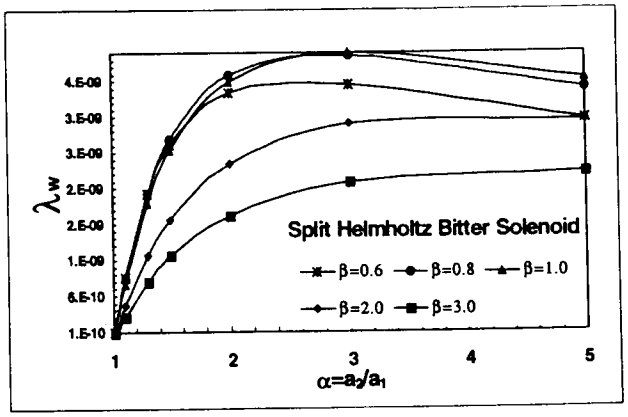

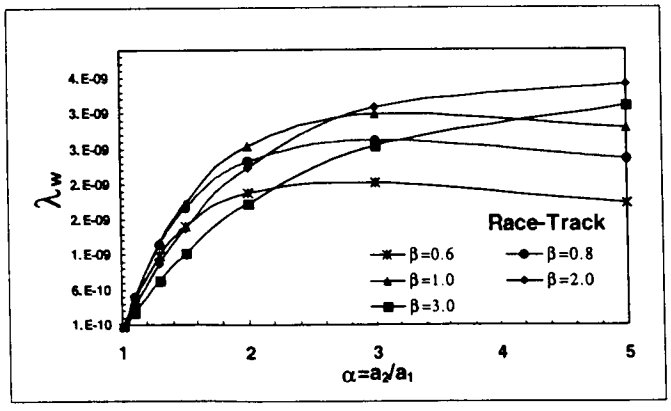

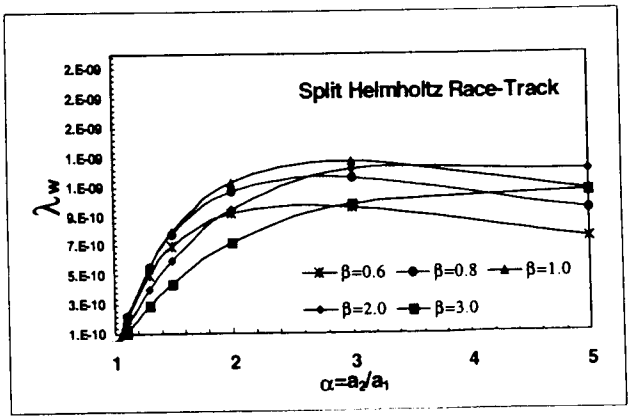

Fig. 3c Levitation factor for resistive Helmholtz split pair relative to power consumption, W.

Fig. 3d Levitation factor for resistive single coil relative to power consumption, W.

R	B_r	B_z	Bt	F_z/x	F_z
m	T	T	T	N/m3	kg/kg
0.000	0.000	16.719	16.719	-2.063E+09	1.031
0.005	0.384	16.736	16.740	-2.071E+09	1.036
0.010	0.772	16.789	16.807	-2.096E+09	1.048
0.015	1.168	16.886	16.926	-2.130E+09	1.065
0.020	1.569	17.037	17.109	-2.154E+09	1.077
0.025	1.967	17.259	17.371	-2.119E+09	1.060
				Average=	1.02590

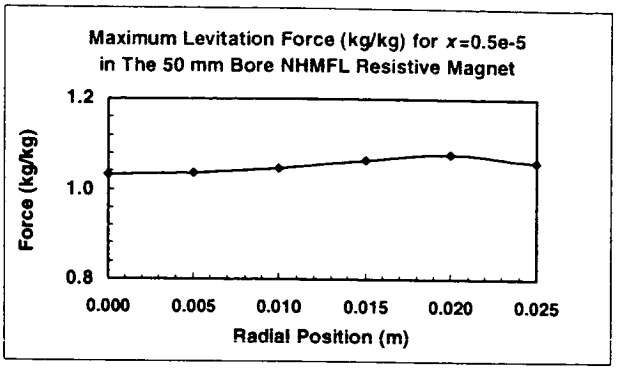

Fig. 4a Levitation force distribution in the NHMFL 50 mm bore, 22 T resistive magnet at z= 0.09 m from mid-plane

R	B_r	B_z	Bt	F_z/x	F_z
m	T	T	T	N/m3	kg/kg
0.000	0.000	0.000	0.000	-7.80E+08	0.9360
0.000	0.000	15.728	15.728	-7.88E+08	0.9454
0.020	0.613	15.742	15.754	-8.12E+08	0.9741
0.040	1.249	15.783	15.832	-8.53E+08	1.0234
0.060	1.935	15.844	15.962	-9.08E+08	1.0898
0.080	2.715	15.905	16.135	-9.51E+08	1.1416
				Average=	1.0655

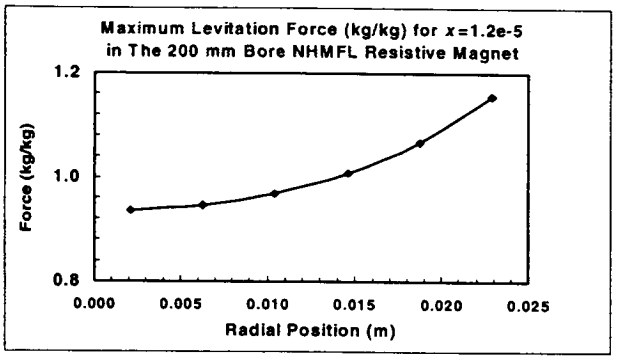

Fig. 4b Levitation force distribution in the NHMFL 200 mm, 20 T bore resistive magnet at z = 0.17 m from mid-plane

R	B_r	B_z	Bt	F_z/x	F_z
m	T	T	T	N/m3	kg/kg
0.000	0.000	0.000	0.000	-1.03E+09	1.0345
0.000	0.000	-19.278	19.278	-1.04E+09	1.0422
0.040	-2.708	-19.312	19.501	-1.07E+09	1.0671
0.080	-5.467	-19.413	20.168	-1.12E+09	1.1170
0.120	-8.336	-19.574	21.275	-1.21E+09	1.2076
0.160	-11.398	-19.781	22.830	-1.38E+09	1.3759
				Average=	1.19902

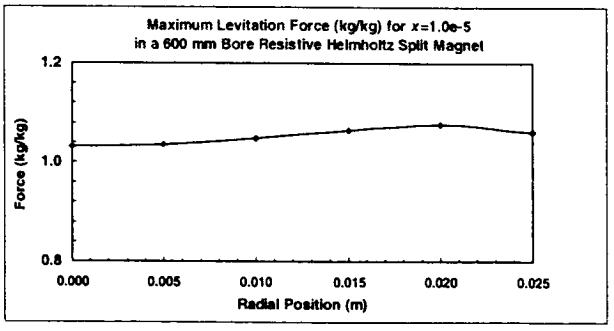

Fig. 4c Levitation force distribution in a 600 mm bore, 38 T maximum field resistive split Helmholtz magnet at z = -0.29 mm from mid-plane.

Session 7 -- Maglev 2

Chairman: Hans Schneider-Muntau
National High Magnetic Field Laboratory (NHMFL)

MAGLEV PIPELINE TO IMPROVE GRAIN SHIPMENTS FROM AMERICA TO ASIA

Ernst G. Knolle
Knolle Magnetrans
South San Francisco, CA

SUMMARY

Magnetic levitation (Maglev) technology has been advanced to a level where several versions, and combinations thereof, can be considered 'proven technology'. For instance, in Disneyland, an amusement park owned by Walt Disney World Inc. in California, U.S.A., a system, called the PeopleMover, has been in operation since 1975. (ref. 1) . While the PeopleMover's linear induction motors (LIMs) operate at low speed, faster LIMs were designed (ref. 2), built and successfully tested (ref. 3) in the late 1970s at the Transportation Test Center near Pueblo, Colorado, U.S.A. This technology has now also been adapted for use to levitate and propel grain containers over long distances, such as from grain producing areas of the U.S.A.to the West Coast, at high speed and low cost, for subsequent shipment by large bulk grain carriers to Asia. Capacity requirements, logistics and financial feasibility of such a project was analyzed.

INTRODUCTION

The Present Trade Routes of American Grain to Asia

According to the US Department of Agriculture (USDA) roughly 50 million tons of grain are exported from America to Asia annually, of which about 17 million tons are transported by rail, at a rate of several unit trains/day, along the Canadian border from grain producing areas to the West Coast of the U.S.A. for shipment to Asia out of Portland, Oregon. (A unit train along this route consists of about 100 hopper cars, each carrying 100 tons of grain.) The other 33 million tons are mostly carried in barges down the Mississippi river to New Orleans, where they are reloaded into ocean going ships, which then have a much longer route to Asia than ships out of Portland. Bulk carrier sizes in present North America to Asia trade are limited by river channels, locks and canals to about 50,000 tons. Figure 1 shows a map of the Pacific rim area with present and proposed routes.

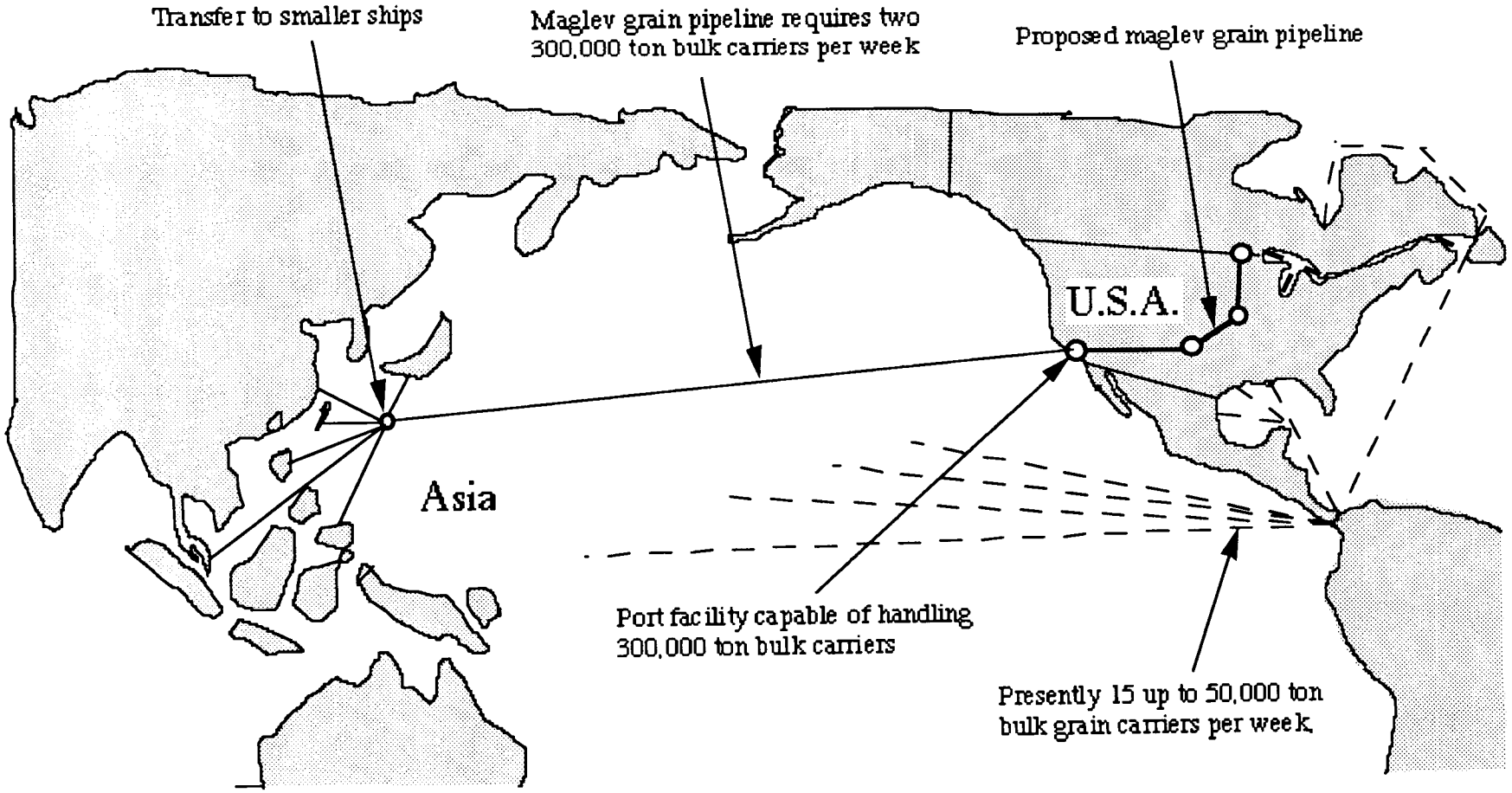

Figure 1. America to Asia route map

Costs of Shipping to Asia via Mississippi River

The cost (ref. 4), via the Mississippi River, imbedded in a ship load of 50,000 tones of grain arriving in Asia, breaks down to approximately $6 million for grain producing farmers, $6 million for transportation and storage from farmers' fields to on-board ship in New Orleans, and $2 million for the ocean voyage to Asia, for a total of $14 million. Factors in these costs include: Long-haul trucks 10¢/ton-mile (6¢/ton-Km), storage $1.00/ton-month, Mississippi barges 2¢/ton-mile (1.2¢/ton-Km), short-haul railroads 5¢/ton-mile (3¢/ton-Km), empty ship waiting for loading in New Orleans $4,000/day, loaded ship waiting to get through Panama Canal $8,000/day and Panama Canal fee $200,000 for passages back and forth.

Costs of Shipping to Asia via Railroad to California

The cost, via railroad to California, imbedded in a 50,000 ton ship load of grain arriving in Asia, breaks down to approximately $6 million for grain producing farmers (as above), $5 million for transportation and storage from farmers' fields to railroad loading docks in Topeka, Kansas, $2 million for the rail trip to California and $1 million for the ocean voyage to Asia, for a total of $14 million, which equals the above Mississippi route. There is presently very little grain going along this route. Tracks may not be of high enough quality to carry unit trains consisting of 168 covered hopper cars, each carrying 98 short tons of grain, at speeds of up to 70 miles (130 Km) per hour. To fill one 50,000 ton ship requires three unit train loads. To go back and forth, if all goes well, between Kansas and California takes 4 days. A fully loaded train (rolling stock plus load) represents a capital investment of $20 million. Fig. 2 shows a typical covered hopper car which railroads use to transport grain. The transport charge from Kansas to California is about $3,500 per car. However, reservations need to be made months in advance, a practice which has caused extreme consternations and is generally dubbed as the "Grain Hopper Crisis". Crop yields and harvest times fluctuate, sometimes greatly, according to the weather. As a result, hopper cars are often sitting idle in some locations, and in others they are in short supply. Having reserved them in advance is still no guarantee that they will be there when needed. To the railroads, the cost of delaying a 168-car unit train when empty is $1,000/day and when full $2000/day.

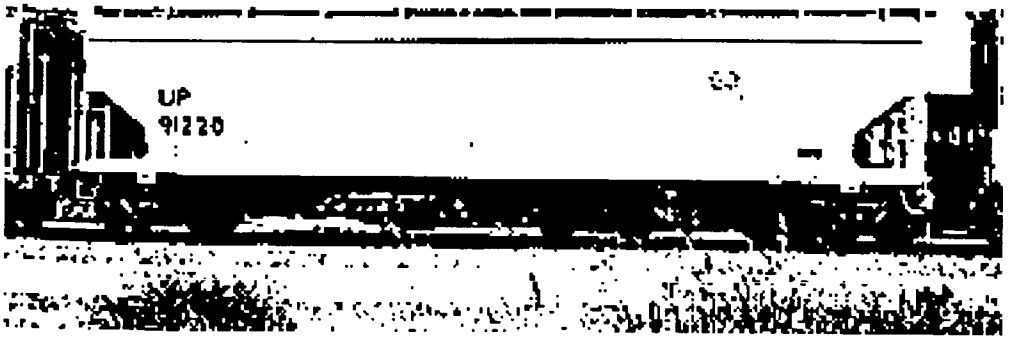

Figure 2. Railroad covered hopper car capable of carrying 98 tons of grain.

Cost Estimate of Shipping to Asia via Maglev Pipeline to California

Unlike the "Cost of Shipping to Asia via Railroad to California" route, a maglev grain pipeline would not compete directly with the Mississippi river route. Instead, the plan is to stay clear of the Mississippi as much as possible, passing through good farming areas and reaching above Kansas to Minnesota. The upper reaches of the Mississippi are often not navigable for long periods of time due to ice, low water levels and floods. These areas are also where farms have frequently failed and land lies fallow because of inadequate or too costly transportation. With an all-weather maglev grain pipeline close by, running unimpeded continuously 24 hours a day, transportation costs to it and storage costs would be greatly reduced, thus creating a boom to the presently economically depressed area.

The cost imbedded in a ship load of 50,000 tons of grain arriving in Asia via this maglev grain pipeline, breaks down to approximately $6 million for the grain producing farmers (as above), $2 million for transportation and storage from farmers' fields to the maglev grain pipeline, $1 million for the maglev pipeline to California and $1 million for the ocean voyage to Asia, for a total of $10 million. This is more than a 25% cost reduction over present modes of transportation, despite the fact that the maglev grain pipeline would be comparatively a high capital investment project. Table 1 shows a comparison of cost distributions of the three routes described above on a dollars per ton basis.

Table 1. Grain to Asia Cost Distribution Comparison, Dollars per Ton

	Via Mississippi River	Via Railroad to California	Via Maglev to California
	$/ton	$/ton	$/ton
Farmers	120	120	120
Railroads & Barges	120	140	40
Maglev Pipeline	-	-	20
Ocean Shipping	40	20	20
Total	280	280	200

Logistic Advantage of Maglev Grain Pipeline over Present Methods

Currently carriers arrive and depart intermittently and irregularly. Therefore, storage facilities (silos) are needed to hold the grain at every transfer point. After harvest, the grain is first stored on the farm. Then it is taken by truck to a railroad, where it is stored a second time. After that the railroad takes it to the Mississippi river to be stored a third time. Then, finally river barges take the grain to an overseas loading dock where it is put into silos for a fourth time.

A maglev grain pipeline is a continuous system capable of running 24 hours a day. Thus, there is less of a need to store grain. Assume a maglev system with 8-inch diameter containers at speeds of 50 miles (80 Km) per hour is in operation. Table 2 shows that it could move grain at a rate of 52,000 tons/day, or 40 tons per minute. Grain is taken directly from farmers' silos to the pipeline's intake hopper and sent directly non-stop to the West Coast where it is stored in silos for the second and last time at an overseas loading dock. Even the West Coast storage may be avoided, or reduced, if ship loading could be organized in a continuous fashion. Hence, with a maglev grain pipeline 50% and possibly 75% of all present silos could be dispensed with. Consequently, cost savings are passed on to grain farmers and Asian consumers.

There are even more savings in this approach. As shown in Figure 1, ships coming in and out of Southern California ports can, like super tankers, be of the largest possible size, 300,000 tons, while the ships presently carrying grain out of non-California ports, due to restrictions in river channels, locks and the Panama Canal, are limited to about 50,000 tons. Hence, one super tanker size ship could take the place of six smaller ships. To take care of all the present grain exports to Asia only two super carrier size ships per week are needed. This would result in reductions in shipping costs.

BASIC COMPONENTS OF A MAGLEV GRAIN PIPELINE

Permanent Magnets in Repulsion as the Means of Suspension

The grain is put into containers which are suspended by permanent magnets in repulsion (ref. 5) as shown in Figure 3. Not shown are lateral guidance controls, which can be either mechanical or magnetic (ref. 6). A particular advantage of using permanent magnets in repulsion is that they require no power to levitate and the containers always remain levitated even when the system is turned off and has stopped. New magnetic compounds virtually last forever in this application.

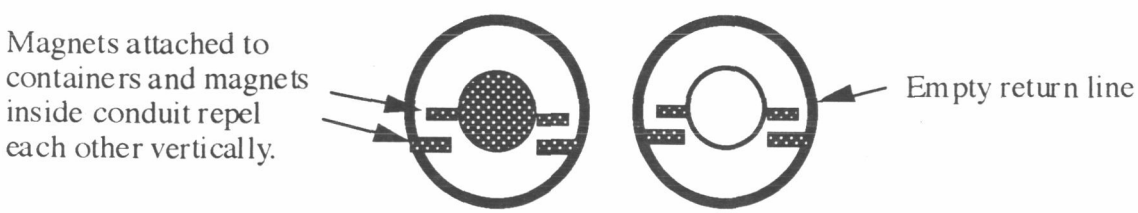

Figure 3. Typical cross section of maglev grain pipeline.

Electric Linear Induction Motors (LIM) for Propulsion

The primary portion of a typical LIM is shown in Figure 4. The secondary to this LIM consists of a metal sandwich or platen attached to the bottoms of the containers. The speed of the shown LIM can be varied by varying the frequency of the supplied power. For instance, the speed can be reduced from 200 to 100 miles (320 to 160 Km) per hour by reducing the frequency from 150 to 75 cycles per second (cps). The LIM can also be reversed for braking. A power supply with appropriate controls would be required to meet the full range of possible operating needs.

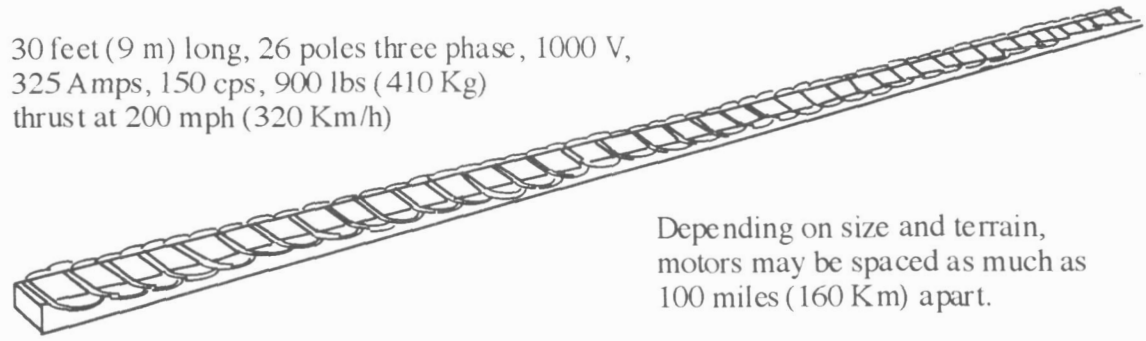

Figure 4. Typical high speed high performance linear induction motor (LIM).

Dynamic Mechanical Loading and Unloading

The containers are flexibly attached to each other end to end and move in unison. A short distance before the end of the line is a cam that forces alternate container joints to diverge onto upper and lower tracks (ref. 7). This causes the containers to fold up against each other and slow down, the last stages of which are shown in Figure 5. After they have completely folded, they pass through either a filling or a dumping station followed by a U-turn. Figure 6 shows a low cost elevated cross-country version of the pipeline.

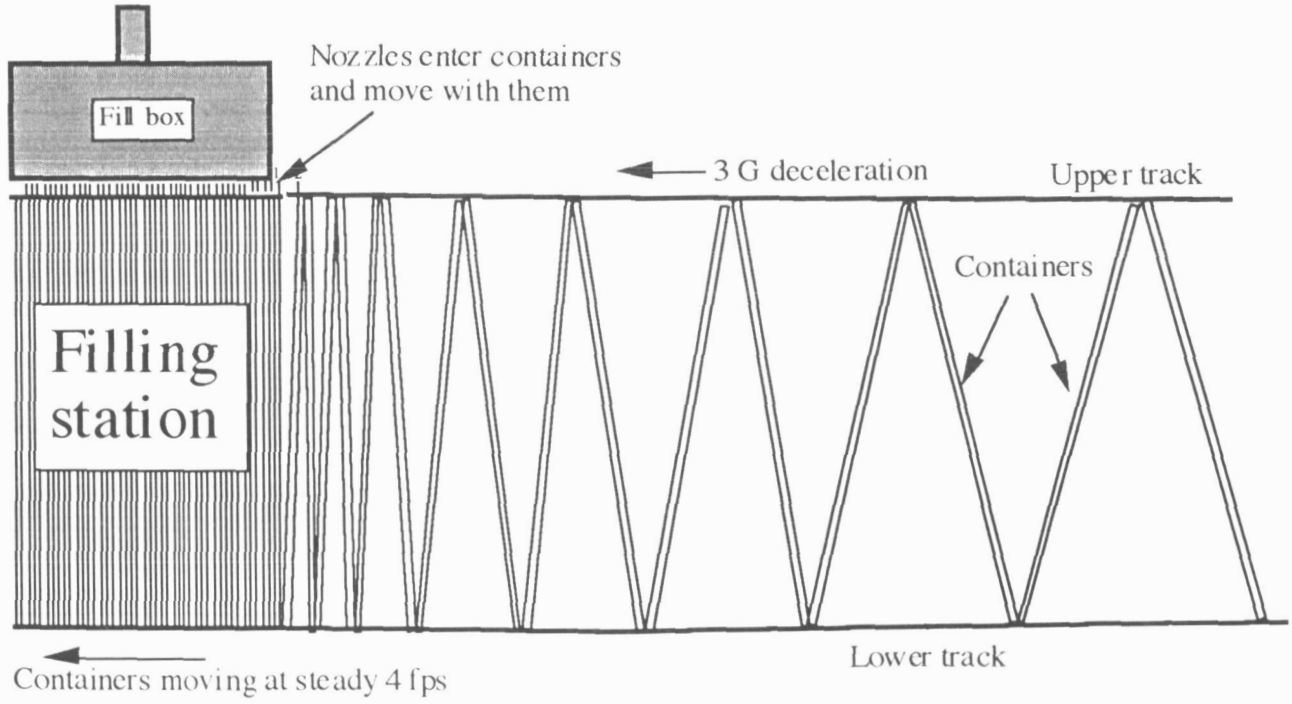

Figure 5. Typical folding and filling of containers..

Comments on Figure 5. Figure 5 is a cutout from a drawing that shows a 200 mph (310 Km/h) system. While this might be a look into the future in bulk materials transportation, initial speeds of between 50 and 100 mph (80 and 160 Km/h) would be advocated with provisions to step the speed up to a higher level later.

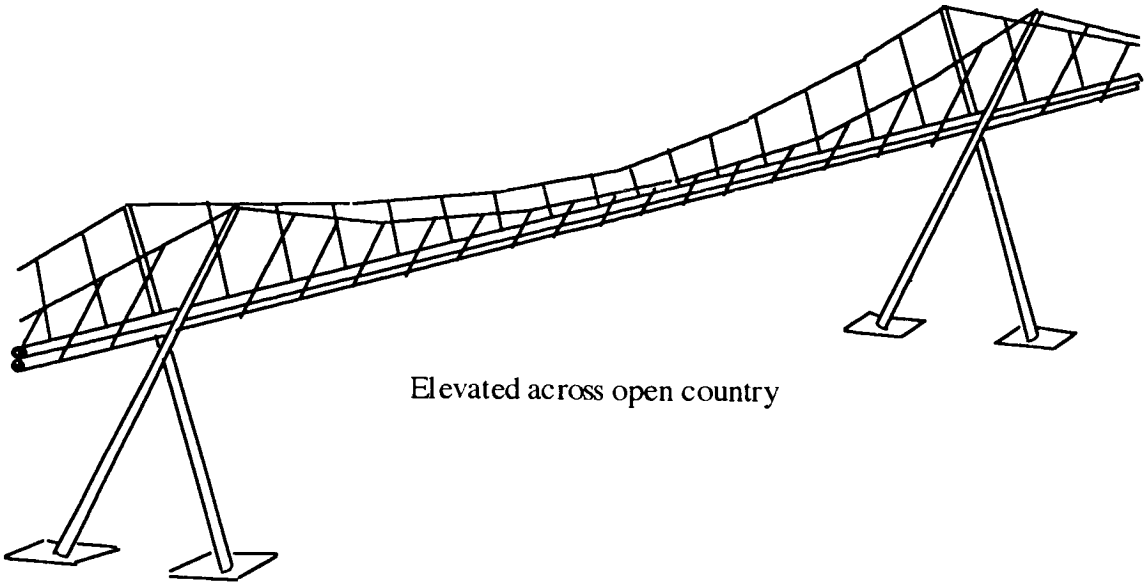

Figure 6. Typical low-cost elevated design of maglev grain pipeline.

SPECIAL REQUIREMENTS FOR TRANSPORTING GRAIN IN CONTAINERS

Unlike the Alaska maglev crude oil pipeline proposal, described in Reference 6, where the only requirement was for the oil to be hot during filling and again during emptying, grain transported in containers should be kept within a specific temperature range and moisture content throughout the trip. When grain is in a condition outside these desirable ranges, the containers should be capable of improving on those conditions. For instance, when grain with too much moisture passes through hot dry regions of Arizona and California, containers should have sensing devices which open vents to remove excess moisture.

Temperature Range. Cold temperatures are generally not injurious to grain. On the contrary, the danger of spoilage disappears when temperatures approach freezing. High temperatures require dryer grain. At about 115^{0}F (46^{0}C) grain with moisture content exceeding 12 percent would suffer heat damage.

Moisture Content. Grain may have from 9 to 13.5 percent moisture. At moisture levels around 12 percent, grain becomes difficult to store for several months. At levels over 14 percent, grain may spoil in a matter of weeks, which is especially true for newly harvested grain.

Insects Removal. While the grain is in the containers, the air around it could be replaced with CO_2 or nitrogen, or a low level fumigants could be added to the air to kill insects.

Ventilation to Reduce Moisture. If grain has too much moisture and when it should also be fumigated, the time available should be shared. The fumigants should be applied first. Then after a few hours, remote controls could trigger vents to open for fumigant to exit and drying air to enter.

MAGLEV PIPELINE COST AND CAPACITY

Construction Cost. A detailed cost estimate shows that, if a medium size maglev grain pipeline had been built in 1996 as an elevated system as shown in Figure 6, it would probably have cost about $500,000 per mile ($300,000 per Km). Not included in this estimate are the costs of (1) right-of-ways, (2) power generators if needed, (3) service roads and (4) end facilities. The elevated design is preferred because of the continued need for very straight alignment similar to overhead electric wires or catenaries of high speed railroads.

Table 2. Assorted Carrying Capacities of Maglev Grain Pipeline, Tons per Day

Container diameter (inches)	(cm)	Speed 25 mph (40 Km/h)	Speed 50 mph (80 Km/h)	Speed 75 mph (120 Km/h)	Speed 100 mph (160 Km/h)
3	7.5	3,700	7,400	11,100	14,800
4	10	6,500	13,000	19,500	26,000
6	15	15,000	30,000	45,000	60,000
8	20	26,000	52,000	78,000	104,000
12	30	60,000	120,000	180,000	240,000

Conversion factors for grain, used in Table 2, are (a) 35 bushels (100 hectoliter) = one ton, (b) 0.8 bushel = one cubic foot (28 liters), (c) grain weight 48 pounds per cubic foot (0.78 Kg per liter).

Size, Speed and Capacity. The carrying capacity of the pipeline is determined by multiplying the container cross-sectional area with the system velocity. The cross-sectional area is determined by the elected container diameter. However, the speed can be changed at any time later which in turn changes system capacity. Table 2 shows the pipeline capacities for various sizes and speeds when running continuously for 24 hours.

FINANCIAL FEASIBILITY

Basic Considerations

In the paper "Maglev Crude Oil Pipeline", Ref. 6, an extensive financial analysis was included to show that if the Alaska crude oil pipeline had been constructed as a maglev crude oil pipeline, as herein proposed for grain, some $10 million per day could have been saved. That analysis was based on recorded financial data as reported to the U.S. Federal Energy Regulatory Commission. This data also shows that the Alaska pipeline was not a true private enterprise because (1) profit was arbitrarily restricted to 6% and (2) interest during construction was not capitalized. The reason for not including these two items on the books was obvious. The Alaska pipeline would have gone bankrupt before it even could have started to operate.

Unlike the Alaska crude oil pipeline, where solid recorded cost data was available to compare with, here, for this proposed grain pipeline project across more than half of North America, there is nothing to compare costs with. All we can go by is the knowledge that two railroads have growing business parallel to the proposed route. One of them moves about 17 million tons/year, and the other is just starting, but may have trouble with inadequate tracks. Their combined present annual income from grain transportation to the West Coast is around $600 million. Additional 33 million tons of grain could be transported along this route representing an additional $1,200 million annually.

Sharing Line with Passenger Service

Not included in considerations of financial feasibility is the likelihood of sharing the maglev pipeline's elevated structure with the light weight passenger transit system, the Knolle Magnetrans (ref. 8, 9 & 10). For instance, the 300 mile portion of the grain pipeline in California may be combined with a Los Angeles to Las Vegas passenger Magnetrans, which could bring in additional gross revenues of $200 million per year. Sharing the grain pipeline structure with passenger service in other locations may also be lucrative. Airlines have long recognized that combining freight and passengers is profitable and keeps rates low for customers.

When Undertaken by Private Enterprise

Figure 6 shows how the 1,500 mile (2,400 Km) maglev grain pipeline across North America would financially fare after construction is completed. Shown are three levels of costs per mile, which could possibly occur, and correspondingly elected freight rates in magnitudes that would assure amortization of capital over approximately 15 years, while paying all require taxes and a return on equity of 20% per year at a debt ratio of 70%.

Comments on Figure 6. A serious effort was made to produce highly realistic data for this graph. For instance, with the pipeline's 1997 estimated cost of $4 million/mile ($2.5 million/Km) and having a length of 1,500 miles (2,400 Km), the beginning of the curve is shown in year one at close to $12,000 million and not $6,000 million (4 x 1,500 = 6,000). This is because estimated inflation of 5% was added during each of the 5 years of construction, and also, estimated annual interest during construction (cost of money) of 15% was included (capitalized) as construction cost. The longer the construction period, the

heavier is the capitalized 'cost of money' burden. The construction period was estimated as 5 years. If it could be reduced to 3 years, it would save over $2,000 million in initial capital requirement.

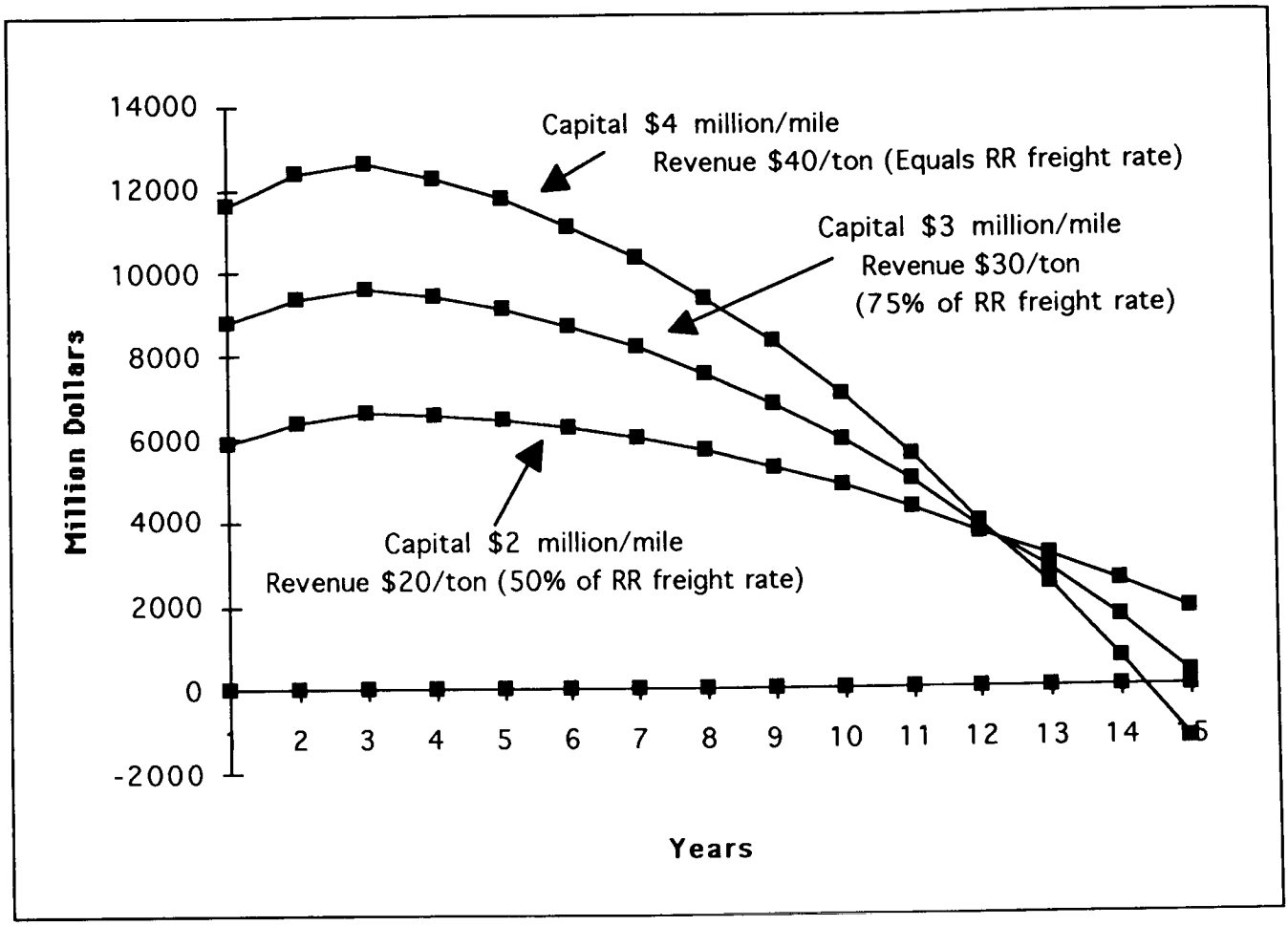

Figure 6. Amortization of capital investment for a 1,500 mile (2,400 Km) maglev grain pipeline from Midwest America to California, assuming capital investment of $4 million/mile ($2.5 million/Km), $3 million/mile ($1.9 million/Km) and $2 million/mile ($1.2 million/Km) with respective revenues of $40/ton, $30/ton and $20/ton.

CONCLUSION

Farm failures are a serious problem in America. The cost of farm equipment, and energy to run it, is rising, but not farm income. Grain transportation, storage and handling costs are excessive. Railroads lack adequate tracks. Maglev pipeline technology could greatly reduce the need for intermediate handling and storage of grain (cut out the middle men), could transport grain more efficiently and reduce overall costs considerably, from which both grain producers (farmers) and Asian consumers would greatly benefit.

Included in this paper is a financial analysis, indicating that a 1,500 mile (2,400 Km) maglev grain pipeline would be financially feasible across the American West. It would be a profitable tax paying enterprise when undertaken by private enterprise.

REFERENCES

1. Yen, A.M., Henderson, C., Sakasita, M. & Roddin, M.; *Assessment of the WEDway Peoplemover System at Walt Disney World*, US Department of Transportation, report No. UMTA-IT-06-0135-77-5, 1977

2. Nonaka, S. and Higuchi, T.; *Design Strategy of Single-Sided Linear Induction Motors for Propulsion of Vehicles*, IEEE Trans., Cat, No. 87CH2443-0, pp. 1-11, 1987.

3. Laithwaite, E. R. & Chirgwin, K.; *Transport Without Wheels*, Westview Press, Boulder, Colorado, pp. 37-59, 1977.

4. Research staff; *Grain Transportation, Agricultural Market Service, Wheat Yearbook*, etc., Economic Research Services, Transportation and Marketing Division, U.S. Department of Agriculture, continuously updated periodicals.

5. Strnat, K. J., *Rare-Earth Permanent Magnets: Two Decades of New Magnetic Materials*, ASM, Paper No. 8617-005, 1986.

6 .Knolle, E.; *Maglev Crude Oil Pipeline,* NASA Conference Publication 3247, Langley Research Center, pp. 671-684, 1993.

7. Knolle, E.; *Bulk Material Conveyor*, U.S. Patent No. 4,024,947, 1977.

8. Knolle, E.; *Magnetrans High Speed Maglev People Mover,* ASCE Library of Congress Catalog Card No: 89-17833, ISBN 0-87262-73.1-4, pp. 871-880, 1989.

9. Knolle, E.; *Knolle Magnetrans, a Magnetically Levitated Train System*, NASA Conference Publication 3152, pp. 907-918, 1991.

10. Schneider, J., *Magnetrans*, Supported Technologies, Innovative Transportation Technologies (ITT) Web site, <http://weber.u.washington.edu/~jbs/itrans/>, 1997.

MATHEMATICAL TREATMENT OF SUPERCONDUCTING LINEAR SYNCHRONOUS MOTOR

Tetsuzo Sakamoto
Department of Control Engineering, Kyushu Institute of Technology
Tobata, Kitakyushu 804, Japan

SUMMARY

The paper deals with the superconducting linear synchronous motor with application to the propulsion system of a high-speed transportation maglev vehicle. The system is composed of superconducting magnets (SCMs) on the vehicle and linear synchronous motor armature windings on the ground. The suitable coordinate system on the speed control may be *dq*-axis fixed on the SCMs.

The system variables are formulated viewing from the *dq0*-axes and the block diagram is constructed accordingly. A speed control system is then designed with appropriate disturbance compensations included, and it is confirmed from computer simulations that it works well under disturbed conditions.

INTRODUCTION

The superconducting linear synchronous motor (LSMs) is suitable for the propulsion of a high-speed transportation maglev vehicle; the power factor and efficiency are kept high even for a large gap between the superconducting magnets (SCMs) and the LSM armature windings.

There are mainly two types of operation for a synchronous motor in terms of the source voltage determination: they are "separately-controlled type" and "self-controlled type". On the former, the armature current flows in the circuit passively depending on the magnitude of the load. The current phase lags or leads from the source voltage, which is determined from the magnitude relation for the applied voltage and the speed emf induced from the field. The load is often referred to using the variable called load angle, because the phase angle between the applied voltage and the speed emf increases monotonically as the load increases, where no load corresponds to zero load angle. If the load exceeds the maximum value, which is called pullout power, then the motor loses synchronism. On the other hand, the source voltage of the self-controlled type is generated in such a way that the armature current flows in phase with the induced speed emf, which realizes zero lateral force, and high power factor. The current always lags behind the source voltage. In this case, however, the phase angle between the applied voltage and the induced speed emf never becomes zero for even no load. Accordingly the load angle does not mean the load magnitude for this type, and then it does not have a practical meaning. The applied voltage is produced by a variable voltage variable frequency (VVVF) power source according to the signals from position detectors. Therefore, this operation never loses synchronism as long as the detector works normally. This paper discusses the treatment of the self-controlled type linear synchronous motor.

Dawson et al. (ref. 1) discussed the fundamental characteristics of a superconducting LSM in a three-phase coordinate system assuming a fundamental component of magnetic field, and constructed a control system having vehicle speed and force angle as feedback signals, and voltage and frequency as

manipulated variables. Maki et al. (ref. 2) showed detailed computer simulations of electrodynamic variables in terms of three-phase coordinate system, but they did not refer to the combination with the control system. Although Ikeda presented a block diagram of the speed control system constructed in dq-axes (ref. 3), it ended up with a qualitative discussion with respect to electrodynamic variables. The author has presented an exact analysis of the propulsion system in $dq0$-axes with space harmonics of magnetic field included, and defined the thrust coefficient (ref. 4), making it possible to understand the characteristics quantitatively in a similar way as DC motor. The block diagram can be constructed almost exactly as it is in the practical maglev vehicle by using mathematical modeling, where any uncertainty is not retained in the formulation with respect to the propulsion system. Consequently, the three-power converter system employed at the new test track of Japan Railway in Yamanashi, where the propulsion power is supplied in sections from three inverters, is easily included in the block diagram. In this paper, the analysis is shown using the configurations of the test vehicles developed by Japan Railway.

ANALYSIS, MODELS, AND SPEED CONTROL SYSTEM

Propulsion force is provided by the interaction between the vehicle-borne SCMs and the armature windings with air core on the guideway. The SCMs are arranged in a concentrated manner so that the passenger cabin is not exposed into strong magnetic field, and at the same time the total weight of SCM becomes minimum.

Figure 1 shows the first of two models we discuss here, which has three SCM's arranged with two pole-pitch spaces in the longitudinal direction. The armature coil is installed in the form of two layers of 240-degree coil pitch arrangement as shown in the figure. The other form of armature coil has a single layer of 120-degree coil pitch, and it is treated as a special case for the 240-degree configuration in the formulation. The coordinate systems (x,y,z) and (x',y',z') are fixed on the vehicle and the guideway, respectively. The electromagnetic field problem is formulated through two stages: i) to derive the magnetic field equations considering the SCM as the source; ii) to formulate the interaction between the armature currents and the SCM's, i.e., induced emf, and forces. The magnetic field is derived by means of a magnetic vector potential or a magnetic scalar potential; the latter is simple. The physical meaning of using the magnetic scalar potential is to regard the SCM as a magnetic charge layer. Let the *mmf* function of SCM array located at $y = d_s$ be $f_s(x,z)$, and then the next equation holds

$$M_S = e_y f_S(x,z)/h_S \tag{1}$$

where M_s is the magnetization vector, e_y is the y-component unit vector, and h_s is the thickness of

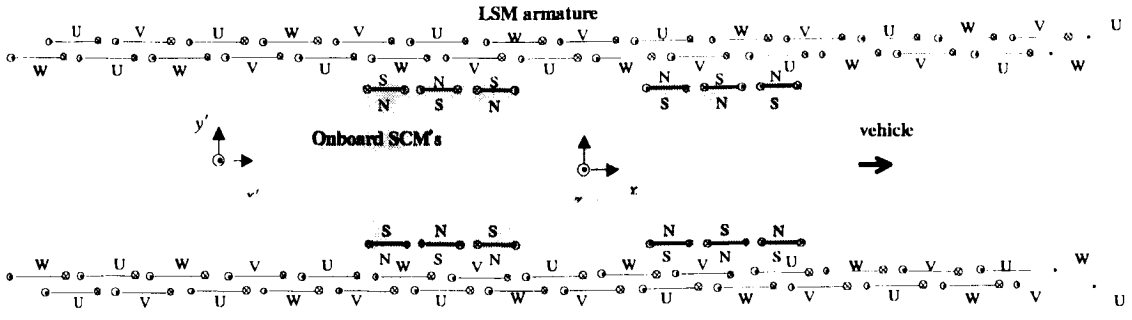

Figure 1. LSM armature windings and onboard SCM's (Model 1)

the SCM. Hence the magnetisation charge density is given by the divergence,

$$\rho_M = -\nabla \cdot \boldsymbol{M}_S \tag{2}$$

If we assume that the thickness of the SCM is infinitely small, the magnetic scalar potential has a discontituity of magnitude as the dipole moment per unit area $\rho_M h_S = f_s(x,z)$ at the double layer (ref.5). Then the governing equations for the potential are written as

$$\nabla^2 \phi_m = 0 \qquad (y \neq d_s) \tag{3.a}$$

$$\begin{cases} \phi_m^o(x,y,z) - \phi_m^i(x,y,z) = f_s(x,z) & (y = d_s) \\ \phi_m^o(x,y,z) + \phi_m^i(x,y,z) = 0 & (y = d_s) \end{cases} \tag{3.b}$$

where

$$\phi_m = \begin{cases} \phi_m^o & (y \geq d_s) \\ \phi_m^i & (y \leq d_s) \end{cases}$$

$$\boldsymbol{H}_S = (H_{Sx}, H_{Sy}, H_{Sz}) = -\nabla \phi_m$$

We then obtain the scalar magnetic potential as

$$\phi_m^{o,i} = \sum_{k=1,3,\cdots} \sum_{m=1,3,\cdots} \pm \frac{a_s(k,m)}{2} \sin \alpha_k x \cos \alpha_m z \cdot e^{\mp \beta_{km}(y-d_s)} \tag{4}$$

where

$\alpha_k = \pi k / L$, $\alpha_m = \pi m / H$, $\beta_{km} = \sqrt{\alpha_k^2 + \alpha_m^2}$

$$a_S(k,m) = \frac{32 n_s I_s}{\pi^2 km} \sin(\alpha_k \frac{l_s}{2}) \sin(\alpha_m \frac{w_s}{2}) \frac{\cos(3\alpha_k \tau/2)}{\cos(\alpha_k \tau/2)} \cdot \sin(5\alpha_k \tau/2)$$

$n_S I_S$: *mmf* of SCM, l_S , w_S : length and width of SCM, τ : pole pitch .

The flux linkages of armature windings for the three phases, the length of which corresponds to one section, are given by

$$\psi_U = \sum_{l=1}^{N_a/2} \left\{ \int_{x_{al}-\frac{3\tau}{2}-\frac{l_a}{2}-\lambda}^{x_{al}-\frac{3\tau}{2}+\frac{l_a}{2}-\lambda} \int_{-\frac{w_a}{2}}^{\frac{w_a}{2}} \mu_0 n_a H_{sy}(x', d_a - \frac{c_a}{2}, z') dx' dz' + \int_{x_{al}-\frac{\tau}{2}-\frac{l_a}{2}-\lambda}^{x_{al}-\frac{\tau}{2}+\frac{l_a}{2}-\lambda} \int_{-\frac{w_a}{2}}^{\frac{w_a}{2}} \mu_0 n_a H_{sy}(x', d_a + \frac{c_a}{2}, z') dx' dz' \right\}$$

$$\psi_V = \sum_{l=1}^{N_a/2} \left\{ \int_{x_{al}+\frac{7\tau}{6}-\frac{l_a}{2}-\lambda}^{x_{al}+\frac{7\tau}{6}+\frac{l_a}{2}-\lambda} \int_{-\frac{w_a}{2}}^{\frac{w_a}{2}} \mu_0 n_a H_{sy}(x', d_a - \frac{c_a}{2}, z') dx' dz' + \int_{x_{al}-\frac{5\tau}{6}-\frac{l_a}{2}-\lambda}^{x_{al}-\frac{5\tau}{6}+\frac{l_a}{2}-\lambda} \int_{-\frac{w_a}{2}}^{\frac{w_a}{2}} \mu_0 n_a H_{sy}(x', d_a + \frac{c_a}{2}, z') dx' dz' \right\}$$

$$\psi_W = \sum_{l=1}^{N_a/2} \left\{ \int_{x_{al}-\frac{\tau}{6}-\frac{l_a}{2}-\lambda}^{x_{al}-\frac{\tau}{6}+\frac{l_a}{2}-\lambda} \int_{-\frac{w_a}{2}}^{\frac{w_a}{2}} \mu_0 n_a H_{sy}(x', d_a - \frac{c_a}{2}, z') dx' dz' + \int_{x_{al}-\frac{11\tau}{6}-\frac{l_a}{2}-\lambda}^{x_{al}-\frac{11\tau}{6}+\frac{l_a}{2}-\lambda} \int_{-\frac{w_a}{2}}^{\frac{w_a}{2}} \mu_0 n_a H_{sy}(x', d_a + \frac{c_a}{2}, z') dx' dz' \right\} \tag{5}$$

where N_a is the number of cells, which is defined as one cell for two pole-pitch length, l_a, w_a : length and width of armature coil, c_a : distance between two layers, d_a : lateral position of armature coil, n_a : number of turn of armature coil, $x_{al} = (2 - N_a)\tau + 4(l-1)\tau$, $\lambda = 0$ (240-degree type), $\lambda = \tau/6$ (120-

degree type), and the section is located at $-N_a\tau \le x' \le N_a\tau$.

The induced counter emf of armature coil is obtained by the equation

$$E_\zeta = \frac{d\psi_\zeta}{dt} \quad (\zeta = \mathrm{U, V, W}) \tag{6}$$

Now, we aim here to view the electrical variables from the $dq0$-axes, where the zero-sequence component appears due to the existence of the neutral line, i.e., $i_U + i_V + i_W \neq 0$. A transformation matrix that maps from three-phase axis to $dq0$-axeswith the power held constant is written as

$$C = \sqrt{\frac{2}{3}} \begin{pmatrix} \cos\theta_{dq} & \cos(\theta_{dq} - \frac{2\pi}{3}) & \cos(\theta_{dq} + \frac{2\pi}{3}) \\ -\sin\theta_{dq} & -\sin(\theta_{dq} - \frac{2\pi}{3}) & -\sin(\theta_{dq} + \frac{2\pi}{3}) \\ \frac{1}{\sqrt{2}} & \frac{1}{\sqrt{2}} & \frac{1}{\sqrt{2}} \end{pmatrix} \tag{7}$$

where $\theta_{dq} = \frac{x_1 + \lambda}{\tau}\pi$, $x_1(t) = x' - x = \int_{t_s}^{t} v_x(u)du$, $v_x(t)$: vehicle speed

In three-phase axes, the vector voltage equation becomes

$$\begin{pmatrix} V_U \\ V_V \\ V_W \end{pmatrix} = \begin{pmatrix} R & 0 & 0 \\ 0 & R & 0 \\ 0 & 0 & R \end{pmatrix} \begin{pmatrix} i_U \\ i_V \\ i_W \end{pmatrix} + \begin{pmatrix} L & M & M \\ M & L & M \\ M & M & L \end{pmatrix} \frac{d}{dt} \begin{pmatrix} i_U \\ i_V \\ i_W \end{pmatrix} + \begin{pmatrix} E_U \\ E_V \\ E_W \end{pmatrix} \tag{8}$$

Transformation of (7) by the mapping of (6) yields

$$\begin{pmatrix} V_d \\ V_q \\ V_0 \end{pmatrix} = \begin{pmatrix} R + pl_m & -\omega_{dq} l_m & 0 \\ \omega_{dq} l_m & R + pl_m & 0 \\ 0 & 0 & R + p(L + 2M) \end{pmatrix} \begin{pmatrix} i_d \\ i_q \\ i_0 \end{pmatrix} + \begin{pmatrix} E_d \\ E_q \\ E_0 \end{pmatrix} \tag{9}$$

where $V_d, V_q V_0$: source voltages, i_d, i_q, i_0: armature currents, $\omega_{dq} = d\theta_{dq}/dt$, R, L, M : resistance, self inductance, and mutual inductance between phases of armature, $l_m = L - M$. $p = d/dt$.

The interaction between the induced speed emf and the armature currents causes power dissipation, and accordingly leads to energy conversion from electric power to dynamic power via magnetic field. Finally, we get the propulsion force.

$$F_p = (E_U i_U + E_V i_V + E_W i_W)/v_x = (E_d i_d + E_q i_q + E_0 i_0)/v_x \tag{10}$$

otherwise, using the magnetic energy concept,

$$F_p = i^T{}_{dq0} C \left(\frac{dC^T}{dx_1} \psi_{dq0} + C^T \frac{d\psi_{dq0}}{dx_1} \right) \tag{11}$$

where $i_{dq0} = (i_d, i_q, i_0)^T$, $\psi_{dq0} = (\psi_d, \psi_q, \psi_0)^T$

Assuming sufficient control to keep the d-axis and zero-sequence currents at zero, the thrust coefficient K_F is defined as

$$K_F = F_p / i_q \tag{12}$$

And we have

$$K_F = -\sqrt{\frac{2}{3}}\sum_k\sum_m \alpha_k \Psi_{km}\left\{\sin\theta_{dq}\cdot g_{Ukm} + \sin(\theta_{dq}-\frac{2\pi}{3})\cdot g_{Vkm} + \sin(\theta_{dq}+\frac{2\pi}{3})\cdot g_{Wkm}\right\} \tag{13}$$

where

$$g_{Ukm} = e^{\beta_{km}c_a/2}\cos\alpha_k\left(x_1+\frac{3\tau}{2}+\lambda\right) + e^{-\beta_{km}c_a/2}\cos\alpha_k\left(x_1-\frac{\tau}{2}+\lambda\right)$$

$$g_{Vkm} = e^{\beta_{km}c_a/2}\cos\alpha_k\left(x_1-\frac{7\tau}{6}+\lambda\right) + e^{-\beta_{km}c_a/2}\cos\alpha_k\left(x_1+\frac{5\tau}{6}+\lambda\right)$$

$$g_{Wkm} = e^{\beta_{km}c_a/2}\cos\alpha_k\left(x_1+\frac{\tau}{6}+\lambda\right) + e^{-\beta_{km}c_a/2}\cos\alpha_k\left(x_1-\frac{11\tau}{6}+\lambda\right)$$

We also consider the model shown in Figure 2, which has 4-pole concentrated arrangement with 12-pole pitch space. The equations are slightly different from the case of the model-1, because the inner and outer armature coils have different number of turns, while they have the same value in the model-1.

Let's consider a feeding system such that the power is fed to the sections where the vehicle exists from three inverters to minimize the associated losses as shown in Figure 3. The block diagram is constructed based on the voltage equation (9), combining with the feeding system and the controller. We design a PI controller with cascade system, in which every inverter has its own current controller, for the speed control to demonstrate the performance. Moreover, disturbance compensations are added to the system, estimators of the speed emf and for the non-diagonal terms of the coefficient matrix that appears in (9). The variables with the symbol tilde indicate the estimated signals in the block diagram. The signals v'_0, v'_d and v'_q are the outputs of current controllers, whereas v_0, v_d and v_q are the compensated manipulated variables to be output from the inverters. The vehicle mass is denoted by

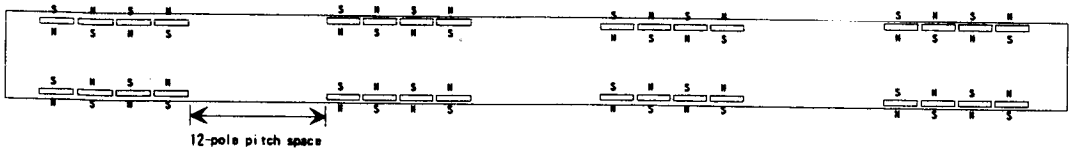

Figure 2. SCM arrangement of Model 2

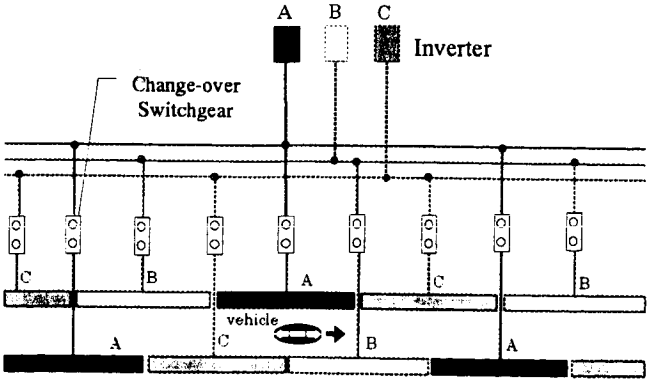

Figure 3. Three-power converter System

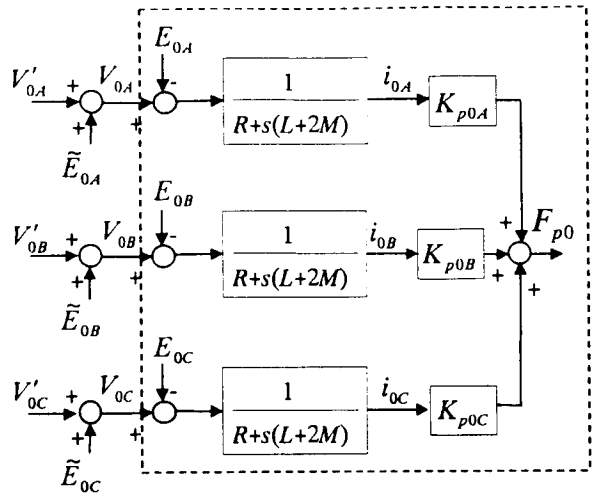

(a) Zero sequence

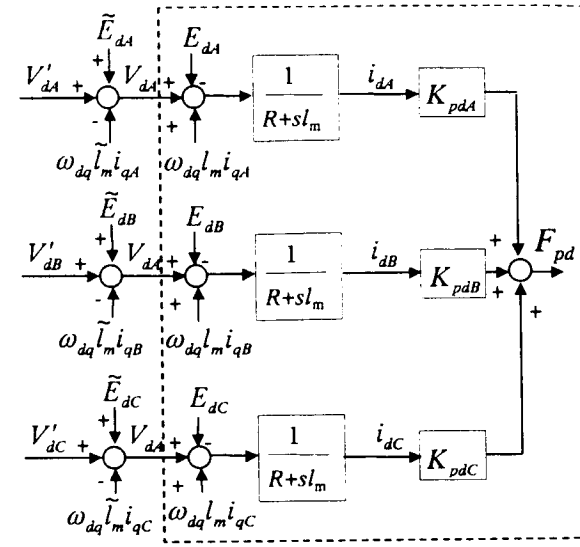

(b) d-axis

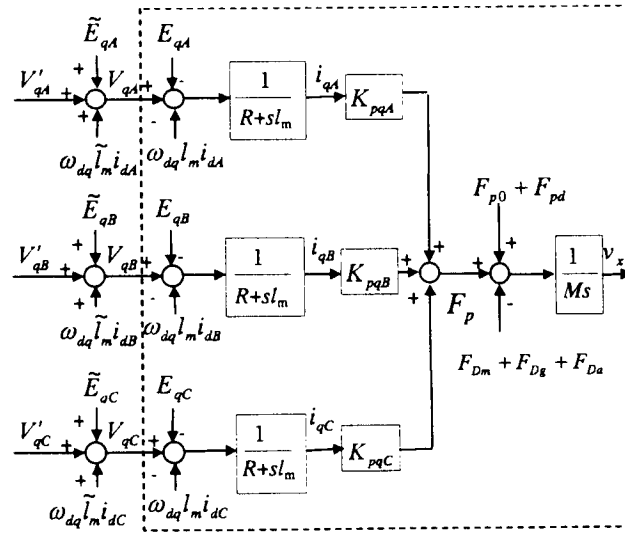

(c) q-axis

Figure 4. Block diagram of the control system

M. The forces F_{Dm}, F_{Dg} and F_{Da} are the drag forces resulting from the loss in magnetic levitation system, guideway gradient and air resistance that is proportional to the square of speed, respectively.

CALCULATED RESULTS

Figure 5 shows the speed emf induced in each one of the three-phase armature coils at the speed of 420km/h, which were calculated for the two cases of the 120-degree coil pitch type and the 240-degree coil pitch type. The comparison indicates that more high frequency components of emf are induced in the case of the 120-degree coil pitch type. As is easily seen, the amplitude increases and decreases when the vehicle enters and leaves the corresponding section, respectively. The thrust coefficients

calculated from (13) are shown in Figure 6. The values are shown for the single section case and the resultant case made up from neighboring sections. The resultant value is kept at some range near the steady value in either case, though the thrust coefficient changes between 0 to the resultant value for the single section. However, one noticeable thing is the severe pulsation for the 120-degree coil pitch type, resulting in possible high frequency dynamic force generation at SCM's even if the armature current itself is well controlled. In that respect, the 240-degree coil pitch type has better characteristics, but it still has a pulsation. It can be concluded that this pulsation appears due to the vehicle design where the number of the concentrated arrangement SCM is an odd number. This design brings about changing of the amplitude of the flux linkage with time for one section coil.

Accordingly, the vehicle should have even number of concentrated SCMs and Figure 7 shows the numerical example calculated for 2-pole concentrated arrangement of SCMs to prove this statement. In this case, the flux linkage amplitude is kept constant while the whole vehicle SCM's are positioned in one section as shown in Figure 7(a). Then the thrust coefficient has a constant value.

Next, we show the speed control simulations using the Model 2 with the three-power converter system. Two significant conditions are assumed: (i) The guideway has a tunnel. (ii) One of the 3 inverters, the inverter C, is disabled, and the corresponding circuit is opened so that unnecessary currents can't flow. Figure 8 shows the results. From the aerodynamic drag force profile, it may be understood that the speed control is working well as a result, because its value solely depends upon the vehicle speed other than the constants of the tunnel. On the normal guideway, the aerodynamic drag is about 50kN, and inside the tunnel it is about 90kN. Although the generated propulsion force follows well the aerodynamic drag except for some area, there appears rippled propulsion force at regular intervals. As mentioned earlier, the thrust coefficient has some steady value that is made from neighboring sections. But, these areas are where the vehicle runs partly on the section C, which is connected to the disabled inverter. Therefore, the thrust coefficient has ripples, producing the rippled forces. Propulsion force is controlled directly by q-axis current. Figure 8(c) shows the applied voltage of q-axis component at each section, where the C-section voltage is 0 from the assumption. During the period that the vehicle runs in the tunnel, the voltage amplitudes have larger values, and their profiles are almost proportional to the aerodynamic drag force. In Figure 8(d), the $dq0$ components of the inverter A are shown. The d-axis voltage has comparatively large value because it needs to cancel the coupling voltage from q-axis. The q-axis current value changes just as required to produce the propulsion force, while d-axis and zero-sequence currents are suppressed at almost zero as can be seen from Figure 8(e). Finally, the vehicle acceleration in the running direction is shown in Figure 8(f). The magnitude is small enough in spite of the rippled propulsion forces at some areas, which coincide with the time that the acceleration occurs. Our speed control system works well under the assumed conditions.

CONCLUSIONS

We have shown a methodology for the mathematical treatment of the superconducting linear synchronous motor, which makes it possible to define the thrust coefficient and to construct the speed control system block diagram. The formulation has been made in $dq0$-axis taking account of the space harmonic magnetic fields and time harmonic induced voltages of armature coils. First, it was found out that the vehicle-borne SCM should be arranged concentrically with even number of SCMs so as to not have rippled propulsion forces. Second, the speed control system was designed with the structure

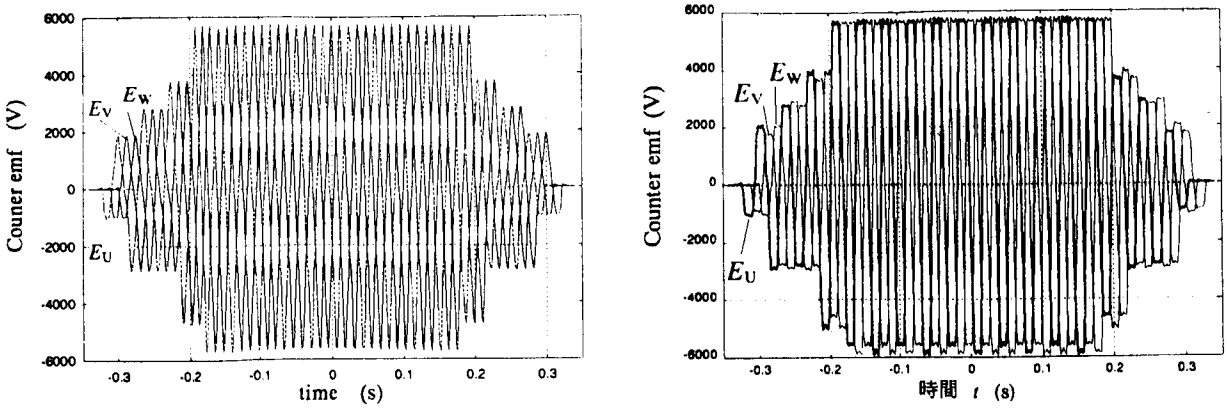

(a) 120-degree coil pitch with single layer

(b) 240-degree coil pitch with double layer

Figure 5. Counter emf for Model 1 (420km/h)

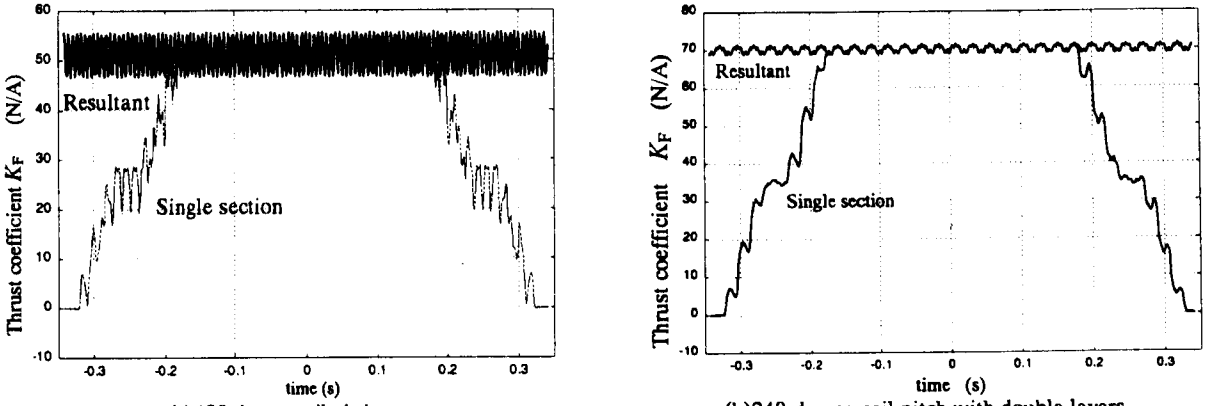

(a) 120-degree coil pitch type

(b)240-degree coil pitch with double layers

Figure 6. Thrust coefficient for Model 1 (420km/h)

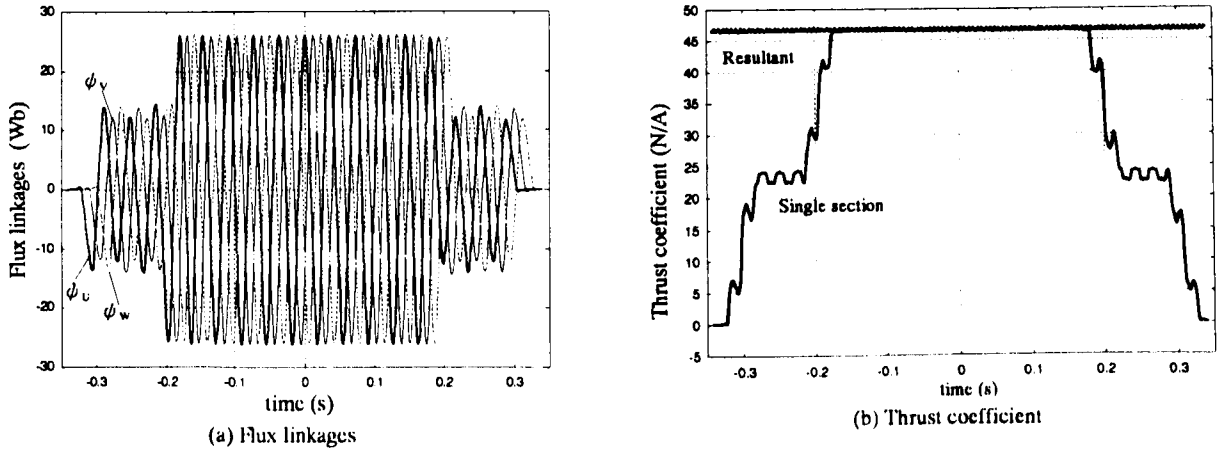

(a) Flux linkages

(b) Thrust coefficient

Figure 7. 2-pole concentrated arrangement of SCM with 4-pole space (420km/h)

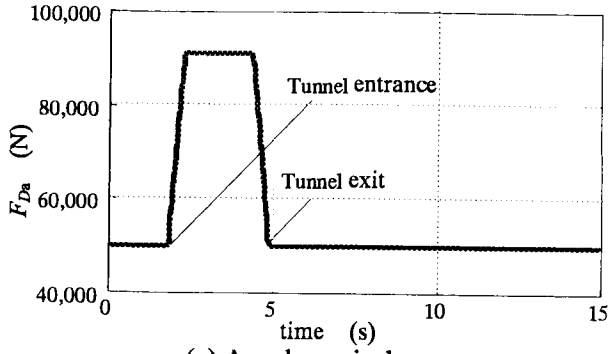

(a) Aerodynamic drag

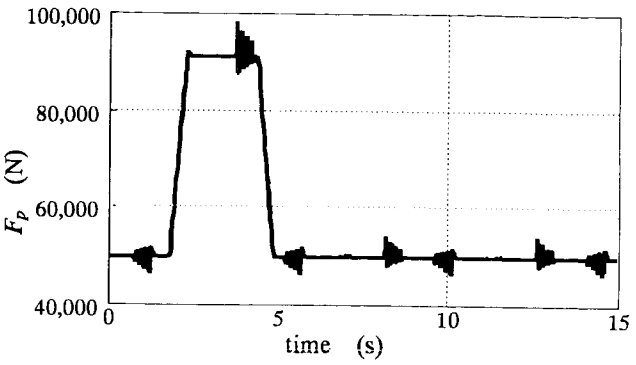

(b) Propulsion force

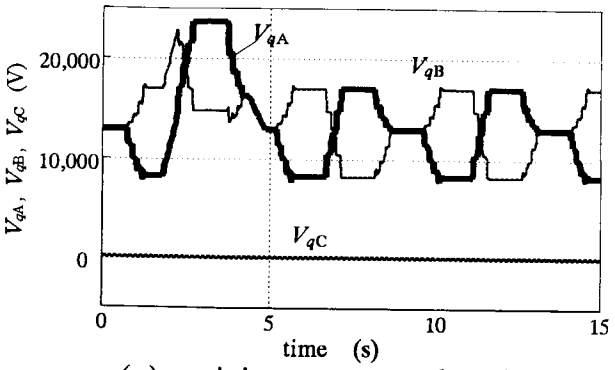

(c) q-axis inverter output voltage for A-, B- and C-section

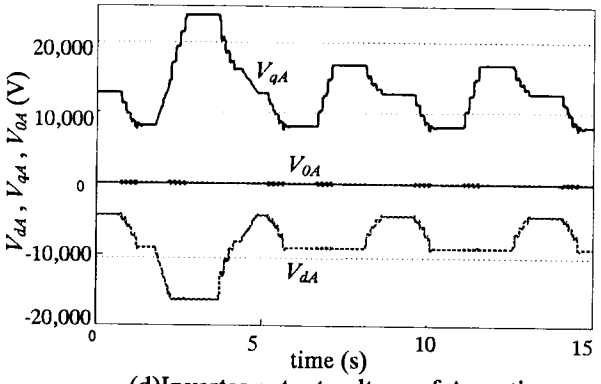

(d)Inverter output voltage of A-section

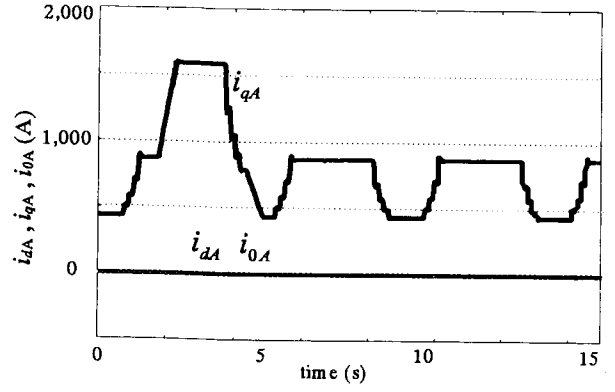

(e) Currents of A-section

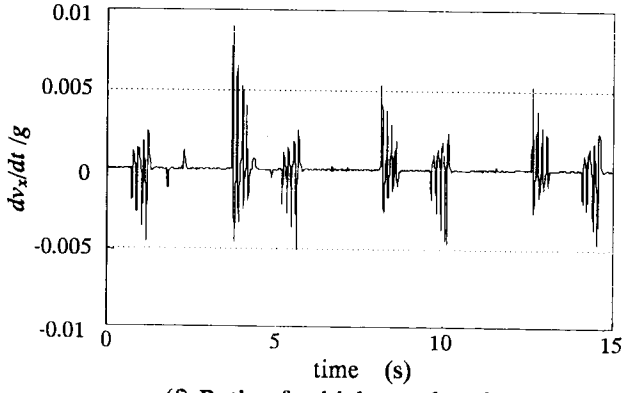

(f) Ratio of vehicle acceleration to gravitational acceleration

Figure 8. Speed control simulation with the disabled inverter C for Model 2 (Speed reference: 550km/h)

of the power feeding system comprised of three inverters. Computer simulations have shown that the speed control system works well under the condition that the guideway has a tunnel and one of the inverters is disabled.

REFERENCES

1. G.E.Dawson, P.C.Sen, D.J.Clarke and S.Lakhavani, Linear Synchronous Motor Feedback Controls, *IEEE Trans. Magn.*, vol.12, pp.885-888, November 1976

2. N.Maki, H.Okuda, J.Fujie and T.Iwahana: A Combined System of Propulsion and Guidance by Linear Synchronous Motors, *IEEE Trans. Power Apparatus and Systems*, vol.96, No.4, pp.1109-1116, 1977

3. H.Ikeda and I.Kawaguchi, Development of Thrust Control System for Linear Synchronous Motor, *Trans. IEE of Japan*, vol.108-D, No.8, pp.757-764 , 1988

4. T. Sakamoto, Analysis of a Superconducting Linear Synchronous Motor Propulsion in Terms of *dq* Variables, *Trans. IEE of Japan,* vol.116-D, No.2, pp.177-182, 1996.

5. W. Panofsky and M. Phillips: Classical Electricity and Magnetism. Addison-Wesley Publ. Co., 1977.

CHARACTERISTICS OF ACTIVE MAGNETIC BEARINGS BIASED WITH PERMANENT MAGNETS ON THE ROTOR

Satoru Fukata
Department of Engineering Design, Kyushu Institute of Design
4-9-1 Shiobaru, Minami-ku, Fukuoka 815, Japan.

Kazuyuki Yutani
Graduate Student, Kyushu University
Fukuoka 812-81, Japan.

SUMMARY

An active magnetic radial bearing is constructed by a combination of permanent magnets for biasing and electromagnets for control. A ring-shaped permanent magnet with axial magnetization is arranged between two rotor cores on a shaft and shares all the pole legs with the electromagnets. The stator is composed of two rings having four pole legs in their inner side and four connecting segments giving the permanent-magnetic flux path. This composition is similar to that of a case where permanent magnets are arranged in the stator. In the non-rotating state, frequency responses of the rotor positioning control system are measured and the transient rotor-motion for impulsive force is tested. The frequency responses are compared with numerical results based on a simple model. In the rotating state, the decay of rotation due to magnetic braking with air friction is examined together with the whirling of the rotor.

INTRODUCTION

A combination of permanent magnets to give bias forces and electromagnets to generate control forces by be useful for the reduction of cost and running energy comsumption of electromagnetic bearings (refs. 1-2). Allaire *et al.* (ref. 3) reviewed work related to this subject, discussed the design and construction, and gave experimental data to show the merit. In this combined magnetic system, the permanent magnets are arranged in the stator in usual, and the stator is shared by two electromagnetic systems in the vertical and horizontal directions. Hence, the magnetic systems interact with each other in general.

In this combination, another arrangement is possible: the permanent magnet is attached to the rotor. This arrangement may have a disadvantage in practice, because there are some problems in the composition of the rotor; however, we can design less interacting magnetic systems with separated stators being homopolar in geometry. The authors (ref. 4) constructed a setup of this arrangement using solid magnet cores, for simplicity, and confirmed that the characteristics are similar to those of the all electromagnetic design. With the separated stators, however, the electromagnetic flux takes an axial path where the magnet core is difficult to laminate. Hence, the response of the electromagnet decays because of eddy current effects. Thus, this arrangement has a merit in the interaction problem but has a demerit in the dynamics. Another demerit is in the setting up of the separate stators into the frame.

To overcome the demerits of this arrangement, without giving up the merit, we consider another stator that is similar to the case of arranging the permanent magnets in the stator. Decoupling control systems are designed with analog PID compensators, neglecting the gyroscopic effect. Frequency responses of

the rotor motion to a disturbance input and the motion for an impulsive force are tested in the non-rotating state. The frequency responses are compared with the numerical results based on a simple model. In the rotating state, the decay of rotation due to magnetic braking with air friction is examined together with the whirling of the rotor.

CONSTRUCTION AND MAGNETIC SYSTEM OF RADIAL BEARINGS

Figure 1 illustrates the construction and the main flux paths of radial magnetic bearings composed of a permanent magnet for biasing and electromagnets for control. A ring-shaped permanent magnet with axial magnetization is arranged between two rotor cores on a shaft of non-ferromagnetic material. The stator is composed of two rings having four pole legs in their inner side and of four connecting segments of ferromagnetic material. The stator rings are made of laminated stacks. The permanent magnetic flux flows radially in the rotor core and goes into the pole leg through the airgap, and passes through the connecting segment to return to the rotor via the other airgap.

The electromagnet coils installed on the radially opposing pole legs are connected in series together with those of the other stator ring and are driven by a single power amplifier. The electromagnetic flux passes down or up the stator pole-leg, through the working airgap and the rotor radially, and enters the radially opposing pole leg. The return flux takes two paths along the stator ring, as shown in the figure. Thus, we can control the total flux by increasing current on one side of the rotor and decreasing current on the other side. A part of the electromagnetic flux may pass the stator axially in the same way as the permanent magnetic flux; but this quantity decreases with increasing frequency because of eddy current effects in the connecting segments that are not laminated for the flux path, in general.

The construction of the stator is similar to that of the case where biasing permanent magnets are

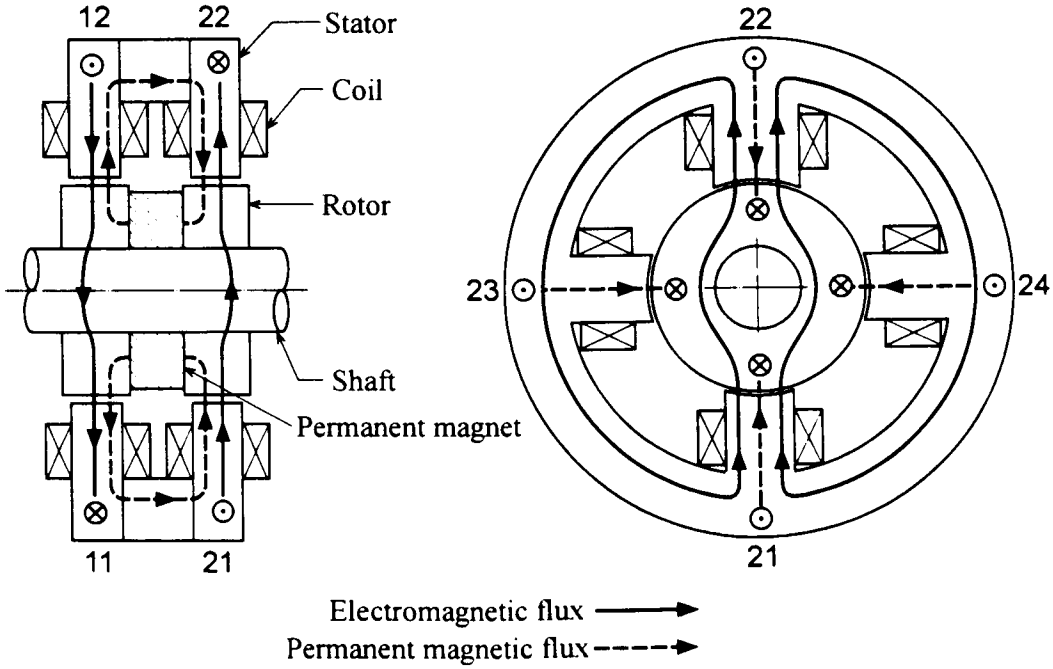

Figure 1. Construction and main flux paths of magnetic radial bearings biased with permanent magnet on the rotor.

located in the stator, where the permanent magnet segments take the place of the connecting segments. With this stator ring connecting the four pole legs, the two magnetic systems are supposed to interact with each other more than with separated stators in ref. 4; however, the response is faster because the electromagnetic flux in large part takes the path of the laminated cores.

Since the composition resembles the case of arranging the permanent magnets in the stator, the magnetic circuit model is derived in a similar way to that in ref. 5. The model may be simplified as in **Fig. 2**, where the left-hand part gives the magnetic parallel circuit of the single stator ring (each path corresponds to a single pole leg), and the right-hand is the equivalent single path of the other stator ring. The symbols F_{ij} and R_{ij} are the magnetomotive force and magnetic resistance of a single pole-leg coil system, and Φ_{ij} is the magnetic flux. The lower part is the axial path in the connecting segments between the two stator rings with the magnetic resistance R_S; the upper is the axial path in the rotor and the permanent magnet with the magnetic resistance R_R. The characteristics of the permanent magnet are considered with the imaginary magnetomotive force F_B and the magnetic internal resistance R_B. In general, since the magnet cores are difficult to laminate in the radial direction, R_S and R_R become larger with frequency because of eddy current effects. Hence, the axial electromagnetic flux may be smaller at higher frequencies.

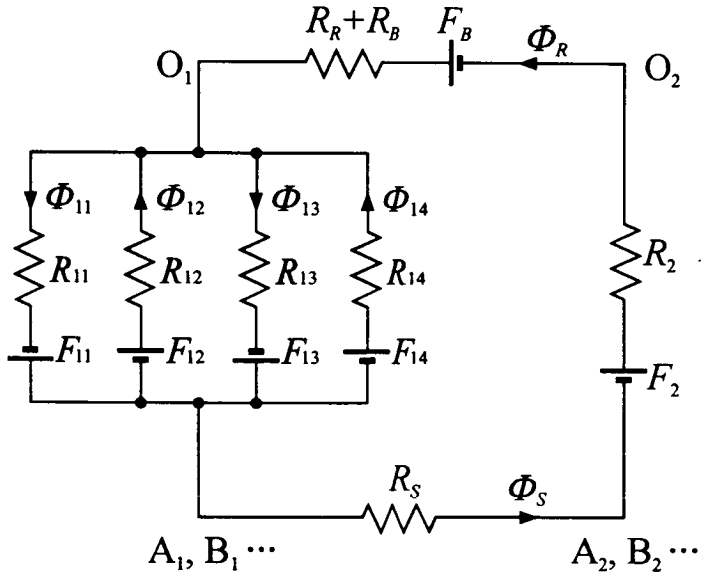

Figure 2. Simplified magnetic circuit.

A DYNAMIC MODEL OF THE MAGNETIC SYSTEM

Symbols

b_j : gain of power amplifier (ratio of output current to input voltage)
c_{Rij} : relative increment of magnetic resistance
e_j : incremental input voltage into power amplifier
I_{j0} : bias coil current

i_j : incremental coil current

$l_{mij\,0}$: equivalent airgap length considering magnetic resistance of magnet core

N_{ij} : turns of magnet coil

Q_{Bij} : equivalent permanent magnetic flux having the unit of current

$Q_{ij\,0}$: similar equivalent bias magnetic flux

q_{ij} : incremental equivalent magnetic flux

R_{ij} : magnetic resistance associated with working airgap

$R_{ij\,0}$: nominal magnetic resistance

R_R : axial magnetic resistance of rotor

R_S : axial magnetic resistance of connecting segments

$R_{T\,0}$: nominal total magnetic resistance

T_{Cj} : time constant of total electromagnet system

T_{Cij} : time constant of individual electromagnet system

T_{Rj} : time constant associated with working airgap variation

Φ_{ij} : magnetic flux associated with working airgap

$\alpha_{i0}, \alpha_{ij\,0}$: ratio between two magnetic resistances

$\Delta\alpha_{ijk}$: difference between α_{ij}

β_{ij} : gain of incremental flux to coil current

μ_0 : permeability of air ($= 4\pi \times 10^{-7}$ H/m)

τ_j : dead time of electromagnet system

We number the pole legs and the working airgaps with *ij* where $I = 1, 2$ for the left- and right-hand stator rings, respectively, $j = 1, 2$ for the lower and upper sides and $j = 3, 4$ for the left- and right-hand sides, respectively, in each stator ring (see Fig.1, for example). The magnet system is referred by 1 for the vertical direction and by 3 for the horizontal direction. These numbers will be used in the subscript to show the associated variables and constants.

Assumption

The analysis of the magnetic system is very complicated in general, as seen in ref. 5. We consider a simple case with the following conditions:

(C1) In the horizontal direction, the dimensions of the magnet system are equal in each stator ring, and

(C2) there is no bias load: no bias current in the electromagnet.

(C3) The nominal working airgap lengths are equal in each direction.

We make the following assumptions:

(A1) Rotor displacement is sufficiently small.

(A2) Incremental magnetic fluxes are sufficiently small.

(A3) Magnetic leakage resistances are constant.

(A4) The recoil permeability of the permanent magnet is equal to that of air.

(A5) Eddy-current effects in the axial flux paths are negligible.

Initial Steady-State Values

For the magnetic fluxes, we use the variables having the unit of current and giving the dynamical characteristics of the fluxes, which are defined by

$$Q_{ij} = \frac{R_{ij0}}{N_{1j}} \Phi_{ij}, \quad i = 1,2;\ j = 1 \sim 4 \tag{1}$$

We denote the initial steady-state values with subscript 0. Then, from the results in ref. 5 obtained under conditions (C1) to (C3), we have the following relations with the nominal working airgap.

$$Q_{ij0} = \beta_{ij} I_{10} + (-1)^{j-1} Q_{Bij},\ j = 1,2; \qquad Q_{i30} = -Q_{i40} = -\frac{N_{11}}{N_{13}} \gamma_{i10} I_{10} + Q_{Bi3} \tag{2}$$

where

$$\frac{1}{R_{i0}} = \sum_{j=1}^{4} \frac{1}{R_{ij0}}, \qquad R_{T0} = R_{10} + R_{20} + R_S + R_R$$

$$\alpha_{i0} = \frac{R_{i0}}{R_{T0}}, \qquad \alpha_{ij0} = \frac{R_{i0}}{R_{ij0}}$$

$$\alpha_{i12} = \frac{N_{i1}}{N_{11}} \alpha_{i10} + \frac{N_{i2}}{N_{11}} \alpha_{i20}, \qquad \Delta\alpha_{i12} = \frac{N_{i1}}{N_{11}} \alpha_{i10} - \frac{N_{i2}}{N_{11}} \alpha_{i20}$$

$$\beta_{ij} = \frac{N_{ij}}{N_{1j}} + (-1)^j \frac{N_{11}}{N_{1j}} \gamma_{i10}$$

$$\gamma_{i10} = \Delta\alpha_{i12} - \alpha_{i0}\left(\Delta\alpha_{112} + \Delta\alpha_{212}\right)$$

The above equations are formulated so that they are applicable to the cases where the right-hand stator ring has no electromagnet coil and/or the dimensions are different on the left- and right-hand sides. Hence, the constants are complicated in form, but become simpler in the case of the same dimensions on both sides. The equivalent permanent-magnetic bias current Q_{Bij} may be given with the data of the permanent magnet; but we may also obtain it directly from the measurement of the magnetic flux densities B_{ij0} by

$$Q_{Bij} = \frac{l_{mij0}}{\mu_0 N_{1j}} B_{ij0} \tag{3}$$

Incremental Magnetic Fluxes

We denote the increments by lower letters. From the results in ref. 5 obtained under assumptions (A1) to (A4), with assumption (A5) we have the following relations for the increments, for $i = 1,2$.

Vertical direction: $j = 1,2$

$$q_{ij} - Q_{ij0}' c_{Ri1} = \beta_{ij} i_1 \tag{4}$$

$$T_{C1} \dot{i}_1 + i_1 + T_{R11} \dot{c}_{R11} + T_{R21} \dot{c}_{R21} = b_1 e_1 (t - \tau_1) \tag{5}$$

Horizontal direction: $j = 3, 4$

$$q_{ij} = \bar{q}_{i3} + (-1)^j \Delta q_{i3}, \qquad \bar{q}_{i3} - Q_{i30} c_{Ri3} = \frac{N_{i3}}{N_{13}} i_3,$$

$$\Delta q_{i3} = \frac{N_{11}}{N_{13}} (\gamma_{i10} i_1 + \gamma_{R1i} I_{10} c_{Ri1}) \tag{6}$$

$$T_{C3} \dot{i}_3 + i_3 + T_{R13} \dot{c}_{R13} + T_{R23} \dot{c}_{R23} = b_3 e_3 (t - \tau_3) \tag{7}$$

where

$$c_{Rij} = \frac{R_{ij}}{R_{ij0}} - 1, \qquad Q_{ij0}' = (-1)^{j-1} \left(Q_{ij0} - \frac{N_{11}}{N_{1j}} \gamma_{R1i} I_{10} \right)$$

$$T_{C1} = \sum_{i=1,\ j=1}^{2} \beta_{ij} T_{Cij}, \qquad T_{C3} = 2(T_{C13} + T_{C23})$$

$$T_{Ri1} = \sum_{j=1}^{2} Q_{ij0}'\ T_{Cij}, \qquad T_{Ri3} = 2 Q_{i30} T_{Ci3}$$

$$\gamma_{R1i} = \alpha_{i12} - \alpha_{i0} (\alpha_{112} + \alpha_{212})$$

In the equations of coil current, eqs. (5) and (7), we added time lags τ_j that may be due to the dynamical characteristics of the power amplifier.

The above model says that the magnet system in the horizontal direction is disturbed by that in the vertical direction, with the effects of the bias coil current I_{10} and the term γ_{i10} that is based on the asymmetry of a pair of electromagnets in the vertical direction. The bias current is given to suspend the rotor against the gravity and a bias load in the vertical direction; c ondition (C2) gives no bias current in the horizontal direction. The relations are complicated by γ_{i10}, but those become much simpler in the symmetric bearing, i.e., γ_{i10} =0 when the dimensions of the magnetic system are equal in the vertical direction.

Net Force in Single Stator Ring

We express the magnetic force as

$$F = \frac{A_h B^2}{2\mu_0} = \frac{A_h}{2\mu_0} \left(\frac{\Phi}{A} \right)^2 = \frac{\mu_0 A_h}{2} \left(\frac{N}{l_{m0}} \right)^2 Q^2 \tag{8}$$

where

$$Q = \frac{R_{m0}}{N} \Phi, \qquad R_{m0} = \frac{l_{m0}}{\mu_0 A}$$

and where A is the area of pole-leg face, A_h its cross-sectional area, B the magnetic flux density, N the turns of magnet coil, l_{m0} the equivalent airgap length and Φ the magnetic flux. Applying this expression to the opposing pole legs, we have the force acting on the rotor as

$$F_{i12} = c_{Fi1} (Q_{i1}^2 - c_{ANi} Q_{i2}^2)$$

where

$$c_{Fi1} = \left[\frac{\mu_0 A_h}{2}\left(\frac{N}{l_{m0}}\right)^2\right]_{i1}, \qquad c_{ANi} = \frac{c_{Fi2}}{c_{Fi1}} = \frac{A_{hi2}}{A_{hi1}}\left(\frac{N_{i2}}{N_{i1}}\right)^2 \tag{9}$$

Then, the net force is given by

$$\Delta F_{i12} = F_{i12} - F_{i120} = f_{i1} + c_{Fi1}\left(q_{i1}{}^2 - c_{ANi}\, q_{i2}{}^2\right)$$

with the incremental force

$$f_{i1} = (k_{Fi1}/2)\left(q_{i1} + c_{Qi1} q_{i2}\right) = k_{Fi1}\bar{q}_{i1}, \qquad 2\bar{q}_{i1} = q_{i1} + c_{Qi1} q_{i2} \tag{10}$$

where

$$k_{Fi1} = 4 c_{Fi1} Q_{i10} = 4\frac{F_{i10}}{Q_{i10}}, \qquad c_{Qi1} = c_{ANi}\frac{-Q_{i20}}{Q_{i10}} = \frac{A_{hi2}}{A_{hi1}}\left(\frac{N_{i2}}{N_{i1}}\right)^2 \frac{-Q_{i20}}{Q_{i10}} \ (>0) \tag{11}$$

For $\bar{q}_{i1}$ in eq. (10), from eq. (4) we have

$$\bar{q}_{i1} - \bar{Q}_{i10}{}' c_{Ri1} = \bar{\beta}_{i1} i_1 \tag{12}$$

where

$$\bar{Q}_{i10}{}' = \frac{1}{2}\left(Q_{i10}{}' + c_{Qi1} Q_{i20}{}'\right), \qquad \bar{\beta}_{i1} = \frac{1}{2}\left(\beta_{i1} + c_{Qi1}\beta_{i2}\right)$$

With the relative increment of the magnetic resistance c_{Ri1}, we take a variable z_i as the vertical displacement of the rotor onto the lower side, positive when the rotor approaches a pole leg numbered by $i1$. Then, c_{Ri1} may be approximated by

$$c_{Ri1} \cong -\frac{z_i}{l_{mi10}} \tag{13}$$

The total incremental force of the two stator rings is given by the summation of the forces of eq. (10) with i=1, 2.

LINEARIZED DYNAMICS OF RIGID-ROTOR-SUPPORTING BEARINGS WITH ELECTROMAGNETS OF EQUAL DYNAMICS

We consider a rigid rotor supported by the two radial bearings. To obtain the resultant incremental force and moment acting on the rotor in a simple form, we add the following conditions:

(C4) The two stator rings have equal dimensions with the electromagnetic system in each bearing [$A_{11}=A_{21}$, $A_{12}=A_{22}$, $N_{11}=N_{12}$, $N_{21}=N_{22}$ and $l_{m110}\,(=l_{m120})=l_{m210}\,(=l_{m220})$].

(C5) The dynamical characteristics of the electromagnet systems are equal in each direction (vertical or horizontal) in the two bearings.

Incremental Force

We take the vertical rotor-displacement z at the center of the bearing, and we assume that the effects of the conical displacement on the magnetic resistances are negligible. In this case, from eqs.

(10), (12), (13) and (5) under condition (C4), we obtain the total incremental force of the single bearing as

$$f_1 = k_{F1} q_1, \qquad T_{C1}\dot{q}_1 + q_1 - a_{10} z = \bar{\beta}_{11} b_1 e_1 (t - \tau_1) \tag{14}$$

where

$$k_{F1} = 2k_{F11}, \qquad a_{10} = \frac{Q_{110}'}{2l_{m110}}\left(1 + c_{Q11} c_{Q11}'\right), \qquad c_{Q11}' = \frac{Q_{120}'}{Q_{110}'} \tag{15}$$

In the second of eq. (14) we have omitted a term with $\dot{z}$ by presuming that it is negligible in general. We note that the above relation is formulated with a single stator ring. This is reflected in the factor of the force.

For the horizontal direction, the disturbing term Δq_{i3} in eq. (6) is cancelled out, and the equation is given by a simple form as a special case of the above result with $\bar{\beta}_{11}$=1, $Q_{110}' = Q_{130}$, $c_{Q11} = c_{Q11}'$=1, etc. For the displacement y, we have

$$f_3 = k_{F3} q_3, \qquad T_{C3}\dot{q}_3 + q_3 - a_{30} y = b_3 e_3 (t - \tau_3) \tag{16}$$

Equations of Rigid-Rotor Motion

We number the two bearings by 1 and 2 on the left- and right-hand sides, respectively, and use these numbers in the subscript of the variables if necessary. We take the sense of the rotor displacement to be positive when going down, as in the above, and the sense of the conical motion to be positive when going down more in bearing 1 than in bearing 2. Then, neglecting the gyroscopic effects in the conical motions, we have the equations of the translatory and conical motions of rigid rotor:

$$m\ddot{z} = f_1 + f_2 + d_z, \qquad J\ddot{\theta} = L_1 f_1 - L_2 f_2 + M(d_z) \tag{17}$$

where z is the translatory displacement of the gravity center of rotor, θ the angle of the conical motion, m the rotor mass, J the moment of inertia, L_j the distance between the gravity center of rotor and the bearing center, f_j the net force in the bearing, d_z a resultant disturbing force acting on the rotor, and $M(d_z)$ the resultant moment of disturbing forces.

The variables z and θ are related with the displacements in two bearings in the rigid-rotor motion by

$$z_1 \cong z + L_1\theta, \qquad z_2 \cong z - L_2\theta$$

For the angle of the conical motion, we take the displacement defined by

$$z_C \equiv \frac{1}{2}(z_1 - z_2) \cong L\theta, \qquad L = \frac{1}{2}(L_1 + L_2) \tag{18}$$

In applying eq. (14) to the two bearings with $T_{C1} = T_{C2}$ under condition (C5), we set

$$2e_z = e_1 + c_{ez} e_2, \qquad 2e_{zC} = \frac{L_1}{L} e_1 - \frac{L_2}{L} c_{ez} e_2 \tag{19}$$

where

$$c_{ez} = c_{kFz} \frac{\bar{\beta}_{21}}{\bar{\beta}_{11}} \frac{b_2}{b_1}, \qquad c_{kFz} = \frac{k_{F2}}{k_{F1}}$$

Then, we obtain the following equations.

$$m\ddot{z} = 2k_{F1}q_z + d_z, \qquad T_{C1}\dot{q}_z + q_z - a_z z - \Delta a_z z_C = \bar{\beta}_{11} b_1 e_z (t - \tau_1) \tag{20}$$

$$m_C \ddot{z}_C = 2k_{F1}q_{zC} + d_{zC}, \qquad T_{C1}\dot{q}_{zC} + q_{zC} - a_{zC} z_C - \Delta a_z z = \bar{\beta}_{11} b_1 e_{zC} (t - \tau_1) \tag{21}$$

where

$$m_C = \frac{J}{L^2}, \qquad d_{zC} = \frac{M(d_z)}{L}$$

$$a_z = \frac{1}{2}(a_{10} + c_{kFz} a_{20}), \qquad a_{zC} = \frac{1}{2}\left[\left(\frac{L_1}{L}\right)^2 a_{10} + \left(\frac{L_2}{L}\right)^2 c_{kFz} a_{20}\right]$$

$$\Delta a_z = \frac{1}{2}\left[\frac{L_1}{L} a_{10} - \frac{L_2}{L} c_{kFz} a_{20}\right]$$

There are no interacting terms $\Delta a_z z_C$ and $\Delta a_z z$ in eqs. (20) and (21) in the case of a symmetric bearing system or in a supporting condition (ref. 6); we may neglect them in many cases. Omitting them, we design the control systems of the two motions with the control variables e_z and e_{zC}. To realize the designed control actions, from eq. (19) we assign the actual control inputs into the electromagnets as follows:

$$e_1 = \frac{L_2}{L} e_z + e_{zC}, \qquad e_2 = \frac{1}{c_{ez}}\left(\frac{L_1}{L} e_z - e_{zC}\right) \tag{22}$$

The similar equations of the horizontal direction are given as a special case of the above results.

EXPERIMENTS

Experimental Setup

Figure 3 shows the mechanical part of the experimental set up of the symmetric radial bearings supporting a symmetric rotor in the horizontal direction. The stator and rotor cores are made of silicon steel strips of 0.2mm thickness. The four stator rings of the two bearings are of equal dimensions. The pole legs are of the same size in the horizontal direction and on the lower side in the vertical direction. The pole legs on the upper side are 25% wider than the others, to give a larger permanent magnet flux to suspend the deadweight of the rotor. A sheet of paper was pasted on the pole-leg faces to prevent direct contact with the rotor. The turns in the electromagnet coils are all the same. The connecting segments may be made of solid iron, but we used silicon steel strips, for convenience.

The rotor cores in the shape of a ring have outer and inner diameters of 50mm and 19mm, respectively, and are guided on a shaft of aluminum. The permanent magnet made of neodymium has an outer diameter of 39mm, an inner diameter of 19mm and a thickness of 7mm. Two spacer rings of aluminum are used to adjust the bias flux. We adjusted its density to be about 0.45T in the nominal working airgap length to suspend the deadweight of the rotor without electromagnet bias current. Four displacement sensors of the eddy current type are used to detect the radial displacement of the rotor. The rotation is given by compressed air blown onto teeth in the middle of the shaft. The primary specifications are given in **Table 1.**

The rotor-position control systems are constructed to realize the decoupling control systems, based on eqs. (20)- (22) with parallel analog PID compensators. The input voltage into the power amplifiers is limited to a value of about 4V to give the maximum coil current of 2.4A that is nearly equal to the

value of current cancelling the bias flux with the nominal working airgap. The gains of the compensators were adjusted experimentally with a sinusoidal input of amplitude 1V in a similar way to the measurement of frequency response shown later. The selected gains gave a phase margin of 32 deg. at 180 Hz and a gain margin of 10dB at about 510Hz in the vertical translatory control system, and 44 deg. at about 200Hz and 9dB at 590Hz, respectively, in the vertical conical control system. We gave similar margins to the horizontal control system.

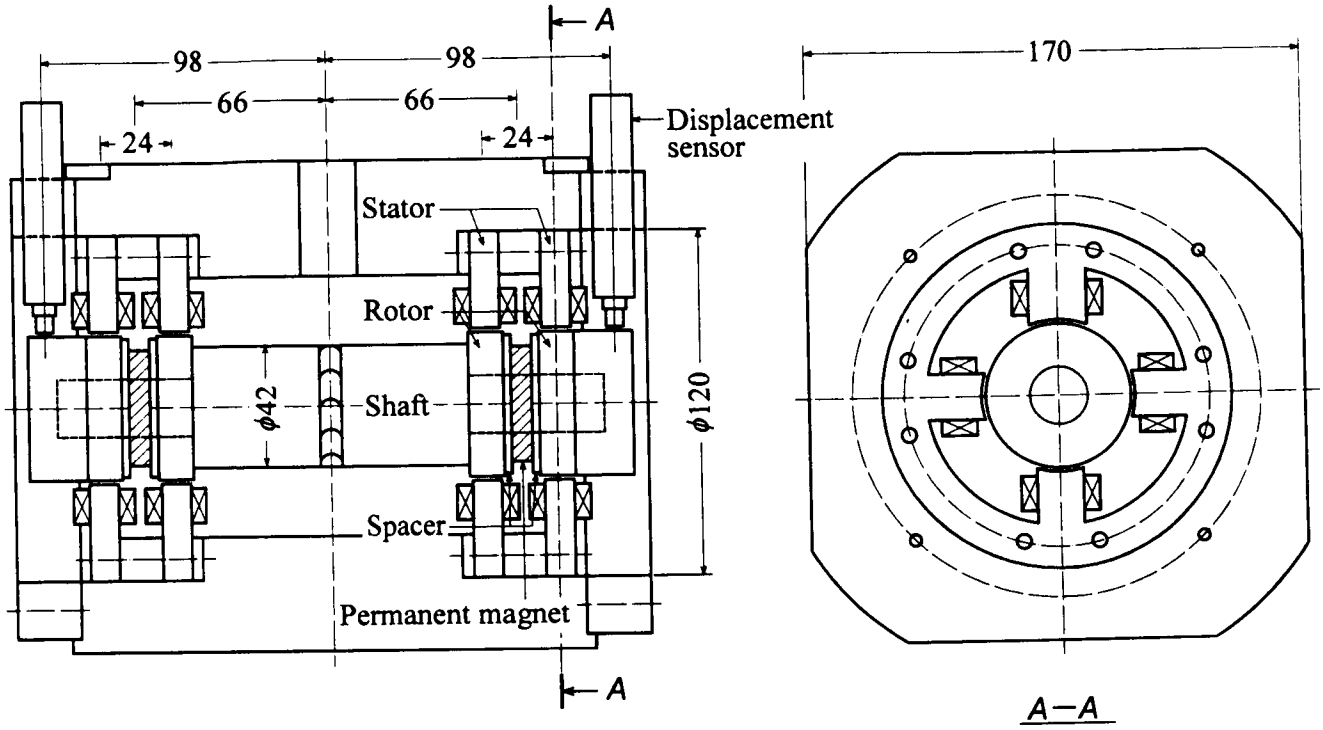

Figure 3. Experimental setup of active magnetic bearings biased with permanent magnets on the rotor.

Frequency Responses of Rotor Motion

In the non-rotating state, we measured frequency responses of the rotor displacement to a non-biasing sinusoidal signal superimposed on the control input of the decoupled control systems: for example, in eq. (20)

$$e_z = \bar{e}_z + e_0 \tag{23}$$

where $\bar{e}_z$ is the control input of the translatory motion and e_0 is the sinusoidal input. **Figure 4** shows by the solid lines the response of the vertical translatory control system with an input amplitude of 1V. The maximum gain at about 35Hz corresponds to a displacement amplitude of 0.12mm. With input amplitude 2V, we obtained a gain response that is very close to this response but slightly lower around the frequency giving the maximum gain (the maximum amplitude is 0.21mm).

Figure 5 shows the response in the vertical conical control system with an amplitude of 1V; the maximum displacement amplitude is estimated to be 0.13mm at about 25Hz. We had a very close response to the amplitude of 1.5V with the maximum amplitude of 0.18mm.

Table 1 Specifications and Data of Experimental Setup

Rotor : Mass		$m = 1.35$	kg
Outer diameter		$D = 50.0\times10^{-3}$	m
Moment of inertia of conical motion		$J = 56.7\times10^{-4}$	kgm^2
Polar moment of inertia		$J_p = 3.94\times10^{-4}$	kgm^2
Distance between bearing centers		$2L_1 = 132\times10^{-3}$	m
Distance between two gap sensors		$2L_{m1} = 196\times10^{-3}$	m
Stator			
Cross-sectional area of pole leg : Upper		$A_{hi2} = 2.0\times10^{-4}$	m^2
Others		$A_{hij} = 1.6\times10^{-4}$	m^2
Working airgap length		$l_{ij0} = 0.6\times10^{-3}$	m
Displacement sensor gain : Translatory		$k_{ST} = 5.0\times10^3$	V/m
Conical		$k_{SC} = 7.4\times10^3$	V/m
Permanent magnet : Bias flux density in airgap		$B_0 = 0.441$	T
Equivalent coil current		$Q_{Bij} = 2.14$	A
Recoil permeability		$\mu_r = 1.0$	
Electromagnet : Turns of coil		$N_{ij} = 100$	
Gain of power amplifier		$b_1 = 0.61$	A/V
Relative permeability of magnet core		$\mu_S = 5{,}000$	
Calculated data			
Bias coil current :	Vertical	$I_{10} = -0.01$	A
	Horizontal	$I_{30} = 0$	A
Bias force :	Lower	$2F_{110} = 24.6$	N
(Single bearing)	Upper	$2F_{120} = 31.2$	N
	Horizontal	$2F_{130} = 24.8$	N
Force constant :	Vertical	$k_{F1} = 46.0$	N/A
(Single bearing)	Horizontal	$k_{F3} = 46.2$	N/A
Instability constant :	Vertical	$a_z = a_{zC} = 3{,}960$	A/m
	Horizontal	$a_y = a_{yC} = 3{,}510$	A/m
Constant		$\bar{\beta}_{11} = 1.12$	A/V
Time constants : Time constant of coil current		$T_{C1} = 0.10\times10^{-3}$	s
Dead time of power amplifier		$\tau_1 = 0.02\times10^{-3}$	s

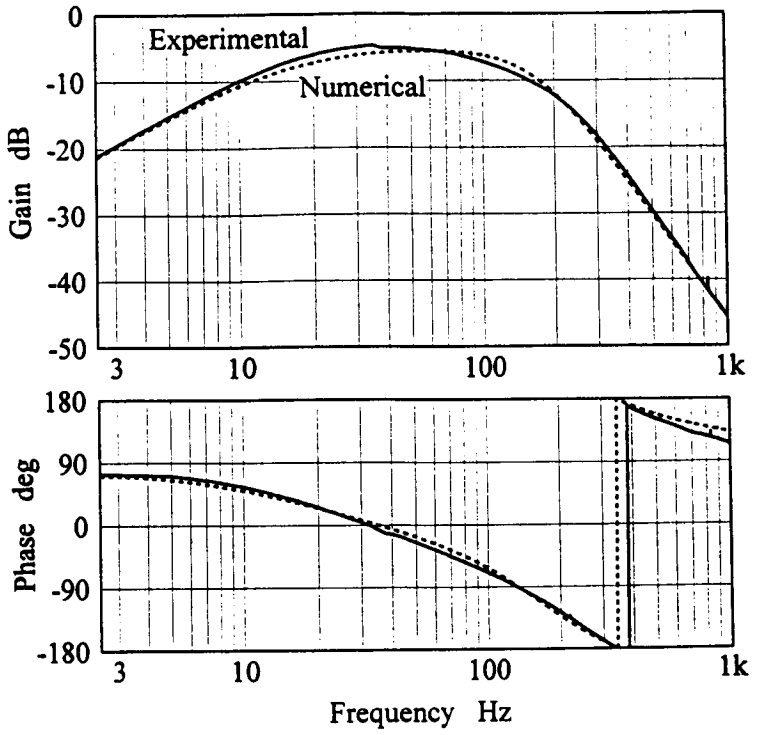

Figure 4. Frequency response of translatory rotor motion.

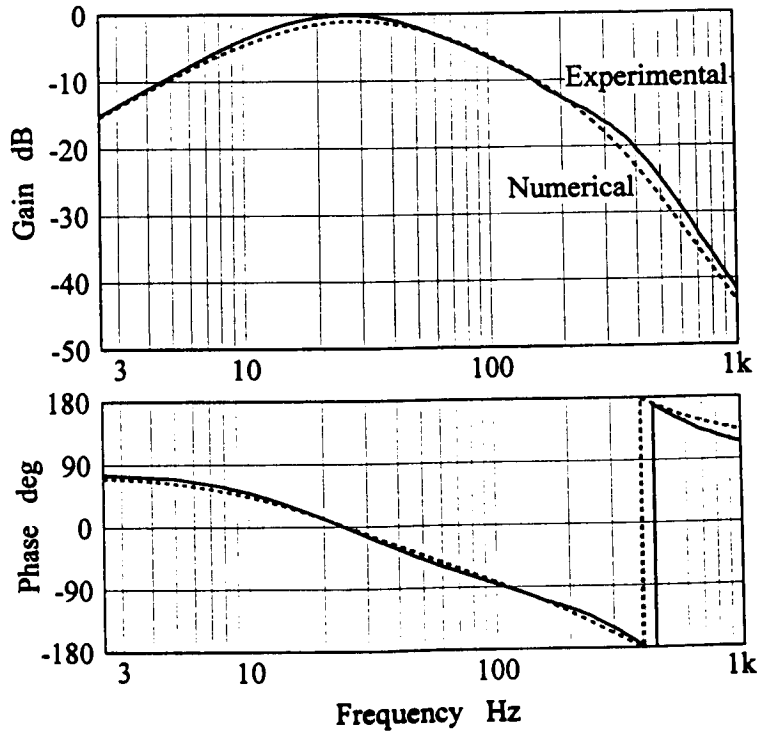

Figure 5. Frequency response of conical rotor motion.

Numerical Results of Frequency Responses

The permanent-magnet flux density was 0.441T on average in the measurement with the nominal airgap. This value is used to calculate the equivalent bias current of eq. (3) and the bias force of eq. (8); we take a value of 5,000 for the relative permeability of the magnet cores. Then, the constants in eqs. (20) and (21) are calculated as in Table 1 when we neglect the electromagnetic flux axially passing through the rotor and the connecting segments ($R_R + R_B = \infty$). In this case, statically, the electromagnetic flux bypassing the horizontal pole legs is calculated to be about 12% of the flux of the vertical lower pole leg, i.e., the flux on the upper side is about 12% more than that on the lower side. The measured values were about 7% and 15%, respectively (the difference of 8% seems to have taken other paths). The time constants of the electromagnet system in eq. (5) are identified from the frequency characteristics of the coil current with the fixed nominal-airgap. We obtained a very good approximation to the characteristics whose values are shown in the lowest part of Table 1.

The numerical frequency responses of eq. (20) with the input of eq. (23) and eq. (21) with the similar input are drawn by the broken lines in Figs. 4 and 5. The gain response of the translatory motion is a little different from the experimental result in the frequencies of about 10Hz to 200Hz, but very close above 200Hz. About the conical motion, there is a little difference under 50Hz and a larger difference above 200Hz. We presently have no idea about these differences.

From the numerical analysis, we see that the gain characteristics depend mainly on the gains of the compensator, in particular, the integral action's gain, in lower frequencies, on the instability constant, a_z or a_{zC}, in the intermediate frequencies, and on the force constant, k_{Fi}, in higher frequencies. We can obtain the gains of the compensator, so that we have good agreement in the lower frequencies.

Transient Motion to Impact

Figure 6 shows the translatory rotor motion and the actual control input into the power amplifier for a vertical impulsive force that directly acts at the center of the shaft in the non-rotating state. The maximum displacement of about 0.4mm is about 70% of the nominal working-airgap length; the rotor was regulated in about 20ms. The input into the power amplifier was attenuated by a factor of 0.69, and the maximum input was designed to be about 2.8V(4 × 0.69). The constant b_1 in Table 1 is given by the series attenuation of this factor and the static gain of the coil current to the input, 0.89.

Decay of Rotation and Whirling of Rotor

We ran the rotor up to 25,000rpm. **Figure 7** gives a decay of rotation due to magnetic braking with air friction without driving. From 25,000rpm the rotation decreases to 1,000rpm in about 5.4min and to zero in about 6.3min. The decay is approximated by the curve given by the equation

$$\dot{\omega} + 3.5 \times 10^{-3}\omega + 2.5 \times 10^{-6}\omega^2 = -1.85, \quad \omega : \text{rad/s} \tag{24}$$

We observed the whirling of the rotor together with the rotation decay. The amplitudes in the vertical and horizontal directions are shown in **Fig. 8.** The whirling is larger in the horizontal direction than in the vertical direction above 16,000rpm, but smaller below it. We had not checked the rotor balancing and had seen that there was an installation error of the sensor target rings for displacement sensing. We suppose these are reasons why the whirling is relatively large.

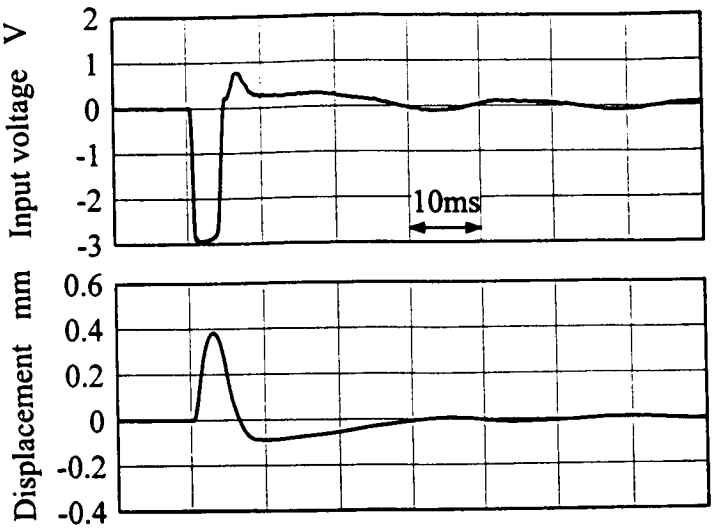

Figure 6. Transient motion to impact.

CONCLUSIONS

We considered the characteristics of the radial magnetic bearings biased with permanent magnets arranged on the rotor. First, we presented a simple linearized model of control force that is similar to that of the all electromagnetic design. Second, in the non-rotating state, we measured the frequency responses of the rotor positioning control and compared those with the numerical results to check the validity of the simple model. We also gave the transient displacement of the rotor for impact directly acting on the rotor. Last, we examined the decay of the rotation mainly due to magnetic braking with the whirling of the rotor. The data obtained show the characteristics similar to those of the all electromagnetic design.

The construction of electromagnets with opposing coils in a series connection gives a property that the time constant of the electromagnet system does not vary so much with working airgap length. This construction may be adopted in the all electromagnetic case as in ref. 7, for example, but may be uncommon to these applications at present. While this construction may lead to the interactions of the magnetic systems, we have not encountered a serious problem in our experiments.

We thank the Nippon Steel Corp. for supplying us the silicon steel strips. We also acknowledge Mr. Fujino, S. for machining the experimental setup, and Undergraduate students Watanabe, T. and Yanai, N. for help in assembling the setup and in the experiment.

REFERENCES

1. *NASA Tech. Brief*, B74-10131, Sept. 1974.

2. *Design News*, 6-11-90, p.156.

3. Allaire, P. E.; *et al*.:: Permanent Magnet Biased Magnetic Bearings-Design, Construction, and Testing, *Proc. 2nd Inter. Sympo. Magnetic Bearings*, pp.175-182, Tokyo, June 1990.

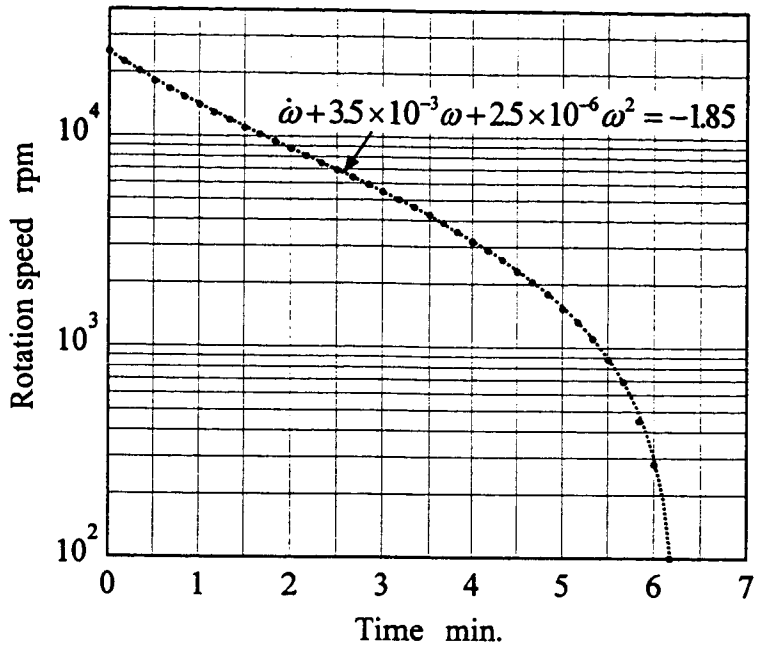

Figure 7. Decay of rotation.

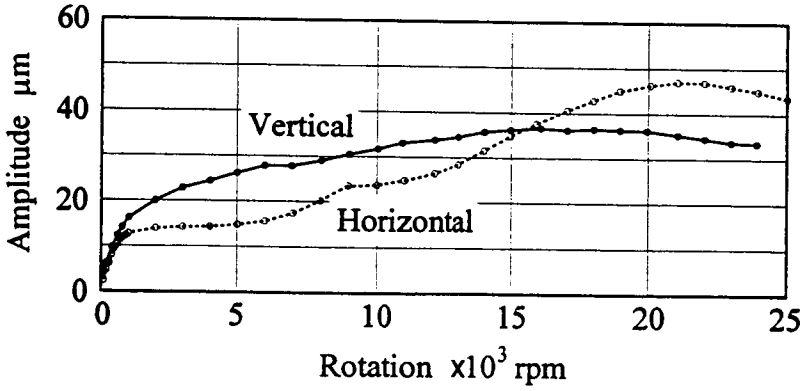

Figure 8. Amplitude of whirling of rotor.

4. Fukata, S.; and Yutani, K.: Dynamics of Permanent-Magnet Biased Active Magnetic Bearings, *Proc. 3rd Inter. Sympo. Magnetic Suspension and Technology,* Part 2, pp. 721-736, July 1996.

5. Fukata, S.; and Yutani, K.: Analysis of Magnetic systems of Magnetic Bearings Biased with Permanent Magnets, *Memoirs of Fac. Engg., Kyushu Univ.*, Vol.57, No.1, pp.17-35, March, 1997.

6. Fukata, S.; and Kouya, T.: Control Systems of Active Magnetic Bearings Based on Decoupling of the Motion of Rigid Rotor, *Technology Report of Kyushu Univ.* (in Japanese), Vol. 60, No. 2, pp.185-191, 1987.

7. Ozeki, et al., Magnetic Bearings Supporting Spindles, *Bearing Engineer* (in Japanese), No. 51, p.55, 1985.

Session 8 -- Modeling 1

Chairmen: Colin P. Britcher, Old Dominion University (ODU)
Atsushi Nakajima, National Aerospace Laboratory (NAL)

A NEW MODEL BASED METHOD FOR THE ACCURATE MEASUREMENT OF MAGNETIC BEARING FORCES

Michael Matros
Institute of Mechatronics
University of Darmstadt, Germany

Joachim Sobotzik
Institute of Mechatronics
University of Darmstadt, Germany

Rainer Nordmann
Institute of Mechatronics
University of Darmstadt, Germany

SUMMARY

Active magnetic bearings (AMB) are typical mechatronic systems. Their employment in rotating machinery offers the possibility for active control of the dynamics of the shaft as well as use as a diagnosis tool. The use of an AMB can make turbomachinery safer and more efficient. In many cases an accurate knowledge of the bearing forces is demanded. A specific example where this topic is relevant is briefly described in this paper. It is a test-rig which was designed for the identification of physical parameters such as stiffness, damping and inertia coefficients of journal bearings, annular seals and others. The AMB are used as exciters in order to apply an artificial and controlled motion on a test shaft. For the identification of the unknown coefficients, it is necessary to measure time dependent displacements and forces, which are acting on the moving shaft, with sufficient accuracy. The measurement of the shaft movement, e.g. by eddy current sensors, with very low errors is state of the art whereas the determination of the bearing forces with high accuracy takes much more effort. A very simple and cheap possibility is based on the measurement of bearing coil currents and the air gap between rotor and magnet (i-s-method). The main advantage of this approach is that no additional sensor devices other than the ones which are required for the control system of the AMB, are necessary. But this method has the disadvantage of neglecting eddy current losses as well as hysteresis and saturation effects of the core material. Hence the measured force is polluted by an error of amplitude and phase with unknown quantities. Due to lamination of the magnets and the magnetized parts of the shaft in combination with comparatively low rotational speeds and excitation frequencies, eddy current losses are of less importance and the error is dominated by the hysteresis. The characteristic of the force error by using the i-s-method is shown by theory and with experimental help. In addition to that, the paper presents a new method that allows a prediction and, hence, correction of errors due to hysteresis and saturation effects. It is based on a model by which the hysteresis of the core material can be simulated. The results of the model are verified by measurements. In a specific test, it is shown

that the error of the force measurement can be reduced from 9% down to 1.5% in amplitude. The phase shift due to hysteresis losses is shown to be less than 2° for the core material used in the test-rig. Hence the capability of the method is proven, which allows a much more accurate identification of rotordynamic coefficients with the test rig. In addition to that, it offers the possibility of precise, simple and cheap force measurement in any machinery where AMB are used for shaft support.

INTRODUCTION

Figure 1 shows a test rig which is designed for the identification of rotordynamic parameters, such as stiffness, damping and masses. The knowledge of these coefficients allows a comprehensive description of the dynamic characteristics of components which are used in fluid handling machinery. The test results of a long annular seal, an impeller and a hydrostatic bearing have been published up to now. Those results can be used for deepening the knowledge about the behavior of the components themselves and their influence on the rotordynamics of the whole turbomachine. The rest rig uses active magnetic bearings (AMB) for rotor support. In parallel, the AMB-system is used to apply a well defined relative motion between rotor and stator, by which the fluid forces in the test-component are generated. In order to identify the rotordynamic coefficients, it is necessary to measure displacements and forces simultaneously. The measurement of displacements is done by eddy current probes with an accuracy of 1% or better.

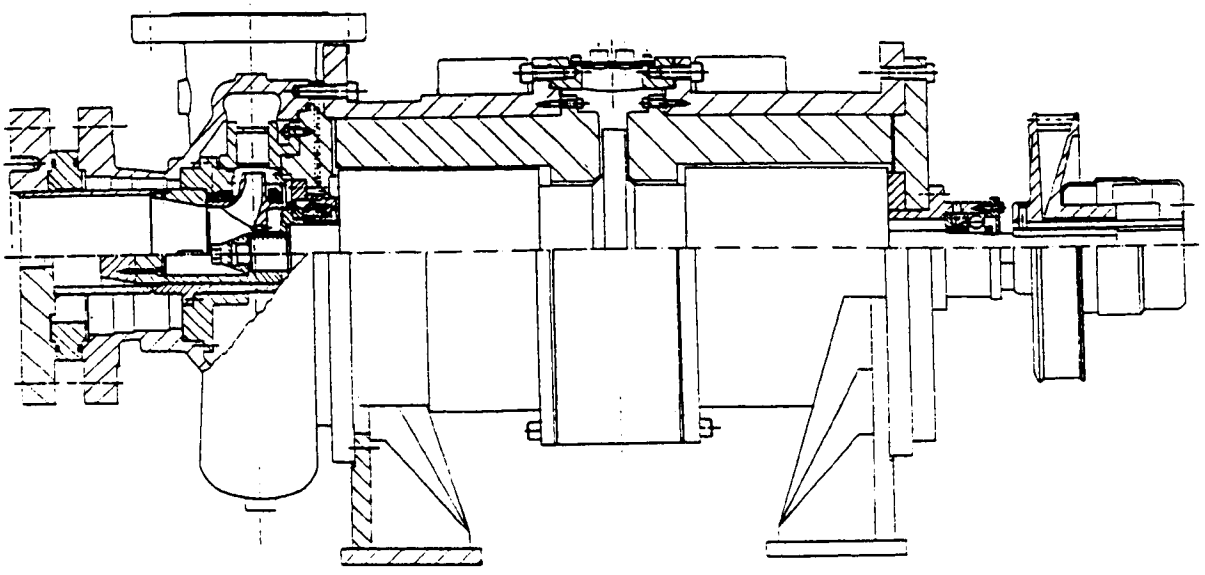

Fig. 1: Sectional drawing of a AMB Component Tester used for identification of physical parameters

The forces are measured indirectly by using values from the magnets. The force, which is acting on the shaft due to a single magnet as shown in Fig. 2, can be calculated from the change of the magnetic field energy in the air gaps. Assuming a homogenous magnetic field in the air gaps and neglecting stray fluxes yields the single force f.

$$f_{real} = \frac{\Phi_L{}^2}{A \cdot \mu_0} \cdot \cos\alpha \quad = \quad \frac{B_L{}^2 \cdot A}{\mu_0} \cdot \cos\alpha \qquad (1)$$

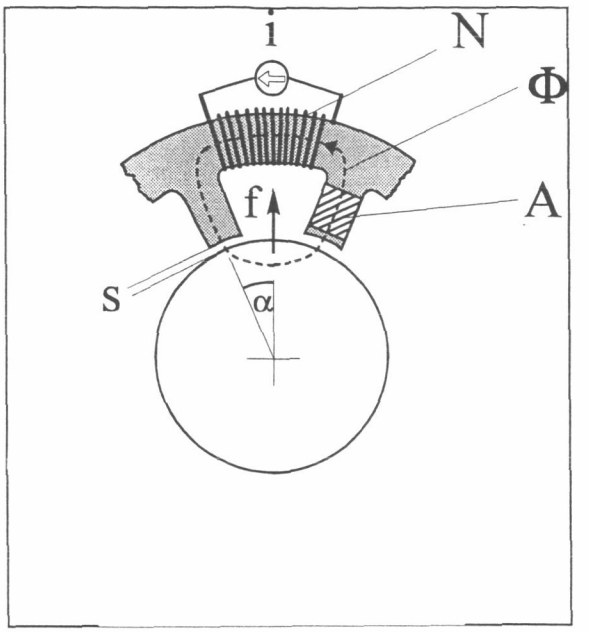

Figure 2: Single magnet of a radial magnetic bearing

The flux density B_L can be substituted by the magnetic field strength H_L.

$$B_L = \mu_0 \cdot H_L \qquad (2)$$

Introducing the formulation for H_L as follows

$$H_L = \frac{1}{2 \cdot s} \cdot \left(N \cdot i - l_{FE} \cdot H_{FE}\right) \qquad (3)$$

allows a formulation for the single force f according to equation (4).

$$f_{real} = A \cdot \mu_0 \cdot \cos\alpha \cdot \frac{1}{4 \cdot s^2} \cdot \left(N \cdot i - l_{FE} \cdot H_{FE}\right)^2 \qquad (4)$$

This formulation contains, besides known geometrical and material dependent values, the coil current I and the air gap s, which are measurable physical values. The magnetic field strength in the laminated core H_{FE} is unknown and not possible to measure. Hence it is neglected, which finally gives a basic equation where the force of a single magnet can be calculated from i and s. Therefore, we call it the i-s-method. The resulting force is not the real force but an indirectly measured force, including error.

$$f_m = \frac{1}{4} \cdot A \cdot \mu_0 \cdot \cos\alpha \cdot N^2 \cdot \frac{i^2}{s^2} \qquad (5)$$

ERRORS DUE TO THE I-S METHOD

Now the consequences of neglecting the field strength in the core material are demonstrated again for a single magnet. The combination of eq. (4) and (5) yields an expression which represents the difference between the measured force by the i-s-method and the real force. Hence it is formulation for the force measurement error.

$$\left(\sqrt{f_m} - \sqrt{f_{real}}\right) = \frac{1}{2 \cdot s} \cdot \sqrt{A \cdot \mu_0 \cdot \cos\alpha} \cdot l_{FE} \cdot H_{FE} \qquad (6)$$

It appears that the measured force is always higher than the real force. It is simple to understand, because the measured coil is not completely transformed in a magnetic force. A part of it has to be used for magnetization of the iron, which is neglected by the i-s-method. It is also obvious now that the force measurement error must be dependent on the properties of the core material and on the real magnetic force because H_{FE} is related to the flux density in the core B_{FE}, which again is related to the real force as it is shown in eq. (7). Hence the characteristics of H_{FE} over B_{FE} is given by a hysteresis loop, which is determined by the material used.

$$\sqrt{f_{real}} = \sqrt{\frac{A \cdot \cos\alpha}{\mu_0}} \cdot B_{FE} \qquad (7)$$

Figure 3 shows the outer hysteresis loop of the material used for the bearings, without the virgin curve.

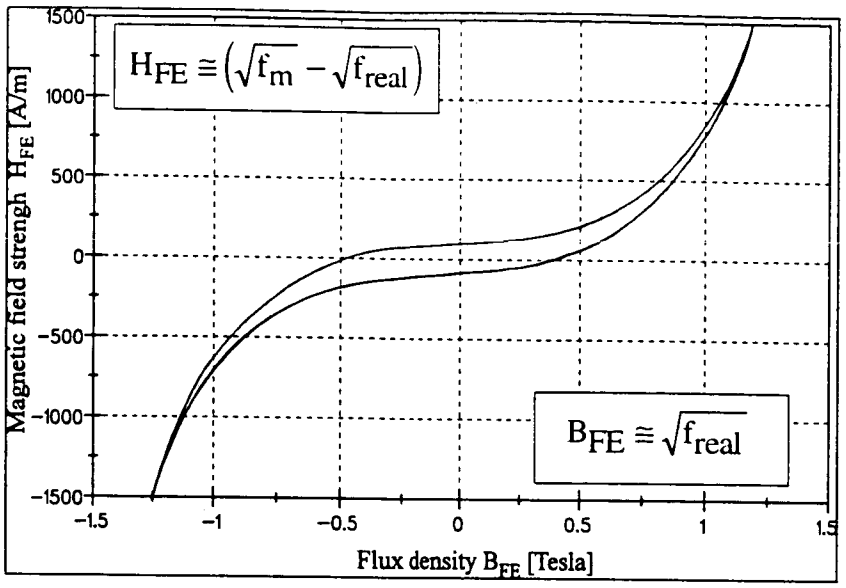

Figure 3: ***Characteristic*** *hysteresis loop of laminated core material*

Following the expressions of eq. (6) and (7) the difference between i-s-measured force and the real force, hence the force measurement error, must have the same characteristic dependence on the real force as is shown in figure 3. This has been proven by an experiment with the test rig. The net real force is measured by calibrated load cells and the i-s-method yields the net measured force. The result for one pair of magnets acting in opposition to each other is presented in figure 4. It shows the typical error characteristic depending on the bearing load. Equation (6) shows that the force measurement error also depends on the air gap s. By calibration this dependence can be eliminated with an electronic circuit. It also has to be noted that the major loop in figure 4 results from two minor loops from both single magnets.

The function f(B) is a formulation of the hysteresis curve and g(B) determines the thickness of the loops. The formulation used is restricted to the points where the upper and the lower curve meet each other, i.e. the case of complete saturation is not treated.

$$f(B) = A_1 \cdot \tan(A_2 \cdot B) \qquad \text{for } |B| \le B_s \tag{9}$$

$$g(B) = \frac{df}{dB} \cdot \left[1 - A_3 \cdot \exp\left(\frac{A_4 \cdot |B|}{B_s - |B|} \right) \right] \qquad \text{for } |B| \le B_s \tag{10}$$

The coefficients A1 ... A4 are calculated iteratively. The characteristic values for the remanent flux density the coercive field strength and the gradients O_i are known for the core material in the bearings.

$$2 \cdot A_2 \cdot \mu_s \cdot H_s = \sin(2 \cdot A_2 \cdot B_s) \tag{11}$$

$$A_1 = H_s \cdot \cot(A_2 \cdot B_s) \tag{12}$$

$$B_s = \frac{1}{A_2} \cdot \operatorname{acos} \sqrt{A_1 \cdot A_2 \cdot \mu_s} \tag{13}$$

$$A_3 = 1 - \frac{1}{A_1 \cdot A_2} \cdot \left(\frac{1}{\mu_c} + \gamma \cdot H_c \right) \tag{14}$$

$$A_4 = \frac{B_r - B_s}{B_r} \cdot \ln\left[\frac{1}{A_3} - \frac{\cos^2(A_2 \cdot B_r)}{A_1 \cdot A_2 \cdot A_3} \cdot \left(\frac{1}{\mu_r} + \gamma \cdot A_1 \cdot \tan(A_2 \cdot B_r) \right) \right] \tag{15}$$

Integration of eq. (8) yields two integral equations, which allows a description of each point of the outer B-H-curve between upper and lower boundaries. The upper and the lower curves of the loop are formulated separately.

$$H_u(B) = f(B) + e^{-\gamma \cdot B} \cdot \int_{-B_{max}}^{B} \left[g(\xi) - \frac{df}{dB}(\xi) \right] \cdot e^{\gamma \cdot \xi} \, d\xi \tag{16}$$

$$H_d(B) = f(B) - e^{\gamma \cdot B} \cdot \int_{B}^{B_{max}} \left[g(\xi) - \frac{df}{dB}(\xi) \right] \cdot e^{-\gamma \cdot \xi} \, d\xi \tag{17}$$

The inner loops of the hysteresis are given by eq. (18) and (19):

$$H_{iu} = f(B) + \cosh\left[\gamma \cdot (B_{min} - B)\right] \cdot \int_{B_{min}}^{B} \left(g(\xi) - \frac{df}{dB}(\xi) \right) \cdot \sinh\left[\gamma \cdot (B_{min} - \xi)\right] d\xi \qquad (18)$$

$$H_{id} = f(B) - \cosh\left[\gamma \cdot (B - B_{max})\right] \cdot \int_{B_{max}}^{B} \left(g(\xi) - \frac{df}{dB}(\xi) \right) \cdot \sinh\left[\gamma \cdot (B_{max} - \xi)\right] d\xi \qquad (19)$$

With the help of equations (1), (4), (5) and the hysteresis equations (16) to (19) the related real magnetic force, which is applied to the shaft by a pair of magnets, can be correlated to the measured force by the i-s-method. Hence, the force error due to neglecting the magnetization of the iron can be calculated.

RESULTS

The measured force error loop from fig. 4 is used to tune the free parameters of the model. It represents the outer hysteresis loop, which is given by eq. (16) and (17). The comparison between simulated and measured results for one pair of radial magnets is shown in figure 5 on the left-hand side.

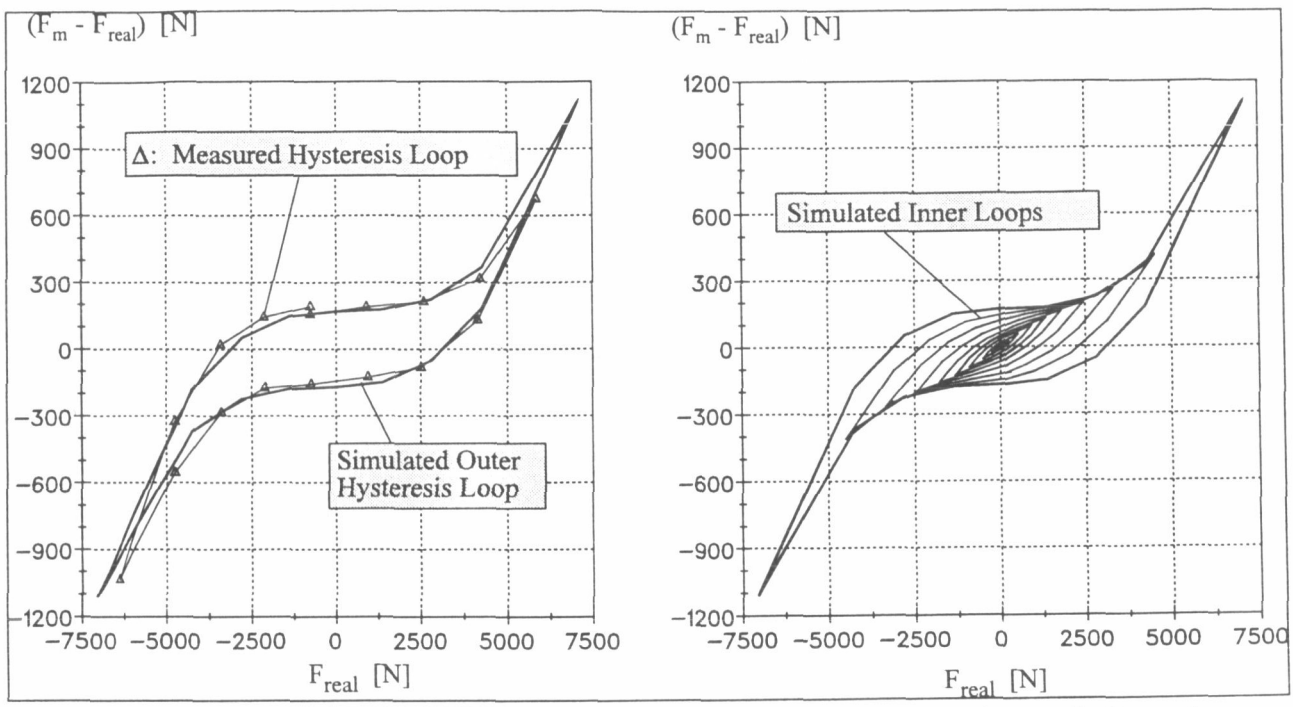

Fig. 5: Correlation of measured and simulated force error ***hysteresis*** *loops (left) and simulated inner loops (right) of one pair of radial magnets*

Specifically in the working range of the magnets there is a very good correlation between theory and experiment. The difference at higher force levels may be the result of incipient saturation of the amplifiers of the magnets.

On the right side of figure 5, some simulated inner loops are presented. Those loops are the basis for calculating the force errors for any desired force amplitude. The end points of the inner loops are drifting away from the outer one when there are no effects from saturation anymore. This results in a minimum of force error at 3200 N force level (see fig. 6). The increase of error for lower real forces is due to the stronger contraction of the loop on the F_{real}-axis.

It should be realized that the i-s force measurement method leads to an error in force amplitude of at least 5.8% for each pair of magnets. Tremendous deviations are expected when the full saturation of the material is reached. In addition to that, it has to be recognized that low force levels result in errors of about 10% for one pair of magnets.

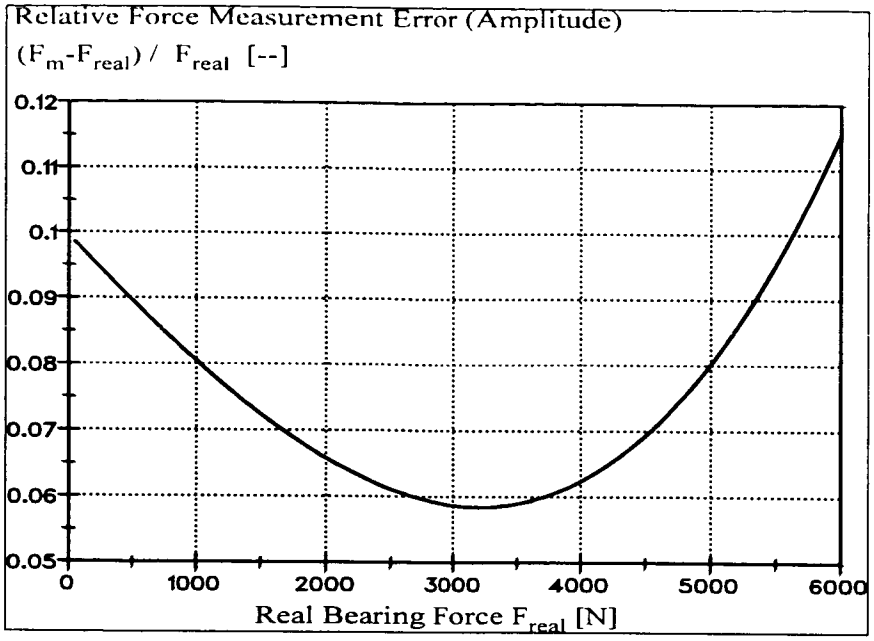

Fig. 6: Model based calculated relative force measurement error due to hysteresis

APPLICATION AND VERIFICATION

In order to test and verify the method, a specific test setup was created, where the AMB test-rig was used for identification of the well known bending stiffness of a clamped beam in the way as described, for example in [1]. In a simplified sketch, figure 6 shows the test configuration.

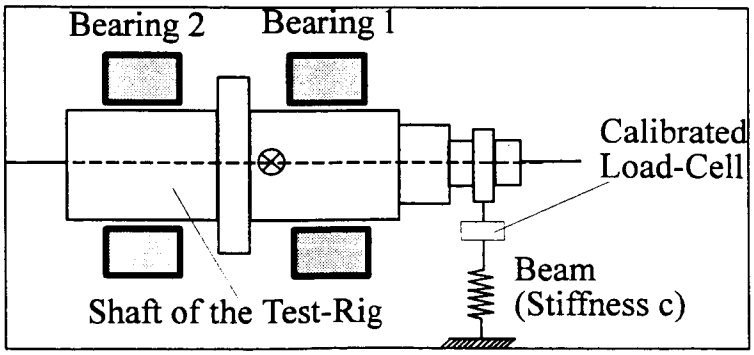

Fig. 6: Sketch of the test configuration for identification of a stiffness

The measured forces at bearing 1 and 2 together with the artificial pure lateral shaft motion are in direct correlation with the beam stiffness c. An additional load cell is used for reference.

The stiffness identified by the load cell is identical to the analytically calculated value of 4.58 MN/m. Using the bearing forces delivered by the i-s-method for identification results in a stiffness of 4.95 MN/m. Hence it is 8% higher than the real value. The application of the model

based error calculation first needs the real forces at the magnetic bearings, which are accurately determined from geometrical values, the mass of the shaft and the real stiffness c of the beam. At bearing 1 there is a force magnitude of F1=237 N and at bearing 2 only F2=53 N is reached. The hysteresis model delivers theoretical relative errors in amplitude of F1=9.5% and F2=9.8%. Hence this theory forecasts a relative error of the stiffness of +9.4%. It has to be noted that for this application the magnitude of the bearing forces are quite low. In spite of that, the result of the error calculation is very close to reality.

SUMMARY AND CONCLUSIONS

It has been demonstrated that the characteristic error of applying the i-s-method for measuring AMB-forces is based on the hysteresis of the magnetized core material. With help of a hysteresis model it was possible to simulate the force error characteristic of a radial bearing used in a test-rig. The method was verified by a specific test.

It has to be noted that the model still does not fully match reality. First of all the rotation of the shaft, which also causes losses in the rotor material, is not included. Furthermore, the effect of frequency dependence on the hysteresis curves was only estimated in this case. All these effects are taken into account by measuring the magnetic flux. The application of Hall Sensors allows force calculations with an accuracy of up to 1.5% for static and 5.5% for dynamic forces.

However, the i-s-method could be applied without additional hardware on existing magnetic bearings and the hysteresis calculation allows a much more accurate identification of physical parameters with help of the AMB's.

REFERENCES

1. Coleman, B.D., Hodgdon, M.L. 1987. , On a Class of Constitutive Relations for Ferromagnetic Hysteresis", Arch. Rational Mech. Anal., 99, No. 4, pp. 375-396

2. Hodgdon, M.L 1988. , Mathematical Theory and Calculations of Magnetic Hysteresis Curves", IEEE Transactions on Magnetics, Vol. 24, No 6, pp.3120-3122

3. Matros, M., Neumer, T. and Nordmann,R. 1994. , Identification of Rotordynamic Coefficients of Centrifugal Pump Components Using Active Magnetic Bearings", Proceedings of the ISROMAC-5, Kaanapali, USA

4. Matros, M., Ziegler, A. and Nordmann, R. 1995. , Fluid Structure Interactions in Annular Seals of Centrifugal Pumps", STLE Tribology Transactions, Vol. 38, pp. 353-363.

APPLICATION OF SELF-SENSING MAGNETIC SUSPENSION TO A LINEAR CARRIER SYSTEM

Takeshi Mizuno
Department of Mechanical Engineering, Saitama University,
Urawa, Saitama, Japan

Eiichi Kitahara
Nissan Motor Co., Ltd.
Tochigi, Japan

Kenji Araki
Saitama University
Urawa, Saitama, Japan

SUMMARY

A magnetically suspended linear carrier system is developed which has electromagnets for suspension on the stator. The electromagnets are used not only for force generation but also for gap sensing so that sensors to be placed along the tracks can be omitted. Permanent magnets for power saving are built in the carrier so that the number of permanent magnets are reduced, compared to systems with permanent magnets in the stator. The virtually zero power suspension is automatically accomplished by applying the observer-based self-sensing suspension method. This paper describes the basic configurations of the developed magnetically suspended carrier system, and demonstrates experimental results on the self-sensing suspension.

INTRODUCTION

Magnetic suspension systems have many advantages over conventional mechanical suspensions:

- no mechanical contact,
- absence of lubrication,
- no contamination due to wear.

Therefore, they are particularly suitable for vacuum and clean-room environments. However, they generally are more costly and need larger space than mechanical suspensions. These are critical obstacles to widening their application fields. The self-sensing or sensorless operation is a promising method of removing these obstacles because it enables the omission of displacement sensors (ref. 1-3).

This paper applies the self-sensing magnetic suspension to a magnetically suspended linear carrier system. The developed system has electromagnets for suspension on the stator. Conventional systems of this configuration have problems related to the measurement of suspension gaps. When probe type gap sensors such as eddy current type sensors are placed on the carrier, wiring or wireless signal transmission from the carrier is necessary. Otherwise, a lot of sensors must be placed along the tracks on the stator; this causes high cost in manufacturing and leads to a time-consuming job in calibrating the sensors. This problem can be overcome by using the self-sensing or sensorless magnetic suspension. The combined use of the electromagnets as actuator and sensor can avoid placing many sensors along the tracks.

One of the promising methods of minimizing the energy required to suspend the carrier is to use hybrid magnets, composed of electromagnets and permanent magnets, and to control the electromagnets to maintain air gap length so that the attractive force by the permanent magnet balances the total weight of the carrier (*virtually zero power* suspension) (ref. 4, 5). However, many permanent magnets are necessary in the carrier systems where the suspension magnets are placed on the stator if conventional hybrid magnets are used. In the developed system, permanent magnets are built in the carrier so that the number of permanent magnets are minimized. Moreover, the virtually zero power suspension is automatically accomplished by applying the observer-based self-sensing suspension methods (ref. 3).

This paper describes the basic configurations of the developed magnetically suspended carrier system, and demonstrates some experimental results of the self-sensing suspension.

DESIGN CONCEPTS

Classification of Conventional Linear Suspension Systems

A number of electromagnetic linear suspension systems of the active type have been developed (ref. 6). Most of them are classified into two types as shown in **Fig. 1.**

(a) Electromagnets and sensors for suspension are put on the carrier (type I),

(b) Electromagnets and sensors for suspension are placed in the stator (type II).

The configuration of (a) has an advantage in cost because of the numbers of electromagnets and sensors necessary for suspending a carrier are independent of the length of the tracks. However, it has a problem of power supply for suspension. Wiring to the carriage causes contamination and also entanglement. Building a battery in the carrier (ref. 5) makes the carrier heavier; the necessity of recharging the on-board battery is also a practical problem.

The configuration of (b) has no such problems related to power supply. However, the numbers of electromagnets and sensors increase in proportion to the length of the track. Placing probe type sensors along the tracks on the stator causes high cost in manufacturing and time-consuming work in calibrating them. The main purpose of this paper is to overcome this problem by using the self-sensing magnetic suspension.

Permanent Magnets for Virtually Zero Power Suspension

The virtually zero power suspension is very effective for power saving, where permanent magnets supply an attractive force balancing the total weight of the carrier with its loads (ref. 5). The conventional zero-power systems use a hybrid magnet which is composed of electromagnets and a permanent magnet as shown in **Fig. 2(a).** However, a lot of permanent magnets are necessary in linear carrier systems of type I when the conventional hybrid magnets are used. The configuration shown in **Fig. 2(b)**, where permanent magnets are built in the carrier, enables the number of permanent magnets to be reduced.

Both the configurations shown in Fig. 2 have a problem that the coil current must overcome the reluctance of the permanent magnet in addition to the air-gap reluctance. **Figure 3** shows a schematic of the configuration of a hybrid magnet developed in this research. The magnetic circuit is designed so that the coil current primarily overcomes only the air-gap reluctance although a permanent magnet is built in the carriage.

Self-Sensing Suspension

In the developed linear carriage system, gap sensors to be placed along the track are omitted by the combined use of electromagnets as force generator and position sensor. These are two categories of such self-sensing methods:

(1) using observer-based controller (ref. 1-3),

(2) superimposing a high-frequency alternating excitation (ref. 7-9).

Method (1) utilizes the controllability and observability of voltage-controlled magnetic suspension systems in which only the coil currents are sensed. The procedures of the control system design follow the classical state-space approach. First, a state feedback controller is designed on the assumption that all the state variables, *i.e.* displacement, velocity and coil currents, are detected. Next, an observer is constructed for estimating all the states from the measured coil currents. Finally, the estimated signals produced by the observer are used in the feedback controller instead of the actual states.

This type of self-sensing magnetic suspension system has a unique characteristic. The stationary values of the coil currents are independent of static load force acting on the suspended object, the power dissipation in the coils automatically becomes zero if the bias flux is provided by permanent magnets. This means that the virtually zero power control is automatically achieved in self-sensing suspension systems (ref. 3) while more sophisticated control algorithms are necessary for the zero power suspension in conventional magnetic suspension systems with displacement feedback (ref. 4, 5). In this research, therefore, method (1) is applied for realizing self-sensing suspension.

DEVELOPED MAGNETICALLY SUSPENDED CARRIAGE SYSTEM

A schematic drawing of the developed linear suspension system is shown by **Fig. 4**. The representative dimensions for the system are listed in **Table 1.** In this system the vertical position, roll, and pitch of the carrier are actively controlled by four electromagnets in the stator. The lateral position and yaw are passively supported. To strengthen the stiffness in the passive direction, grooves are cut on the pole surfaces of the magnets.

Two stations are located at the ends of the track having a length of 865 mm. The acceleration, deceleration and positioning of the carrier in the propulsion direction will be done inside these stations. The carrier runs with inertia between the station where only electromagnets for self-sensing suspension are placed.

EXPERIMENTS

In order to examine the feasibility of the observer-based self-sensing suspension in the developed carrier system, a single-degree-of-freedom model was built for basic experimental study (**Fig. 5**). In this model, the fixed and suspended elements are interchanged with each other because it is technically difficult to constrain the motions of the carrier to one degree of freedom. An electromagnet to be placed in the stator is fixed to an arm, which will be an object to be suspended. This arm is supported at an end with a ball bearing pivot so that it has a single-degree-of-freedom motion. The carrier is fixed to the base.

The DSP-based digital controller is used for the implementation of the designed observer-based self-sensing controllers. A full-order state observer is used in estimating the state variables. The sampling period is 100 msec.

Figure 6 shows the response of one of the designed self-sensing suspension systems when a step-wise disturbance acts on the suspended object. Comparing the detected displacement (a) with its estimated signal (b), we observe that both agree well in the transient, but differ in the stationary;

the stationary value of the estimated displacement does not change due to static disturbance acting on the suspended object. The steady value of the coil current also converges to zero (Fig. 7(c)). These results demonstrate well the characteristics of the observer-based self-sensing suspension systems.

CONCLUSIONS

The design concepts of the developed magnetically suspended carrier system were discussed. The developed system is characterized by

(1) Electromagnets for suspension are placed in the stator.
(2) They work both for force generator and gap sensor (self-sensing operation).
(3) Permanent magnets for power saving are built in the carrier.
(4) The developed hybrid magnet has a magnetic circuit such that the coil current primarily overcomes only the air-gap reluctance.
(5) Virtually zero power control is automatically performed by using the observer-based self-sensing controller.

The experiments carried out with a single-degree-of-freedom model demonstrated that the self-sensing suspension could be realized in a suspension system with the developed hybrid magnet.

Further experimental work is underway to realize the completely contactless transportation of the carrier with the self-sensing suspension.

ACKNOWLEDGMENT

The authors would like to express their gratitude to Mr. H. Ueyama of Koyo Seiko Co. Ltd. for his kind support in manufacturing the experimental setup.

REFERENCES

1. Vischer, D.: Sensorlose und spannungsgesteuerte Magnet-lager. *Doctor Thesis* Nr. 8665, ETH Zurich, 1988.
2. Vischer, D.; and Bleuler, H.: A New Approach to Sensorless and Voltage Controlled AMBs Based on Network Theory Concept. *Proc. 2nd International Symposium on Magnetic Bearings*, Univ. of Tokyo, 1990, pp.301-306.
3. Mizuno, T.; and Bleuler, H.: Self-Sensing Magnetic Bearing Control System Design Using the Geometric Approach. *Control Engineering Practice*, Vol. 3, No. 7, 1995, pp.925-932.
4. Henrikson, C.H.; Lyman, J.; and Studer, P.A.: Magnetically Suspended Momentum Wheels for Spacecraft Stabilization. *AIAA Paper* No. 74-128, 1974.

5. Morishita, M.; Azukizawa, T.; Kanda, S.; Tamura, N.; and Yokoyama, T.: A New Maglev System for Magnetically Levitated Carrier System. *IEEE Trans. on Vehicular Technology*, Vol. 38, No. 4, 1989, pp.230-236.
6. Magnetic Levitation Technical Committee of IEEJ, eds.: Magnetic Suspension Technology. *Corona Publishing Co., Ltd.*, Japan, 1993, pp.102-108 (*in Japanese*).
7. Frazier, R.H.; Gilinson, P.J.Jr.; and Oberbeck, G.A.: Magnetic and Electric Suspensions. *The MIT Press*, 1974, pp.231-284.
8. Okada, Y.; Matsuda, K.; and Nagai, B.: Sensorless Magnetic Levitation Control by Measuring PWM Carrier Frequency Component. *Proc. 3rd International Symposium on Magnetic Bearings, Technomic Publishing Company Inc.*, 1992, pp.176-183.
9. Mizuno, T.; Ishii, T.; and Araki, K.: Realization of Phase-Locked and Frequency-Feedback Magnetic Bearings. *Proc. 4th International Symposium on Magnetic Bearings, Vdf,* 1994, pp.311-316.

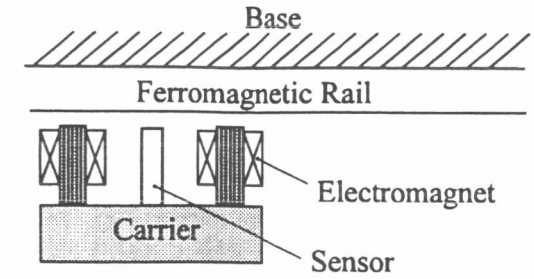

(a) magnets and sensors situated on the carrier

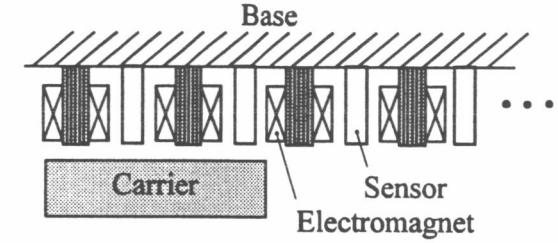

(b) magnets and sensors situated on the stator

Figure 1. Schematic drawing of linear magnetic suspension systems.

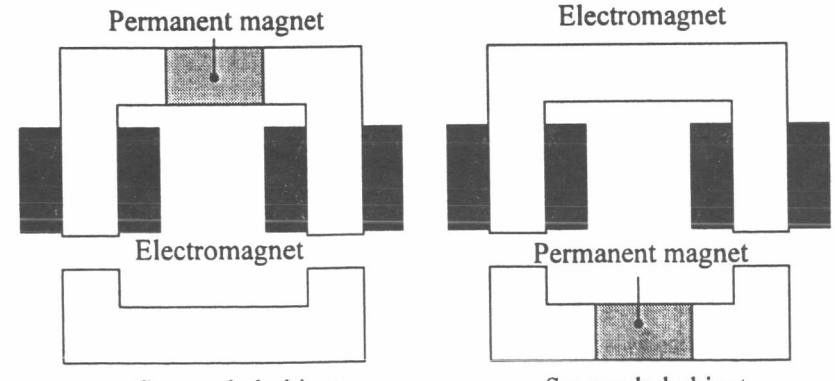

(a) conventional (b) modified

Figure 2. Configuration of a hybrid magnet.

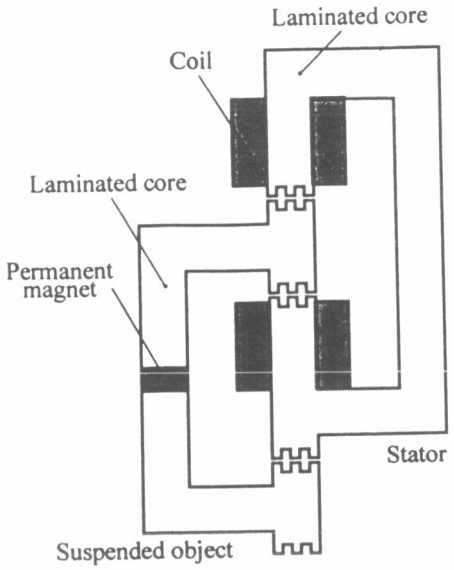

Figure 3. Structure of the developed hybrid magnet.

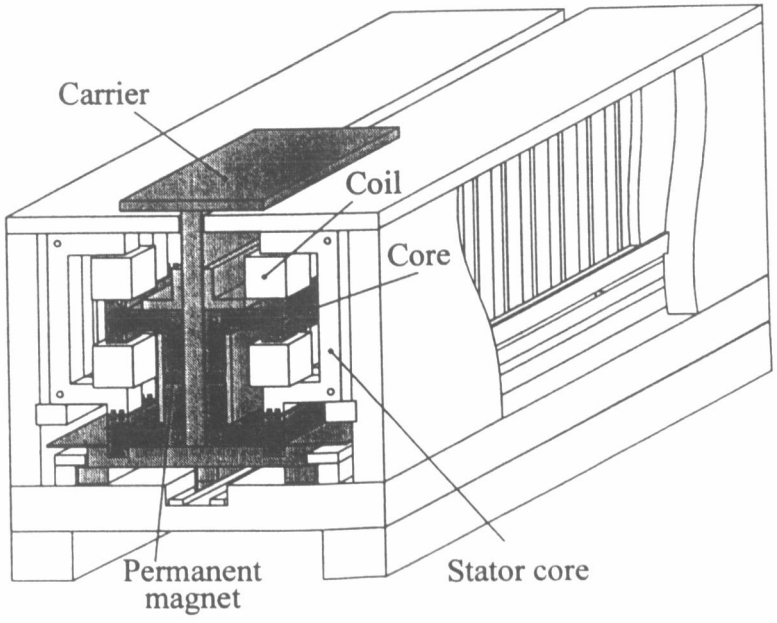

Figure 4. Developed magnetically suspended linear carrier system.

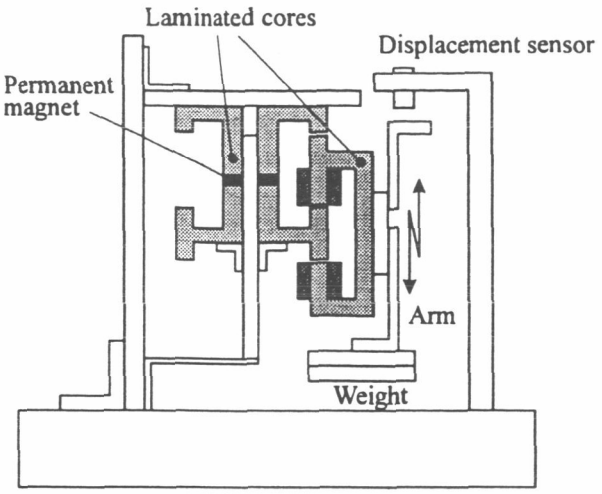

Figure 5. Experimental setup.

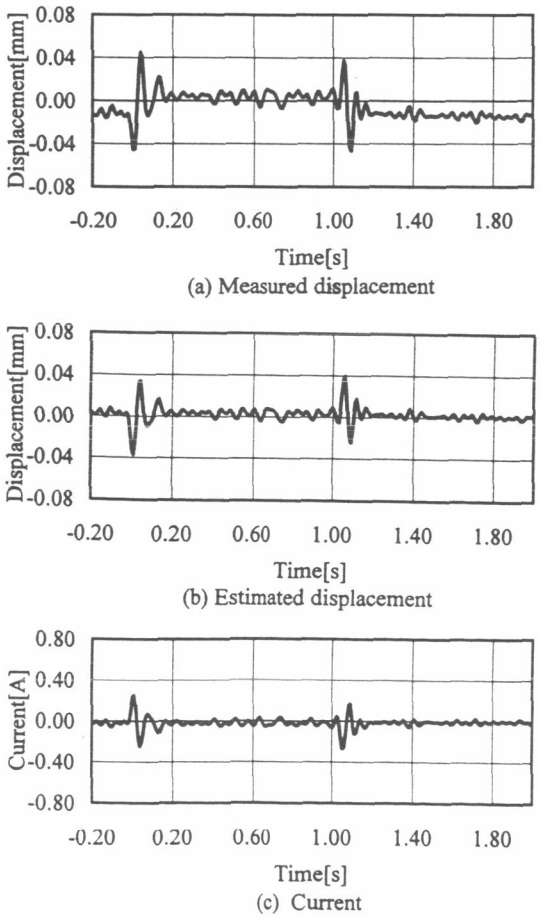

Figure 6. Response of the self-sensing magnetic suspension system when a step-wise disturbance acts on the suspended object.

Table 1. Specifications for the Developed Carrier System

Carrier dimensions	193 mm L × 106 mm W × 133 mm H
Carrier weight	4 kg
Stator (with a track) dimensions	865 mm L × 182 mm W × 177 mm H
Permanent magnet	Neodymium-boron-iron magnet

μ-ANALYSIS AND SYNTHESIS OF A MAGNETIC SUSPENSION SYSTEM CONSIDERING STRUCTURED UNCERTAINTIES

Toru Namerikawa[1], Masayuki Fujita[2], and Fumio Matsumura[1]

[1] Department of Electrical and Computer Engineering, Kanazawa University
2-40-20 Kodatsuno, Kanazawa 920, Japan
e-mail: toru@t.kanazawa-u.ac.jp
[2] School of Information Science, Japan Advanced Institute of Science and Technology
1-1 Asahidai, Tatsunokuchi, Ishikawa 923-12, Japan
e-mail: fujita@jaist.ac.jp

SUMMARY

This paper deals with modeling, structured uncertainties, μ-analysis and synthesis of a magnetic suspension system. First we derive a nominal model of the plant and consider its structured uncertainties, e.g., linearization error, parametric uncertainties, and neglected dynamics. Then we set the interconnection structure which includes the above structurally represented uncertainties. Next we design a robust μ controller which achieves robust performance conditions using the structured singular value μ. Finally we evaluate the proposed interconnection structure and verify robustness and performance of the designed μ controller by experiments.

INTRODUCTION

Magnetic suspension systems can suspend objects without any contact. Increasing use of this technology is now made for various industrial purposes, and it has already been applied to magnetically levitated vehicles, magnetic bearings, etc. [1,2]. Recent overviews and advances in this field are shown in [3]. Since magnetic suspension systems are essentially unstable, a feedback control is indispensable. The problem is that model uncertainties and perturbations often make the systems unstable.

In the robust control of magnetic suspension technology field, these uncertainties have been treated as exogenous disturbances, and unstructured uncertainties [4], however, both uncertainty descriptions caused the conservative analytic results for robust stability/performance tests. In [5], parameter perturbations were considered, and the model uncertainties were described structurally, but the unmodeled dynamics written as unstructured uncertainties is not fully discussed.

In this paper, our novelty is to propose the model and structured uncertainty description of a magnetic suspension system, which contains less conservativeness for robust stability/performance analysis. This is concerned with how to construct a set of plant models. We consider the parametric uncertainties and unmodeled dynamics and linearization error. These uncertainties are structurally described by real/complex numbers/matrices, and for robustness analysis, we employ

the mixed structured singular value (mixed μ) test [6] to reduce conservativeness. Finally we evaluate the proposed model and the robustness and performance of a designed μ controller by several experimental results.

MAGNETIC SUSPENSION SYSTEM

In this section, we derive an ideal model of the system based on physical laws and several assumptions.

Construction

Consider the electromagnetic suspension system shown schematically in Fig. 1. An electromagnet is located at the top of the experimental systems.

The control problem is to levitate the iron ball stably utilizing the electromagnetic force, where a mass M of the iron ball is 1.04kg, and steady state gap X is 5mm. Note that this simple electromagnetic suspension system is unstable, thus feedback control is dispensable. As a gap sensor, a standard induction probe of eddy current type is placed below the ball.

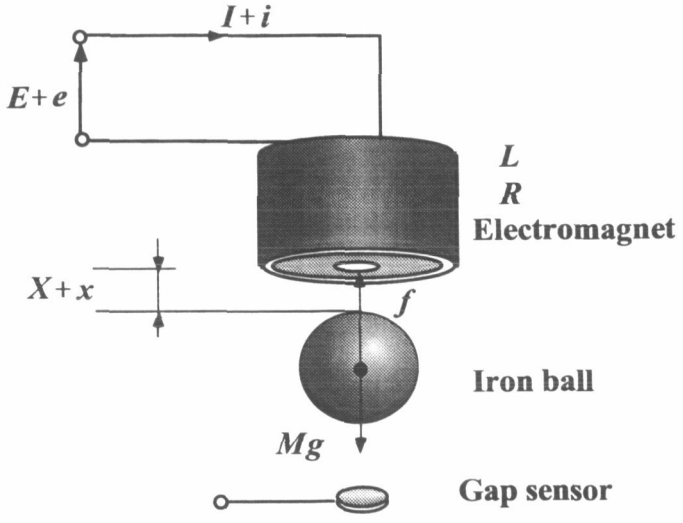

Figure 1: Magnetic Suspension System (M.S.S.)

Mathematical Model

In order to derive a model of the system by physical laws, we introduce following assumptions [1, 2, 4].

[A1] Magnetic flux density and magnetic field do not have any hysteresis, and they are not saturated.

[A2] There is no leakage flux in the magnetic circuit.

[A3] Magnetic permeability of the electromagnet is infinity.

[A4] Eddy current in the magnetic pole can be neglected.

[A5] Coil inductance is constant around the operating point, and an electromotive force due to a motion of the iron ball can be neglected.

These assumptions are almost essential to model this system. Under these assumptions, we derived equations of the motion, the electromagnetic force, and the electric circuit as

$$M\frac{d^2x}{dt^2} = Mg - f, \tag{1}$$

$$f = k\left(\frac{I+i}{X+x+x_0}\right)^2, \tag{2}$$

$$L\frac{di}{dt} + R(I+i) = E + e, \tag{3}$$

where M is a mass of the iron ball, X is a steady gap between the electromagnet (EM) and the iron ball, x is a deviation from X, I is a steady current, i is a deviation from I, E is a steady voltage, e is a deviation from E, f is EM force, k, x_0 are coefficients of f, L is an inductance of EM, and R is a resistance of EM.

Next we linearize the electromagnetic force (2) around the operating point by the Taylor series expansion as

$$f = k\left(\frac{I}{X+x_0}\right)^2 - K_x x + K_i i, \tag{4}$$

$$K_x = 2kI^2/(X+x_0)^3, \quad K_i = 2kI/(X+x_0)^2.$$

From equations (1), (3), (4) and the steady state equations: $Mg = k\left(\frac{I}{X+x_0}\right)^2, RI = E,$ the nominal block diagram of the magnetic suspension system is represented in Fig. 2. With the nominal model parameters in Table 1, a transfer function of the nominal model is given by

$$G_{nom}(s) = \frac{-28.9}{(s+28.8)(s+78.0)(s-78.0)}. \tag{5}$$

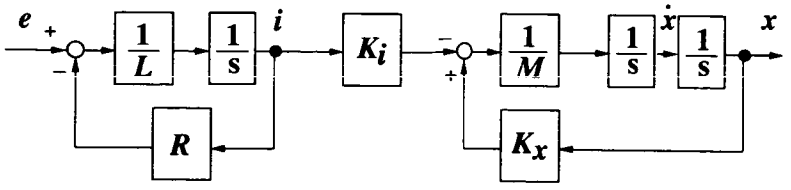

Figure 2: Nominal linear model for M.S.S.

Table 1: Model Parameters

Parameter	Nominal Value	Unit
M	1.04	[kg]
X	5.00 $\times 10^{-3}$	[m]
I	0.789	[A]
k	1.71 $\times 10^{-4}$	$[Nm^2/A^2]$
x_0	-1.80 $\times 10^{-3}$	[m]
K_x	6.27 $\times 10^{3}$	$[N/m]$
K_i	25.7 $\times 10^{-4}$	$[N/A]$
L	0.859	[H]
R	24.76	$[\Omega]$

STRUCTURED UNCERTAINTIES

Note that the model of the plant in Fig. 2 was introduced based on several assumptions and approximations. This model cannot always express the exact behavior of the real plant. We consider model uncertainties between the real physical system and the ideal nominal model, and make a set of plant models. Generally, it is well known that the following items are serious uncertainties [7] and we discuss them in the following:

- linearization error
- parametric uncertainty
- unmodeled dynamics

Linearization Error

There should be model uncertainties caused by linearization of the electromagnetic force around the operating point. In Fig. 3, the current-force (*i-f*) curve at X = 5.0mm is plotted in the upper figure, and gap-force (*x - f*) curve at *I* = 1.15A is in the lower figure, where O denotes measured experimental data at each point, and the solid lines show the determined current-force curve and gap-force curve. The dashed straight lines indicate tangents of each curve at the operating points. These inclinations of tangents are employed as K_i and K_x, respectively. The dash-dot straight lines are sectors of the linearization errors. These data were measured five times at each point. From Fig. 3, the perturbations between tangents and curves become bigger if the operating points move from the original points. These errors were caused by linearization. Here we employ sector bounds to account for linearization error, and describe K_i and K_x as

$$K_i = K_{i0} + k_i\delta_i, \quad \delta_i \in [-1, 1], \tag{6}$$

$$K_x = K_{x0} + k_x\delta_x, \quad \delta_x \in [-1, 1], \tag{7}$$

where K_{i0} and K_{x0} are nominal values, k_i and k_x are weights of uncertainties.

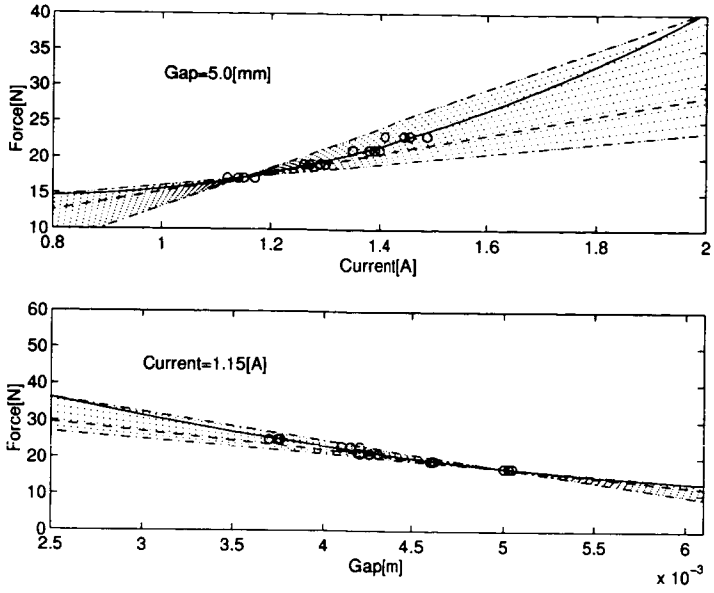

Figure 3: Current-Force Curve and Gap-Force Curve

Parametric Uncertainty

We had better consider the perturbation of a mass of the iron ball M against intentional change of the mass and against unexpected exogenous force disturbances. Hence, with a perturbation we describe it as

$$M = M_0 + k_M \delta_M, \quad \delta_M \in [-1, 1], \tag{8}$$

where, M_0 is the nominal value, and k_M is magnitude of perturbation.

Unmodeled Dynamics

In this section, we discuss the dynamics of the electromagnet which can be represented as $\frac{1}{Ls+R}$. Inductance L and resistance R of the electromagnet have frequency dependent characteristics. Also, measurements of these parameters are very sensitive. Nominal values of L, R are determined as averages of measurements under forcing at 10Hz. Figure 4 shows the experimental data of $\frac{1}{Ls+R}$, where the solid line indicates the nominal frequency response and the dashed lines indicate upper and lower bounds. The dynamics of electromagnet, $\frac{1}{Ls+R}$, are distributed in a frequency dependent belt. Furthermore, if the frequency of the input signal changes, this belt becomes broad. We treat the width of this belt in Fig. 4 as an unstructured uncertainty as below.

$$\frac{1}{Ls+R} = \frac{1}{L_0 s + R_0} + w_i(s)\Delta_i(s), \quad |\Delta_i(jw)| \leq 1. \tag{9}$$

where L_0 and R_0 are the nominal values of L and R, respectively, and $w_i(s) = d_w + c_w(sI_m - A_w)^{-1}b_w$ is a weight of uncertainty. The magnitude of weight $w_i(s)$ is determined as one half of a width of the belt in Fig. 4.

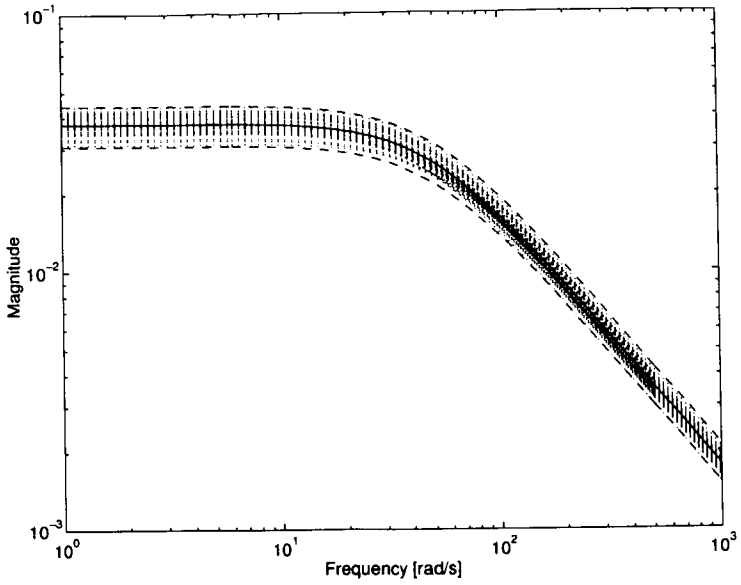

Figure 4: Frequency responses of $\frac{1}{Ls+R}$

Set of Plant Models

We take into account the above three types of uncertainties, and reconstruct the block diagram of the system in Fig. 2. The obtained set of models which includes the above uncertainties is shown in Fig. 5.

μ-ANALYSIS AND SYNTHESIS

Quantization of Uncertainties

In this section, we quantify uncertainties and make a real set of plant models.

Change of the Operating Point

We consider a structurally represented uncertainty caused by a change of the operation point. In this system, the operating point is characterized by a steady state gap X $\{X \mid 3.8 \leq X \leq 6.2\}$.

Perturbation of K_i and K_x

Change of the operating point X causes the other perturbations of parameters, K_i and K_x. In this case, parameters K_i and K_x perturb as $14.1 \leq K_i \leq 37.3$, $5.38 \times 10^3 \leq K_w \leq 7.16 \times 10^3$ $(3.8 \leq X \leq 6.2)$. Then we describe K_i and K_x as below.

$$K_i = 25.7 + 11.6 \cdot \delta_i, \quad \delta_i \in [-1, 1], \tag{10}$$

$$K_x = 6.27 \times 10^3 + 8.90 \times 10^2 \cdot \delta_x, \quad \delta_x \in [-1, 1]. \tag{11}$$

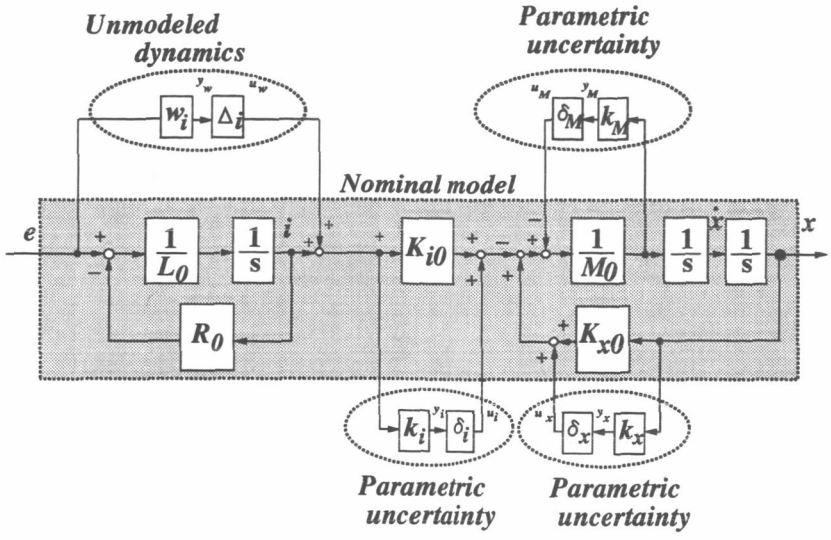

Figure 5: Set of Plant Models with Uncertainties

Dynamical uncertainties

An uncertainty in the electromagnet, $\frac{1}{Ls+R}$, should be also considered. We set the parametric uncertainty of L and R as $0.782 \leq L \leq 0.936$ (9% perturbation) and $24.5 \leq R \leq 25.0$ (1% perturbation). In addition to the above parametric perturbation, we should take into account unmodeled dynamics in the high frequency range. Using an FFT analyzer, we measured them. Finally, we decided a set of electromagnetic dynamics, $\frac{1}{Ls+R}$, as

$$\frac{1}{Ls+R} = \frac{1}{0.859s+24.8} + \frac{1.28 \times 10^{-3}(s+3.20)(s+900)}{(s+25.8)(s+31.4)}\Delta_i(s), \quad |\Delta_i(jw)| \leq 1. \tag{12}$$

From the above discussion in these three subsections, the final quantity of uncertainties are selected in Table 2, where a 7% perturbation of mass M is considered in this case.

Table 2: Quantity of uncertainties

	Value		Value
k_i	11.6	k_x	8.90×10^2
k_M	7.25×10^{-2}	$w_i(s)$	$\frac{1.28\times10^{-3}(s+3.20)(s+900)}{(s+25.8)(s+31.4)}$

Design

Utilizing the structured singular value μ [8, 9], we design the controller which achieves robust performance against various types of uncertainties.

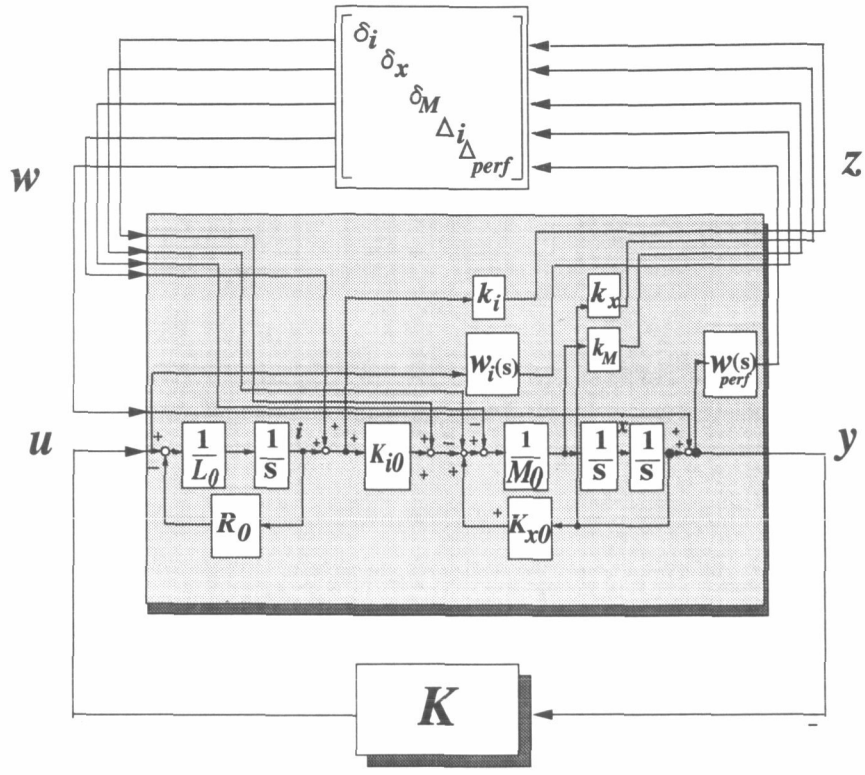

Figure 6: Interconnection Structure

We construct an interconnection structure by LFT representation in Fig. 6, where W_{perf} is a performance specification and also is a weight for a sensitivity function $S := (I + G_{nom}K)^{-1}$. W_{perf} is given by a following equation, and its frequency response is shown in Fig. 7.

$$W_{perf}(s) = \frac{100}{1 + s/0.1}. \tag{13}$$

Next, for the robust performance synthesis, we define the block structure Δ. The perturbation $\Delta(s)$ belongs to the bounded subset

$$\mathbf{B\Delta} := \{\Delta(s) \in \mathbf{\Delta} | \bar{\sigma}(\Delta(j\omega)) < 1\}, \tag{14}$$

where Δ is given by

$$\mathbf{\Delta} := \{\mathrm{diag}[\delta_i, \delta_x, \delta_M, \Delta_i, \Delta_{perf}] : \quad \delta_i, \delta_x, \delta_M \in \mathbf{R}, \Delta_i, \Delta_{perf} \in \mathbf{C}\}. \tag{15}$$

The structured singular value $\mu_\Delta(M)$ is defined for matrices $M \in \mathbf{C}^{n \times n}$ with the block structure Δ as

$$\mu_{\mathbf{\Delta}}(M) := \frac{1}{\min\{\bar{\sigma}(\Delta) : \Delta \in \mathbf{\Delta}, \det(I - M\Delta) = 0\}} \tag{16}$$

unless no $\Delta \in \mathbf{\Delta}$ makes $(I - M\Delta)$ singular, in which case $\mu_\Delta(M) := 0$.

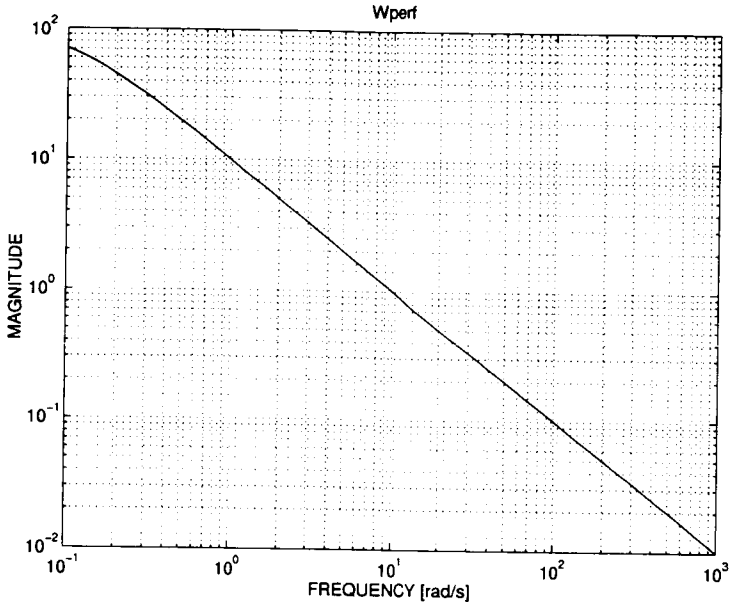

Figure 7: Weighting Function W_{perf}

We then have:
- The closed loop system will have robust performance, i.e., it will be robustly stable and

$$\sup_{\omega \in R} \mu_{\Delta}[F_l(P(j\omega), K(j\omega))(j\omega)] < 1. \tag{17}$$

We apply standard D - K iteration to find the sub-optimal μ controller for the system. We thus iteratively solve the following problem:

$$\sup_{\omega \in R} \inf_{D(\omega)} \{\bar{\sigma}(D(j\omega)F_l(P(j\omega), K(j\omega))(j\omega)D^{-1}(j\omega))\} < 1. \tag{18}$$

After the 3rd iteration, we obtained a controller *K(s)*, where the supremum of μ_{Δ} [F_l(P,*K*)] is 0.9766. Final scaling matrix *D(s)* has 12 states, then *K(s)* has 30 states. We employ the Hankel norm approximation technique to calculate the reduced order system of *K(s)*. Final balanced controller *K(s)* is as follows, and its bode diagram is shown in Fig. 8. The supremum of the $\mu_{\Delta}[F_l(P, \hat{K})]$ is also 0.9766.

$$\begin{aligned}
\hat{K}(s) &= \frac{3.27 \times 10^{10} \times (s+486+885i)(s+486-885i)}{(s+1740)(s+949+1320i)(s+949-1319i)} \\
&\times \frac{(s+389+626i)(s+389-626i)(s+335)(s+79.1)(s+29.5)}{(s+472+794i)(s+472-794i)(s+391+599i)(s+391-599i)(s+348)} \\
&\times \frac{(s+14.7)(s+4.86)(s+2.63)(s+0.175)(s+0.114)}{(s+8.16)(s+2.66)(s+0.210)(s+0.127)(s+0.0778)}
\end{aligned} \tag{19}$$

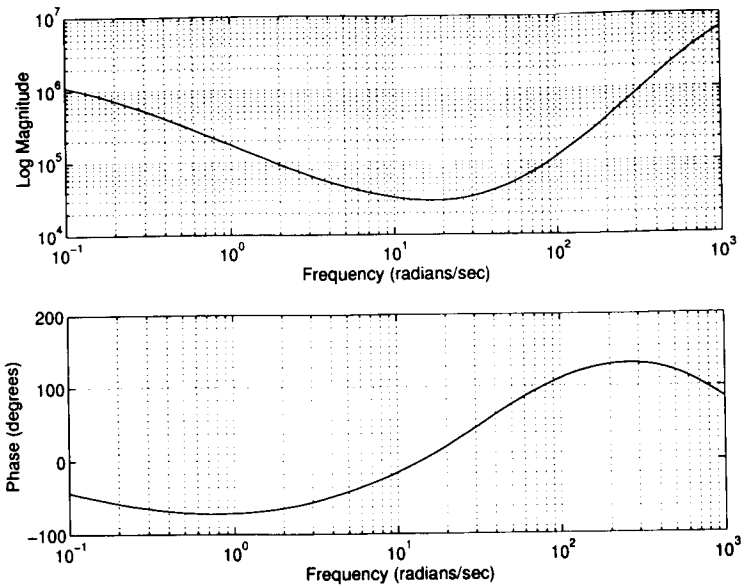

Figure 8: Final Controller $\hat{K}(s)$

A calculated upper bound and lower bound of $\mu_{\Delta}[F_l(P, \hat{K})]$with the controller $\hat{K}(s)$ is shown in Fig. 9., where the two solid lines respectively show upper and lower bounds of μ and the dashed line shows the maximum singular value of $(D(j\omega)F_l(P(j\omega), \hat{K}(j\omega))(j\omega)D^{-1}(j\omega))$.

A peak value of the upper bound of μ is less than 1, then the closed-loop system with considered uncertainties achieves the robust performance condition. This result shows guarantees robust performance against uncertainties caused by a change of operating point $\{X \mid 3.8 \leq X \leq 6.2\}$.

EXPERIMENTAL EVALUATION

In order to evaluate the design process, we implement the obtained controller $\hat{K}(s)$ via a digital controller, and carry out experiments. The sampling period of the controller is 95μs, and a well known Tustin transform was employed for discretization. All experimental results which show a position of the iron ball are shown in Fig. 10.

Evaluation of Nominal Performance

Step response of the position x of the iron ball at X = 5[mm] (nominal steady gap) is shown in Fig. 10(a), which indicates stable levitation with the controller $\hat{K}(s)$ at the nominal steady gap X = 5.0mm. The magnitude of the step-type disturbance is 22 N, which is twice as much as the steady state force. Since it is difficult to give disturbance forces to the iron ball directly, we add a pseudo-disturbance by applying a voltage signal to the control input signal. This figure shows that the nominal performance is fully achieved.

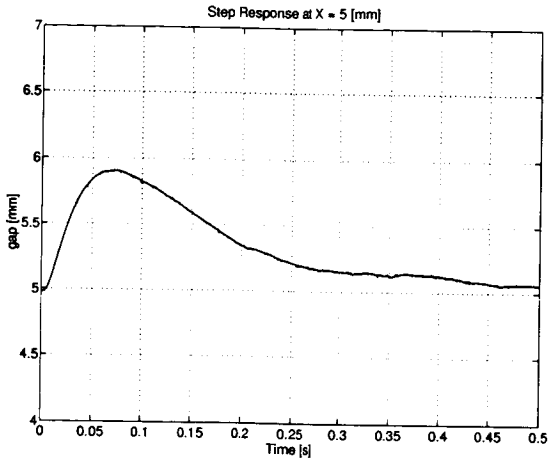

(a) Step Response at $X = 5$[mm]

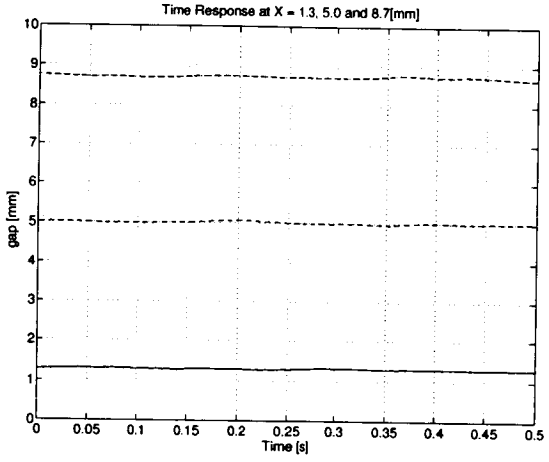

(b) Time Response at $X = 1.3,\ 5.0,\ 8.7$[mm]

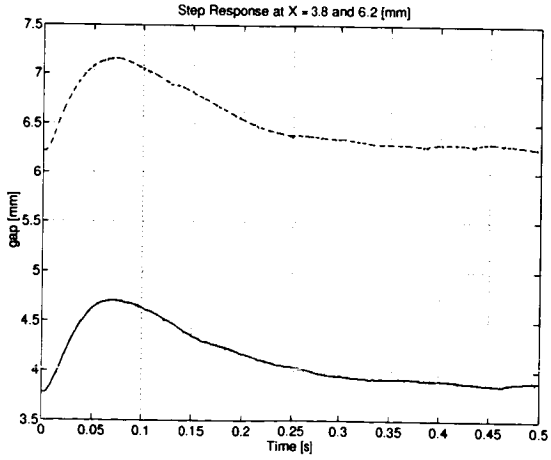

(c) Step Response at $X = 3.8,\ 6.2$[mm]

Figure 10: Experimental Results

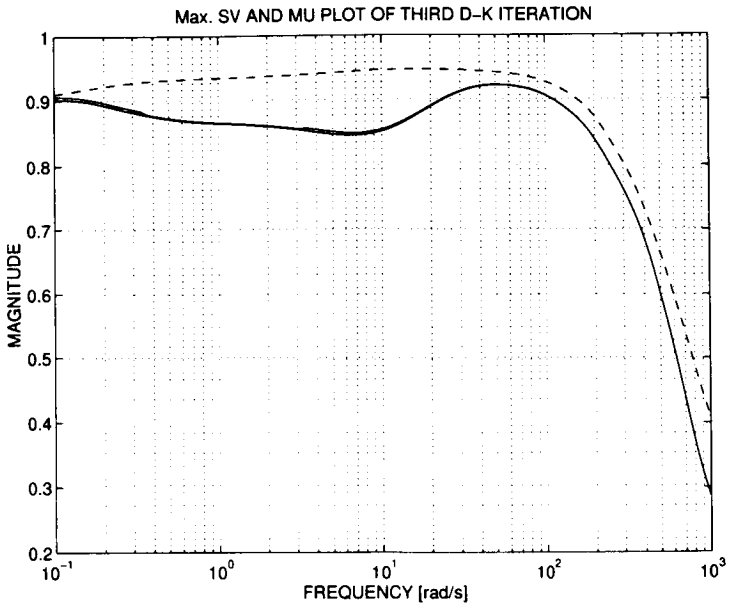

Figure 9: $\mu_{\Delta}[F_l(P,\hat{K})]$ and $\bar{\sigma}[DF_l(P,\hat{K})D^{-1}]$

Evaluation of Robust Stability

Time responses of the controllers $\hat{K}(s)$ are shown in Fig. 10(b), which indicate stable levitation at the steady state gaps $X = 1.3, 5.0, 8.7$ mm. These lines show that the robust stability against the perturbation of X $(1.3 \leq X \leq 8.7)$ is achieved. If we change the steady state gap X to less than $X = 1.3$, or greater than $X = 8.7$, then the system disappointingly becomes unstable.

Evaluation of Robust Performance

For the verification of the robust performance test, we measured time responses against a step-type external disturbance (22 N) at the steady state gaps $X = 3.8$, 6.2mm. Results are shown in Fig. 10(c).

From this result, it can be seen that the controller $\hat{K}(s)$ shows adequate performance comparing the response in Fig. 10(a). We have confirmed $\hat{K}(s)$ achieves robust performance against model perturbances caused by a change of operating point $\{X \mid 3.8 \leq X \leq 6.2\}$.

CONCLUSIONS

In this paper, we proposed a novel set of plant models for a magnetic suspension system considering structured uncertainties.

We transformed the obtained model to the LFT represented interconnection structure with the structured mixed uncertainty. Next we designed a robust controller by μ-analysis and synthesis which achieves robust performance criteria using the structured singular value μ. Finally we evaluated the proposed interconnection structure which contained the structured uncertainties, and also verified robustness and performance of the designed μ controller by experiments.

REFERENCES

[1] P. K. Sinha: *Electromagnetic Suspension: Dynamics and Control, IEE,* Peter Peregrinus, London, 1987.

[2] G. Schweitzer, et al.: *Active Magnetic Bearings,* Hochschulverlag AG an der ETH Zurich, 1994.

[3] F. Matsumura, Ed.: *Proc. of the Fifth Int. Symp. on Magnetic Bearings,* Kanazawa, Japan, Aug. 1996.

[4] M. Fujita, T. Namerikawa, et al.: "*μ*-Synthesis of an Electromagnetic Suspension System," *IEEE Trans. Automatic Control,* Vol. 40, No. 3, pp. 530-536, 1995.

[5] T. Sugie and M. Kawanishi: "Analysis and Design of Magnetic Levitation Systems Considering Physical Parameter Perturbations," *Trans. of ISCIE,* Vol. 8, No. 2, pp. 70-79, 1995.

[6] P. M. Young: " Controller Design with Real Parametric Uncertainty," *Int. J. of Control,* Vol. 65, No. 3, pp. 469-509, 1996.

[7] F. Paganini: *Sets and Constraints in the Analysis of Uncertain Systems,* Ph.D. Thesis, California Institute of Technology, 1996.

[8] G. J. Balas, J. C. Doyle, K. Glover, A. Packard, and R. Smith: *μ-Analysis and Synthesis Toolbox User's Guide*, MUSYN Inc. and Math Works, 1993.

[9] G. Stein and J. C. Doyle: "Beyond Singular Values and Loop Shapes," *J. Guidance,* Vol. 14, No. 1, pp. 5-16, 1991.

Eddy Current Influences on the Dynamic Behaviour of Magnetic Suspension Systems

Colin P. Britcher†, Dale V. Bloodgood‡
Department of Aerospace Engineering
Old Dominion University

Abstract

This report will summarize some results from a multi-year research effort at NASA Langley Research Center aimed at the development of an improved capability for practical modelling of eddy current effects in magnetic suspension systems. Particular attention is paid to large-gap systems, although generic results applicable to both large-gap and small-gap systems are presented. It is shown that eddy currents can significantly affect the dynamic behaviour of magnetic suspension systems, but that these effects can be amenable to modelling and measurement. Theoretical frameworks are presented, together with comparisons of computed and experimental data particularly related to the Large Angle Magnetic Suspension Test Fixture at NASA Langley Research Center, and the Annular Suspension and Pointing System at Old Dominion University. In both cases, practical computations are capable of providing reasonable estimates of important performance-related parameters. The most difficult case is seen to be that of eddy currents in highly permeable material, due to the low skin depths. Problems associated with specification of material properties and areas for future research are discussed.

Background

Whenever a time-varying magnetic flux penetrates a conducting medium, eddy-currents will be generated according to a simple application of Faraday's Law of Induction :

$$\nabla \times \vec{E} + \frac{\partial \vec{B}}{\partial t} = 0 \tag{1}$$

or alternatively :

$$V = N \frac{d\phi}{dt} \tag{2}$$

- where E represents the electric field, B magnetic flux density, V electric potential, N the number of turns in a coil, and ϕ magnetic flux. Two fundamental effects must be considered for a proper understanding of eddy current behaviour, particularly in large-gap suspension systems. These are first, the reactive coupling from the magnetic fluxes required for suspension purposes to the eddy current circuits and second, the resistive dissipation in those circuits. The former effect is the driving term, the second clearly the

† Associate Professor of Aerospace Engineering
‡ Graduate Research Assistant

dissipative term. Further, the signs of terms in equation 1 suggest exclusion (or cancellation) of flux from the eddy current circuits; normally known as Lenz's Law.

Important insight can be gained from consideration of a simple model, resembling a single-turn transformer, with the eddy current circuit being the secondary. The general form of the results are easily shown to be [1] :

$$I_e = I\left(\frac{-L_m s}{R_e + L_e s}\right) \tag{3}$$

- where I, I_e are the driven coil and eddy currents respectively, R_e, L_e, L_m are the resistance, self-inductance and mutual-inductance of the eddy current circuit. If the field component B_j at some location due to a unit current in the primary coil is given by K_j and the corresponding field component due to the eddy current is given by K_{e_j} then :

$$B_j = K_j I + K_{e_j} I_e = \left(1 - \frac{K_{e_j} L_m s}{K_j(R_e + L_e s)}\right) \tag{4}$$

The basic behaviour is illustrated in Figure 1, and is seen to be a roll-off in the magnitude of the useful field, with a phase lag peaking at some "resonant" frequency, then asymptoting to zero phase at high frequency. The frequency of resonance and the magnitude of the peak phase shift (or maximum attentuation) are clearly of great interest. It has previously been shown that order of magnitude estimates can made for simple geometries using standard formulae for single-turn coils and the like [1].

A number of large-gap geometries have been studied and experimental evidence supports the form of equations 3 and 4. Some of these results will be reviewed later in this paper. In the meantime, certain practical difficulties that have been experienced in developing mathematical models will be discussed. The "resonant frequency", or frequency of maximum phase lag from equations 3 or 4, and the maximum phase lag are easily shown to be [1] :

$$\omega_{\phi_{max}} = \sqrt{\frac{R_e^2}{L_e^2 - L_m L_e}} \quad ; \quad \phi_{max} = Tan^{-1}\left(\frac{L_m}{2\sqrt{L_e^2 - L_m L_e}}\right) \tag{5}$$

In the former case, the resistance of the eddy current circuit must be known. One would be forgiven for thinking that estimation of eddy current circuit resistance was a simple matter of inserting material resistivity into simple geometric formulae. This apparently trivial step quickly becomes a significant challenge, when it is realized that the resistivity of common engineering metals varies greatly between different alloys, as illustrated in Table 1, and is often also a function of heat treatment and cold work. Further, any welded, bolted or rivited joints present unknown and practically unmeasurable properties.

Where the "skin depth" or penetration depth of the eddy currents is frequency dependent, modified models are required. Careful consideration of the physics of the problem and

Table 1 - Resitivity of Aluminum Alloys [2]

Type	Resitivity, $\Omega m \times 10^{-8}$
Pure aluminum	2.65
2024-T0	3.4
2024-T3,4	5.7
5083	5.9
6061-T6	4.0

study of classical solutions assists in the formation of suitable models. Exact solutions for eddy currents in certain simplified geometries, such as infinite plates or bars are available [3,4]. The solution to the infinite plate problem, illustrated in Figure 2, is reproduced here for reference. The governing equation is the one-dimensional diffusion equation :

$$\frac{\partial^2 B_z}{\partial y^2} = \sigma \mu_o \mu_r \frac{\partial B_z}{\partial t} \tag{6}$$

- where σ is the material conductivity and can be solved for the geometry given in Figure 2, to give the total magnetic flux across the conductor as :

$$B_{total} = \frac{2}{\alpha} B_{surface} Tanh(\alpha b) \tag{7}$$

- where, δ being the skin depth :

$$\alpha = \sqrt{j\omega\sigma\mu_o\mu_r} = \frac{1+j}{\delta} \tag{8}$$

The behaviour of equation 7 is rather unusual, suggesting that the total flux "rolls-off" at a rate of 10db/decade with a limiting phase lag of 45°. These are exactly half the corresponding values of a simple first-order pole. Similar results have been reported by other authors in small-gap applications [5] and the term "half-order pole" invoked. The term "fractional derivative" is found in materials science and structural dynamics literature, where similar temporal or spatial variations of physical properties have been noticed, albeit in different circumstances [6,7].

This result suggests an ad-hoc adjustment of equation 3 or 4, by a multiplier of the form :

$$\left(\sqrt{\frac{1}{1+\tau s}}\right) \tag{9}$$

- where τ is based on the frequency where the skin depth becomes roughly equal to the effective material thickness. Reference 5 suggests an alternative form, based on an approximate analysis, where the denominator would take the form $\left(1 + \sqrt{\tau s}\right)$. However, the form given in equation 9 is recommended here as being more consistent with other literature. The response predicted by equation 9, illustrated in Figure 3, shows broad correlation with observed behaviours. It should be noted that the integration of equation 9

into equation 3 and 4 requires some care. Where an electromagnet coil is closely coupled to an iron core, the flux penetration into the core, hence its magnetization, would lag according to equation 9. Where currents are being excited in non-magnetic, conducting media the situation is more complex. The flux penetration into the conductor will lag the driving field, suggesting a lag in the eddy current, but it should be noted that the driving field is itself strongly modified in the region of the conductor during the flux penetration process. Further analysis is required in this area. The remainder of this paper will review some experimental and computational results related to actual suspension and levitation systems.

Practical Examples

Three suspension systems have been used during the course of this work for experimental evaluation of eddy current effects. Each system, together with representative experimental and computational results will now be briefly introduced. Experimental data relies on direct flux measurements with a Hall probe; computational results employ the finite element computer code ELEKTRA [10]

The Large-Angle Magnetic Suspension Test Fixture

The Large Angle Magnetic Suspension Test Fixture (LAMSTF) is a laboratory-scale levitation device comprising five conventional electromagnets arranged in a circular configuration, levitating a small suspended element containing a cylindrical permanent magnet core. The core is magnetized along the long axis of the cylinder, which in turn is horizontal. The suspended element can be controlled in five degrees of freedom [8,9]. Figure 4 shows the original layout of the system. The aluminum sensor frame and baseplate are worthy of note.

When LAMSTF was first commissioned, a discrepancy was discovered in the dynamic model, mainly manifested in the "pitch" degree-of-freedom (rotation of the suspended element about a lateral, horizontal axis). Extensive computations and measurements of the effects of eddy currents in the metallic support plate and position sensor structure indicated that the problem was mainly due to eddy currents induced in parts of the sensor structure. In fact, later replacement of this structure and the mounting plate with non-conducting material removed the discrepancy in the dynamic behaviour.

Many results have been previously published [1], but Figure 5 summarizes some important results.

The 6DOF-8C/2L system

A variety of "planar array" magnetic configurations were studied with the objective of developing a LAMSTF-like system with 6 degree-of-freedom control. The naming convention indicates that the system developed indeed achieves six degree-of-freedom

control (6DOF) by using eight control coils (8C) and two D.C. coils providing a background "levitation" field (2L). This configuration, illustrated in Figure 6, is far from the only possibility. The system was developed with the minimum of metallic structure (although iron cores are used in the eight control electromagnets), so the dynamic model proved to be quite reliable. However, a much larger system of a comparable configuration, the Large-Gap Magnetic Suspension System, is currently being developed at NASA Langley [11], where the levitation coils will be low-temperature superconductors. Eddy currents in the walls of the aluminum helium/nitrogen dewars containing these electromagnets were a real concern. The 6DOF-8C/2L system has therefore been used for a variety of verification experiments, repeating and extending work previously carried out with LAMSTF.

Figure 7 shows measured and computed results from the 6DOF-8C/L2 system for the case where a thin aluminum plate is placed between the control coils and the suspended element. Agreement is considered reasonable, despite some uncertainty in the resistivity of the actual aluminum alloy used. Readers are encouraged to compare the form of the responses in Figure 7 with the trends shown in Figure 3.

The Annular Suspension and Pointing System

The Annular Suspension and Pointing System (ASPS), shown in Figure 8, is a sophisticated prototype of a payload pointing and vibration isolation system for space payloads [12,13]. It comprises an annular iron rotor, suspended and controlled in six degrees-of-freedom by five magnetic bearing assemblies and one bidirectional linear motor. There is interest in developing advanced systems of similar configuration, so the existing hardware is being used to study modelling and control techniques. The achievable bandwidth of the magnetic bearings is of interest, either as a prerequisite to provision of higher system bandwidths, or to permit effective application of more sophisticated controller design techniques.

Computational modelling of the ASPS bearing stations has been attempted, albeit with some difficulties caused by the highly permeable iron cores used. This presents computational difficulties at the iron-air interface, particularly during the eddy current computations, as well as problems is specifying precise material properties. Nevertheless, it is clear that fluctuating coil currents provoke heavily damped flux waves propagating inwards through the iron electromagnet cores. This is the expectation from classical analysis, such as that presented earlier for the flat plate case, and can be captured in computations, as illustrated in Figure 9.

Discussion and Conclusions

It has been shown that significant attentuation and phase shift of unsteady magnetic fields can occur in magnetic suspension and levitation systems. Accurate predictions are necessary for controller design purposes, as is a simple linear model. It has been shown

that simple models can be developed, albeit with an awkward "fractional derivative" term. Further research in this latter area is warranted.

Acknowledgements

This work was supported by NASA Langley Research Center under Grant NAG-1-1056 and Cooperative Agreement NCC-1-248. The Technical Monitor was Nelson J. Groom of the Guidance and Control Branch.

References

1. Britcher, C.P.; Foster, L.: Modelling of eddy currents related to the large angle Magnetic Suspension Test Fixture. 2nd International Symposium on Magnetic Suspension Technology, Seattle, WA, August 1995. NASA CP-3247.
2. Solid State Physics - Nonferrous Metals.
3. Stoll, R.L.: The Analysis of Eddy Currents, Clarendon, 1974.
4. Smythe, W.R.: Static and Dynamic Electricity, 3rd edition, McGraw-Hill, 1967.
5. Feeley, J.J.: A simple dynamic model for eddy currents in a magnetic actuator. IEEE Transactions on Magnetics, March 1996.
6. Torvik, P.J.; Bagley, R.L.: On the appearance of fractional derivatives in the behaviour of real materials. ASME Journal of Applied Mechanics, 1994.
7. Rossikhin, Y.A.; Shitikova, M.V.: Applications of fractional calculus to dynamic problems of linear and nonlinear hereditary mechanics of solids. Applied Mechanics Reviews, January 1997.
8. Britcher, C.P.; Ghofrani, M.; Britton, T.C.; Groom, N.J.: The large-angle magnetic suspension test fixture. International Symposium on Magnetic Suspension Technology, Hampton, VA, August 1991. NASA CP-3152.
9. Britcher, C.P.; Ghofrani, M.: A magnetic suspension system with a large angular range. Review of Scientific Instruments, July 1993.
10. Vector Fields Incorporated. ELEKTRA Reference Manual.
11. Groom, N.J.: Description of the Large Gap Magnetic Suspension Ground-Based Experiment. Technology 2000, published as NASA CP-3109, V.2, 1991
12. Cunningham, D.C. et. al.: Design of the annular suspension and pointing system. NASA CR-3343, October 1980.
13. Britcher, C.P.; Groom, N.J.: Current and future development of the annular suspension and pointing system. 4th International Symposium on Magnetic Bearings, Zurich, August 1994.

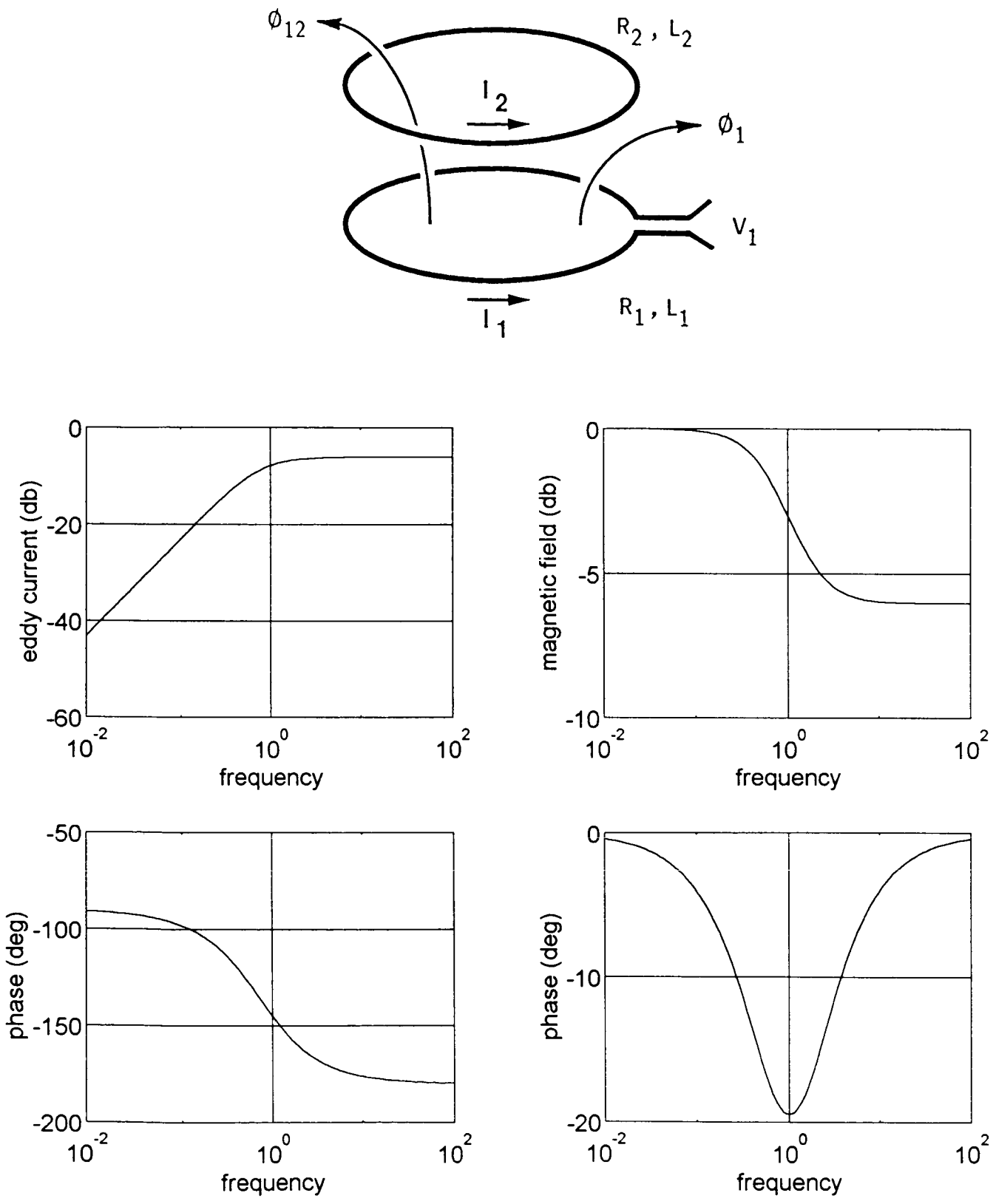

Figure 1 - Transformer Model and Predicted Response
Reasonant frequency adjusted to 1 unit, low/high frequency amplitude ratio = 0.5

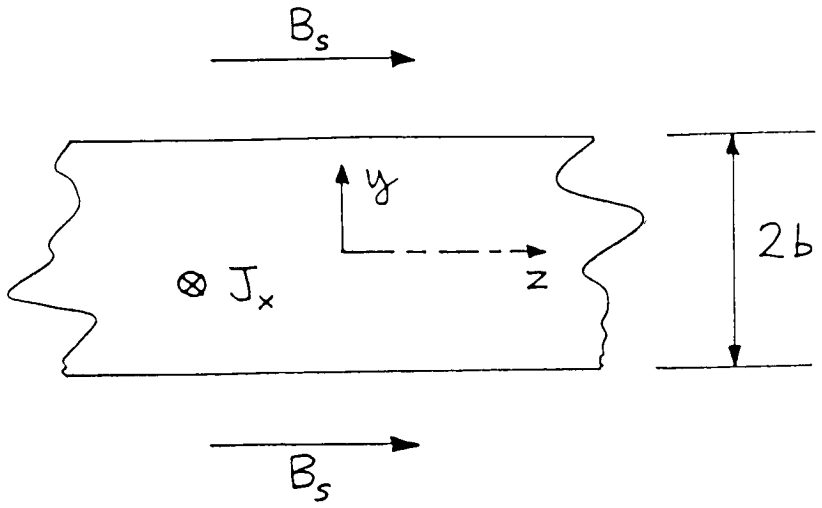

Figure 2 - Eddy Currents in an Infinite Flat Plate
Description of geometry

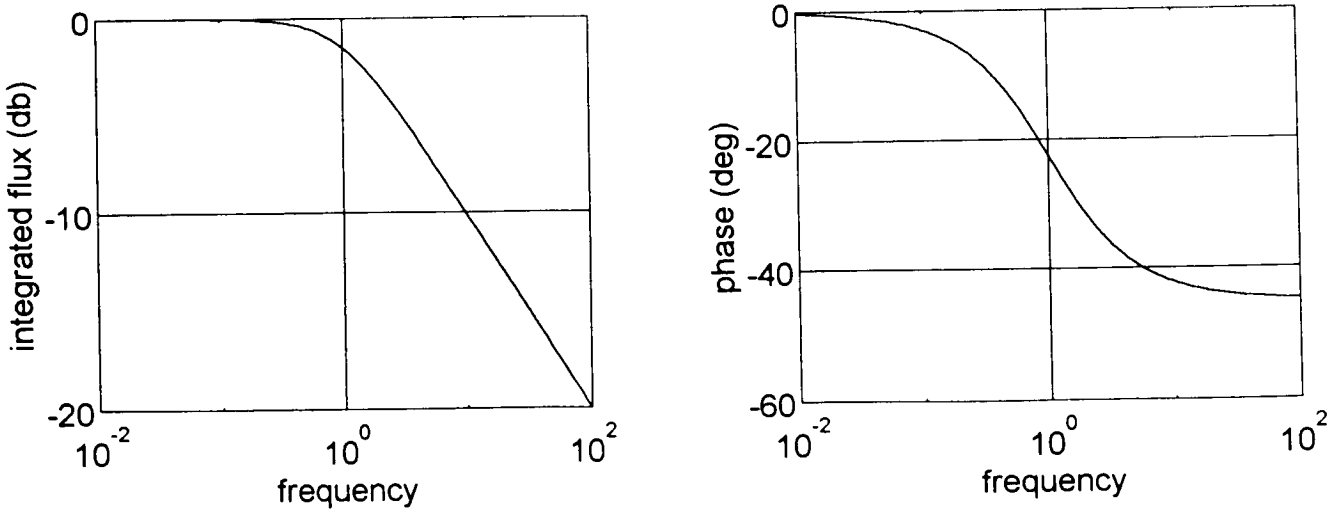

Figure 3 - Response of Half-Order Pole

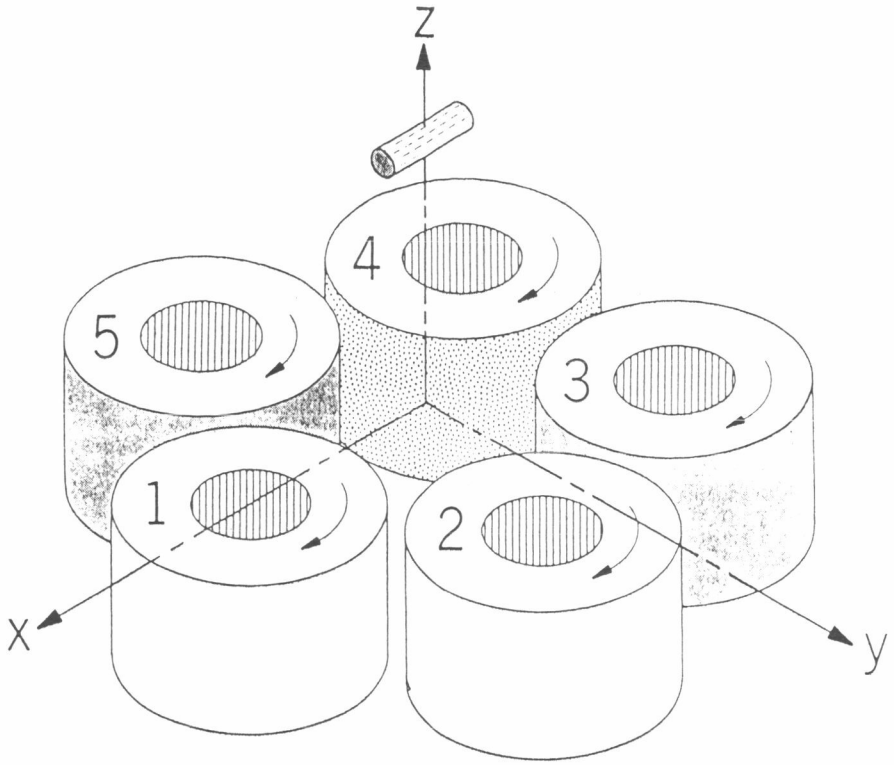

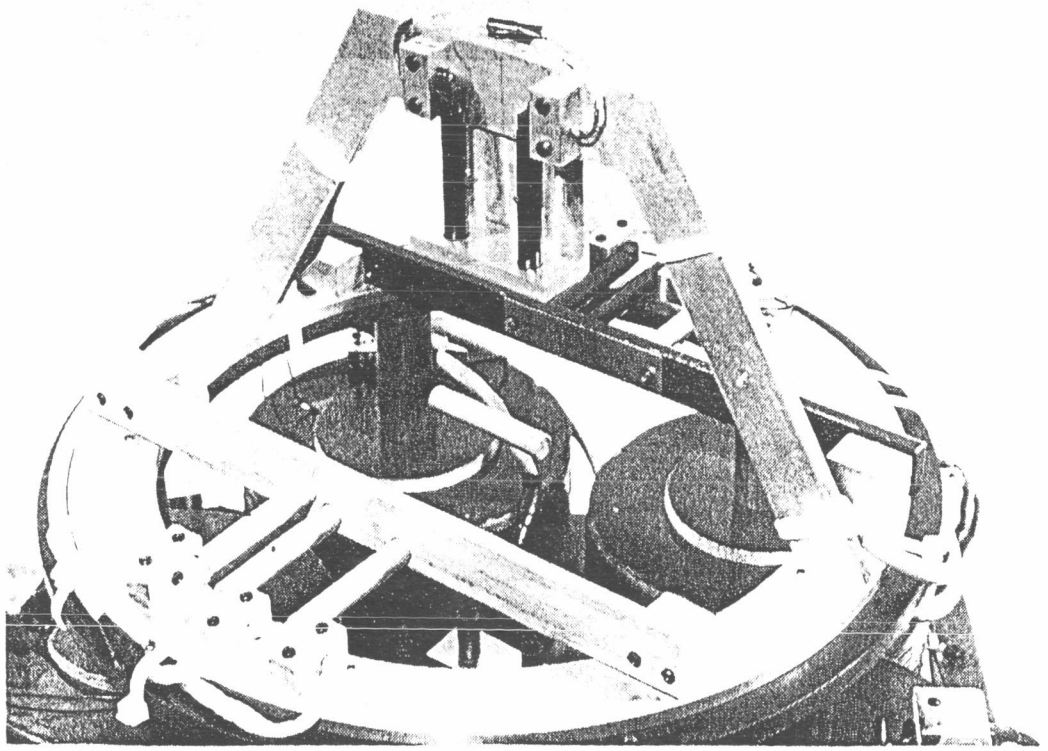

Figure 4 - The Large Angle Magnetic Suspension Test Fixture

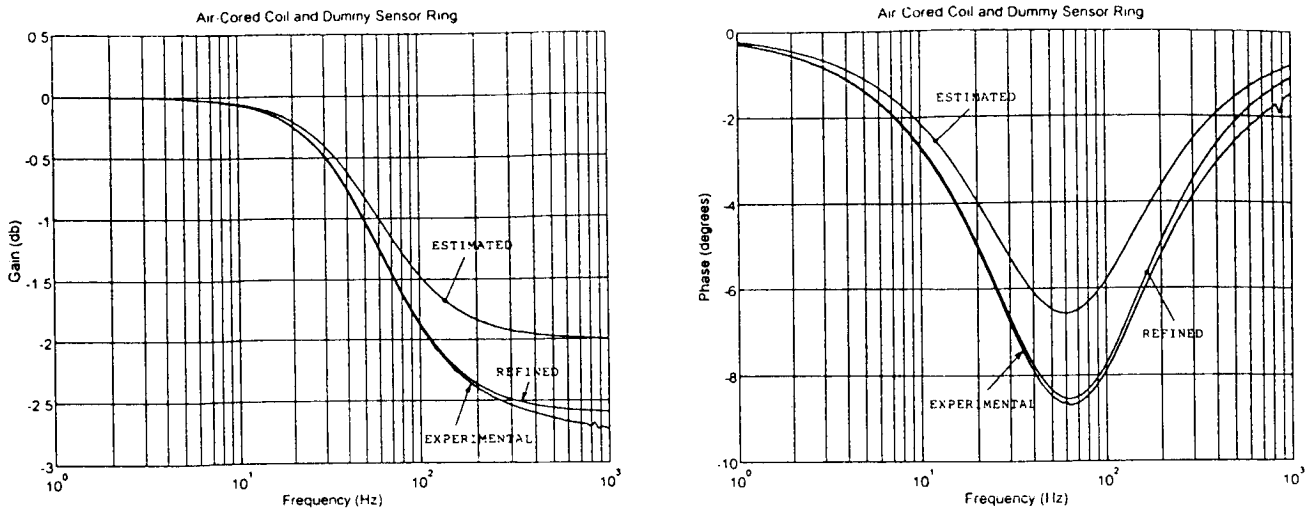

Figure 5 - Typical Results for Eddy Current Effects in LAMSTF
Vertical field at centroid of levitated model, partial simulated sensor frame [1]

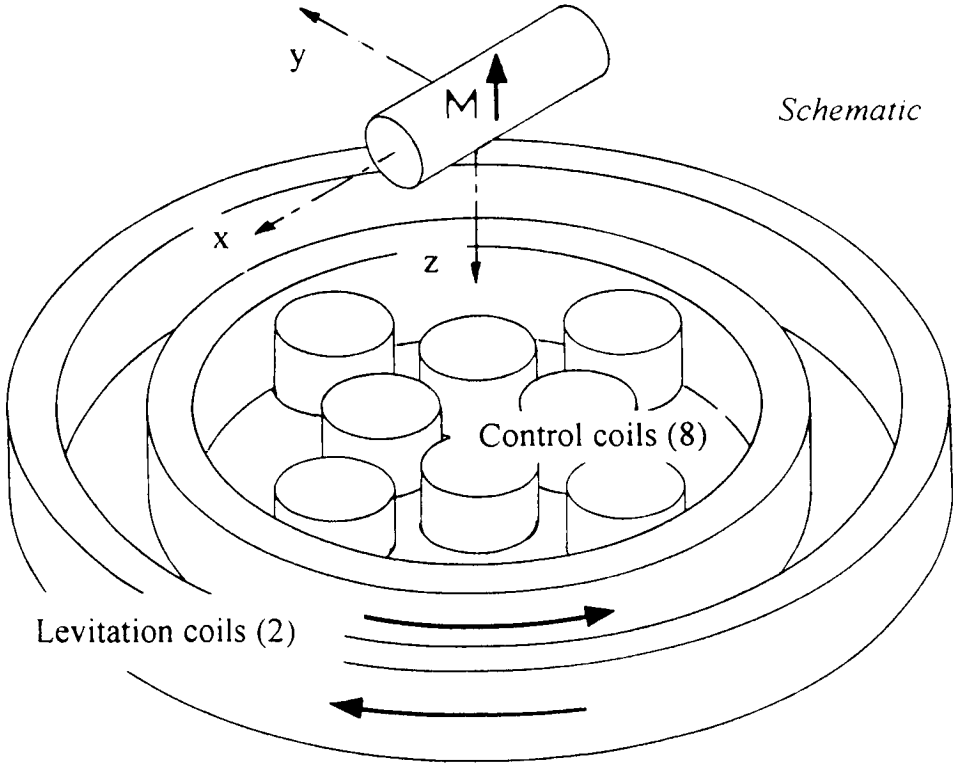

Figure 6 - The 6DOF-8C/2L Levitation Configuration
Schematic

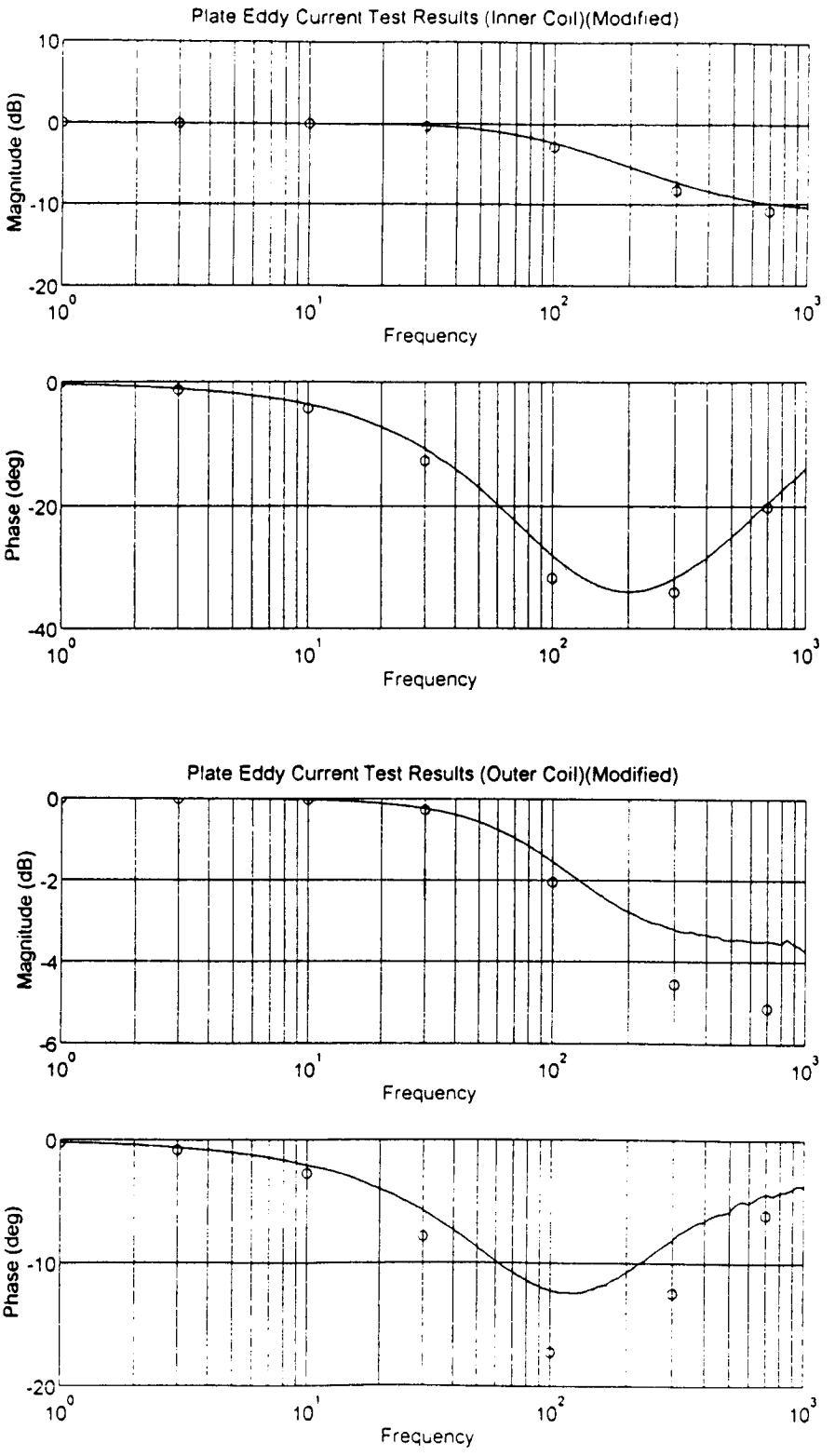

Figure 7 - Typical Results for the 6DOF-8C/2 L System
One inner control coil energized (upper graphs)
One outer control coil energized (lower graph)

Figure 8 - The Annular Suspension and Pointing System Schematic

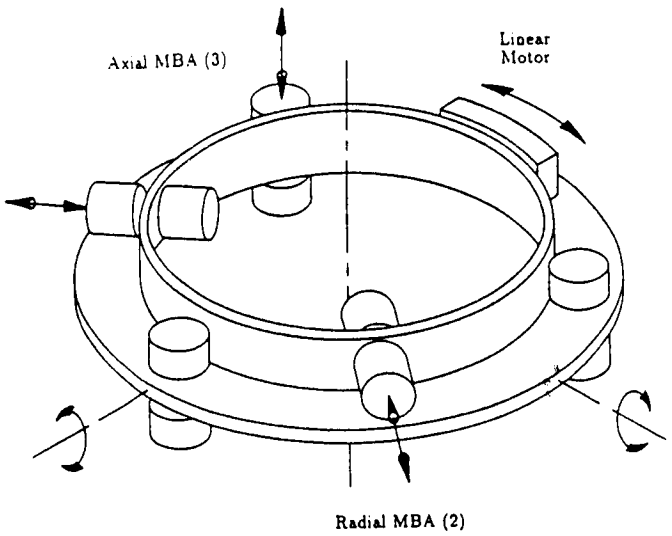

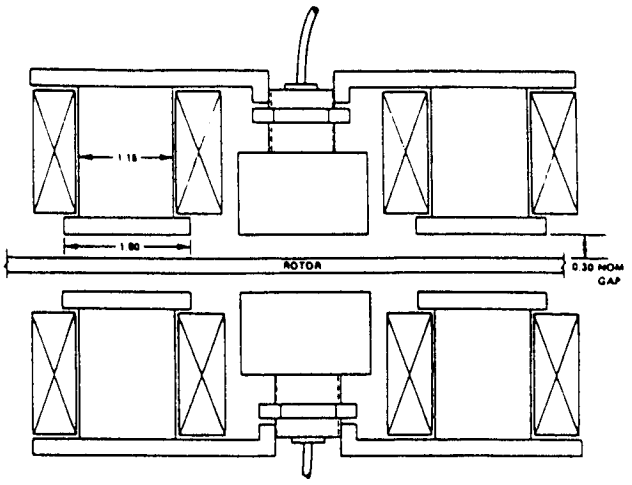

ASPS Axial Bearing Station (dimensions in inches)

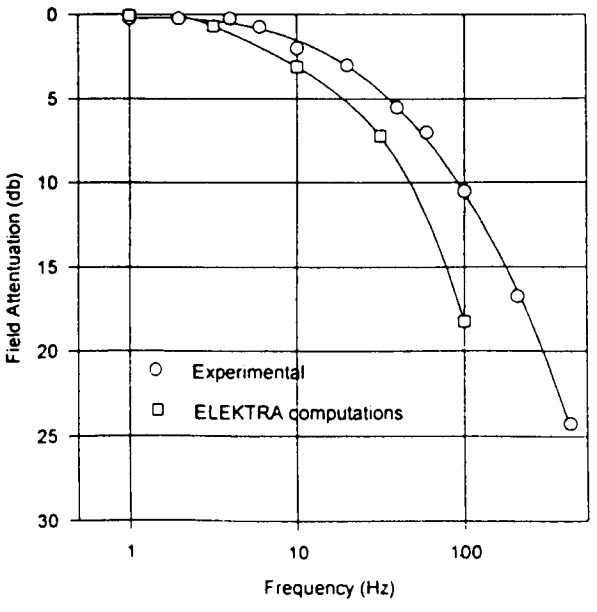

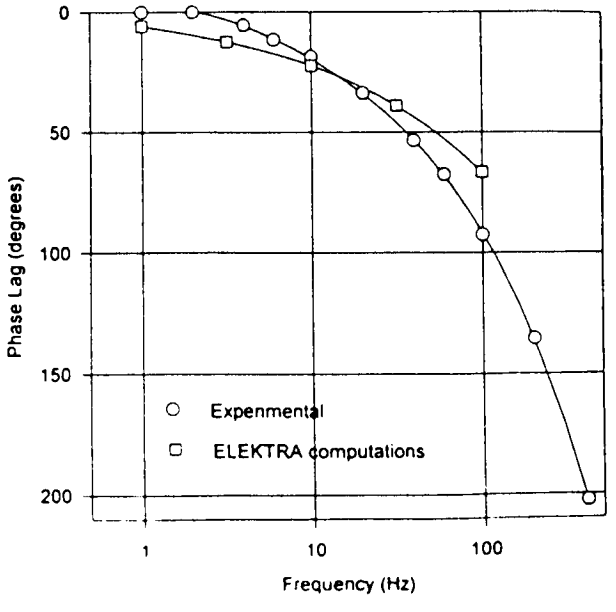

Figure 9 - ELEKTRA Results for Air-Gap Flux

Session 9 -- Maglev 3

Chairman: Nelson J. Groom
NASA Langley Research Center

TEST RESULTS FROM A LARGE SCALE, HIGH SPEED EDS MAGLEV WHEEL TEST FACILITY

Marc T. Thompson, Ph.D. [1]
Consultant
19 Commonwealth Road
Watertown, MA 02172
(617) 923-1392 *marctt@mit.edu*

Anthony Kondoleon
Charles Stark Draper Laboratory
Cambridge, MA 02139

SUMMARY

The Laboratory for Electromagnetic and Electronic Systems at the Massachusetts Institute of Technology and the Charles Stark Draper Laboratory, for the past few years, have been testing an innovative Electrodynamic Suspension (EDS) system for Maglev applications on their large scale, high speed wheel test facility. Magnetically-levitated high-speed ground transportation technology is a potential solution to increasing highway and air corridor congestion. The Intermodal Surface Transportation Efficiency Act of 1992 (ISTEA) mandated the development of a prototype Maglev demonstration system. **In 1993, a team of MIT, Draper, Bechtel, Hughes Electronics, and** General Motors completed one of four System Concept Definition studies of Maglev systems in the National Maglev Initiative (NMI). This team concept was based on Electrodynamic Levitation and Guidance (EDS) using superconducting magnets and a special arrangement of electrical conductors on the guideway.

The magnetic suspension system was the most important, but least understood part of proposed EDS Maglev systems. Thorough understanding of such systems, with verified analytical design techniques, were essential to formulating improved designs for successful full scale systems. Since the original NMI study, a new "flux-canceling" Maglev geometry has been developed, and the test fixture described in this paper experimentally confirms the predictions and models derived in the course of this study. New design and analytic techniques for Maglev guideway structures have been developed. The test wheel has been successfully run at speeds simulating that of a full-scale Maglev system and resultant data has been taken at speeds significantly higher than the Maglev drag peak.

SYSTEM OVERVIEW

Earlier tests on a similar EDS suspension were done by the MIT/Draper team, with results given in [Kondoleon, et. al.]. During the course of that testing, it was found that the performance of the aluminum guideway conductors was inadequate, due to poor electrical joints, and the results indicated a drag peak above the maximum wheel speed of 1000 RPM. Therefore, a new test wheel was designed with copper conductors. This paper covers the design and test of the 2-meter diameter

[1] Formerly from the Laboratory for Electromagnetic and Electronic Systems, Massachusetts Institute of Technology, Cambridge, MA 02139

wheel, with capability to test at speeds up to 1000 RPM (84 meters/second linear peripheral speed). Two companion papers in these *Proceedings* discuss the development of modeling techniques for EDS Maglev and basic issues related to magnetic control of ride quality, and the history and design detail of the entire project is discussed in the Ph.D. thesis by Marc Thompson.

Iron-Core Levitation Magnet Design

A linearized view of the magnet with copper coils is shown *Fig. 1.* The magnet core is constructed with laser-cut laminations of 0.9 mm thick M19 transformer steel. The core laminations were bonded together with epoxy which was thinned with ketone. The epoxy was thinned so that it would not take up a significant fraction of the core volume. A thin layer of epoxy was sprayed on each lamination. The laminations were then stacked and the structure was pre-cured at 50C for 1 hour. After pre-curing, the structure was then cured at 180 C for 1 hour. The laminations for the pole faces were cut to accommodate a coil bend radius of 1 centimeter to meet a minimum practical radius for a high-temperature superconducting coil. A sample of the lamination stack-up was tested at room temperature, at elevated temperature, and at 77K in a liquid nitrogen bath. There was no damage evident due to differential thermal expansion under repeated testing.

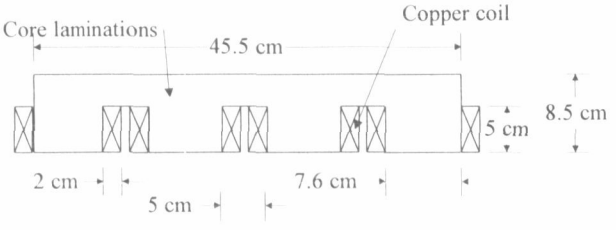

(a) Side view of linearized iron-core magnet with copper coils

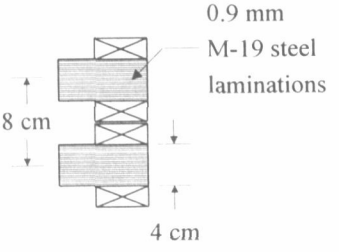

(b) Rear view of dual-row magnet

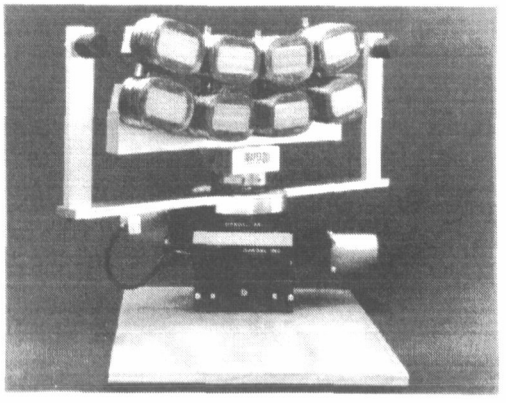

(c) Iron-core magnet, mounted to multi-axis force sensor, showing capacitive position sensors

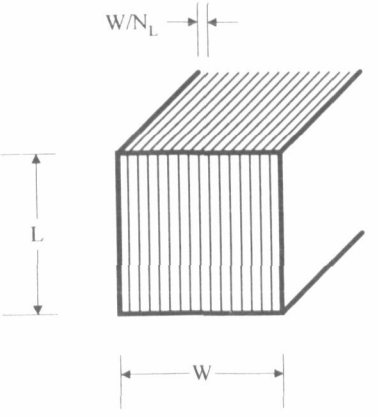

(d) Core laminations

Fig. 1. Detail of magnet design

Eight copper coils were wound with 18 gauge copper magnet wire on an arbor with the same geometry as the magnet polefaces. The final copper coil design had 550 turns in a winding window of 5 cm × 2 cm. The design limit of the copper coils is 8 amps in still air (with current density $J \approx$ 1000 A/cm^2) and 20 Amps when operating in the liquid nitrogen bath ($J \approx 2500$ A/cm^2). The measured resistance of each coil is 3.4 Ω at 300K and 0.442 Ω when cooled to 77K, corresponding to a maximum copper power dissipation per coil of ~200 Watts.

The core laminations were sized by considering the power dissipation per unit length in a section of the core made up of N laminations (*Fig. 1d*) is calculated to be [Zahn]:

$$P \approx \frac{\sigma L W^3 (dB/dt)^2}{16 N_L^2} \qquad [1.]$$

The power loss may be made arbitrarily small by reducing the thickness of the lamination. With a core design with $\sigma \approx 10^6$ (Ωm)$^{-1}$, $N_L = 40$ and expected AC fields of $\Delta B < 0.5$ Tesla at frequencies $f <$ 10 Hz, the power loss in the core is calculated to be less than a Watt.

The magnets were designed so that the top row of coils are operated in a North-South-North-South arrangement (*Fig. 2a*), while the bottom row is offset by one half-cycle. The resultant magnet behaves as a magnetic octapole. A significant advantage of the magnetic octapole is the rapid far-field falloff in the field, which will reduce the shielding required to maintain a low magnetic field in the passenger cabin [Thornton, et. al., 1993].

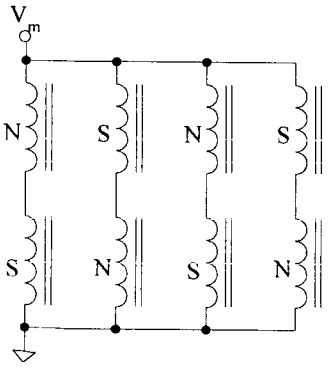

(a) Magnet wiring for flux-canceling Maglev

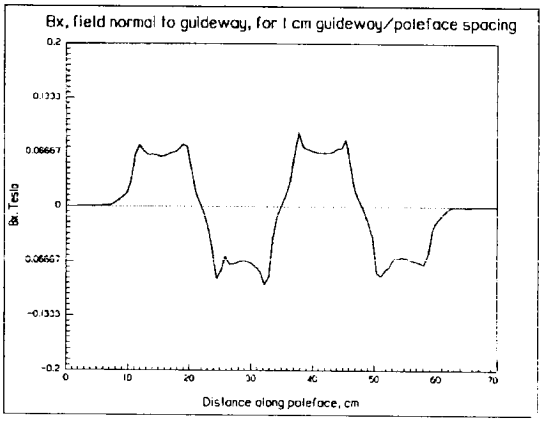

(b) Results of finite element analysis, NI = 2200 Ampere-turns per coil

Fig. 2. Flux-canceling Maglev electrical wiring

Finite element analyses were run on the non-linear iron core design (*Fig. 2b*). The flux density normal to the guideway (B_x) was calculated at a distance $x = 1$ cm from the poleface of the magnet, which is the nominal setpoint for guideway-to-poleface setting. This analysis was checked against measurements taken with a Gaussmeter on the magnet operating with copper coils. The measured value at the center of the poleface was $B_x = 0.069$ Tesla, which matches the calculated value to within a few percent. The finite element analysis was also used to optimize the thickness of the magnet back-iron, so that the weight of the magnet was minimized while insuring that the iron does not saturate for normal operating levels.

Guideway and Test Wheel Mechanical Design

The guideway conductor pattern was constructed from 0.093" thick sheets of 1/2 hard #110 copper. The repeating conductor pattern was cut with an Omax high-pressure numerically-controlled water jet cutter, from 35"×12" sections of copper (*Fig. 3a*) in a 60° section. The water jet cutter has a high-pressure jet 0.030" in diameter and garnet dust is injected into the water stream as an abrasive to increase cutting speed and efficiency. The originally-designed guideway geometry was adjusted to accommodate a minimum cutting line width of 0.030."

The water jet cutting proved to be a more economical method than other methods for copper cutting. The thin slot width does not allow an efficient milling operation. Laser cutting for thick sheets is difficult due to the high thermal conductivity and reflectivity of copper. Wire-EDM is a precision process, but is costly and slow. The water cutting resulted in an acceptable mechanical tolerances of a few thousandths of an inch. Each 60° section took approximately 1 hour to cut. For a production operation, the conductor pattern could be punched out of sheets of copper.

After the individual guideway sections were cut, the inner face of the copper conductor pattern was painted with an electrically-insulating high temperature stove paint. The paint is specified to maintain its integrity to temperatures of 1000 F intermittently, 800F continuous. The 12 guideway sections were then screwed together with brass, round-head #2-58 screws (*Fig. 3b*) spaced approximately 5 inches apart along the outer and inner rim edges. The resulting ring of copper conductors was brazed along the inner and outer diameters, using a 50% lap joint for additional shear strength. The edge of each section was beveled approximately 0.030" so that the solder joint would have higher strength to withstand the shear force due to hoop tension. After the soldering operation, the heads of the screws were ground off.

A silver bearing solder (94% tin, 6% silver) was used for the braze joint. The solder has high strength and a relatively low melting temperature of 535 °F and a yield strength approximately 3 times higher than low cost lead/tin solder. This solder was chosen over a higher-temperature silver-bearing braze joint (where the melting temperature is ~1000-1500 °F) as the lower temperature results in significantly less thermal stress on the copper conductors during assembly.

After brazing, the eccentricity of the copper ring was measured, and found to be true within 1/16 of an inch. A precision mold was constructed, and a composite disk of fiberglass cloth and epoxy 5/8" thick was constructed over the copper conductors with the conductors near one surface of the disk. A step in the fiberglass disk construction process is shown in *Fig. 3c*, with the finished test wheel shown mounted and ready for operation in *Fig. 3d*. A transparent coating of epoxy was used on the front face of the wheel so that the copper conductor pattern is visible.

Test Wheel Safety Testing

The wheel resonant frequencies were calculated so that vibration may be monitored during wheel operation. During wheel acceleration, or if there is a static or dynamic unbalance, wheel resonances will be excited. This analysis is for purposes of calculating first-order resonant frequencies only. In order to calculate various wheel resonant frequencies (or "critical speeds"), a lumped-parameter model was used to calculate the lowest natural frequencies for several different vibration modes. During wheel operation, wheel resonances were monitored using an accelerometer.

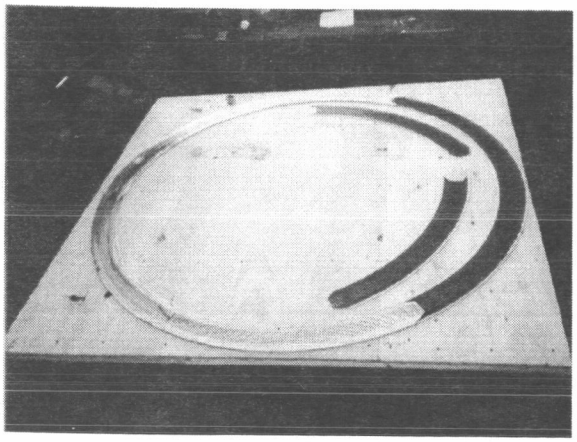

(a) Copper sections coated with non-conductive paint and aligned

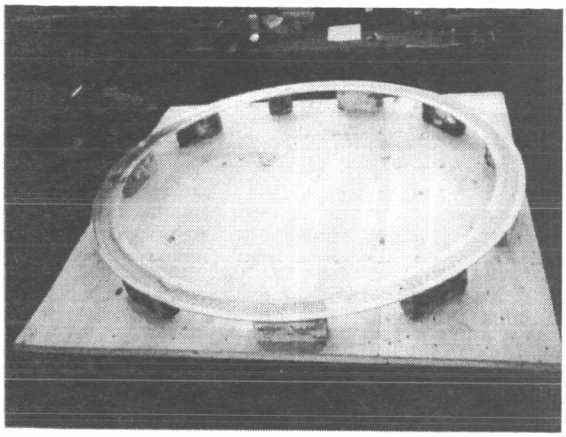

(b) Sections bolted and aligned and ready for brazing

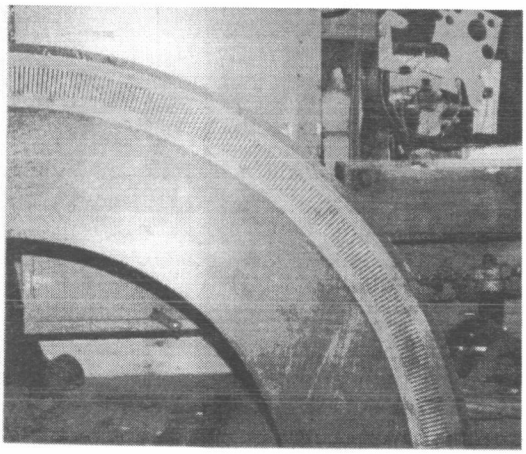

(c) Conductors embedded in fiberglass rim. This is the final seep prior to bolt-hole drilling of the disk and alignment with aluminum hub.

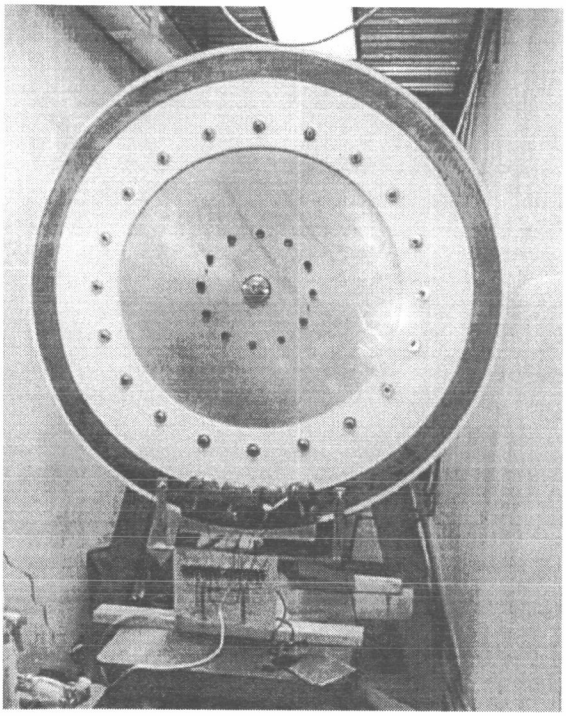

(d) Completed test wheel ready for operation

Fig. 3. Steps in Maglev test wheel construction

Bending and torsional resonances due to the stresses in the aluminum axle were calculated by using standard beam bending and torsion approximations [Den Hartog]. For disk flexure, a vibration mode when the disk itself deforms similarly to the vibration of a drum head, the frequencies of vibration may be found by assuming that the disk behaves as a circular plate (*Fig. 4*) [Blevins, pp. 240] with appropriate boundary conditions. For a disk with a free outer edge, the resonant frequencies are given by:

$$f_{ij} = \frac{\lambda_{ij}^2}{2\pi a^2}\sqrt{\frac{Et^3}{12\gamma(1-\nu^2)}} \qquad [2.]$$

where a is the radius of the disk, E is the Young's modulus of the material in the disk, t is disk thickness, γ is mass per unit area of disk, and ν is the Poisson's ratio. The 3 lowest natural frequencies are found from $\lambda_{ij}^2 = 5.253$, 9.084 and 12.23. The constants λ_{ij}^2 depend on the natural mode shape of interest.

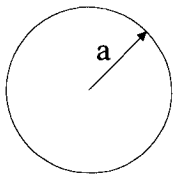

Fig. 4. Circular plate geometry for calculation of flexural resonant modes

This calculation assumes that the disk is of homogeneous material and of constant thickness and is freely supported. The test wheel as built is comprised of fiberglass, copper, and aluminum of varying thickness and is supported by the 3" diameter aluminum axle. In order to calculate resonant modes for disk flexure, average values were used for disk thickness, density, Young's modulus, and Poisson's ratio with calculated results for disk flexure modes (*Table 1*) surprisingly close to the measurements made with accelerometers. The torsional mode may be excited during normal wheel operation at speeds near 230 RPM, but was not noticed during normal operation. Disk flexure modes should not be excited as they are at frequencies higher than the maximum equivalent test wheel operating frequency.

Table 1. Test wheel resonant frequencies

Resonance	***Calculated mode***	***Measured***	***Wheel speed (RPM)***
Torsional	3.85 Hz	---	231
Bending	76.3	---	4580
Disk flexure modes	29.6 Hz, 51, 69	21.9 Hz, 50, 69	1314, 2976, 4116

Air Bearing Design

The air bearing allows low friction, one degree-of-freedom motion of the magnet in the vertical direction. The bearing is under load due to magnetic guidance and drag forces. The bearing allows free motion of the magnet assembly vertically, while constraining the magnet in the other 5 degrees-of-freedom. Further details of the air bearing theory and construction are discussed in [Chiu].

The bearing housings are designed to slide on an alumina shaft 4"×1.36"×30" (10cm×3.5cm×76cm). Before assembly, the alumina shafts were cleaned with sulfuric acid. The air supply was cleaned and dried with a Wilkerson Model X06 desiccant dryer and an ARO 129121-400 Filter/Regulator Unit The bearings are designed to operate with a nominal air gap of 5-15 μm (0.2-0.6 mils). After initial assembly it was found that the main bearing would ground out with torque about the vertical axis of ~ 6 Newton-meters. A secondary outrigger bearing was added to compensate for this torque. Test data shows good performance when the bearing is operated at an air pressure of 140 P.S.I. with z torques up to 16 N-m, with resultant damping of less than 1%. The maximum torque during normal test wheel operation is approximately 25 N-m, so steps were taken to increase the

torque load-bearing capability. With preloading, the load bearing capability of the bearing can be doubled. The air bearing was then tested and it was found that the damping ratio was low, approximately 1% *(Fig. 5d)*.

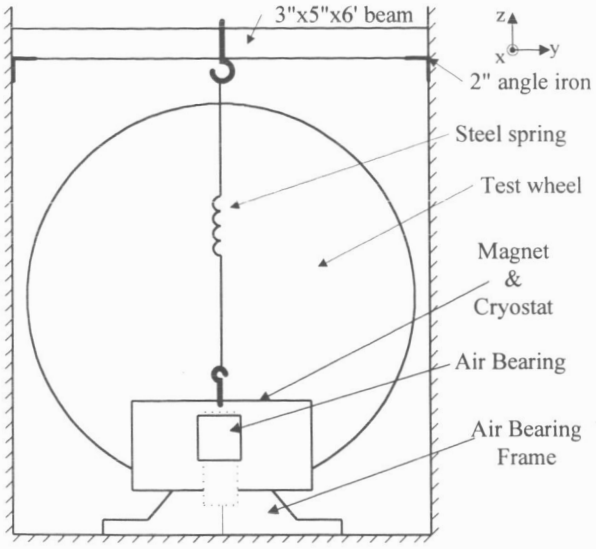

(a) Air bearing schematic view

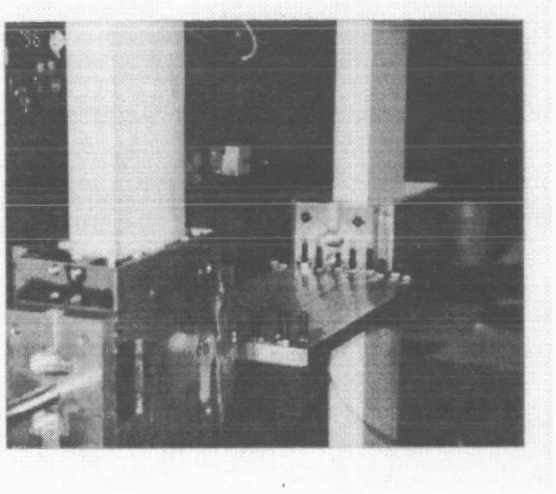

(b) Main and outrigger air bearings, shown sliding on alumina shafts

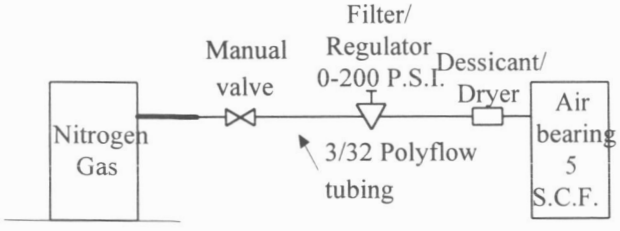

(c) Details of air bearing piping

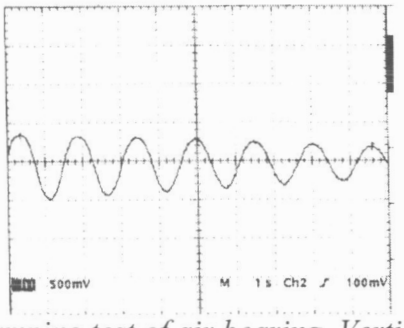

(d) Damping test of air bearing. Vertical 1 cm/division. Oscillation due to steel spring is at approximately 0.6 Hz

Fig. 5. Magnet and air bearing setup

Prototype Superconducting Coil Design and Testing

High-temperature superconducting coils were designed which may be used to retrofit the existing magnet. Several prototype pancake coils were constructed from Bi-2223 superconductor, with HTSC tape dimensions as show in *Table 2* [Haldar]. The cross sectional area of the tape is $A_t = 7.4\times10^{-7}$ m^2, and the area of the superconductor is $A_{sc} = 1.8\times10^{-7}$ m^2, or 25% of the total area. In between each turns of the coil, there is an insulator made of polyimide tape (Kapton) 0.0027" (76 μm) in thickness. After winding and before epoxy impregnation, the edges of the Kapton tape were trimmed off with a razor. A winding width of 1 cm was designed (*Fig. 7a*). Ideally, this would

accommodate $N = 36$ turns per pancake, but due to the bulging of the winding $N = 30$ was wound per coil. After winding, the coil was impregnated with Stycast 2850-GT low-temperature epoxy. The coil was cured at 70 °C for 24 hours.

Table 2. High temperature superconducting tape specification[2]

Tape width	$2a = 3.7$ mm
Tape thickness	$t = 0.2$ mm
I_c at 77K, zero field	11.2 A[3]
Total superconductor area	1.8×10^{-7} m^2
% superconductor	25%
J_c at 77K	6200 A/cm^2
J_{eng} at 77K	1550 A/cm^2
Maximum tensile strain	0.2 %
Maximum bending strain	0.4%

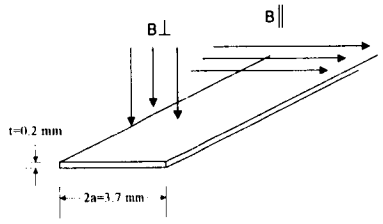

(a) Definition of perpendicular and parallel fields

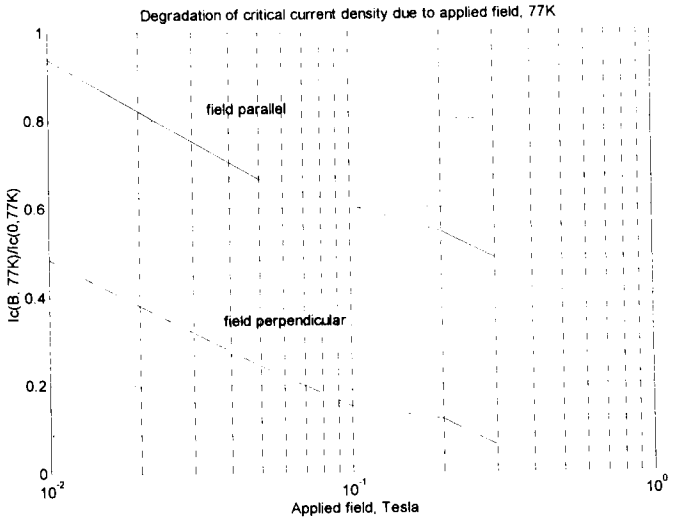

(b) Data from IGC BSCCO-2223 tape [Haldar]

Fig. 6. Degradation of I_c as a function of applied field orientation for HTSC tape

An approximate value for the self-inductance of each pancake coil can be found by using an expression for the inductance of a rectangle of rectangular wire is [Terman, pp. 53]:

$$L = 0.92N^2\left\{(s_1+s_2)\log_{10}\left(\frac{2s_1s_2}{w+t}\right) - s_1\log_{10}(s_1+g) - s_2\log_{10}(s_2+g)\right\} + 0.4N^2\left\{2g - \frac{s_1+s_2}{2} + 0.447(w+t)\right\} \qquad [3.]$$

where L is in microHenries, N is the number of turns in the rectangular coil, s_1 and s_2 are the mean outer lengths of the rectangle side (in meters), w is the width of the rectangle cross section, t is the

[2] Data from Intermagnetics General Corporation

[3] At the time of this writing, tapes with $I_c = 40$A at 77K, 0T are available [Iwasa]

thickness of the rectangle cross section, and g is the diagonal length of the coil cross-section. This model shows good agreement with finite-element analysis and measurements on the prototype coil (*Table 3*).

An I/V curve was generated for the prototype pancake coil (*Fig. 7b*). Results show that the critical current of the coil was degraded by approximately 50% during the winding process, perhaps due to the crude solder connections or the 2 centimeter bend radius[4]. With a tape thickness $t = 0.2$ mm and a minimum bend radius of $\rho = 2$ cm a maximum bending strain of $\varepsilon = t/2\rho = 0.5\%$ is predicted, which is sufficient to degrade the critical current density [Haldar]. However, the coil performs better than a copper coil of identical geometry up to approximately 17 Amperes. For operation as a Maglev magnet coil, the anisotropy of the tape with regard to degradation of critical current due to perpendicular fields makes it advantageous to keep the HTSC material from the poleface area where leakage flux is of the greatest magnitude.

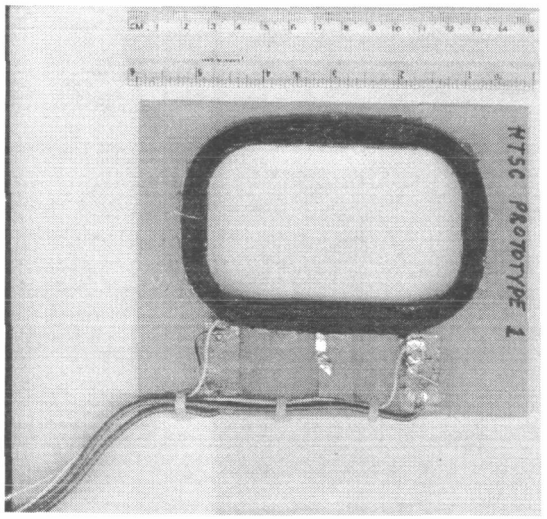

(a) Prototype HTSC coil, mounted and strain-relieved. Shown are large current wires and voltage taps for voltage sensing.

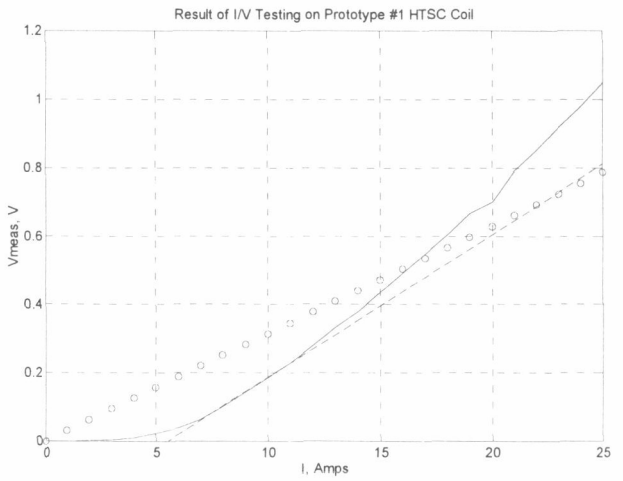

(b) Results of I/V testing with prototype coil, 77K, zero field. Horizontal axis: coil current; Vertical axis: measured voltage at current taps. Solid line --- measurements. Dotted line, prediction, based on $I_c = 5.5$ Amps. ooo --- Comparison with copper coil of same geometry

Fig. 7. Prototype HTSC coil

Table 3. Prototype HTSC coil electrical parameters

	Calculated	***Finite Element Analysis***	***Measurement @ 1 kHz***
R @ 300K	0.3206 Ω	---	0.47 Ω
R @ 77K (when normal)	0.0641 Ω	---	---
L	167 μH	166 μH	155 μH

[4] In this measurement, the actual critical current density if the 10 μV/cm criterion is used is approximately 2 Amperes.

Cryostat and Liquid Nitrogen Delivery System

The cryostat (*Fig. 8)* was designed to hold the iron-core magnet in a liquid nitrogen bath. Level sensors were installed in the cryostat so a nitrogen delivery system can maintain a constant level of coolant over the magnets. The vessel was constructed from sheets of 1/8" thick G-10 fiberglass/epoxy composite, with the corner seams sealed with 2" wide strips of fiberglass boat tape and Emerson and Cuming Stycast™ 2850-GT epoxy. 5 outer walls of the cryostat were insulated with 1" thick Styrofoam. The front face of the cryostat, where the magnetic polefaces are flush, was milled out to a 1/16" thickness, with the magnet polefaces fitting into the groove. The necessary tight spacing between the magnet pole faces and the test wheel did not allow insulation on this face. The aluminum support braces keep the front face of the vessel flush when differential thermal expansion occurs. An outer layer of 1/16" phenolic on 5 faces of the vessel protects the Styrofoam insulation from damage.

The capacity of the cryostat is approximately 8 liters of liquid nitrogen. The latent heat of evaporation of nitrogen at 77 K is $h_L = 161$ J/cm^3. The total cooling requirement includes heat leak from the cryostat and power dissipation from the copper coils. Heat flux leak through the G-10 and Styrofoam insulation was calculated to be $q_{leak,cond.} \approx 150$ W/m^2, corresponding to a heat leak due to conduction of approximately 30 Watts. Radiative heat transfer is a few Watts. The fill rate was measured with the magnets not operating, and was approximately 0.8 liters/hour corresponding to a cryostat heat leak of ~35 Watts. A liquid nitrogen delivery system was designed to maintain a constant level of liquid nitrogen in the cryostat under all operating conditions.

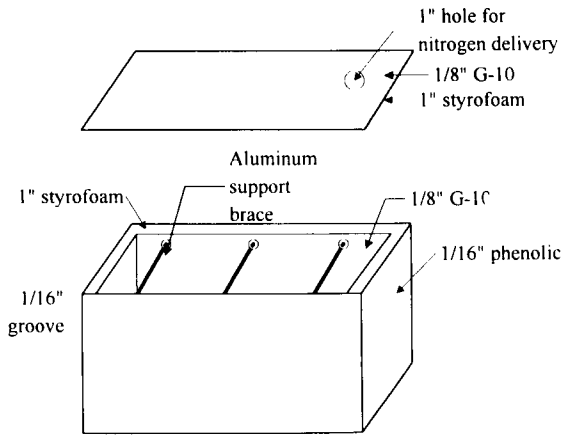

Fig. 8. Cryostat

Test Wheel Speed Control and Data Acquisition System

The data acquisition and test wheel control system (*Fig. 9*) is a computerized station for real time acquisition, processing, display, and storage of sensor data during tests in the facility. The system is comprised of a Macintosh IIfx data acquisition computer, electronics console, motor controllers, specialized software and external sensors. Key parameters are monitored during tests in the facility. Summary data is recorded in the form of plots and spreadsheet compatible data files. Sensors include the multi-axis force sensor to measure forces and torques acting upon the test article, gap sensors to measure the coil to wheel gap, rotation sensors to measure wheel speed, and temperature sensors to measure shaft bearing temperature. The data acquisition and control computer contains 8M RAM and a 240M hard drive, a National Instruments NB-MIO-16 analog/digital

interface card with 16 multiplexed channels of analog input, 8 bits of digital I/O, and 3 counter/timers. Four analog channels are used to acquire gap and temperature sensor data, eight channels have been allocated for coil current measurement and two of the counters for measuring wheel speed. The computer also has two serial ports. One of these is used for communicating with the digital interface of the multi axis force sensor using RS-232 protocol, while the other port is connected to the main motor controller.

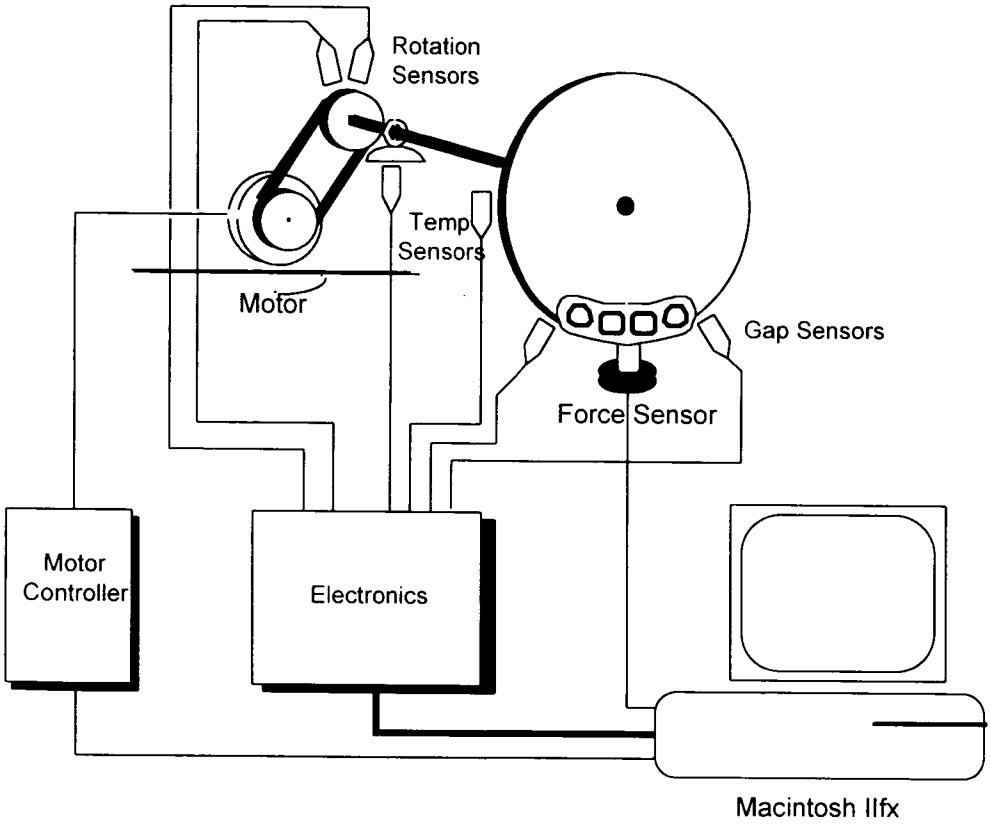

Fig. 9. Data acquisition system and test wheel speed control

TEST RESULTS

Maglev Force Measurements using Force Sensor

The initial testing was done with the magnet mounted to a 6 degree-of-freedom force sensor. The procedure for making basic measurements of forces and moments was as follows:

- The magnet was positioned near the test wheel in the desired vertical (z) and horizontal (x) positions.
- The test wheel was run at the speed corresponding to the desired linear velocity.
- The data acquisition system was activated, beginning a 4 second sampling of force and torque data from the force sensor.
- In the middle of the sampling period, the power supply driving the coils was turned on, and the resulting force transient was measured (*Fig. 10a,b*).

By doing multiple force measurements at different vertical magnet positions and test wheel speeds, Maglev lift (z force), drag (y), and guidance force (x) profiles were calculated (*Fig. 10c,d*) based on the data from the wheel tests. A companion paper in these proceedings describes a model which predicts the lift and drag force profiles with good results.

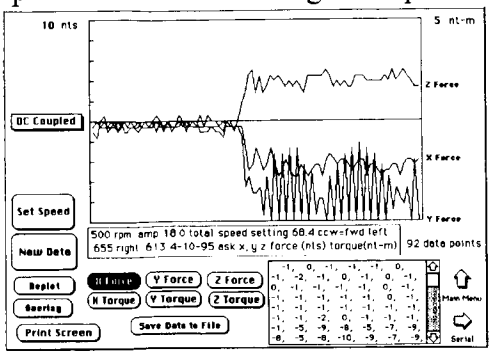

(a) Data acquisition screen showing x force (guidance), y force (drag) and z force (levitation)

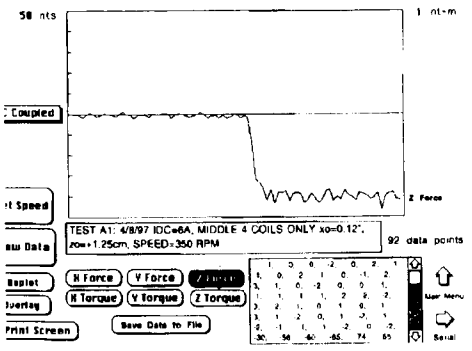

(b) Magnetic lift measurement, showing approximately -50 Newtons of lift at 350 RPM

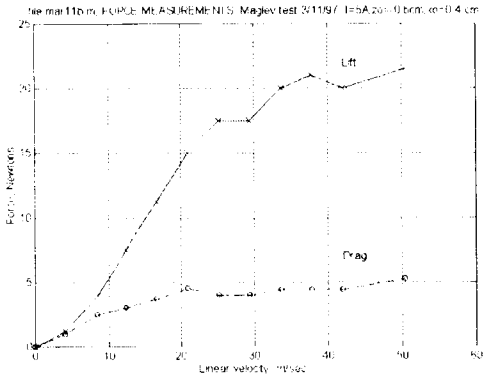

(c) Magnet below null position at z = -0.4 cm

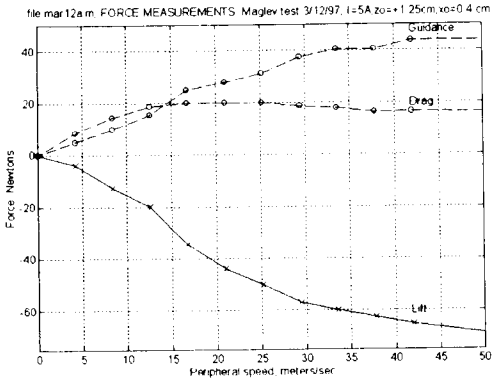

(d) Magnet above null position at z = 1.45 cm

Fig. 10. Lift, drag, and guidance force measurements at different vertical (z) displacements

Vertical Dynamic Tests using Air Bearing and Active Vertical Position Control

In order to test the concept of varying the lift force by using differential current control, a control current source was connected as in *Fig. 11a*. The test wheel was run at 350 RPM. Each of the coils was energized with 6 Amps DC by the main power supply V_m. A 12 Amp peak-to-peak square wave driven by the control current source I_c and the resultant measured lift force is shown *Fig. 11b*. The magnet was set above the null position, and hence the average lift force is negative. This test verifies that it is possible to control the vertical force by controlling the magnet nodes shown in the figure. The advantage of driving at these points is that the effective inductance at the coil terminals is decreased by mutual coupling between magnet coils.

In a follow-up experiment, the air bearing was energized and the magnet was allowed to bounce freely under active current excitation. The DC current for these tests was set to 5 Amperes, the test wheel was set to 350 RPM (30 meters/second peripheral speed), and an underdamped vertical resonant frequency of 1.15 Hz was measured corresponding. In *Fig. 12a*, the differential control terminals are driven with a 12 A p-p, 0.2 Hz current signal. The bottom trace shows little motion, as

the magnet is driven well below the resonant frequency. In *Fig. 12b*, the magnet is driven with a current at 1.1 Hz, near the measured resonant frequency. As expected, there is significant vertical deflection of the magnet.

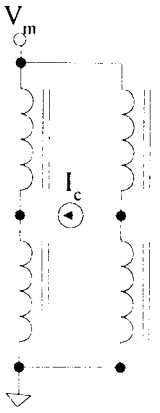

(a) Magnet wiring for differential lift measurement

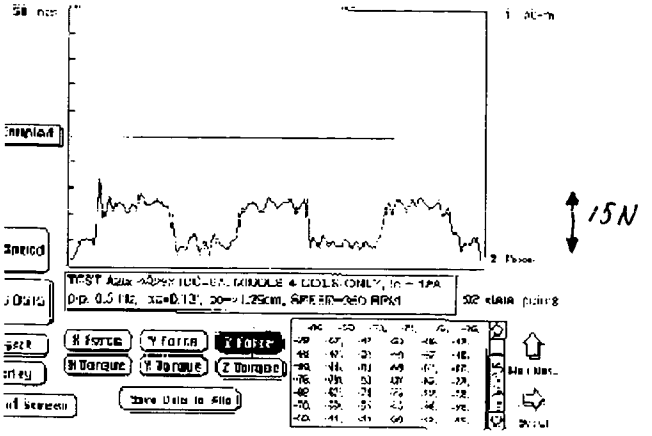

(b) Magnet driven with square wave of control current. Lift force measurement, DC current = 6 Amps/coil, control current = 12 Amp square wave at 0.5 Hz

Fig. 11. Differential lift measurement

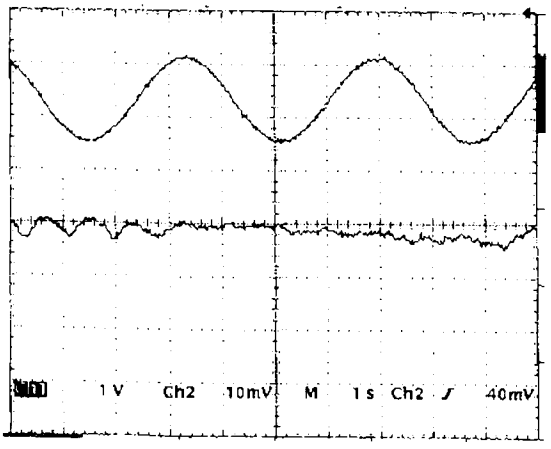

(a) Magnet driven well below resonance Top trace: magnet current, 5 Amps/div. Bottom trace: magnet vertical deflection, 1 cm/div.

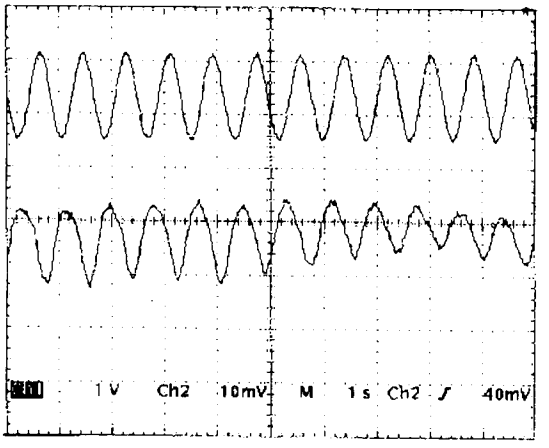

(b) Magnet driven near resonant frequency f = 1.15 Hz. Top trace: magnet current, 5 Amps/div. Bottom trace: magnet vertical deflection, 1 cm/div.

Fig. 12. System driven with sinusoidal current at differential drive terminals

With the air bearing energized and the control system deactivated, the vertical magnet position was perturbed approximately +1 centimeter from the equilibrium position and the resultant transient decay of magnet position was observed (*Fig. 13a*). The oscillatory behavior is at 1.15 Hz with a damping ratio of approximately 1%, corresponding to the expected underdamped EDS response. A similar experiment was run, but with the control system energized with a simple P.I.D.

controller *(Fig. 13b)*. The resultant magnet vertical position response is much more damped ($\varsigma \sim$ 40%) showing that the control system is operating correctly. Further improvement can be made in the transient response by adjusting the loop parameters. This test shows that it is possible to use an active secondary magnetic suspension for ride quality control with this geometry.

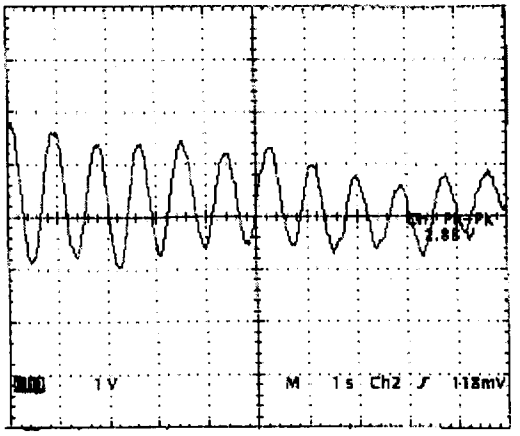

(a) Control system not operating
Initial deflection ~ 1 cm; magnet bounces at EDS natural frequency 1.15 Hz

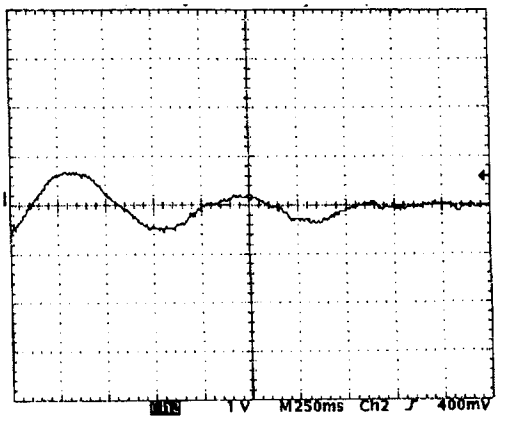

(b) Active damping enabled, using PID controller, damping ratio ~40%. (Note change in time scale)

Fig. 13. Performance of active secondary magnetic suspension

CONCLUSIONS

The successful design and test of a rotating wheel test facility for the study of Maglev electrodynamic suspensions has been demonstrated in this work. The 1/5-scale model suspension described is a starting point for the design of a full-scale, high-efficiency EDS suspension based on high temperature superconducting coils. Development of this model suspension has resulted in improvements and inventions for EDS Maglev, including: the use of an iron core for EDS Maglev, with its associated benefits and costs; verification of operation of the "flux-canceling" topology, including tests of lift force, drag force, and guidance force; use of differential control for controlling vertical forces; AC coil currents for the generation of lift at zero train velocity; use of an active secondary magnetic suspension for ride quality control; and development of scaling laws based on circuit models for the prediction of the performance of a full-scale Maglev system. The test facility operates at linear peripheral speeds exceeding the Maglev drag peak with sufficient safety and mechanical tolerance. At maximum rated test wheel speed, the linear peripheral speed is 84 meters/second, significantly higher than the drag peak velocity. Therefore, both low speed and high speed tests have been done.

Of note is the design of a new low-cost guideway structure which offers good electrical performance. Although much of the guideway conductor design was driven by requirements for high strength to withstand rotating forces, the design could be suitably modified for a full-scale linear guideway where centrifugal force is not an issue. A one degree-of-freedom air bearing was developed which allows low friction vertical motion of the Maglev magnet. The motivation for use of the air bearing was that EDS suspensions are lightly damped and in order to get meaningful test data the mechanical fixturing must have low damping.

Final tests were done using a novel active secondary magnetic suspension. It was shown that it is possible to actively control the magnet position to achieve good ride quality with modest power requirements by using differential current control of the magnets. This opens up the door to the possibility of using HTSC in an active secondary suspension, to take advantage of the robustness of HTSC with regard to AC currents and background fields. These suspension concepts could be further extended to guide the train as it travels down the track by utilizing active horizontal control.

ACKNOWLEDGMENTS

Thanks are due to the U.S. Department of Transportation, Federal Railroad Administration, through the Volpe National Transportation Systems Center, Cambridge, MA, which funded this work, Intermagnetics General Corporation, which provided the superconducting tape used to construct the HTSC coils, Mr. Michael Chiu and Dr. Jeff Roblee who assisted in the design of the air bearing system, and Prof. Richard D. Thornton of the Massachusetts Institute of Technology, who reviewed the work.

REFERENCES

[1] R. D. Blevins, *Formulas for Natural Frequency and Mode Shapes*, R. E. Krieger, Malabar Florida, 1984

[2] M. Chiu, "Low-Cost, Highly-Damped, Precision Linear Motion Using Porous Carbon Air Bearings and Epoxy Replication," Master's Thesis, Massachusetts Institute of Technology, Department of Mechanical Engineering, 1994

[3] J. Den Hartog, *Mechanical Vibrations*, 4th ed., Dover Publications, Inc. New York, 1985

[4] P. Haldar, J. G. Hoehn Jr., J. A. Rice, L. R. Motowidlo, U. Balachandran, C. A. Youngdahl, J. E. Tkaczyk and P. J. Bednarcqyk, "Fabrication and Properties of High-Tc Tapes and Coils Made from Silver-Clad Bi-2223 Superconductors." *IEEE Transactions on Applied Superconductivity*, vol. 3, 1127-30 (1993)

[5] Y. Iwasa, personal communication, 1997

[6] A. Kondoleon, D. Seltzer, R. D. Thornton, and M. T. Thompson, "Development of a Large Scale High Speed Wheel Test Facility," *Proceedings of the Third International Symposium on Magnetic Suspension Technology*, NASA Conference Publication 3336, part 2, pp. 523-534, Dec. 13-15, 1995

[7] F. E. Terman, *Radio Engineers' Handbook*, McGraw-Hill, New York, 1943

[8] M. T. Thompson, "High Temperature Superconducting Magnetic Suspension for Maglev," Ph.D. Thesis, Department of Electrical Engineering and Computer Science, Massachusetts Institute of Technology, May 1997

[9] M. T. Thompson and R. D. Thornton, "Modeling of HTSC-Based Iron Core Flux Canceling Electrodynamic Suspension for Maglev," these *Proceedings*

[10] R. D. Thornton, D. Perreault and T. Clark, "Linear Synchronous Motors for Maglev," *U.S. Dept. of Transportation, Federal Railroad Administration Report DOT/FRA/NMI-92/13*, January 1993

[11] R. D. Thornton and M. T. Thompson, "Magnetically Based Ride Quality Control for an Electrodynamic Maglev Suspension," these *Proceedings*

[12] M. Zahn, *Electromagnetic Field Theory: A Problem Solving Approach*, Krieger Publishing Company, Malabar Florida, 1987

MAGNETICALLY BASED RIDE QUALITY CONTROL FOR AN ELECTRODYNAMIC MAGLEV SUSPENSION

Richard D. Thornton, ScD.
Massachusetts Institute of Technology, Cambridge, MA 02139
MagneMotion, Inc., 142V North Road, Sudbury, MA 01776
thornton@mit.edu, mmi-rdt@magnemotion.com

Marc T. Thompson, PhD.[1]
Consultant
19 Commonwealth Road, Watertown, MA 20172
marctt@mit.edu

SUMMARY

ElectroDynamic Suspensions are highly undamped and require some form of active control or a secondary suspension to achieve adequate ride quality. This paper reports on efforts to develop a version of EDS that uses controllable magnetic forces to eliminate the need for any secondary suspension. The magnetic forces act directly on the guideway and avoid the need to have unsprung weight and a secondary suspension. It is shown that the energy required to effect this control can be less than 1% of the energy stored in the suspension magnets, so a modest size controller can be used. The same controller can also provide lift at very low speeds and thereby eliminate the need for a separate low speed suspension system.

INTRODUCTION

ElectroDynamic magnetic Suspension, called EDS and referred to as repulsive Maglev because it relies on repulsive magnetic forces, has the capability of allowing high speed transportation with a relatively large gap between the vehicle and guideway. In 1966 Danby and Powell proposed an EDS system using superconducting magnets with a "null flux" suspension that offered reduced magnetic drag. Subsequent researchers in the U.S., Japan, Germany, the UK and Canada have come up with a variety of further innovations, but there are still a number of technical problems that need resolution.

To date the only commercial Maglev implementations have used the electromagnetic suspension in which electromagnets support a vehicle with attractive force to a steel guideway. While EMS may be a preferred option for lower speed designs, it has the fundamental disadvantage of requiring a small gap between vehicle and guideway, typically less than a centimeter, and requiring active control to maintain the gap. The

[1] Formerly from the Laboratory for Electromagnetic and Electronic Systems, Massachusetts Institute of Technology, Cambridge MA 02139

promise of EDS is that this gap can be increased by a factor of 5 or more, and therefore guideway tolerances are relaxed and cost might be reduced. Another purported advantage of EDS is that it can be inherently stable and not dependent on feedback to maintain a constant gap. Unfortunately this advantage is not as real as it appears because all EDS designs are highly underdamped and, in certain cases, even unstable. Other disadvantages of EDS are higher power requirements for suspension, higher external magnetic fields and the need for a separate low speed suspension system.

The foremost obstacle to installing any high speed ground transportation system is the high cost, but the key issue is the high cost of constructing a guideway, and this issue is not unique to Maglev. Many researchers are now convinced that, for new installations, if Maglev technology were fully developed it would be less expensive than a high speed train if all installation and operating costs are included. This is particularly true if the Maglev system can provide shorter travel times and more frequent service which, in turn, attracts more users so that the capital cost per user is reduced. The reason for the EMS preference has been its apparently lower cost because it uses a relatively simpler technology with fewer unknowns. German Maglev developers have shown that EMS can operate successfully at speeds over 400 km/h, so the problem is to improve EDS to the point that, for high speed travel, it has enough advantages to compete with both EMS designs and high speed rail.

We believe that in order to achieve wide acceptance EDS designers must face squarely the following problems:

- The cost of manufacturing and installing suspension and propulsion components on the guideway must be comparable to EMS designs;
- The suspension system must have a power loss that is comparable to power loss in EMS designs;
- All EDS suspension designs are highly underdamped and it is imperative to find practical means to damp oscillations and provide high ride quality;
- External magnetic fields associated with onboard superconducting magnets must be reduced, particularly in the passenger compartments.
- It is highly desirable to eliminate the need for a separate low speed suspension system because this adds to the cost, weight and complexity of both the vehicle and the guideway.
- Any superconducting vehicle magnets must be able to operate reliably in a hostile transportation environment.

This and two companion papers [19, 20] report the latest results of MIT research to develop an improved EDS design that addresses all of these issues.

SUMMARY OF PRIOR EDS STABILITY RESEARCH

The problem of stability has long been recognized as one of the fundamental design challenges for the successful commercialization of electrodynamic Maglev. The stability of Maglev vehicles is of considerable interest due to its effects on passenger safety and structural requirements. Many theoretical and several experimental studies have been done to illustrate this problem.

Woods et. al. [1970] considered the stability of a levitated superconducting current ring and evaluated passive damping techniques as well as active stabilization. Davis and Wilkie [1971], Fink and Hobrecht [1971], and Reitz and Davis [1972] studied the problem of infinitely-long wires traveling over an infinite conducting sheet and found vertical and transitional instabilities in the absence of air drag.

This problem of negative magnetic damping was studied by Yamada et. al. [1974] who built an experimental facility in 1973. A ferrite magnet was suspended and allowed to vibrate near a rotating aluminum drum. The damping behavior of the system was observed at various operating speeds, and it was found that negative damping exists for linear velocities above a critical velocity. For a full-scale train traveling over a sheet guideway, these results extrapolated to negative damping for train speeds higher than ~60 km/hour.

Iwasa [1973] and later Iwamoto et. al. [1974] applied the impedance-modeling method to predict lift and drag forces and to study the static and dynamic stability of various vehicle-guideway configurations. Iwamoto predicts a negative damping coefficient for train speed over ~50 m/sec traveling over a trace with discrete loops. Iwamoto recommends using passive damping to achieve good ride quality.

The conclusion of many of these early studies was that some form of damping is needed for acceptable ride quality, even in the presence of aerodynamic drag. Passive damping devices were considered, but the use of passive conducting plates or tuned coils between the lift magnets and the sheet guideway did not provide sufficient damping for the expected guideway roughness. It was concluded that some sort of secondary suspension or active control is needed.

The MIT team of Kolm, Thornton, Brown and Iwasa [1975] studied the stability of the EDS Magneplane system with a 1/25th-scale model, and found the suspension to be underdamped and prone to catastrophic accelerations. One important development for vertical control was the use of the linear synchronous motor for heave damping.

Later stability studies have focused on dynamic instabilities and the effects of mode coupling. Chu and Moon [1983], demonstrated instabilities in a 2 D.O.F. electrodynamic

Maglev model, showing limit cycle oscillations at operating speeds near the Maglev drag peak. Due to the small scale of their model, aerodynamics significantly affected their results. In other experiments, Moon [1977] reports results from a rotating wheel test facility for study of lateral, heave, roll, yaw, and pitch motions. A yaw-roll instability was observed.

The most detailed study of instabilities to date in EDS Maglev has been performed by the Maglev group at the Argonne National Laboratory [Chen, et. al, 1995], [Cai et. al, 1996]. Suspension instabilities of EDS systems with 3 and 5 degrees-of-freedom (D.O.F.) have been evaluated by computer simulation. Their results show that coupling effects among the 5 D.O.F. play an important role and that there are several potential instabilities. The instabilities depend on the equilibrium air gap, which in turn is determined by the vehicle mass, passenger load, and guideway design.

An active secondary suspension using high-temperature superconductors has been built and analyzed by the MIT group of Thornton and Thompson with help from Kondoleon and Draper Laboratory [1995-1997]. With scaling law studies and tests on a rotating test wheel facility, it was shown that it is possible to actively control the magnet position to achieve good ride quality with reasonable levels of power and energy from the control source.

It should be noted that many of the reported instabilities are related to the propulsion means. If a constant propulsive force is used, instability can arise because the magnetic drag decreases with increasing speed. In many cases the use of a constant speed propulsion, or the use of feedback control for the linear motor, would eliminate the instability.

THE PROBLEM OF RIDE QUALITY CONTROL

The Birmingham, England airport shuttle used only an active electromagnetic suspension and the combination of speed and air gap was such that no secondary suspension was required. The Birmingham system had a remarkably good record of reliability, and was advertised as having no moving parts except the doors! It is the goal of the work reported here to develop similar active suspension options for electrodynamic systems which, because of their larger air gap, have the potential to operate at high speeds.

A controllable magnetic primary suspension has a big advantage over an uncontrolled primary suspension combined with an active mechanical secondary suspension: the magnetic force acts directly on the guideway and does not require that there be any "unsprung" weight. EMS systems have the same advantage, but the air gap is so small that an active primary suspension has not been deemed sufficient to give adequate ride

quality at high speeds. In 1972 an MIT research project demonstrated the ability of an LSM to produce controllable vertical forces on a Maglev vehicle, and this allowed the damping of heave motion [8]. By mounting the LSM in different configurations it is possible to counteract sway as well as heave, but since the force acts uniformly over the whole vehicle it is not possible to control pitch or yaw. Therefore, additional magnetic forces are needed to augment the LSM forces.

In principal one could directly control the current in the vehicles suspension magnets, but this is impractical because of the large energy storage associated with these magnets. This is particularly true of the most common design which uses a single array of low temperature superconducting coils without any ferromagnetic material in the flux path. Such designs have large external fields with a very large magnetic energy storage, and this energy must be changed relatively fast to provide good ride quality. Moreover, the low temperature superconducting wire can not tolerate large AC components of current without requiring very large refrigeration power to overcome the AC losses.

The design reported here incorporates three features, each of which contributes to making it feasible to construct a controllable magnetic suspension:

- The vehicle magnets use high temperature superconducting wire that is able to tolerate substantial AC current without excessive power loss;
- The vehicle magnets use an iron core which greatly reduces the amount of energy stored in the field;
- The suspension uses the flux canceling design for which a small differential magnetic field can produce a significant force.

Taken together, these features make it possible to have a reasonable amount of power control the ride quality for a suspension that can tolerate several centimeters of vertical motion.

A SIMPLIFIED MODEL OF FLUX CANCELING SUSPENSION

Prior publications and a companion paper [19] provide a detailed description of the Flux Canceling Suspension system, but for this paper we use the simpler model shown in Figure 1. This Figure represents the vehicle magnets by two wave windings and the guideway by a simple ladder. Each vehicle has two identical suspension systems, one on each side of the vehicle. The guideway can be a channel, with the guideway ladder mounted on the inside vertical walls of the channel, or the guideway can be a monorail, with the guideway ladder mounted on the outside of the monorail. The suspension forces are shear forces between the guideway and vehicle and any lateral forces are balanced by

lateral forces on a separate suspension system on the other side of the vehicle. For this paper we only consider the suspension forces for a single system. The same ideas can be applied to control guidance forces, but guidance is not discussed in this paper.

In Figure 1 the heavier lines show the ends of two wave windings and the lighter lines show a guideway ladder. The two structures are laterally displaced by a distance that is much less than h, the height of the ladder. The actual vehicle magnets consist of windings on the poles of a ferromagnetic structure and the guideway uses more vertical members and a more elaborate arrangement in order to minimize unwanted eddy currents, but this simple model is adequate for the analysis of an active suspension system. The analysis assumes the vehicle is moving with respect to the guideway, so there is the potential for the vehicle to induce AC currents in the guideway and thereby produce vertical lift forces on the vehicle.

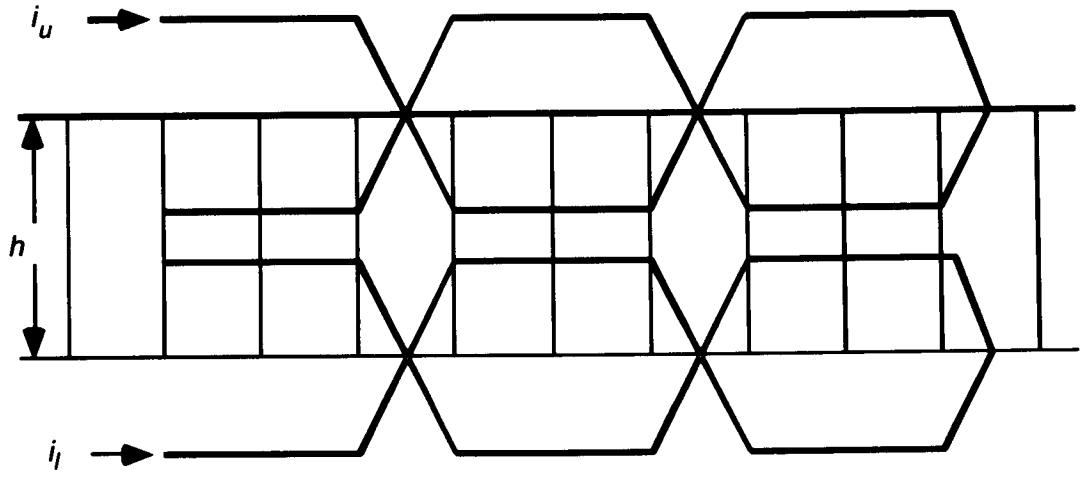

Figure 1. Simplified Flux Canceling Suspension.

In Fig.1 the lower and upper magnet currents are labeled i_l and i_u. Assuming these two currents are constant and equal, if the vehicle coils are vertically centered with respect to the guideway ladder, as shown in Figure 1, then there is no induced current in the ladder and no force on the vehicle. If the vehicle is displaced either up or down, then there is an induced current that creates a restoring force; i.e. the suspension behaves like a magnetic spring. Note that even though there is considerable power loss in the guideway ladder, the suspension is undamped except for minor losses due to aerodynamic effects and eddy currents that are not represented in this simplified model.

The key to the analysis is to note the functional dependence of vertical force on currents. Although the currents in the rung and side elements in the ladder have a complex behavior, we can imagine a composite RMS current, called i_R, that characterizes the

behavior. In order to simplify the analysis define sum and difference values of the vehicle coil currents. The sum i_s is the suspension current that is used to control the equilibrium position and the difference i_c is the control current that is used to control ride quality:

$$\begin{aligned} i_s &= i_l + i_u \\ i_c &= i_l - i_u \end{aligned} \tag{1}$$

If the vehicle is going fast enough to be on the high speed side of the drag peak, then we can express the effective guideway current as:

$$i_g = k_1 \left(i_s y + i_c h_e \right) \tag{2}$$

where k_1 is a proportionality constant that depends on many details of the design, y is the vertical displacement of the vehicle from equilibrium, and h_e is an effective height that determines the induced voltage; in a typical design h_e is about $0.4h$, where h is the height of the guideway as shown in Fig. 1.

Given i_g we can express the vertical lift force F_y as:

$$F_y = k_2 i_g i_s \tag{3}$$

where k_2 is another proportionality constant that depends on the design details.

Define y_0 as the displacement y at equilibrium when the vertical force equals the weight of the vehicle, mg. Then, combining Eqs. 1 to 3 we have:

$$F_y = mg \left(1 + \frac{i_c h_e}{i_s y_0} \right) \tag{4}$$

We interpret Equation 4 as follows. If we wish to exert a control force, say a controllable force up to 0.2g, then we need to make the second term in parenthesis in Eq. 4 have a value of up to 0.2. For a typical full scale design h_e = 0.2 m and y_0 = 0.1 m, so the control current needs to be only about 10% as large as the suspension current. This 0.2g of control force is in addition to any force produced by the LSM, which can also be on the order of 0.2 g, either up or down. Since the vehicle is suspended by a long array of magnets, each can have its own control system, exactly as with EMS designs. Then it is possible to provide controllable pitch forces, and if the same ideas are applied to guidance it is possible to produce controllable yaw forces.

In order to control the ride quality we separate each of the wave windings in Fig. 1 into two equal parts and connect them in the bridge configuration shown in Fig. 2.

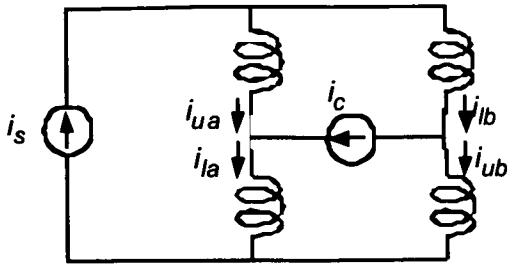

Figure 2. Bridge connection of vehicle windings.

The suspension current i_s excites the bridge so as to control the sum of the magnet currents and the control current i_c excites the bridge so as to control the difference of the magnet currents. In this way we have a simple way to provide only the differential current required for ride quality control.

An important point to note is that there are mutual inductances between the various coils in Fig. 2, and the inductance seen by the suspension current source is typically about twice as large as the inductance seen by the control current. This reduction in control circuit inductance reduces still further the power and energy needs to effect ride quality control. In short, it takes less than 1% as much energy to effect a 0.2 g control force as it does to provide the equilibrium suspension force. For a typical design the power and energy required for good ride quality can be less than the power and energy required to control the magnets in an EMS system.

Experimental results to substantiate this type of control are reported in companion papers in these proceedings [19, 20] and in more detail in an MIT thesis [18].

ZERO SPEED SUSPENSION

The ride quality control hardware can also be used to effect suspension at zero speed. To do this the control current is connected so as to only excite the upper magnet current in Fig. 1. The controller then applies a low frequency sine wave, on the order of 10 Hz, and this induces AC current in the guideway and produces lift. When the vehicle is resting on the guideway the displacement from equilibrium is relatively large so that by exciting only the upper magnets a large current is induced in the guideway ladder. In practice a multiplicity of controllers would be used, each driving only a single magnet, and the excitation currents would be phased so as to minimize pulsating forces. This means of supplying zero speed lift would produce excessive power loss in the guideway if allowed to persist, but in practice it would only be used for a few seconds until the

vehicle speed is past the drag peak. With the suspension system described in this paper the drag peak can be less than 10 m/sec and when this transition speed is reached the normal EDS mode would be activated.

Preliminary experiments have been done to prove the feasibility of low speed lift, but more work is needed to design a working system.

CONCLUSIONS

When an EDS system is built with a Flux Canceling suspension using iron core magnets and high temperature superconducting wire, it is possible to use magnetic forces to control ride quality and eliminate the need for a secondary suspension. This same system can also be used to provide zero speed lift and eliminate the need for a separate low speed suspension system. More work is needed to optimize the design, but initial experiments are very encouraging.

REFERENCES

[1] C. H. Woods, R. K. Cooper, V. K. Neil, and C. E. Taylor, "Stability Analysis of a Levitated Superconducting Current Ring Stabilized by Feedback and Eddy Currents," *Journal of Applied Physics*, vol. 41, no. 8, July 1970, pp. 3295-3305

[2] H. J. Fink and C. E. Hobrecht, "Instability of Vehicles Levitated by Eddy Current Repulsion --- Case of an Infinitely Long Current Loop," *Journal of Applied Physics*, vol. 42, no. 9, August 1971, pp. 3446-3450

[3] L. C. Davis and D. F. Wilkie, "Analysis of Motion of Magnetic Levitation Systems: Implications for High-Speed Vehicles," *Journal of Applied Physics*, vol. 42, no. 12, November 1971, pp. 4779-4793

[4] J. R. Reitz and L. C. Davis, "Force on a Rectangular Coil Moving above a Conducting Slab," *Journal of Applied Physics*, vol. 43, No. 4, April 1972, pp. 1547-1553

[5] Y. Iwasa, "Electromagnetic flight stability by model impedance simulation," *Journal of Applied Physics*, vol. 44, 1973, pp. 858-862

[6] T. Yamada, M. Iwamoto and T. Ito, "Magnetic Damping Force in Inductive Magnetic Levitation System for High-Speed Trains," *Electrical Engineering in Japan*, vol. 94, no. 1, 1974, pp. 80-84

[7] M. Iwamoto, T. Yamada, and E. Ohno, "Magnetic Damping Force in Electrodynamically Suspended Trains," *IEEE Transactions on Magnetics*, vol. MAG-10, (1974), pp. 458-461

[8] W. S. Brown, "A 1/25 Scale Magneplane," Ph.D. Thesis, Department of Electrical Engineering and Computer Science, Massachusetts Institute of Technology, October 1975

[9] Y. Iwasa, W. S. Brown, and C. B. Wallace, "An Operational 1/25-scale Magneplane System with Superconducting Coils," *IEEE Transactions on Magnetics*, vol. MAG-11, no. 5, September 1975, pp. 1490-1492

[10] H. H. Kolm, R. D. Thornton, Y. Iwasa, and W. S. Brown, "The magneplane system," *Cryogenics*, July 1975, pp. 377-384

[11] F. C. Moon, "Vibration Problems in Magnetic Levitation and Propulsion," *Transport Without Wheels*, E. Laithwaite Editor, Elek Science, London 1977 pp. 122-161

[12] L. M. Holmes, "Stability of magnetic levitation," *Journal of Applied Physics*, vol. 49, no. 6, June 1978, pp. 3102-3109

[13] D. Chu and F. C. Moon, "Dynamic Instabilities in Magnetically Levitated Models," *Journal of Applied Physics*, vol. 54, no. 3, March 1983, pp. 1619-1625

[14] F. C. Moon, "Chaotic Vibrations of a Magnet Near a Superconductor," *Physics Letters A*, vol. 132, no. 5, 10 October 1988 pp. 249-252

[15] S. S. Chen, S Zhu, and Y. Cai, "On Unsteady-Motion Theory of Magnetic Forces for Maglev Systems," *Journal of Sound and Vibration*, vol. 188, no. 4, pp. 529-543, 1995

[16] Y. Cai, D. M. Rote, T. M. Mulcahy, Z. Wang, S. S. Chen and S. Zhu, "Dyanmic Stability of Repulsive-Force Maglev Suspension Systems," Argonne National Laboratory report ANL-96/18, November 1996

[17] A. Kondoleon, D. Seltzer, R. D. Thornton, and M. T. Thompson, "Development of a Large Scale High Speed Wheel Test Facility," *Proceedings of the Third International Symposium on Magnetic Suspension Technology*, NASA Conference Publication 3336, part 2, pp. 523-534, Dec. 13-15, 1995

[18] M. T. Thompson, "High Temperature Superconducting Magnetic Suspension for Maglev," Ph.D. Thesis, Department of Electrical Engineering and Computer Science, Massachusetts Institute of Technology, May 1997

[19] M. T. Thompson and R. D. Thornton, "Modeling of HTSC-Based Iron Core Flux Canceling Electrodynamic Suspension for Maglev," these *Proceedings*

[20] M. T. Thompson and A. Kondoleon, "Test Results from a Large Scale, High Speed EDS MAGLEV Wheel Test Facility," these *Proceedings*

ELECTROMAGNETIC LAUNCHERS FOR SPACE APPLICATIONS: COILGUNS FOR REPETITIVE LAUNCHING

M. D. Driga
Professor, Department of Electrical and Computer Engineering
The University of Texas at Austin
Austin, Texas, 78712 USA

ABSTRACT

Electromagnetic macroparticle accelerators or electromagnetic launchers (EMLs) are frequently mentioned as a new approach to launching payloads into space, from earth, to interplanetary space propulsion ,or to test facilities for space applications.

The advantages of such EMLs are due to the fact that electromagnetic thrust forces are distributed over the entire space of the vehicle being launched, are substantially more controllable, and permit projectile velocities well beyond the ones achievable with explosives, because of the absence of some thermodynamic constraints.

This paper considers the idea that a solution to markedly improve the technology is to abandon the simple and coarse d.c. railgun in favor of a.c. polyphase induction coilgun launchers powered by heteropolar compulsators The theory of such a coilgun launchers is presented and an example of their conceptual design is given.

BACKGROUND

The old idea [1] of electromagnetic launchers (EMLs) has received new attention in the last two decades due to the fact that electromagnetic thrust forces can be distributed over the entire length of vehicles been launched, are substantially more controllable and permit projectile velocities well beyond the ones achievable with explosives. Under funding from DARPA and the U.S. Army, numerous applications of the EML technology have been reported at the EML Symposia held every two years.

While the vast majority of such papers concern a variety of anti-armor applications, due to the promise of hypervelocity defeating advanced armor, at virtually all of the symposia (beginning with the one in 1980 in San Diego, CA, up to the one in 1995 in Baltimore, MD), the theory that EML technology can provide a cost-effective means of launching and propelling material into space, thus opening the door to exploration of solar system and beyond, was advanced frequently [2, 3].

Several simplistic conceptual designs were performed in order to obtain a first-order calibration of the EML technology involved in achieving an orbital mission. In such a mission, almost the entire propulsion energy needed is provided by EML technology: the projectile is launched from the ground, travels to the atmosphere, and reaches its launch apogee at 200-800 miles for Low Earth Orbit (LEO) or even 22,000 miles for Geosynchronous Orbit (GEO), at which point it fires its circularization rocket.

Another study was performed by NASA Lewis Research Center [4] in conjunction with Battelle Columbus and employed a railgun system, having as a power supply a large number of homopolar generators and inductors distributed along the railgun. The mission of such an EML system was to dispose of nuclear waste by launching it into the solar system. The concept was to process spent fuel rods into a nuclear waste payload and launch the payloads from the earth's surface into the solar system.

A few years ago, a preliminary conceptual design of an electromagnetic accelerator (EMA) was performed at the Center for Electromechanics (CEM), The Univ. of Texas at Austin, under NASA Langley sponsorship [5]. This EML accelerator had a task of accelerating space vehicle models up to 10,000 Gees for studying their flight behavior in actual re-entry conditions (i.e. real velocities atmosphere, and pressures) in a proposed hypersonic real gas-free flight test facility. In the proposed system, the models, ranging in length from 0.1 to 0.6m, and in mass, from 5 to 10kg, were to carry complex measuring instrumentation. In the test, range altitudes from sea level to 120km and test atmospheres of air, nitrogen, and carbon dioxide were to be simulated - for a velocity of interest between 2 and 6km/sec with a possible extension to 11km/sec.

Both basic topological concepts for the accelerators were considered: the coilgun (heteropolar) principle and the railgun (homopolar) principle [6, 7]. The coilgun EML was designed to accelerate a 14 kg mass to a 6 km/sec velocity with the provision that by adding additional accelerator stages and the corresponding power supplies, a 10 kg mass will be accelerated to 11 km/sec. The railgun system was designed only to accelerate a mass of 14 kg to 6 km/sec.

This paper will outline the principle of the coaxial induction accelerators and will show the result of the preliminary conceptual design for such type of accelerator. It is the author's belief that for space applications, the induction coilguns are superior to the railgun EML. Presently, however, the railguns appear to be leading the competition between the two types of accelerators and there are several reasons explaining why they enjoy such popularity.

Railguns are the simplest of the EMLs and it is natural that they should be developed first. They undoubtedly benefit from the fact that virtually anyone with access to a laboratory can fabricate a small railgun which will accelerate a projectile. This advantage of simplicity is compounded by the scaling relationships for the two concepts. Whereas the inductance gradient of the railgun is essentially independent of scale, the comparable gradient for induction launchers is quite sensitive to it, improving dramatically in larger accelerators. Thus, it is quite difficult to build a small-scale coaxial launcher with impressive performance.

Moreover, the railgun, a homopolar accelerator, has had the benefit of the existence of the pulsed homopolar generator in conjunction with an inductor and an opening switch, an inherently compatible power supply that had been developed for other programs (fig. 1). The induction launchers enjoyed no such benefit and have suffered as a result. In fact, much of the effort expended on the development of coaxial accelerators to date, when viewed in this light, appears to have been directed toward forcing the accelerator to conform to existing power supplies.

In this paper, it is considered that the optimal power supply for a coilgun (a heteropolar accelerator) are heteropolar, rotating electrical machines of synchronous, pulsed types [8], in configurations capable of producing accelerated, linearly traveling magnetic fields [9, 10, 11].

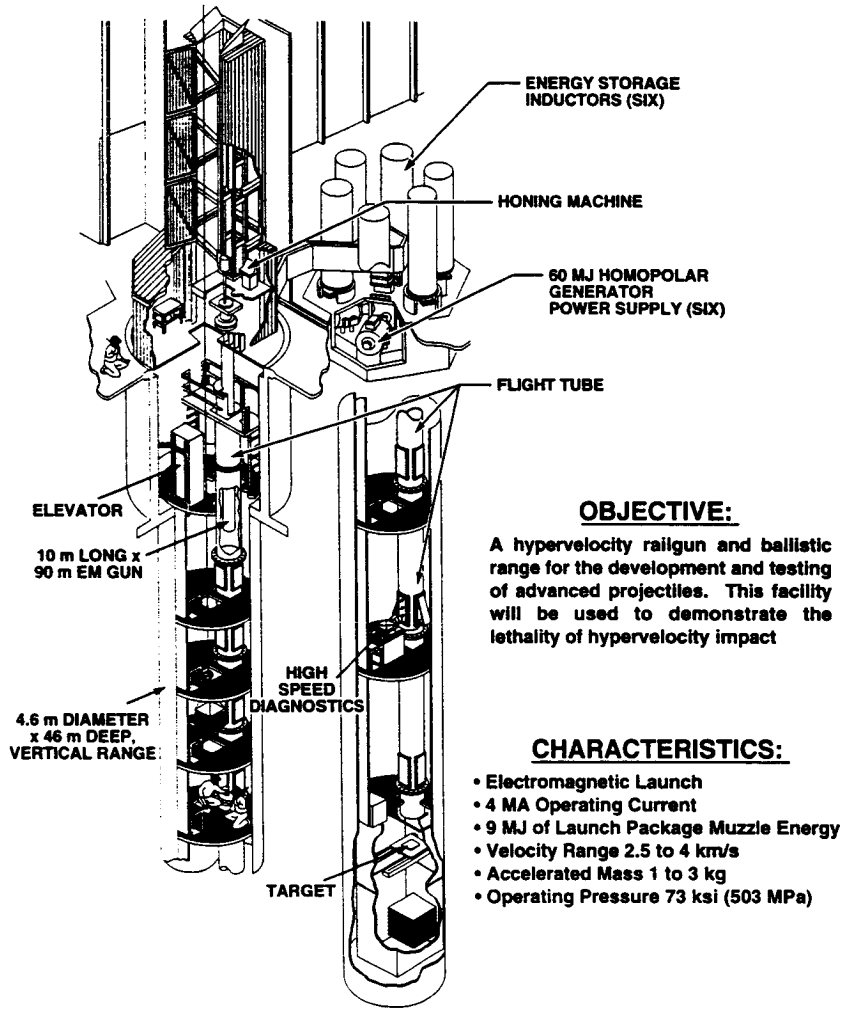

Figure 1. A laboratory railgun electromagnetic launcher (CEM, UT, Austin)

ACCELERATED TRAVELING FIELDS

Figure 2 presents a segment of a stator winding of a coaxial launcher with identical coils. The stator winding is assumed to have a constant polar pitch τ. In the typical 3-phase winding of a conventional induction motor, the 3-phase system of currents energizing the stator produce a traveling rotating wave progressing with a speed:

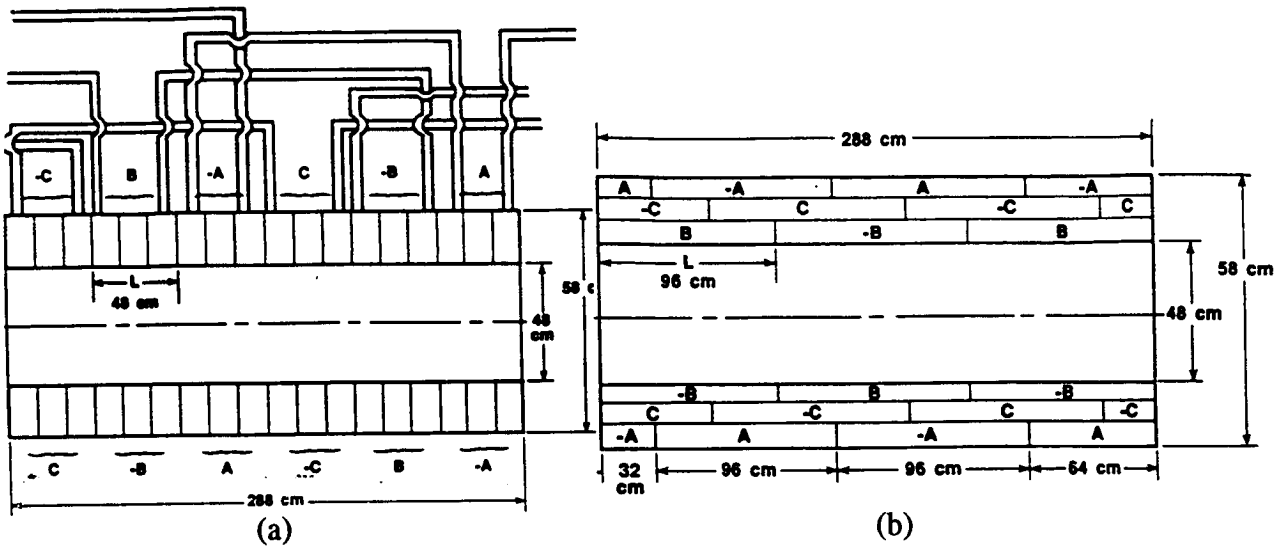

Figure 2. Segment of stator winding of a coilgun launcher: a) non-layered, b) layered.

$$n_s = \frac{120f}{p} \quad \text{where} \quad n_s = \text{synchronous rpm of the field wave} \tag{1}$$

f = frequency of the excitation current
p = number of poles.

In the tubular linear induction launcher in (fig. 2), the velocity of the magnetic field traveling down the launcher is:

$$V_s = 2\tau f \quad \text{where} \quad V_s = \text{traveling field velocity (m/s)} \tag{2}$$

τ = polar pitch (m).
f = frequency of the excitation currents (H_z)

The velocity, V, can be controlled along the launcher barrel by varying either frequency, f, or the polar pitch, τ, or both. The need for controlling the velocity of the traveling magnetic wave in order to obtain an accelerating field wave arises from efficiency considerations.

From the theory of the conventional induction motor it is known that the efficiency for starting operation (expressed in energy terms) is less the 50%. For each unit of energy stored kinetically in the rotor, an equal or greater amount is dissipated in the Joule heating of the rotor by slip losses.

In exactly the same manner, a projectile accelerated from rest by a constant velocity traveling field will be subject to the same slip losses, which amount to W_{PJ}, for the entire launch period:

$$W_{PJ} = \int_{o}^{t} F_p s V_{TF} dt = m_p V_{TF} \int_{TF_o}^{t} s \frac{dv}{dt} dt. \tag{3}$$

Changing the integration limits:

$$W_{PJ} = m_p V_{TF} \int_{o}^{V_{TF}} \left(1 - \frac{v}{V_{TF}}\right) dv \quad \text{where:} \quad F_p = \text{force applied to projectile (N)} \tag{4}$$

m_p = projectile mass (kg)
V_{TF} = speed of traveling field (m/s)
v = instantaneous speed of projectile (m/s)

$$\text{and } s = \frac{V_{TF} - v}{V_{TF}} \times 100 = \text{slip (percent)}. \tag{5}$$

Accelerating from rest to the speed of the traveling field and neglecting friction losses gives a minimum energy loss of:

$$W_{PJ} = m_p V_{TF} \left[v - \frac{v^2}{2V_{TF}} \right]_{o}^{V_{TF}} = \frac{1}{2} m_p V_{TF}^2. \tag{6}$$

Actually, the projectile does not reach the speed of the traveling field (fig. 3a) and the energy loss is given by:

$$W_{PJ1} = \int_{o}^{V_M} m_p (V_{TF} - v) dv = m_p \left(V_{TF} \bullet V_M - \frac{V_M^2}{2} \right) \tag{7}$$

where V_M = projectile output velocity (at the muzzle of the launcher).

For a two-staged system (fig. 3b) comprising two traveling field speeds, the energy loss decreases considerably:

$$W_{PJ2} = \int_{o}^{V_i} m_p (V_{TF1} - v) dv + \int_{V_i}^{V_M} m_p (V_{TF2} - v) dv. \tag{8}$$

$$\text{If the intermediary speed } V_i = \frac{V_M}{2} \text{ and } V_{TF2} = 2V_{TF1}, \text{ then } W_{PJ2} = \frac{m_p V_M}{2} \left(\frac{3}{2} V_{TF2} - V_M \right). \tag{9}$$

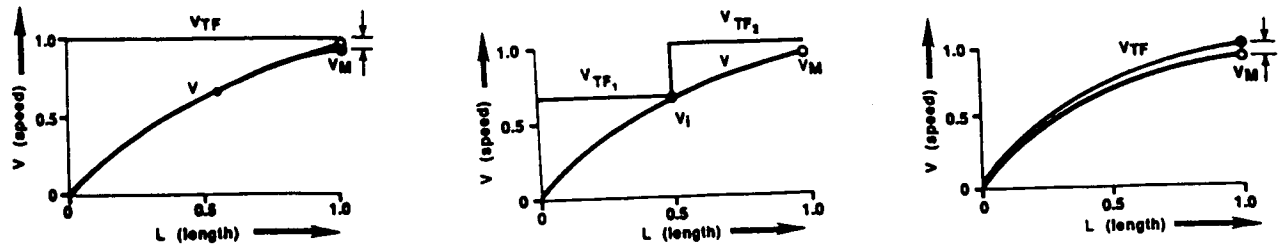

Figure 3. Influence of traveling field velocity change on the launch efficiency. a) No change; b) Two-step change; c) Continuous change.

The number of stages can be further increased, improving the energy efficiency and reducing to a minimum the Joule loss in the projectile, (fig. 3c). At the limit, this corresponds to a continuous increase in the pole pitch or a continuous change in the frequency of the currents, producing a traveling field. The accelerating traveling field will ideally be followed closely by the projectile, keeping the slip and, consequently, the losses, at constant, low values. The manner of obtaining an accelerating field is to continuously vary the supply frequency. This way, the armature is accelerated down an essentially constant pitch stator winding, the driving frequency increasing with armature velocity. Of course, this is just the opposite of what happens in an alternator or compulsator as inertially stored energy is extracted. A combination of the two solutions above could be chosen - a pole pitch variation combined with a change in the power supply frequency.

ELECTROMAGNETIC PRINCIPLES

Eliminating the use of iron for the magnetic circuit permits an increase in electrical machine performance, especially for pulsed operation. For induction accelerators, this means that the analytical tools of equivalent circuits and the theory and methodology of design related to such tools must undergo significant modifications. The equivalent circuit variants (fig. 4) consider series and take into account both parts of the accelerators - the projectile filled segment and the rest of the barrel, which is many times longer. The first section of the equivalent circuit corresponds to the length of the projectile (neglecting all the edge effects), the second takes into account the rest of the barrel $(L - \ell)$ where, in addition to the energy loss in the stator, only reactive power is consumed.

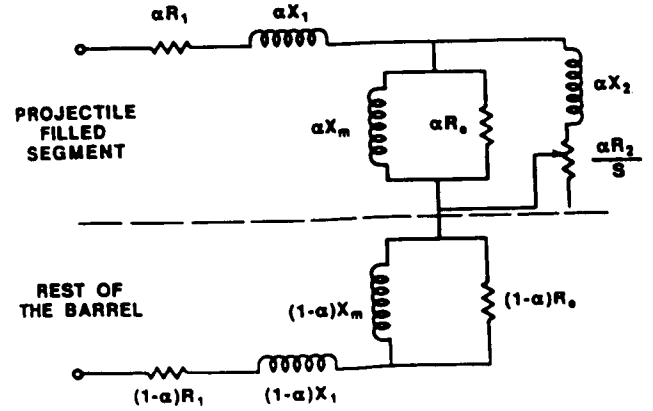

Figures 4. Series equivalent circuit of the coilgun induction accelerator.

Using a similar treatment as in classical theory of linear induction motors [9, 10], in the short secondary variant, the accelerating force is:

$$F = \frac{\left(I_2^2 R_2 \bullet X_m^{\,2}\right)\left(\frac{\ell}{L}\right)}{V_s^2\left[\left(\frac{R_2}{S}\right)^2 + X_m^{\,2}\right]} \tag{10}$$

Optimizing the system for a maximum force-to-loss ratio, assuming a constant stator resistance, R_1, the value of the product between the force and the speed of the traveling field, FV_s, per unit stator loss results:

$$\frac{FV_s}{R_1 I_1^2} = \frac{\frac{\ell}{L} s\left(\frac{R_2}{R_1}\right)\left[1+\left(\frac{Xm}{R_1}\right)^2\right]}{\left(\frac{L-\ell}{L}\right)\left[\left(\frac{R_2}{R_1}+s^2\right)+\left(\frac{R_2}{X_m}\right)^2\right]+\frac{\ell}{L}\left[s^2+\left(\frac{R_2}{X_m}\right)^2\right]\left[1+\left(\frac{X_m}{R_1}\right)^2\right]} \tag{11}$$

which can be optimized further by considering $R_2 X_m$ as a variable

where: R_1 and R_2 - resistances of the primary and secondary circuits
X_m = magnetizing reactance
s = slip
I_1 = stator current.

Onuki and Laithwaite [10] propose an optimization looking for the minimum stator length with the additional requirement of a permissible heat loss based on Euler-Lagrange's equations:

$$\frac{\partial}{\partial v_s}\left[\frac{m_p V}{2FR_2\left(\frac{1}{X_1}+\frac{1}{X_m}\right)V_{TF}\frac{(v_s-v)}{(v_s-v)^2+\left[R_2\left(\frac{1}{X_1}+\frac{1}{X_m}\right)V_{TF}\right]^2}}\right] + \lambda\frac{\partial m_p(v_s-v)}{\partial v_s} = 0 \tag{12}$$

where: λ = Lagrange multipliers imposing the constraints mentioned above.

It has been shown that efficiency considerations exclude the use of an induction accelerator with uniform properties per unit length of stator. A continuously varying pitch, a continuously increasing supply frequency during the launch, or a combination of both requires

changes in the use of the equivalent circuit as a tool for modeling of the machine properties. For a computer-based design, a time marching procedure, continuously changing the parameters of the equivalent circuit as the projectile advances through the barrel was used. Such an iterative procedure takes into account the influence of the transient processes produced by switching the symmetric system of voltages into the accelerator, and also the influence of parameter variations (supply frequency, reactances, polar pitch, resistance change due to field diffusion and temperature rise) [5, 11].

The stator winding is a three-phase tubular winding producing a traveling wave of magnetic flux along the barrel when energized. Usually, one phase of the stator winding is made of a series of alternatively polarized coils spaced apart at a distance equal to the polar pitch and producing alone a standing magnetic flux wave, which pulsates in time with the frequency of the sinusoidal current flowing through the winding. The succession and relative disposition of all three phases is shown in fig. 2a, which illustrates a segment of one of the barrel windings. Each phase coil has an even number of turns, half of direct, half of inverse polarity. The coils of all three phases produce the traveling field wave by superposition.

The serious disadvantage of the standard configuration winding with the interphase connections is that they form an additional outside structure, which the voluminous, and since the connections require the same cross-sectional area as the winding itself, the design of the bus structure is important. Also, the projectile following the traveling wave is subjected continuously to phase-to-phase electric potentials. Because of these drawbacks, the winding selected for design is a layered, distributed winding shown in fig. 2b.

Each layer (inner, middle, and outer) carries only one phase, and the total magnetomotive force (mmf) is obtained by superposition and by the choice of the phase angle between different layers. For a given segment of length L, the sum of different mmf's is:

$$mmf = \overline{B} - \frac{1}{3}\overline{C} - \frac{1}{3}\overline{A}. \tag{13}$$

The condition for a symmetric polyphase system of mmf is:

$$\overline{A} + \overline{B} + \overline{C} = 0, \text{ at any moment} \tag{14}$$

$$\text{then } \overline{B} = -\overline{C} - \overline{A} \tag{15}$$

or, substituting in the original relation for the winding segment of length L:

$$\overline{B} - \frac{1}{3}\left(\overline{C} + \overline{A}\right) = \overline{B} + \frac{1}{3}\overline{B} = \frac{4}{3}\overline{B}. \tag{16}$$

Comparing figs. 2a and 2b, it can be seen that the distance over which phase B is spread is twice as much in the distributed winding. Then for equal conditions, the resulting mmf of the traveling wave is only 4/3 X 1/2 = 2/3 or 66% of the original concentrated winding.

However, the loss of 1/3 of the mmf represents a favorable trade-off, not only for the elimination of complicated phase interconnections, but also for an easy manufacturing process. The windings for a phase run continuously, only the polarity being successively reversed. Insulation between phases is applied uniformly. The projectile traveling down the barrel sees along the stator a distributed voltage which, for all positions, is relatively small, requiring comparatively thin layers of insulation.

A PRELIMINARY COILGUN ACCELERATION DESIGN

The system shown in fig. 5 is comprised of a modular coaxial accelerator, each module being energized by its own pulsed electrical machine. The 14-kg projectile (sabot and payload) is accelerated at a constant acceleration of 10,000 gees, to an exit velocity of 6 km/s by the traveling magnetic wave produced by the currents in the three-phase stator. An additional requirement was to launch a similar projectile (14 kg) to almost double the velocity (11 km/s). Table I presents different options in which the second requirement can be accommodated.

Table I. Operating Envelope.

Exit Velocity (km/s)	Projectile Mass (kg)	Acceleration A (gees)	Launch Length (m)	Launch Time (ms)
6	14	10,000	188	61.2
11	14	10,000	620	112
11	14	18,333	336	61.2
11	14	32,800	188	34.4

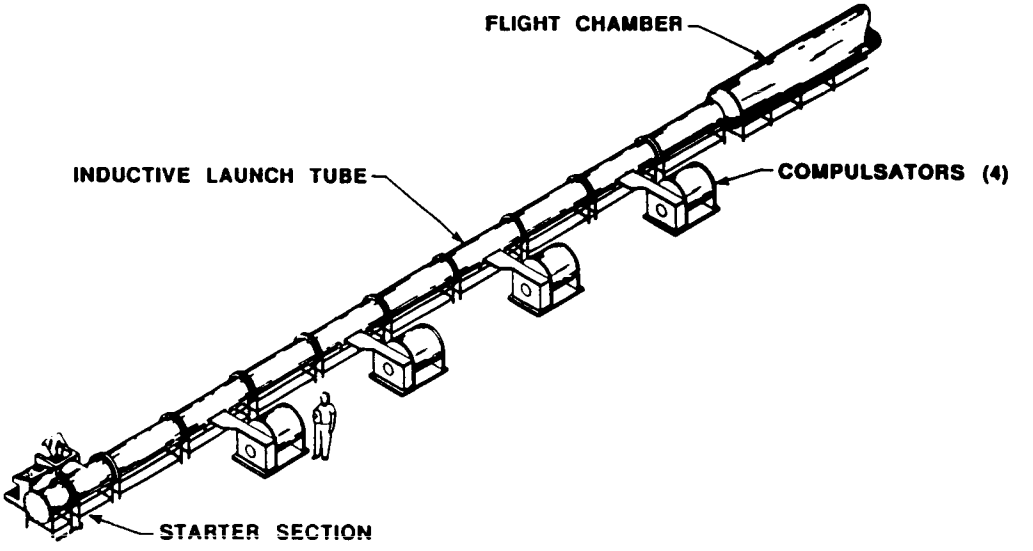

Figure 5. Schematic of a modular coaxial accelerator.

The last design option was chosen, such that the same accelerator is used to launch the 14 kg load at 11 km/s. Due to the modular construction of the barrel, only a small number of connections must be changed. In addition, the number of power supplies, their size, and frequency ratings must be increased.

The three main components of the system are: the launcher, the pulsed electrical machines representing the power supply, and the projectile. The launcher has a ideal length of 188 m and an actual length of 192 m, excluding the "starter coil" which is 1.2 m long and an end coil, 6 m long, the total length approaching 200 m. The standard unit coil which forms the base of the modular construction is 0.15 m long. For the 6 km/s variant, the accelerator is divided into four electrically independent, but magnetically series-connected, segments. Each part is 48 m long and has 14, 8, 7, and 7 segments, respectively, each segment having a different pole pitch in order to match the power supply instantaneous frequency with the velocity of the armature passing through each respective segment.

The power supply is configured of four compulsators storing 179, 211, 242, and 274 MJ. While the projectile is passing through the segment, only half of the stored energy is used. The frequency and voltage of the alternators drops to 70% of the initial value (for instance in the last stage, the frequency drops from 480 to 340 Hz). The current per elementary turn is maintained constant at 477 kA, the impedance dropping at the same rate as the voltage and frequency. The initial voltage of the machines varies from 8.73 kV for the first generator to 29.9 kV for the fourth one.

The above values for the currents and voltages are rms and per phase. Fig. 6 gives the diagram of the frequency and voltage variation for each compensated alternator in the discharge time for each of the parts of the launcher. At the bottom of the diagram, the energy stored by each compulsator is given.

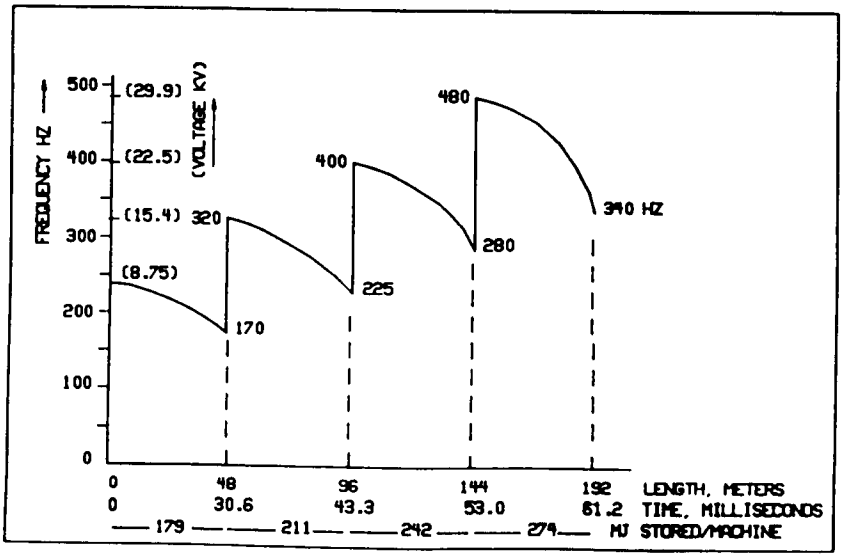

Figure 6. Diagram of frequency and voltage variation for the compulsators used for the modular launcher.

The armature is an aluminum shell. Provisions are made to initially cool the armature to liquid nitrogen temperature. A start-up coil will induce an initial current in the armature, thus assuring the maintenance of the "slip" and the corresponding losses at a reasonable value. When the mass of 14 kg to 6 km/s is accelerated, the exit kinetic energy of the projectile is:

$$W_p = \frac{1}{2}mV^2 = \frac{1}{2}(14)(6{,}000)^2 = 252\times 10^6 J \tag{17}$$

For constant acceleration of 10,000 gees = 98,000 m/s^2, the ideal length of the launcher is:

$$S = \frac{V^2}{2a} = \frac{(6{,}000)^2}{98{,}100} = 183.5\ \ m. \tag{18}$$

Connections between segments of the stator winding increase this length to 188 m. Additional starting coils and final segment extends the length to 196 m.

The launch time is:

$$t = \frac{V}{a} = \frac{6{,}000}{98{,}000} = 61.16\times 10^{-3} s. \tag{19}$$

The average axial force acting on the projectile in the direction of motion is:

$$F = ma = 1.373\times 10^6 N. \tag{20}$$

The need to induce the entire secondary current in the early moments of the launching requires the larger dimensions of the stator coils in the initial stages of the accelerator. A substantial reduction in the size of these coils is achieved by using a "starter segment" whose role is to induce the secondary current in the projectile just before launching.

ACKNOWLEDGEMENT

The support from the U.S. Army, Contract DAAH04-96-0-0197 is gratefully acknowledged.

REFERENCES

1. Fauchon, ALO Villepleé. Canons Electriques, (book), Berger-Levrault, Paris, 1920.

2. Palmer, M. R. & A. E. Dabin. Electromagnetic Space Launch, IEEE Transactions on Magnetics, Jan 1989, Vol 25, No. 1, pp. 493-400.

3. Driga, M. D. & Bilby, C., et. al. "A Lunar Electromagnetic Launcher, Paper No. LBS-88-073, Proceedings of Symposium on Lunar Bases and Space Activities in 21 Century, Houston, TX, April 5-7, 1988.

4. Rice, E. E., et. al. Preliminary Feasibility Assessment for Earth to Space Electromagnetic Launchers, IEEE Transactions on Magnetics, Jan 1989, Vol, 25, No. 1, pp. 9-16.

5. Gully, H. J., Driga, M. D., & Weldon, W. F. A Feasibility Study of a Hypersonic Real-Gas Facility - Final Report, NASA-Langley Grant NAG1-721, Jan 1988.

6. Driga, M. D. & Weldon, W. F. Induction Launcher Design Consideration, IEEE Transactions on Magnetics, Vol MAG 25, No. 1, 1989, pp. 153-158.

7. Weldon, W. F. & Driga, M. D. Traveling Wave Accelerator, U. S. Patent No. 4,870,888, Oct 3, 1989.

8. Driga, M. D. A Generalized Goodness Factor for Rotating Electrical Machines for Hypervelocity Accelerators, Proceedings of the 6th European Symposium on Electromagnetic Launch Technology, The Hague, Netherlands, May 25-28, 1997, pp. 435-444.

9. Laithwaite, E. R. Induction Machines for Special Purposes. (book), Chemical Publishing Co., London, England, 1966.

10. Onuki, T. & Laithwaite, E. R. Optimized Design of Linear Inductor Motor Accelerators, Proceedings of IEEE, Vol 118, Feb 1971, pp. 349-355.

11. Kitzmiller, J. R., et. al. Laboratory Testing of the Pulse Power System for the Cannon Caliber Electromagnetic Gun System, IEEE Transaction on Magnetics, No. 1, Jan 1997, pp. 443-448.

Session 10 -- Controls 2

Chairman: Colin P. Britcher
Old Dominion University (ODU)

ELIMINATION OF UNBALANCE VIBRATIONS IN VARIABLE SPEED MAGNETIC BEARINGS USING DISCRETE-TIME Q-PARAMETERIZATION CONTROL

JunHo Lee
Department of Electrical and Computer Engineering, Kanazawa University
2-40-20 Kodatsuno, Kanazawa 920, Japan

Abdelfatah M. Mohamed
Dept. of Electrical and Electronics Engineering, Assiut University

Fumio Matsumura
Department of Electrical and Computer Engineering, Kanazawa University
2-40-20 Kodatsuno, Kanazawa 920, Japan

ABSTRACT

In this paper we propose a controller design methodology using the discrete-time Q-parameterization control for variable speed magnetic bearings in order to achieve elimination of unbalance vibrations. Rotor unbalance usually generates sinusoidal disturbance forces, with frequency equal to the rotational speed. So in order to achieve asymptotic rejection of these disturbance forces, the Q-parameterization controller free parameter Q is chosen such that the controller has poles on the unit circle at $z = \exp^{jp_kT_s}$ for the different speeds of rotation p_k (T_s is the sampling period). First, we give a mathematical model for the magnetic bearing in state space form. Second, we explain the proposed discrete-time Q-parameterization controller design methodology. The controller free parameter Q is assumed to be a proper stable transfer function whose order equals twice the number of operating speeds. Third, we show that the controller free parameter which satisfies the design objectives can be obtained by simply solving a set of linear equations rather than solving a complicated optimization problem. We also show that the controller order equals: Number of degrees of freedom × (order of Q +3). Finally, several simulation and experimental results were obtained to evaluate the proposed controller. The results obtained showed the effectiveness of the proposed controller in eliminating the unbalance vibrations at the different speeds of rotation.

Keywords: Q-parameterization, Magnetic bearings, Vibrations, Rotor unbalance.

INTRODUCTION

Unbalance in the rotor of rotating machines causes vibrations due to the sinusoidal disturbance forces generated by the unbalance. This problem can be solved using active controlled magnetic bearing systems. There are several papers in the literature which deal with this problem [1]-[7] using either feedback control or Notch filters to eliminate these vibrations.

The Q-parameterization theory [8]-[9] provides a good tool for the controller design of magnetic bearing systems in order to achieve elimination of rotor vibrations [5]. This is because the controller free Q-parameter can be chosen such that asymptotic rejection of sinusoidal disturbances is achieved. The order of the Q-parameterization controller equals the order of the plant plus the order of the free parameter Q while in the other methods, the order of the controller equals the order of the plant plus the order of the weighting functions. Usually the Q-parameterization controller has lower order.

In this paper we extend the controller design methodology developed in [5] to achieve unbalance compensation for variable speed magnetic bearing systems, moreover we design the controller in the discrete-time domain. Since the frequency of the unbalance sinusoidal disturbance forces equals the rotational speed, we can

achieve asymptotic rejection of these variable frequency disturbances by designing a controller which has poles on the unit circle at $z = \exp^{jp_k T_s}$ for the different speeds of rotation p_k, $k = 1, 2, ...r$ where r is the number of operating speeds and T_s is the sampling period. This can be done by a suitable choice of the controller free parameter Q . The controller free parameter Q is assumed to be a proper stable transfer function whose order equals twice the number of operating speeds. With this assumption the controller order is shown to equal: Number of degrees of freedom × (order of Q +3). We also show in this paper that the controller free parameter Q which satisfy our design objectives can be obtained by simply solving a set of linear equations rather than solving a complicated optimization problem as for example in the H_∞ synthesis control. A 36 state controller is obtained for the magnetic bearing operating at three different speeds. Several simulation and experimental results were obtained. The results showed that vibrations are eliminated at the different operating speeds using the proposed controller.

MATHEMATICAL MODEL FOR THE MAGNETIC BEARING

A- Equations of Motion

Consider the magnetic bearing system shown in Fig. 1.

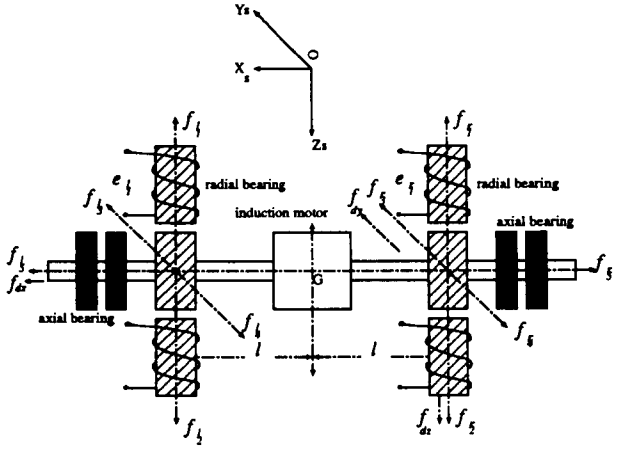

Fig. 1 Schematic diagram of the magnetic bearing system.

Table 1: Parameters of the Magnetic Bearing [9]

Parameter	Symbol	Value	Unit
Mass of the Rotor	m	1.39×10^{1}	kg
Moment of Inertia about X	J_x	1.348×10^{-2}	kg · m^2
Moment of Inertia about Y	J_y	2.326×10^{-1}	kg · m^2
Distance between Mass Center and Electromagnet	l	1.30×10^{-1}	m
Steady Attractive Force	$F_{l1,r1}$	9.09×10	N
	$F_{l2\sim4,r2\sim4}$	2.20×10	N
Disturbance Forces	$f_{dy}, f_{d\psi}, f_{dz}, f_{d\theta}$	?	N
Steady Current	$I_{l1,r1}$	6.3×10^{-1}	A
	$I_{l2\sim4,r2\sim4}$	3.1×10^{-1}	A
Steady Gap	G_{oj}	5.5×10^{-4}	m
Resistance	R	1.07×10	Ω
Inductance	L	2.85×10^{-1}	H
Rotational speed	p	$2\pi30, 2\pi20, 2\pi10$	rad/sec

Assuming that the rotor is a rigid floating body, the fundamental equations of motion of the rotor for the four radial degrees of freedom [5] are

$$
\begin{aligned}
\ddot{y}_s &= \frac{\alpha y_s}{m} + \frac{1}{m}(f_{l3} - f_{l4} + f_{r3} - f_{r4} + f_{dy}) \\
\ddot{z}_s &= \frac{\alpha z_s}{m} + \frac{1}{m}(f_{l2} - f_{l1} + f_{r2} - f_{r1} + mg + f_{dz}) \\
\ddot{\theta} &= -\frac{pJ_x}{J_y}\dot{\psi} + \frac{l}{J_y}(f_{l1} - f_{l2} + \frac{1}{2}f_{d\theta} + f_{r2} - f_{r1} + \frac{1}{2}f_{d\theta}) \\
\ddot{\psi} &= \frac{pJ_x}{J_y}\dot{\theta} + \frac{l}{J_y}(f_{l3} - f_{l4} + \frac{1}{2}f_{d\psi} + f_{r4} - f_{r3} + \frac{1}{2}f_{d\psi})
\end{aligned} \tag{1}
$$

The axial motion (**X** motion) is independent of the radial motion ($\mathbf{Y}, \mathbf{Z}, \mathbf{\Theta}, \mathbf{\Psi}$), can be controlled separately and it is not considered in this paper. All the parameters in Eq. (1) are defined in Table 1.

B- Electromagnetic Equations

1- Force Equation

The electromagnetic force f_j produced by the j th electromagnet can be expressed in terms of the coil current i_j and the gap length g_j as follows:

$$
f_j = k(\frac{i_j}{g_j})^2, \quad j = l1, l2, l3, l4, r1, r2, r3, r4 \tag{2}
$$

where k is a constant

2- Coil **Voltage** Equation

The voltage e_j across the j th electromagnet coil, can also be expressed in terms of i_j, electromagnet coil inductance L, and electromagnet coil resistance R as follows:

$$
e_j = L\frac{di_j}{dt} + Ri_j, \quad j = l1, l2, l3, l4, r1, r2, r3, r4 \tag{3}
$$

C- Linearization

Let F_{oj}, I_{oj}, G_{oj}, and E_{oj} be the nominal values of the force, coil current, gap length and electromagnet voltage of the jth electromagnet respectively, and let f'_j, i'_j, g'_j, e'_j be the deviation of these quantities from their nominal values. Then we can write $f_j = F_{oj} + f'_j$, $i_j = I_{oj} + i'_j$, $g_j = G_{oj} + g'_j$, $e_j = E_{oj} + e'_j$, where

$$
\begin{aligned}
f'_j &= c_j i'_j + d_j g'_j, \\
e'_j &= L\frac{di'_j}{dt} + Ri'_j
\end{aligned} \tag{4}
$$

and $c_j, , d_j$ are the linearization constants which are given by

$$
\begin{aligned}
c_j &= \frac{2kI_{oj}}{G_{oj}^2}, \\
d_j &= \frac{-2kI_{oj}^2}{G_{oj}^3}
\end{aligned} \tag{5}
$$

The gap deviations vector $\mathbf{g}$ can be expressed in terms of $y_s, z_s, \theta, \psi, l$ as follows:

$$\mathbf{g} = \begin{pmatrix} g'_{l1} \\ g'_{r1} \\ g'_{l3} \\ g'_{r3} \end{pmatrix} = - \begin{pmatrix} g'_{l2} \\ g'_{r2} \\ g'_{l4} \\ g'_{r4} \end{pmatrix} = \begin{pmatrix} (z_s - l\theta) \\ (z_s + l\theta) \\ (-y_s - l\psi) \\ (-y_s + l\psi) \end{pmatrix}. \tag{6}$$

Note that for the horizontal shaft magnetic bearing system

$$c_{l1} = c_{r1},\ c_{l2} = c_{r2},\ \ c_{l3} = c_{l4} = c_{r3} = c_{r4}$$
$$d_{l1} = d_{r1},\ d_{l2} = d_{r2},\ \ d_{l3} = d_{l4} = d_{r3} = d_{r4}$$

Assume that the coil voltages are controlled such that

$$e'_{l1} = -e'_{l2},\ e'_{r1} = -e'_{r2},\ \ e'_{l3} = -e'_{l4},\ e'_{r3} = -e'_{r4} \tag{7}$$

then we have

$$i'_{l1} = -i'_{l2},\ i'_{r1} = -i'_{r2},\ \ i'_{l3} = -i'_{l4},\ i'_{r3} = -i'_{r4} \tag{8}$$

$$\begin{aligned} f'_{l1} - f'_{l2} &= (c_{l1} + c_{l2})i'_{l1} + (d_{l1} + d_{l2})g'_{l1} \\ f'_{r1} - f'_{r2} &= (c_{r1} + c_{r2})i'_{r1} + (d_{r1} + d_{r2})g'_{r1} \\ f'_{l3} - f'_{l4} &= 2c_{l3}i'_{l3} + 2d_{l3}g'_{l3} \\ f'_{r3} - f'_{r4} &= 2c_{r3}i'_{r3} + 2d_{r3}g'_{r3} \end{aligned} \tag{9}$$

Also from Equation (6), we have

$$\begin{aligned} (g'_{l3} + g'_{r3}) &= -2y_s \\ (g'_{l1} + g'_{r1}) &= 2z_s \\ (g'_{l1} - g'_{r1}) &= -2l\theta \\ (g'_{l3} - g'_{r3}) &= -2l\psi \end{aligned} \tag{10}$$

Substituting Equations (9)–(10) in Equation (1), we then have

$$\begin{aligned} \ddot{y}_s &= \frac{1}{m}(\alpha - 4d_{l3})y_s + \frac{2}{m}c_{l3}(i'_{l3} + i'_{r3}) + \frac{1}{m}f_{dy} \\ \ddot{z}_s &= \frac{1}{m}(\alpha - 2(d_{l1} + d_{l2}))z_s - \frac{1}{m}(c_{l1} + c_{l2})(i'_{l1} + i'_{r2}) + \frac{1}{m}f_{dz} \\ \ddot{\theta} &= -\frac{pJ_x}{J_y}\dot{\psi} + \frac{l}{J_y}\Big((d_{l1} + d_{l2})(-2l\theta) + (c_{l1} + c_{l2})(i'_{l1} - i'_{r1})\Big) + \frac{l}{J_y}f_{d\theta} \\ \ddot{\psi} &= \frac{pJ_x}{J_y}\dot{\theta} + \frac{l}{J_y}\Big(2d_{l3}(-2l\psi) + 2c_{l3}(i'_{l3} - i'_{r3})\Big) + \frac{l}{J_y}f_{d\psi} \end{aligned} \tag{11}$$

Let $e_y = e'_{l3} + e'_{r3},\ \ e_z = e'_{l1} + e'_{r1},\ \ e_\theta = e'_{l1} - e'_{r1},\ \ e_\psi = e'_{l3} - e'_{r3}$,

then from Equation (4) we have

$$\begin{aligned} e_y &= L\frac{d(i'_{l3} + i'_{r3})}{dt} + R(i'_{l3} + i'_{r3}) \\ e_z &= L\frac{d(i'_{l1} + i'_{r1})}{dt} + R(i'_{l1} + i'_{r1}) \\ e_\theta &= L\frac{d(i'_{l1} - i'_{r1})}{dt} + R(i'_{l1} - i'_{r1}) \\ e_\psi &= L\frac{d(i'_{l3} - i'_{r3})}{dt} + R(i'_{l3} - i'_{r3}) \end{aligned} \tag{12}$$

D- State Space Representation

Let

$$\mathbf{x_y} = \begin{pmatrix} y_s \\ \dot{y}_s \\ i_y \end{pmatrix}, \ \mathbf{x_z} = \begin{pmatrix} z_s \\ \dot{z}_s \\ i_z \end{pmatrix}, \ \mathbf{x}_\theta = \begin{pmatrix} l\theta \\ l\dot{\theta} \\ i_\theta \end{pmatrix}, \ \mathbf{x}_\psi = \begin{pmatrix} l\psi \\ l\dot{\psi} \\ i_\psi \end{pmatrix},$$

$$\mathbf{x_g} = \begin{pmatrix} \mathbf{x_y} \\ \mathbf{x}_\psi \\ \mathbf{x_z} \\ \mathbf{x}_\theta \end{pmatrix}, \ \mathbf{u} = \begin{pmatrix} u_y \\ u_\psi \\ u_z \\ u_\theta \end{pmatrix} = \begin{pmatrix} e_y \\ e_\psi \\ e_z \\ e_\theta \end{pmatrix}, \ \mathbf{y} = \begin{pmatrix} y_s \\ l\psi \\ z_s \\ l\theta \end{pmatrix}, \ \mathbf{f_d} = \begin{pmatrix} f_{dy} \\ f_{d\psi} \\ f_{dz} \\ f_{d\theta} \end{pmatrix}, \ \mathbf{z_r} = \begin{pmatrix} y_s \\ l\psi \\ z_s \\ l\theta \end{pmatrix}$$

Then from Equations (11) and (12) we have

$$\begin{aligned} \dot{\mathbf{x}}_\mathbf{g} &= \mathbf{A_g}(p)\mathbf{x_g} + \mathbf{B_g}(\mathbf{u}+\mathbf{v}) + \mathbf{E_g}\mathbf{f_d} \\ \mathbf{y} &= \mathbf{C_g}\mathbf{x_g} + \mathbf{n} \\ \mathbf{z_r} &= \mathbf{C_g}\mathbf{x_g}, \end{aligned} \tag{13}$$

where $\mathbf{z_r}$ is the variable that needs to be regulated, $\mathbf{v}$ represents actuator noise, $\mathbf{n}$ represents sensor noise and

$$\mathbf{A_g}(p) = \begin{pmatrix} A_y & \mathbf{0} & \mathbf{0} & \mathbf{0} \\ \mathbf{0} & A_\psi & \mathbf{0} & A_{\psi\theta} \\ \mathbf{0} & \mathbf{0} & A_z & \mathbf{0} \\ \mathbf{0} & A_{\theta\psi} & \mathbf{0} & A_\theta \end{pmatrix}, \ \mathbf{B_g} = \begin{pmatrix} b_y & \mathbf{0} & \mathbf{0} & \mathbf{0} \\ \mathbf{0} & b_\psi & \mathbf{0} & \mathbf{0} \\ \mathbf{0} & \mathbf{0} & b_z & \mathbf{0} \\ \mathbf{0} & \mathbf{0} & \mathbf{0} & b_\theta \end{pmatrix},$$

$$\mathbf{C_g} = \begin{pmatrix} c_y & \mathbf{0} & \mathbf{0} & \mathbf{0} \\ \mathbf{0} & c_\psi & \mathbf{0} & \mathbf{0} \\ \mathbf{0} & \mathbf{0} & c_z & \mathbf{0} \\ \mathbf{0} & \mathbf{0} & \mathbf{0} & c_\theta \end{pmatrix}, \ \mathbf{E} = \begin{pmatrix} e_{dy} & \mathbf{0} & \mathbf{0} & \mathbf{0} \\ \mathbf{0} & e_{d\psi} & \mathbf{0} & \mathbf{0} \\ \mathbf{0} & \mathbf{0} & e_{dz} & \mathbf{0} \\ \mathbf{0} & \mathbf{0} & \mathbf{0} & e_{d\theta} \end{pmatrix},$$

$$A_y = \begin{pmatrix} 0 & 1 & 0 \\ \frac{(\alpha-4d_{l3})}{m} & 0 & \frac{2c_{l3}}{m} \\ 0 & 0 & \frac{-R}{L} \end{pmatrix}, \ A_z = \begin{pmatrix} 0 & 1 & 0 \\ \frac{(\alpha-2(d_{l1}+d_{l2}))}{m} & 0 & \frac{-(c_{l1}+c_{l2})}{m} \\ 0 & 0 & \frac{-R}{L} \end{pmatrix},$$

$$A_\theta = \begin{pmatrix} 0 & 1 & 0 \\ \frac{-2(d_{l1}+d_{l2})}{m_1} & 0 & \frac{(c_{l1}+c_{l2})}{m_1} \\ 0 & 0 & \frac{-R}{L} \end{pmatrix}, \ A_\psi = \begin{pmatrix} 0 & 1 & 0 \\ \frac{-4d_{l3}}{m_1} & 0 & \frac{2c_{l3}}{m_1} \\ 0 & 0 & \frac{-R}{L} \end{pmatrix},$$

$$A_{\theta\psi} = \begin{pmatrix} 0 & 0 & 0 \\ 0 & \frac{-pJ_x}{J_y} & 0 \\ 0 & 0 & 0 \end{pmatrix}, \ A_{\psi\theta} = \begin{pmatrix} 0 & 0 & 0 \\ 0 & \frac{pJ_x}{J_y} & 0 \\ 0 & 0 & 0 \end{pmatrix},$$

$$b_y = b_z = b_\theta = b_\psi = \begin{pmatrix} 0 \\ 0 \\ \frac{1}{L} \end{pmatrix}, \ c_y = c_z = c_\theta = c_\psi = (1 \quad 0 \quad 0),$$

$$e_{dy} = e_{dz} = \begin{pmatrix} 0 \\ \frac{1}{m} \\ 0 \end{pmatrix}, \ e_{d\theta} = e_{d\psi} = \begin{pmatrix} 0 \\ \frac{1}{m_1} \\ 0 \end{pmatrix}, \ m_1 = J_y/l^2$$

The subscripts y, z, θ and ψ denote the $\mathbf{Y}$, $\mathbf{Z}$, $\mathbf{\Theta}$ and $\mathbf{\Psi}$ motions respectively. Note that if the rotational speed $p = 0$ the system can be divided into four separate SISO systems. However if $p \neq 0$ the system can be divided into three separate subsystems, two SISO systems and one, two-input two-output system. In both cases the electromagnets coil voltage are given as follows

$$\begin{aligned} e'_{l1} &= -e'_{l2} = (u_z + u_\theta)/2, \\ e'_{r1} &= -e'_{r2} = (u_z - u_\theta)/2, \\ e'_{l3} &= -e'_{l4} = (u_y + u_\psi)/2, \\ e'_{r3} &= -e'_{r4} = (u_y - u_\psi)/2 \end{aligned} \tag{14}$$

In this paper we design the controller for $p = 0$.

DISCRETE-TIME Q-PARAMETERIZATION CONTROL

The discretization of each subsystem defined by Eq. (14) using a zero order hold at a sampling time of T_s *sec* [15] yields the following SISO discrete-time control system:

$$\begin{aligned} x(k+1) &= A_d x(k) + b_d u(k) + b_d v(k) + e_d f_d(k) \\ y(k) &= c_d(k) + n(k) \\ z_r(k) &= c_d x(k) \end{aligned} \tag{15}$$

A- The Q-parameterization theory

The Q-parameterization theory [11]-[12] states that the set of all stabilizing controllers of a given plant $G(z)$ can characterized by one free parameter (one-parameter-control feedback) or two free parameters (two-parameter-control feedback) namely Q_1 and Q_2 .

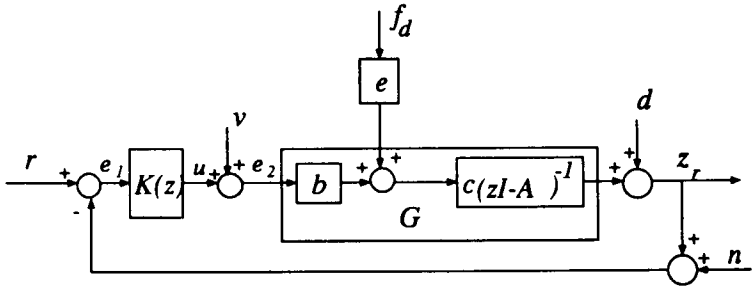

Fig. 2 One-Parameter-Control Feedback System.

Consider the one-parameter-control feedback system shown in Fig. 2, for controlling any of the SISO subsystems described by Eq. (13), where $z_{ref} \in \mathbb{R}$ is the reference (command) input signal, $v \in \mathbb{R}$ is the actuator noise, $n \in \mathbb{R}$ is the sensor noise, $f_d \in \mathbb{R}$ is the disturbance force, $d \in \mathbb{R}$ is the output disturbance, $u \in \mathbb{R}$ is the controller output, $z \in \mathbb{R}$ is the plant output to be regulated, and $K \in R$ is the stabilizing controller for $G(s)$. Note that v, n, and f_d may also represent model uncertainties. In order to characterize the set of all stabilizing controllers K for $G(z)$, first we need to construct a doubly coprime factorization (see [11] for details) $N, D, \tilde{N}, \tilde{D}, X, Y, \tilde{X}, \tilde{Y} \in RH_\infty$ for $G(z)$. First we choose real matrices f_1 and f_2 such that the matrices $A_o := A_d - b_d f_1$ and $\tilde{A}_o := A_d - f_2 c_d$ are stable (all the eigenvalues of A_o and $\tilde{A}_o$ lie inside the unit circle), then the doubly coprime factorization $N(z), D(z), \tilde{N}(z), \tilde{D}(z), X(z), Y(z), \tilde{X}(z), \tilde{Y}(z) \in RH_\infty$ for $G(z)$ is given as follows

$$\begin{aligned} N(z) &= c_d(zI - A_o)^{-1} b_k \\ D(z) &= I - f_1(zI - A_o)^{-1} b_d \\ \tilde{N}(z) &= c_d(zI - \tilde{A}_o)^{-1} b_d \\ \tilde{D}(z) &= I - c_d(sI - \tilde{A}_o)^{-1} f_2 \\ X(z) &= f_1(zI - \tilde{A}_o)^{-1} f_2 \\ Y(z) &= I + f_1(zI - \tilde{A}_o)^{-1} b_d \\ \tilde{X}(z) &= f_1(zI - A_o)^{-1} f_2 \\ \tilde{Y}(z) &= I + c_d(zI - A_o)^{-1} f_2 \end{aligned} \tag{16}$$

Then the set of all stabilizing controllers for $G(z)$ is given by

$$K(z) = \{(Y(z) - Q(z)\tilde{N}(z))^{-1}(X(z) + Q(z)\tilde{D}(z)),\ Q(z) \in RH_\infty,\ \left|Y(z) - Q(z)\tilde{N}(z)\right| \neq 0\}. \tag{17}$$

B- Controller Objectives

The following controller objectives are imposed

1. We need to achieve robust stability against speed and other parameter variation; and achieve fast and well damped transient response
2. We need to achieve rejection of low frequency **disturbances**
3. We need to achieve asymptotic rejection of the class of sinusoidal disturbance with frequency equal to the rotational speed p, in order to compensate for the unbalance.

C- Controller Synthesis

1. In order to satisfy requirement No. 1, the closed loop poles must be located at a prescribed region in the open left half plane. This can be achieved by choosing $N, D, \tilde{N}, \tilde{D}, X, Y, \tilde{X}, \tilde{Y}, Q \in D_s$ where D_s is a subset of RH_∞ defined as shown in Fig. 3.

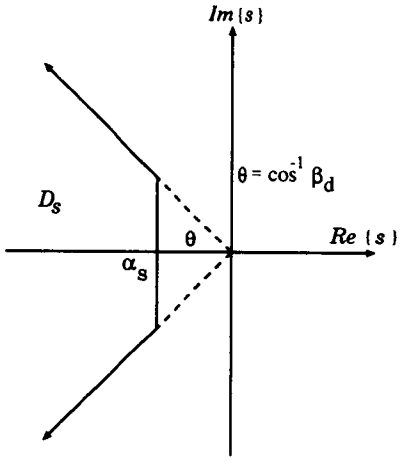

Fig. 3 Generalized region of stability.

2. In order to satisfy requirement No. 2, the controller must have a pole at $z = 1$. This can be achieved by choosing $Q(z)$ such that the following identity holds

$$K(z = 1) = \infty \tag{18}$$

From Eq. (17), $Q(z)$ must satisfy the following Equation

$$Y(z = 1) - Q(z = 1)\tilde{N}(z = 1) = 0 \tag{19}$$

3. In order to satisfy requirement No. 3, the controller free parameter $Q(z)$ must be chosen such that the controller has poles at $z = \exp^{\pm jpT_s}$. This can be achieved by choosing $Q(z)$ such that the following identity holds

$$K(z = \exp^{jpT_s}) = \infty \tag{20}$$

Let us assume that the operating speeds of the magnetic bearing are $p_1, p_2, ...p_r$. Then at each operating speed the frequency of the generated unbalance sinusoidal disturbance forces equals p_k, $k = 1, 2, ...r$. In order

to achieve asymptotic rejection for the class of sinusoidal disturbance with variable frequencies, the following condition is imposed on $Q(z)$

$$K(z = \exp^{jp_kT_s}) = \infty, \qquad k = 1, 2, ...r \tag{21}$$

From Equation (17) we have

$$Y(z = \exp^{jp_kT_s}) - Q(z = \exp^{jp_kT_s})\tilde{N}(z = \exp^{jp_kT_s}) = 0, \qquad k = 1, 2, ...r \tag{22}$$

Equations (22) are in fact $2r$ equations, r equations for the real part and r equations for the imaginary part. Equations (19) and (22) indicate that we have $2r + 1$ equations in $Q(z)$, this suggests that $Q(z)$ can take the form

$$Q(z) = a_0 + \frac{a_1}{(z - z_1)} + \frac{a_2}{(z - z_2)} + ...+ \frac{a_n}{(z - z_n)} \tag{23}$$

where $a_0, a_1, ...a_n \in \mathbb{R}$ are free design parameters and $z_1, z_2, ...z_n > \alpha_s \in \mathbb{R}$ are fixed. Note that Q is a proper stable transfer function whose order equals twice the number of operating speeds.

Theoretically we should be able to design a controller which achieves asymptotic rejection for the class of sinusoidal disturbance of variable frequencies. However in this case as the order of Q gets higher, so does the controller. In this case the practical implementation of the controller becomes difficult. Model reduction techniques [14] must be used to reduce the order of the controller. In this paper we design a controller for magnetic bearings rotating at three different speeds p_1, p_2, and p_3 , so $Q(z)$ is chosen as follows:

$$Q(z) = a_0 + \frac{a_1}{(z - z_1)} + \frac{a_2}{(z - z_2)} + \frac{a_3}{(z - z_3)} + \frac{a_4}{(z - z_4)} + \frac{a_5}{(z - z_5)} + \frac{a_6}{(z - z_6)} \tag{24}$$

Then we have

$$Q(z = 1) = a_0 + \frac{a_1}{(1 - z_1)} + \frac{a_2}{(1 - z_2)} + \frac{a_3}{(1 - z_3)} + \frac{a_4}{(1 - z_4)} + \frac{a_5}{(1 - z_5)} + \frac{a_6}{(1 - z_6)} \tag{25}$$

$$Q(zp_k) = a_0 + \frac{a_1}{(zp_k - z_1)} + \frac{a_2}{(zp_k - z_2)} + \frac{a_3}{(zp_k - z_3)} + \frac{a_4}{(zp_k - z_4)} + \frac{a_5}{(zp_k - z_5)} + \frac{a_6}{(zp_k - z_6)}, \qquad k = 1, 2, 3 \tag{26}$$

where $zp_k = \exp^{jp_kT_s}$ Eqs. (25) and (26) are in fact seven linear equations in the seven unknown free design parameters a_0, a_1, a_2, a_3, a_4, a_5, a_6 . In order to solve Eqs. (25) and (26) for a_0, a_1, a_2, a_3, a_4, a_5, a_6 we need first to solve Eqs. (19) and (22) for $Q(z = 1)$ and $Q(z = \exp^{jp_kT_s})$, $k = 1, 2, 3$. Eqs. (19) and (22) are also linear equations in $Q(z = 1)$ and $Q(z = \exp^{jp_kT_s})$, $k = 1, 2, 3$. From Eqs. (19) and (22) we have

$$\begin{aligned} Q(z = 1) &= Y(z = 1)\tilde{N}^{-1}(z = 1), \\ Q(z = \exp^{jp_kT_s}) &= Y(z = \exp^{jp_kT_s})\tilde{N}^{-1}(z = \exp^{jp_kT_s}), \qquad k = 1, 2, 3 \end{aligned} \tag{27}$$

Then the design parameters a_0, a_1, a_2, a_3, a_4, a_5, a_6 can easily be found by solving the following set of linear equations: Let $zpp_{kj} = 1/(zp_k - z_j)$, $k = 1, 2, 3$, $j = 1, 2, ...6$. Then we have

$$\begin{pmatrix} a_0 \\ a_1 \\ a_2 \\ a_3 \\ a_4 \\ a_5 \\ a_6 \end{pmatrix} = \begin{pmatrix} 1 & 1/(1-z_1) & 1/(1-z_2) & 1/(1-z_3) & 1/(1-z_4) & 1/(1-z_5) & 1/(1-z_6) \\ 1 & \Re(zpp_{11}) & \Re(zpp_{12}) & \Re(zpp_{13}) & \Re(zpp_{14}) & \Re(zpp_{15}) & \Re(zpp_{16}) \\ 0 & \Im(zpp_{11}) & \Im(zpp_{12}) & \Im(zpp_{13}) & \Im(zpp_{14}) & \Im(zpp_{15}) & \Im(zpp_{16}) \\ 1 & \Re(zpp_{21}) & \Re(zpp_{22}) & \Re(zpp_{23}) & \Re(zpp_{24}) & \Re(zpp_{25}) & \Re(zpp_{26}) \\ 0 & \Im(zpp_{21}) & \Im(zpp_{22}) & \Im(zpp_{23}) & \Im(zpp_{24}) & \Im(zpp_{25}) & \Im(zpp_{26}) \\ 1 & \Re(zpp_{31}) & \Re(zpp_{32}) & \Re(zpp_{33}) & \Re(zpp_{34}) & \Re(zpp_{35}) & \Re(zpp_{36}) \\ 0 & \Im(zpp_{31}) & \Im(zpp_{32}) & \Im(zpp_{33}) & \Im(zpp_{34}) & \Im(zpp_{35}) & \Im(zpp_{36}) \end{pmatrix}^{-1} \begin{pmatrix} Q(z = 1) \\ \Re(Q(z = zp_1)) \\ \Im(Q(z = zp_1)) \\ \Re(Q(z = zp_2)) \\ \Im(Q(z = zp_2)) \\ \Re(Q(z = zp_3)) \\ \Im(Q(z = zp_3)) \end{pmatrix} \tag{28}$$

where $\Re(\bullet)$ and $\Im(\bullet)$ denotes the real and imaginary parts of ($\bullet$).

RESULTS AND SIMULATION

The method of controller design discussed in section IV is applied to a magnetic bearing system whose parameters are given in Table 1. The μ synthesis Toolbox [16] with Simulink were used for the design and simulation. The system is discretized using a zero order hold at a sampling time $T_s = 158\mu sec$. The controller $\mathbf{K}(s)$ is designed at a speed $p = 0$ rad/sec and must be able to keep the system stable for a speed range $(0 - 2\pi 250)$ rad/sec. The operating speeds are assumed to be $p_1 = 2\pi 30$ rad/sec, $p_2 = 2\pi 20$ rad/sec, and $p_3 = 2\pi 10$ rad/sec. The generalized region of stability D_s is defined by the following parameters: $\alpha_s = 0.995$, $\beta_d = 0.707$ to insure a certain degree of stability against parameter variation and to get fast and well damped transient response. $z_1 = 0.99$, $z_2 = 0.981$, $z_3 = 0.984$, $z_4 = 0.981$, $z_5 = 0.978$, $z_6 = 0.975$. The following results are obtained: The controller free parameters $a_0, a_1, a_2, a_3, a_4, a_5, a_6$ which satisfies Eqs. (19) and (22), for each subsystem of Eq. (13) were found to be

$$
\begin{aligned}
Y-\text{motion}: \; a_0 &= 7.7\times 10^7,\; a_1 = 1.44\times 10^7,\; a_2 = -1.589\times 10^8 a_3 = 6.649\times 10^8,\; a_4 = -1.325\times 10^9,\\
&\quad a_5 = 1.262\times 10^9,\; a_6 = -4.618\times 10^8\\
\Psi-\text{motion}: \; a_0 &= 7.63\times 10^7,\; a_1 = 1.427\times 10^7,\; a_2 = -1.574\times 10^8 a_3 = 6.583\times 10^8,\; a_4 = -1.312\times 10^9,\\
&\quad a_5 = 1.250\times 10^9,\; a_6 = -4.573\times 10^8\\
Z-\text{motion}: \; a_0 &= -5.258\times 10^7,\; a_1 = -9.55\times 10^6,\; a_2 = 1.053\times 10^8 a_3 = -4.406\times 10^8,\; a_4 = 8.782\times 10^8,\\
&\quad a_5 = -8.369\times 10^8,\; a_6 = 3.061\times 10^8\\
\Theta-\text{motion}: \; a_0 &= 5.209\times 10^7,\; a_1 = 9.461\times 10^6,\; a_2 = -1.043\times 10^8 a_3 = 4.363\times 10^8,\; a_4 = -8.696\times 10^8,\\
&\quad a_5 = 8.288\times 10^8,\; a_6 = -3.031\times 10^8
\end{aligned}
\tag{29}
$$

Substituting the Q 's in Eq. (17) we get (after model reduction) a 9 state controller for each of the four subsystems. The overall controller of the whole system has 36 states and is formulated as follows:

$$
\mathbf{K}(z) = \begin{pmatrix} K_Y(z) & 0 & 0 & 0 \\ 0 & K_\Psi(z) & 0 & 0 \\ 0 & 0 & K_Z(z) & 0 \\ 0 & 0 & 0 & K_\Theta(z) \end{pmatrix} \tag{30}
$$

where $K_Y(z)$, $K_\Psi(z)$, $K_Z(z)$, $K_\Theta(z)$ are the controllers of the Y, Ψ, Z, Θ subsystems respectively.

Table 2: Controller order Vs. Number of operating speeds

Number of operating speeds	Degree of controller
$r = 1$	20
$r = 2$	28
$r = 3$	36
$r = 4$	44
$r = 5$	52
$r = 6$	60
...	...
$r = N$	No.of degrees of freedom $\times(2N + 3)$

An interesting observation from the controller design procedure explained in the previous section is shown in Table 2. Table 2 shows a relationship between the number of operating speeds and the degree of the controller. We can conclude from this table that the degree of the controller equals: number of degrees of freedom $\times(2N+3)$ where N is the number of operating speeds or equals: number of degrees of freedom $\times$ (order of Q +3).

A plot of the singular values of the loop gain GK is shown in Fig. 4. High loop gain at low frequency and low gain at high frequency are achieved. A plot of the singular values of sensitivity is shown in Fig. 5. From Fig. 5 we can see that the sensitivity is small at low frequencies which means good disturbance rejection for the

class of step disturbances and approaches zero at the frequencies $\omega_1 = 2\pi 30$ rad/sec, $\omega_2 = 2\pi 20$ rad/sec and $\omega_3 = 2\pi 10$ rad/sec which means asymptotic rejection of the unbalance sinusoidal disturbance forces at these speeds.

In this design, we ignored the interference terms, which express the gyroscopic effect, as $p = 0$. We therefore verify the robust stability of the system against the changes in the rotor speed. Let the perturbed plant $p \neq 0$ be denoted by G_p and the additive perturbation Δ_p from G is as follows:

$$\Delta_p = G_p - G \tag{31}$$

The robust stability is guaranteed if the following inequality holds:

$$\overline{\sigma}(\Delta_p) < \frac{1}{\overline{\sigma}(K(I+GK)^{-1})} \tag{32}$$

Fig. 6 shows the singular values plot of $1/\overline{\sigma}(K(I+GK)^{-1}$ and $\overline{\sigma}(\Delta_p)$ at $p = 2\pi 250$ rad/sec. From Fig. 6 we can see that the system is stable up to a speed $p = 2\pi 250$ rad/sec. Fig. 7, Fig. 8, Fig 9 show the gap deviations due to unbalance and electromagnet forces acting on the rotor. In Fig. 7, 8, and 9 we can see the good suppression of the imbalance forces at the variable three design speeds.

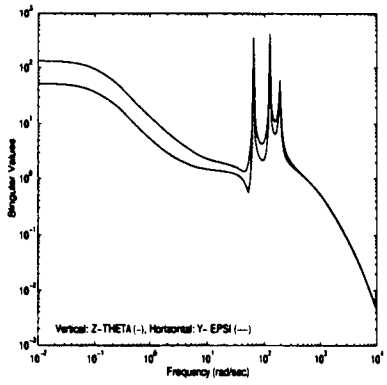

Fig. 4 Singular values of the loop gain GK.

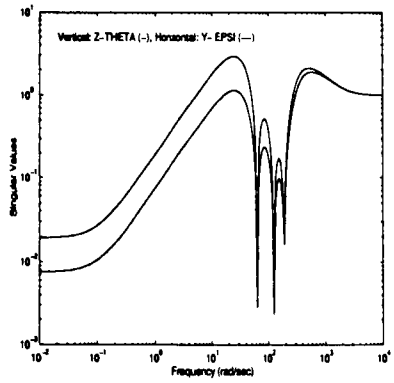

Fig. 5 Singular values of the sensitivity.

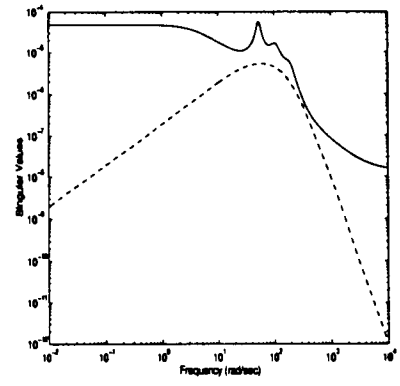

Fig. 6 $1/\overline{\sigma}(K(I+GK)^{-1})$ (-) and $\overline{\sigma}(\Delta_p)$ (- -) $p = 2\pi 250$.

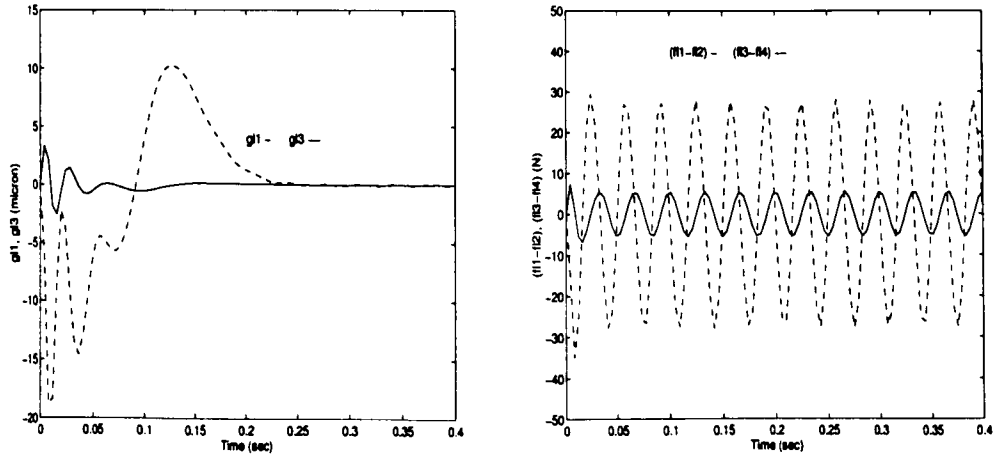

Fig. 7 Airgap variations due to unbalance and magnetic forces acting on the bearing for $p = 2\pi 30$.

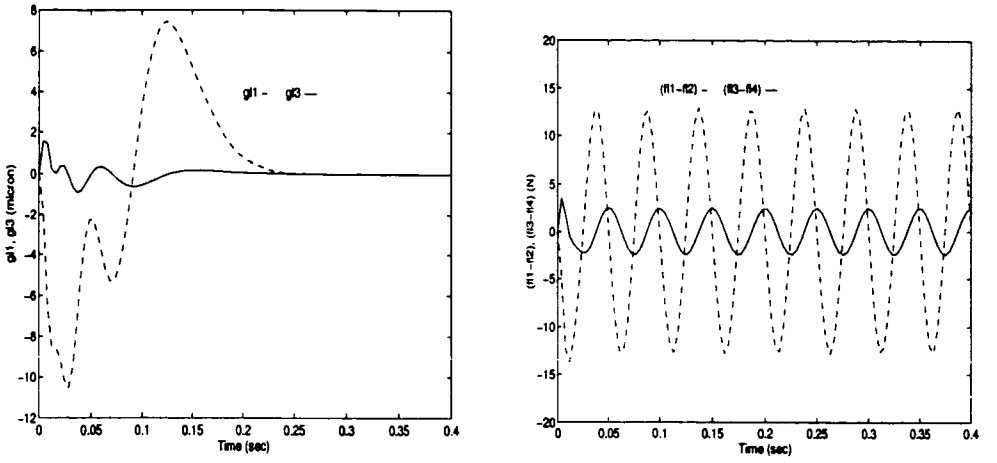

Fig. 8 Airgap variations due to unbalance and magnetic forces acting on the bearing for $p = 2\pi 20$.

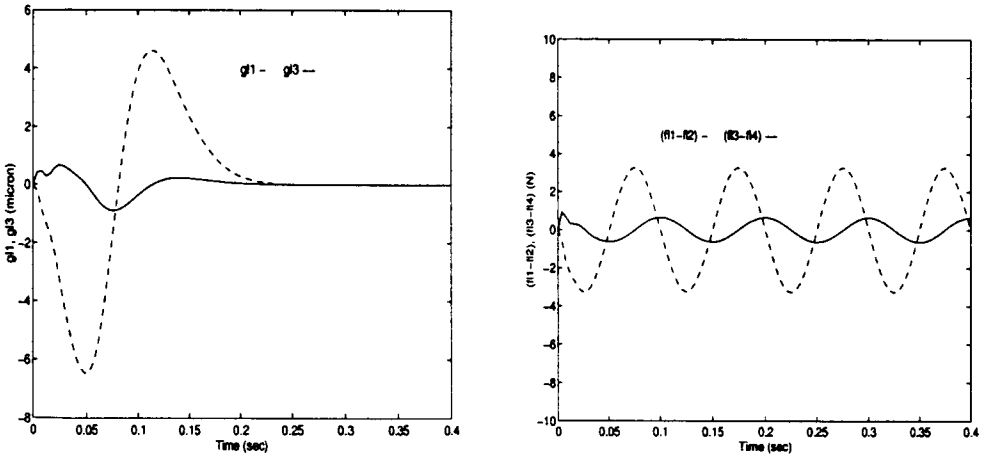

Fig. 9 Airgap variations due to unbalance and magnetic forces acting on the bearing for $p = 2\pi 10$.

CONCLUSIONS

In this paper we employed the discrete-time Q-parameterization control to design a controller which achieves elimination of unbalance vibrations in variable speed magnetic bearings. The free controller parameter is chosen such that the controller has poles on the unit circle at $z = \exp^{jp_k T_s}$ for the different speeds of rotation p_k , and satisfies other control objectives. This insures asymptotic rejection of the unbalance disturbance forces generated by the unbalance. The controller free parameter Q is assumed to be a proper stable transfer function whose order equals twice the number of operating speeds. We showed that the free controller parameter is obtained by solving a set of linear equations rather than solving a complicated optimization problem. We also showed that the controller order equals: Number of degrees of freedom $\times$ (order of Q +3). The controller is designed at speed $p = 0$ and the good simulation results that were obtained at speeds $p = 2\pi 30$ rad/sec, $p = 2\pi 20$ rad/sec and $p = 2\pi 10$ rad/sec showed the robustness of the proposed controller.

Elimination of unbalance vibrations in a variable speed magnetic bearing can also be achieved by making the rotor rotate around its axis of inertia at the different operating speeds (automatic balancing). In this case the rotor will be free from vibrations. This can be done using the same procedures explained in section III and [5].

References

1. Mizuno, T., and Higuchi, T., "Design of Magnetic Bearing Controllers Based on Disturbance Estimation," Proceedings of the 2nd International Symposium on Magnetic Bearings, pp. 281-88, July 12-14, 1990, Tokyo Japan.
2. Larsonneur R., and Herzog, R., "Feedforward Compensation of Unbalance: New Results and Application Examples," Proceedings ITUAM Symposium on Active Control of Vibration, pp. 45-52, Septmber 1994, Bath, U.K.
3. Knospe, C. R., "Robustness of Unbalance Response Controllers," Proceedings of the 3rd International Symposium on Magnetic Bearings, pp. 580-589, Virginia, USA, July 1992.
4. Herzog, R., Bühler , P., Gähler , C., and Larsonneur, R., "Unbalance Compensation Using Generalized Notch Filters in the Multivariable Feedback of Magnetic Bearings," *IEEE Transactions on Control System Technology,* Vol. 4, No. 5, pp. 580-586, September. 1996.
5. Mohamed, A., and Busch-Vishniac, I.,"Imbalance Compensation and Automatic Balancing in Magnetic Bearing Systems Using The Q-Parameterization Theory," *IEEE Transactions on Control System Technology,* Vol. 3, No. 2, pp. 202-211, June 1995.
6. Matsumura, F., Namerikawa, T., Hagiwara, K., and Fujita, M., "Application of Gain Scheduled H_∞ Robust Controllers to a Magnetic Bearing," *IEEE Transactions on Control System Technology,* Vol. 4, No. 5, pp. 484-493, September 1996.
7. Sivrioglu, S., and Nonami, K., "LMI Based Gain Scheduled H_∞ Controller Design for AMB Systems under Gyroscopic and Unbalance Disturbance," Proceedings of the 5th International Symposium on Magnetic Bearings, pp.191-196, August 28-30, 1996, Kanazawa, Japan.
8. Vidyasagar, M., Control System Synthesis: a Factorization Approach, Cambridge, Mass.: MIT Press, 1985.
9. Boyd, S., Barratt, C., *Linear Controller Design: Limits Of Performance,* Prentice Hall Information and Science Series New Jersey 1991.
10. McFarlane, D. and Glover, K.,"Robust Controller Design Using Normalized Coprime Factor Plant Descriptions," *Lecture Notes in Control and Information Sciences,* Vol. 138, Springer-Verlag, 1990.
11. Ogata, K., *Discrete Time Control Systems,* Prentice-Hall Inc., Englewood Cliffs, New Jersey 1987.
12. Balas, G., Doyle, J. C., Glover, K., Packard, A., and Smith, R., μ *-Analysis and Synthesis Toolbox*, The Math Works Inc., 1993.

ANGULAR COORDINATE REPETITIVE CONTROL OF MAGNETIC BEARINGS

Yohji Okada, Bunshu Nagai and Katsuhiko Karino
Department of Mechanical Engineering, Ibaraki University
4-12-1 Nakanarusawa, Hitachi 316 JAPAN
Phone +81-294-38-5025, Fax +81-294-38-1229
E-mail: okada@mech.ibaraki.ac.jp

SUMMARY

New repetitive control is applied to active magnetic bearings. It is intended for rotor magnetic bearing systems to reduce unbalance response automatically. Repetitive control is a kind of servo control which is expected to follow periodic command. The follow-up property is based on internal model principles, that is, the controller includes a repetitive-type transfer function. The system also has noise rejection properties from the repetitive disturbance produced by the rotor imbalance. A simple experiment is performed to confirm the proposed technique. The results show good disturbance rejection properties and robustness.

INTRODUCTION

Magnetic bearings have merits of supporting a rotor without physical contact [1] and producing a canceling force to the rotor disturbance. Unbalance response is one of the biggest problems for rotary machinery. Several methods are proposed to cancel this unbalance excitation: Mizuno and Higuchi proposed a disturbance observer-based controller [2]; Hisatani and Koizumi proposed an adaptive filter type controller [3]; Knospe and Tamer proposed a new technique called open loop control [4]. They are fundamentally based on a constant speed controller and requires an adaptive technique for the rotational speed. A rotary machine usually changes its speed. Standard disturbance cancellation control with constant time sampling does not work properly, because the internal model does not exactly match the variable speed imbalance.

This paper proposed a new type of repetitive control which uses angular coordinate sampling intervals [5], [6]. The frequency of this repetitive controller is automatically equalized to the rotor speed and is expected to reduce the rotor unbalance vibration. First, the plant is stabilized with the local PID controller which uses constant time sampling. Then the stabilized magnetic bearing is transformed into the angular coordinates of the rotor at the operating speed. Finally, the angular coordinate repetitive controller is designed using optimal regulator theory [6].

A test apparatus is made to confirm the proposed technique. The results are compared with and without repetitive control. The effect of rotor speed change and the robustness are also tested and discussed. The results show good unbalance rejection properties and robustness and robustness of the proposed repetitive controller.

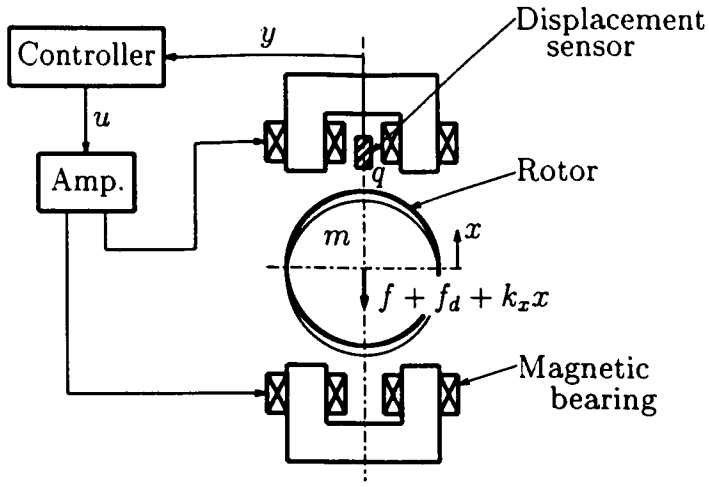

Figure 1: Model of magnetic bearing system

Table 1: The symbols of magnetic bearing system

m	:	Rotor mass	[kg]
k_x	:	Negative stiffness of magnetic bearing	[N/m]
K_f	:	Force factor of actuator	[N/V]
q	:	Sensor gain	[V/m]
x	:	Rotor displacement	[m]
u	:	Control input	[V]
y	:	Sensor output	[V]
f	:	Control force	[N]
f_d	:	Disturbance	[N]

MODELING AND LOCAL PID CONTROL

It is assumed that the coupling between two radial magnetic bearings are ignored and they can be controlled individually. This simplified radial magnetic bearing is shown schematically in Fig. 1. The symbols used are shown in Table 1. Only the vertical degree-of-freedom is indicated in the figure, and another set is necessary to control the horizontal position.

Equations of Motion

Assuming that each control degree is independent, we have the following equation of motion in each direction.

$$m\frac{d^2x(t)}{dt^2} = f(t) + f_d(t) + k_x x(t) \quad f(t) = K_f u(t) \tag{1}$$

Equation (1) can be transformed into the following state equation.

$$\begin{cases} \dot{\boldsymbol{x}}(t) &= \boldsymbol{A}_c\boldsymbol{x}(t) + \boldsymbol{B}_c u(t) + \boldsymbol{E}_c f_d(t) \\ y(t) &= \boldsymbol{C}_c\boldsymbol{x}(t) \end{cases} \tag{2}$$

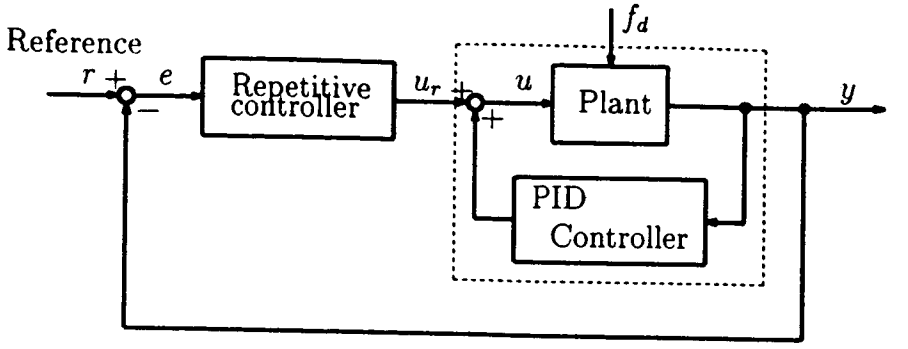

Figure 2: Block diagram of repetitive control system

$$A_c = \begin{bmatrix} 0 & 1 \\ 0 & 0 \end{bmatrix} \quad B_c = \begin{bmatrix} 0 \\ \frac{K_f}{m} \end{bmatrix} \quad E_c = \begin{bmatrix} 0 \\ \frac{1}{m} \end{bmatrix}$$

$$C_c = \begin{bmatrix} q & 0 \end{bmatrix} \quad x(t) = \begin{bmatrix} x(t) & \dot{x}(t) \end{bmatrix}^T$$

PID Control

The stabilizing controller used is the standard PID controller for each control degree of freedom.

$$G(s) = K_p + K_i\frac{1}{s} + K_d s \tag{3}$$

In this paper, Digital Signal Processor (DSP, TI TMS320C30) is used. The following digital PID controller

$$\begin{cases} x_1[k+1] &= e^{-T/T_d}x[k] + u[k] \\ x_2[k+1] &= x_2[k] + Tu[k] \\ y[k] &= \frac{K_d}{T}(e^{-T/T_d} - 1)x_1[k] + K_i x_2[k] + (K_p + \frac{K_d}{T})u[k] \end{cases} \tag{4}$$

$u[k]$: input signal
$x_1[k], x_2[k]$: state variables
$y[k]$: output signal

is installed, where T is the sampling interval and T_D is the derivative time constant [sec], respectively.

ANGULAR COORDINATE REPETITIVE CONTROL

PID controllers can stabilize rotor-magnetic bearing systems. However, unbalance excitation is one of the biggest problems of rotary machines. In the paper, angular coordinate repetitive control is proposed to reduce the unbalance response. First, the system is stabilized using the local PID controller, and then it is transformed into the angular coordinate of shaft position.

Table 2: The signals of repetitive control system

u	:	Control input	[V]
u_r	:	Repetitive control input	[V]
y	:	Control output	[V]
f_{dt}	:	Disturbance	[N]
r	:	Reference	[V]
e	:	Error	[V]

Finally, the repetitive controller is designed using optimal regulator theory. The designed controller has a strong merit that is independent from the rotational speed and the unbalance excitation is automatically reduced by this controller.

Transformation from Time Coordinate to Angular Coordinate

The control system is schematically shown in Fig. 2. The meaning of signals used is summarized in Table 2. The local PID controller is included in the control object of the repetitive controller which is shown in the dotted block in Fig. 2. This control object is written by the following state equation, where $d(t)$ indicates the periodic disturbance.

$$\begin{cases} \dfrac{d\boldsymbol{x}(t)}{dt} &= \boldsymbol{A'}_c\boldsymbol{x}(t) + \boldsymbol{B}_c u_r(t) + \boldsymbol{E}_c d(t) \\ y(t) &= \boldsymbol{C}_c\boldsymbol{x}(t) \end{cases} \tag{5}$$

$$\boldsymbol{A'}_c = \begin{bmatrix} 0 & 1 \\ \dfrac{K_f K_p}{m} & \dfrac{K_f K_d}{m} \end{bmatrix}$$

Next, let us transform the system into the angular coordinate domain. The transformation requires the following necessary condition.

$$\omega(t) = \frac{d\theta}{dt} > 0 \quad {}^{\forall}t > 0 \tag{6}$$

This requires the existence of the inverse function $t = t(\theta)$ from the rotating angular function $\theta = \theta(t)$. If the necessary condition of eqn. (6) is satisfied, then we can transform eqn. (5) into the following angular coordinate plant equation.

$$\begin{cases} \dfrac{d\boldsymbol{x}(\theta)}{d\theta} &= \tilde{\boldsymbol{A}}_c\boldsymbol{x}(\theta) + \tilde{\boldsymbol{B}}_c u_r(\theta) + \tilde{\boldsymbol{E}}_c d(\theta) \\ y(\theta) &= \tilde{\boldsymbol{C}}_c\boldsymbol{x}(\theta) \end{cases} \tag{7}$$

$$\tilde{\boldsymbol{A}}_c = \frac{\boldsymbol{A'}_c}{\omega_r} \quad \tilde{\boldsymbol{B}}_c = \frac{\boldsymbol{B}_c}{\omega_r} \quad \tilde{\boldsymbol{C}}_c = \boldsymbol{C}_c \quad \tilde{\boldsymbol{E}}_c = \frac{\boldsymbol{E}_c}{\omega_r}$$

Equation (7) is the linearly approximate transformation from t to θ around the operating speed ω_r [rad/s]. Finally eqn. (7) is discretized using the following sampling angle

$$\Delta\theta = \frac{2\pi}{N} \text{ [rad]} \tag{8}$$

where N is the sampling number of one repetitive period in angular coordinate digital control.

Design of Repetitive Controller

Now the state equation is expanded to include the error of the signal. The expanded system includes the original control object as well as the repetitive error model. First we need to discretize the control object eqn. (7) using the sampling interval of eqn. (8). The control object and the error equations are written by

$$\begin{aligned} \boldsymbol{x}[k+1] &= \boldsymbol{A}\boldsymbol{x}[k] + \boldsymbol{B}u_r[k] + \boldsymbol{E}d[k] && (9)\\ y[k] &= \boldsymbol{C}\boldsymbol{x}[k] && (10)\\ e[k] &= r[k] - y[k] && (11) \end{aligned}$$

Next a new operator α is defined by

$$\alpha \equiv 1 - z^{-N} \tag{12}$$

where N is the sampling stage number of the repetitive period. That is, let L [sec] be the period of the repetitive disturbance and T_r be the sampling interval, we have the relation of $L = Nt_r$. Remember that z is the angular coordinate sampling operator and change its time interval. The operator α means the difference between the signal and the N sample advanced signal. Applying α to eqn. (11), we have

$$\alpha e[k+1] = \alpha r[k+1] - \alpha y[k+1] \tag{13}$$

Substitute eqns. (9) and (10) into eqn. (13), we have

$$\begin{aligned} e[k+1] &= e[k-N+1] + \alpha r[k+1] \\ &\quad -\boldsymbol{C}\boldsymbol{A}\alpha\boldsymbol{x}[k] - \boldsymbol{C}\boldsymbol{B}\alpha u_r[k] - \boldsymbol{C}\boldsymbol{E}\alpha d[k] \end{aligned} \tag{14}$$

Applying α to eqn. (9), we have

$$\alpha\boldsymbol{x}[k+1] = \boldsymbol{A}\alpha\boldsymbol{x}[k] + \boldsymbol{B}\alpha u_r[k] + \boldsymbol{E}\alpha d[k] \tag{15}$$

Considering the periodic property of the reference and disturbance signals and combining eqns. (14) and (15), we can get the expanded state equation of eqn. (16). Where X is an expanded state variable.

$$\boldsymbol{X}[k+1] = \boldsymbol{\Phi}\boldsymbol{X}[k] + \boldsymbol{G}\alpha u_r[k] \tag{16}$$

$$\boldsymbol{\Phi} = \begin{bmatrix} 0 & \cdots & 0 & 1 & -\boldsymbol{C}\boldsymbol{A} \\ 1 & \cdots & 0 & 0 & \boldsymbol{0} \\ \vdots & \ddots & \vdots & \vdots & \vdots \\ 0 & \cdots & 1 & 0 & \boldsymbol{0} \\ 0 & \cdots & 0 & 0 & \boldsymbol{A} \end{bmatrix} \quad \boldsymbol{G} = \begin{bmatrix} -\boldsymbol{C}\boldsymbol{B} \\ 0 \\ \vdots \\ 0 \\ \boldsymbol{B} \end{bmatrix}$$

$$\boldsymbol{X}[k] = \begin{bmatrix} e[k] & e[k-1] & \cdots & e[k-N+1] & \alpha\boldsymbol{x}[k] \end{bmatrix}^T$$

The controller is designed using optimum regulator theory. The performance index J is defined by

$$J = \sum_{k=0}^{\infty} \left\{ \boldsymbol{X}^T[k]\boldsymbol{Q}\boldsymbol{X}[k] + \alpha u_r^T[k] h \alpha u_r[k] \right\} \tag{17}$$

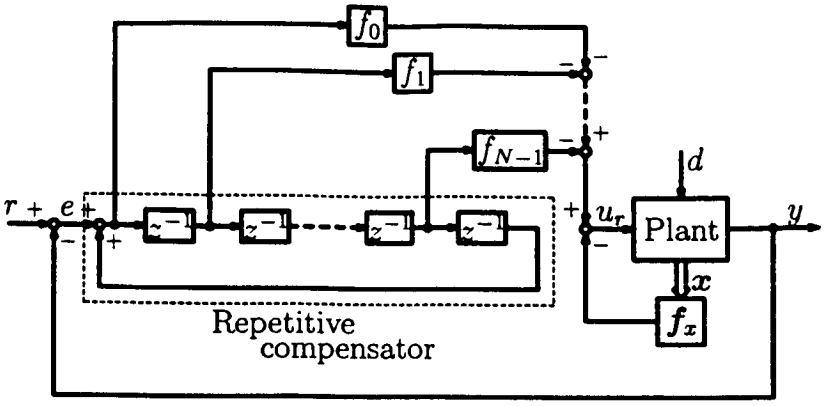

Figure 3: Block diagram of optimal repetitive control system

Where Q is the positive semi-definite weighting matrix for state variable and h is positive definite weight for actuating signal, respectively. Minimizing J, we have the following optimum actuating signal,

$$\begin{aligned} \alpha u_r[k] &= -\left[f_0 \;\; f_1 \;\; \cdots \;\; f_{N-1} \;\; \boldsymbol{f}_x \right] \boldsymbol{X}[k] \\ &= -\left[f_0 \;\; f_1 \;\; \cdots \;\; f_{N-1} \right] \begin{bmatrix} e[k] \\ e[k-1] \\ \vdots \\ e[k-N+1] \end{bmatrix} - \boldsymbol{f}_x \alpha \boldsymbol{x}[k] \end{aligned} \tag{18}$$

The feedback gains are given by eqn. (19), where P is the positive definite symmetric solution of the Riccati equation (20).

$$\left[f_0 \;\; f_1 \;\; \cdots \;\; f_{N-1} \;\; \boldsymbol{f}_x \right] = \left[h + \boldsymbol{G}^T \boldsymbol{P} \boldsymbol{G} \right]^{-1} \boldsymbol{G}^T \boldsymbol{P} \boldsymbol{\Phi} \tag{19}$$

$$\boldsymbol{P} = \boldsymbol{Q} + \boldsymbol{\Phi}^T \boldsymbol{P} \boldsymbol{\Phi} - \boldsymbol{\Phi}^T \boldsymbol{P} \boldsymbol{G} \left[h + \boldsymbol{G}^T \boldsymbol{P} \boldsymbol{G} \right]^{-1} \boldsymbol{G} \boldsymbol{P} \boldsymbol{\Phi} \tag{20}$$

The optimum repetitive control system is schematically shown in Fig. 3. Remember that the local PID controller is included in the control object of the repetitive controller which is shown in the dotted block in Fig. 2.

EXPERIMENTAL RESULTS AND CONSIDERATIONS

To confirm the proposed technique, a test apparatus was made and tested. A schematic of the experimental setup is shown below.

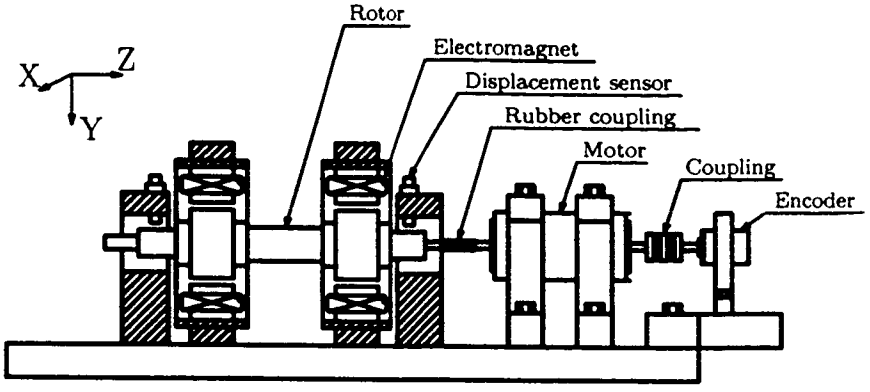

Figure 4: Scheme of experimental setup

Control System

As mentioned before, a digital control system is used, employing a digital signal processor. The control system is shown schematically in Fig. 5. The system parameters used are

m	=	0.403	[kg]
K_f	=	2.104	[N/V]
q	=	1000	[V/m]
K_p	=	4000	[V/m]
K_d	=	25	[V·s/m]
K_i	=	0 (for PD) or 0.35 (for PID)	[V/s·m]
T	=	0.0001	[sec]

The repetitive controller is designed using the nominal rotating speed of $\omega = 2\pi$ x 20 [rad/s] = 20 [Hz]. The repetitive sampling stage number is N = 15. The Riccati equation is solved using the following weightings;

$$Q(1,1) = 10.0 \quad , \quad h = 1.0$$

Results and Discussions

Figure 6 shows the time response of the rotor which runs at 20 [Hz]. In this case, integral control is not used to clarify the effect. The static disturbance is considered as a kind of periodic function and is expected to be canceled with the repetitive control. First the rotor runs without repetitive control. Then the repetitive control is turned on at the sampling number of 130. The periodic disturbances as well as the static error is quickly decreased without increasing the actuating signal. These results indicate the superiority of the proposed optimum repetitive control.

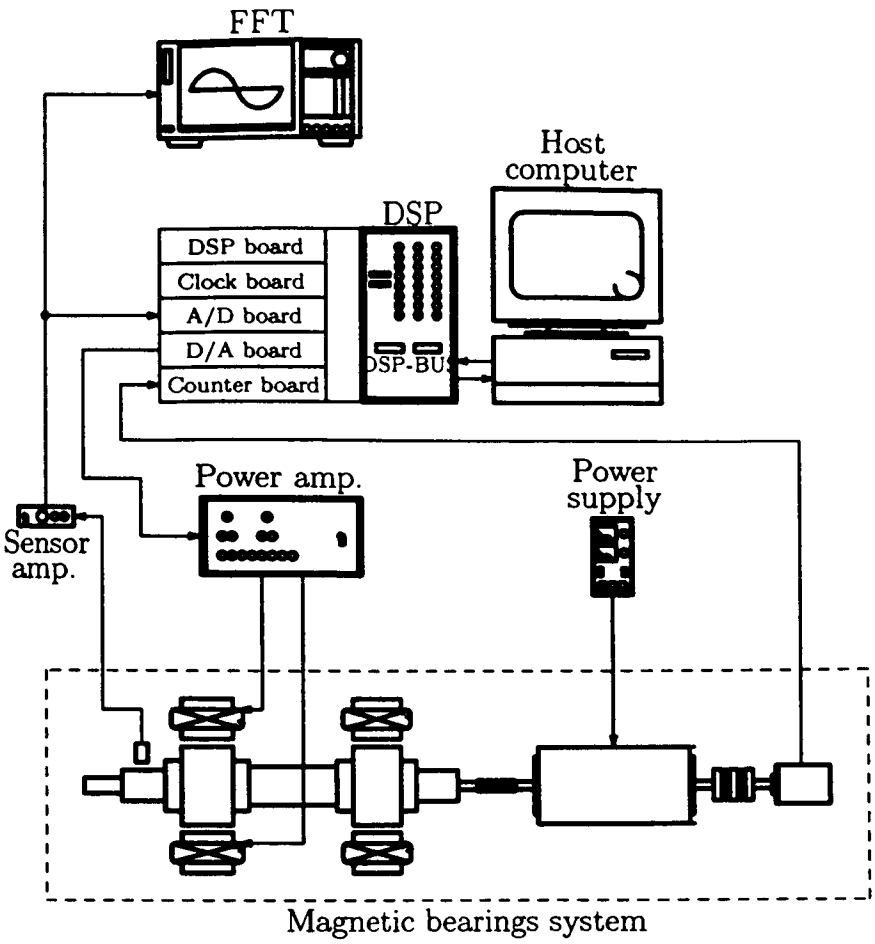

Figure 5: Control system of magnetic bearings

Next, the robustness of the rotational speed change is tested and the results are shown in Fig. 7. The controller is designed using the nominal speed of 20 [Hz], while the responses are tested by changing the rotational speed of 15, 20 and 25 [Hz]. The response with the repetitive controller is indicated by the solid line and is compared with the response without repetitive control. Unbalance response is always reduced even though the rotational speed changes about 25%. These responses indicate the robustness of the proposed optimum repetitive controller.

Finally, repetitive control is applied to the PID controlled magnetic bearings. The responses are shown in Fig. 8. The top graph indicates the horizontal displacement. First, the rotor runs at 20 [Hz] without repetitive control. The repetitive control is turned on at the sampling of 80 and the periodic response decays quickly. The middle graph indicates the expanded response for 500 or 560 sampling which is compared with the response without the good disturbance rejection property of the proposed repetitive control.

In this paper, the repetitive number for one revolution is chosen as 15 and it is relatively small. However, the optimum repetitive controlled indicates relatively good unbalance rejection properties. Increasing the sampling number will decrease higher order repetitive unbalance. Hence a repetition number more than 30 is recommended for the practical digital control system.

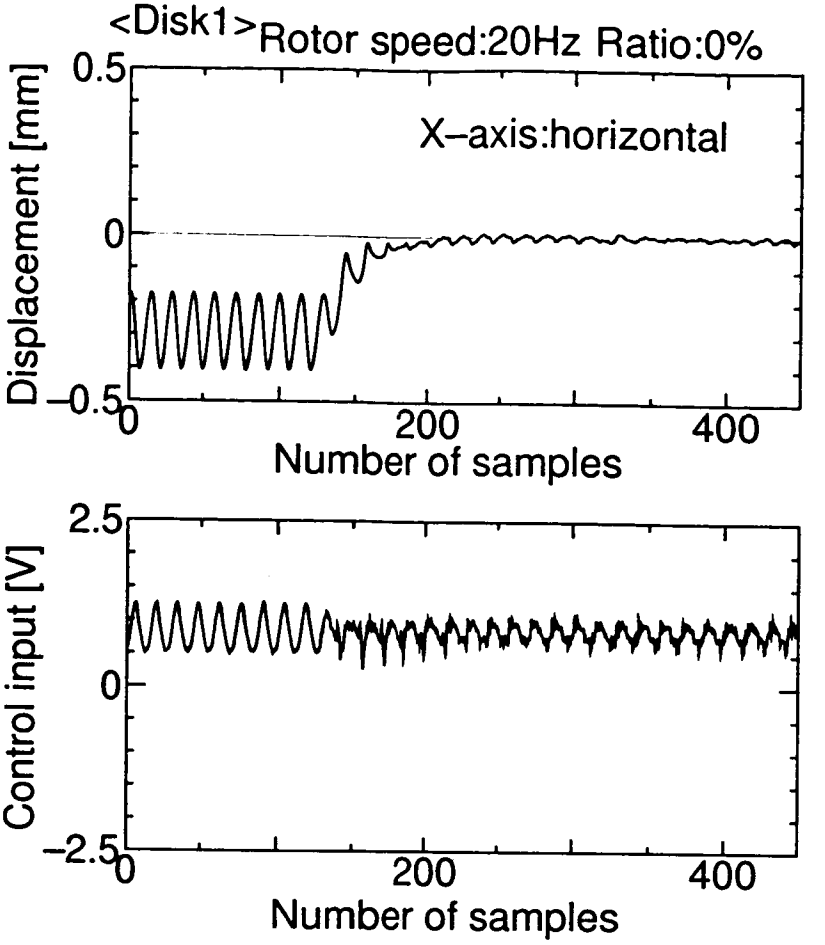

Figure 6: Transient response of optimal repetitive control system

CONCLUSIONS

A new repetitive control is proposed using the angular coordinate sampling domain. The controller is designed using the optimum regulator theory. The designed controller is applied to a solid rotor and tested. The following results are obtained.

- The angular coordinate repetitive controller can reduce the unbalance response automatically even though the rotating speed changes.
- The repetitive control system is perfectly stabilized by optimum regulator theory.
- It is argued that the proposed repetitive control is one of the most suitable unbalance cancellation techniques for rotating machinery.

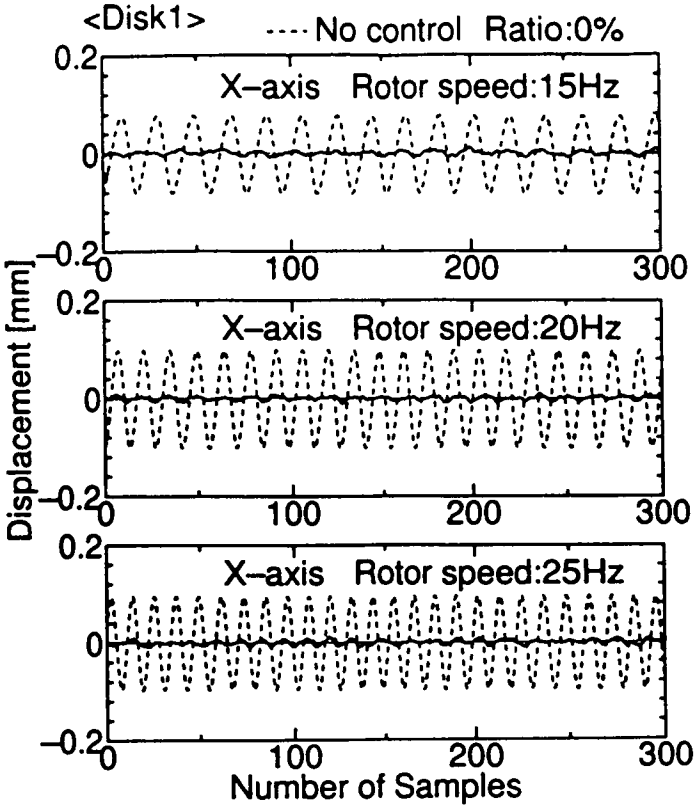

Figure 7: Time response of optimal repetitive control system

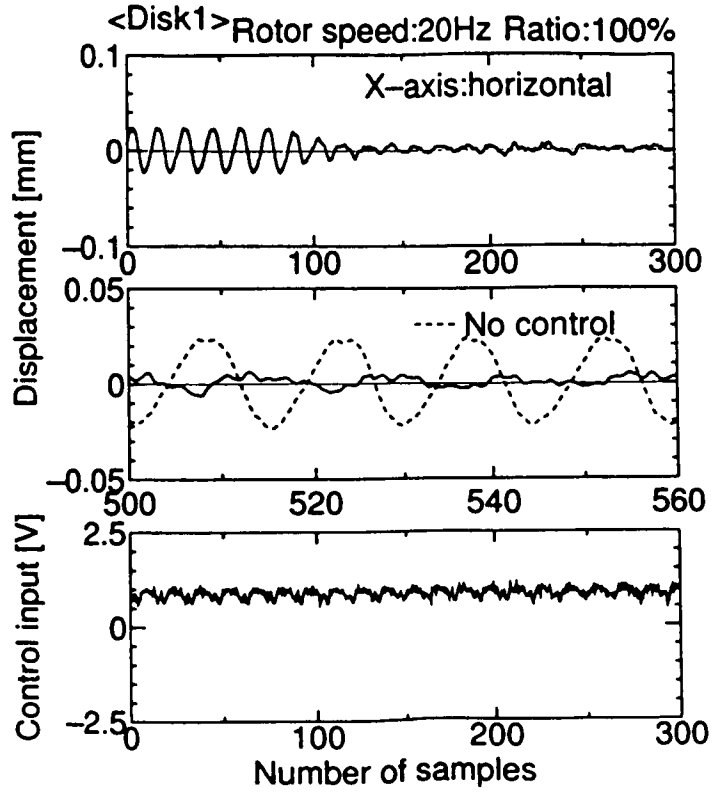

Figure 8: Response of disturbance cancellation and optimal repetitive control system

References

[1] M. Dussaux: *The Industrial Application of the Active Magnetic Bearings Technology.* Proc. of the 2nd Int. Symposium on Magnetic Bearings, July 12-14, 1990, Tokyo, p. 33.

[2] T. Mizuno and T. Higuchi: *Design of Magnetic Bearing Controllers Based on Disturbance Estimation.* Proc. of the 2nd Int. Symposium on Magnetic Bearings, July 12-14, 1990, Tokyo, p. 281.

[3] M. Hisatani and T. Koizumi: *Adaptive Filtering for Unbalance Vibration Suppression.* Proc. of the 4th Int. Symposium on Magnetic Bearings, August 23-26, 1994, Zurich, p. 125.

[4] C. R. Knospe and S. M. Tamer: *Experiments in Robust Unbalance Response Control.* Proc. of the 5th Int. Symposium on Magnetic Bearings, August 28-20, 1996, Kanazawa, p. 131.

[5] M. Nakano, et. al.: *A New Approach to Reject Angle Dependent Disturbances in Constant Speed Rotation Control Systems.* Trans. of IEE, Japan, 112-D, 1992, p. 409-414 (in Japanese).

[6] S. Kon, et.al.: *High Precision Control for Electrical Machine with Periodic Disturbances Based on Optimal Repetitive Control.* Trans. of IEE, Japan, 115-D, 1995, p. 843-851 (in Japanese).

Session 11 -- High Tc 2

Chairman: Hans Schneider-Muntau
National High Magnetic Field Laboratory (NHMFL)

Electromaglev System of a YBCO Bulk Superconductor

K.Sawa, H.Horiuchi, K.Nishi
Faculty of Science and Technology
Keio University
Kouhoku-ku, Yokohama 223 Japan

Y.Iwasa, M.Tsuda, H.Lee
Francis Bitter National Magnet Laboratory
Massachusetts Institute of Technology
Cambridge, Masacchusetts

K. Nagashima, T.Miyamoto, M.Murakami
ISTEC
Minato-ku, Tokyo105 Japan

H.Fujimoto,
Railway Technical Research Institute, JR

SUMMARY

This paper describes an "Electromaglev" system, in which a HTS sample, that is, a YBCO disk or ring, is stably levitated in a DC magnetic field generated by electromagnets placed under the levitated object. The most versatile and useful features of this system are: (1) easily adjustable levitation height - it is made possible by varying the electromagnet coil current, (2) large levitation height - it is feasible by sufficiently large electromagnets. This levitation system is theoretically and experimentally discussed from the view of levitation stability. Consequently, for stable levitation, specifically pitch stability, magnetic flux is required to be trapped in the YBCO disk as the disk is initially cooled from the normal state to the superconducting state in the presence of an external magnetic field. Further, the levitation height can be controlled by the coil current. The range of the maximum levitation height achieved by a 40mm diameter (with a 30mm diameter hole) YBCO ring was 100mm.

1. INTRODUCTION

The magnetic levitation of high-temperature superconducting (HTS) materials is applied, for example, to magnetic bearings. A permanent magnet disk levitated stably above a superconducting disk, generally of $YBa_2Cu_3O_{7-\delta}$ (YBCO), is a familiar phenomenon of HTS [1-3]. The levitation is achieved by a repulsive force created between the magnetic field of the permanent magnet disk and that induced in the YBCO disk. Levitation is stable. With a system in which both disks are permanent magnets, however, levitation is unstable, because such a system violates requirements set forth by a corollary of Lenz's law. The corollary may be stated as follows: for stable levitation, spatial current flow in at least one of the two disks must have more than one degree of freedom. Note that the amperian current in each of the two permanent magnet disks has only one degree of freedom - in the azimuthal direction. If one of the permanent magnet disks is replaced with a superconducting disk, on the other hand, because induced supercurrents in the disk can flow, both in the azimuthal and radial directions, the currents have two degrees of freedom, making it possible for the other permanent magnet disk to be levitated stably above the superconductor. In the "electromaglev" system, first investigated by Krasnyuk and Mitrofanov in 1990 [4] and studied comprehensively here, the levitated object is an HTS bulk sample rather than a permanent magnet disk. Also, a magnetic field is generated by electromagnets rather than by a permanent magnet. Figure 1 shows a schematic drawing of an "electromaglev" system, in which a superconducting YBCO disk, $2R_d$ diameter and S_d thick, is levitated above a magnet system comprised of two electromagnets referred to as the Outside Coil and Inside Coil. A steel plate on which the two coils are placed enhances the field in the top half of the space. In constrast to this electromaglev system, we may refer to the more common system in which a permanent magnet disk is levitated above a bulk HTS disk as a passive system.

The most versatile and useful features of the "electromaglev" system, as opposed to the passive system, are: 1) readily adjustable levitation height, made possible by varying currents in the electromagnets; and 2) "large" levitation heights, made feasible by using sufficiently large electromagnets. In this paper the condition of stable levitation is theoretically and experimentally discussed for two types of YBCO bulk, 40mm diameter ring (30mm diameter hole) and 100mm diameter disk. For stable levitation a proper amount of magnetic flux is required to be trapped in the YBCO objects by the field cooling. We have succeeded in achieving a maximum levitation height of 100mm with the ring.

2. "ELECTROMAGLEV" SYSTEM

The system used in the experiment is basically equivalent to that shown in Figure 1. For a new system, a large double pancake structure coil has been used as the Outside Coil with its companion Inside Coil to achieve greater levitation height. Figure 2 shows the cross section of the new Outside Coil placed on steel plates. It also shows the detail of the winding, whose conductor is of copper, 1mm thick and 8.25mm high. Turns are separated by insulating spaces, each 3mm wide, placed every 10mm along the conductor.

A 40mm diameter ring and two 100mm diameter disks, both of YBCO, are used as the floating objects. Since the levitation stability is greatly affected by the homogeneity of YBCO bulk crystal, a magnetic flux is trapped in the YBCO bulk and the flux distribution is measured by a Hall probe. Figures 3 and 4 show the results. Figure 3 shows the flux distribution of the ring, which is axially symmetric. Figure 4 shows that of the 100mm diameter disks. Figure 4a shows the flux distribution of a permanent magnet used to apply a flux to the disks; its distribution is very uniform both in the radial and azimuthal directions. Figures 4b and 4c show the flux distributions due to the trapped flux, respectively, for Disks 1 and 2. Although both distributions are not uniform, Disk 1 may be somewhat better than Disk 2.

3. BASIC IDEA FOR STABILITY

The stable levitation is achieved by a repulsive force created between the field induced in the YBCO disk and that of electromagnets [5-6]. For stable levitation, spatial current flow in the disk must have more than one degree of freedom. In this system, though the disk provides two degrees of freedom for its supercurrent, that is not sufficient. To achieve lateral and pitch stability for the levitating disk, the magnetic field created by the electromagnets must satisfy the following spatial requirements, which are derived from consideration of Lorentz force acting on the supercurrent, Id, induced in the disk (see Figure 5):

$$\left[\left(\frac{\partial B_z}{\partial r}\right)_{(R_d,z)} > 0\right]_{Lateral\ Stability} \tag{1}$$

$$\left[\left(\frac{\partial B_r B_z}{\partial z}\right)_{(R_d,z)} < 0\right]_{Pitch\ Stability} \tag{2}$$

4. EXPERIMENTAL RESULTS

As stated in section 3, stable levitation needs to achieve lateral and pitch stability. Exciting currents are obtained to generate flux distributions satisfying equations (1) and (2). Figure 6 shows the flux distributions generated by the coil currents I_1 and I_2. From Figure 6a the B_z distribution at current I_2 less than 40A is found to satisfy the lateral stability of equation (1). However, Figure 6b shows the pitch stability to be difficult to realize, especially at lower height z. The higher the current I_2 becomes, the more easily the pitch stability can be realized. From these results we choose 40A as the optimal current I_2. The levitation tests were tried under the condition of I_2=40A,but stable levitation, especially pitch stability, could not be achieved. In all tests, the ring tilted, finally levitating vertically (Figure 7) as the Outside Coil current was increased.

The experiment has demonstrated that in addition to field requirements of equations (1) and (2), the presence of a trapped flux in a disk (or a ring) is another necessary condition for stable levitation. Experimentally, this trapped flux may be induced in the disk through what we call a field-cooling (FC) process, in which a flux may be trapped in the disk when it is cooled from the normal state to the superconducting state in the presence of a magnetic field generated by the electromagnets. Table 1 presents levitation data for the ring. The 1st and 2nd columns give, respectively, currents, I_1 for Outside Coil and I_2 for Inside Coil used to generate an external field during FC; 3rd column gives I_2, held constant, as I_1 was raised to achieve levitation: 4th column gives I_1 when the ring begins levitation, but it also gives I_1 at that time if the ring starts tilting before levitation: 5th column gives the ring's approximate tilt angle at maximum levitation height: Note that to achieve tilt-free levitation the ring must be field-cooled with I_1 above 210A when I_2 is 40A. Figure 8 shows the variation of levitation starting current and maximum levitation height with FC current. The maximum levitation height is shown to decrease with FC current.

The levitation experiment was conducted with two 100mm diameter YBCO disks, each 20mm thick. Table 2 presents a summary of data for the disks. It was not possible to achieve stable levitation for Disk 2 even with I_1=200A, a level sufficient for stable levitation for Disk 1. This inferior behavior of Disk 2 in companion with Disk 1 behavior may be a reflection of Disk 2's homogeneity of field distribution that is poorer than Disk 1's as mentioned in Section 2. Data presented in each table clearly indicate that a trapped flux is essential for stable levitation: with no field cooling, i.e., I_1=0, the first row in each table shows a right-angle tilted levitation.

5. DISCUSSION

For stable levitation, especially tilt-free levitation, field cooling is indispensable. Here, it is elucidated how the trapped flux by the field cooling works for stable levitation. Assuming an axially long HTS bulk the Bean model is used for the superconducting current distribution.

Figure 9 presents the supercurrent distribution in the HTS bulk in an external magnetic field H_d with zero field cooling. The bulk is levitated by Lorentz forces generated between the supercurrent I_d and external magnetic field H_d. Equations (1) and (2) are spatial requirements for stable levitation. As stated above, actually, both requirements are not sufficient to achieve tilt free levitation.

For a HTS bulk with a trapped flux induced through the field cooling process, Figure 10 shows its supercurrent distribution in an external magnetic field H_d. The outside supercurrent penetrates a thickness δ_j into the bulk to eliminate the external magnetic field, and the trapped supercurrent remains inside. Certainly an external field becomes so large that the trapped supercurrent will be cancelled ($H_d \geqq 2H_{d0}$). At the presence of an external field the existence of the inside supercurrent is very different from the bulk with zero field cooling. This will be related to pitch stability.

Now, the disk is assumed to be tilted by $\Delta\theta$ about – y axis as shown in Figure 11. As stated in the section 3 if $(\partial B_r B_z/\partial z)\ r=r_1 < 0$, a restoring force will be generated in the outside supercurrent I_d. On the other hand, since the inside supercurrent has an opposite direction of moment, its restoring force decreases if $(\partial B_r B_z/\partial z)\ r=r_0 < 0$. However, $(\partial B_r B_z/\partial z)$ generally becomes positive at small radial distance r as shown in Figure 12. In that case the inside suppercurrent can contribute to enhance the restoring force.

From the above consideration the radial distribution of the supercurrent is an important factor for pitch stability. In this discussion the Bean model is used as the supercurrent distribution. But the floating object is a thin ring or disk, where the Bean model is not effective. More comprehensive two-parameter models such as Chen and Kim's are needed to better estimate the supercurrent distribution[7].

6. CONCLUSIONS

We have proposed an "Electromaglev" system in which levitation height is controlled by electromagnets. In this paper, levitation behaviors including stability and maximum levitation

height were investigated in a system comprised of new large electromagnets and two types of YBCO samples, 40mm Φ ring (I.D. 30mm) and 100mm Φ disks.

For stable and tilt-free levitation, the trapped flux induced through a field cooling process is found to be indispensable. Furthermore, pitch stability requires a supercurrent flow both in the azimuthal and radial directions.

It has been demonstrated that new electromaglev systems can levitate YBCO samples stably and tilt-free. Levitation height may be easily controlled by means of the magnetic field generated by the system's electromagnets. A maximum stable, tilt-free levitation height of ~100mm Φ and 17-mm thick (0.85kg disks) has been demonstrated.

REFERENCES

[1] F.C.Moon, K-C.Weng, and P-Z.Chang, "Dynamic magnetic forces in superconducting ceramic," *J. Appl. Phys.*66, 5643(1983)

[2] Takeshi Takatomi, John J.Boland, and Derk B.Dove, "Magnetic field controlled levitation and suspension of a magnet above and below type II superconductors," *Appl.Phys.Lett.*55,1454

[3] Masato Murakami, Terutugu Oyama, Hiroyuki Fujimoto, Takahiro Taguchi, Satoshi Gotoh, Yuh Shiohara, Naoki Kshizuka, and Shoji Tanaka, "Large levitation force due to flux pinning in YBCuO superconductors fabricated by melt-powder-melt-growth processes," Japanese *J.Appl.Phys.29*,L1991(1990)

[4] N.N.Krasnyuk and V.P.Mitrofanov, "Levitation of ceramic $YBa_2Cu_3O_{7-y}$ in magnetic field," Superconductivity 3, 303 (1990)

[5] Yukikazu Iwasa and Haigun Lee, "'Electromaglev'-magnetic levitation of a superconducting disk with a DC field generated by electromagnets: Part 1 Theoretical and experimental results on operating modes, lift-to-weight ratio, and supension stifness," *Cryogenics* 37(1997)

[6] Yukikazu Iwasa, Haigun Lee, Koichiro Sawa,and Masato Murakami, "Active magnetic levitation with YBCO samples," Advances in superconductivity IX [Proc.9th International Sympo. Superconductivity (ISS'96) October 21-24, 1996 Sapporo],Eds.S.Nakajima and M.Murakami (Springer-Verlag, Tokyo,1997)

[7] J H P Watson and I Younas, "Current and field distribution within short cylindrical superconductors," *Supercond.Sci.Technol.*8 (1995) 799-805

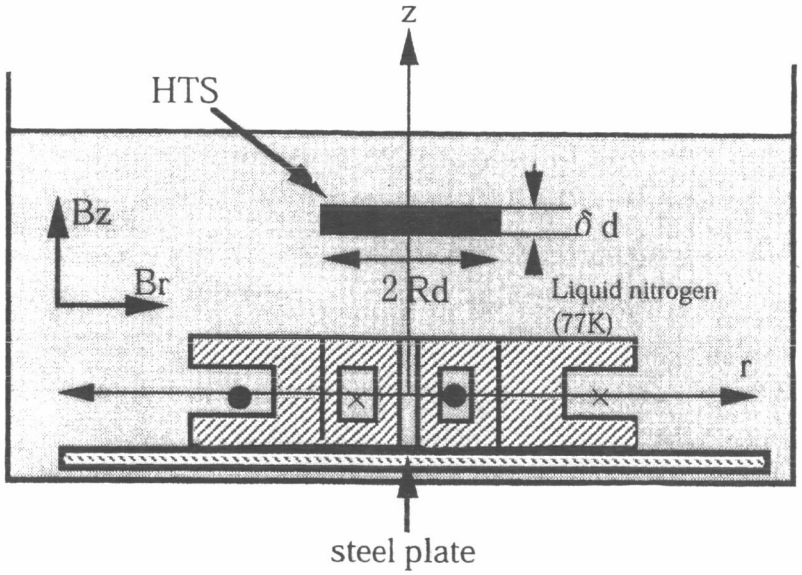

Fig.1 Experimental setup

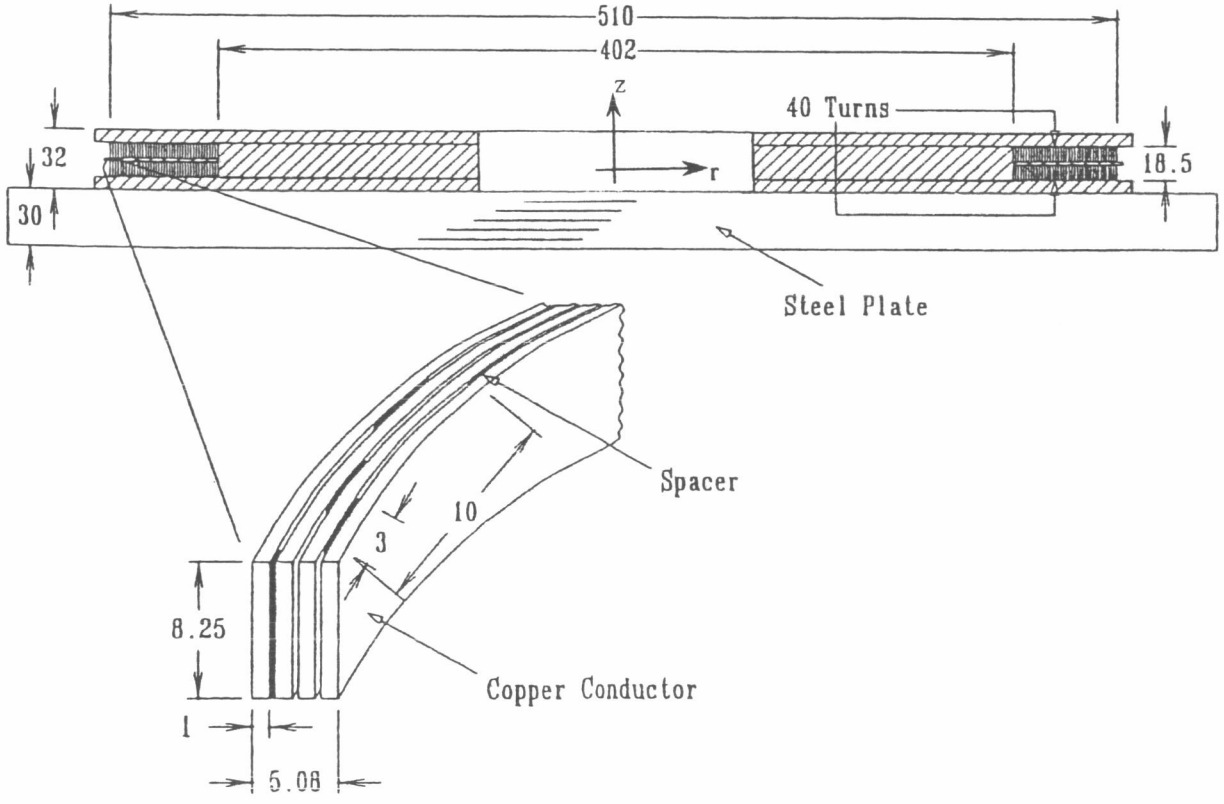

Fig.2 Cross sectional view and winding details of a double pancake coil placed on a steel plate. Dimensions are in mm

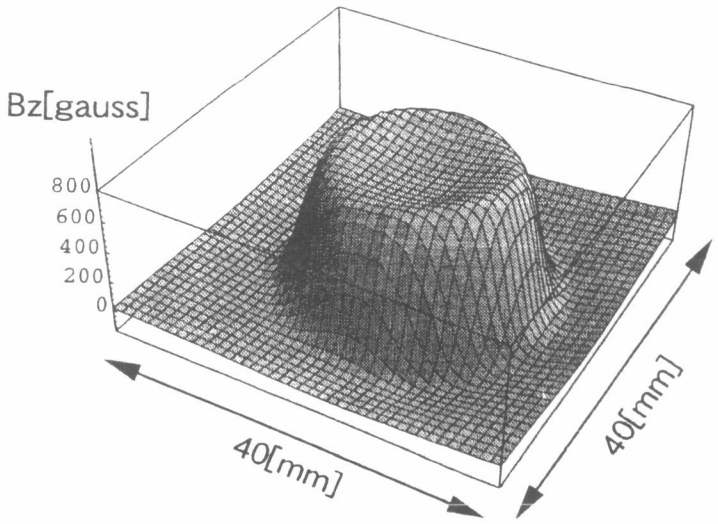

(a) 3D representation

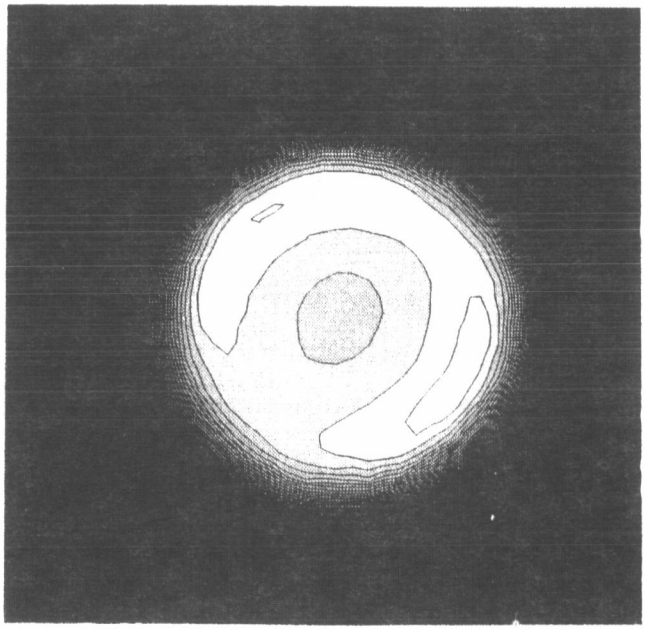

(b) Contour line representation

Fig.3 Magnetic flux density distribution of trapped flux in the ring

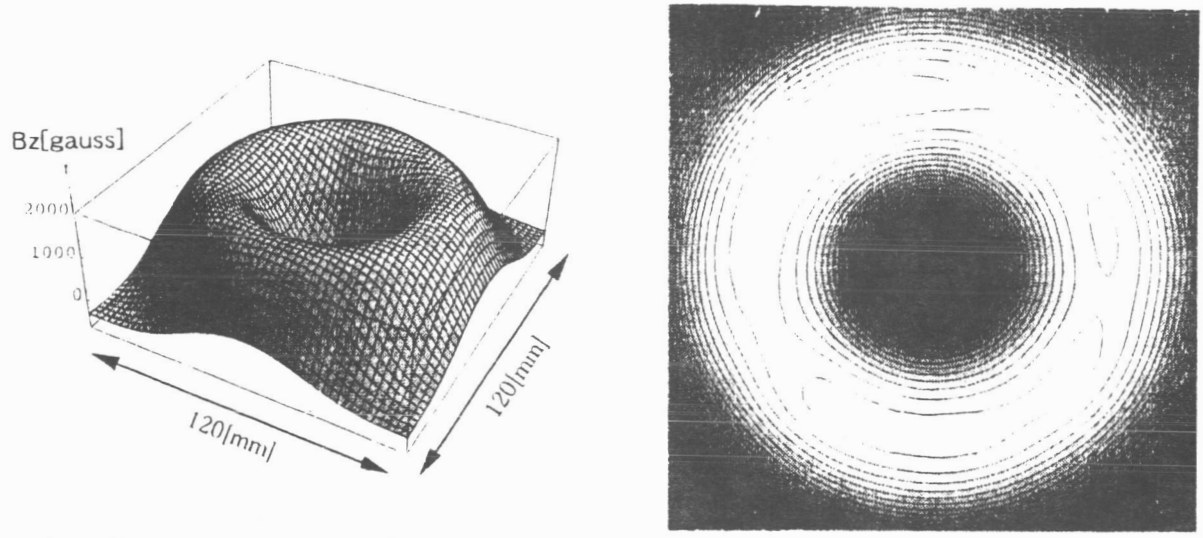

(a) Bz distribution of the permanent magnet used in the field cooling

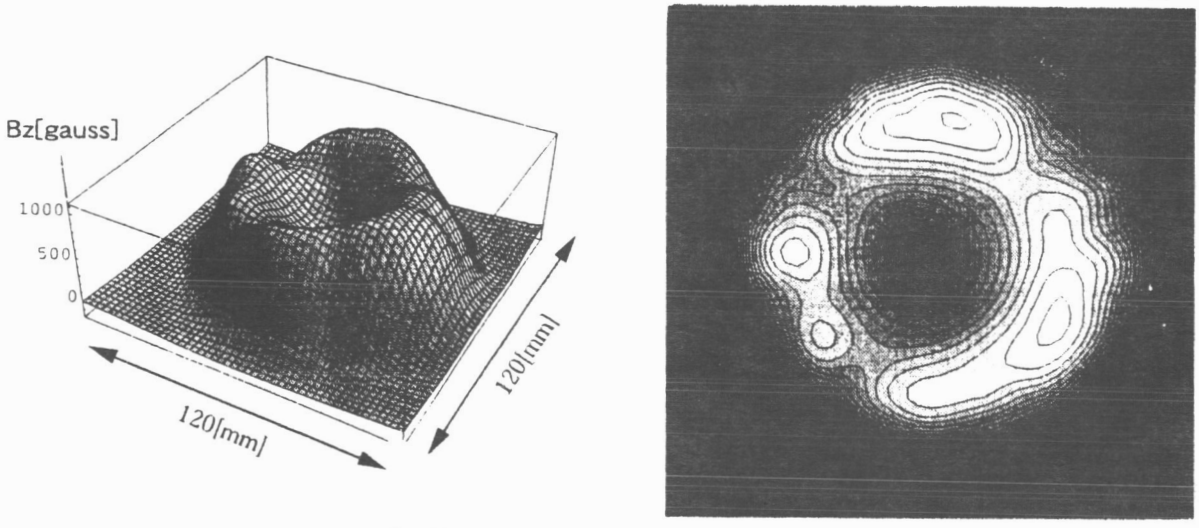

(b) Bz distribution of Disk 1

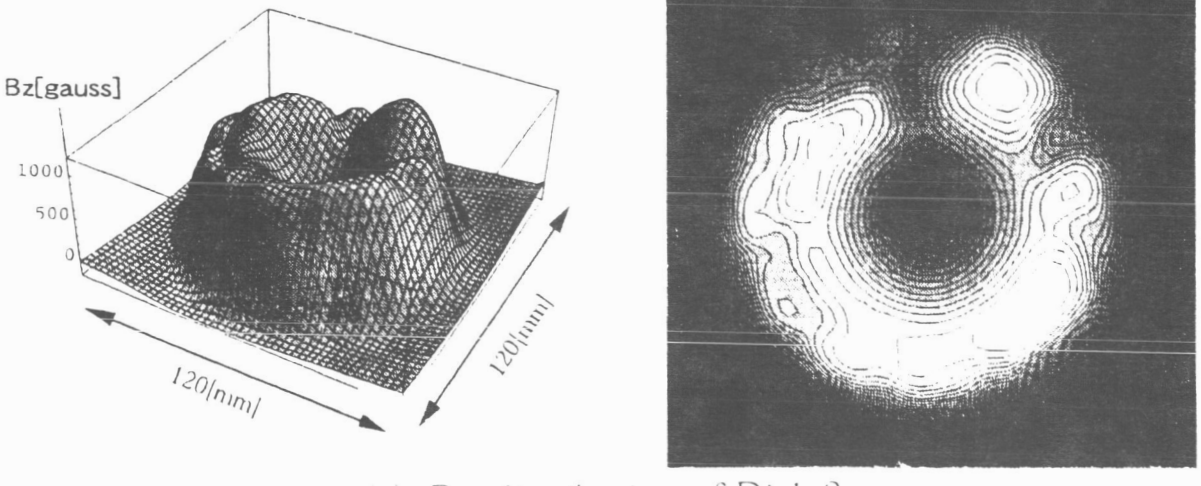

(c) Bz distribution of Disk 2

Fig.4 Magnetic flux density distribution of trapped flux in Disks

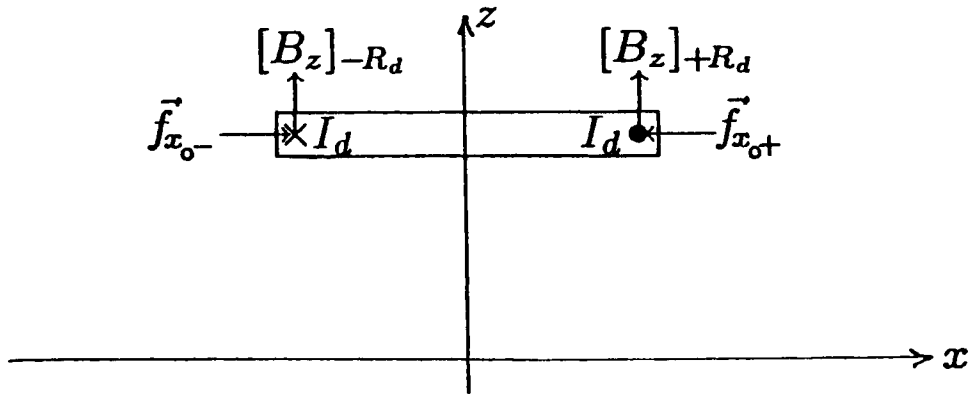

(a) Lateral-direction force

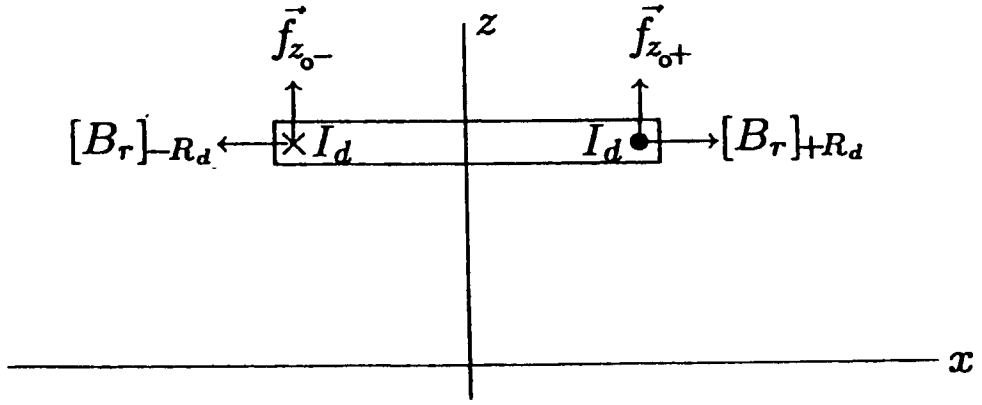

(b) Pitch-direction force

Fig.5 Schematic drawings of a levitated disk subjected to lateral and pitch-direction force

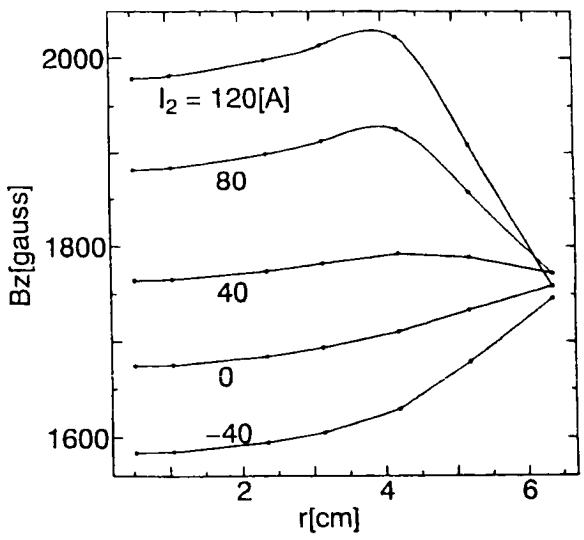

(a) r - Bz (z=2.06[cm],I_1=400[A])

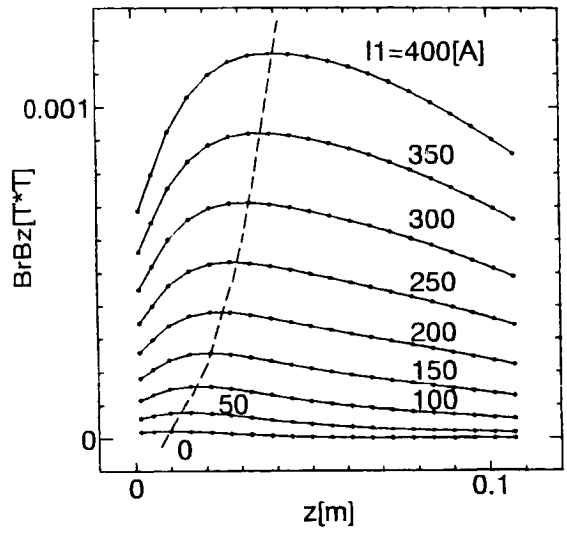

(b) z - BrBz (r=2.1[cm],I_2=40[A])

Fig.6 Magnetic flux density distribution for levitation stability

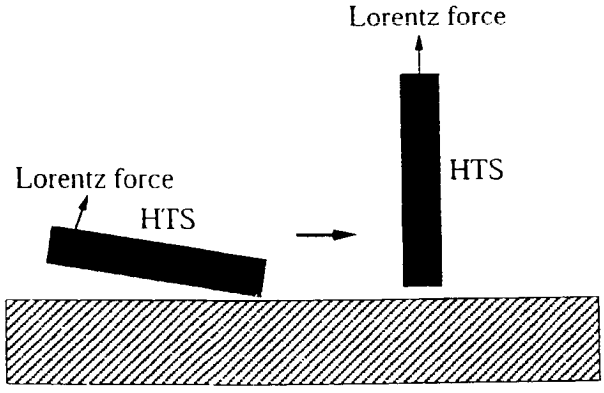

Fig.7 Schematic view of unstable levitation

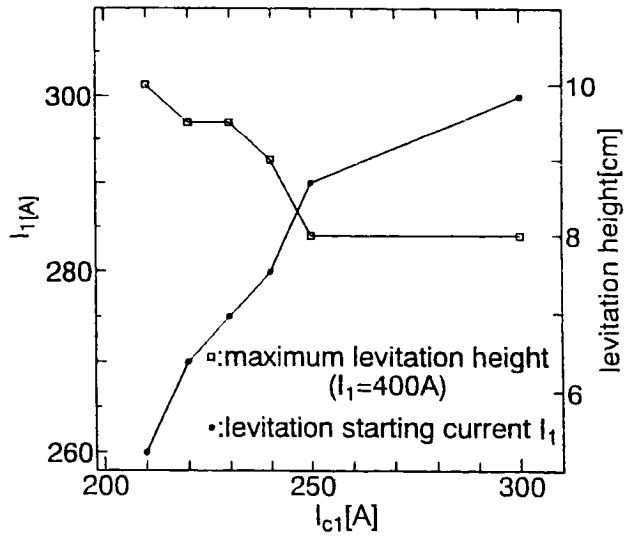

Fig.8 Levitation starting current and levitation height (I_{c2}=40[A])

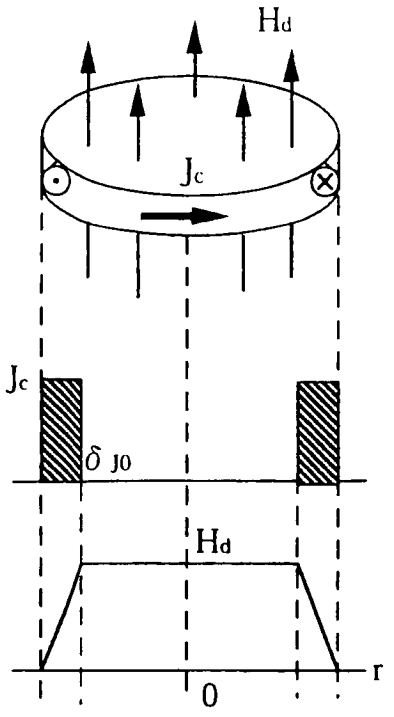

Fig.9 Supercurrent and magnetic field of a disk with a flux trapped by F.C.

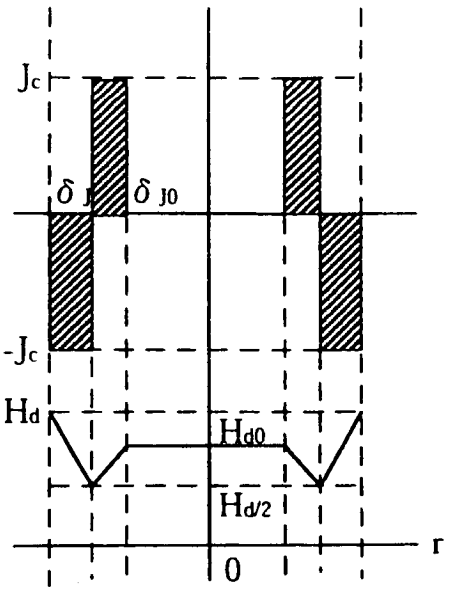

Fig.10 Supercurrent and magnetic field of a F.C. disk in an external field Hd

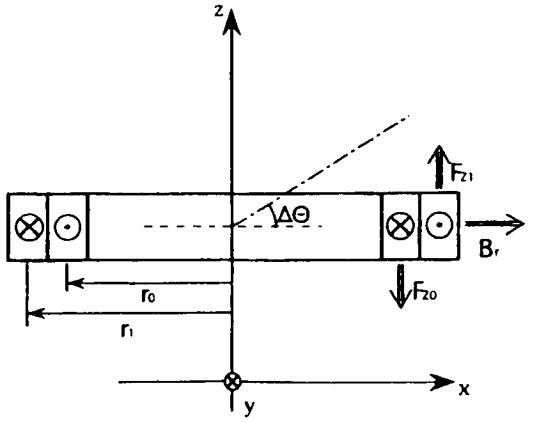

Fig.11 z-direction forces acting on each current layer

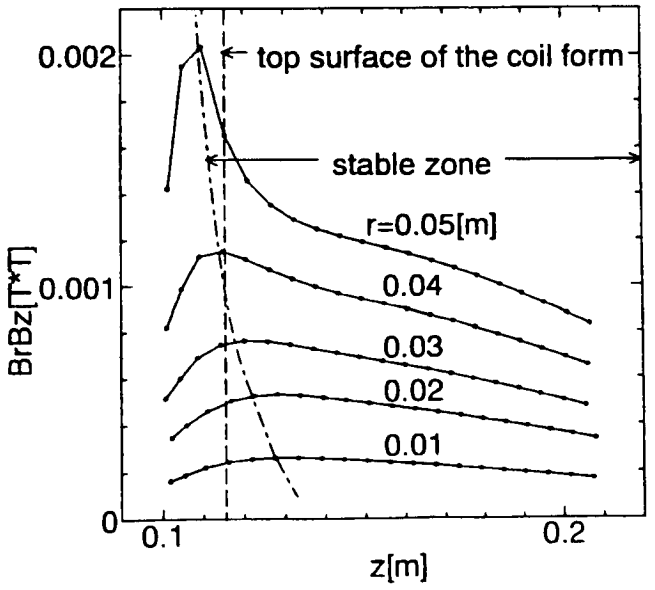

Fig.12 z - BrBz relation with a parameter of radial distance r (I1=250[A], I2=40[A])

Table 1 Levitation data for the ring

field cooling current		I_2[A]	tilting starting current	levitation starting current	tilting angle
I_1[A]	I_2[A]		I_1[A]	I_1[A]	[°]
0	40	40	60	275	90
50	40	40	120	360	90
100	40	40	150	310	45
150	40	40	190	310	45
200	40	40	310		10
210	40	40	260		0
220	40	40	270		0
230	40	40	275		0
240	40	40	280		0
250	40	40	290		0
300	40	40	300		0

Table 2 Levitation data for disks

DISK 1					
field cooling current		I_2[A]	levitation starting current	tilting angle	levitation height
I_1[A]	I_2[A]		I_1[A]	[°]	h[cm] (I_1[A])
0	0	−40	255	90	4 (425)
200	40	40	300	0	8 (425)
250	40	40	375	0	6～7 (450)
200	−40	−40	350	20	7～8 (425)
255	−40	−40	375	5	7～8 (450)
DISK 2					
200	40	40	340	30	5～6 (425)

LEVITATION FORCE PROPERTIES OF BULK SUPERCONDUCTORS FOR MAGNETIC BEARINGS

Hidekazu Teshima, Mitsuru Morita, and Takayuki Kaneko
Advanced Technology Research Laboratories, Nippon Steel Corporation
3-35-1 Ida, Nakahara-ku, Kawasaki 211, Japan

SUMMARY

Because superconducting levitation using high-temperature superconducting bulk materials is essentially stable, the possibility that completely noncontact and passive bearings can be realized without any control exists. In this study, an investigation was experimentally made into the basic properties of superconducting levitation force using large-size, high-performance Y-Ba-Cu-O bulk superconductors. It became apparent that an orientation of the c-axis of bulk superconductors and a reduction in the number of divided portions of samples by increasing the sample size are effective in improving the levitation force. It was also found that a sufficient sample thickness of bulk superconductors is about 10 mm. Furthermore, a near-net shape process was proposed for the processing of optimum-shaped materials for bulk superconductors.

INTRODUCTION

Magnetic bearings, which can support objects in a noncontact manner, have excellent features, such as high efficiency, high-speed rotation, low friction loss, cleanness, low noise and long life, and have been applied in various industrial fields. Because the magnetic bearings so far put into practical use are based on the levitation between two magnets, which is essentially unstable (ref.1), it was necessary to stabilize the levitation using a control mechanism. However, because superconducting levitation using high-temperature superconducting bulk materials is essentially stable (ref.2), the possibility that completely noncontact and passive bearings can be realized without any control has come up. Furthermore, expectations of practical use of superconducting magnetic bearings grew all the more because high-performance, large-size bulk superconductors were developed (ref.3) and it became possible to obtain high levitation forces (ref.4).

One of the fields to which superconducting magnetic bearings can be applied is bearings for energy storage systems for flywheels. In energy storage systems the overall efficiency is a very important index. In long-period energy storage, however, bearing losses provide a great cause of a decrease in the overall efficiency. It is needless to say that losses by friction are great in contact-type mechanical bearings. In active (controlled) magnetic bearings, which belong to the noncontact type, also, the power required by control lowers the overall efficiency. Because superconducting magnetic bearings do not require control;, it is expected that the overall efficiency of a system rises even if the disadvantage that bulk superconductors are cooled to liquid nitrogen temperature is taken into consideration. For this reason, the development of flywheel energy storage systems using high-temperature superconducting levitation is being actively conducted in various countries of the world (ref.5-11).

A major premise for the practical application of a superconducting flywheel system is that superconducting levitation can really support a flywheel of weight at a practical application level. Although a high value of 2.7kgf/cm^2 at a levitation gap of 0 mm is reported as the levitation force with a single bulk superconductor (ref.4), it is not clear what the levitation force is when multiple bulk superconductors are used. Even in a large-size application where multiple bulk superconductors must be used, it is necessary to arrange bulk superconductors in an optimum manner in order to realize a high levitation force. However, high-performance bulk superconductors have only recently been developed and data on the superconducting levitation necessary for the optimum design of bulk superconductors used in superconducting magnetic bearings are insufficient. In this paper, an investigation was experimentally made into the basic properties of superconducting levitation using large-size, high-performance Y-Ba-Cu-O bulk superconductors.

PRINCIPLE OF HIGH-TEMPERATURE SUPERCONDUCTING LEVITATION AND BULK SUPERCONDUCTORS

Principle of High-Temperature Superconducting Levitation

Figure 1 is a schematic diagram of high-temperature superconducting levitation using the pinning effect. The magnetic lines coming out of the magnet are fixed by pinning centers to the bulk superconductor, that is, they are pinned and, therefore, the strength of stability relative to the levitation position works in both horizontal and vertical directions, resulting in stable levitation. However, it is only in the direction in

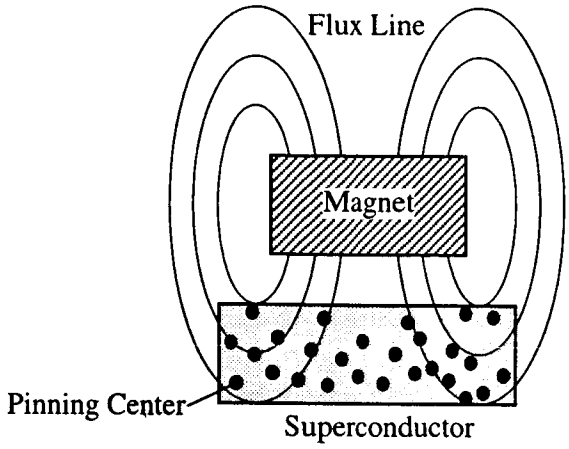

Figure 1 Schematic diagram of high-temperature superconducting levitation by the pinning effect.

which the magnetic field is nonuniform that the strength of stability (restoring force) works. In the flywheel application, therefore, the resistance to rotation can be reduced to a negligible degree by making the magnetic field distribution uniform in the rotation direction.

Although it has been pointed out that the levitation force is very small in **superconducting leviation** using the Meissner effect, it is possible to enhance the levitation force in **superconducting levitation** using the pinning effect by improving the properties and size of bulk superconductors. In other words, the levitation force increases in proportion to the product of critical current density (J_c) and sample size in the superconducting levitation using the pinning effect (ref.12). In recent years, a high levitation force has been realized for a single bulk superconductor owing to the development of high-performance, large-size bulk superconductors (ref.3-4).

High-Temperature Bulk Superconductors

In order to increase the levitation force, the high-temperature superconducting bulk materials used in the levitation application must be large-size ones of high J_c. For this reason, Y-Ba-Cu-O bulk superconductors processed by a melt-process called the modified Quench & Melt Growth (QMG) process were used in this experiment. Figure 2 shows the photographs of the appearance of an as-grown bulk superconductor and its microstructure. In the modified QMG process, a high Jc value is realized by finely dispersing the nonsuperconducting phase Y_2BaCuO_5 (211 phase), which is an effective pinning center, in the superconducting phase $YBa_2Cu_3O_x$ (123 phase). In Fig.2 (b), the matrix is the 123 phase and black

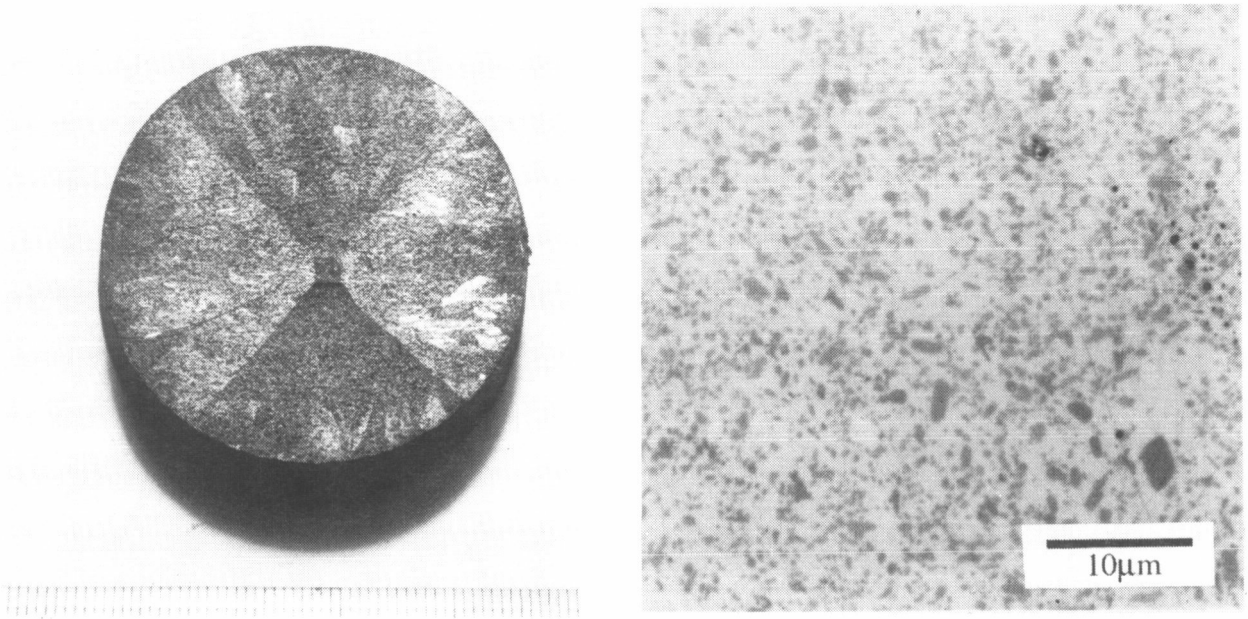

(a) (b)

Figure 2 Photographs of (a) the appearance of an as-grown bulk superconductor and (b) its microstructure.

spots of about 1 μm are the 211 phase. The J_c value is more than 10,000A/cm^2 even at a liquid nitrogen temperature of 77K and in a magnetic field of 1T. For the sample size, on the other hand, it is necessary to increase the size by excluding high-angle grain boundaries with the above fine structure kept unchanged. In the modified QMG process, the sample size is increased by controlling grain growth and crystallographic direction by a seeding technique. In Fig.2 (a), what is observed in the center of the bulk superconductor is a seed crystal.

The processing conditions for the bulk superconductors used in this experiment are as follows. First of all, the raw material powders Y_2O_3, BaO_2 and CuO were weighted out at a ratio of 1.3: 1.7: 2.4. This ratio corresponds to a proportion of the 211 phase of 30 mol %. Then 0.5 wt. % of Pt powders was added to these weighted-out powders and thoroughly mixed. After that, precursors were pressed by uni-directional duct pressing and cold isostatic pressing (CIP). The precursors were then brought into a partial-melt state by heating up to 1150°C and grains were caused to grow by using a Sm-Ba-Cu-O seed crystal while conducting slow cooling. After that, the precursors were made thoroughly superconducting by oxygen annealing.

Figure 3 shows the appearance of high-temperature bulk superconductors which are presently

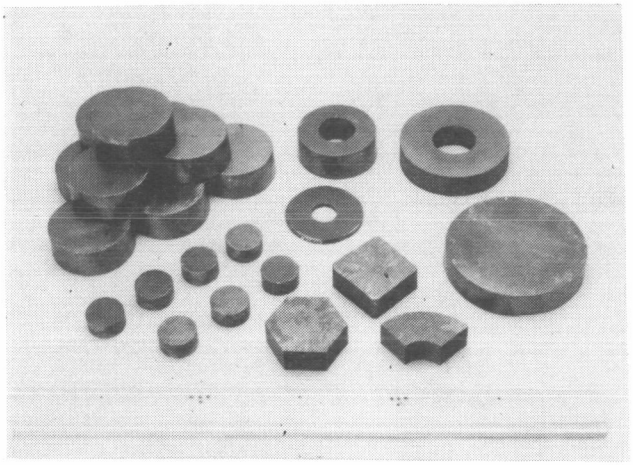

Figure 3 Appearance of bulk superconductors commercially available.

commercially available. Although bulk superconductors are oxides, they have relatively good formability and can be formed in various shapes as shown in Fig.3. For a small-size application, bulk superconductors may be formed in a disc shape or ring shape. At present, bulk superconductors up to about 100 mm in diameter can be obtained. For applications of large size, bulk superconductors are formed in a hexagon or sector shape and multiple bulk superconductors are arranged in a disc or ring shape. However, an optimum arrangement that maximizes the superconducting levitation force is not well known at the present stage, because basic data on the relationship between the superconducting levitation force and the shape, size, crystallographic direction, etc., of bulk superconductors are insufficient.

Method of Measuring Superconducting Levitation Force

Figure 4 shows the arrangement of the measuring device of superconducting levitation force used in this experiment. This device is an improvement upon a device for measuring mechanical strength of metallic materials, such as tensile strength and compressive strength. The bulk superconductor is fixed in a cooling container and cooled with liquid nitrogen. The magnet is attached to a magnet holder above the bulk superconductor and can be vertically moved by a drive system for changing the distance from the bulk superconductor. The levitation force is measured by a load cell . The relationship between the bulk superconductor-magnet distance and the levitation force can be measured by recording the signals of the controller controlling the drive system and those of the load cell. In this experiment, the bulk superconductor is always cooled under the condition of zero magnetic field cooling, that is, the bulk superconductor is cooled before the magnet is brought near to it.

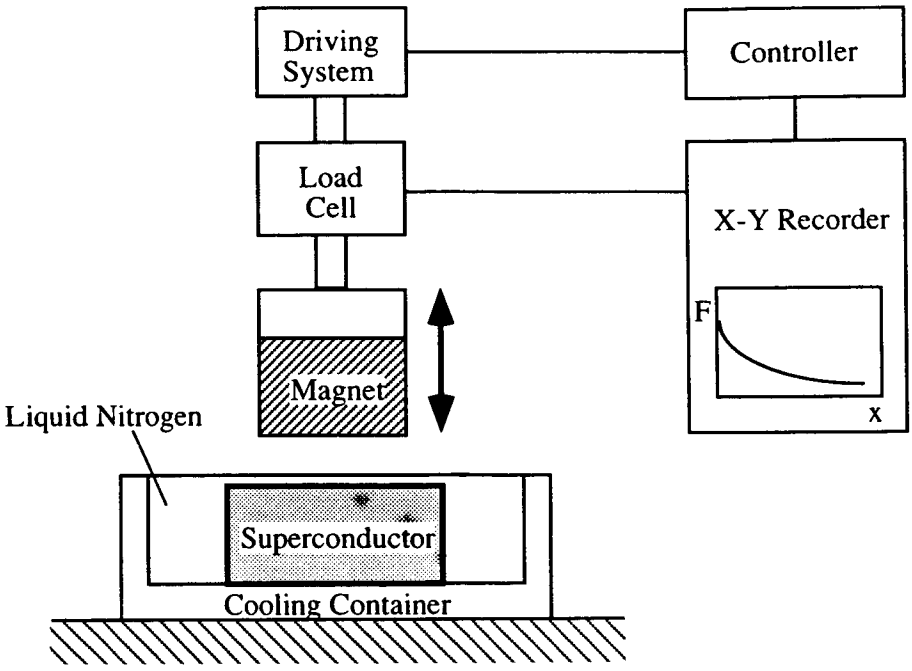

Figure 4 Composition of measuring device of superconducting levitation force.

RESULTS AND DISCUSSION

Superconducting Levitation Force and Crystallographic Direction

High-temperature superconductors have great anisotropy. Therefore, the relationship between superconducting levitation force and crystallographic direction was first investigated. Two cubic specimen with 10 mm sides were cut out from a c-axis oriented disc-shaped bulk superconductor 46 mm in diameter in such a manner that the grain axes should be the same as the directions of the sides; that is, the cubic specimens were cut out so that a c-axis oriented plane and an a-axis oriented plane could be obtained. A Pr-Fe-B rare earth permanent magnet 18 mm in diameter was used in measuring the levitation force. The surface magnetic flux density of this magnet was about 0.45T.

Table 1 shows the levitation force at a levitation gap of 0 mm on c-axis oriented planes and a-axis oriented planes. It was found that the levitation force on c-axis oriented planes is about twice that on a-axis oriented planes. It might be thought that this phenomenon reflects the fact that in high-temperature superconductors, superconducting currents are apt to flow on a plane perpendicular to the c-axis (i.e., the a-b

Table I. Superconducting levitation forces of c-axis oriented planes and a-axis oriented planes.

Sample No.	c-axis oriented (up side)	c-aixs oriented (down side)	a-axis oriented (side 1)	a-axis oriented (side 2)
1	0.81 kgf	0.70kgf	0.43 kgf	0.40 kgf
2	0.70 kgf	0.77 kgf	0.46 kgf	0.45 kgf

plane or the Cu-O plane). In order to increase the superconducting levitation force, therefore, it is important to orient the c-axis of a bulk superconductor in the direction of the magnetic field.

Superconducting Levitation Force and Sample Size

Next, the relationship between the superconducting levitation force and the size of the bulk superconductor was investigated. The superconducting levitation force was measured in disc-shaped bulk superconductors 33.0, 46.9 and 77.3 mm in diameter using Pr-Fe-B rare earth permanent magnets 18, 25 and 43 mm, respectively, in diameter. In this experiment, the ratio of bulk superconductors to permanent magnets was kept almost constant (1: 0.53-0.57). The surface magnetic flux density of all magnets was about 0.45T. Figure 5 shows the trapped magnetic flux density distribution of each superconductor. From the fact that the trapped magnetic flux density distribution has a single peak, it is apparent that this is a good bulk superconductor which does not contain a weak link in it.

Figure 6 shows the relationship between the bulk superconductor-magnet distance and the superconducting levitation force in each sample. It should be noted that the superconducting levitation force in Fig.6 is the superconducting levitation force per unit area of magnet. It became apparent that the superconducting levitation force increases with increasing sample size. The preponderance of large samples was especially remarkable when the bulk superconductor-magnet distance was great. Because an actual system is used at a finite levitation gap, an increase in the sample size is very effective in improving the superconducting levitation force of the whole system.

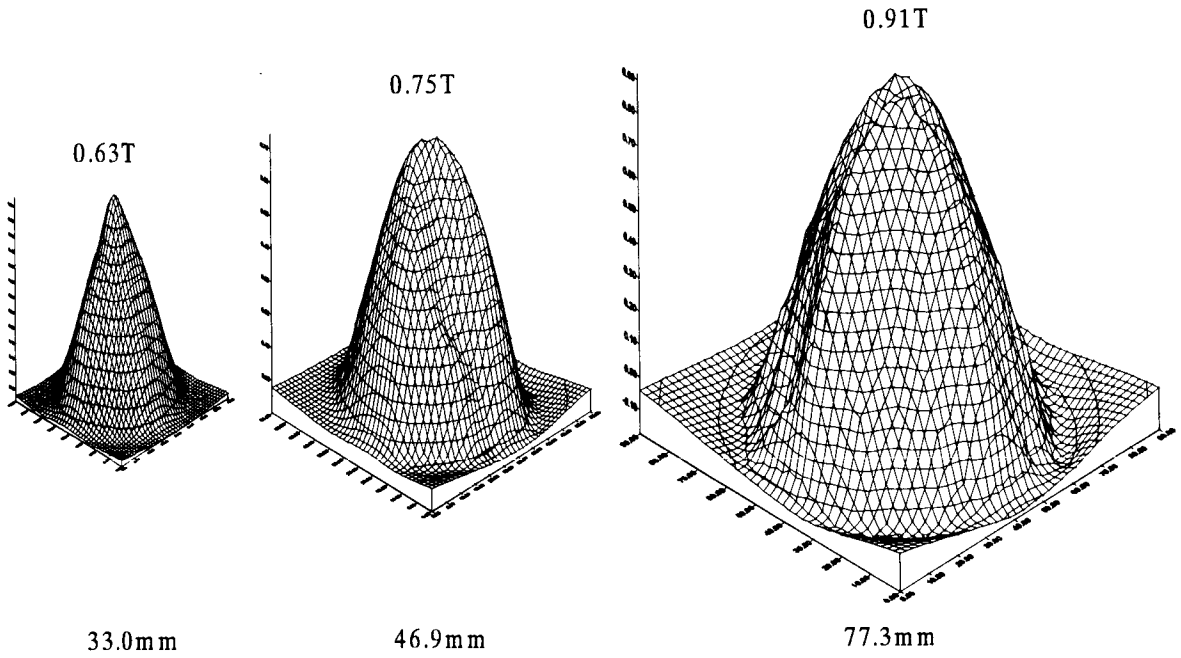

Figure 5 Trapped magnetic flux density of bulk superconductors 33.0, 46.9 and 77.3 mm in diameter.

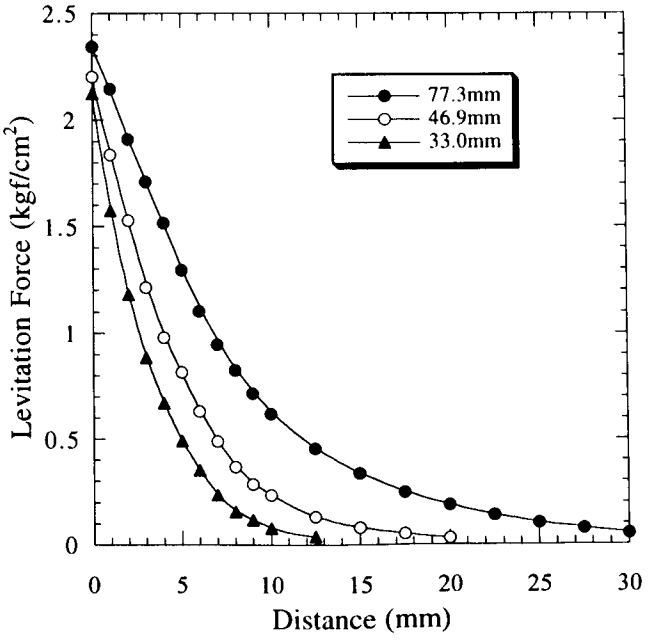

Figure 6 Levitation force characteristics curves of bulk superconductors 33.0, 46.9 and 77.3 mm in diameter (relationship between the bulk superconductor-magnet distance and the superconducting levitation force).

Superconducting Levitation Force and Sample Thickness

The relationship between the superconducting levitation force and the thickness of bulk superconductor was also investigated. As shown in Fig.7 (a), one disc-shaped bulk superconductor 46 mm in diameter was sliced into five thin discs 3 mm in thickness and the thickness was adjusted by stacking them. A Pr-Fe-B rare earth permanent magnet with a surface magnetic flux density of 0.45 T was used. Figure 7 (b) shows the results of an experiment conducted to investigate the relationship between the superconducting levitation force and the thickness of bulk superconductor at a levitation gap of 0 mm. It is apparent that the levitation force almost reaches its maximum when the sample thickness is 6 mm. It might safely be said that thickness of about 10 mm are sufficient when bulk superconductors are used in superconducting bearings.

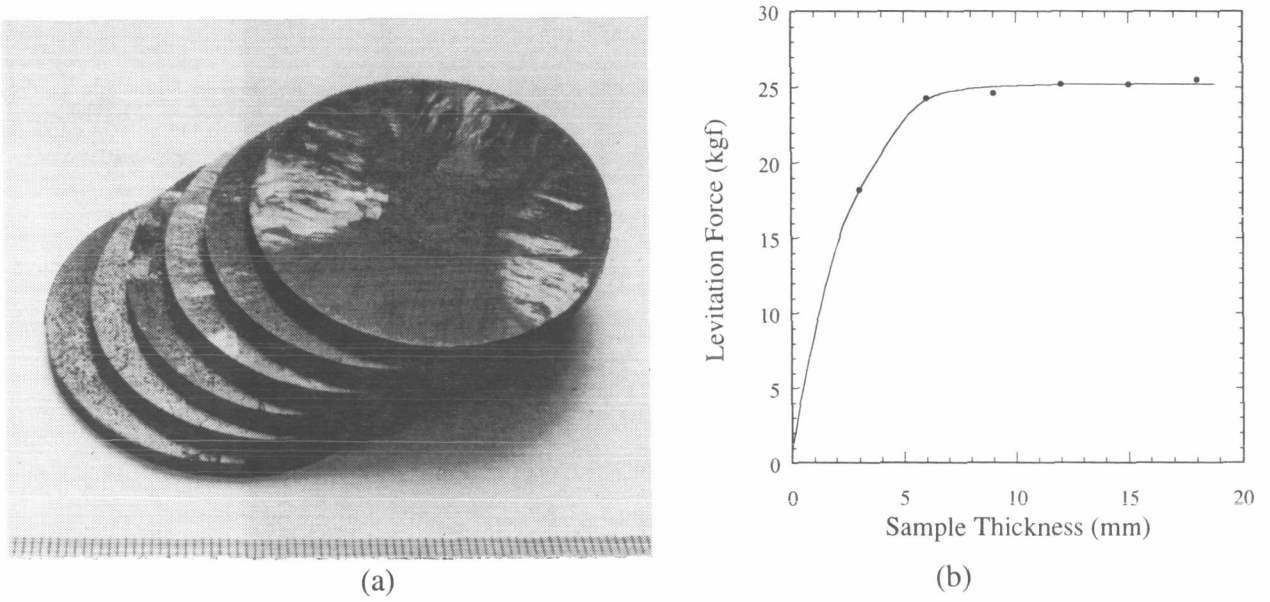

(a) (b)

Figure 7 (a) Photograph of a disc of bulk superconductor 3 mm in thickness and (b) relationship between the superconducting levitation force and the sample thickness.

Superconducting Levitation Force and Sample Dividing

The superconducting levitation force was investigated in a case where one bulk superconductor was divided. In this experiment, a disc-shaped bulk superconductor 30 mm in diameter was used and divided

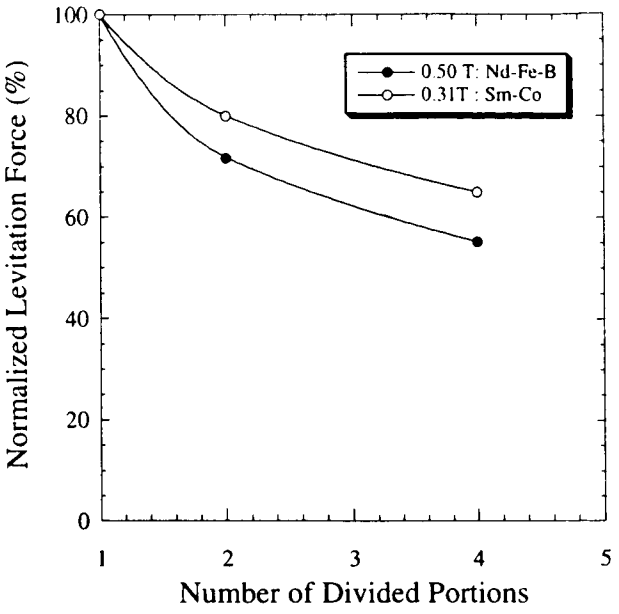

Figure 8 Relationship between the superconducting levitation force and the number of divided portions of sample.

into two portions and four portions. Two kinds of magnets were used; they are a Sm-Co rare earth permanent magnet 50 mm in diameter with a surface magnetic flux density of 0.32 T and a Nd-Fe-B rare earth permanent magnet 50 mm in diameter with a surface magnetic flux density of 0.50 T. Figure 8 shows the result of an experiment conducted to investigate the relationship between the superconducting levitation force and the number of divided portions of sample. In Fig.8, the levitation force is normalized by the value of the undivided sample. The superconducting levitation force decreased when a bulk superconductor was divided. It is found that the degree of decrease in the levitation force is remarkable when a magnet of a large surface magnetic flux density is used.

Hysteresis of Characteristic Curve of Superconducting Levitation Force

Because the superconducting levitation force is generated by the pinning of the magnetic flux lines that penetrate the interior of a bulk superconductor, hysteresis occurs essentially in the characteristic curves of superconducting levitation force when the magnet is brought nearer to and away from the bulk superconductor. The existence of hysteresis means that the levitation position is not definitely determined for the same load. In other words, when some force is applied to a levitating object and great displacement occurs, this object does not return to the original stable levitation position and levitates in another position in

a stable manner. This is not desirable in practical systems and it is necessary to reduce hysteresis.

Figure 9 shows the levitation force characteristics curves of bulk superconductors with different superconducting levitation forces. It became apparent that the hysteresis is large in a sample with a small levitation force. Conversely, the hysteresis became very small when the levitation force was large. As is apparent form this, the hysteresis of characteristic curves of superconducting levitation force can be decreased by improving the properties of bulk superconductors. To what extent the properties of bulk superconductors are to be improved is determined by the allowable range of practical systems.

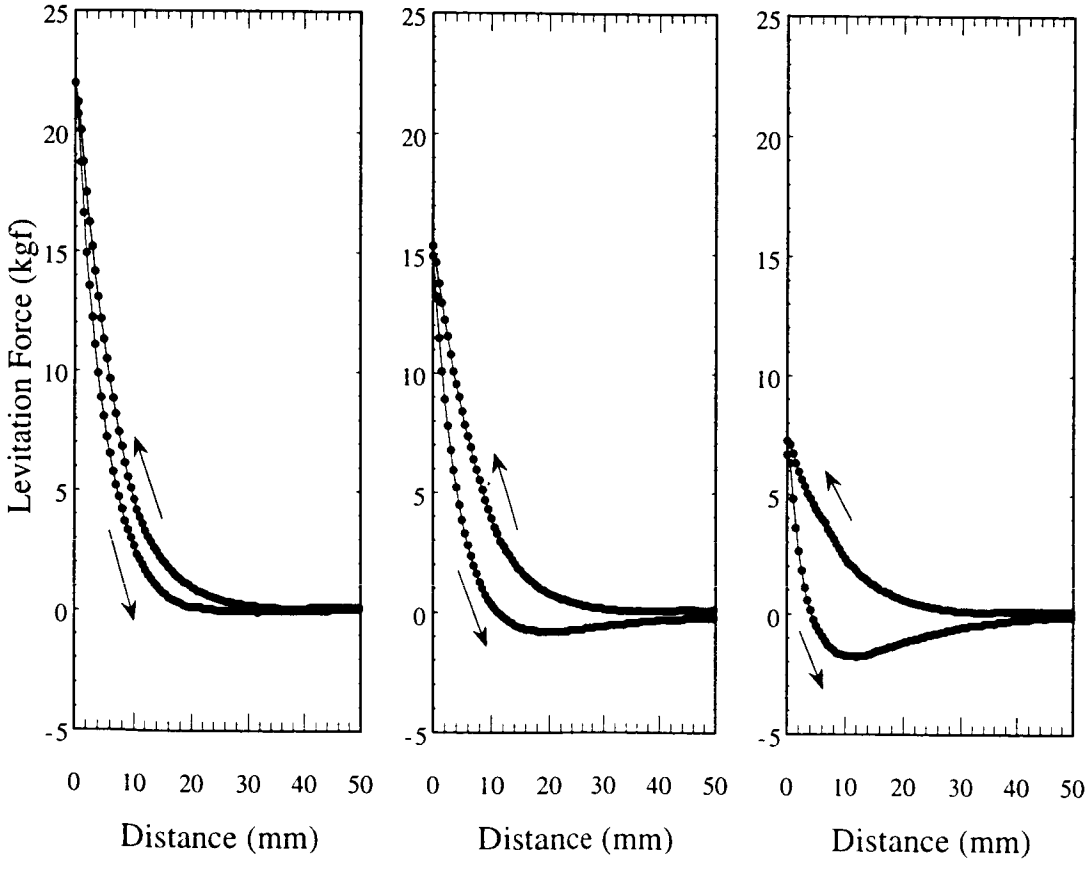

Figure 9 Examples of levitation force characteristic curve of bulk superconductors with different superconducting levitation forces.

Process of Fabricating Optimum-Shaped Materials

From the above experiments it became apparent that it is necessary to increase the size of a bulk superconductor and to reduce the number of divided portions of the superconductor part in order to improve the superconducting levitation force. In bulk superconductors for large-size superconducting magnetic bearings, therefore, it is desirable to densely arrange hexagon- or sector-shaped bulk superconductors. In obtaining bulk superconductors of such shapes, so far a disc-shaped sample was prepared and then cut into the final shape as shown in Fig.10 (a). However, it is difficult to fabricate large samples which do not include grain boundaries (that is, maintain high performance) and it is desirable that the region in which grains are caused to grow be minimized as far as possible.

For this reason, the near-net shape (NNS) process shown in Fig.10 (b) was tried. A precursor that has a shape close to the final one was used and grains were caused to grow. Thus, only the working of fine adjustment was conducted in the final shape-forming process. In the modified QMG process, the precursor is heated to about 1150 °C at which the 123 phase decomposes. However, because the 211 phase is contained, the shape of the precursor is maintained and, then it is possible to adopt such processes. In the NNS process, portions that are cut off during the shape-forming process and become useless are small in quantity, contributing to a reduction of the raw material cost. Figure 11 shows an example of a bulk superconductor made by the NNS process. There was no problem in grain growth and properties compared with the conventional process.

CONCLUSIONS

In this study, an investigation was experimentally made into the basic properties of superconducting levitation force using large-size, high-performance Y-Ba-Cu-O bulk superconductors made by the modified QMG process. It became apparent that an orientation of the c-axis of bulk superconductors and a reduction in the number of divided portions of samples by increasing the sample size are effective in improving the levitation force. It also became apparent that thickness of about 10 mm are sufficient as the sample thickness of bulk superconductors. The near-net shape process was proposed in order to make optimum-shaped bulk superconductors. At present, the basic properties of superconducting levitation force are being investigated with respect to the arrangement of axial bearings and radial bearings in a ring shape that is closer to the practical shape.

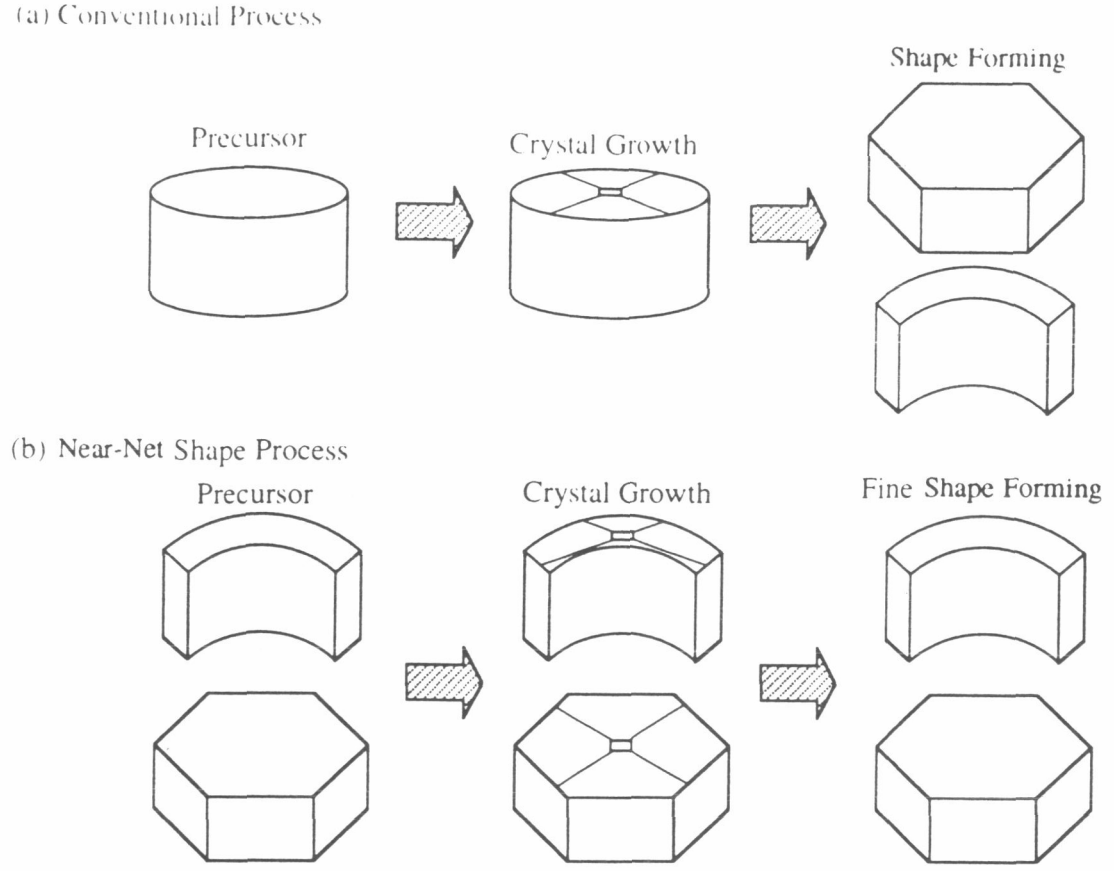

Figure 10 Processing processes by (a) the conventional process and (b) the near net shape process.

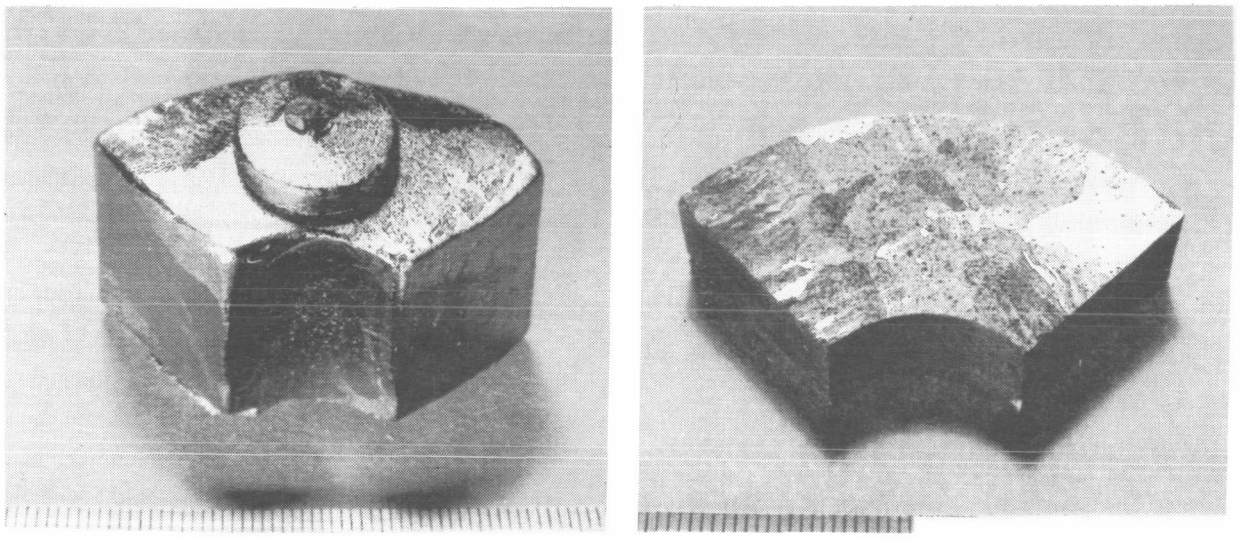

Figure 11 Bulk superconductor made by the near net shape process.

ACKNOWLEDGMENT

A part of this work was supported by New Energy and Industrial Development Organization (NEDO) under the project of the High-temperature Superconducting Flywheel Energy Storage System.

REFERENCES

1. Earnshaw S.: On the nature of the molecular forces which regulate the constitution of the luminiferous ether. Trans. Camb. Phil. Soc., 7, Part I,1842, pp.97-112.
2. Hellman F., Gyorgy E. M., Johnson D. W., Jr., O'Brayan H. M., and Sherwood R. C. : Levitation of a magnet over a flat type II superconductor. J. Appl. Phys. 63, 1988, pp.447-450.
3. Morita M., Sawamura M., Takebayashi S., Kimura K., Teshima H., Tanaka M., Miyamoto K., and Hashimoto M. : Processing and properties of QMG materials. Physica C, 235-240, 1994, pp.209-212
4. Teshima H., Morita M., and Hashimoto M. : Comparison of the levitation forces of melt-processed YBaCuO superconductors for different magnets. Physica C, 269, 1996, pp.15-21.
5. Higasa H., Ishikawa F., Kawauchi N., Yokoyama S., Nakamura S., Imaizumi H., and Ito N. : Experiment of a 100 Wh-class power storage system using high-Tc superconducting magnetic bearing. Advances in Superconductivity VI (ISS'93), 1993, pp.1249-1252.
6. Suzuki T., Suzuki H., Endo M., Yasaka Y., Morishita H., Takaichi H., and Murakami M. : Fundamental characteristics of prototype ring-shaped flywheel generator with superconducting levitated magnetic bearing. Advances in Superconductivity VI (ISS'93), 1993, pp.1237-1242.
7. Nagaya S., Hirano N., Minami M., and Kawashima H. : The study of the high-Tc superconducting flywheel for energy storage system. Proc. of the 1995 int. workshop on Superconductivity, Maui, U.S.A., 1995, pp.158-161.
8. Teshima H., Tawara T., and Shimada R. : Ring-shaped flywheel energy storage systems with superconducting levitation. Proc. of the Power Conversion Conference (PCC), Nagaoka, Japan, 1997, pp.701-706.
9. Bornemann H. J., Ritter T., Urban C., Zaitsev O., Weber K., and Rietschel H. : Low friction in a flywheel system with passive superconducting magnetic bearings. Applied Superconductivity, vol.2, No.7/8, 1994, pp.439-447.
10. Hull J. R., Mulcahy T. M., Uherka K. L., Erck R. A., and Abboud R. G. : Flywheel energy storage

using superconducting magnetic bearings. Applied Superconductivity, vol.2, No.7/8, 1994, pp.449-455.

11. Chen Q. Y., Xia Z., Ma K. B., McMichael C. K., Lamb M., Cooley R. S., Fowler P. C., and Chu W. K. : Hybrid high Tc superconducting magnetic bearings for flywheel energy storage systems. Applied Superconductivity, vol.2, No.7/8, 1994, pp.457-464.
12. Murakami M. : Levitation and suspension (Chapter 14) of Melt processed high-temperature superconductors. World Scientific, Singapore, 1992, pp.271-291.

Session 12 -- Bearings 2

Chairman: Yohji Okada
Ibaraki University

2-AXIS ACTIVELY CONTROLLED MAGNETIC BEARINGS

Atsushi Nakajima,
National Aerospace Laboratory

Naoki Kakuta and Tomohiro Soeda
Hosei University

Gen Shibata and Tomoyuki Sekine
Mitsubishi Precision Co.Ltd.

SUMMARY

Microsatellites are characterized as better, faster, cheaper spacecraft, and their effective utilization is actively studied by universities, national institutes and private companies. Owing to technology innovations, small and lightweight on-board components are fabricated with high mission performances. For example, 3-axis attitude control is required for 50kg-class microsatellites. In order to satisfy such demands,weight, mass and power consumption of each sensor and actuator are strictly limited. The National Aerospace Laboratory (NAL) has been developing magnetic bearings for attitude control actuators such as reaction and momentum wheels. Several types of magnetic bearings have been manufactured and evaluated and resulted in the advantage of 2-axis magnetic bearings with a potential miniaturization. In this paper, the development histories of 2-axis magnetic bearings in NAL and recent small magnetic bearing reaction wheels for microsatellite attitude control actuators are described. The design goal is a small size magnetic bearing reaction wheel, which has the characteristics of approximately 1.5kg weight, 100mm diameter and 0.2Nms angular momentum at 6,000 rpm.

INTRODUCTION

Magnetic bearings are now practically used in fields of industry such as turbo-molecular pumps to obtain ultra high vacuum and precise positioning mechanisms applied for semi-conductor manufacturing systems. Several types of magnetic bearings for space applications have been researched and developed by NAL (refs. 1 and 2). 2-axis actively controlled magnetic bearings have the characteristics of simple construction, low power consumption and adequate dimensions for a flywheel system. These features have potential applications for practical use of magnetic bearing reaction wheels as attitude control actuators of spacecraft. In 1986, the research model of a 2-axis actively controlled magnetic bearing flywheel developed by NAL was launched and on-orbit experiments were done to evaluate the fundamental magnetic bearing system such as the launch lock mechanisms, levitation, rotation and damping characteristics.

In recent years, small satellite utilization is actively increasing, especially 50kg-class microsatellites which are focused on low cost performance by the researchers of institutes and universities. They proposed various missions, which required high performance attitude control systems such as 3-axis attitude stabilization adopted in large satellite systems (ref. 3). Since microsatellite bus systems are limited by volume and weight, then the actuator is also required to have small size and light-weight performances.

This paper describes the development of a small-size magnetic bearing reaction wheel for the application to small and microsatellites attitude actuator. They have potential characteristics of miniaturization of onboard components with high rotational speed and low vibration.

PIGGYBACK MICROSATELLITES

Many small and microsatellites have been launched as piggyback payloads in conjunction with the larger primary satellite. Large launchers such as H-II, Ariane IV and V, Delta-II etc. have sometimes provided mass margins in excess of the primary payloads. Piggyback satellites can be included making effective use of this mass margin, often providing very cost effective launching into orbit.

Since 1990, the SPWS (Small Payload Workshop) was organized as a non-government working group for the study of active utilization of piggyback satellites in the fields of technology demonstration, communication and earth observations. The activities of the SPWS has mainly focused on the mission proposals of small and microsatellites, information exchange among national institutes, universities and private companies in the world.

In 1995, the SPWS summarized and analyzed 61 proposed mission ideas. The proposed missions are divided into 4 categories, which are technology experiments, observations, communications and biological experiments. More than 50% are concentrated on science and technology missions such as in-orbit verifications of satellite bus system, components, materials like semi-conductors, robotics, tethers and another technological items. Missions related to the Earth and astronomical observations and survey of debris distributions take second place, about 30% of the total. Some demands for satellite attitude control systems are also requested. The almost microsatellites, launched in the past, have adopted gravity gradient attitude stabilization or slow tumbling (forced spinning or no active attitude control) because of the limited budget and requested attitude accuracy. The results of the questionnaires, on the contrary, show that more than 50% of missions require 3-axis attitude stabilization in order to meet future extensive demands such as high

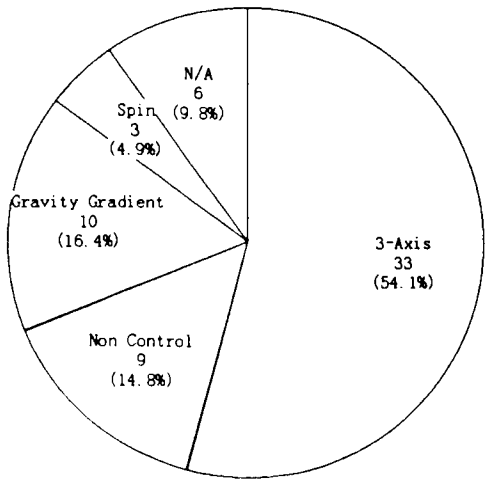

Fig.1 Attitude Requirements for Microsat

bit-rate data transmission, high accuracy pointing, fixing to the inertial frame, micro-gravity environment and so on. Low-cost, simplified 3-axis attitude control packages must be developed as soon as possible. Fig. 1 shows the required attitude control distribution. Small-sized reaction wheels or a momentum wheel with magnetic suspension will be candidates as actuators.

MAGNETIC BEARINGS WITH PERMANENT MAGNETS

Magnetic bearings used for suspending rotating bodies must constrain the five degree-of-freedom (DOF) motion of the body, leaving the motion about the rotational axis out of consideration, three DOF being assigned perpendicular to the rotation axis. Principally, each direction of motion may be actively controlled or passively stabilized with the help of permanent magnets, as long as at least one axis is actively controlled. Thus, various types of magnetic bearings have been proposed, ranging from an axial-active and radial-passive type (one axis active control) to a five DOF active control type.

Utilization of permanent magnets in the magnetic bearings not only provides passive stabilization but it also helps the control system to overcome the inherently nonlinear relationships between the electromagnetic quantities (e.g. coil current, gap flux density etc.) and the resultant forces by a technique called "flux density modulation". Another advantage of permanent magnet utilization is that it enables the "Virtually zero power" method capable of minimizing (or nulling) the power consumption in the control coils by balancing the constant external force (e.g. gravitational force) with the unbalance force produced by the permanent magnets.

The passive stiffness is produced by the sum of restoring forces acting on the magnetic pole pieces. Fig.2(a) shows the magnetic flux distribution chart calculated by finite element method (FEM). The magnetic fluxes generated by the permanet magnet pass through all magnetic pole pieces and are concentrated on the central pieces. A specially magnified detail drawing of the central pieces is

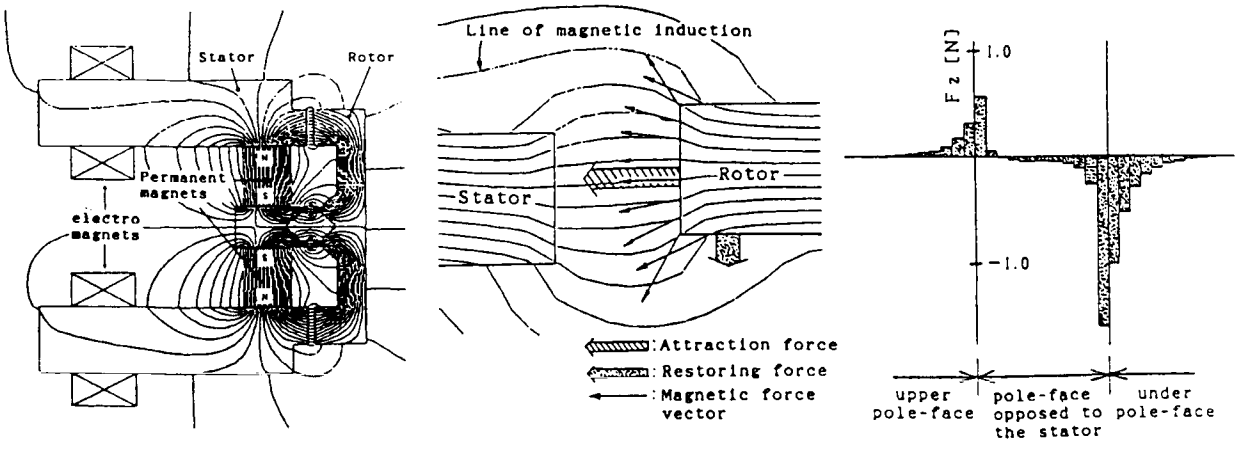

(a) Magnetic Flux Distribution (b) Force Vector (c) Force Distribution

Fig.2 Magnetic Attraction and Restoring Force Acting on the Pole Pieces

shown in Fig. 2(b). The magnetic force vector of each corresponding magnetic flux is expressed by a straight line with an arrow head and the vector sum is decomposed into attraction force and restoring force. The attraction force is controlled by electromagnets which is shown in Fig.2(a) and the restoring force supports the rotor mass passively. The force distribution on the magnetic pole-face is shown in Fig. 2(c). The restoring force is highly concentrated on the extreme edge of the magnetic pole pieces. Then the restoring force is roughly proportional to the number of edges and the flux density.

2–AXIS ACTIVELY CONTROLLED MAGNETIC BEARINGS

2-axis active magnetic bearings have a relatively simple arrangement and easy construction. The most preferable feature of this type is its virtually flat-shaped form, which enables the achievement of a high moment of inertia/mass ratio flywheel. From this point of view, it is possible to realize a high capacity angular momentum with minimum weight and manufacturing cost. Since 1980, NAL has studied and manufactured, by way of trial, several types of two DOF magnetic bearings and found that they have a high potential for applications such as a reaction wheel.

Fig.3 shows the principle of 2-axis actively controlled magnetic bearings developed by NAL. The magnetic forces act on the pole pieces on G1, G2 and G3, two of which (G1 and G3) are so-called magnetically modulated gaps where magnetic flux densities are modulated by radial electromagnets whereas G2 is a non-modulated gap. This non-modulated gap plays an important part where magnetic flux density is very high, therefore both axial and tilting stiffness can be made high. There are two ring-shaped permanent magnets on the stator side only. Eight electromagnet

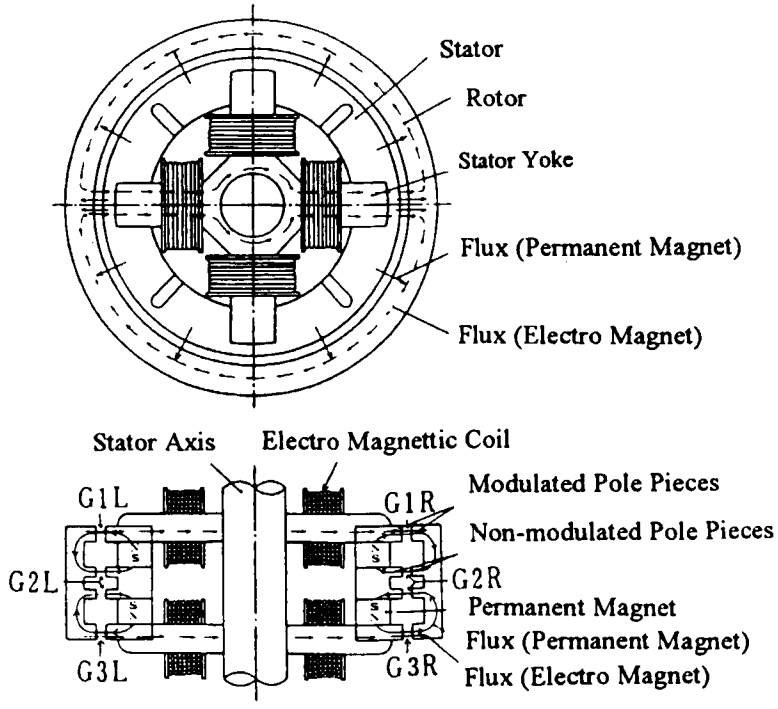

Fig.3 Cross Sectional View of 2-axis Actively Controlled Magnetic Bearings

coils are wound around both upper and lower cross-shaped stator yokes to modulate the two gaps (G1 and G3) for levitation. The arrow lines represent the magnetic flux flows generated by the permanent magnets. Two closed loops are generated and both lines commonly pass through the non-modulated gap G2. The dashed lines represent the flux flows generated by the electromagnets, which pass only G1 and G3 and modulate the biased flux generated by permanent magnets. Eddy current type gap sensors (which are not shown in the figure) detect the radial displacement for radial active control.

2-Axis Actively Controlled Magnetic Bearing Flywheel for Space Experiment

In order to evaluate the on-orbit characteristic of a 2-axis actively controlled magnetic bearing flywheel, the research flight model (RFM) was manufactured and launched into orbit in 1986. Experimental items are:

(1) manufacturing of a magnetic bearing flywheel for space flight model
(2) functional test of the launch lock mechanism
(3) measurements of the damping characteristic of the passively stabilized axis
(4) comparison of ground test data with space experimental results, especially
(5) levitation characteristics

A cross sectional view of the RFM is shown in Fig. 4. It was composed of axially magnetized samarium-cobalt permanent magnets, electromagnetic coils for x- and y-axis control, two pairs of eddy current type position sensors to detect the radial displacements of the rotor, a flywheel to accumulate an angular momentum, emergency ball bearings and launch lock mechanism which fasten the rotating part with elastic metal plates and 2 mm diameter twisted wire. An additional four position sensors are mounted on the bottom base of the stator to detect the axial displacement of the rotor by adding the four output signals to measure the rotor's tilting motions about the x- and y-axis by subtracting each pair of sensors. A pair of electromagnetic coils are additionally wound around stator yokes to excite a tilting oscillation for the purpose of damping characteristics measurement.

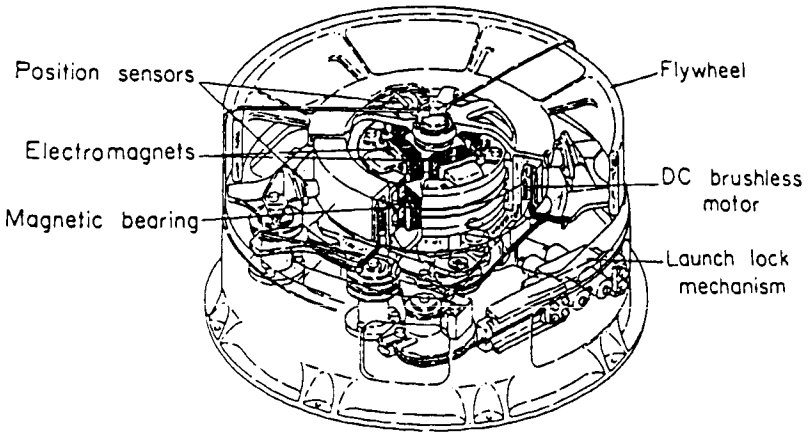

Fig.4 Cross-sectional View of Magnetic Bearing Flywheel for Space Experiment

Several environmental tests were performed before system integration. Random vibration level for each direction is about 14.5 Grms and the temperature range is −20 ～ +50℃. Dimensions and specifications are shown in Table 1. In order to measure several features of magnetic bearings, this RFM was not designed in conformity to the purpose of direct application for spacecraft from the view point of dimension and weight because of the additional sensors and coils for experiments. All on-orbit experiments were carried out successfully.

Table 1 Characteristics of Magnetic Bearing Flywheel for Space Experiment

items		measured values
Axial stiffness	[N/m]	8.3×10^4
Radial control force	[N/A]	4.8×10
Dimension	[mm]	270 (dia.) × 127 (machine body) , 200 × 252 × 151(electronics)
Weight	[kg]	7.23 (machine body) , 5.10 (electronics)
Rotation speed	[rpm]	1,000 (only for this exp.)
Power consumption	[W]	3 (suspension) , 7 (at 1,000 rpm)

Flat-shaped 2-axis Actively Controlled Magnetic Bearing Reaction Wheel

Fig.5 shows a flat shaped reaction wheel. The design goals of this model are to reduce weight, dimensions (especially height) and power consumption, and to increase angular momentum, bearing stiffness and reliability. The magnetic bearings were installed at the outside of the stator, then the mass concentration to the outer part of the wheel could be satisfied. This installation has brought about high moment/mass ratio and high stiffness of the magnetic bearings. The values of stiffness are measured dynamically by modal analysis using the impulse hammering test. The characteristics are shown in Table 2. The damping ratios are also measured and their values are over 0.3 for radial directions and over 0.01 for axial and around radial directions.

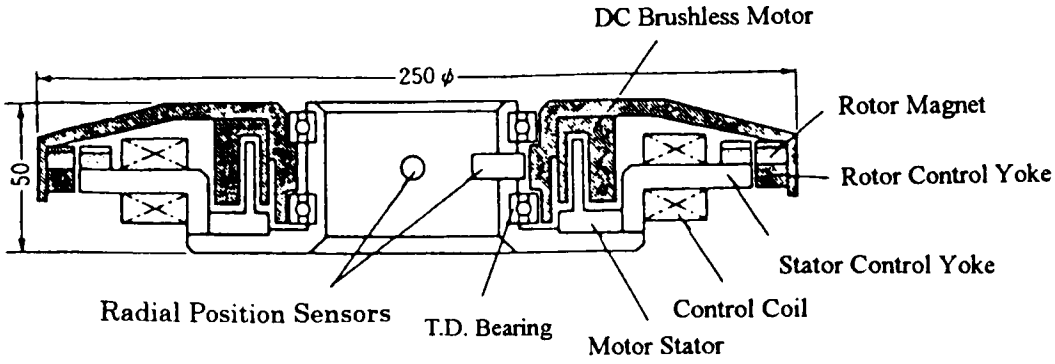

Fig.5 Flat-shaped Magnetic Bearing Reaction Wheel

Table 2 Characteristics of Flat-shaped Magnetic Bearing Reaction Wheel

items		measured values
Axial stiffness	Ka [N/m]	3.2×10^5
Radial stiffness	Kr [N/m]	7.6×10^5
Orthogonal stiffness	Ke [Nm/rad]	1.5×10^3
Dimension	[mm]	$\phi 250\times50$
Rotor weight	[kg]	2.4
Angular momentum (at 3,000 rpm)	[Nms]	7.5

SMALL MAGNETIC BEARING REACTION WHEEL FOR MICROSATELLITE ATTITUDE CONTROL

A small size magnetic bearing reaction wheel for the attitude control of microsatellites has been designed and is now being manufactured (ref. 4). The design baseline is similar to the reaction wheel described in the previous section (flat-shaped reaction wheel). The design parameters are shown in Table 3 and the sectional view of the construction is shown in Fig. 6. The required maximum angular momentum is 0.2 [Nms], where the rotation speed is at 6,000 [rpm].

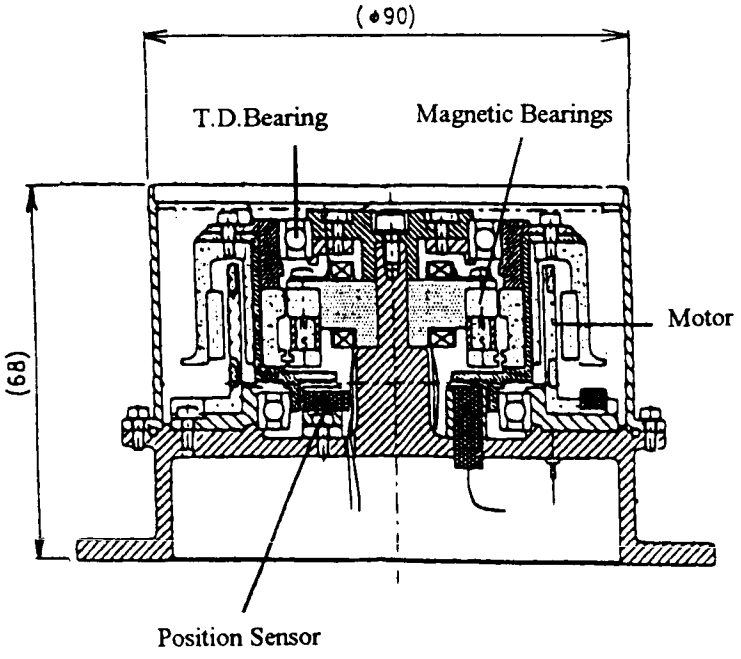

Fig.6 Small Magnetic Bearing Reaction Wheel

Table 3 Design Parameters of Small Magnetic Bearing Reaction Wheel

items	design values
Dimension	ϕ 90 × 70[mm]
Weight	1.5[Kg]
Angular momentum	0.2[Nms] (at 6,000rpm)
Torque	0.005[Nm]
Permanent magnet (for magnetic bearings)	R26H(SINETSU Rare Earth)
Maximum energy-product	210[KJ/m^3]
Dimension	outer diameter ϕ 37[mm] , inside diameter ϕ 30[mm] height 6[mm]
Magnetic pole Dimension	outer diameter ϕ 50 × 14[mm]
Face width	5[mm] × 1(Modulating magnetic pole) 1[mm] × 2(non-modulating magnetic pole)
Magnetic flux density	
Modulating magnetic pole	0.41[T]
Non-modulating magnetic pole	0.68[T]

CONCLUDING REMARKS

Research and development activities of magnetic bearings, especially emphasizing a 2-axis actively controlled type developed by NAL are overviewed. For large satellites, magnetic bearing reaction wheels are already practically used and sufficient characteristics are demonstrated. In the past, microsatellites are usually passively stabilized by gravity gradient torque, as an example. According to the high-quality mission requirements for microsatellite attitude control system, 3-axis stabilization is necessary. NAL is now developing a small magnetic bearing reaction wheel for microsatellite application and will be actually used as attitude control actuators for piggyback microsatellites, under development in NAL, which will be launched within a few years.

REFERENCES

(1) A.Nakajima : Research and Development of Magnetic Bearing Flywheels for Attitude Control of Spacecraft, Proc.of 1st International Symposium on Magnetic Bearings, Zurich, 1988

(2) A.Nakajima and C.Murakami : Research and Development of Magnetic Bearings, Proc.of 16th ISTS, Sapporo, 1988.

(3) A.Nakajima and T.Hayashi : A Future View of Micro-Satellites, - As Piggy-back Satellites of H-II Launcher -, 20th ISTS, Gifu, 1996.

(4) A.Nakajima et.al. : Development of Magnetic Bearing Flywheel, 41st Symposium on Space Science and Technology, JSASS, 97-13-7, Sapporo, 1997.

COMPARATIVE STUDIES OF LEVITATION AND CONTROL PERFORMANCES OF TWO TYPES OF SINGLE-AXIS CONTROLLED REPULSIVE TYPE MAGNETIC BEARING

S. C. Mukhopadhyay, T. Ohji, T. Kuwahara, M. Iwahara, S. Yamada and F. Matsumura
Laboratory of Magnetic Field Control and Applications,
Faculty of Engineering, Kanazawa University,
Kodatsuno 2-40-20 Kanazawa 920 Japan

SUMMARY

Single-axis controlled repulsive type magnetic bearings have the advantages of simplified control schemes and less numerous electromagnets. The bearing system employed can be one of two types of machine configurations: (1) Vertical-shaft machines, (2) Horizontal-shaft machines. Prototype models of each type have been developed and experiments conducted in our laboratory. This paper discusses different aspects such as design of bearing systems and configuration, levitation, control, vibration and disturbance attenuation characteristics etc. of two types of schemes of repulsive type magnetic bearings. The controllers of both systems have been configured around digital signal processors.

INTRODUCTION

In recent times, magnetic bearings offering numerous advantages such as long life, extreme reliability, frictionless nature, lubrication free operation, low losses, adjustable damping and stiffness characteristics are becoming indispensable in applications such as turbomolecular pumps, space applications, vacuum and clean room atmosphere, fly-wheel energy storage systems and so on. Because in the presence of active control in active magnetic bearings (AMB) the stiffness and damping characteristics can be adjusted according to requirements along the controlled axis, AMBs are more commonly used in critical industrial applications but incur more cost, need complicated controllers and lots of electromagnets. Repulsive type magnetic bearings consisting of permanent magnets and controlled electromagnets have the advantages of a lower number of electromagnets and simplified control schemes compared to active magnetic bearings. Many research papers have been published on magnetic bearings using permanent magnets (PM) [1-4]. But the satisfactory operation of this type of

magnetic bearing system is strongly dependent on the characteristic of the permanent magnet and its configuration in the bearing system. The permanent magnet configuration is very important because it determines the characteristics along the passive axis. The bearing system employed can be one of two types of machine configurations - (1) Vertical-shaft machines and (2) Horizontal-shaft machines. In type (1) the levitation force and stiffness characteristics are decoupled from each other resulting in simpler magnet configurations. In type (2) the levitation force and stiffness characteristics are coupled to each other and there must be a trade-off between the two to obtain an optimum characteristic. Prototype models of each type have been developed and experiments conducted in our laboratory. This paper discusses the different aspects such as design of bearing systems and configuration, levitation, control, vibration and disturbance attenuation characteristics etc. of two types of schemes of repulsive type magnetic bearings. The controllers of both the systems have been configured around digital signal processors.

CONFIGURATION OF BEARING SYSTEM FOR VERTICAL-SHAFT MACHINE

The system configuration developed in our laboratory is shown in Fig. 1 and the corresponding PM configuration is shown in Fig. 2. Both that stator and rotor permanent magnet are made of strontium-ferrite magnet. One gap sensor is used to detect the position of the rotor along the vertical direction, one electromagnet is used for rotor positioning, and the control is provided along the vertical axis. Improvement of either levitation force or radial stiffness can be done without sacrificing the other. The active control axis is the same as the levitation direction in this scheme. The principal data are: length of rotor = 420mm, mass of rotor = 5.5kg, diameter of rotor = 200mm.

CONFIGURATION OF BEARING SYSTEM FOR HORIZONTAL-SHAFT MACHINE

The system developed in the laboratory is shown in Fig. 3. The rotor is levitated due to the repulsive force acting between the stator and rotor permanent magnets along the vertical-axis. The unstable system is stabilized by active control along the horizontal axis. No active control has been provided along the vertical axis. Since the rotor is levitated due to the repulsive force, the symmetrical PM configuration described earlier cannot be used in this configuration. In order to achieve better disturbance attenuation characteristics, higher stiffness is desirable, which has been achieved by an optimum configuration of permanent magnets. The configuration of permanent magnets for this type

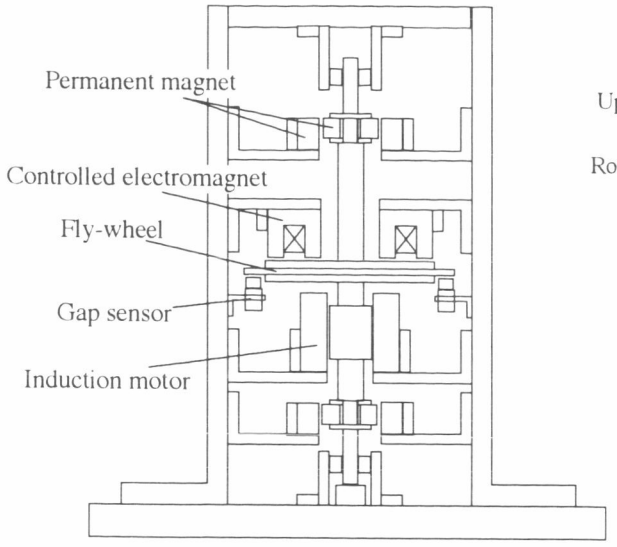

Figure 1. Bearing system configuration.
(Vertical-shaft machine)

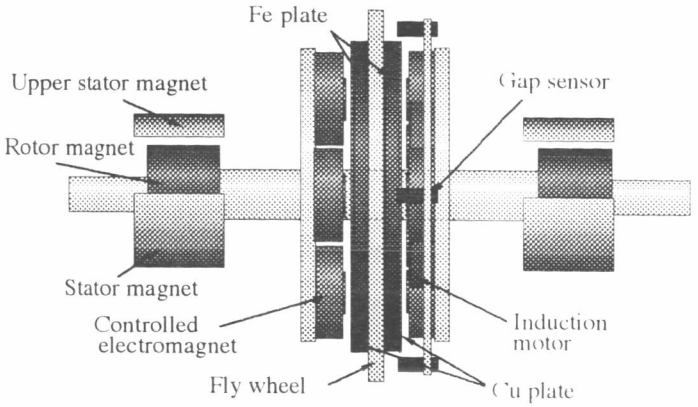

Figure 3. Bearing system configuration.
(Horizontal-shaft machine)

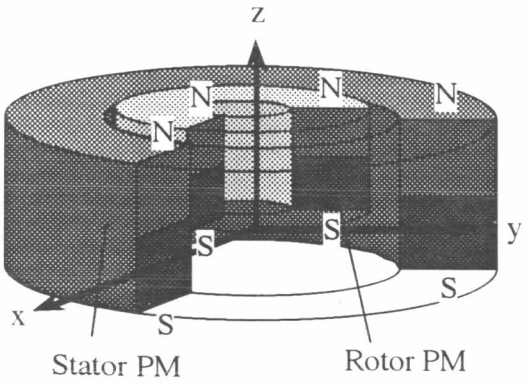

Figure 2. PM configuration.
(Vertical-shaft machine)

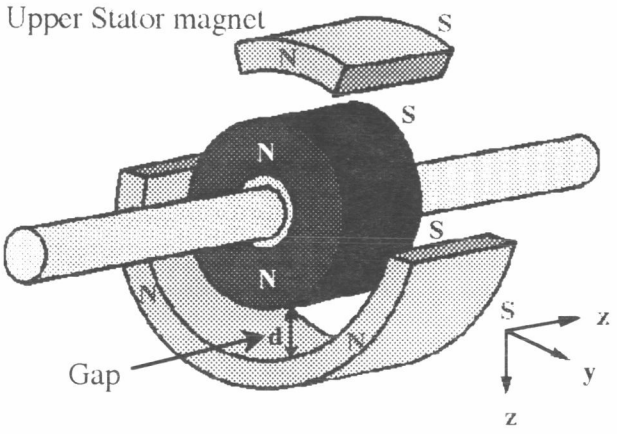

Figure 4. PM configuration
(Horizontal-shaft machine)

of magnetic bearing system is shown in Fig. 4. The stator permanent magnet is made of Neodymium-iron-boron (Nd-Fe-B) material and the rotor is of Strontium-ferrite material. The motor used in this study is a normal induction motor. Four electromagnets are used for the axial control but they are not separately controlled, all are connected in series. A gap sensor is used to sense rotor position and is of eddy-current type giving an output of 1V/mm. The principal data are: length of rotor = 510mm, mass of rotor = 8kg, diameter of rotor = 220mm.

LEVITATION AND STIFFNESS CHARACTERISTICS

In permanent magnet bearing systems, it is very important to know the force and stiffness characteristics operating between the stator and rotor permanent magnets. We have analyzed the above

characteristics with the help of the finite element method. Since attenuation of disturbance along the uncontrolled passive radial direction is very important for the stability of the system, higher stiffness is desirable.

With the help of three-dimensional finite element analysis, the repulsive force and stiffness characteristics are calculated for the vertical-shaft machine. The force as well as stiffness depend on the material characteristic and the configuration of PMs in the system. We have calculated the repulsive forces for two types of PM materials. If only the rotor material is replaced by Nd-Fe-B magnet, the improvement is not significant but if both stator and rotor PM is replaced by Nd-Fe-B magnet, a great improvement of the characteristics are observed. Fig. 5 shows the relative characteristics along the vertical axis and Fig. 6 is that for the horizontal axis. Since control is provided along the vertical axis, the passive stiffness along that axis is not so important. Fig. 7 shows the stiffness characteristic along the radial direction.

Another method by which the repulsive force and stiffness characteristics can be improved is by providing a small gap between the permanent magnets of the stator PM assembly or rotor PM assembly. Fig. 8 shows the characteristic where a gap of 1mm has been provided in the rotor PM assembly and the stator is kept as it is. It is seen that there is a slight improvement in repulsive force.

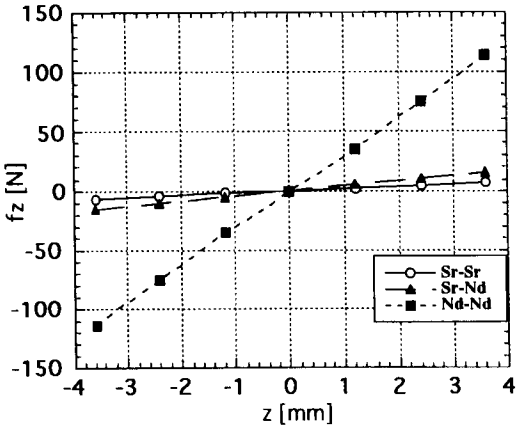

Figure 5. Repulsive force characteristic for different material along vertical-direction.

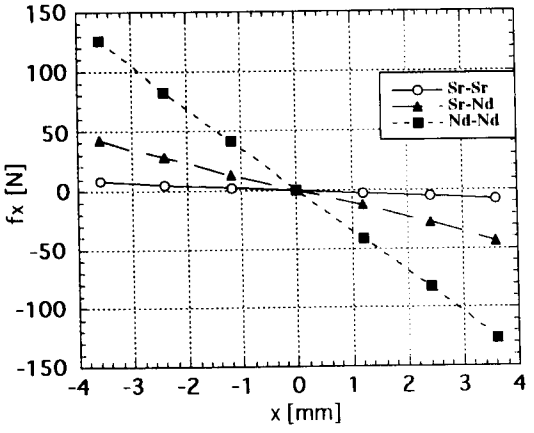

Figure 6. Repulsive force characteristic for different material along radial-direction.

Instead of configuring the Pms as NSNS.., if it is configured as NSSN..and is provided with a small gap between two successive magnets, both the stiffness and the levitation force are improved. This has been described in detail in [5]. This configuration needs a complicated arrangement for holding the magnets in their respective positions.

Since the vertical-shaft configuration is a well established one, we will not go into great detail. We have developed a simple laboratory model using low cost strontium-ferrite magnets with NSNS configuration. The experimental characteristics are measured and are shown in Fig. 9 and 10 respectively.

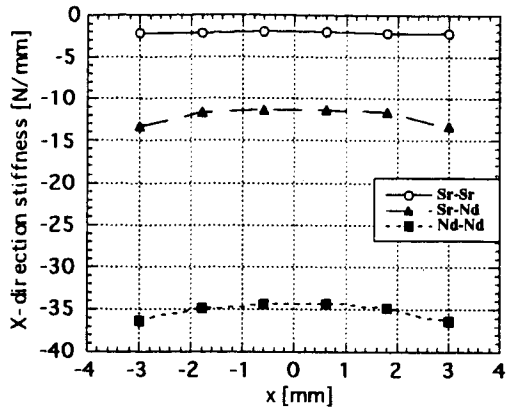

Figure 7. Stiffness characteristic for different material along radial-direction.

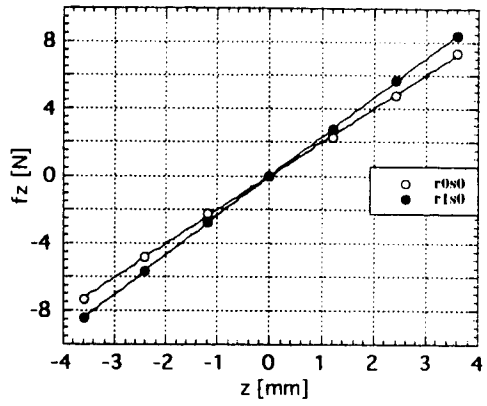

Figure 8. Repulsive force characteristic having gap in PM assembly.

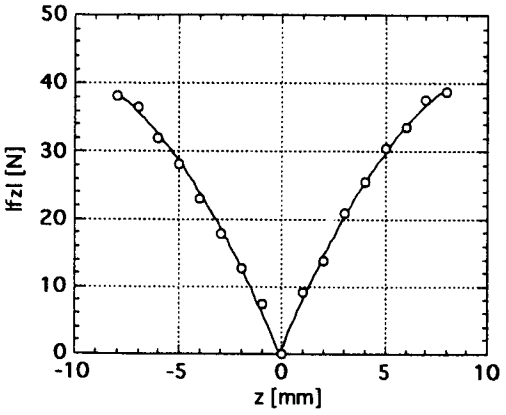

Figure 9. Experimental levitation force for system #1.

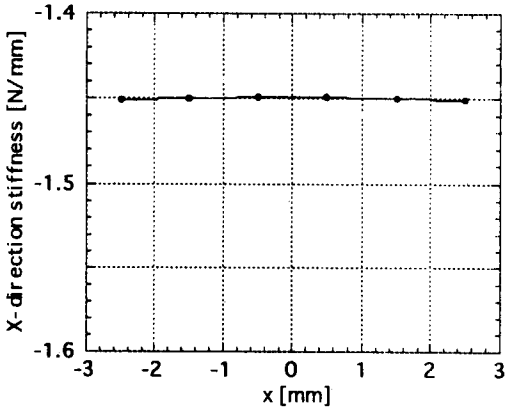

Figure 10. Experimental stiffness characteristic for system #1.

For the horizontal-shaft configuration, the symmetrical PM configuration as discussed earlier will be of no use as it results in zero levitation force along the vertical axis. In order to achieve better radial stiffness, a section of PM is placed on the upper half of the stator. Fig. 11 shows the 2-dimensional view of the PM configuration. Placement of the upper stator permanent magnet will reduce the levitation force, so the arc length θ should be selected critically. With the help of FE analysis a trade-off has been achieved. The PM configuration shown in Fig. 4 is an open boundary problem and is not an axi-symmetric one if three-dimensional view is taken. Using three-dimensional finite element analysis, more precise results can be obtained at the cost of a large computer memory requirement and long computation time. Considering the movement of the rotor with respect to the stator configuration, the model can be reduced to a two-dimensional one for the analysis to be made more practical, yet obtaining relatively precise results. Also, the complexity of three-dimensional analysis can be avoided. The sectional view of Fig. 4 has been shown in Fig. 12 for two-dimensional finite element analysis. Different two-dimensional views are obtained when the bearing system is cut at different angles; the

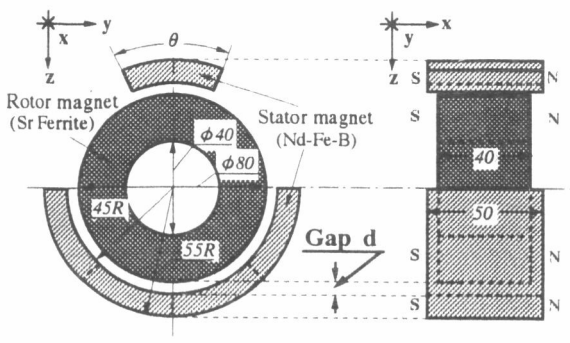

Figure 11. 2-D of PM configuration of system #2.

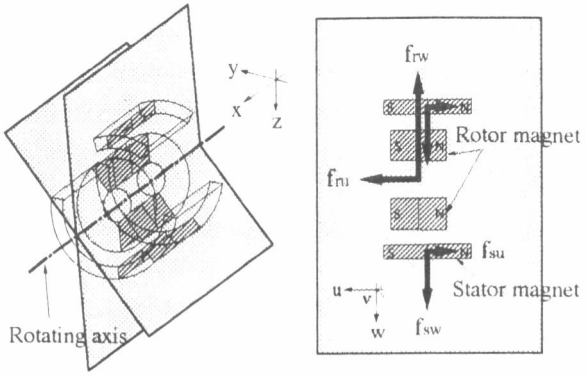

Figure 12. Sectional view of PM configuration.

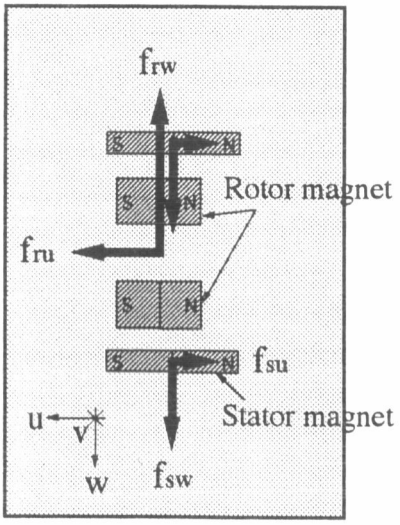

(a) 2-D view of section near 90° cutting angle.

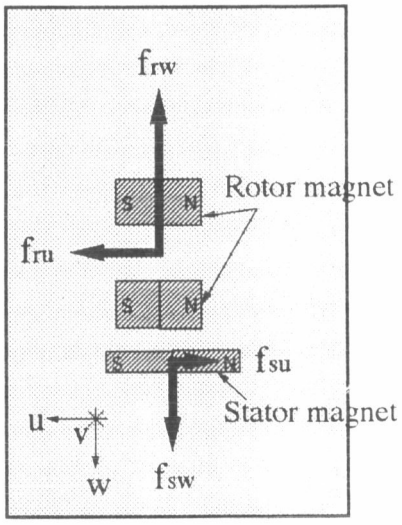

(b) 2-D view of section near 0° cutting angle.

Figure 13. 2-D view of the model.

cutting plane makes with the horizontal plane passing through the rotating axis.

Fig. 13a shows the view when the cutting plane makes an angle of nearly 90° with the horizontal plane and Fig. 13b shows the view when the cutting plane makes nearly 0° with the horizontal plane. We have taken 19 such views of each rotor position with respect to the stator at 10° intervals along the rotor surface. For the field analysis MSC markets the software package

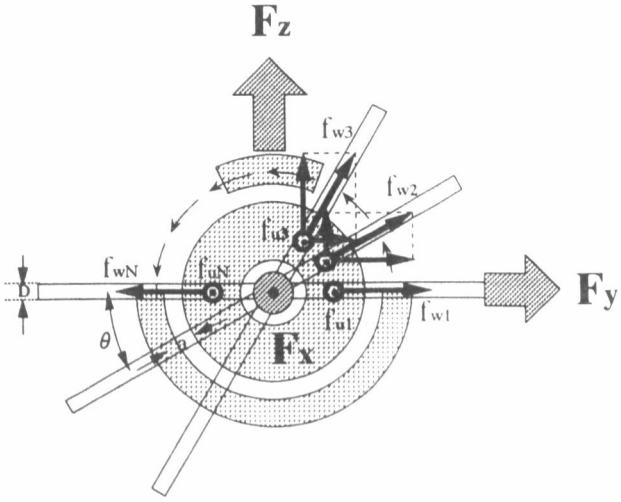

Figure 14. Forces on rotor section.

EMAS, which has been used and the repulsive forces f_{ru}, f_{su}, f_{rw} and f_{sw} as shown in Fig. 12 are calculated from the field solution. Resultant forces along u and w are given by

$$f_u = |f_{ru} - f_{su}| \quad \text{------(1)} \qquad f_w = |f_{rw} - f_{sw}| \quad \text{------(2)}$$

Fig. 14 shows all the forces acting on different sections of the model. By adding the forces vectorially the resultant forces along the three axes x, y and z are given by

$$F_x = f_{u1} + f_{u2} + ... + f_{uN} \quad \text{------(3)}$$

$$F_y = f_{w1}\cos\theta_1 + f_{w2}\cos\theta_2 + ... + f_{wN}\cos\theta_N \quad \text{----(4)}$$

$$F_z = f_{w1}\sin\theta_1 + f_{w2}\sin\theta_2 + ... + f_{wN}\sin\theta_N \quad \text{----(5)}$$

This method of calculation forms a two-dimensional database which helps to understand easily the variation of repulsive forces with rotor movement. In order to find the optimum PM configuration by changing the upper PM section, we have calculated the forces and stiffness characteristics along the vertical i.e., the z-direction.

By changing the arc section θ we have calculated the force and stiffness characteristics. Fig. 15a and b shows the variation of repulsive force and stiffness characteristics with the gap distance for different values of θ. It is seen that higher stiffness is achieved at the cost of repulsive force. Since higher repulsive force is necessary from the levitation point of view, a trade-off between the two is achieved and $\theta = 45°$ is chosen for our laboratory model.

The levitation and stiffness have also been analyzed by the three-dimensional finite element method and also measured experimentally. Fig. 16a and b shows the levitation and stiffness characteristics by 2-D, 3-D and experimental methods for the laboratory model.

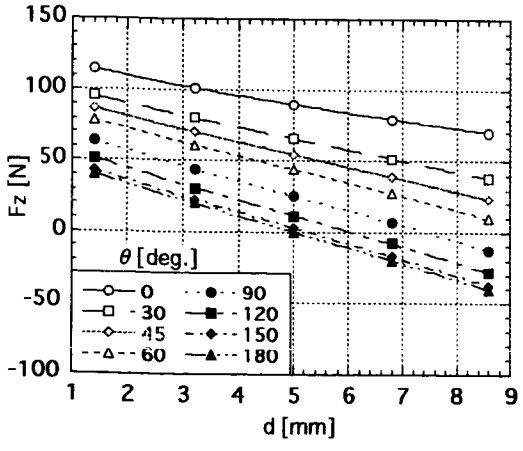

Figure 15(a). Variation of repulsive force with gap-distance for different sections.

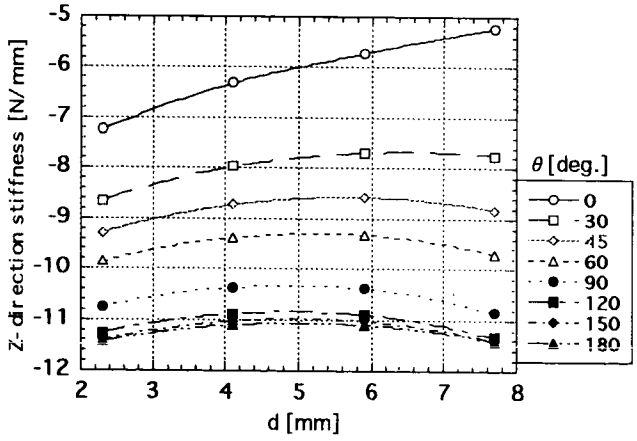

Figure 15(b). Stiffness characteristic for different sections.

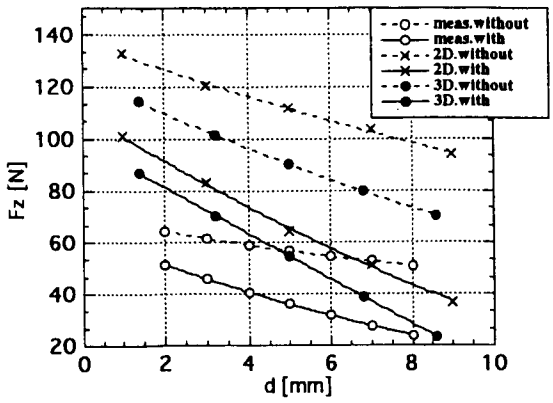

Figure 16(a). Comparative values of repulsive forces.

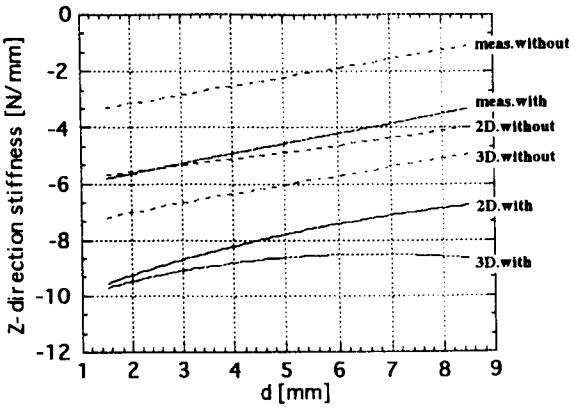

Figure 16(b). Comparative stiffness characteristics.

SYSTEM MODELING

Both the systems are expressed in the form of state-space models. The modeling of repulsive type magnetic bearings have been described in detail in [6]. In this section, simplified models of two systems have been considered. For this purpose, the operating forces are expressed analytically.

The repulsive force characteristic along the controlled axis can be expressed as

$$f_{PM,i} = S_i \cdot x + F_{0,i} \qquad \text{-------(6)}$$

where I=1 for system #1 (Vertical-shaft machine) and I=2 for system #2 (Horizontal-shaft machine). S_i is the slope of characteristic of system #2 and is expressed as N/m. $F_{o,i}$ is the force at the nominal operating point for system #1, in N. x is the displacement from the nominal operating point.

The electromagnet quantities are expressed by

$$e_i = L_i \frac{di_i}{dt} + R_i i_i \qquad \text{-----(7)}$$

$$f_i = k\left(\frac{i_i}{g_i}\right)^2 \qquad \text{-----(8)}$$

where L_i and R_i are the inductance and resistance of the electromagnet of system #1. k is a constant which depends on the structure of the magnet and the number of turns.

Assuming all the four electromagnets used for system #2 are identical, the total operating forces will be four times that given by eqn (8).

Linearizing the operating characteristic of the electromagnet around the normal equilibrium operating point and expressing by the deviated quantities from the steady state values, we get

$$e_i' = L_i \frac{di_i'}{dt} + R_i i_i' \qquad \text{----(9)}$$

$$f_i' = 2F_{e,i}\left(\frac{i_i'}{I_{0,i}} - \frac{g_i'}{W}\right) \qquad \text{----(10)}$$

where Fe, Io and W are the force, current and gap-distance at the nominal operating point. At steady-state, the following relationships hold good.

$$For\ system\ \#\ 1, \quad F_{e1} + 2F_{01} - m_1 g = 0 \quad -----(11)$$

$$For\ system\ \#\ 2, \quad 4F_{e2} - 2F_{02} = 0 \quad -----(12)$$

The dynamic equation of motion is given by,

$$For\ system\ \#\ 1, \quad m_1 \frac{d^2 x_1}{dt^2} = f_{e1} + 2f_{01} - m_1 g \quad ----(13)$$

$$For\ system\ \#\ 2, \quad m_2 \frac{d^2 x_2}{dt^2} = 4f_{e2} + 2f_{02} \quad -----(14)$$

All the variable parameters are linearized around the nominal operating point. Taking the gap-deviation from the nominal point, its derivative and the current deviation from the nominal point, the state-space model is given by,

$$\frac{d}{dt}\begin{bmatrix} x' \\ \dot{x}' \\ i' \end{bmatrix} = \begin{bmatrix} 0 & 1 & 0 \\ \frac{2S}{m} + \frac{2}{mW}\sum_i F_i & 0 & \frac{2}{mI}\sum_i F_i \\ 0 & 0 & -\frac{r}{L} \end{bmatrix} \begin{bmatrix} x' \\ \dot{x}' \\ i' \end{bmatrix} + \begin{bmatrix} 0 \\ 0 \\ \frac{1}{L} \end{bmatrix} e' \quad ----(15)$$

$$y = \begin{bmatrix} 1 & 0 & 0 \end{bmatrix} \begin{bmatrix} x' \\ \dot{x}' \\ i' \end{bmatrix} \quad ----(16)$$

The parameters used in the model are explained below.

x'	: Gap derivation from nominal state
i'	: Current derivation of electromagnet from nominal state
e'	: Incremental input voltage to electromagnet
m	: Mass of rotor
F_i	: Attractive force at steady state
I	: Nominal current
W	: Nominal gap
r	: Resistance of electromagnet
L	: Inductance of electromagnet
R,S	: Constant used in permanent magnet equation

The performance of the system represented by the state-space model in eqns. (15) and (16) has been simulated with the help of MATLAB. The block diagram representation of the model for the performance simulation is shown in Fig. 17. The values of different parameters used in the model are listed in Table 1. Using the values of the parameters, the A and B matrices are given by,
for system #1,

$$A_1 = \begin{bmatrix} 0 & 1 & 0 \\ 7547.9 & 0 & 12.03 \\ 0 & 0 & -68.05 \end{bmatrix} \quad B_1 = \begin{bmatrix} 0 \\ 0 \\ 27.78 \end{bmatrix} \quad ----(17)$$

for system #2,

$$A_2 = \begin{bmatrix} 0 & 1 & 0 \\ 5585 & 0 & 2.654 \\ 0 & 0 & -60.5 \end{bmatrix} \quad B_2 = \begin{bmatrix} 0 \\ 0 \\ 5.165 \end{bmatrix} \quad ----(18)$$

Fig. 18 shows the simulated response characteristics of system #1 and Fig. 19 is that for system #2.

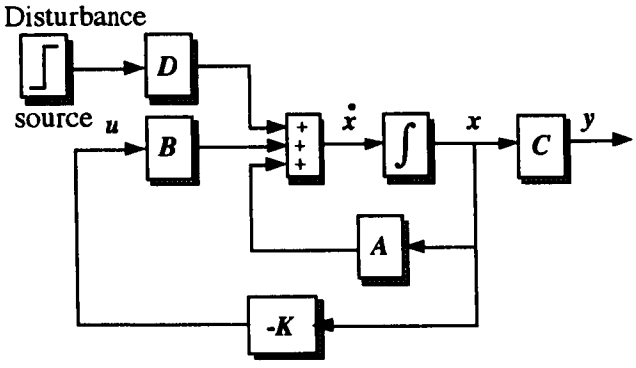

Figure 17. Simulation block diagram.

Table 1. Main parameters of systems.

PARAMETER	SYSTEM#1	SYSTEM#2
m	5.5kg	8kg
S	0.49×10^{4} N/m	1.18×10^{4} N/m
F_0	15.97 N	11.76 N
F_e	21.46 N	5.88 N
L	0.036 H	0.194 H
R	2.45 Ohm	11.72 Ohm
I_0	0.48 A	1.0 A
W	0.001 m	0.002 m

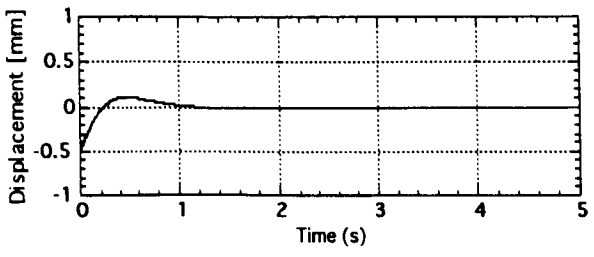

Figure 18. Simulated response of system #1.

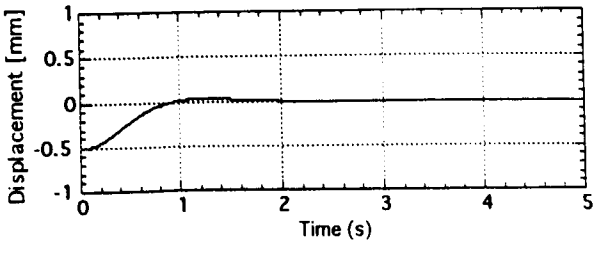

Figure 19. Simulated response of system #2.

Using eqns (15) and (16) for the stability of the system which is unstable in nature, an optimum integral type servo control system has been constructed. Using the Matlab control system toolbox, the Riccati equation is solved to obtain the feedback coefficients. The experiments are carried out by configuring the controller around the digital signal processor. The block diagram representation of the control system is shown in Fig. 20. The inputs to the controller are the gap-deviation, its derivative and the current deviation of the electromagnet. The output is the control signal to the power amplifier. The DAC output is represented as

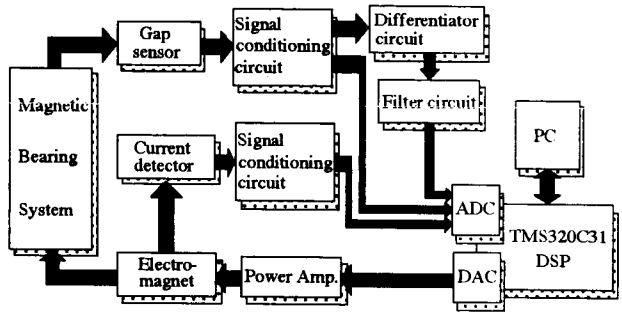

Figure 20. Controller block diagram representation.

$$e' = -\left(k_1 x' + k_2 \frac{dx'}{dt} + k_3 i' + \int x'\,dt\right) \quad -----(19)$$

With the help of the controller, the rotors are stabilized. Fig. 21 shows the vibration characteristic along the control axis of the vertical-shaft machine. Fig. 22 shows that of horizontal-shaft machine. It is seen that the level of vibration is similar. This is due to the fact that the same type of controller has been employed for the axial stabilization.

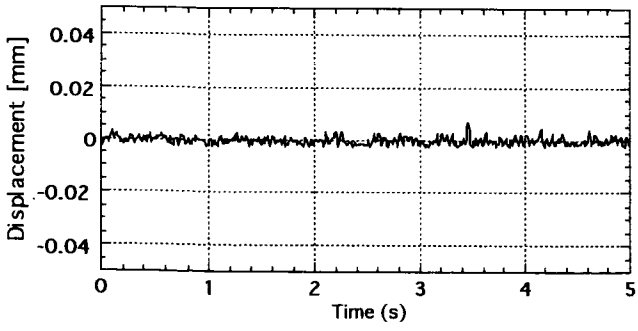

Figure 21. Vibration characteristic of system #1.

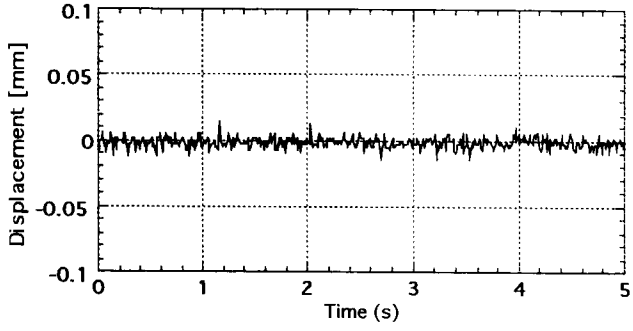

Figure 22. Vibration characteristic of system #2.

The important thing to be considered is the disturbance attenuation characteristic along the passive control axis of the two systems. Since the PM configuration for system #1 is symmetrical, disturbances along the passive radial direction will be damped out to zero with time. The higher the stiffness, the faster the stabilization. But in system #2, the presence of an upper stator magnet has a strong influence [7]. When disturbances are created, the system shows overshoot and returns back

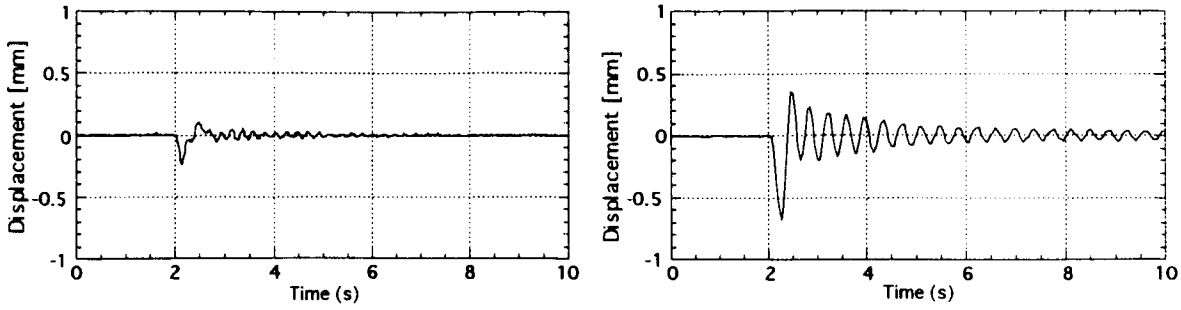

(a) With upper stator magnet. (b) Without upper stator magnet.

Figure 23. Disturbance characteristic at zero speed.

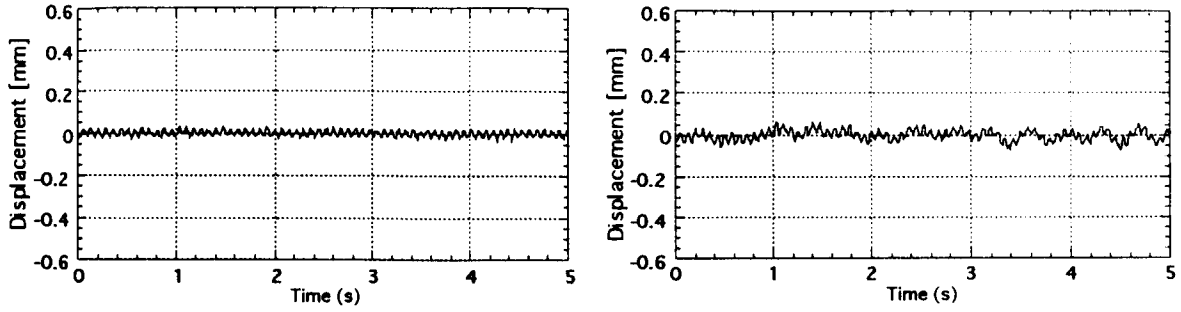

(a) With upper stator magnet. (b) Without upper stator magnet.

Figure 24. Vibration characteristic at 800rpm.

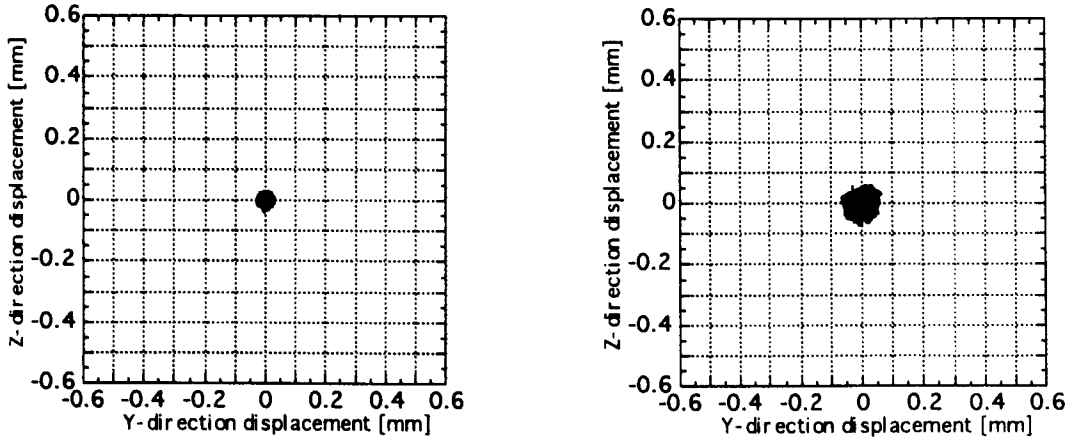

(a) With upper stator magnet. (b) Without upper stator magnet.

Figure 25. z-axis vibration vs. y-axis vibration at 800rpm.

to the original state after some time. Fig. 23a and b shows the disturbance characteristics at zero speed with and without the upper stator magnet respectively. It is seen from Fig. 23 that for the same magnitude of disturbing force the effect is almost one-third in the case with an upper stator magnet system compared to that without an upper stator magnet system. In order to verify the response characteristic while the rotor is in motion, the motor is driven at low speed. Due to the presence of harmonic torques, there is a lot of disturbing force during low speed operation of the motor. Fig. 24a and b shows vibration characteristics at 800rpm with and without the upper stator magnet. Fig. 25a

and b shows the y-axis vibration vs. z-axis vibration characteristics at 800rpm. It is seen that the vibration level is less for the system with the upper stator magnet.

CONCLUSION

In this paper, we have discussed two types of single-axis controlled repulsive type magnetic bearing systems. Their configuration, permanent magnet arrangement, levitation, stiffness characteristics and control performances have been described. For the horizontal-shaft machine, an optimum permanent magnet configuration has been obtained which reduces the levitation force but improves the radial stiffness characteristic. The choice of the system type depends on the application and system requirements.

REFERENCES

1. J. P. Yonnet, "Passive Magnetic Bearing with Permanent Magnets," *IEEE Trans. on Magnetics,* Vol-MAG 14, No. 5, pp. 803-805, Sept. 1978.
2. J. P. Yonnet, "Passive Magnetic Bearing and Couplings," *IEEE Trans. on Magnetics,* Vol-MAG 17, No. 1, pp. 1169-1173, Sept. 1981.
3. J. P. Yonnet, S. Hemmerlin, E. Rulliere and G. L. Emarquand, " Analytical Calculation of Permanent Magnet Couplings," *IEEE Trans, on Magnetics,* Vol-MAG 29, No. 6, pp. 2932-2934, Nov. 1993.
4. J. Delamare, E. Rulliere and J. P. Yonnet, "Classification and Synthesis of Permanent Magnet Bearing Configuration," *IEEE Trans. on Magnetics,* Vol-MAG 31, No. 6, pp. 4190-4192, Nov. 1995.
5. J. P. Yonnet, "Analytical Calculation of Magnetic Bearings," *Proc. of Fifth International Workshop on Rare Earth-Cobalt Permanent Magnets and their Applications,* June 7-10, 1981, pp. 199-216, Virginia, USA.
6. S. C. Mukhopadhyay, T. Ohji, M. Iwahara, S. Yamada and F. Matsumura, "A New Repulsion Type Magnetic Bearing," *Proc. of IEEE PEDS,* Vol. 1, pp. 12-18, Singapore, May 26-29, 1997.
7. S. C. Mukhopadhyay, T. Ohji, S. Yamada and F. Matsumura, "Disturbance Attenuation and Faster Stabilization via Permanent Magnet Placement on Repulsion Type Magnetic Bearing," *Proc. of IEEE PEDS,* Vol. 1, pp. 255-261, Singapore, May 26-29, 1997.

Session 13 -- Applications

Chairman: Nelson J. Groom
NASA Langley Research Center

HIGH POWER ELECTRICAL MACHINES FOR SPACE APPLICATIONS ELECTROMAGNETIC LAUNCHERS (QUALITY FUNCTIONS AND GOODNESS FACTORS)

M. D. Driga
Professor, Department of Electrical and Computer Engineering
The University of Texas at Austin
Austin, Texas, 78712 USA

ABSTRACT

In order to drastically increase the power and energy densities of the pulsed electrical machines for space applications electromagnetic launchers a "system approach" of the entire electromechanical and electrodynamical chain must be adapted. A unified treatment and optimization of both rotating power supplies and accelerators leads to a set of goodness functions and quality factors exploring the relative merits of the system. Such quality indicators must be based on a rigorous theoretical foundation from both electrodynamical and electromechanical points of view.

For electromechanical aspects, the general theory of electrical machines, together with Kron's tensorial formulations for transient and pulsed conversion lead to a quality indication as a "goodness factor" or "goodness function" generalized from steady state to pulsed electrical machines and, further, to systems of machines (rotating power supply, self-excitation system, accelerator).

By using Maxwell's equations for moving media and the notion of flux derivative, three different formulations for electromagnetic forces in electrical machines are introduced and interrelated leading to an assessment for the electromagnetic recoil and for the distribution of forces in air core and iron core advanced machines and electromagnetic accelerators.

BACKGROUND

For many years, the Electromagnetic Launchers (EMLs) have been proposed as alternative means for space launching. After more than one decade of experimentation with different electromagnetic guns and launchers (under U. S. Army and DARPA sponsorship), the issue of the size of the electric power supplies for such devices has emerged as one of the most critical which may determine if any practical space or military use is to be expected in the foreseeable future.

The power supplies used for significant electromagnetic gun experiments have been capacitors, inductors, or high-voltage electrical machines. The homopolar machine is a very

low-voltage electrical machine and does not have the capability of delivering the high level of power required by the electromagnetic launcher. The inductor charged relatively slowly by the homopolar and the opening explosive switch represent, jointly, the power supply [1].

It is always understood that the power supply has also, like the ones mentioned above, the capability of storing the necessary energy and a common way of characterizing the power supplies is by the specific stored energy, while strongly implying that sufficient means (such as high output voltage and low internal impedance) exist in order to deliver such energy in an extremely short period of time.

The variables of state, uniquely defining the stored energy , are the electric field intensity *E(v/m)* for capacitor films, the magnetic flux density *B(T)* for inductors, and the peripheral velocity *u(m/sec)* for the flywheel part of electrical machines, for the power supplies considered here in which the energy is stored in electric field, magnetic field, and as kinetic energy, respectively.

Taking into account the demonstrated state-of-the-art technology only, we arrive at the energy density levels listed in the Table 1. Table 1 shows that the balance is heavily tilted in favor of high-voltage, electrical machines, with kinetic energy store. A strong implication is that the power supply has the means of transferring very rapidly such energy to the load: high voltage output and small internal impedance.

Table 1. Performance energy density levels for different media of storage.

Energy storage medium	Energy density J/m^3	Demonstrated levels of performance J/m^3
1. Electric energy density	$w_E \frac{\varepsilon E^2}{2}$	$9.1\times10^6 \begin{cases} E = 1.6\times10^4 \frac{v}{mil} \\ \varepsilon = 5\varepsilon_0 \end{cases}$
2. Magnetic energy density	$w_M = \frac{B^2}{2\mu_0}$	$1.0\times10^8 \begin{cases} B = 16\ Tesla \\ \mu = \mu_0 \end{cases}$
3. Kinetic energy density	$w_K = \rho\frac{v^2}{2}$	$1.2\times10^9 \begin{cases} u = 1,150 \frac{m}{\sec} \\ \rho = 1,800 \frac{kg}{m^3} \end{cases}$

The present paper tries to advance the idea that directions for drastic improvements in space application of EML and their power supplies must come from a unified treatment and optimization of both introducing a system of quality (or goodness) factors and functions applicable to the entire "electromechanical chain" (power supply and launcher), in a system approach.

Maxwell's Equations for Media in Motion

The expression for Maxwell's equations customarily used do not contain explicitly the motion of the media so important for machines and accelerators. As an example, the very important ones, Ampere's Law and Faraday's Law, respectively, are:

$$\oint_{e_2} \overline{H} \bullet d\overline{l} = \iint_{s_{ac}} \overline{J} \bullet \overline{ds} + \frac{d}{dt} \iint_{s_{c2}} \overline{D} \bullet ds \qquad \oint_{e_1} \overline{E} \bullet d\overline{l} = -\frac{d}{dt} \iint_{s_{d1}} \overline{B} \bullet \overline{ds} \qquad (1)\ \&\ (2)$$

In the moving media, both the curve on which the circulation is taken *(c)* and the surfaces through which the flux is considered *(s_C)* are moving and by using the known formula for flux derivative, the two Maxwell's equations above become:

$$\oint_C \overline{H} \bullet \overline{dl} = \iint_{S_c} [\overline{J} \bullet \overline{ds} + \frac{\partial \overline{D}}{\partial t} \bullet \overline{ds}] + \iint_{S_c} \overline{u} \bullet div\ \overline{D}\ \overline{ds} + \iint_{S_c} curl\ (\overline{D} \times \overline{u}) \overline{ds} \qquad (1a)$$

$$\oint_C \overline{E} \bullet \overline{dl} = -\iint_{S_C} \frac{\partial \overline{B}}{\partial t} \bullet \overline{ds} - \iint_{S_C} \overline{u} div\ \overline{B} \bullet \overline{ds} - \iint_{S_C} curl\ (\overline{B} \times \overline{u}) \overline{ds} \qquad (2a)$$

or in differential form:

$$curl\ \overline{H} = \overline{J} + \frac{\partial \overline{D}}{\partial t} + \overline{u}\ \ div\ \ \overline{D} + \ curl\ \ (\overline{D} \times \overline{u}) \qquad (1b)$$

$$curl\ \overline{E} = -\frac{\partial \overline{B}}{\partial t} - \overline{u} div \overline{B} - curl\ \ (\overline{B} \times \overline{u}) \qquad (2b)$$

In the objects of our considerations, electrical machines, projectiles moving in electromagnetic field and electromagnetic launchers, we assume that a point in motion maintains its electromagnetic properties ε and μ (the substantial derivative is zero $\frac{ds\mu}{dt} = \frac{\partial \mu}{\partial t} + \overline{u} grad \mu$). Then, the partial derivatives of $\overline{D}$ and $\overline{B}$, vectors determining the electric and magnetic flux are replaced by their flux derivatives, with respect to time:

$$\frac{\partial D}{\partial} \rightarrow \frac{d_f \overline{D}}{dt} \quad \text{and} \quad \frac{\partial \overline{B}}{\partial} \rightarrow \frac{d_f \overline{B}}{dt} \qquad (3)$$

Then the fundamental balance of energy for electromagnetic field in a volume v surrounded by a closed surface s_v through which we calculate the Poynting's vector will transform, replacing the partial derivatives, with respect to time, with the flux derivatives into:

$$-\oint_{s_v} \oint (\overline{E} \times \overline{H}) \bullet \overline{ds} = \iiint_v \overline{E} \overline{J} dv + \iiint_v \left(\overline{E} \bullet \frac{\partial_f \overline{D}}{\partial t} + \overline{H} \bullet \frac{\partial_f \overline{B}}{\partial t} \right) dv \qquad (4)$$

which considers not only the electrodynamic phenomena, but also the electromechanical power conversion effects, due to the media motion.

Forces in electrical machines and electromagnetic accelerators

The fundamental balance of power [1, 5] will permit us to find the electromagnetic forces in three different formalisms:

1. As the global forces: generalized Lagrangian forces acting along generalized coordinates;
2. As a distribution of body forces in the projectile, accelerator, and power supply; and
3. As stresses using the artificial method of Maxwell's electromagnetic stress tensor, and as a generalization finding the origin and distribution of the recoil forces.

The theoretical tools which transform the expressions for forces, from a formalism to another are the constancy of the magnetic flux as the constraint for the Lagrangian transformation and the complex and subtle notion of flux derivative [1].

1. As a Lagrangian transformation, we choose one in which the sum of the Poynting's vector flux and the Joule losses is equal to zero during the transformation. Such constraint reduces the expression (4) to:

$$P_J + P_{S_o} = -\int_v \iiint \left(\bar{E} \frac{d_f \bar{D}}{dt} + \bar{H} \frac{d_f \bar{D}}{dt} \right) dv = 0 \tag{5}$$

$\frac{d_f \bar{D}}{dt} = 0$ and $\frac{d_f B}{dt} = 0$ lead to the constraints $\psi_{el_{s_o}}$, $\Phi_{m_{s_o}} = const.$ (5a)

The only significant way to enforce the constraint is to keep fluxes (electric and magnetic) constant and, consequently, their derivative zero. Then the change in the energy must equal mechanical work and, as a result:

$$F_j = -\left(\frac{\partial W_{el}}{\partial x_j} \right)_{\psi_e = const.} - \left(\frac{\partial W_m}{\partial x_j} \right)_{\Phi_m = const.} \tag{6}$$

Formulas (5 and 6) show that the constancy of the flux (electric or magnetic) comes naturally from Maxwell's equations and the conservation of energy.

2. The body forces (forces per unit volume) are obtained as an extension of (6a, b), differentiating with respect to time to find the power:

$$-\left(\frac{dW}{dt}\right)_{\substack{\Psi_e=const \\ \Phi_m=const}} = \frac{dL}{dt} = \int\int\int_v \bar{f} \cdot \bar{u}\, dv \tag{6a}$$

again by using the method of flux derivative, we obtain for the body force $\bar{f}$ an expression (7) containing six terms.

$$\bar{f} = \bar{f}_e + f_m = \rho_v \bar{E} - \frac{E^2}{2} \bullet grad\varepsilon + grad\left(\frac{E^2}{2}\tau\frac{\partial\varepsilon}{\partial\tau}\right) + \bar{J}\times\bar{B} - \frac{H^2}{2} \bullet grad\mu + grad\left(\frac{H^2}{2}\tau\frac{\partial\mu}{\partial\tau}\right) \tag{7}$$

If the magnetostriction term is considered to be less significant to the object of our research, the remaining two terms in the magnetic body force,

$$f_m = \bar{J}\times\bar{B} - \frac{H^2}{2} \bullet grad\mu \tag{7a}$$

are very significant in showing the difference between iron core and air core machines. Fig. 1 shows an illustration of how the forces split in $\bar{J}\times\bar{B}$ forces and forces applied to the ferromagnetic materials of the slot making it obvious why in the ferromagnetic machines the majority of the stresses will apply on the strong ferromagnetic walls and a significantly smaller amount on the fragile windings. For the air core structures, we are able to use a much larger flux density - obtaining much larger power densities, at the price of a substantially higher excitation magnetomotive forces (obtained usually by self-excitation).

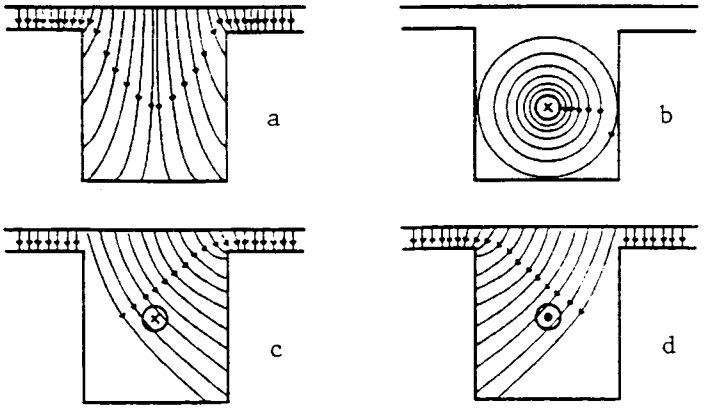

Figure 1. Why a large part of electromagnetic forces stress the ferromagnetic material.

3. The electromagnetic (Maxwell's) stress tensor gives as a third formalism [1] in which the global electromagnetic force *F(N)* is obtained by integrating stresses $\bar{T}_u$ over an area s_v which, in turn, balances the body forces of electromagnetic origin , integrated over the volume *V*:

$$\bar{F} = \int_v \int\int \bar{f} dv = \oint\oint \bar{T}_n \, ds \tag{8}$$

We obtain in the final the three components of the tensor on the three axes (x, y, z):

$$\begin{aligned} \Gamma_x &= \left[E_x \bar{D} + H_x \bar{B} - i \left(\frac{\varepsilon E^2}{2} + \frac{\mu H^2}{2} \right) \right] \\ \Gamma_y &= \left[E_y \bar{D} + H_y \bar{B} - j \left(\frac{\varepsilon E^2}{2} + \frac{\mu H^2}{2} \right) \right] \\ \Gamma_z &= \left[E_z \bar{D} + H_z \bar{B} - k \left(\frac{\varepsilon E^2}{2} + \frac{\mu H^2}{2} \right) \right] \end{aligned} \tag{8c}$$

However, if the regime is not stationary, the equation (8) becomes:

$$\bar{F} + \frac{d}{dt} \int_v \int\int (\bar{D} \times \bar{B}) dv = \oint_{s_0} \oint (\bar{T}) (-\bar{n}) ds \tag{8a}$$

leading to the fact that the resultant force in an isolated mechanical system interacting with an electromagnetic system is zero; expressed in terms of the mechanical and electromagnetic momentum where the electromagnetic momentum is $\bar{D} \times \bar{B} = \varepsilon\mu \bar{E} \times \bar{H} = \varepsilon\mu \bar{S}$).

Considering the mechanical momentum in addition to the electromagnetic one:

$$\frac{d}{dt} \left[G_{mech.} + \int_v \int\int (\bar{D} \times \bar{B}) dv \right] = 0 \tag{8d}$$

The conservation of momentum applies to the sum of both mechanical and electromagnetic momentum.

The expression above is important in evaluating the design questions related to recoil in electromagnetic guns. The volume integral of the electromagnetic force density, the Maxwell's stress tensor, and the electromagnetic momentum become tools in defining and calculating globally and locally the recoil in electromagnetic accelerators [1].

Intrinsic Characteristics of the Rotating Pulsed Power Supplies (RPPS) for Electromagnetic Launchers (EML)

The peculiar nature, "the strangeness", of the RPPS for EML is due not only to constraints related to their very high energy and very high power ratings under conditions of

extreme transient characteristics (they operate under load for few milliseconds only), but also to strong differences with respect to other electromechanical power converters.

1) One, casually disregarded, but carrying important theoretical implication, is that such machines belong not to the customary constant voltage systems, but to a totally new world of constant current systems in which the supplied current is always the same and the voltage is variable, according to the power required by the load. Pestarini [12] has described in detail such a world mainly for d.c. machines, calling them Metadynes, and patenting numerous applications - the majority in complex drive systems.

Laithwaite alluded to it [6] and, as Pestarini did years before him, commented about how unprepared the common electrical machine designer is to adapt himself to a system of reference diametrically opposite to the usual practice and requirements.

2) The second intrinsic characteristic of the RPPS is the so-called "compensation." The compensation is actually a misnomer for a complex phenomenon used by the electrical machine designer to adapt the characteristics of the power supply to those needed by the electromagnetic launcher. The term is borrowed from the theory of operation of d. c. machines in which the armature current flows in series through a separate winding (compensation winding) embedded in the pole-pieces of the machine stator, canceling in large part the magnetic field of armature reaction. The success of the operation is assured by the constant (and opposite) relative position in space of the two magnetic fields - armature reaction and compensation - maintained by the brush and commutator system.

In the first approximation, the notion of armature reaction compensation can be generalized to a synchronous generator by using a conductive uniform shield - placed on the excitation poles and opposing the armature. During the machine discharge into the low impedance load (such as the electromagnetic launcher), image currents in the shield produce a magnetic field opposite to the armature reaction field, canceling a large part of it and achieving an important reduction of the internal impedance of the power supply, thus increasing the efficiency of the power transfer. A refinement of the method involves an anisotropic shield, permitting compensation while reducing losses by providing magnetic decoupling during the self-excitation process.

Armature reaction compensation applied to pulsed synchronous generators by means of a conductive shield (continuous or partially distributed) is always imperfect due to the phase shift of the induced currents and their resultant magnetic field and the transient field penetration. Such apparent imperfections are actually used by electrical machine designers in order to achieve the goal of variability of the internal electromagnetic field structure of the RPPS in order to adapt itself to the continuous changing power requirements of the EML and launch package in every instant of acceleration [2, 3, 4]. For example, to the condition of a constant acceleration impressed on the projectile requiring, generally, a constant current power supply under a variable, continuously increasing voltage, which drops sharply at the end of launching.

Phasorial formalism in the Blondel's two reaction theory of synchronous machines, as well as in Doherty and Nickle's, and in Park's transformation [9, 10, 11] shows that the general theory of electrical machinery was conceived for steady-state analysis. Even Kron's [11] generalized theory and its "Application of Tensors to the Analysis of Rotating Machines" is still, in large part, devoted to the same type of treatment. However, the generalized electrical machine theory and the notion of primitive machines offers the best analytical tools for the treatment and evaluation of quality factors (goodness) of the RPPS for EMLs.

Fig. 2 shows the diagram of a synchronous machine as a primitive machine with fictitious axis coils, using the two-axis (direct, *D*, and quadrature *Q*) theory [10]. When compared to the normal, primitive machine, takes into account the compensation winding as a nonuniformly-distributed shield. It can characterize in this way a wide spectrum of "compensation" windings, from continuous shields to very selective and asymmetrical windings, obtained through modification of the parameters of the *m* winding in the direct axis and the *n* windings in the quadrature axis, correspondingly.

Since the pulsed power supply has a highly transient behavior, the equations are written using operational calculus formalism, replacing the phasor formalism used for steady state. The equations for the system of coils are written in function of

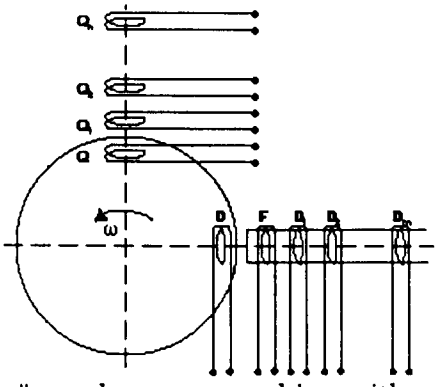

Figure 2. Generalized "primitive" synchronous machine with several (nonuniform) compensation windings.

their self and mutual inductances and, for armature coils including the rotation voltage term, leading in the case of fig. 2 to a set of $(m + 2)$ equations containing $(m + 2)$ currents, as well as the excitation (field) voltage v_f and the magnetic flux linkage in the direct axis ψ_d. The relation between the Laplace transforms of flux, current, and voltage is:

$$\overline{\psi}_d = \frac{X_d(p)}{\omega_O}\overline{i}_d + \frac{G(p)}{\omega_O}\overline{v}_f \qquad (10)$$

where ω_0 allows for the proper dimensionality in (1) above.

$X_d(p) = \dfrac{a_{(m+1)}p^{m+1} + a_m p^m + \ldots + a_1 p + a_0}{b_{(m+1)}p^{m+1} + b_m p^m + \ldots + b_1 p + b_0}$ is the direct-axis operational impedance . $G(p)$ has the same denominator as $X_d(p)$, but a numerator of m order only. For the quadrature axis, the elimination of currents from a set of $(n + 1)$ equations gives, similarly:

$$\overline{\psi}_q = \frac{X_q(p)}{\omega_0}\overline{i}_q \tag{10}$$

where $X_q(p)$ is the quadrature axis operational impedance being the quotient of two polynomials of order n while $\overline{\psi_q}$ is the Laplace transform of the magnetic flux in the quadrature axis.

Equations (9) and (10) apply to the transient regimes. During the steady state operating condition when all the variables in the two-axis reference frame are constant, $p = 0$ and as an example, the direct axis operational impedance $X_d(p)$ degenerates into the direct axis synchronous reactance X_d.

Despite idealizations and linearizations, the operational impedances, $X_d(p)$ and $X_{(q)}(p)$, characterize and define very efficiently a large spectrum of different transient behaviors of RPPS for EMLs. In a preliminary design characterization, the direct axis operational impedance $X_d(p)$ is often used in the form of an operational admittance $Y_d(p)$ expanded into partial fractions. As an example, in the well-known short-circuit characterization of synchronous generators:

$$Y_d(p) = \frac{1}{X_d(p)} = \frac{(1 + T_{d'_0}p)(1 + T_{d''_0}p)}{(1 + T_{d'}p)(1 + T_{d''}p)}Y_d \tag{11}$$

where $T_{d'_0}$, $T_{d''_0}$, $T_{d'}$, and $T_{d''}$ are the principal time constants of the synchronous machine. After expanding into partial fractions and using the canonical notations, we obtain the classical:

$$Y_d(p) = \frac{1}{X_{d'}} + \left(\frac{1}{X_{d'}} - \frac{1}{X_d}\right)\frac{T_{d'}p}{1 + T_{d'}p} + \left(\frac{1}{X_{d''}} - \frac{1}{X_{d'}}\right)\frac{T_{d''}p}{1 + T_{d''}p}. \tag{11a}$$

The last partial fraction represents the compensation winding as one of the three branches in parallel in the equivalent, modified, direct axis equivalent circuit. A similar modified quadrature axis equivalent admittance is used for design evaluation. It is interesting to see the operational admittance transformed for sinusoidal changes of frequency ω in which replacing p by $j\omega$, we obtain the operational admittance frequency locus in fig. 3 (direct axis).

An alternative approach is the use of Kron's re-establishment of transient dynamical equations from the equivalent circuits and the introduction, by using Kron's method of reference frames, of an interconnection clause [11]. In the first approach (fig. 4), if the transient equations of the machine (pulsed generator) or of a group of machines (pulsed generator and electromagnetic launcher) are required, they can be obtained from the equivalent circuit containing the variable frequency f_{dS}, feature. The transient system is found by replacing f by the p/j operator, where j is the imaginary unit. The transformation for the reference frames is described in [11]. The interconnection clause is used not only to study the power supply (compensated synchronous generator) together with the electromagnetic launcher, but also to include the process of self-excitation as the interconnection of separate equivalent circuits.

Quality Indicators and Electrodynamics Similitude Criteria for Classical Electrical Machines

The theory of electrical machine design [7, 8, 9] called in [13] "an esoteric preoccupation of the few" uses a complex methodology to arrive to an optimal design. Such methodology can be formally checked and verified at each logical step, the procedures, being almost canonical, matured for more than a century and reaching asymptotically a level which has remained almost flat for the last forty years. Several quality indicators, similitude criteria, and scaling laws will be reminded to the reader.

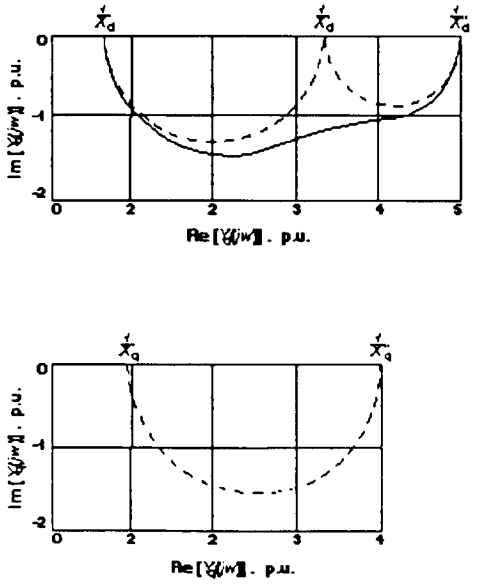

Figure 3. Operational admittance direct axis (d).

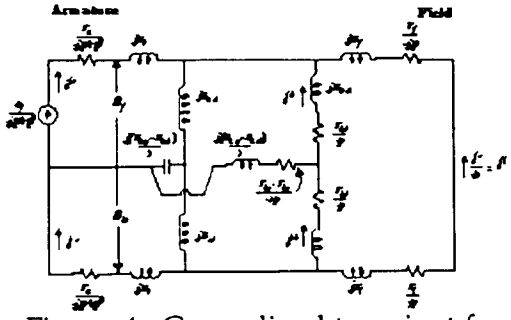

Figure 4. Generalized transient frequency locus on equivalent circuit (Kron).

Electrodynamics Similitude and Scaling Relations

The apparent interior power: $S_i = mEI \ (VA)$ is the product of number of phases m, phase current $I(A)$ and phase electromotive force $E(v)$. $E = \pi\sqrt{2}\Phi f w k_w (V)$ where: Φ is the

fundamental of main magnetic flux *(Wb)*, $f = pn$ = frequency (rps), and k_w = winding factor. The flux Φ can be expressed as:

$$\Phi = B_\delta \frac{2}{\pi} \tau_p l_i \tag{12}$$

where: B_δ = flux density in the air gap *(T)*, τ_p - polar pitch *(m)*, and l_i i= ideal length *(m)*. If the phase current I is expressed in terms of the sheet of current density $A(A/m)$:

$$A = \frac{2mIw}{\pi D} \tag{13}$$

Substituting (13), (14), and (15) in (13'), the fundamental formula relating the apparent power, geometrical dimension and the rotational velocity n (rps) is obtained:

$$S_i = \frac{\pi k_w}{2\sqrt{2}}(2p\Phi)(\pi DA)\ \ n = \frac{\pi^2 k_w}{\sqrt{2}} D^2 l_i\ \ n\ \ AB_\delta = (2p)\sqrt{2} f\ \ k_w(\tau_p)^2 l_i B_\delta A. \tag{14, 15, 16}$$

For classical machines, the expressions (16a, b, c) are usually translated in the simple form of a "machine constant" as the power per unit speed obtained from the armature unit volume. A more elaborate analysis shows that the power increases faster than the cube of the linear dimensions of the electric machine, let the current density J be expressed as:

$$J = \frac{At_1}{H_{cu} b_{cu}} = \frac{A}{h_c \beta\ k_{cu}} \left(\frac{A}{m^2}\right),\ \beta = \frac{b_c}{t_1},\ \text{and}\ k_{cu} = h_{cu} b_{cu} / h_c b_c \tag{17a, b, c}$$

where h_c is the height of the slot and , the ratio between the slot width to the slot pitch, and the copper filling coefficient of the slot. The average flux density along the tooth is obtained from:

$$B\zeta k_{Fe} = B_\delta \tag{18}$$

where $\zeta = \frac{b}{t_1}$ is the ratio between the average width of the tooth to the slot pitch and k_{Fe} is the

ratio between the net length of the active ferromagnetic iron to the total length of the armature. Then, (14, 15, 16) can be transformed as:

$$S_i = \frac{\pi^2 k_w}{\sqrt{2}} \beta k_{cu} \zeta k_{Fe} D^2 l_i n h_c JB = (2p) f \sqrt{2}\ \ k_w \frac{\tau^4}{\lambda} k_{cu}\ \ \beta_1 JB\ (\text{where } \delta = \tau / l_i), \tag{19a, b}$$

leading to the conclusion that in electrical machines, with similar geometry the apparent power increases proportionally to the linear dimensions to the fourth:

$S_i = kL^4$ or $L = \frac{1}{k'} \sqrt[4]{S_i}$ or $L = \frac{1}{k'} (S_i)^{\frac{1}{4}}$. The weight of machine G is: $G = k_2 L^3 = k_2' (S_i)^{\frac{3}{4}}$.

Active Conductor Electromagnetic Power Conversion Densities

In spite of the appearance of describing the local power density, the density obtained previously is an average one since its definition involves the rated apparent power of the entire machine.

The local power density in the condition of lossless electromechanical power conversion per unit volume of active conductor of the generator, is:

$$-\left(\bar{J}\times\bar{B}\right)\bullet\bar{u}=\left(\bar{u}\times\bar{B}\right)\bullet\bar{J} \tag{20}$$

which, multiplied by the elementary volume, *dv* is the truly local definition of instantaneous conversion. The "active conductor" is the seat of the power conversion and by the principle of equality of action and reaction, is equally felt in both the stator and rotor of the electromechanical converter.

The flux density $\bar{B}$ in expression (12) is the vectorial sum of the impressed excitation field $\bar{B}_{imp}$ and the induced field by the armature reaction, $\bar{B}_{a,ind}$ (invoking the Lenz rule) such that:

$$\left[-\bar{J}\times\left(\bar{B}_{imp}-\bar{B}_{a,ind}\right)\right]\bullet\bar{u}=\left[\bar{u}\times\left(\bar{B}_{imp}-\bar{B}_{a,ind}\right)\right]\bullet\bar{J}. \tag{21}$$

A "compulsator" exploits the manner in which the two $\bar{B}$ vectors add (or rather subtract) in different moments of discharge. Controlling the compensation, by eliminating partially the direct axis shield and allowing the armature reaction in the initial moment of discharge to almost completely demagnetize the armature field $B_{imp}-B_{a,ind}\approx 0$; and gradually, after that to reach a high degree of compensation in the latest moments of launching, the machine will apply a voltage linearly increasing from zero to maximum, the ideal one for EMLs.

For large RPPS, this solution leads to a more compact system than the one proposed in [14] by Driga in which, in a polyphase compensated generator, the output wave shape, and magnitude are solid-state controlled, thus decoupling the velocity of the generator and output wave control. The same relation applies to the launcher in which the back *emf* is locally described as the motional field $\left(\bar{u}_a\times\bar{B}_a\right)$, increasing linearly with the projectile velocity $\bar{u}_a$ and, for a constant current (and constant acceleration), increasing ideally from zero to the exit velocity.

The "Goodness Factor" Criterion: Is It Too Simplistic?

The criterion of "Goodness" of an electrical machine was introduced by Laithwaite in [6] as a means of comparing the relative performance (from the design point of view) of different electrical machines. It had to be an objective measure of the ability of the electrical machine to convert power electromechanically - a property which is more general than, for example, the efficiency which can be increased at the expense of other indicators of vital importance to the machine operation.

Since the electromechanical power conversion is determined by the coupling of the electric and magnetic circuits, Laithwaite defined it as the proportionality:

$$G \approx \frac{1}{\text{Resistance}} \times \frac{1}{\text{Reluctance}} \times \text{ frequency or } G \approx \left(\frac{A_e}{\rho l_e}\right) \times \left(\frac{\mu_0 A_m}{l_m}\right) \times f. \tag{22}$$

This is a simplistic approach to quality of a design and is based on the ability of an electric circuit to produce current *(I)* for a given electromotive force *(E)*, namely (I/E) combined with the ability of a magnetic circuit to produce flux for a given magnetomotive force *I'*, namely (Φ/I). The product (I/E) X (Φ/I) is made dimensionless by multiplying it with the frequency. It is an imperfect approach to "goodness," but leads to interesting inferences. For instance: In the example considered by Laithwaite [6], the length of the magnetic circuit is equal to the thickness of the gap. What happens to the "goodness factor" in the case of air core machines considered, almost exclusively as RPPS for EMLs and made entirely of "gap?"

According to the previous paragraph, the generalization of the "goodness factor" for pulsed, transient machines requires the replacement of the simple reluctance and resistance by corresponding very complex operational impedances in a dimensionless form, containing (as suggested by Kron) a connection clause. Such clause permits adding to the same expression the contribution of the launcher and the self-excitation stages, considered as intermediate interconnected machines. In such generalized "goodness factor," the frequency is replaced by the square root of the ratio between the machine discharge time t_d and the thermal time constant of the power supply τ_t namely $\sqrt{\frac{t_d}{\tau_t}}$. This factor takes into account the scaling of the machine from steady-state to short pulse discharge. Then the "generalized goodness" is

$$GG \approx \frac{\overline{Y}_1(p) \bullet \overline{Y}_2(p) \ldots \overline{Y}_k(p)}{\omega_{01} \bullet \omega_{02} \ldots \omega_{0k}} \sqrt{\frac{t_d}{\tau_t}} \tag{23}$$

where the factors ω_{01} ... ω_{0k} at the denominator make dimensionless the product of the partial operational admittances at the numerator.

CONCLUSION

By using Maxwell's equations for moving media, three different formulations for electromagnetic forces in electrical machines are introduced, obtaining from them a definite quality assessment for the electromagnetic recoil and force distribution in air and iron core machines.

The introduction of a generalized "goodness factor" for rotating pulsed power supplies and for electromagnetic launchers is possible through the use of interconnected operational admittances, not only for the power supply, but for accelerator and self-excitation system, as well. Such a "goodness factor" is actually a complex transient function describing the comparative interplay of several magnetic and electric circuits in the condition of rapid conversion. Additionally, several other quality indicators and similitude criteria from the classical electrical machine theory must be taken into account.

ACKNOWELDGEMENT

The support from the U. S. Army, Contract DAAH04-96-0-0197 is gratefully acknowledged.

REFERENCES

[1] M. D. Driga, Electromagnetic Launch Technology Assessment (Forces and Electromechanical Power Conversion). DARPA Report No. R-6266, DAAH01-88-0-0131, 1990, 122 pages.
[2] W. F. Weldon, M. D. Driga, and H. H. Woodson, "Compensated Pulsed Alternator," U. S. Patent 4,200,831, April 29, 1980.
[3] M. D. Driga, et al., "Design of Compensated Pulsed Alternators with Current Waveform Flexibility," Proceedings of the 7th IEEE Pulsed Power Conference, Washington, D. C., June 28 - July 1, 1987.
[4] M. D. Driga, et al, "Advanced Compulsator Designs," IEEE Transactions on Magnetics, Vol MAG 25, pp. 142-146, January, 1989.
[5] M. D. Driga, A Generalized Goodness Factor Criterion Applied to Advanced Rotating Electrical Machines for Hypervelocity Accelerators? Proceedings of the 6th European Symposium on Electromagnetic Launch Technology. The Hague 25-28 May, 1997, pp. 435-444.
[6] Eric R. Laithwaite, Induction Machines for Special Purposes, Chemical Publishing Co., 1966.
[7] R. Richter, Elektrische Maschinen, Band 1, 2, Birkhauser Verlag, Basel, 1967.
[8] E. Levi, M. Panzer. Electromechanical Power Conversion. Dover Publications, Inc., New York, 1974.
[9] J. Chatelain, "Machines Electriques," Vol 1, 2, Dunod, Paris, 1993.
[10] B. Adkins, R. G. Harley. "The General Theory of Alternating Current Machines. "Chapman and Hall, 1986.
[11] G. Kron, Application of Tensors to the Analysis of Rotating Electrical Machinery, General Electric Review, 1942.
[12] Joseph M. Pestarini, Metadyne Statics (1952), MIT Press and John Wiley and Sons, Inc.
[13] H. C. J. de Jong, A. C. Motor Design: Rotating Magnetic Fields in a Changing Environment, Hemisphere Publishing Corporation, 1989.

[14] M. D. Driga, "Metadynes as Pulsed Power Electrical Machines for Use in Advanced Robotics." The 10th IEEE Pulsed Power Conference Proceedings, pp. 1005-1012.
[15] J. R. Kitzmiller, et al, Laboratory Testing of the Pulse Power System for the Cannon Caliber Electromagnetic Gun System (CCEMG), IEEE Transactions on Magnetics, No. 1, January, 1997, pp. 443-448.

SUPERCONDUCTIVE SOLENOID FOR THE NAL 60CM MSBS

Hideo Sawada, Takashi Kohno, and Tetsuya Kunimasu
National Aerospace Laboratory
7-44-1 Jindaijihigashi-machi Chofu-shi, Tokyo, Japan

SUMMARY

The model position sensing system at the NAL 60-cm MSBS has been improved to provide a more accurate measurement of lateral positions by using an additional sensing camera mounted at the upper side of the test section. The MSBS is equipped with a model holding system in order to establish safe model release and capture. The holding system has a balance to monitor the load on the model while the system holds it. Suitable dimensions of the cylindrical model core for the MSBS are estimated. A larger MSBS for the 1.25 m high Reynolds number supersonic wind tunnel is designed by scaling up the dimensions of the 60-cm MSBS. A superconductive solenoid core is inevitable if suspending a model magnetically in the high Reynolds number supersonic wind tunnel. The proposed goal of the cylindrical core is 0.9m long and 74mm in diameter, with 80kA/cm^2 current density. In order to examine its feasibility, a superconductive solenoid model core of 300mm long and 45kA/cm^2 current density has been designed and built.

INTRODUCTION

Magnetic Suspension and Balance Systems (MSBS) provide an ideal way of supporting a model for wind tunnel tests because the force to support the model is generated by a magnetic field which is controlled by coils arranged outside the test section. Any mechanical support system is not needed in the flow field inside the test section. Then the support interference problem does not exist except for very special test conditions like hypersonic flow containing ionized atoms. Besides the fact that the MSBS is an interference free support system, it is very suitable to carry out difficult tests like dynamic tests. It is much easier to change the model attitude over a wide range by the MSBS than by mechanical support systems. This feature of the MSBS will improve tunnel data productivity. Many MSBSs have been built up to 1970s but only a few are in operation presently.

The NAL 10-cm MSBS was developed in 1985 and the 60-cm MSBS was developed in 1991 at the National Aerospace Laboratory (NAL).[1] The 10-cm MSBS has been used for basic research like rolling moment control [2] and dynamic calibration tests with measured magnetic field intensity around the test section[3,4] A specially designed model is controlled in 6 degrees of freedom in the 10-cm MSBS. The 60-cm MSBS has the largest test section in the world in the sense of the dimensions. The coil arrangement in the 60-cm MSBS is the same as in the 10-cm MSBS as shown in Figure 1. The coil drive units are 5 for the MSBS. The model can be suspended in 5 degrees of freedom with the exception of its rolling motion about the model body axis.

The model size is large enough to allow some type of apparatus to be installed inside it. A rolling motion suppression system inside the model has been developed, which has a fiber optic gyro for the motion. The model attitude and its motion will be measured with sensors installed inside the model in the near future.

Another merit of the bigger model is the potential use of the superconductive solenoid model core. In order to generate large magnetic forces balancing the aerodynamic load, both a strong magnetic field and large magnetic moment of the model core are needed. The permanent magnet or ferromagnetic material like soft iron is used as a model core in the small MSBSs. In the case of large wind tunnel models, there is sufficient room inside the model. Then, the superconductive solenoid core can be mounted inside the model, which can generate a much larger magnetic moment than permanent magnet cores. A superconductive solenoid model core was designed and was suspended successfully in a MSBS at Southampton University supported by NASA.[5,6] A detailed feasibility study of a superconductive solenoid model core to meet a large transonic wind tunnel was carried out[7] and a large model core was designed and built[8]. But the model core has not been used in a large MSBS. There is not a large enough MSBS in the word such that the performance of the core may be tested in it.

The feasibility of the superconductive solenoid as a model core for the high Reynolds number supersonic wind tunnel has been studied with the 60-cm MSBS since 1996 at NAL. The improvements of the 60-cm MSBS in order to examine the superconductive solenoid core and goals of the core for the high Reynolds number supersonic wind tunnel and the specifications of the prototype model core, which was ordered and was built by a manufacturer, will be described in this paper.

SYMBOLS

(x,y,z)	... coordinate system, See Figure 1.
(ϕ,θ,ψ)	... rolling, pitching , and yawing angles of a model
H	... magnetic field intensity (Hx,Hy,Hz)
M	.... moment (Nm) (Mx,My,Mz)
F	... force (N) (Fx,Fy,Fz)

IMPROVEMENTS OF THE 60-CM MSBS

A model with a cylindrical permanent magnet core inside it was successfully suspended in 3 degrees of freedom at the NAL 60-cm MSBS in 1993. Presently, a model with the same core can be suspended in 5 degrees of freedom except for rolling motion about the axis of the core. In order to get more stable control in the lateral direction, an additional model position sensing camera was mounted on the upper side of the test section together with the original sensing camera. Before a model is suspended, it sometimes becomes very unstable near its stand. The complete model suspension was confirmed by inspection. This was a potential danger. The MSBS was equipped with a model holding system to avoid the unexpected unstable motion and the danger. The MSBS was also equipped with a monitoring system for the model load and the contact between the model and the system.

Description of the NAL 60-cm MSBS

Details of the NAL 60-cm MSBS are described in References 1 to 4, so only the main features of it

will be described here. There are two iron rings perpendicular to the wind axis (x axis) as shown in Figure 2. Each has four pole surfaces. The coils 1 to 4 are attached asymmetrically to the upstream iron ring. The coils 5 to 8 are attached to the downstream ring similarly. The magnetic field surrounded by the four pole surfaces in each ring can be controlled by the coil currents. The four coils are always excited in pairs, for example, coils 1 and 3. For pure vertical force the pair coils of (1,3) and (5,7) are excited so that a vertical field exists between the vertical pair poles of each ring. Similarly, for horizontal force the pair coils of (2,4) and (6,8) are excited. A pair of air cored coils, (0, 9) causes drag force along x axis. The distance between the poles of the coil pairs is 640 mm. The specifications of the coils are listed in Table 1. Hz and Hy of the magnetic field intensity and their derivatives with x can be controlled by adjusting the four pair coil currents. Hx derivative with x can be controlled with the two air cored coils.

coil #	turn number	dimensions	purposes
0,9	50	620 x 620	drag
1,3,5,7	97 + 97	200 x 200	lift, pitch moment
2,4,6,8	100	200 x 200	side force yawing moment, and rolling moment
coil drive units		60V, 75A	5 units
bias coil drive units		1000 W	2 units
model core		300 $^{\Phi}$ x 600 cylindrical permanent magnet (Fe-Cr-Co)	
control		5 degree of freedom except for rolling motion control	

Table 1 Specifications of the NAL 60-cm MSBS

A model core of the 60-cm MSBS is a permanent cylindrical magnet magnetized along its principal axis. It is 50 mm in diameter and 300 mm long and a TOKIN K-5 type Fe-Cr-Co magnet. Five coil drive units for the coil pairs range from -75 to 75 A at 60V. A bias coil for generating additional lifting force is driven by two constant current power units of 1000 W, which range from 0 to 100 A. The coils are cooled with ambient air and they can be operated for about 1 hour.

The magnetic field was measured with an F.W.BELL Co. type 9903 gauss-meter using coil currents required to magnetically suspend the model. The measured Hz is plotted with respect to x coordinate in three lift coil current cases as shown in Figure 3. The figure suggests that the derivative of Hz with x is proportional to the current. Hx is also plotted with x in three drag coil currents as shown in Figure 4.

Improved Model Position Sensing System

The model position sensing system developed at NAL had poor accuracy in the lateral position because the position was evaluated with the model image size focused on the 3 CCD line sensors. The measured lateral position was worse in its accuracy than the longitudinal position by about 1 order as described in Ref. 1. The response speed of the lateral motion was much slower than of the longitudinal motion due to the poor accuracy of the position when the model position was measured with only one camera mounted at the side of the MSBS. In order to improve the lateral motion control, another model position sensing camera was mounted at the upper side. The camera measures y coordinate and yaw angle, ψ of the model. The expected accuracy of the measured y coordinate and yaw angle, ψ with the additional camera is the same as those measured with the original camera. The calibration test results show good resolution as shown in Table 2. Some examples of the results are also shown in Figure 5.

Each camera is connected to a computer and both measured data sets are gathered synchronously in a computer. The computer evaluates the model position based on these data sets and adjusts the coil currents accordingly. Large noise radiated from the power units affects the accuracy of the measured position significantly. All position data are modified with low pass filters of 10Hz cut-off frequency before evaluating the model position.

	resolution
x	0.07 mm
y	0.06 mm
z	0.04 mm
θ	0.02°
ψ	0.02°

Table 2 Resolution of the Improved Model Position Sensing System

Model Holding System

Before a model is suspended, it is laid on a stand made of wood. After suspending the model completely without any contact to the stand, the stand is removed by hand. The process is very dangerous when the model starts to move suddenly for some reason. The model was occasionally balanced on an edge of the stand. If the model was lifted rapidly to clear the stand, the model started to move with a periodical motion or dropped down from the stand during the early tests. It was very difficult to determine a way of lifting up the model safely from the stand in the early stages.

In order to avoid model damage and personnel accidents, the 60-cm MSBS was equipped with a model holding system. The system can suppress unexpected model motion byholdingit strongly and can release the model gradually by monitoring the model position and load on it.

The system was designed to hold the model horizontally at the center of the test section as shown in Figure 6. The held model position can be changed by 200 mm vertically about the center while the system holds it. The model can be moved to the positive *y* direction from the center. The arm part of the system can be moved out from the test section completely after releasing the model. The arm can also be moved back to the holding position automatically through sequential procedures. In order to establish accurate positioning repeatability, 5 photo switches are used. The system is driven by 5 hydraulic actuators. All parts are made with non-ferromagnetic materials. The arm can hold the model solidly even if 98 N vertical or horizontal forces and 30 N axial force act on it, respectively. The shape of the part holding a model was designed specially not to prevent the two sensing cameras from measuring the model position. The system can hold the model up to 93mm in diameter. The system works well during MSBS operation presently.

Force Monitoring System

When the model holding system holds a model in the 60-cm MSBS, various forces act on the model. After confirming the model is in balance, the model can be released. In order to know that the model is in balance, the model holding system is equipped with a force balance as shown in Fig. 6. The specifications

of the balance are listed in Table 3. The force and moment acting on and about the model gravity center can be estimated from the obtained data. If the output from the balance vanishes, it suggests that the model has left the system completely. After the model is released from the system completely, the arm is moved out of the test section quickly.

shape : 67^{ϕ} x 27^{h},	mass : 180 g
fx, fy < 100 N,	fz < 200 N
Mx,My,Mz < 6.3 Nm	
data rate : 0.4883 Hz	

Table 3 Specifications of the Balance for the Magnetic Force Monitoring System

Calibration tests for the balance were carried out with an empty model shell at the 60-cm MSBS. The magnetic field effect on the balance output was measured. If the effect is negligible small, aerodynamic load will be measured accurately after the wind tunnel test as has been mentioned in Reference 9. The temporal results obtained show there is little effect as shown in Figure 7.

MODEL CORES FOR THE NAL 60-CM MSBS

Permanent Magnet Cores

The original model core for the NAL 60-cm MSBS is a cylindrical permanent magnet since the design stage of the system. The MSBS is not equipped with magnetization coils. As a result, a soft iron core cannot be used with the MSBS.

Magnetic force acting on a cylindrical permanent magnet core is proportional to its magnetic moment. The magnetic moment is approximated by the product of the residual magnetic induction and the core volume. However, the available residual magnetic induction is limited to around 1.2 to 1.4T at present. The model must be suspended against the gravity force by the magnetic force. In addition to the gravity force, the vertical upward magnetic force component, *Fz*, must be as large as possible. In the case of the 60-cm MSBS, Figure 8 predicts that Alnico magnets are the most suitable for the size of the model core for the 60-cm MSBS. If the shape is changed, the suitable magnet will be other magnetic material like the Nd-Fe-B magnet. Figure 9 shows the net lifting force of the cylindrical magnet for the 60-cm MSBS with respect to its diameter. There is a suitable diameter for each cylindrical magnet of constant length. The present magnet core is near the most suitable shape. The net lifting force will be up to 17N at the MSBS even if the shape is designed very well. If a tunnel model is aircraft shaped, the model mass including the wing and control surfaces must be less than 1.7kg plus the magnet mass. Although the aerodynamic force acting on a tunnel model reduces the lifting coil currents, the model must be supported in no flow by the magnetic force. Then, the model mass must be less than 1.7kg. If the model does not contain any instrumentation, it will be possible to build such a light model. If the model includes some control system inside it, it will become impossible to build a model lighter than 1.7kg. So, the net lifting force must be as large as possible.

Superconductive Solenoid Core

In place of the permanent magnet, the superconductive solenoid can be used as a model core for the 60-cm MSBS. The solenoid can generate a much larger magnetic moment than the permanent magnet if the sizes are the same. This means that the solenoid core can generate a magnetic force several times larger than a permanent magnet core. However, the coil must be thermally insulated with a light and strong special cryostat because the current mode is established at very low temperature around liquid helium temperature. The discovery of high temperature superconductive materials will make the superconductive solenoid core more feasible.

By adjusting the coil current, the magnetic moment of the solenoid can be adjusted easily. It is very convenient to control the coil currents because the power units for driving the coils can be operated in similar conditions independently of the aerodynamic load. This means that the aerodynamic load can be measured accurately independent of the load magnitude.

A superconductive solenoid model was successfully suspended in the Southampton University's MSBS. The cryostat for the coil looks very complicated because it contains the solenoid plus various apparatus for gaseous helium exhaust and protection diodes against the quench and leads for large current and a switch for the permanent current mode change and support system for the solenoid inside the cryostat against the large magnetic force.

Because the required thickness of thermal insulation remains independent of scale, the solenoid diameter in the cryostat must become smaller rapidly as the cryostat diameter decreases. Then, the magnetic moment of the model core will be small at a small MSBS. If the model core diameter is 50 mm, the solenoid diameter is expected to be about 35 mm at most. If the core is 300 mm long, the solenoid length will be about 150mm at most. The attainable magnetic moment of the solenoid is not large enough that the magnetic force can suspend the model for the 60-cm MSBS. As a result, the cylindrical permanent magnet core is much better than the superconductive solenoid core for the 60-cm MSBS if the shape is limited to a suitable scale for aeronautical wind tunnel tests. In case of wind tunnel models like aircraft, the superconductive solenoid core will be suitable for a larger MSBS whose test section is above 1m at least. In the case of a thick body, the superconductive solenoid can still be available as a wind tunnel model core in smaller sized MSBSs.

MODEL CORES FOR THE HIGH REYNOLDS NUMBER SUPERSONIC WIND TUNNEL

The High Reynolds Number Supersonic Wind Tunnel

It is necessary to conduct wind tunnel tests at the same Reynolds number as in flight conditions in order to predict airplane performance from the obtained wind tunnel tests. Many wind tunnels have been designed to meet the conditions of Reynolds number match. Higher wind tunnel pressure provides higher Reynolds number flow generally. However, the aerodynamic load on the model becomes large in a highly pressurized wind tunnel, especially at transonic and low supersonic speeds. The load could exceed the limits of even mechanical support systems. The load also causes some distortion of the model shape.

Cryogenic wind tunnels were successfully designed and operated which can generate high Reynolds number flow by decreasing the fluid temperature in smaller test sections than ambient temperature wind tunnels. The dynamic pressure, which is proportional to the model load, remains independent of the temperature. Then cryogenic wind tunnels are very suitable for MSBSs. For example, in a low speed cryogenic wind tunnel, the fluid temperature is cooled to around 100K. Then the density becomes about three times as large as the ambient one at constant pressure. The viscosity of the fluid will become 0.38 times smaller than the ambient one. As a result the Reynolds number will become about 8 times as large as at ambient at the same flow speed if the pressure remains constant. However, the dynamic pressure will remain constant. So, the cryogenic wind tunnel is better in the sense of the model load than the pressurized wind tunnel. The fluid temperature ranges from 90 K to 150 K in the cryogenic wind tunnel. The low fluid temperature makes the cryostat thermal insulation thinner or the operation time of the cryostat longer in case of using the superconductive solenoid core. Also, the high temperature superconductive material will exaggerate the tendency much more because the temperature is around 100 K.

Magnetic Force Required at the Proposed Wind Tunnel

There are no high Reynolds number supersonic wind tunnels in the world presently. The Society of Japanese Aerospace Companies, Inc. proposed a high Reynolds number supersonic wind tunnel with a 1.25 m x 1.25 m test section.[10] This tunnel is a cryogenic one and the tunnel pressure ranges from 1 to 5 bar. The tunnel temperature is about 170 K at Mach number 2.0. Supposing a supersonic transport model for this tunnel, the fuselage will be 2000 mm long and about 91 mm in diameter. The attainable largest Reynolds number in the tunnel is still much lower than that of a proposed huge supersonic transport in flight.

We investigated the feasibility of a suitable superconductive solenoid core for this model. The aerodynamic load on the wind tunnel model will be 6000 N in lift and 900 N in drag. The aerodynamic moment about the model gravity center is estimated to be small because the core gravity center can be located at the aerodynamic load center. These values are estimated from the aerodynamic coefficients during the cruising flight. They are not so definite because the model attitude will be changed during the tests.

A Superconductive Solenoid Core

If the MSBS for the tunnel is two times as large as the 60-cm MSBS, the gradient of Hz and Hx with x will reduce to a quarter of the Hz and Hx of the 60-cm MSBS, respectively. Because the model is 2000 mm long, the winding length could become 900 mm at least. It is reasonable to be subdivided into three 300 mm long solenoids to avoid a single long solenoid. Judging from the fuselage diameter of 91 mm, the cryostat for the solenoid is about 87 mm in diameter. The solenoid diameter is 72 mm because thermal insulation must be installed between the solenoid and the cryostat shell. The cryostat is still 1200 mm in overall length because various apparatus for the superconductive solenoid and the gaseous helium exhaust system and so on must be included completely in a space of 300 mm long.

Supposing the NbTi superconductive solenoid of 900 mm long and 72 mm in outer diameter and 43 mm inner diameter and 45 kA/cm^2 current density, the magnetic forces are 550 N lift and 135 N drag forces in the 1.3-m MSBS, which is scaled up by two times of the 60-cm MSBS and the same coil turn number of electromagnets and power units. The obtainable forces are about 1/11 in lift and 1/7 in drag of the required

magnitudes. More efficient magnetic circuits, larger power units, and larger numbers of coil turns are required as the specifications of the new MSBS for the 1.25-m supersonic wind tunnel in addition to the higher performance of the superconductive solenoid core.

From the experience of designing the two MSBSs at NAL, the temporal goals of the improvement of the MSBS performance are chosen as shown in Table 4. The large increase in the coil turn number may cause some trouble in the cooling system of the coils and a huge inductance problem. A 600 ampere power unit for coil drive is sold by a company presently. The improvement of the magnetic circuit of the MSBS by 20% in its efficiency seems possible according to magnetic field simulation results. The remaining goal is the superconductive solenoid core with higher current density. The goals except the last one look very promising with commonly available technology.

the new MSBS for the proposed wind tunnel	
coil turn number of the lift coil	: 200 + 200
coil turn number of the drag coil	: 200
maximum current of the lift coil	: 600 A
maximum current of the drag coil	: 300 A
derivative of *Hz* with *x* at 600 A lift coil	: 91000 AT/m^2
derivative of *Hx* with *x* at 300 A drag coil	: 19800 AT/m^2
goal of the solenoid performance	
dimensions	: 72$^{\phi}$ mm x 42$^{\phi}$ mm x 300 mm x 3 pieces
current density	: 75 kA/cm^2
goal for the cryostat performance	
lifetime	: 2 hours

Table 4 Goals of the Model Core for the Proposed Wind Tunnel

A Prototype Superconductive Solenoid Core

A 900 mm long solenoid is too long for the MSBS. A superconductive solenoid core was designed and built in 1997 by Cryogenics Co., which is the same shape as the required one except its length as shown in Figure 10 and Table 5. The new cryostat is 600 mm long and the solenoid is 300 mm long. By examining the performance of the prototype solenoid core, the feasibility of the long core for the new MSBS will be studied. The solenoid is limited to 300mm which is as long as the permanent magnet core. The diameter of the core is 87mm which is the goal in Table 4. The superconductive material is NbTi and works at 4.2 K. The maximum magnetic moment is above 0.0047 Wb·m. The duration time of the persistant current mode is above 1 hour. For about 20 minutes, the operator must establish the permanent current mode and disconnect the liquid helium transfer tube and current leads. It will take 20 minutes to suspend the model magnetically and carry out some tests and capture the model by the model holding system. Next, the operator must connect the current leads and sink the current from the solenoid. The duration time seems long enough for the above mentioned procedure.

Magnet			
Field achieved in test at 4.2K	Specified: 6.5 T	Actual:	>6.5 T
Coil inductance:	Specified: N/A	Actual:	~7 H
Current density at 6.5T:	Specified: >25 kA/cm2	Actual:	45.1 kA/cm2
Calculated magnetic moment at 6.5T:	Specified: >0.0047 Wb.m	Actual:	0.0057 Wb.m
Magnet bore:	Specified: 35 mm	Actual:	43 mm
Overall diameter:	Specified: 75 mm	Actual:	72 mm
Overall length:	Specified: N/A	Actual:	348 mm
Winding length:	Specified: 300 mm	Actual:	300 mm
Distance from base to field center:	Specified: N/A	Actual:	156.5 mm
Cryostat			
Cryostat length:	Specified: 600 mm	Actual:	600 mm
Cryostat outside diameter:	Specified: 87 mm	Actual:	87 mm

Table 5 Superconductive solenoid core specifications for the 60-cm MSBS

All parts for the solenoid operation are installed completely inside a cylindrical region of 87 mm in diameter. This condition is necessary to install the cryostat into a wind tunnel model easily. The vaporized gas from the liquid helium is exhausted through a slender pipe periodically. During exhausting the gas, the aerodynamic forces cannot be measured because the flow around the model is disturbed by the exhausted gas jet. The solenoid will be immersed in the liquid helium. The pressure in the cryostat remains around 1 bar by exhausting the excessive gas. The mass of the cryostat is about 8 kg.

The magnetic force on the solenoid can be evaluated from the measured magnetic field in the 60-cm MSBS. The obtained results are plotted in Figure 11. Even at the very low current density of the solenoid, the magnetic lifting force is enough to lift up the cryostat as shown in the figure.

Next Step for the Superconductive Solenoid Core

As mentioned as goals for the solenoid performance in Table 4, the required solenoid is 3 times as long as the present solenoid and the current density is also 3 times as large as the present one. The elongation of the solenoid seems easy because the three present solenoids can be lined up in a new long cryostat. The goal of the current density is 75kA/cm2. It appears impossible to accomplish this value by using the NbTi superconductive material. Other material like Nb_3Sn or Nb_3Al will be needed. However, just improving the material is not enough to reach the goal. One of the solutions may be to operate the solenoid at a much lower temperature, around 1K, by the use of ^3He. Other is to redesign the cryostat to make the solenoid as large as possible.

The strong magnetic field generated by the solenoid may magnetize the iron rings of the MSBS unexpectedly if it is too strong. It could be very dangerous for the suspended model because the magnetic field may become uncontrollable by the unexpected magnetization. The estimated magnetic field induced by the solenoid will change by concentrating the magnetic flux at the ferromagnetic materials in the magnetic field. In order to avoid this phenomenon, it is best not to use the electromagnets for the MSBS. Much iron material is used for the iron rings at the 60-cm MSBS. The magnetic field induced by the solenoid must be sufficiently weak around the ferromagnetic materials like the iron coil cores not to be

magnetized strongly. This means there is an upper limit value of the current density for the solenoid of the 60-cm MSBS. This effect will be much reduced for the larger MSBS because the magnetic field intensity induced by the solenoid reduces rapidly in inverse proportion to the square of the distance between the solenoid and the ferromagnetic material.

CONCLUDING REMARKS

The original model position sensing system was improved by adding another sensing camera mounted at the upper side of the 60-cm MSBS. Measured y coordinate and yawing angle, ψ,of the model are as accurate as the other measured positions like the z coordinate with the original sensing camera mounted on the side of the MSBS.

The 60-cm MSBS is equipped with a model holding system in order to release safely and hold the suspended model. This system is inevitable for tests of a superconductive solenoid core because it is very dangerous to put the excited solenoid on a stand in the MSBS manually. The system is used to hold and release a permanent magnet cored model presently.

The model holding system is equipped with a model load monitoring system. The system can measure the load at various coil currents at various model positions.

It is impossible to build a suitable sized superconductive solenoid for the 60-cm MSBS because the solenoid inside the cryostat must be too small.

A cylindrical model core of Alnico magnet is the most suitable of available permanent magnets for the 60-cm MSBS. The attainable net lifting force is up to 17N with 130A lifting coil current. A model must be designed within the gravity force of 17 N except for the core weight.

The cryogenic wind tunnel has a much smaller test section and smaller dynamic pressure than other ambient temperature wind tunnels when they generate the same Reynolds number flow in their test sections. These features of the cryogenic tunnel is very suitable for the MSBS. Besides, the low temperature of the fluid is good for the cryostat of the superconductive solenoid. The MSBS is a very attractive system, especially for the cryogenic high Reynolds number supersonic wind tunnel.

A superconductive solenoid core for the cryogenic high Reynolds number supersonic wind tunnel is specified. As a first step to make the solenoid, a 300 mm long superconductive solenoid core was designed and built in 1997. The dimensions of the cryostat are 87 mm in diameter and 600 mm long and below 8 kg in mass. The NbTi superconductive solenoid is 72 mm in diameter and 300 mm long and 45 kA/cm^2 at highest current density. The solenoid is immersed in liquid helium at around 4.2 K. The lifetime is about 1 hour. The largest magnetic lifting force is estimated at 500 N at the 60-cm MSBS although it has not been examined at NAL.

We plan to examine the performance of the superconductive solenoid and the cryostat and the suspension performance in the near future.

REFERENCES

1. H.Sawada, H.Kanda, and H.Suenaga : "The10cm x 10cm Magnetic Suspension and Balance System at the National Aerospace Laboratory." AIAA 91-0397, 1991
2. H.Sawada and H.Suenaga : "Status of MSBS Study at NAL", NASA CP 3247, 1994, pp. 275-289

3. H.Sawada and H.Suenaga : "Magnetic Suspension and Balance Systems at NAL." Pacific International Conference on Aerospace Science and Technology, Conference Proceedings Vol. 2, 1993, pp. 1014-1021
4. H.Sawada, H.Suenaga and T.Kohno : "Status of MSBS Study at NAL in 1995." NASA CP 336, 1996, pp. 505-519
5. C.P.Britcher : "Progress Toward Magnetic Suspension and Balance Systems for Large Wind Tunnels." Journal of Aircraft, Vol. 22, No. 4, April, 1995 pp. 264-269
6. J.Eskins : "Further Investigation into Calibration Techniques for a Magnetic Suspension and Balance System." NASA CR-178056, 1986
7. R.W.Boom, M.K.Abdelsalam, Y.M.Eyssa, and G.E.McIntosh : "Magnetic Suspension and Balance System Advanced Study-Phase II." NASA CR 4327, 1990
8. M.J.Goodyer : "Southampton University's Contributions to the Technology of Magnetic Levitation Applied to Wind Tunnel Testing." Pacific International Conference on Aerospace Science and Technology, Conference Proceedings Vol. 2, 1993, pp. 1006-1013
9. C.P.Britcher : "Large Superconductive Model Core Developed by Madison Magnetics." MSBS News Letter edited by R.Kilgore, No. 7, June, 1990, pp. 3
10. Sawada, K. Suzuki, A. Hanzawa, T. Kohno, and T. Kunimasu: "The NAL 0.2m Supersonic Wind Tunnel." NAL TR-1302T, July, 1996

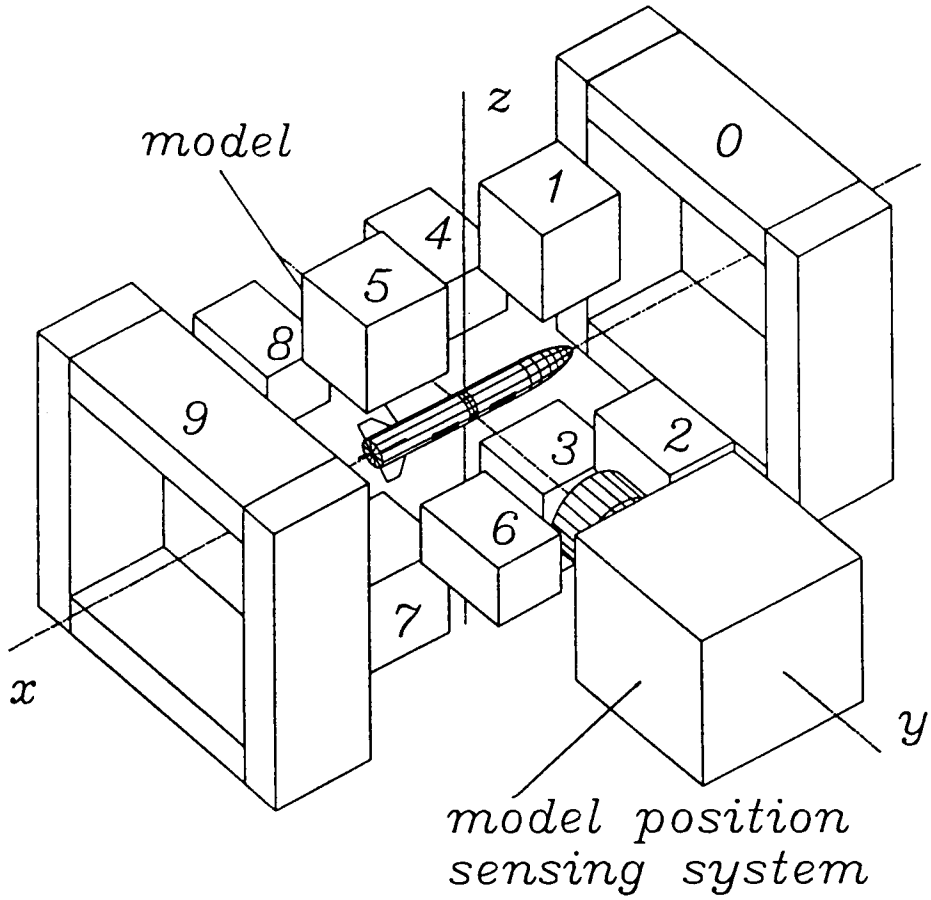

Figure 1 Coil Arrangement of the NAL 60-cm MSBS

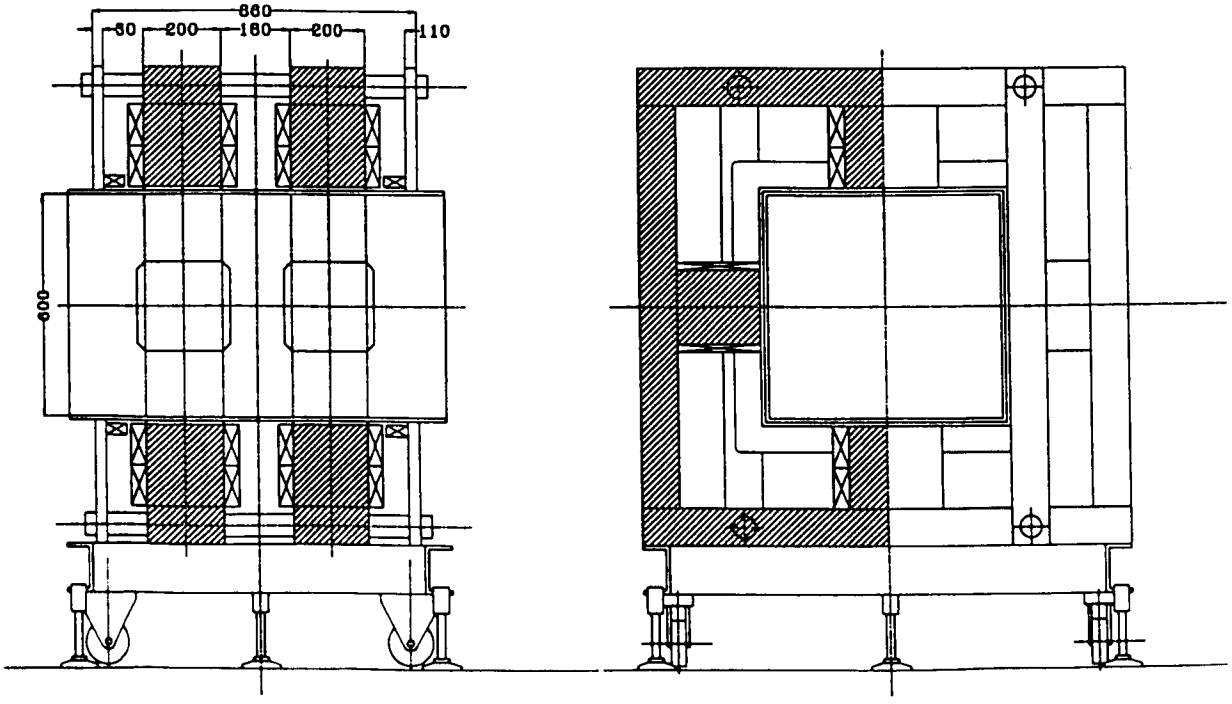

Figure 2 The 60-cm MSBS

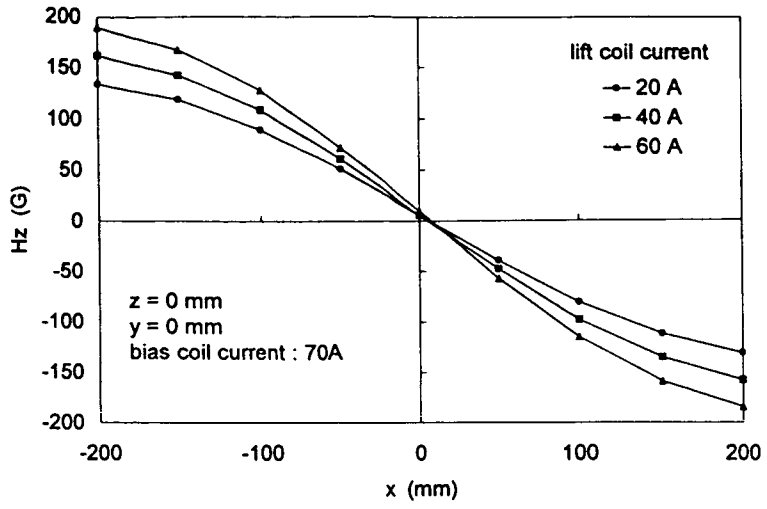

Figure 3 *Hz* Measured in the 60-cm MSBS

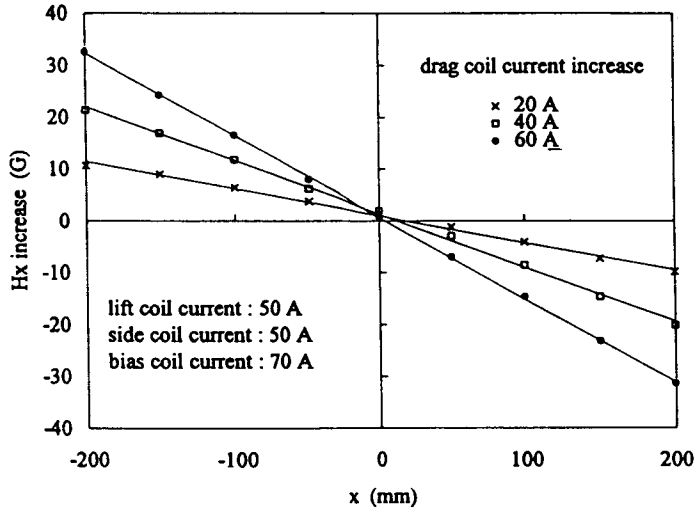

Figure 4 *Hx* Measured in the 60-cm MSBS

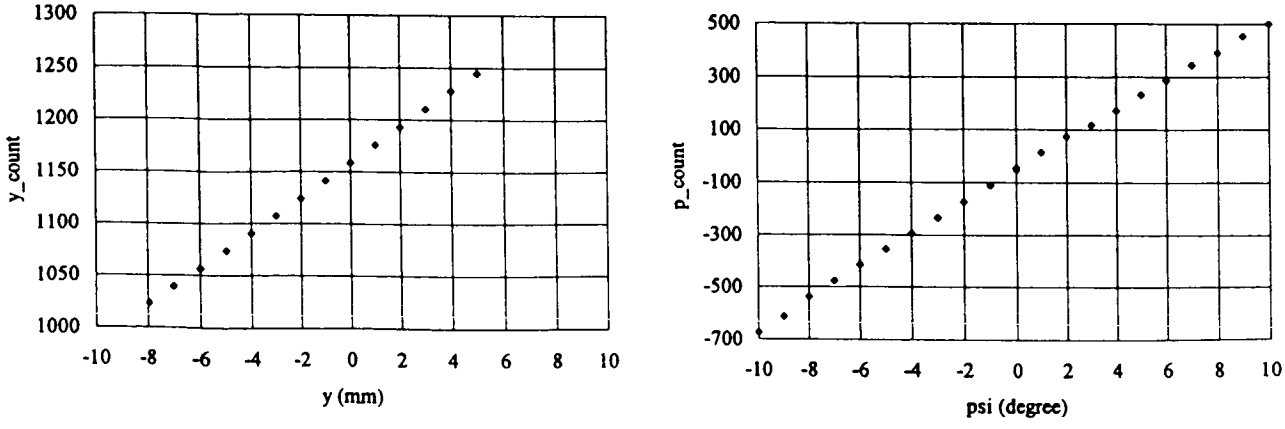

Figure 5 Calibration Test Results of the Improved Model Position Sensing System

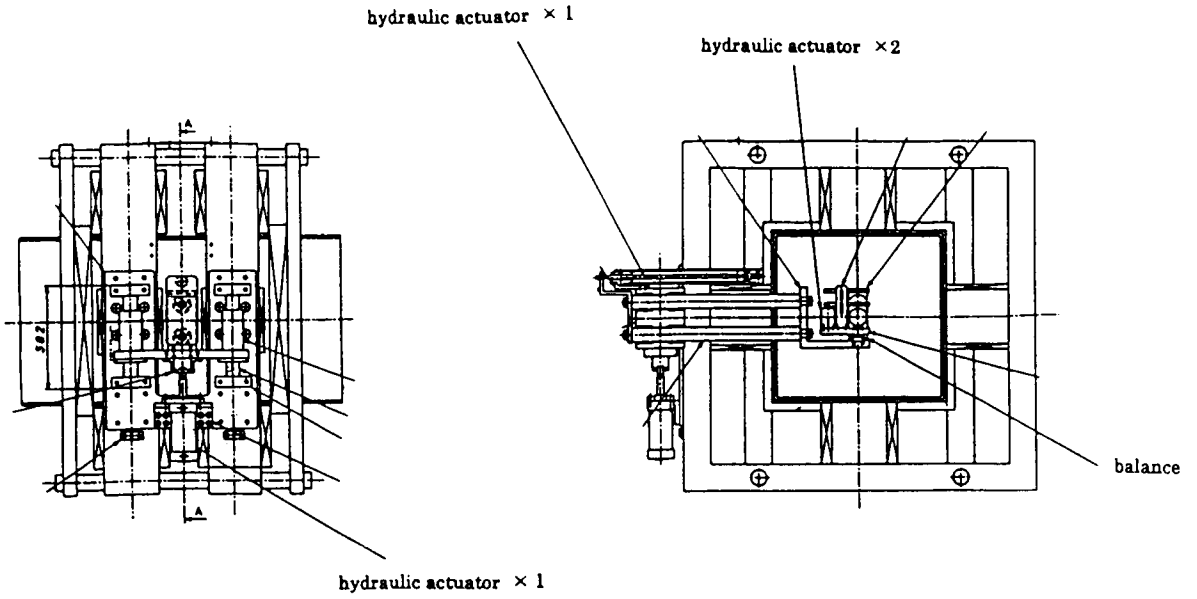

Figure 6 Model Holding System

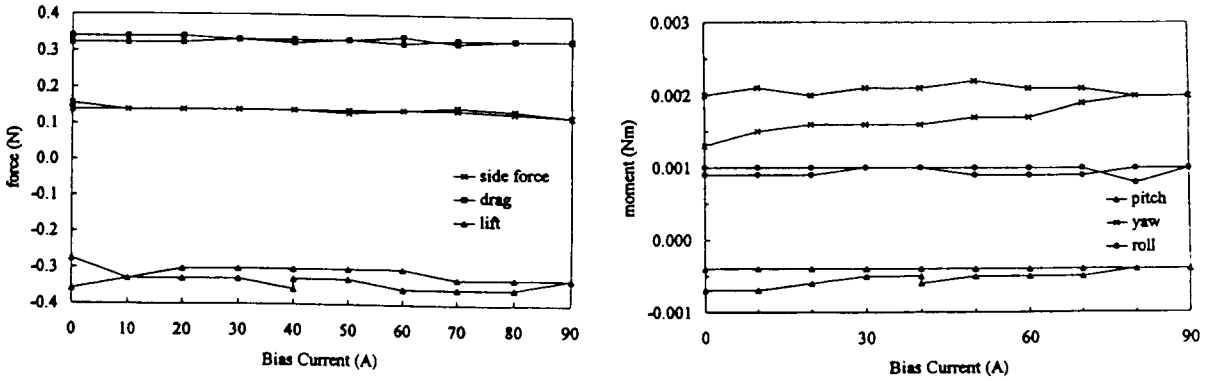

Figure 7 Model Holding System Effect on the Balance Output

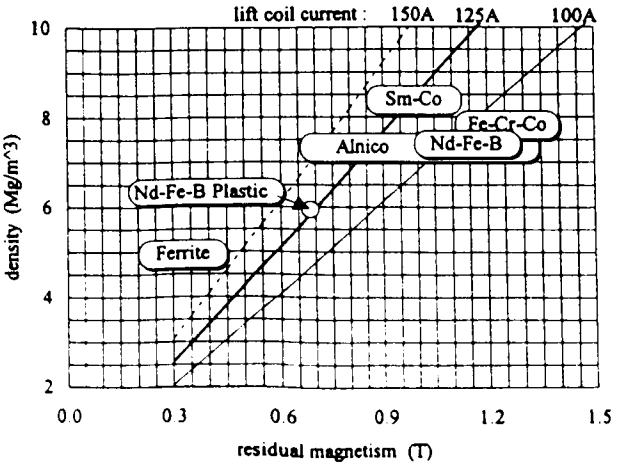

Figure 8 Performance of The Permanent Magnet Core for the 60 cm MSBS

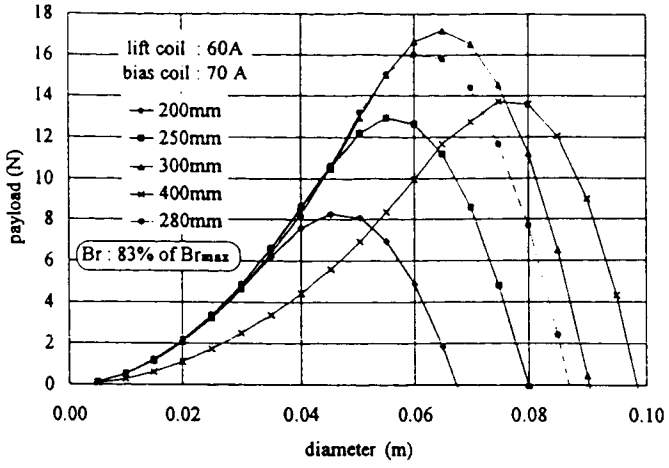

Figure 9 Alnico Magnet Performance at the 60-cm MSBS

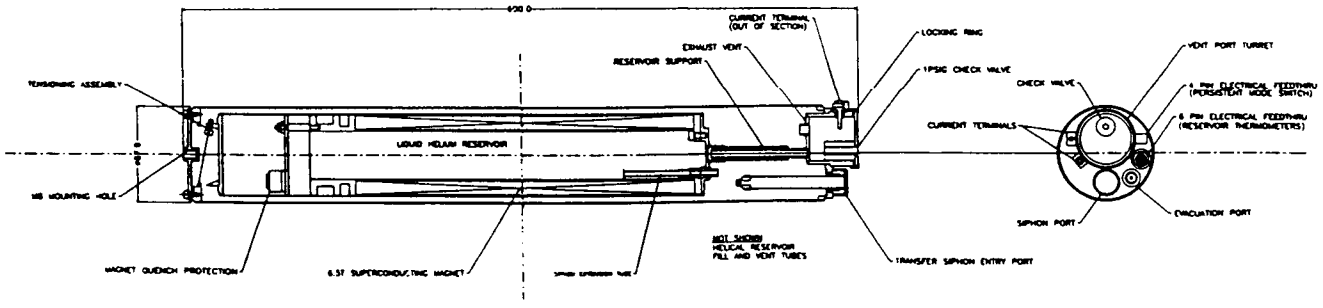

Figure 10 The Superconductive Solenoid Core for the 60-cm MSBS

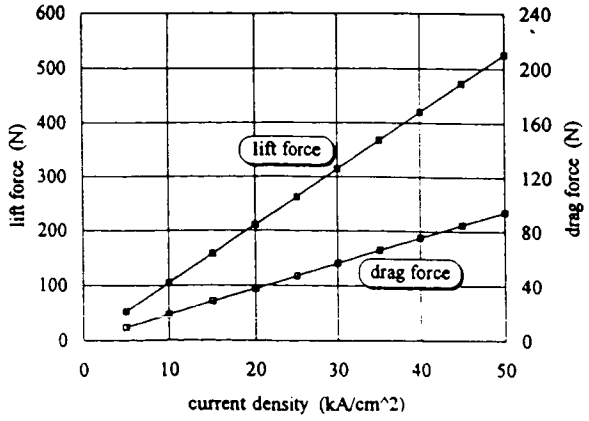

Figure 11 The Evaluated Magnetic Force Acting on the Superconductive Solenoid

NONLINEAR ROBUST CONTROL AND ITS APPLICATION TO MAGNETIC SUSPENSION TECHNOLOGY[1]

Victor S. Voronkov
Research Institute for Applied Mathematics and Cybernetics (NII PMK)
of Nizhny Novgorod State University, Nizhny Novgorod, Russia

SUMMARY

Nonlinear robust control is a development of the modern robust approach to the stability of linear control systems. For nonlinear systems, this approach was used in the theory of absolute stability. The absolute stability methods are bounded as a rule by the class of stable SISO-objects. However, magnetic suspension technology deals with unstable and MIMO-objects in the general case.

Design of stabilizing systems for magnetic suspension may effectively be carried out on the basis of a proposed approach to nonlinear robust control synthesis. The proposed approach is based on the criterion of the Maximum Region of Attraction for stabilizing equilibrium in the phase space of a closed loop system. Actually the same criterion is used in absolute stability theory whose methods allow relation of the topological identity, the phase space structure of the system with the nonlinear control, to the phase space structure of the linear system.

The analytical solution of the synthesis problem in a form of a nonlinear robust control law allows the determination of the dependence of the optimal regulator's structure and parameters from the objects. The theoretical background of using regulators has been added to the base of the proposed synthesizing approach and new nonlinear robust control laws for stabilizing magnetic suspension systems have been found.

One of the new control laws is the control of angular motion of a shaft in magnetic bearings with gyroscopic effects. Finding this law required the development of the suggested approach from unstable to stable objects having conservative stability.

INTRODUCTION

Taking into account the realistic restrictions of the control action makes a mathematical model of a stabilizing system nonlinear. It results in an attractive region concept for a stabilizing equilibrium in the phase space of a closed loop system. In a nonlinear system, unstable periodic motions are the main cause of inadmissible reduction of a region of attraction, as shown in [1].

In order to avoid these unstable periodic motions, the original approach to synthesizing control laws for unstable objects is suggested in [2]. In this approach, the control law is synthesized from the criterion of attaining the Maximal Region of Attraction (MRA-criterion) of stabilizing equilibrium in the phase space of a closed loop system.

[1] This research has been done under support from the RBRF (project 97-01-00669)

The synthesizing results give the theoretical background for many regulators used in magnetic suspension technology [3]. As shown in [4] for the simplest magnetic suspension, a control synthesized from MRA-criterion satisfied a number of conventional quality performance criteria simultaneously.

The shaft magnetic suspension attracts researchers [5] by its practical significance and as a more complex object having a control system which stabilizes the shaft position in three translational degrees of freedom and two angular ones. Synthesis of nonlinear robust control of a shaft magnetic suspension has been done in [6] using a series of simplifying suppositions. One of these suppositions is the neglect of the gyroscopic effect. As shown in [7], increasing the shaft rotation speed leads to stability loss of the magnetic suspension stabilizing system. In order to account for the gyroscopic effect one may accept the simplified supposition about consideration of only angular degrees of freedom of the shaft with respect to its mass center for synthesis of restricted control of the shaft magnetic suspension with accounting for the gyroscopic effect.

PROBLEM STATEMENT

Under the accepted supposition, the shaft in the Active Magnetic Bearings (AMB) may be considered as a solid with the fixed point as shown in Fig. 1. The fixed point O of the shaft coincides with its mass center. The origin of the fixed coordinate system O, ξ, η, ζ is placed at this point. The mobile coordinate system O, ξ', η', ζ' is connected with the principal axes of the shaft and axis O, ζ' is directed along the axis of its rotation. The position of this axis is given by angles θ_1, θ_2 in the fixed coordinate system. The control forces from AMB $F_{1\text{-}4}$ are found in two planes where the AMB are placed as shown in Fig. 1. Let these planes be placed symmetrically with respect to point 0 at the distance $\pm l/2$.

In the case of small angles, the shaft dynamics are given by following equations

$$J\frac{d^2\theta_1}{dt^2} + J_\zeta\Omega\frac{d\theta_2}{dt} - \frac{al^2}{4}\theta_1 = -\frac{l}{2}(F_1 - F_3)$$

$$J\frac{d^2\theta_2}{dt^2} - J_\zeta\Omega\frac{d\theta_1}{dt} - \frac{al^2}{4}\theta_2 = -\frac{l}{2}(F_2 - F_4)$$

where $J_\xi = J_\eta = J$, J_ζ are the moments of inertia for the axial symmetrical shaft with respect to principal axes, Ω is the angular speed of the shaft, supposed as constant, m is the mass of the shaft, a is the negative stiffness of the AMB, l is the distance between planes of top and bottom AMB. It is supposed also that control actions are restricted $|F_{\xi,\eta}| \le F^*$.

By introduction of the time scale $t_m = \sqrt{\frac{4J}{al^2}}$ the mathematical model of the control object may be presented in the standard dimensionless form

$$\frac{d\mathbf{x}}{dt} = \mathbf{A}\mathbf{x} + \mathbf{B}\mathbf{u} \tag{1}$$

$$\mathbf{A} = \begin{pmatrix} 0 & 1 & 0 & 0 \\ 1 & 0 & 0 & -H \\ 0 & 0 & 0 & 1 \\ 0 & H & 1 & 0 \end{pmatrix}, \quad \mathbf{B} = \begin{pmatrix} 0 & 0 \\ -1 & 0 \\ 0 & 0 \\ 0 & -1 \end{pmatrix}.$$

$$|u_{1,2}| \le u^+,$$

where the vector of phase coordinates has the following components:

$$x_1 = \theta_1, \quad x_2 = l_m \frac{d\theta_1}{dt}, \quad x_3 = \theta_2, \quad x_4 = l_m \frac{d\theta_2}{dt}.$$

$H = \frac{J_\xi \Omega l_m}{J}$ is a parameter describing the ratio of the inertia moments of the shaft and the rotation speed, $u_1 = \frac{F_\eta l_2}{mgl_1}$, $u_2 = \frac{F_\xi l_2}{mgl_1}$ are the control actions restricted by the magnitude $u^+ = \frac{F^+ l_2}{mgl_1}$ Using the symmetry of equations (1) allows us to reduce its order in half by the complex variables

$$z_1 = x_1 + ix_3; \quad z_2 = x_2 + ix_4; \quad v = u_1 + iu_2, \tag{2}$$

where $(i = \sqrt{-1})$. As a result the mathematical model of the object may be presented either in the standard form of the complex phase space

$$\frac{d\mathbf{z}}{dt} = \mathbf{A_c z} + \mathbf{B_c} v, \tag{3}$$

$$\mathbf{A_c} = \begin{pmatrix} 0 & 1 \\ 1 & iH \end{pmatrix}, \quad \mathbf{B_c} = \begin{pmatrix} 0 \\ -1 \end{pmatrix},$$

or as a differential equation of second order

$$\frac{d^2 z_1}{dt^2} - iH \frac{dz_1}{dt} - z_1 = -v \tag{4}$$

with respect to the complex variable z_1. These equations contain the complex function of admissible controls v, whose components $u_1 = Rev$, $u_2 = Imv$ are supposed as the simplest piece-wise linear functions as shown in Fig. 2

$$\begin{aligned} &\mathbf{u} = \beta\sigma, |\beta\sigma| \le u^+, u_{1,2} = u^+, \beta\sigma \ge u^+, \\ &u_{1,2} = -u^+, -u^+ \ge \beta\sigma, \quad \sigma = \mathbf{C(H)x}, \end{aligned} \tag{5}$$

where β is some scalar and C(H) is some feedback control matrix which depends on H. The problem consists in synthesizing this function as some dependence from the state space variables of the object which provides a stabilization of the axis shaft vertical position under the maximal admissible initial departures in the phase coordinates for given control restrictions or under the minimal admissible control restrictions for given angular initial departures of the shaft. In this case the quality control performance will be some optimal structure of the phase space for the closed loop system.

LINEAR ANALYSIS OF UNCONTROLLED OBJECT

Synthesis of a control law from the MRA-criterion is carried out based on the eigen-motions for an uncontrolled object. These motions are given by the eigenvalues of matrix A_c, or by the roots of a characteristic equation for an uncontrolled object (3), (4)

$$\chi(\lambda) = \lambda^2 - iH\lambda - 1 = 0$$

The solution of this quadratic equation has the following analytical expression

$$\lambda_{1,2} = \frac{1}{2}(iH \pm \sqrt{4 - H^2}) \tag{6}$$

The dependence of the roots (6) from the parameter H is illustrated by the upper half complex plane in Fig. 3. The dependence of the complex conjugate roots to (6) and noted by sign (*) is shown in the bottom half of this plane. The whole Fig. 3 shows the dependence of the matrix A eigenvalues from the parameter H for object (1). The following specific points in this dependence conforming to the behavior of the roots may be stated. The first point conforms to the shaft without rotation when $H = 0$ and

$$\lambda_1 = \lambda_1^* = 1, \quad \lambda_2 = \lambda_2^* = -1.$$

In this case, there are two positive eigenvalues of the matrix A that relate to instability of the nonrotational shaft due to a negative stiffness of AMB. The second specific point conforms to the beginning of the shaft gyroscopic stabilization when $H = 2$ and

$$\lambda_1 = \lambda_2 = i; \quad \lambda_1^* = \lambda_2^* = -i.$$

In this case, all eigenvalues of the matrix A are imaginary ones and the shaft has conservative stability. The portions of the dependence $\lambda(H)$ which characterizes the stability of the control object may also be deduced. The first portion conforms to the range (0,2) of parameter H. This portion is characteristic of the object instability as far as the roots (6) in this case

$$\lambda_1 = r + i\frac{H}{2}, \quad \lambda_1^* = r - i\frac{H}{2} \tag{7}$$

have the positive real part $r > 0$. The second portion conforms to the range $H \geq 2$. It is characteristic of the object's conservative stability. In this case, all eigenvalues of the matrix A are imaginary ones

$$\lambda_1 = i\omega_P, \quad \lambda_1^* = -i\omega_P, \quad \lambda_2 = i\omega_N, \quad \lambda_2^* = -i\omega_N. \tag{8}$$

where ω_P and ω_N denote the precessional and nutational frequencies of the high rotational speed shaft. For $H > 1$ these frequencies are approximately equal to $\omega_P = 1/H$, $\omega_N = H$. By this means, the studied problem deals with the object with stability without control dependencies from one parameter H. Parameter H characterizes the shaft rotational speed which may be changed from zero to some final value H_m. It is proposed that the point $H = 2$ lies within the range of the admissible values of this parameter. In this case, the changing range of parameter H is divided in two parts on indication of the object stability. The object is unstable when $0 \leq H < 2$, and it has conservative stability when $H \geq 2$.

SYNTHESIZING A NONLINEAR ROBUST CONTROL OF THE UNSTABLE SHAFT

The optimum structure of the closed loop system phase space is the nonlinear robust control performance providing the fulfillment of the MRA-criterion. Synthesis of a nonlinear robust

control for an unstable shaft is carried out using the approach suggested in [2]. With respect to this approach the equations (3) are transformed to canonical form

$$\frac{dy}{dt} = \Lambda y - v$$

where A is the Jordan form of the matrix A_c. This transformation may be carried out by means of a linear transformation of variables

$$y = Dx, \quad D = \begin{pmatrix} 1/\lambda_1 & 1 \\ 1/\lambda_2 & 1 \end{pmatrix}$$

Next is separated the unstable part of the object conforming to the matrix A_c eigenvalue having the positive real part

$$\frac{dy_1}{dt} = \lambda_1 y_1 - v \tag{9}$$

where $y_1 = \frac{z_1}{\lambda_1} + z_1$ is the unstable variable of the object. Nonlinear robust control v is synthesized in a class of the simplest piece-wise linear functions (5) satisfying the following conditions [2]:

a) dependence of control upon unstable variable only; b) asymptotic stability of the system's unstable part under this control. If the control dependence from the feedback signal in a linear area control function is

$$v = \beta\sigma, \quad \sigma = \lambda_1 y_1, \quad \beta > 1 \tag{10}$$

then these conditions are satisfied. The transition from variables y to variable x in this dependence by the use of (2), (7) defines the feedback matrix in (5)

$$\mathbf{C}_1(\mathbf{H}) = \begin{pmatrix} 1 & r(H) & 0 & -\frac{H}{2} \\ 0 & \frac{H}{2} & 1 & r(H) \end{pmatrix} \tag{11}$$

for nonlinear robust control of the unstable shaft when $0 \le H < 2$. The results of the changing roots within the parameter range $0 \le H < 2$ is shown in Fig. 3 by dashline for different values of parameter β.

SYNTHESIZING A NONLINEAR ROBUST CONTROL UNDER SHAFT GYROSCOPIC STABILIZATION

In case of sufficiently great angular momentum of the shaft ($H \ge 2$), i.e. when the gyroscopic stability condition is fulfilled, the control's main goal is provision of the asymptotical attenuation for undamping precessional and nutational modes of the appropriate frequencies ω_P, ω_N. The best control performance may be achieved also by the use of MRA-criterion under the synthesis problem solution. Only in contrast to the unstable object having the bounded region of controllability in this case the maximal region of attraction is coincident with the whole phase space. In this case a robust indication of synthesis of control with respect to an uncertainty of its nonlinear characteristic will be the absolute stability [8] of a closed loop system. For synthesis of

control providing the system absolute stability in some class of nonlinear functions it is comfortable to use the object mathematical model (4) and to carry out the variable substitution to a rotational coordinate system

$$z_1 = wexp(i\omega t) \tag{12}$$

where ω is a new complex variable which change in time takes place with some cycle frequency ω. In new variables, equation (4) has a view of an undamped oscillator also

$$\frac{d^2w}{dt^2} + i(2\omega - H)\frac{dw}{dt} + k(\omega)w = vexp(-i\omega t) \tag{13}$$

At the same time its natural frequency

$$k(\omega) = H\omega - \omega^2 - 1 > 0 \tag{14}$$

in the contract to (4) may be positive explicitly. Really, inequality (14) is fulfilled under the gyroscopic stabilization condition if the cycle frequency in (12) is chosen within the range $[\omega_P, \omega_N]$ determined by the cycle frequencies of the shaft precession and nutation. It is illustrated by dependence $k(\omega)$ shown in Fig. 4 under condition $H > 2$. The values of the natural frequencies ω_P, ω_N are given by the intersecting points of the curve $k(\omega)$ with the abscissa axis. The choice of the cycle frequency value in the variable substitution (12) is realized in the maximum point of this dependence $\omega = \omega_m = \frac{H}{2}$ when $k(\frac{H}{2}) = \frac{H^2}{4} - 1$. For achievement of the system (13) absolute stability, i.e. for obtaining transient asymptotical stability and of the equilibrium state uniqueness (placed in the origin), control action is chosen as a monotone function from only a variable velocity

$$vexp(-i\omega t) = u(\frac{dw}{dt}). \tag{15}$$

For the simplest piece-wise linear functions (5), i.e. the linear functions with restrictions on the level u^+, it is not difficult to show that the absolute stability condition for the closed loop system (13), (15) is fulfilled. The coefficient β value must be sufficiently great with the aim of transient velocity increasing and of its aperiodicity. Therefore the choice of this coefficient value is accomplished from an aperiodicity transient condition

$$\beta \geq \frac{1}{2}\sqrt{k(\frac{H_m}{2})} \tag{16}$$

in the closed loop system for any values of parameter H from the range $2 < H \leq H_m$. To obtain the control as seen in (5) the inverse variable substitution

$$\frac{dw}{dt} = (\frac{dz_1}{dt} - i\omega z_1)exp(-i\omega t)$$

and transition from complex variable z_1 to variables x is fulfilled. As a result the feedback matrix

$$C_2(H) = \begin{pmatrix} 0 & 1 & \frac{H}{2} & 0 \\ -\frac{H}{2} & 0 & 0 & 1 \end{pmatrix} \tag{17}$$

for the absolute stability system of the high rotational speed shaft control is determined.

PHASE SPACE STRUCTURE OF SYNTHESIZED SYSTEM

The phase space structure of the synthesized system is optional from the MRA-criteria for nonlinear robust control. The view of these maximal regions of attraction for synthesized systems depends on the parameter H value. The phase space structure is considered for three specific values of this parameter: $H = 0$; $0 < H < 2$; $H \geq 2$. The first two cases conform to the unstable object. In these cases the phase plane of the systems unstable parts gives an indication of the whole four-dimensional phase space structure of the closed loop system [2]. In the case of nonrotational shaft (when $H = 0$ and there are two coinciding positive roots $\lambda_1 > 0$) the structure of the unstable variables y_1^+, y_2^+ is shown in Fig. 5a. In the case of a slowly rotating shaft (when $0 < H < 2$ and there are two complex conjugate roots λ_1, λ_1^* with positive real parts) the structure of phase plane for the real and imaginary parts of the unstable variable y_1 is shown in Fig. 5b. The bounded maximal region of attraction for stabilizing equilibrium is the specific feature of the phase space structure in these cases. The third case of the high rotational speed shaft conforms to its conservative stability. In this case the closed loop system under the proposed control embodies absolute stability. The phase space structure of that system is topologically equivalent to the structure of the four dimensional stable linear system.

CONCLUSION

The analytical expression of the nonlinear robust control law adapted to shaft rotational speed is obtained. This expression coincides with one obtained earlier for the nonrotational shaft and shows the differences arising from accounting for gyroscopic effects. These specifications consist of the appearance of the cross feedbacks in the control for each angle and radical distinctions of the control law from and relating to the gyroscopic stabilization. The control law is suddenly changed in the point $H = 2$ that takes into account sudden changing of the object stability property. Obtaining this solution became possible due to use of the unified MRA-criterion and made it possible to obtain the nonlinear robust control. The obtained control robustness resides in the maximal region of attraction under the nonlinear control function uncertainty given by the Hurwitz angle. By this means the robust approach widely used in the stability theory of linear systems at present has been successfully developed for nonlinear systems. For the objects having a conservative stability the nonlinear robust control is the development of absolute stability theory.

ACKNOWLEDGMENT

The author is thankful to Prof. G. G. Denisov for useful discussions and remarks of that problem.

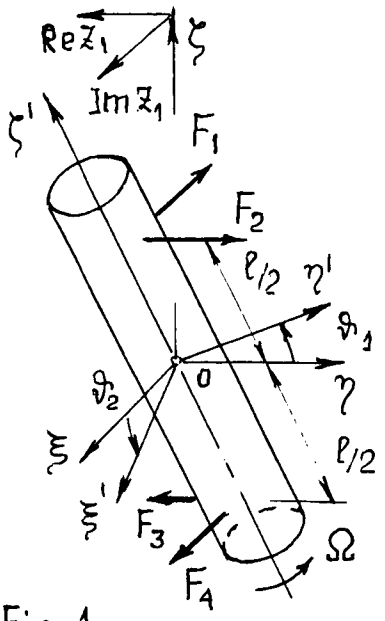

Fig. 1

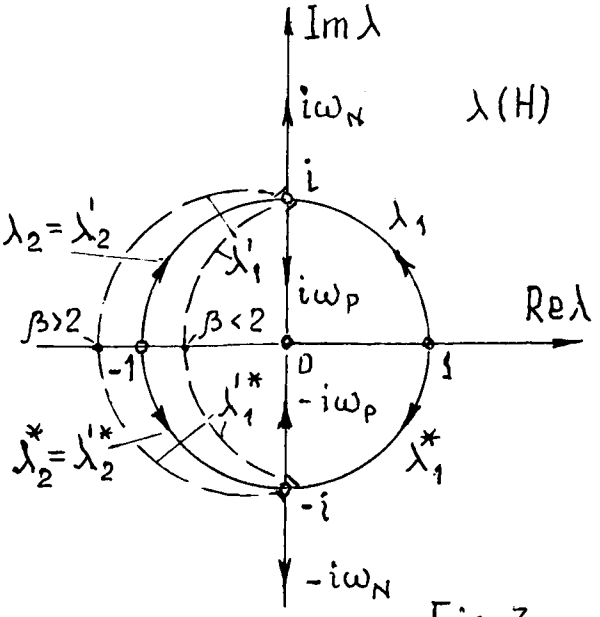

Fig. 3

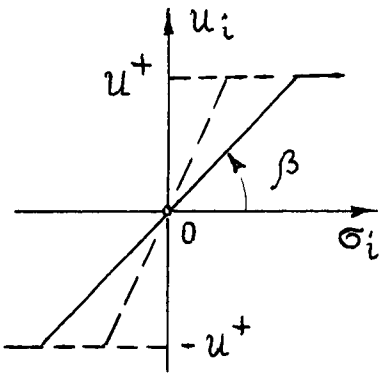

Fig. 2

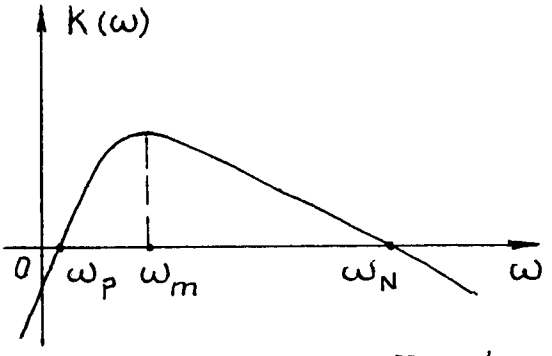

Fig. 4

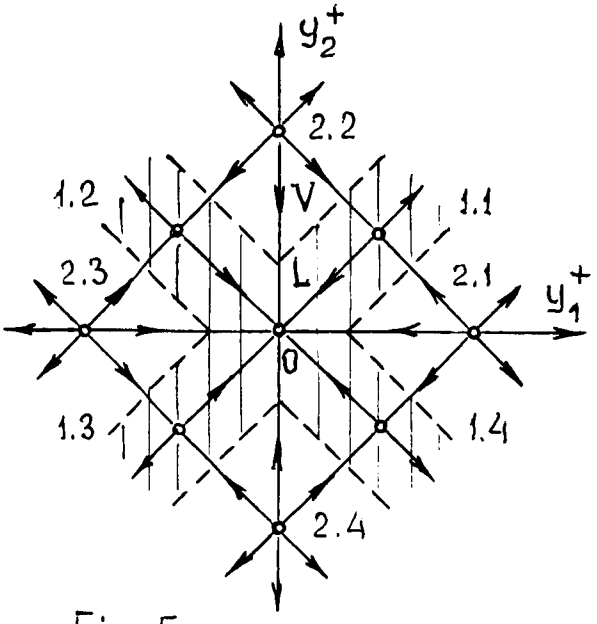

Fig. 5 a

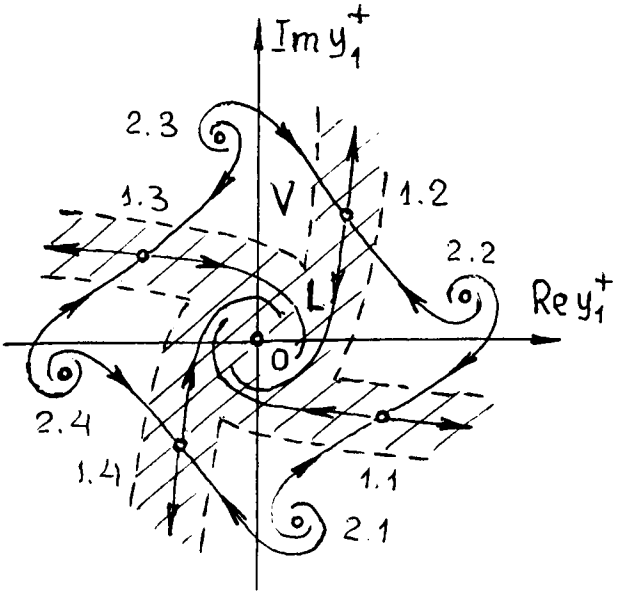

Fig. 5 b

REFERENCES

1. Voronkov, V.S.; Pozdeyev, O.D.: Research of Systems for Stabilizing a Magnetic Bearings. *Mechanics of Solid*, No. 4, 1980, pp. 30-39.

2. Voronkov, V.S.: Synthesizing of Robust Nonlinear Control for Unstable Objects. *Journal of Computer and Systems Sciences International*, No. 6, 1996, pp. 58-66.

3. Kuzin, A.V.: Progress of Magnetic Suspension Systems and Magnetic Bearings in USSR. *Proceedings of International Symposium on Magnetic Suspension Technology.* NASA CP-3152, 1992, pp. 331-359.

4. Belova, E.V.; Voronkov, V.S.: The Quality Performances of Synthesizing Control Laws for an Unstable Object From the Criterion of Obtaining the Maximum Region of Attraction. *Proceedings 3rd International Conference on Motion and Vibration Control,* Tokyo: JSME, Vol. 3, 1996, pp. 455-459.

5. Schweitzer, G.; Bleuler, H.; Traxler, A.: *Active Magnetic Bearings*, Zurich: ETH, 1994.

6. Voronkov, V.S.: The Shaft Stabilization in Active Magnetic Bearings. *Mechanics of Solid*, No. 4, 1991, pp. 63-70.

7. Voronkov, V.S.; Gryaznov, K.V.; Gryaznova, N.Yu.: Robustness of the Stabilizing System in the Magnetic Suspension of a Rotating Shaft. *Proceedings 4th International Symposium on Magnetic Bearings.* Zurich: ETH, 1994, pp. 41-45.

8. Aizerman, M.A.: *Theory of Automatic Control.* Moscow: "Nauka", 1966.

EFFICIENT METHOD OF FORCE CALCULATION FOR BIASED MAGNETIC BEARINGS

Maciej Hippner
University of Natal
Durban, South Africa

Zbigniew Piech
United Technologies Research Center
East Hartford, CT, USA

SUMMARY

Magnetic field in biased radial magnetic bearings is of a three dimensional nature. This means that if a high accuracy is required, design, analysis, and performance calculations of such a bearing would call for a three dimensional (3-D) finite element analysis. Unfortunately 3-D finite element analysis is both time consuming and requires significant computer resources. For force (load) calculation purposes, this 3-D problem can be reduced to a two dimensional one. Such a move significantly reduces both time required to design a finite element model as well as the solution time. It also opens new opportunities e.g. makes parametric analysis and optimisation of the bearing much more viable. The proposed method was verified on a prototype high speed (35,000 rpm, 125 lb) homopolar radial magnetic bearing with a permanent magnet bias. Force acting on the rotor of the bearing was calculated using both 3-D and 2-D finite element models of the magnetic bearing. The values obtained from the FE analysis were compared with the force measured on the prototype bearing. The agreement between the calculated and measured values was very good.

INTRODUCTION

A magnetic bearing system can be advantageous for rotating machinery due to the absence of mechanical wear, elimination of lubricating oil, and ability to operate at higher speeds than mechanical bearings. The forces required to support the rotating shaft are developed by an electromagnetic actuator, typically a part of a feedback control system. The electromagnetic actuator of a magnetic bearing has a rotating member (rotor) and a stationary member (stator) concentrically located with respect to each other. The rotor may be located concentrically internal or external to the stator. A magnetic bearing uses adjustable electromagnetic force generated by a current flowing through coils wrapped around the stator poles and controlled by a control circuit, to adjust the distance between the stator and rotor. Also, proximity sensors are typically used to measure the length of the gap and to provide input signals to the control circuit. In addition to the variable electromagnetic control flux, a magnetic bearing may also have a constant DC bias flux, which premagnetizes the working air gaps to a specified level of the magnetic flux density. The bias linearizes the control laws of the bearing. In some configurations, with a homopolar bias, a permanent magnet can be used to provide the bias flux, eliminating the ohmic losses associated with the bias coils.

Magnetic drag and iron losses are created whenever the rotor rotates within a spatially varying magnetic bias.

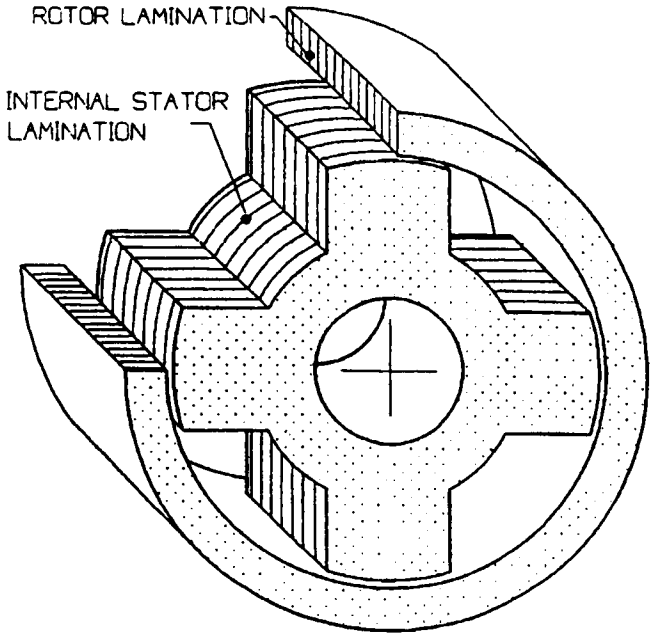

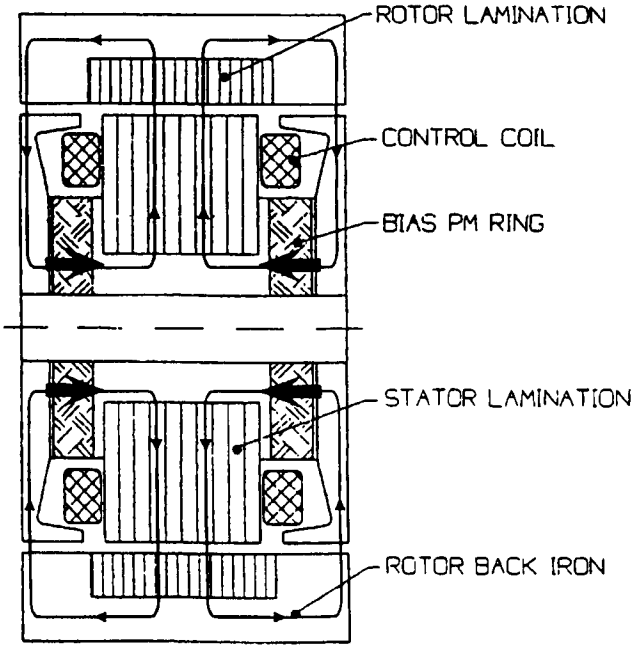

Fig. 1 (a) and (b)

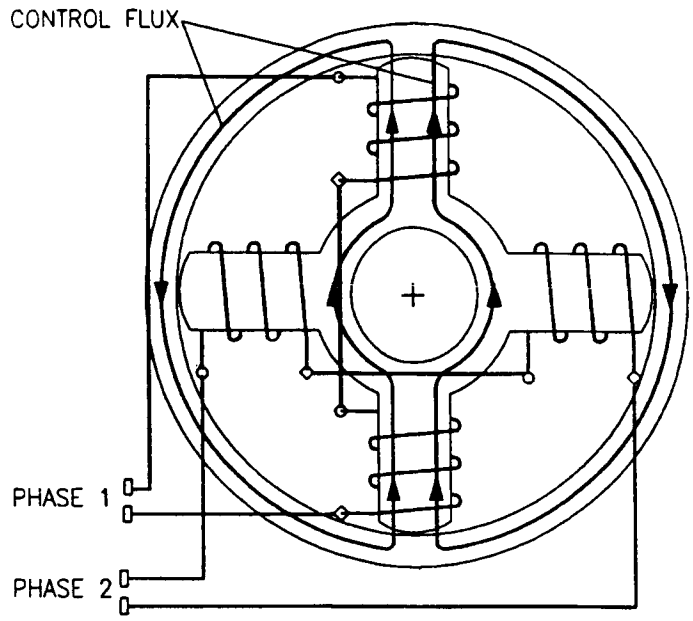

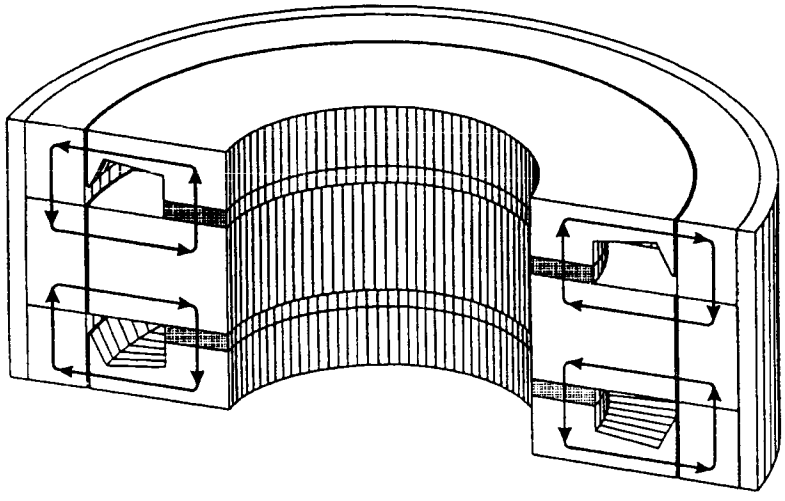

Fig. 1 (c) and (d)

Fig. 1. Permanent magnet biased radial magnetic bearing with external rotor: (a) simplified general layout, (b) longitudinal section showing bias flux path, (c) cross-section showing control flux path for the case when phase 1 carries control current, (d) 3-d view showing bias flux path

Novel homopolar magnetic bearing concepts were described and patented by Malsky [1] and Meeks [2]. These concepts employ a homopolar flux to bias the stator poles to the same polarity, e.g. all are 'north' poles. Control windings direct the flux at opposite poles to one side of the stator or the other to produce a control force in the axis of the poles. Fig. 1 shows the configuration of the homopolar bearing with four poles, described in the patent [1]. The rotor lamination is subjected to a time varying magnetic flux as it rotates through the spatially varying time-invariant bias flux. The perceived advantage of the homopolar bearing is that the bias flux is of one polarity, hence the variation in the rotor flux will be reduced, and the rotor losses should be reduced relative to a heteropolar magnetic bearing.

To design 3-D finite element (FE) model which fully reflects a complex 3-D distribution of both bias and control magnetic fluxes, as well as to perform magnetic field analysis is a very time consuming task. For the designer of a magnetic bearing the most interesting parameter is the magnetic force acting on the rotor. Since this force is created mostly in the air gap between the stator and rotor, the FE model can be reduced to two dimensions. To account for the bias magnetic flux, which is generated by permanent magnets located in the "third dimension", specific boundary conditions are required.

THE METHOD

The relationship between the magnetic flux density **B** and magnetic vector potential **A** is given by:

$$\mathbf{B} = curl\,\mathbf{A} \tag{1}$$

For polar coordinates eq. (1) translates into:

$$B_r = \frac{1}{r}\frac{\partial A}{\partial \theta}\,; \qquad B_\theta = -\frac{\partial A}{\partial r} \tag{2}$$

Magnetic flux lines generated by the permanent magnet (bias flux) enter the rotor of the magnetic bearing (arc AB) perpendicularly. This can be expressed by:

$$\frac{\partial A}{\partial r} = \frac{\partial A}{\partial n} = 0 \tag{3}$$

Therefore, the natural Neumann boundary condition applies on this boundary (arc AB). The same applies to the inner arc CD, through which the bias magnetic flux leaves the stator.

The magnetic flux per unit length in z-direction Φ_{AB} is given by:

$$\Phi_{AB} = \int_A^B B_{AB}(\theta)\; r_{AB}\; d\theta \tag{4}$$

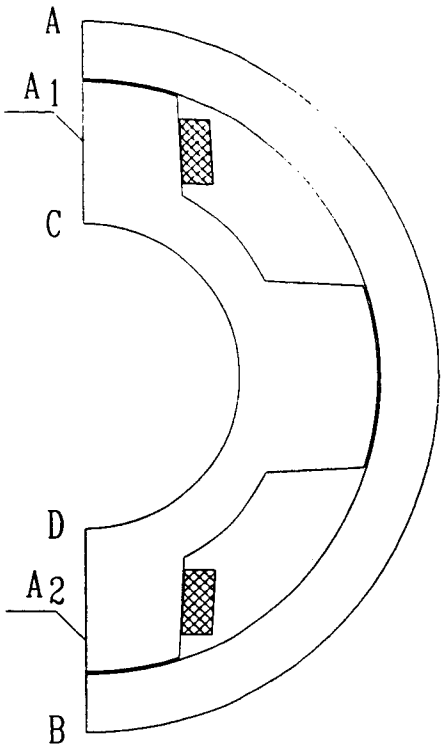

Fig. 2. Finite element 2 D model of biased radial magnetic bearing

Since, according to eq. (2) and eq.(3), the azimuthal component of the magnetic flux density $B_\theta = 0$,

$$\Phi_{AB} = \int_A^B \left(\frac{1}{r_{AB}} \frac{\partial A}{\partial \theta}\right) r_{AB}\, d\theta = A_B - A_A \tag{5}$$

The magnetic flux density along the arc AB (per unit length in z-direction):

$$B = B_r = \frac{\Phi_{AB}}{\pi\, r_{AB}} = \frac{A_B - A_A}{\pi\, r_{AB}} \tag{6}$$

Since the magnetic bearing is symmetrical with respect to the lines AC and DB (or with respect to the planes associated with these two lines, if the depth of the bearing (z-dimension) is taken into account) the magnetic vector potential A is constant along both line AC and DB and equals A_1 and A_2 respectively. This means the Dirichlet boundary conditions apply to these two boundaries.

Concluding, the magnetic flux and magnetic flux density are proportional to the difference between A_1 and A_2 and are given by:

$$\Phi_{AB} = A_2 - A_1 \tag{7}$$

$$B_r = \frac{1}{\pi r_{AB}} (A_2 - A_1) \tag{8}$$

Assuming: $A_1 = -A_2 = A$

$$A = 0.5\, \Phi_{AB} \tag{9}$$

or

$$A = 0.5\, \pi\, r_{AB}\, B \tag{10}$$

Eq. (9) and eq. (10) do not take into account nonlinearity of ferromagnetic materials and usually complex geometry of a magnetic bearing. For those reasons values calculated using the above equations should be further adjusted until the required value, e.g. of flux density in the air gap, is reached.

In other words the 2-D FE modelling procedure appears as follows. A 2-D FE model of the bearing, as shown in Fig. 2, is built. The bias flux, produced by two ring permanent magnets which lay beyond the plane of the FE model, is enforced by setting the difference between A_2 and A_1 to the value obtained from eq. (10), using the required value of the flux density B in the air gap between the stator and rotor. The solution process is then started. The value of the magnetic flux density in the air gap, obtained from this solution, is compared with the value required. Any discrepancy is reduced by correcting the difference between A_2 and A_1 and solving the FE problem again. This cycle is repeated until the required value of the magnetic flux density is reached. Usually a couple of such iterations suffices. The 2-D FE model is now ready for force calculations.

RESULTS

The method introduced in the paper was applied to force calculation of a high speed (35 000 rpm) radial, homopolar magnetic bearing with a permanent magnet bias, designed for a flywheel energy storage system [3]. Both 2-D and 3-D FE models of the bearing were built and the results of force calculations with the help of these models were verified experimentally.

Calculated Results and Experimental Verification

Force acting on the rotor was calculated using both 3-D and 2-D finite element models of the magnetic bearing. In both cases the virtual work method of force calculation, based on the magnetic field solution, was used [4, 5]. The values obtained from the FE analysis were compared with the force measured on the prototype bearing. As can seen from Table 1, the agreement between calculated and measured values is very good (4 %).

Table 1. Comparison of calculated and measured force acting on the rotor; control winding current 10 A.

Force [N]		
Calculated		Measured
2-D FE model	3-D FE model	-
512	523	534

CONCLUSIONS

The method of magnetic bearing force calculation, presented in the paper, replaces time and resources consuming 3-D finite element modelling with a much faster and cheaper 2-D FE modelling. Despite its simplicity, the method offers very good accuracy.

The method was also successfully applied to the calculation of magnetic bearing stiffness and other constants.

REFERENCES

1. Malsky; "High-Speed, Low-Loss Antifriction Bearing Assembly", US Patent No. 5,179,308; 1993.

2. Meeks C.R.: "Magnetic Bearing Structure", US Patent No. 5,111,102; 1992.

3. Piech Z., Hippner M., Colby S.R.: "Low Loss Active Radial Magnetic Bearing", Fifth International Symposium on Magnetic Bearings, Kanazawa, Japan, August 1996, pp. 301-306

4. Coulomb J.L.: "A Methodology for the Determination of Global Electromechanical Quantities from a Finite Element Analysis and its Application to the Evaluation of Magnetic Forces, Torques and Stiffness", IEEE Trans. on Magn., vol. 19, no. 6, November 1983

5. Lowther D.A., Silvester P.P.: "Computer Aided Design in Magnetics". Springer-Verlag, 1986

REPORT DOCUMENTATION PAGE

Form Approved
OMB No. 07704-0188

1. AGENCY USE ONLY *(Leave blank)*	2. REPORT DATE	3. REPORT TYPE AND DATES COVERED
	May 1998	Conference Publication

4. TITLE AND SUBTITLE
Fourth International Symposium on Magnetic Suspension Technology

5. FUNDING NUMBERS
WU 522-24-21-04

6. AUTHOR(S)
Nelson J. Groom and Colin P. Britcher, Editors

7. PERFORMING ORGANIZATION NAME(S) AND ADDRESS(ES)
NASA Langley Research Center
Hampton, VA 23681-2199

8. PERFORMING ORGANIZATION REPORT NUMBER
L-17735

9. SPONSORING/MONITORING AGENCY NAME(S) AND ADDRESS(ES)
National Aeronautics and Space Administration
Washington, DC 20546-0001

10. SPONSORING/MONITORING AGENCY REPORT NUMBER
NASA/CP-1998-207654

11. SUPPLEMENTARY NOTES
Groom: Langley Research Center, Hampton, VA; Britcher: Old Dominion University, Norfolk, VA.

12a. DISTRIBUTION/AVAILABILITY STATEMENT
Unclassified–Unlimited
Subject Category 18 Distribution: Standard
Availability: NASA CASI (301) 621-0390

12b. DISTRIBUTION CODE

13. ABSTRACT ***(Maximum 200 words)***

In order to examine the state of technology of all areas of magnetic suspension and to review recent developments in sensors, controls, superconducting magnet technology, and design/implementation practices, the Fourth International Symposium on Magnetic Suspension Technology was held at The Nagaragawa Convention Center in Gifu, Japan, on October 30–November 1, 1997.

The symposium included 13 sessions in which a total of 35 papers were presented. The technical sessions covered the areas of maglev, controls, high critical temperature (*Tc*) superconductivity, bearings, magnetic suspension and balance systems (MSBS), levitation, modeling, and applications. A list of attendees is included in the document.

14. SUBJECT TERMS	15. NUMBER OF PAGES
Magnetic bearings; Magnetic suspension; Large gap magnetic suspension; Small gap magnetic suspension; Maglev; Sensors; Superconducting magnetic suspension systems; Control systems	445
	16. PRICE CODE A19

17. SECURITY CLASSIFICATION OF REPORT	18. SECURITY CLASSIFICATION OF THIS PAGE	19. SECURITY CLASSIFICATION OF ABSTRACT	20. LIMITATION OF ABSTRACT
Unclassified	Unclassified	Unclassified	